Physics of Atomic Nuclei, Vol. 68, No. 7, 2005, pp. 1079–1086. From Yadernaya Fizika, Vol. 68, No. 7, 2005, pp. 1123–1130.

NUCLEI
Experiment

Alpha-Cluster States in ^{18}O*

V. Z. Goldberg[1),2)], K.-M. Källman[3)], T. Lönnroth[3)], P. Manngård[4)], and B. B. Skorodumov[5)]**

Received August 3, 2004; in final form, October 30, 2004

Abstract—The excitation function of elastic α-particle scattering on ^{14}C has been measured in the laboratory energy range 16.3–19.2 MeV using a backscattering technique with a thick target. These data were analyzed together with the old low-energy data of G.L. Morgan *et al.* in the framework of the R-matrix formalism. Spin–parity assignments were made for 32 states in ^{18}O in the excitation range 9–20 MeV. The estimates of the widths of the states are also presented. The 0^+ and 0^- α-cluster bands appeared to be well separated by 5.6 MeV (as in ^{16}O and ^{20}Ne). We have not found a confirmation of existence of the negative-parity molecular states proposed by M. Gai *et al.* We observed an effect of a doubling of α-cluster levels in ^{18}O similar to that found in ^{22}Ne. © *2005 Pleiades Publishing, Inc.*

1. INTRODUCTION

The α-cluster structures of light $N = Z$ atomic nuclei, ^{8}Be, ^{12}C, ^{16}O, ^{20}Ne, and so on, have been a goal of long-term investigations. However, it was only recently shown (see [1, 2]) that similar α-cluster structures can be observed in the $N > Z$ nucleus ^{22}Ne. These data were obtained in $^{18}\mathrm{O} + \alpha$-particle elastic scattering. These works also claimed the surprising finding of a doubling of the α-cluster states in ^{22}Ne, corresponding to well-known states in ^{20}Ne and ^{16}O. Subsequent theoretical work [3] supported this experimental finding. Evidently, the data on the ^{18}O α-cluster states, which might be obtained in the $^{14}\mathrm{C} + \alpha$ interaction, would be very useful for a better understanding of the phenomenon in question. The available experimental data on the α-cluster structure in ^{18}O are fairly scarce. An interesting piece of experimental evidence for cluster structure of low-lying states in ^{18}O was found in the observation and classification of $E1$ transitions by Gai *et al.* [4]. For the higher members of the band, which should manifest their α-cluster nature by large reduced widths, no quantitative data are available. They made a surprising suggestion that alternative-parity molecular bands in ^{18}O were mixed and were formed by 0^+ (3.63 MeV), 1^- (4.46 MeV), 2^+ (5.26 MeV), 3^- (8.29 MeV), and 4^+ (10.26 MeV). The ^{16}O and ^{20}Ne nuclei do not demonstrate such molecular bands. On the contrary, the $K^\pi = 0^+$ and 0^- states are well separated by several MeV. There is no definite experimental information about the lowest members of the $K = 0^-$ α-cluster band in ^{18}O. The known 1^- levels have small α-particle reduced widths and exhibit nonselective weak $E1$ transitions [4]. Zhao *et al.* [5] observed a broad peak of "unknown origin" in the α-particle spectra of the β-delayed α-particle emission from ^{18}N. This finding was also experimentally consistent with a broad 1^- state around 9.0-MeV excitation energy in ^{18}O. A search for this state in β-delayed neutron decay of ^{18}N was unsuccessful [6]. A single experiment on elastic resonance scattering of α particles on ^{14}C was performed 35 years ago [7]. The authors of that work used a carbon target enriched to 31% in ^{14}C to study the reaction $^{14}\mathrm{C}(\alpha, \alpha)^{14}\mathrm{C}$ over the bombarding energy range 3.5–16.5 MeV. Yield curves at eight angles were measured over the entire energy range. An analysis was attempted only for the data below 8.2 MeV and spin assignments were made for several strong resonances, but only qualitative estimates of the α strength for some sharp strong resonances were given. With the aim to obtain more information on α-cluster states in ^{18}O, we reanalyzed the old data on elastic resonance scattering of α particles on ^{14}C [7] using the figures of that work. These data were analyzed for the excitation region 3.5–8.5 MeV. We have also made new measurements of the excitation functions and angular distributions of the elastic scattering of α particles

*The text was submitted by the authors in English.

[1)]Texas A&M University, College Station, USA.
[2)]Russian Research Centre Kurchatov Institute, pl. Kurchatova 1, Moscow, 123182 Russia.
[3)]Department of Physics, Åbo Akademi, Turku, Finland.
[4)]Swedish Polytechnic, Vasa, Finland.
[5)]Physics Department, University of Notre Dame, Notre Dame, USA.
**e-mail: goldberg@comp.tamu.edu

on a ^{14}C target in the energy region 16.3–19.2 MeV using a novel thick-target method [8].

2. EXPERIMENTAL PROCEDURE AND ANALYSIS

The old data of [7] were obtained in a conventional way using helium ions from a tandem accelerator. Generally, data were taken in intervals of 20 keV, and in the vicinity of some resonances below 8.3-MeV bombarding energy, these steps were reduced to either 5 or 10 keV. The claimed uncertainty in the cross sections is about 25%. We have observed large discrepancies (about a factor of two) in the absolute values, while the shapes were similar, in the calculated and measured excitation functions at a few angles. The reason for these discrepancies could not be cleared up due to absence of feedback with the authors of the experimental work. Taking into account the character of the experimental data, as taken from the graphs, the level assignments should be considered as a "preliminary" result.

The new experimental data in the high-energy region of the $\alpha + {}^{14}$C elastic scattering from 16.3 to 19.2 MeV were obtained at the Åbo Akademi isochronous 103-cm cyclotron. We used our thick-target method [8], which is based on the ideas of backscattering element analysis. The method allows one to measure the desired elastic-scattering energy range in rather large lab-energy steps, thus substantially saving beam time. The measurements of continuous excitation functions were made with four movable detectors set in 13 laboratory angles, at 170° and 160°–124° in steps of 3° and 4°, and using a fixed monitor at −20°. The ^{14}C targets, enriched to 71% in ^{14}C, were thick enough only to degrade the beam energy by 100 keV when tilted by 45° with respect to the beam direction. Absolute values of cross sections were obtained with about 10% precision.

The purpose of the present analysis was to obtain properties of the main structures in the elastic scattering data with as few parameters as possible. The excitation functions shown in Figs. 1 and 2 were analyzed according to the procedure outlined in [9] and successfully used by the Wisconsin group (see [10] and references therein). The scattering amplitude was separated into a nonresonant term plus the sum of resonant partial waves. For spinless particles, the scattering amplitude can be written as

$$f(\theta) = f_{\mathrm{C}}(\theta) + \rho(\theta)\exp(i\chi) \qquad (1)$$
$$- \frac{i}{2k}\sum_m (2l_m+1)\frac{\Gamma_{l_m}}{\Gamma}\left[\exp(2i\beta_{l_m}) - 1\right]$$
$$\times \exp\left(2i(\phi_{l_m} + \omega_l)\right) P_{l_m}(\cos\theta),$$

where ρ and χ are the background amplitude and phase shift, β_{l_m} is a resonant phase shift, ϕ_{l_m} is a relative background phase shift, and $f_{\mathrm{C}}(\theta)$ and ω_l are the Coulomb amplitude and phase shift. Then the cross section will be

$$\frac{d\sigma}{d\Omega} = |f(\theta)|^2. \qquad (2)$$

The resonance phase shift is given by

$$\beta_{l_m} = \arctan\left[\frac{\Gamma}{2(E_{\mathrm{res}_m} - E)}\right]. \qquad (3)$$

In order to reduce the number of free parameters, the background amplitude ρ and the background phase shift χ were taken to be zero. The phase shifts ϕ_{l_m} were fixed for each resonance and were not varied with energy and angle.

Some examples of the fits to the angular distributions, which were measured in [7], are given in Fig. 2. As can be seen, there is qualitative agreement between the experimental data and calculations. Table 1 gives the resonance parameters of the fit. It is difficult to confirm that the fits we have obtained are unique. Attention was paid to the stability of the evaluated resonance parameters and to the possibilities of an alternative description. In particular, it was found that the inclusion of different combinations of weak resonances can improve the general agreement, but they do not greatly affect the parameters of the resonances of Table 1.

3. RESULTS

Figures 1 and 2 give examples of the data and their description in terms of Breit–Wigner resonances. The strong high-spin resonances, which were found at high energy, manifest themselves as rapidly oscillating functions versus angle, as $P_l^2(\cos\theta)$ functions. Therefore, besides the R-matrix analysis, several angular distributions corresponding to the maxima in the excitation function were tested. Figure 3 gives examples of ℓ-value determination. The extracted resonance parameters are given in Table 1. In the following, we comment on the different energy regions.

In the analysis, the prominent peaks that could be related to levels with large α-cluster widths were investigated, and only some weak resonances were included to get more confidence in the extracted parameters of the dominant structures. Alternative spin assignments for weak resonances are given in Table 1 in parentheses.

An important uncertainty in the analysis of the low-energy region is the spin determination of the level at $E_{\mathrm{lab}} = 3.6$ MeV, which is assigned a 1^- value. Due to the weak angular dependence of low-order

Table 1. Summary of resonance parameters for structures observed in the $\alpha + {}^{14}$C elastic-scattering excitation function

Level	J^π	$E_{\rm res}$, MeV $\pm$ keV	E_x, MeV	Γ_α, keV	$\Gamma_\alpha/\Gamma_{\rm tot}$	Reference
1	$1^-, (0^+)$	3.600^{+150}_{-30}	9.027	500^{+150}_{-50}	0.80 ± 0.20	This work
2	2^+	3.710 ± 10	9.113	380^{+5}_{-15}	0.12	This work
3	3^-	4.070 ± 20	9.393	200 ± 20	0.79 ± 0.10	This work
	(2^+)		9.33			[11]
4	(1^-)	4.470 ± 20	9.704	180 ± 30	0.40 ± 0.10	This work
	(2^-)		9.65			[12]
5	3^-	4.480 ± 15	9.711	75 ± 10	0.27 ± 0.05	This work
6	3^-	4.560 ± 20	9.774	300 ± 30	0.90 ± 0.10	This work
7	$0^+, (2^+)$	4.650 ± 30	9.844	400 ± 50	$1.0_{-0.2}$	This work
8	(1^-)	4.780	9.945	300	0.30	This work
9	3^-	4.980 ± 10	10.100	45 ± 8	0.35 ± 0.07	This work
	3^-	4.97	10.10	Large		[7]
10	4^+	5.220 ± 10	10.287	30 ± 7	0.90 ± 0.10	This work
	4^+	5.23	10.29	Large		[7]
	4^+		10.30			[11]
11	3^-	5.320 ± 10	10.365	45 ± 8	0.30 ± 0.06	This work
	3^-	5.34	10.38	Large		[7]
12	2^+	5.400 ± 150	10.427	500 ± 150	0.40 ± 0.10	This work
13	1^-	5.450 ± 100	10.466	800^{+200}_{-100}	$1.0_{-0.2}$	This work
14	3^-	5.840 ± 30	10.769	180 ± 40	0.45 ± 0.15	This work
15	(0^+)	5.940	10.847	250	0.80	This work
16	(3^-)	6.300	11.127	600	0.80	This work
17	4^+	6.670 ± 5	11.415	45	0.90 ± 0.10	This work
	4^+	6.67	11.42	Large		[7]
18	5^-	6.920 ± 10	11.609	60 ± 5	0.90 ± 0.10	This work
	5^-	6.93	11.62	Large		[7]
	$5^-, 6^+$		11.59			[11]
	$5^-, 6^+$		11.60			[12]
19	6^+	7.030 ± 10	11.695	35 ± 5	$1.0_{-0.1}$	This work
	6^+	7.03	11.69	Large		[7]
20	5^-	7.830 ± 10	12.317	80 ± 10	$1.0_{-0.1}$	This work
	5^-	7.85	12.33	Large		[7]
21	6^+	8.100 ± 10	12.527	32 ± 5	$1.0_{-0.1}$	This work
	6^+	8.10	12.53	Large		[7]
	5^-		12.60			[12]
22	7^-	15.700	18.438	60	0.13	This work
23	7^-	16.050 ± 30	18.710	320	0.63	This work
	5^-		18.95	350		[12]
24	7^-	16.660 ± 40	19.185	145	0.34	This work
25	7^-	17.010 ± 30	19.456	113	0.46	This work
26	7^-	17.260 ± 40	19.651	52	0.24	This work
27	5^-	17.550 ± 50	19.876	21	0.12	This work
28	7^-	17.600	19.916	43	0.06	This work
29	8^+	18.000	20.227	326	0.35	This work
30	6^+	18.450	20.577	36	0.24	This work
31	6^+	18.800	20.849	170	0.30	This work
32	6^+	19.300	21.238	67	0.25	This work

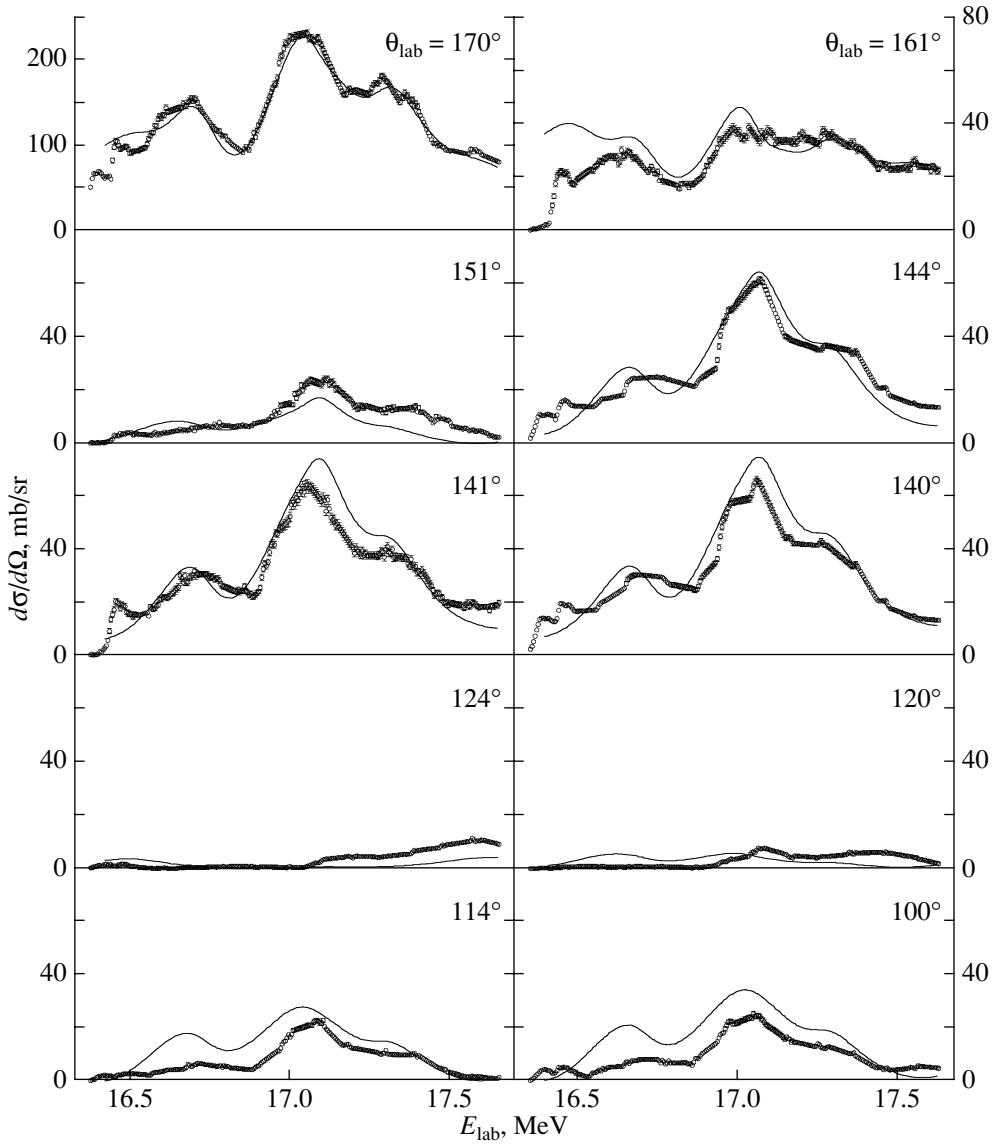

Fig. 1. Experimental data and the fits for the high-energy region of the $\alpha+^{14}$C elastic scattering from 16.3 to 17.7 MeV.

polynomials and the absence of measured excitation functions at angles smaller than 90°, it was not possible to exclude the 0^+ value for that level. In addition, there are local deviations in absolute cross sections in some regions between fits and the experimental data. This disagreement could be partly attributed to the contribution of the resonances outside the energy region investigated.

Fairly broad 1^- and 2^+ resonances were found in the energy region above $E_\alpha = 5$ MeV. The shape of these resonances could not be fitted with a zero-phase Breit–Wigner expression. For this reason, one should include a phase dependence for these resonances. In fact, we observed that a 1% change in the phase improved the fit. We leave these corrections to future analysis, which also should take into account the background, and in the framework of the present approach, we give large uncertainties in the positions of the broad levels and in their widths.

In the intermediate-energy region, between 6.2 and 8.5 MeV, in the previous work [7], the spins were identified by the qualitative behavior of the excitation functions, and for the 4^+ level at 6.67 MeV, only a tentative assignment was made. We have fitted the regions around the peak at all the measured angles and extracted the parameters for the levels in the vicinity of maxima in the angular distributions. The spin assignments thus obtained are in fair agreement with the earlier analysis [7]. Also, it can be seen in Table 1 that the present results agree with data obtained by other methods.

The analysis in the region covered by the present

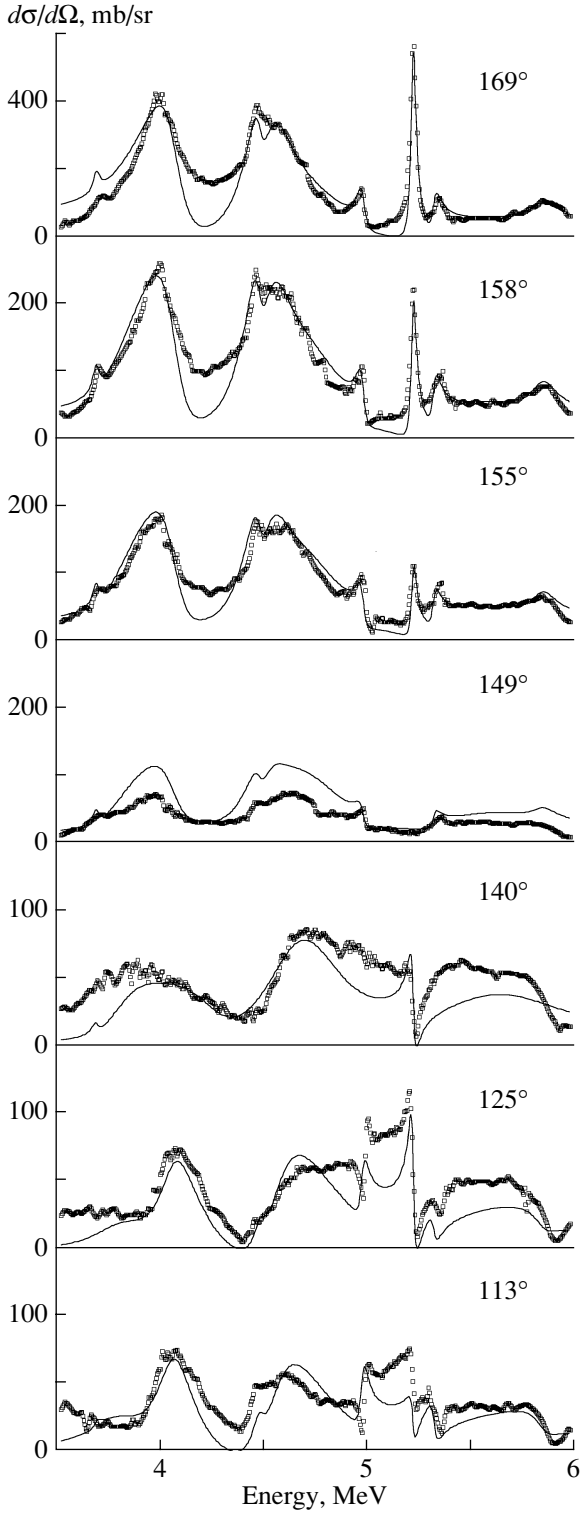

Fig. 2. Low-energy $\alpha + {}^{14}$C elastic scattering adopted from the graphs in [7] and the fits.

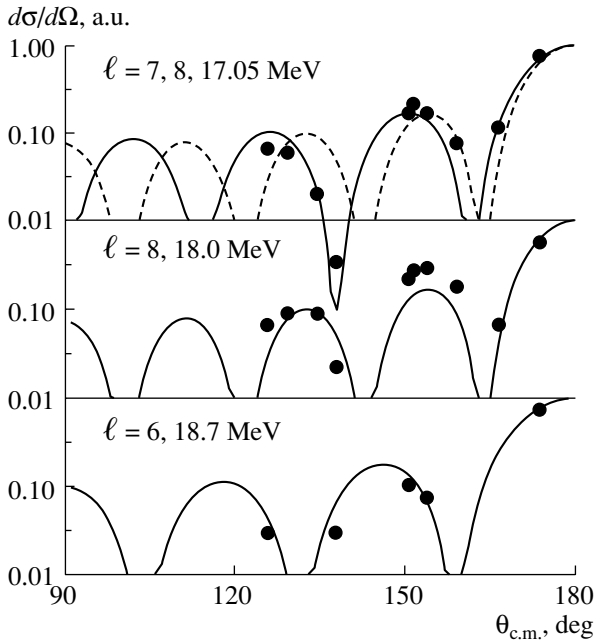

Fig. 3. Illustration to ℓ-value determination for some high-lying resonances. It is clearly seen (top panel) that $\ell = 7$ (solid curve) fits the data very well, whereas $\ell = 8$ (dashed curve) does not. The middle and bottom panels correspond to $\ell = 8$ and 6, respectively.

measurements, $E_\alpha = 16.3$–19.2 MeV, suffers from the absence of data outside both borders. Strong resonances outside the region can influence the calculated excitation functions. The region is dominated by 7^- resonances. This is evident if the measured angular distributions are compared with a squared Legendre polynomial of order 7. The deep minima at 90° definitely exclude the nearest 6^+ or 8^+ assignments. Due to rather broad structures in comparison with the c.m.-energy interval of about 2.3 MeV, it was necessary to include some strong resonances outside of this region. For those, only tentative parameters were found. Tentative parameters were also used for some weak resonances that were evident only at the minima of the 7^- levels. These resonances were included to obtain more reliable assignments of the parameters of the main 7^- states.

4. DISCUSSION

It is evident that α clusterization is a rather general phenomenon, at least for light nuclei. Also, many α-cluster states have α-particle reduced widths that are close to the Wigner limit. Therefore, it seems natural to use a potential approach to describe the common features of the α-cluster states in atomic nuclei as well as (potential) elastic scattering of α particles. (For the formulation of the goals and earlier activity in this direction, see [13, 14].) Reidemeister and Michel [15] considered the lowest $\alpha + {}^{14}$C molecular bands in ^{18}O using the potential model. The parameters of the model were fixed using elastic scattering

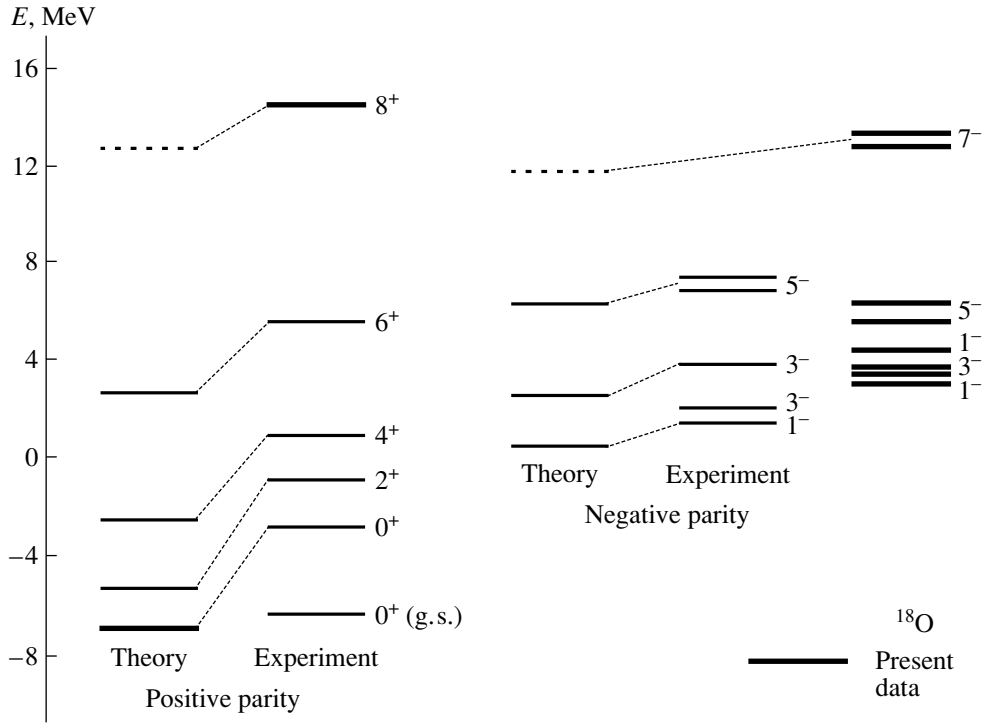

Fig. 4. Potential-model [15] predictions for α-cluster states in ^{18}O.

in the energy region 28–54 MeV and were in general agreement with those ones found [16] for the $\alpha + {}^{12}$C and $\alpha + {}^{16}$O cases. Figure 4 presents results of the calculations of [15] together with experimental results. The previous experimental results [17] include levels up to 6^+ of the positive-parity band, based on the (0^+) excited state at 3.63 MeV, and the states in the second column represent the negative-parity band, which is a tentative compilation from [15]. Our data for the negative-parity cluster band are in the right column. Only the levels with large reduced α-particle widths have been chosen for the comparison. We show a 1^- level at 9.027 MeV as the lowest level of the negative-parity band (however, we could not totally exclude a 0^+ assignment for this level). At 9.0-MeV excitation energy in ^{18}O, a broad structure with $\Gamma \sim 500$ keV, populated in the β decay of the ^{18}N nucleus, was observed [5], and a 0^+ assignment should be excluded due to β-decay selection rules. Simultaneously, the α-cluster structure of this level explains why the search for this level using β-delayed neutron decay of ^{18}N was unsuccessful [6]. (Unfortunately, this level would be a source of serious background in an experiment for parity violation, which is planned by the authors of [5].) We also added calculations, as well as experimental data, for the levels with the highest spins in both bands, the 8^+ and 7^- states. It is seen that there is general agreement between calculations and the data in Fig. 4. The slight global shift in energy observed in Fig. 4 could easily be compensated, as was noted in [15], by a slight decrease in the volume integral of the potential, an effect

Table 2. Comparison of relative excitation energies E^* vs. threshold energies (7.17 and 6.23 MeV, respectively) and reduced widths in ^{16}O (left) and ^{18}O (right)

J^π	$E_{\rm res}$, MeV	Γ_α, MeV	J^π	$E_{\rm res}$, MeV	Γ_α, MeV
1^-	2.41	1.33	1^-	2.80	0.44
4^+	3.19	1.54	3^-	3.15	1.02
3^-	4.43	1.31	3^-	3.52	0.97
5^-	7.49	1.32	4^+	4.06	0.23
6^+	9.11	1.35	1^-	4.24	0.25
7^-	13.69	0.78	4^+	5.19	0.09
			5^-	5.38	0.51
			6^+	5.46	2.48
			5^-	6.09	0.36
			6^+	6.30	0.78
			7^-	12.48	0.39
			7^-	12.99	0.11
			7^-	13.25	0.35
			7^-	13.45	0.05
			7^-	13.86	0.12

expected from both antisymmetrization and dispersion relation effects. Before, this agreement seemed questionable, because the available negative-parity levels were too narrow to be considered as α-cluster states [15]. The present data with reduced widths of ~ 0.5 of the single-particle limit (see below) make the agreement much more reliable, although both the analysis and the experimental data around 9-MeV excitation energy deserve a more careful examination. Detailed theoretical results were presented in the article of Descouvemont and Baye [18]. They used antisymmetric $\alpha + {}^{14}\mathrm{C}_{\mathrm{g.s.}}$ and $\alpha + {}^{14}\mathrm{C}(2_1^+)$ wave functions in generator coordinate formalism to investigate molecular bands in ^{18}O. These calculations give well-separated (by about by 6 MeV) 0^+ and 0^- α-cluster bands, as predicted in earlier studies (see, for instance, [19]). Several detailed predictions of [18] agree remarkably with our findings. They predicted the band head of the 0^- molecular band, a broad 1^- state at 9.6-MeV excitation energy, and a very small splitting between 1^- and 3^- states of the band. As can be seen in Fig. 4, we found 1^- cluster states at 9-MeV energy and two 3^- states were positioned between the 1^- states. Also, the prediction for the 8^+ state of the 0^+ band, at 17.7 MeV, appeared to be very close to the observed level at 18 MeV. Table 2 gives a compilation of well-known α-cluster levels in ^{16}O with these ones found in ^{18}O. The reduced widths of ^{18}O are given relative to the widths of the corresponding levels in ^{16}O. To obtain an estimate of the absolute values of the reduced widths, we have calculated the single-particle widths in the Woods–Saxon potential, which generates a spectrum of α-cluster levels similar to that found in ^{18}O [2]. The potential parameters used are $V = -300$ MeV, $r_0 = 1.1$ fm, and $a = 0.7$ fm. As an example, the absolute reduced width of the 6^+ level is 0.33 of the single-particle (or α) width, which is given by the potential. One can conclude from the data in Table 2 that the general features of levels in ^{16}O and ^{18}O have much in common. Therefore, one can conclude that there is strong theoretical and experimental evidence for the main negative-parity cluster band in ^{18}O to be well separated from the positive-parity band, starting with a (0^+) state at 3.63 MeV. In this sense, the situation is very similar to the ^{16}O or ^{20}Ne cases and differs from the ideas [4] on the existence of the negative-parity α-cluster band in question at a much lower excitation energy. (It is worthwhile to note that no fully microscopic calculation of the resonating group method or the generator coordinate method has succeeded to support the existence of this "mixed" parity band. The only exception is a semimicroscopic orthogonality-condition model calculation [20], which was specially designed to reproduce these features. Obviously, this study does not bring conclusive information about the very existence of the band.) Although there exist quantitative differences in the results of the calculations, they all predict the existence of molecular bands that are decoupled in parity. However, no former calculations predicted a doubling of α-cluster states for $N = Z + 2$ nuclei, ^{18}O or ^{22}Ne, which was observed in [1, 2]. Rogachev *et al.* [1] put forth speculations of an exotic nuclear analog to the Josephson effect to explain the doubling. Recently [3], the effect of the doubling of the negative-parity $\alpha +$ cluster states in ^{22}Ne was interpreted as a strong mixing of $\alpha + {}^{18}\mathrm{O}^*$ configurations. The present work presents new evidence for the doubling of the states in ^{18}O (see Fig. 4). Indeed, there are only two close 5^- resonances, both with large α widths (see also Table 1), and two 3^- resonances included in Fig. 4 have reduced widths five times larger than the others. Therefore, one can conclude that the doubling in question is a more general feature of the α clusterization than it would seem after observation of the effect in ^{22}Ne. It is interesting whether the explanation [3], based on the considerations of the specific nuclear configurations in ^{22}Ne, could be applied to a new case of ^{18}O.

5. CONCLUSION

The present work has demonstrated a rich α-cluster structure in the ^{18}O nucleus. In particular, we have found new experimental evidence for positive- and negative-parity α-cluster bands in ^{18}O. Their global characteristics, including an upward energy shift of the negative-parity band, are in accordance with most theoretical predictions and are similar to those in the ^{16}O and ^{20}Ne nuclei. Thus, the additional two neutrons do not affect the global α-cluster structure; however, we have observed the doubling of the cluster levels in ^{18}O, which seems analogous to the findings in ^{22}Ne. As it seems, some common explanation should be found for this phenomena. We have analyzed only part of the available old data. We believe that it will be more reliable and more rewarding to make new measurements and to use the old data mainly as an additional reference. We hope this work will stimulate new efforts to obtain more detailed experimental data and a better analysis. The energy region near the α-particle threshold in ^{18}O is of special interest.

ACKNOWLEDGMENTS

The Russian authors are grateful for financial support from the Academy of Finland, during 2004 under decision 207797. The authors are also indebted to the Department of Energy for grant no. DE-FC03-93ER40773.

REFERENCES

1. G. V. Rogachev, V. Z. Goldberg, T. Lönnroth, *et al.*, Phys. Rev. C **64**, 051302R (2001).
2. V. Z. Goldberg, G. V. Rogachev, W. H. Trzaska, *et al.*, Phys. Rev. C **69**, 024602 (2004).
3. M. Dufour and P. Descouvemont, Nucl. Phys. A **726**, 53 (2003).
4. M. Gai, M. Ruscev, D. A. Bromley, and J. W. Olness, Phys. Rev. C **43**, 2127 (1991).
5. Z. Zhao, M. Gai, B. J. Lund, *et al.*, Phys. Rev. C **39**, 1985 (1989).
6. K. W. Scheller, J. Görres, J. G. Ross, *et al.*, Phys. Rev. C **49**, 46 (1994).
7. G. L. Morgan, D. R. Tilley, G. E. Mitchell, *et al.*, Phys. Lett. B **32**, 353 (1970); Nucl. Phys. A **148**, 480 (1970).
8. K.-M. Källman, V. Z. Goldberg, T. Lönnroth, *et al.*, Nucl. Instrum. Methods Phys. Res. A **338**, 413 (1994).
9. S. R. Riedhauser, Phys. Rev. C **29**, 1961 (1984).
10. C. A. Davis and R. Abegg, Nucl. Phys. A **571**, 265 (1994).
11. W. D. M. Rae and R. K. Bhowmik, Nucl. Phys. A **427**, 142 (1984).
12. K. P. Artemov, V. Z. Goldberg, M. S. Golovkov, *et al.*, Yad. Fiz. **37**, 1351 (1983) [Sov. J. Nucl. Phys. **37**, 805 (1983)].
13. V. Z. Goldberg, V. P. Rudakov, and V. A. Timofeev, Yad. Fiz. **19**, 503 (1974) [Sov. J. Nucl. Phys. **19**, 253 (1974)].
14. V. Z. Goldberg, K. A. Gridnev, and V. M. Semenov, Bull. Acad. Sci. USSR, Phys. Ser. **52**, 38 (1974).
15. G. Reidemeister and F. Michel, Phys. Rev. C **47**, 1846 (1993).
16. F. Michel *et al.*, Phys. Rev. C **28**, 1904 (1983).
17. D. R. Tilley, H. R. Weller, C. M. Cheves, and R. M. Chasteller, Nucl. Phys. A **595**, 1 (1995).
18. P. Descouvemont and D. Baye, Phys. Rev. C **31**, 2274 (1985).
19. H. Horiuchi, Prog. Theor. Phys. Suppl. **62**, 90 (1977).
20. H. J. Assenbaum, K. Langanke, and A. Weiguny, Z. Phys. A **318**, 35 (1984).

Physics of Atomic Nuclei, Vol. 68, No. 7, 2005, pp. 1087–1095. Translated from Yadernaya Fizika, Vol. 68, No. 7, 2005, pp. 1131–1140.

NUCLEI
Experiment

$J^\pi = 0^-$ Levels in ^{156}Gd and ^{158}Gd

E. P. Grigoriev*

St. Petersburg State University, St. Petersburg, Russia

Received January 13, 2004; in final form, July 7, 2004

Abstract—The 0^- states in the ^{156}Gd nucleus at $E = 1952.38$ keV and in the ^{158}Gd nucleus at $E = 2269.16$ keV are established on the basis of an analysis of available data on even–even deformed nuclei. From data on the deexcitation of the levels and on the probability of their population by beta transitions, it is found that these states have a two-particle proton structure. A comparison of our data with information about the 0^- levels in the ^{170}Yb and ^{176}Hf nuclei makes it possible to conclude that $K^\pi = 0^-$ two-particle states exist at an excitation energy of about 2 MeV and higher. © *2005 Pleiades Publishing, Inc.*

1. INTRODUCTION

In the rare-earth region, only a few excited levels of spin–parity $J^\pi = 0^-$ have been discovered in deformed even–even nuclei. Their number is much smaller than the numbers of levels characterized by the spin–parities of 0^+, 1^+, 1^-, etc. This is not an accidental fact. The first and foremost reason for this is associated with a theoretical treatment of 0^- states. The simplest shell model assumes that two-particle proton or neutron states of even–even nuclei are formed via the rupture of a pair in the ground state with the transition of one of the nucleons to a higher lying level. As a result, there arises a doublet of states such that $\Omega = \Omega_1 + \Omega_2$ or $\Omega = \Omega_1 - \Omega_2$ in it, where Ω_i is the projection of the total angular momentum of the respective nucleon onto the symmetry axis. The energy of excited states is obtained by adding, to the pair energy of $E \approx 1.5$ MeV, the difference of the single-particle energies of the nucleons being considered. There can arise the rupture of a pair at the Fermi surface, in which case a particle–particle level is formed, or the rupture of a pair occurring below the Fermi surface, in which case the emerging excited state is of a particle–hole character. The positions of the levels in a doublet is determined by the Galagher–Moshkovsky law. A systematics shows that the respective splitting is 100 to 200 keV.

Upon taking into account, in the Hamiltonian, collective motion in a nucleus, there arises the collectivization of $K^\pi = 0^-$ states. Because of the symmetry properties of the wave functions, states of even angular momenta, including $J^\pi = 0^-$ states, disappear in the corresponding rotational bands. In experiments, one observes bands that contain 1^-, 3^-, 5^-, etc., levels, but which do not contain states of even angular momenta, including $J^\pi = 0^-$ states. These states are collective, and they are of special interest from the point of view of their interpretation. In discovering them, one clarifies the position of the boundary below which there occurs the collectivization of octupole-type levels. States of spin–parity 0^- are observed at an excitation energy of about 2 MeV and higher.

It should be borne in mind that there exist experimental difficulties that hinder the discovery of 0^- levels. Their decay to the ground state of even–even nuclei may occur only via second-order effects—for example, through a "nuclear–electron bridge" involving the emission of an electron (but not of a photon). Only an $M2$ transition, whose relative intensity is usually modest, can proceed to the first 2^+ level. The deexcitation spectrum is dominated by $M1$ transitions 1^- levels and $E2$ transitions to 2^- levels. Also possible are $E1$ transitions to 1^+ levels, which usually lie higher than levels of octupole bands. Levels of spin–parity 0^- were observed in the beta decay of parent nuclei, but they were not observed in nucleon-transfer reactions or in $(n, n'\gamma)$ reactions.

2. 0^- LEVEL AT 1952.38(1) keV IN ^{156}Gd

2.1. Identification of the 0^- Level

The 0^- level at 1952.41 keV was preliminarily identified in [1, 2] on the basis of data on ^{156}Eu decay with allowance for the results obtained by studying (n, γ) reactions with filtered neutrons. This identification was accepted in the review article of Reich [3], and the energy of the level was refined there to be 1952.385(7) keV by invoking data on the relevant (n, γ) reaction with thermal neutrons [4]. In previous studies included in the review article of Helmer [5], the level in question was established, but it was assigned

*e-mail: epgrig@nuclpc1.phys.spbu.ru

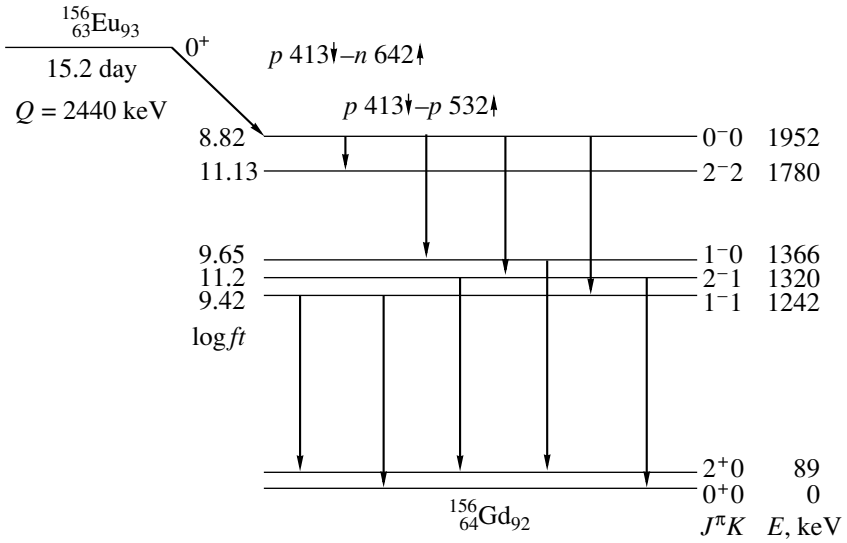

Fig. 1. Fragment of the diagram of ^{156}Eu decay: population and depopulation of the $J^\pi = 0^-, 1^-$, and 2^- levels.

a spin–parity of $J^\pi = 1^-$. Figure 1 shows a fragment of the diagram of ^{156}Gd levels.

The quantum numbers 0^- found experimentally were confirmed on the basis of an analysis of the intensities of primary $M1$ gamma transitions arising upon the capture of 1.9- and 58-keV neutrons [6, 7].

For case of 1.9-keV neutrons, whose scattering is dominated by the s wave, the value of $I_\gamma = 8.9(5)$ arb. units was obtained for the relative intensity of primary gamma transitions. For the same normalization, the value of $I_\gamma = 14$ arb. units is expected according to the statistical model if $J^\pi = 1^-$ or 2^-; but if $J^\pi = 0^-$ or 3^-, the predicted value is $I_\gamma = 7$ arb. units. The prediction of the statistical model at $J^\pi = 0^-$ is in agreement with experimental data. It should be noted that 3^- levels are not populated in the decays of the ^{156}Eu nucleus, whose ground state has the spin–parity of $J^\pi = 0^+$.

In experiments with neutrons of energy $E_n = 58$ keV, the fraction of the p wave is 40%, and the statistical model predicts $I_\gamma = 22$ arb. units for 0^- levels, 60 arb. units for 1^- and 2^- levels, 38 arb. units for 3^- levels, and 15 arb. units for 4^- levels. In ^{156}Gd, there is a 1952.36-keV level of known spin–parity 4^- near the level at 1952.38 keV under study. Subtracting $I_\gamma = 15$ arb. units, which is the fraction of population of the 4^- level, from $I_\gamma = 44(9)$ arb. units, which is the total intensity of population of the two levels in question, we find that the level being considered is populated with an intensity of 29(9) arb. units, which also favors the $J^\pi = 0^-$ assignment for this level. A complete table of experimental data from experiments with filtered neutrons can be found in [6].

The 0^- state is deexcited only via $M1$ and $E2$ transitions to negative-parity levels (see Table 1). A systematics indicates that 1^- levels are deexcited by strong $E1$ transitions to the ground and the first excited state; at the same time, no such transitions were observed from the level at 1952.38 keV. This circumstance alone gives sufficient grounds to prefer the $J^\pi = 0^-$ to the 1^- assignment. The gamma transition to the ground state from the 0^- level is impossible; only the 1872.87-keV $M2$ transition is expected to proceed to the first 2^+ level, but this transition has not yet been observed.

On the basis of data on the levels of ^{156}Gd and on the spectrum of gamma transitions in the relevant (n, γ) reaction, the diagram of the deexcitation of the level in question was supplemented with a 171.870-keV transition, which was included in Table 1. The inclusion of this transition in the set of transitions that depopulate the 0^- level was motivated by ambiguities in determining its position in the level diagram. According to data refined in [3, 4], two levels have very close energies: the 0^- level at 1952.385(7) and the 4^- level at 1952.364(9) keV. From each of these, there can proceed a 171.870(11)-keV transition or one of the components if this is a doublet of levels. The transition intensity indicated in Table 1 must be considered as an upper limit, and this circumstance is taken into account in Table 2.

2.2. Quantum Numbers of the Level

Information about the asymptotic quantum numbers of a 0^- level can be deduced from the results of the calculations based on the quasiparticle vibrational model [8]. The 0^- neutron level characterized

Table 1. Deexcitation of the 0^- level at 1952.38 keV in ^{156}Gd

$J^\pi K_f$	E_f, keV	^{156}Eu			(n,γ)		
		E_γ, keV	I_γ, arb. units	σL	E_γ, keV	I_γ, arb.units	σL
1^-1	1242.480(7)	709.86(5)	9.03	$M1$	709.942(9)	26	$M1$
2^-1	1319.658(2)	632.79(8)	0.40	$E2$	632.719(9)	<3.0	$E2$
1^-0	1366.462(4)	585.90(4)	0.54	$M1$	585.830(15)	1.6	$M1\,(+E2)$
2^-2	1780.486(9)	–	–		171.870(11)	<0.18	$E2$

Note: Here and in Tables 2, 4, and 5, $J^\pi K_f$ are the quantum numbers of the final state, while E_f is its energy.

by the asymptotic quantum numbers $Nn_z\Lambda$ $n651\uparrow - n521\uparrow$ of two unpaired neutrons is expected at an energy of 2.0 MeV, while the 0^-, $n402\downarrow - n521\uparrow$ level is expected at 2.3 MeV; as to the 0^- proton level of quantum numbers $p532\uparrow - p413\downarrow$, it is expected at an energy of 2.4 MeV. This seems to give grounds to prefer the first two-neutron version, although the error of the calculations is estimated at 0.2 MeV. In order to establish the structure of the levels, one can employ the Galagher–Moshkovsky law. The 3^-, $n651\uparrow + n521\uparrow$ state is expected to be the upper one in the doublet of levels in the two-neutron version. The possible candidates have energies of 1936, 2011, and 2024 keV. It is difficult to indicate that which is a partner of the 0^- level. Considering $E1$ transitions from the level at 1934 keV, we can assume that its quantum number satisfies the condition $K < 2$ and that it is not a member of the doublet being studied. Under the assumption that the 0^- level has a proton structure, its 5^- partner must have a lower energy. No such level has been observed so far.

An analysis of the beta decay of ^{156}Eu, 0^+ leads to important conclusions. In accordance with the Nilsson diagram of levels, the structure of the ^{156}Eu ground state has the form $p413\downarrow - n642\uparrow$. The beta transition to the 0^- level at 1952.385 keV is impossible if we assume that this level has the neutron structure considered above—this would be a two-particle transition changing the states of two nucleons. In the case of a proton structure, there occurs the $n642\uparrow \to p532\uparrow$ transformation. Here, one deals with a nonhindered first-order-forbidden beta transition $1u$. The experimental value of $\log ft = 8.82$ is somewhat higher than what is obtained from a systematics of such transitions. This result can be explained by the fact that the final state is already occupied by a nucleon pair—that is, by the effect of Pauli blocking. From Fig. 2, one can see that the state that is populated is below the Fermi surface.

In [8], there is information about levels excited in the relevant neutron-transfer reaction (d, p). Among these, there is no state at 1952 keV, and this may be indicative of its two-proton character, but numerical estimates are required here for drawing a correct conclusion.

2.3. Deexcitation of the 0^- Level

It is of interest to establish or to estimate the partial half-lives with respect to gamma transitions deexciting the 0^- level and the respective hindrance factors. The investigation of the ^{170}Yb nucleus in [9] provides an example of such an analysis. In this nucleus, the deexcitation of the 0^- level at 2819.6 keV proceeds via 16 gamma transitions. It was shown that the $M2$ $0^- \to 2^+$ transition is hindered by a factor of 200 and that the hindrance factors for $M1$ transitions proceeding to low-lying octupole states lie in the range 10^3–10^4. The transition to the head of the $K^\pi = 2^-$, $J^\pi = 2^-$ band at 1717.85 keV was taken for a reference one. Adopting the same hypothesis for the ^{156}Gd nucleus—that is, assuming that the 171.87-keV $E2$ transition proceeding to the 2^- level at 1780.486 keV has a single-particle partial half-life, $T^0 = T_{\rm sp}$—we find that the resulting hindrance factors of $F_{\rm h} = 30$ and 10^3 to 10^4 for, respectively, the competing $E2$ transition to the 2^-2 level and the $M1$ transition from the same 0^- level (Table 2) are close to the expected values. These results should be treated as the respective lower limits.

The calculations were performed in the following way. Taking, for the 171.87-keV transition, $T^0 = 7 \times 10^{-8}$ s for a reference value, we calculate the "experimental" partial half-lives $T_i = T^0 I_0/I_i$. For ^{156}Gd, we have $T_i = 1.3 \times 10^{-8}/I_i$ s. The hindrance factor for the ith transition is determined from the relation $F_{\rm h} = T_i/T_{\rm sp}$.

The set of data quoted above suggests that the 0^- state at 1952.38 keV involves a two-proton component. Concurrently, we cannot rule out the possibility that an admixed part of the two-neutron wave function is also present there. Unfortunately, there are no grounds for establishing the rotational levels of the band built on the 0^- bandhead.

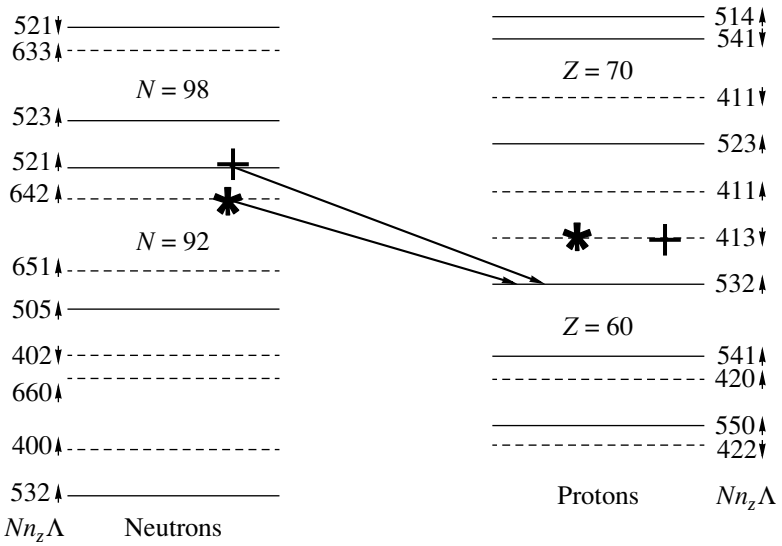

Fig. 2. Fragment of the Nilsson diagram for (asterisks) $^{156}_{63}Eu_{93}$ and (crosses) $^{158}_{65}Eu_{95}$ (+) in accordance with [8]. Shown in the figure are the beta transitions from ^{156}Eu to the 0^- level in ^{156}Gd and from ^{158}Eu to the 0^- level in ^{158}Gd.

3. $J = 1$ LEVEL AT 2267.15(12) keV AND $J^\pi = 0^-$ LEVEL AT 2269.16(1) keV IN ^{158}Gd

A very rich spectrum of levels in the even–even deformed nucleus ^{158}Gd that are excited in the beta decay of ^{158}Eu, 1^-, and in various nuclear reactions, among which (n, γ) and $(n, n'\gamma)$ are the most important [10–12], was investigated. A detailed analysis of available information about the excited states of ^{158}Gd was performed in [13, 14], and new levels were discovered there; in addition, the energies and quantum numbers were refined for some states. Also, a few doublets of closely spaced levels were revealed. One of these contains a $J^\pi = 0^-$ state.

3.1. $J = 1$ Level at 2267.15(12) keV

At an energy of about 2268 keV, there are two closely lying levels (not one, as was indicated in the review article of Helmer [10]). Inelastic photon scattering results in the excitation of states characterized by a high probability of decay to the ground (0^+) and the first excited (2^+) state. The spin–parities of those excited states are $J^\pi = 1^+$, 1^-, and sometimes 2^+. Usually, their decays to other, higher lying, levels are not observed.

In ^{158}Gd, the state at $E = 2268$ keV is excited in the relevant (γ, γ') reaction; it is deexcited via dipole transitions, so that its spin is $J = 1$. In Table 3, it is shown that this state manifests itself in the corresponding $(n, n'\gamma)$ reaction and in ^{158}Eu decay. In all of the three cases, the ratio of the intensities takes the same value within the errors. The 2267- and 2188-keV transitions were not observed in the (n, γ) reaction because of a low sensitivity of the spectrometer in this energy region. The energies of the transitions and of the level were fixed according to data on the respective $(n, n'\gamma)$ reaction from [12], where the smallest error was indicated. The energies of gamma transitions in ^{158}Eu in the range $E = 2.0–2.5$ MeV are somewhat overestimated, as was clarified by considering some gamma transitions in this region. Considering that the level at 2267.15 keV is populated with an intensity of 0.09% in the beta decay of ^{158}Eu, we obtain the value of $\log ft = 8.6$ for this beta-decay branch.

In the decay of ^{158}Eu, only one transition from Table 3 was associated with the deexcitation of the level at 2267.15 keV. The position of the more intense 2268.2-keV transition in the energy-level diagram could not be found. From a comparison of the data in Table 3, it follows that, in all of the three processes, both transitions proceed from the level at 2267.15 keV. Transitions of close energy may be involved in the deexcitation of the level at 2269.16 keV, but these transitions are characterized by a much lower intensity. They were not included in Table 4, which shows the deexcitation of the level at 2269.16 keV, because there are no data on these transitions.

3.2. 0^- Level at 2269.16(3) keV

3.2.1. Identification of the 0^- level. In the preceding section, it was shown that the $J^\pi = 0^-$ level in ^{156}Gd is populated in the beta decay of ^{156}Eu, 0^+. There is a similar situation in the neighboring

Table 2. Hindrance factors for gamma transitions deexciting the 0^- level at 1952.38 keV in ^{156}Gd

$J^\pi K_f$	E_γ, keV	I_γ, arb. units	σL	T_{sp}, s	T_i, s	F_h
1^-1	709.86	100	$M1$	7×10^{-14}	1.3×10^{-10}	2000
2^-1	632.79	4.4	$E2$	1×10^{-10}	3×10^{-9}	30
1^-0	585.90	6.0	$M1$	2×10^{-13}	2×10^{-9}	10 000
2^-2	171.87	$<0.18^*$	$E2$	7×10^{-8}	$\equiv 7 \times 10^{-8}$	$\equiv 1$

* The value of $I_\gamma = 0.18$ should be considered as an upper limit on a transition intensity. Accordingly, the hindrance factors F_h for other gamma transitions may increase.

Table 3. Deexcitation of the $J = 1$ level at 2267.15 keV

(γ, γ')		$(n, n'\gamma)$			^{158}Eu		
E_γ, keV	I_γ, arb. units	E_γ, keV	I_γ, arb. units		E_γ, keV	I_γ, arb. units	
2268	100	2267.04(12)	37(3)	100	2268.2(5)	0.21(3)	100
2188	41(11)	2187.9(4)	20(2)	54(7)	2189.3(8)	0.09(2)	43(12)

nucleus ^{158}Gd. Figure 3 shows a fragment of the energy-level diagram for ^{158}Gd. The $J^\pi = 1^-$ parent nucleus ^{158}Eu of beta-decay energy $Q = 3485$ keV decays to levels of the daughter nuclide ^{158}Gd [10]. Among these, a state at 2269.29 keV was discovered and was assigned a spin of $J = 1$, its refined energy being 2269.16 keV. However, its deexcitation (see Table 4) proved to be similar to the deexcitation of the 0^- level in ^{156}Gd (see Table 1). In either case, three final levels have identical quantum numbers. The present consideration made it possible to supplement the diagram of deexcitation of this level with the 1245.1(4)-keV transition to the 2^- level of the $K^\pi = 1^-$ octupole band. Its position in the diagram of ^{158}Eu decay could not been found. The spectrum of the relevant (n, γ) reaction features a transition of close energy, 1244.58 keV, but its relative intensity of $I_\gamma = 10.6$ arb. units proved to be 40 times higher than that in the decay of ^{158}Eu, so that a very weak component of the possible $\gamma 1245$ keV doublet refers to the deexcitation of the 0^- level. The 2189.3-keV transition proceeding from the level at 2267.15 keV to the first excited 2^+ level (see Table 3 and Fig. 3) was excluded from the spectrum. The above comments and refinements furnish further pieces of evidence in support of the 0^- assignment.

3.2.2. Quantum numbers of the level. The asymptotic quantum numbers of the 0^- level are determined from calculations based on the quasiparticle vibrational model [8]. One expects an $n642\uparrow - n523\downarrow$ two-neutron state at 1.8 MeV, an $n651\uparrow - n521\uparrow$ two-neutron state at 2.2 MeV, and a $p532\uparrow - p413\downarrow$ two-proton state at 2.3 MeV. In two cases, the partner state in the doublet has a spin–parity of $J^\pi = 5^-$ and lies higher than the 0^- level, in accordance with the Galagher–Moshkovsky law.

An analysis of beta decay leads to a more certain result. According to the Nilsson model, the features of the ^{158}Eu ground state are $J^\pi = 1^-$ and $p413\downarrow - n521\uparrow$. A value of $\log ft \approx 6$ is expected for the allowed hindered ah decay $n521\uparrow \to p532\downarrow$ to a two-proton state. The higher observed value of $\log ft = 7.26$ is likely to be associated with the Pauli blocking effect, as in the neighboring nucleus ^{156}Gd (Fig. 2). Beta decay to neutron states would be of a two-particle character—that is, it would be accompanied by a change in the state of two nucleons—or would be the beta transition $n651\uparrow \to p413\downarrow$, which is very strongly hindered in the asymptotic quantum numbers.

3.2.3. Deexcitation of the 0^- level. The hindrance factors F_h for deexcitation gamma transitions were determined by applying the same procedure as in the case of ^{156}Gd. The gamma transition to the $J^\pi K = 2^-2$ level was not observed (recall that, in the case of ^{156}Gd, the analogous transition was used for normalization in estimating the hindrance factors F_h). The energy of this transition was expected to be 475 keV. It was assumed that the $E2$ transition to the $J^\pi K = 2^-1$ level is hindered by a factor of 30, as in ^{156}Gd. The results are displayed in 5.

The hindrance factors for $M1$ transitions to 1^- states are 10^2 to 10^3, this being in agreement with a systematics. They proved to be much less than those in the neighboring nuclei ^{156}Gd. We cannot rule out

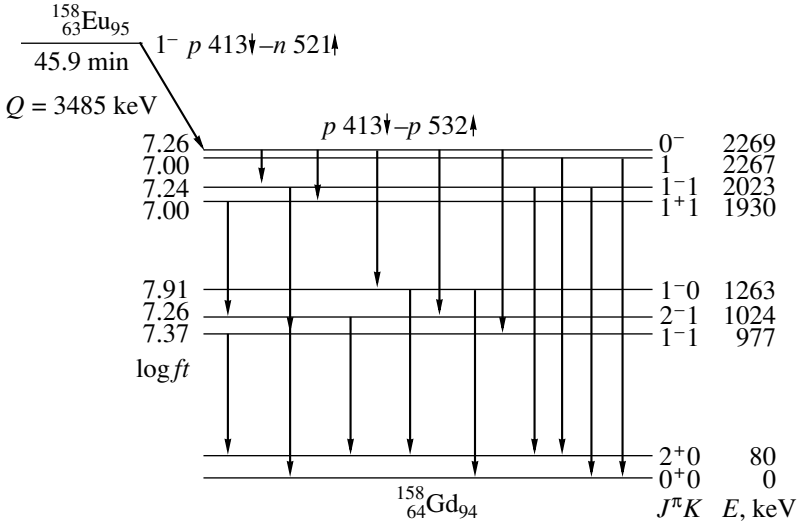

Fig. 3. Fragment of the decay diagram for ^{158}Eu: population and depopulation of the $J^\pi = 0^-, 1^-, 2^-$, and 1^+ levels.

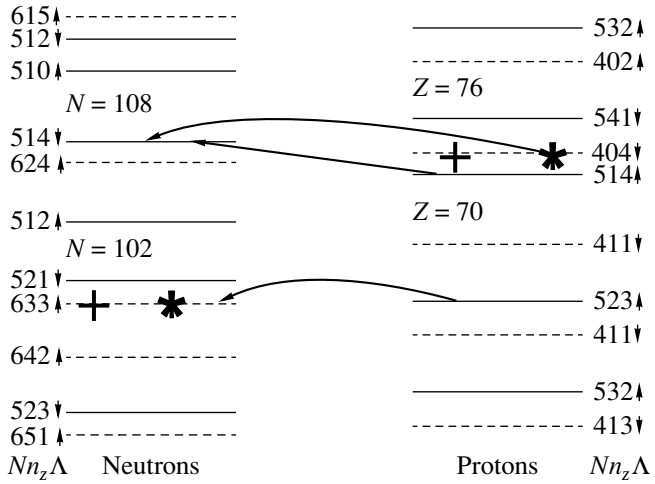

Fig. 4. Fragment of the Nilsson diagram for (asterisks) $^{170}_{71}$Lu$_{99}$ and (crosses) $^{176}_{73}$Ta$_{103}$: (straight line with an arrow) formation of the 0^- four-particle state in ^{176}Hf and (bent lines with arrow) two versions of the formation of two-particle states in ^{170}Yb.

the possibility that this is associated with the choice of normalization for partial half-lives for both nuclei. It is necessary to measure the lifetimes of relevant levels, but this is a difficult experimental task.

4. COMPARISON OF THE PROPERTIES OF LEVELS IN THE ^{156}Gd, ^{158}Gd, ^{170}Yb, AND ^{176}Hf NUCLEI

The properties of the ^{156}Gd and ^{158}Gd nuclei were compared with allowance for information about the ^{170}Yb nucleus, in which five excited states of spin–parity $J^\pi = 0^-$ are known [9, 15, 16], and about the ^{176}Hf nucleus, where two such states were found [17]. Table 6 presents available data on the probabilities of beta decay to the 0^- levels in daughter nuclei.

4.1. 0^- Levels in ^{170}Yb

First of all, it should be noted that the $J^\pi = 0^+$, $p404\downarrow - n633\uparrow$ state of ^{170}Lu decays to two-particle 0^- states via unhindered first-order-forbidden beta transitions $1u$. Two versions are possible here.

(i) There occurs the $p523\uparrow \to n633\uparrow$ transformation. From Fig. 4, it can be seen that all neutron levels up to $N = 100$ are filled in $^{170}_{70}$Yb$_{100}$. A $p404\downarrow - p523\uparrow$ particle–hole state arises in a proton well.

(ii) There occurs the $1u$ beta decay $p404\downarrow \to n514\downarrow$. As a result, a $n633\uparrow - n514\downarrow$ two-neutron state of spin–parity 0^- is formed in ^{170}Yb.

Usually, $1u$ beta transitions are characterized by $\log ft = 6-7$. It is necessary to find out why there arises an additional hindrance factor of 100. It can

Table 4. Deexcitation of the 0^- level at 2269.16(3) keV in ^{158}Gd

$J^\pi K_f$	E_f, keV	^{158}Eu			(n,γ)		
		E_γ, keV	I_γ, arb. units	σL	E_γ, keV	I_γ, arb. units	σL
1^-1	977.147(2)	1292.3(2)	0.89(11)	–	1292	<5	–
2^-1	1023.695(3)	1245.1(4)*	0.10(4)	–	1244.58(13)	<10.6	–
1^-0	1263.514(3)	1005.4(3)	4.1(5)	–	1005.8(9)	11.3(12)	–
1^-1	2023.76(5)	245.33(17)	0.32(4)	$M1, E2$	245.417(5)	0.68(5)	$M1, E2$

* This transition was introduced in the present study.

Table 5. Hindrance factors for gamma transitions deexciting the 0^- level at 2269.16 keV in ^{158}Gd

$J^\pi K_f$	E_γ, keV	I_γ, arb.units	σL	T_{sp}, s	T_i, s	F_h
1^-1	1292.3	22	$M1$	1.1×10^{-14}	1.3×10^{-11}	1200
2^-1	1245.1	2.4	$E2$	4×10^{-12}	$\equiv 1.2 \times 10^{-10}$	$\equiv 30$
1^-0	1005.4	100	$M1$	2.4×10^{-14}	3×10^{-12}	120
1^-	245.33	7.8	$M1$	1.6×10^{-12}	4×10^{-11}	30
2^-2	475	<10	$E2$	4×10^{-10}	$>3 \times 10^{-10}$	>0.1

be deduced from the data in Fig. 4 that, in the decay of ^{170}Lu, this factor is not associated with the Pauli blocking effect. Calculations within realistic models are required for explaining the above result.

These results can be compared with the data on ^{156}Eu decay in Fig. 1. The large experimental value of $\log ft = 8.82$ can be associated with the fact that the beta transition $n642\uparrow \to p532\uparrow$, which was considered in Section 2 for ^{156}Gd, proceeds to the already filled level of structure $p532\uparrow$, as can be seen from the fragment of the Nilsson diagram in Fig. 2.

Let us compare the beta decay of ^{156}Eu to two $K^\pi = 0^-$ levels in ^{156}Gd. By these, we mean the $J^\pi = 0^-$ state found at 1952.38 keV and the 1^-0 level at 1366.46 keV. The beta decay to this level ($\log ft = 9.65$) may proceed through the same wave-function component as in the 0^- state—that is, $n642\uparrow \to p532\uparrow$. According to the calculation performed in [8], however, its fraction in the wave function of the 1^-0 collective state at 1366.46 keV is 3.8%, and one can expect that the probability of the beta decay in question is 15 times lower than that to the 0^- level. However, the calculations in [8] also indicate that the wave function for the 1^-0 level has a 6% admixture of the wave function for the $n642\uparrow - n523\downarrow$ state, and a $1u$ beta transition is possible through this admixed wave function as well. In view of the possible errors in the calculations, no glaring discrepancy in the population of the 0^-0 and 1^-0 levels can be revealed.

In the case where the structure of the level being considered is $n402\downarrow - n521\uparrow$ or $n651\uparrow - n521\uparrow$, beta decay to neutron levels has a two-particle character, changing the state of two nucleons. Its probability is extremely small in this case.

4.2. 0^- Levels in the ^{176}Hf Nucleus

The ^{176}Hf nucleus is the fourth nucleus in which 0^- levels were observed. The levels were excited in the beta decay of ^{176}Ta [17]; their energy was refined in the compilation of Browne and Huo Junde [18]. The lowest of the 0^- states has an energy of 1818.91 keV. It was included in the $K^\pi = 0^-$ band. This is somewhat bizarre, since, in all deformed rare-earth nuclei, low-lying $K^\pi = 0^-$ bands are of a collective character; therefore, they do not contain even-spin states. In ^{176}Hf, the band in question is partitioned into two pairs of levels: the 1^- and 3^- levels at, respectively, 1643.43 and 1710.43 keV form the first pair, while the 0^- and 2^- levels at, respectively, 1818.92 and 1856.99 keV form the second pair. In [17], there is no unambiguous experimental evidence that the level at 1818.92 keV has a spin–parity of 0^-. It should be noted that one transition from this level comes to the 1^- "rotational" level at 1643.43 keV; possibly, the transition to the 2^- level at 1247.68 keV also comes from it. In view of the aforementioned ambiguity, a dedicated discussion on the level at 1818.92 keV is required.

Table 6. Beta decay to $J^\pi = 0^-, 1^-, 1^+$, and 2^- levels

Nucleu	Initial state		Final state			log ft
	J^π	Nucleus, $Nn_z\Lambda$	E_{expt}, keV, $J^\pi K_f$	$Nn_z\Lambda$	E_{calc}, MeV	
^{156}Gd	0^+	^{156}Eu $p413\downarrow - n642\uparrow$	1952.38, 0^-	$p413\downarrow - p532\uparrow$	2.4	8.82
				$n651\uparrow - n521\uparrow$	2.0	
				$n402\downarrow - n521\uparrow$	2.3	
			1242.48, 1^-1	Collective		9.42
			1319.66, 2^-1	Collective		11.2
			1366.46, 1^-0	Collective		9.65
^{170}Yb	0^+	^{170}Lu $p404\downarrow - n633\uparrow$	2052.48, 0^-	$p404\downarrow - p523\uparrow$	2.3	9.40
			2351.54, 0^-	n514$\downarrow - n633\uparrow$	2.2	8.02
			2367.48, 0^-	$n642\uparrow - n512\uparrow$	2.0	7.72
			2497.91, 0^-			8.27
			2819.6, 0^-			7.16
			1364.5, 1^-1	Collective		9.04
			1397.0, 2^-1	Collective		–
			1512.3, 1^-0	Collective		9.20
^{158}Gd	1^-	^{158}Eu $p413\downarrow - n521\uparrow$	2269.16, 0^-	$p413\downarrow - n532\uparrow$	2.3	7.26
				$n642\uparrow - n523\downarrow$	2.1	
				$n651\uparrow - n521\uparrow$	2.2	
			977.15, 1^-1	Collective		7.37
			1023.70, 2^-1	Collective		7.26
			1263.51, 1^-0	Collective		7.91
			1847.80, 1^+1			7.55
			1930.17, 1^+1			7.00
^{176}Hf	1^-	^{176}Ta $p404\downarrow - n512\uparrow$	2912.27, 0^-	$[p404\downarrow - n512\uparrow] - [p514\uparrow - n514\downarrow]$		4.7
			1247.69, 2^-2	Collective		7.11
			1643.41, 1^-0	$n633\uparrow - n514\downarrow$, 93%*		7.42
			1722.05, 1^-1	$p514\uparrow - p404\downarrow$, 93%*		7.74

* The fraction of the wave function according to the calculation in [8].

The structure $p404\downarrow - n512\uparrow$ of the $J^\pi = 1^-$ level in ^{176}Ta ($Z = 73$, $N = 103$) was determined according to the Nilsson diagram (see Fig. 4). According to the calculations in [8], which were based on the quasiparticle vibrational model, the lowest 0^- state in ^{176}Hf has an energy of 1.7 MeV and the structure $n633! \uparrow - n514\downarrow$. It cannot be populated in the beta decay of ^{176}Ta. In experiments, one observes the beta transition to the 1^-0 level at 1643.43 keV ($\log ft = 7.42$). It can proceed owing to the admixture generated in the wave function by the $J^\pi K = 1^-1$ state at 1722.05 keV. The beta decay to this state is characterized by $\log ft = 7.74$. The structure $p514\uparrow - p404\downarrow$ of the 1^-1 level corresponds to the ah transition $p514\uparrow \to n512\uparrow$, which is hindered in the quantum number Λ. The present calculation revealed that there occurs a Coriolis mixing of states in the $K = 0$ and $K = 1$ bands, the mixing parameters being within the ranges that follow from the systematics reported by the present author in [19].

The second 0^- level in ^{176}Hf was discovered at an excitaion energy of 2912.27 keV. Its spin and parity were established on the basis of deexcitation transitions, while its structure was found by using the small value of $\log ft = 5.2$, which corresponds to the au beta transition $p514\uparrow - n514\downarrow$ (see Fig. 4). The only 0^- four-particle state established in the rare-earth region ($[p404\downarrow - n512\uparrow] - [p514\uparrow - n514\downarrow]$) is not of a collective character. Therefore, it is beyond any doubt that this level is associated with the rotational band that contains the 1^- level at 2920.26 keV and the 2^- level at 2969.07 keV [17, 18]. Both are populated by au beta transitions characterized by $\log ft = 5.0$ and 5.4, respectively. Data on the 0^- level in the ^{176}Hf nucleus are included in Table 6.

5. CONCLUSION

The problem of determining the boundary between $K^\pi = 0^-$ levels of collective and single-particle nature has been formulated. In addition to the known examples of the $J^\pi = 0^-$ levels in the ^{170}Yb and ^{176}Hf nuclei, information about the analogous levels and about their properties has been obtained for ^{156}Gd and ^{158}Gd at an excitation energy of about 2 MeV. As to the rotational bands associated with them, they can only be hypothesized. At $E = 2912.27$ keV, a rotational band that involves 0^-, 1^-, and 2^- levels, whose excitation nature is four-particle rather than collective, manifested itself in the ^{176}Hf nucleus. Scanty available data suggest that $K^\pi = 0^-$ noncollective states—in particular, a $J^\pi = 0^-$ state—may manifest themselves in even–even nuclides from the rare-earth region at an excitation energy of about 2 MeV.

This problem deals with states of positive parity. In the $K^\pi = 0^+$ collective bands, there are no levels of odd spin (1, 3, 5, ...). Here, there arises an additional difficulty. It is necessary to determine the quantum number K for known $J^\pi = 1^+$ states. Unfortunately, Alaga rules do not provide a reliable criterion for establishing K for $E > 2$ MeV. This is suggested by a very large scatter of values of $R = B(M1; 1 \to 2^+)/B(M1; 1 \to 0^+)$ for gamma transitions to the ground-state band. The scatter of R values is explained by a different mixing of wave functions in almost all of the $J^\pi = 1^+$ states above 2 MeV. The same reason complicates the analysis of the properties of $K^\pi = 0^-$ levels.

REFERENCES

1. E. P. Grigoriev *et al.*, in *43rd Meeting on Nuclear Spectroscopy and Structure of Nuclei, St. Petersburg, 1993*, p. 85.
2. E. P. Grigoriev and E. B. Bogomolova, in *Proceedings of the St. Petersburg Nuclear Physics Institute School, St. Petersburg, 1995*, p. 155.
3. C. W. Reich, Nucl. Data Sheets **99**, 753 (2003).
4. J. Klora *et al.*, Nucl. Phys. A **561**, 1 (1993).
5. R. G. Helmer, Nucl. Data Sheets **49**, 383 (1986).
6. E. P. Grigoriev and A. V. Murzin, in *VII International Seminar on Interaction of Neutrons with Nuclei (ISINN-7), Dubna, 1999*, p. 332.
7. E. P. Grigoriev and A. V. Murzin, in *50th Meeting on Nuclear Spectroscopy and Nuclear Structure, St. Petersburg, 2000*, p. 156.
8. E. P. Grigoriev and V. G. Soloviev, *Structure of Even Deformed Nuclei* (Nauka, Moscow, 1974) [in Russian].
9. E. P. Grigor'ev, Yad. Fiz. **52**, 915 (1990) [Sov. J. Nucl. Phys. **52**, 581 (1990)].
10. R. G. Helmer, Nucl. Data Sheets **77**, 471 (1996).
11. H. G. Börner *et al.*, Phys. Rev. C **59**, 2432 (1999).
12. E. P. Grigoriev, Yad. Fiz. **64**, 1329 (2001) [Phys. At. Nucl. **64**, 1254 (2001)].
13. E. P. Grigoriev, in *53rd Meeting on Nuclear Spectroscopy and Nuclear Structure, St. Petersburg, 2003*, p. 96.
14. E. P. Grigoriev and I. N. Kuz'mina, in *53rd Meeting on Nuclear Spectroscopy and Nuclear Structure of Atomic, St. Petersburg, 2003*, p. 97.
15. B. S. Dzhelepov *et al.*, *Decay Schemes for Radioactive Nucleus, A = 169, 170* (Nauka, Leningrad, 1988) [in Russian].
16. C. M. Baglin, Nucl. Data Sheets **96**, 611 (2002).
17. F. M. Bernthal *et al.*, Phys. Rev. C **3**, 1294 (1971).
18. E. Browne and Huo Junde, Nucl. Data Sheets **84**, 337 (1998).
19. E. P. Grigoriev, Fiz. Élem. Chastits At. Yadra **31**, 869 (2000) [Phys. Part. Nucl. **31**, 764 (2000)].

Translated by A. Isaakyan

Physics of Atomic Nuclei, Vol. 68, No. 7, 2005, pp. 1096–1100. Translated from Yadernaya Fizika, Vol. 68, No. 7, 2005, pp. 1141–1145.

NUCLEI
Experiment

Cold-Neutron Storage Owing to Diffusion Reflection

S. S. Arzumanov, L. N. Bondarenko*, P. Geltenbort[1)], V. I. Morozov, and Yu. N. Panin

Russian Research Centre Kurchatov Institute, pl. Kurchatova 1, Moscow, 123182 Russia

Received June 10, 2004

Abstract—Results are presented that were obtained from experiments devoted to storing very cold neutrons in vessels whose walls are made from structures involving a spatial inhomogeneity of the average Fermi potential. The possibility of storing neutrons owing to diffusion reflection from the walls is shown, and prospects of elaborating the method are discussed. © *2005 Pleiades Publishing, Inc.*

The discovery of the confinement of ultracold neutrons gave a strong impetus to studying the fundamental properties of the neutron. Advances in these realms were due to a considerable increase in the time of residence of neutrons within measuring facilities owing to their storage. However, the interval of speeds for neutrons that can be stored within vessels owing to a total reflection from media characterized by a positive coherent-nuclear-scattering length is rather modest, 0–7 m/s. In view of this, it is of interest to seek radically new methods, those for storing neutrons of higher speed, their fraction in the reactor-moderator spectrum being much higher. In [1], it was shown that the phenomenon of diffusion reflection from inhomogeneous media can be used to store neutrons.

In the present article, we describe experiments devoted to storing cold neutrons in vessels whose walls are manufactured from artificial structures that are characterized by a pronounced spatial inhomogeneity of the average Fermi potential (boundary energy). Neutrons incident to the walls return to a vacuum upon diffusion reflection, and this ensures neutron storage in the volume of the vessel.

DESCRIPTION OF THE METHOD

Let us consider the interaction between a neutron of energy E and a structure of thickness l consisting of the main phase in which the second phase is embedded in the form of small grains, the boundary energies of the substances of the first and the second phase being $E_{\lim 1}$ and $E_{\lim 2} \neq E_{\lim 1}$, respectively. If the energy of the neutrons is higher than the boundary energy in both phases, either the neutrons are reflected at the phase boundaries, or their trajectory is refracted. In this case, the motion of a neutron acquires a diffusion character, with the result that it has three possibilities: that of returning to a vacuum (this corresponds to reflection), that of traversing the structure layer, and that of undergoing absorption or inelastic scattering to the region of thermal energies. The diffusion process is characterized by the diffusion length L; if $L \ll l$, the transmitted neutron flux becomes negligible, the bulk of neutrons being reflected. It was shown in [2] that, for an isotropic neutron flux incident to such a structure, the probability of losses per collision with the wall is given by

$$\mu = \frac{4}{\bar{\nu}}\left(1 - \frac{E_{\lim 1}}{E}\right)\sqrt{\frac{D}{\tau}}, \qquad (1)$$

where $\bar{\nu}$ is the mean speed of neutrons in the structure; D is the diffusion coefficient, which depends on the difference of $E_{\lim 1}$ and $E_{\lim 2}$, the dimensions of the grains, and their relative concentration in the volume of the main phase; and τ is the neutron lifetime in the structure with respect to the capture and inelastic-scattering channels, which are characterized by the cross sections σ_c and σ_{in}. In a vessel whose walls have such a structure, the number of neutrons as a function of time t, $N(t)$, is expected to behave as $N(t) = N(0)\exp(-\lambda_l t)$, where the probability of losses per unit time is $\lambda_l = 1/\tau_{st} = p\mu$, with p and τ_{st} being, respectively, the frequency of collisions with the wall and the neutron-storage time. In order to minimize the quantity μ, one must obviously create artificial inhomogeneous structures that possess the minimum possible diffusion coefficient and the longest possible neutron lifetime in the structure.

In [2, 3], it was shown that, in order to store cold neutrons of speed in the range 7–50 m/s, it is necessary to employ structures where the characteristic size of spatial inhomogeneities of the potential is larger than and, at the same time, is commensurate

[1)]Institut Laue-Langevin, rue Jules Horowitz 6, BP156-38042 Grenoble Cedex 9, France.

*e-mail: bond@foton.polyn.kiae.su

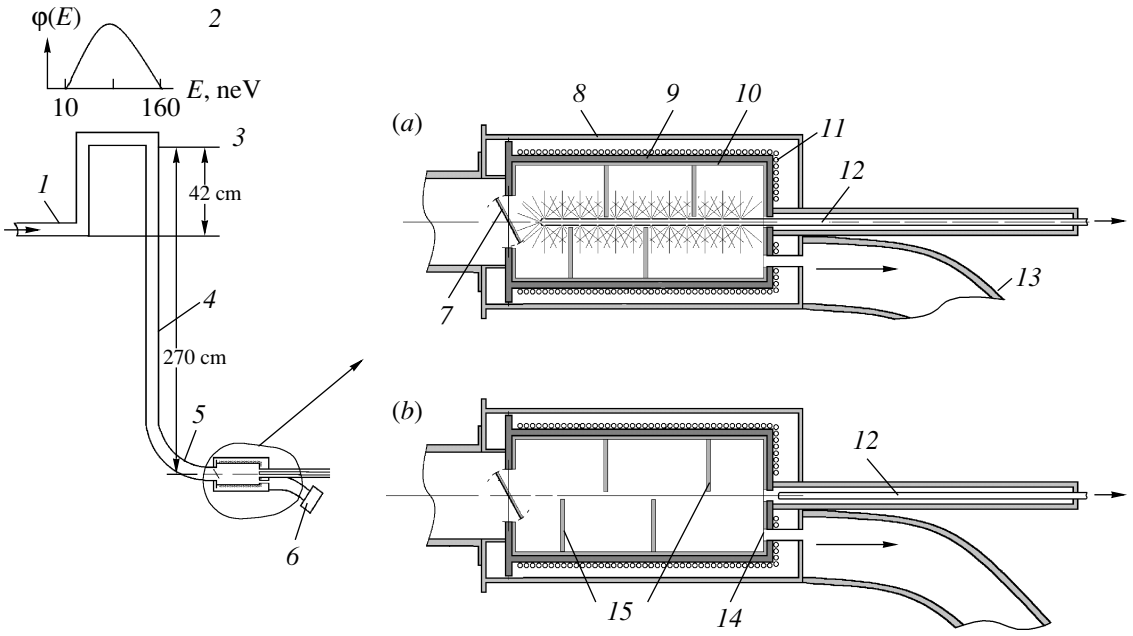

Fig. 1. Layout of the experimental facility used: (*1*) input neutron guide, (*2*) energy spectrum of neutrons in the upper horizontal neutron guide (*3*), (*4*) vertical neutron guide, (*5*) bent channel, (*6*) neutron detector, (*7*) input shutter, (*8*) vacuum chamber, (*9*) copper storage vessel, (*10*) deposited-substance layer, (*11*) pipes of the system for cooling the storage vessel with liquid nitrogen, (*12*) gas-phase injector for layer deposition, (*13*) neutron guide of the detector, (*14*) hole for neutron passage to the detector, and (*15*) copper diaphragms. Shown in the figure are the injector positions during (*a*) surface-layer deposition and (*b*) neutron storage.

with the neutron wavelength of 80 to 600 nm. Estimations show that, by cooling, to low temperatures, structures manufactured from materials in which the capture and inelastic-scattering cross sections are small (beryllium, carbon, deuterium, oxygen, fluorine), the probability μ of losses can be suppressed to a level of 10^{-3} to 10^{-2}.

DESCRIPTION OF THE EXPERIMENTAL FACILITY USED

In order to test directly the possibility of storing cold neutrons in vessels whose wall are made from artificial structures, we employed the facility shown in Fig. 1. Neutrons were stored in a copper vessel (*9*) whose walls were covered with layers of reflecting structures (*10*). By using a П-shaped neutron guide from stainless steel, ultracold neutrons from a source (*1*) whose spectrum fell within the range 50–200 neV were raised to an altitude of 42 cm, their spectrum (*2*) being softened to 10–160 neV. Further, neutrons fell in the gravity field along a vertical neutron guide (*4*) to a depth of 270 cm and, along a bent channel (*5*), arrived at the storage vessel, having a mean speed of 8.3 m/s and the boundaries of the spectrum at 7.4 and 9.2 m/s.

The storage vessel 30 cm in length and 9.2 cm in diameter was installed in a vacuum chamber (*8*) evacuated to a pressure of 10^{-5} mbar. Pipes for cooling the vessel with liquid nitrogen (*11*), which made it possible to change the vessel temperature in the range 100–300 K, were arranged at the outer surface of the vessel. The inlet hole equipped with a fast shutter (*7*) for letting neutrons in the vessel and for subsequently locking them there was at the front flange of the vessel. At the rear flange, there was a small hole (*14*) of area 5 cm^2, through which neutrons accumulated in the vessel flew to a detector (*6*) along a bent neutron guide from nickel (*13*). For the detector, we used a gas

Table

Structure type	T, K	τ_{st}, s	μ, 10^{-2}
Teflon	300	0.11(1)	6.4(6)
	100	0.22(3)	3.2(4)
Graphite–liquid fluoropolymer	300	0.17(3)	4.1(7)
	100	0.22(2)	3.2(3)
Diamond–liquid fluoropolymer	300	0.27(3)	2.6(3)
	100	0.37(4)	1.9(2)
Condensate heavy water	100	0.82(6)	0.86(6)

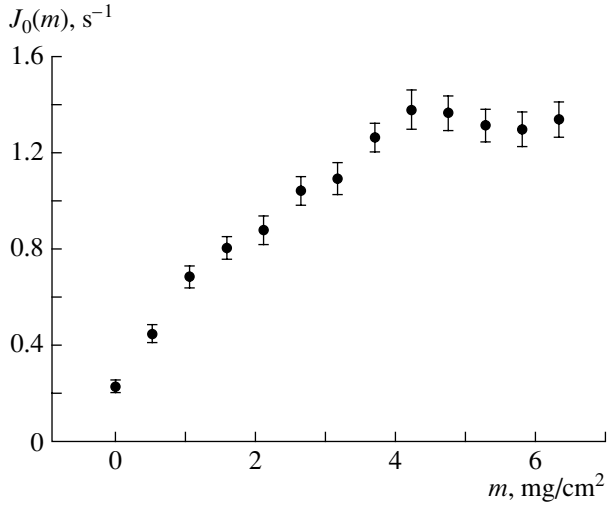

Fig. 2. Detector counting rate as a function of the mass m of condensed water for an open position of the shutter. In the absence of the condensate at the walls ($m = 0$), the detector records a low flux of neutrons hitting it upon reflection from the walls of the copper vessel.

proportional counter based on ^{3}He. In order to prevent a direct passage of neutrons from the inlet hole to the detector, four copper diaphragms (*15*) covered with a reflecting-structure layer were installed within the vessel, each diaphragm covering half of the vessel cross section.

Reflecting layers of the following four kinds were deposited onto the inner surface of the vessel:

(i) solid-state fluoropolymer $(CF_2)_n$ (industrial Teflon) 1 mm thick characterized by a boundary speed of 5 m/s (the spatial inhomogeneity of the potential there was due to the presence of giant molecules featuring structural distortions);

(ii) mixture of liquid fluoropolymer $(OCFCF_3CF_2)_n$ and a graphite micropowder of grain size 5 to 20 μm (the packing density was 0.2 to 0.3; the layer thickness was 0.5 mm; the boundary velocity was 5.6 m/s in graphite and 4.65 m/s in the fluoropolymer; the difference of the boundary energies between the phases was $u_0 = 88$ neV);

(iii) mixture of a liquid fluoropolymer and a diamond micropowder of grain size 250 nm (the packing density was 0.2 to 0.3; the layer thickness was 0.3 mm; the boundary speed in diamond was 7.65 m/s; and the difference of the boundary energies in the two phases was $u_0 = 200$ neV);

(iv) low-temperature microcrystal condensate of a heavy-water vapor (the boundary velocity was 5.0 m/s; the condensate had the form of a vacuum–ice structure whose properties of importance were the following: the difference of the boundary energies between the two phases was $u_0 = 125$ neV; the crystalline-grain size was on the order of 10^2 to 10^3 nm; and the packing density was 0.2 to 0.4).

The coating was created via the condensation of heavy-water vapor through a movable evaporator (*12*) onto the vessel surface cooled to 100 K. The evaporator had the form of a cylindrical pipe 1.2 cm in diameter heated from inside. There were 100 holes of total area 1 cm^2 in the side surface of the pipe. In order to implement condensation, the evaporator was introduced in the volume of the evacuated vessel, whereupon helium was supplied to the vessel under a pressure of 3 to 4 mbar (Fig. 1*a*). After performing the condensation of water vapor onto the vessel surface, the evaporator was withdrawn from the storage volume, helium was evacuated, and neutrons were stored (Fig. 1*b*).

In order to fill the vessel with neutrons, the inlet shutter was opened for 3 to 5 s, which was necessary for maximum filling; after that, it was closed, which took 0.05 s. Within the interval of filling and storing, we measured the detector counting rate as a function of time, $J(t)$. After closing the vessel, the detector counting rate behaved as

$$J(t) = J(0)\exp(-t/\tau),$$

where $1/\tau = 1/\tau_{st} + 1/\tau_d$; here, τ_{st} is the time of neutron storage in the vessel, while $\tau_d = 1.28(12)$ s is the time it takes for neutrons flowing from the hole in the vessel to reach the detector. From the value obtained for τ, we determined the time τ_{st} and the probability of losses,

$$\mu = 4\Omega/(\nu S\tau_{st}),$$

where $\Omega = 2 \times 10^3$ cm^3 is the volume of the vessel and $S = 1.3 \times 10^3$ cm^2 is the area of the inner surface.

RESULTS OF THE MEASUREMENTS

Neutron storage owing to diffusion reflection was observed for all coatings studied here (see table).

From the table, it can be seen that the best result was obtained for a fine-grained heavy-water condensate. Figure 2 shows the detector counting rate as a function of the condensed-water mass m for the case where the shutter is open. In the absence of a condensate at the walls ($m = 0$), the detector records a low flux of neutrons that hit it upon undergoing reflections from the walls of the copper vessel. With increasing condensed-layer mass and with increasing diffusion-reflection probability, the detector counting rate becomes higher owing to an increase in the number of neutrons in the vessel. As soon as the condensed-layer thickness begins to exceed the diffusion length considerably, so that the penetration of neutrons through the layer becomes insignificant, the

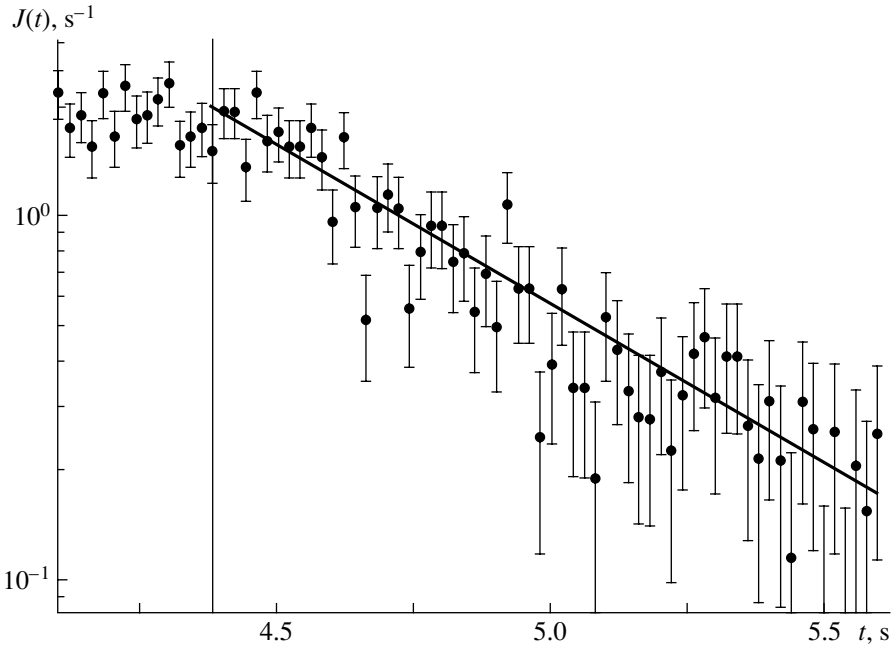

Fig. 3. Detector counting rate as a function of time for a condensed layer of mass $m = 6.7$ mg/cm^2. Upon closing the shutter ($t = 4.4$ s), the number of neutrons in the vessel decreases exponentially, the characteristic time being $\tau = 0.50(3)$ s.

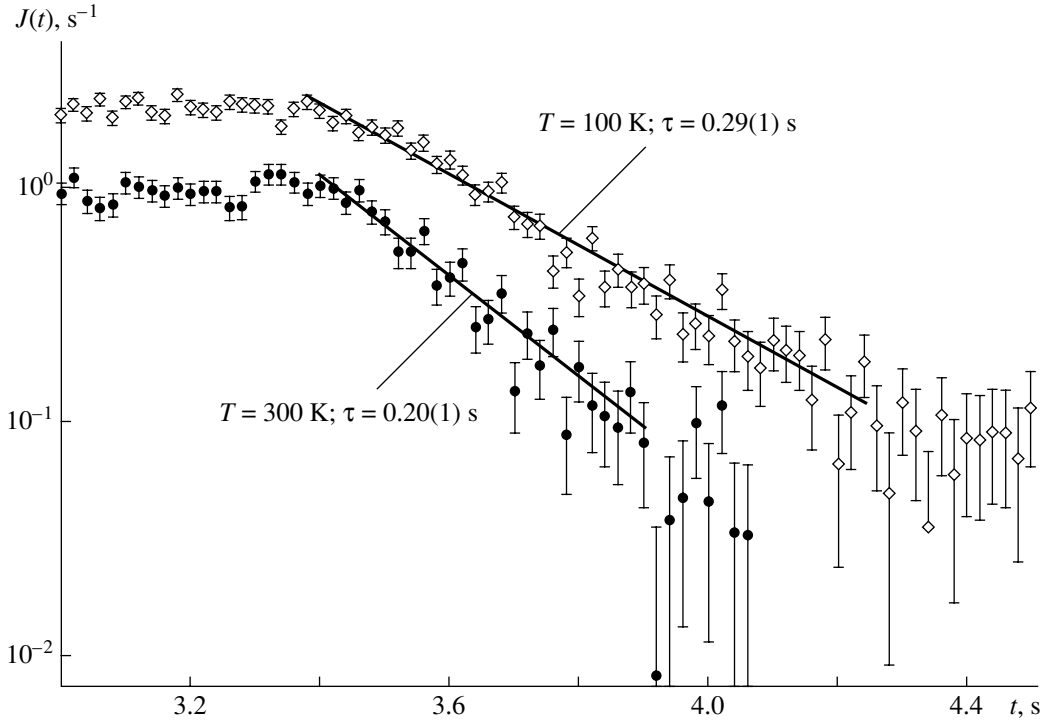

Fig. 4. Detector counting rate as a function of time for the vessel whose inner surface is coated with a mixture of a diamond powder and a liquid fluoropolymer at temperatures of 300 and 100 K. With decreasing temperature, the probability of neutron losses decreases owing to the reduction of the cross section for inelastic scattering, which is the main channel of neutron escape.

counting rate stabilizes. Figure 3 displays the detector counting rate as a function of time for a condensed layer of thickness $m = 6.7$ mg/cm^2. After closing the shutter ($t = 4.4$ s), the number of neutrons in the vessel decreases exponentially, the characteristic time being $\tau = 0.50(3)$ s. This is suggested by the fact that the counting rate decreases with the same characteristic time. Taking into account the leakage of neutrons to the detector, we estimate the time of storage in the vessel at $\tau_{st} = 0.82(6)$ s. At a neutron mean free path of 6.5 cm and a collision frequency of 142 s^{-1}, this corresponds to a value of $\mu = 8.6 \times 10^{-3}$ for the coefficient of losses; that is, a neutron undergoes about 120 diffusion reflections before leaving the volume of the vessel.

Figure 4 shows the detector counting rate as a function of time for the case where the vessel walls are coated with a mixture of a diamond powder and a liquid fluoropolymer at temperatures of 300 and 100 K. One can see that, at the lower temperature value, the probability of neutron losses is lower owing to a decrease in the cross section for inelastic scattering, which is main channel of neutron escape here. However, the effect associated with the decrease in the inelastic-scattering cross section σ_{in} is insignificant, since, according to (1), $\mu \propto \sqrt{(\sigma_{in} + \sigma_c)}$ At $T = 100$ K, the storage time is $\tau_{st} = 0.37(4)$ s, the corresponding value of the coefficient of losses is $\mu = 1.9 \times 10^{-2}$, and the number of diffusion reflections prior to escape is 50.

From the very first results, it can be seen that Teflon, mixtures of liquid fluoropolymer with graphite and diamond powders, and a heavy-water condensate are efficient cold-neutron reflectors that can be used in accumulating neutrons in vessels, as well as in other problems that require a short-term storage of cold neutrons. In particular, they can be employed as reflectors and storage units in ultracold-neutron sources based on cooling cold neutrons in superfluid helium [4] and on using nanoparticles [5]. A further development of the method would require seeking structures that would make it possible to reduce the resulting coefficients of losses to a level of 10^{-3}. The creation of nanostructures (characterized by a grain size of about 10 nm), where a vacuum, which does not contribute to absorption, plays the role of the main phase and where the difference of the effective potentials is maximal, is an obvious way to achieve this goal. In particular, structures from diamond nanoparticles at temperatures of 4 to 80 K and nanocrystal condensates of heavy water and, possibly, of oxygen at temperatures of about 4 K seem promising.

ACKNOWLEDGMENTS

We are grateful to S.T. Belyaev and V.V. Nesvizhevsky for stimulating discussions and support of these investigations.

This work was supported by the Russian Foundation for Basic Research (project no. 03-02-16323-a).

REFERENCES

1. A. Steyerl *et al.*, Z. Phys. A **267**, 379 (1974).
2. S. S. Arzumanov *et al.*, Preprint IAÉ-6321/2 (Institute of Atomic Energy, Moscow, 2004).
3. V. I. Morozov *et al.*, in *Proceedings of the ISINN-10, Dubna, 2003*, pp. 307, 376.
4. R. Golub and J. M. Pendlebury, Phys. Lett. A **62**, 337 (1977).
5. V. V. Nesvizhevsky *et al.*, Yad. Fiz. **65**, 426 (2002) [Phys. At. Nucl. **65**, 400 (2002)].

Translated by A. Isaakyan

Physics of Atomic Nuclei, Vol. 68, No. 7, 2005, pp. 1101–1103. Translated from Yadernaya Fizika, Vol. 68, No. 7, 2005, pp. 1146–1148.

NUCLEI
Experiment

Analysis of the Phase Tunneling Time for Cold Neutrons through a Neutron Interference Filter

A. K. Zaichenko and V. S. Olkhovsky*

Institute for Nuclear Research, National Academy of Sciences of Ukraine, pr. Nauki 47, Kiev, 252028 Ukraine

Received July 20, 2004

Abstract—Explicit expressions are obtained for the energy dependence of the particle transmission coefficient and phase tunneling time through two rectangular barriers near resonance. The resonance half-width and the phase tunneling time for neutrons in resonance are calculated. © *2005 Pleiades Publishing, Inc.*

1. INTRODUCTION

The duration of the neutron interaction with the so-called neutron interference filter has been measured recently [1]. The potential structure of the filter comprised two rectangular barriers separated by a potential well. The neutron precession phase shift during the interaction was a directly measurable quantity. The Larmor neutron tunneling time in the resonance corresponding to the quasi-bound state of neutrons in the potential well between the barriers was found from the measured phase shift. The measured tunneling time was also compared with the calculated phase tunneling time in [1]. In this paper, we analyze the energy dependence of the particle phase tunneling time through the double barrier near resonance.

2. THE RESONANCE CONDITION

Let us consider the tunneling of particles with an effective mass m and energy E through two identical rectangular barriers of width a and height U_0 separated by distance l. In this case, the amplitude of the transmitted wave is defined by the relation [2, 3]

$$A_T(k) = \exp(-2ika)/D(k), \tag{1}$$

where

$$D(k) = \cosh^2(qa) + \frac{1}{4}\sinh^2(qa)[\sigma^2\cos(2kl) - \delta^2] + i\sinh(qa)\left[\delta\cosh(qa) + \frac{1}{4}\sigma^2\sinh(qa)\sin(2kl)\right], \tag{2}$$

$k = \sqrt{2mE}/\hbar$, $q = \sqrt{2m(U_0 - E)}/\hbar$, $\delta = (q^2 - k^2)/kq$, and $\sigma = (k^2 + q^2)/kq$. Since $|A_T(k)|^2 = 1$ [2–5] in resonance, the resonance can be defined by the condition

$$|D(k)|^2 = 1. \tag{3}$$

Substituting (2) into (3) yields the equation

$$\cot(kl) = -(1/2)\delta\tanh(qa). \tag{4}$$

This equation is the same general resonance condition as Eq. (3). Therefore, it can be used to determine the resonance values of any of the parameters a, k, l, m (for electrons [6]), and U_0 (if all of the remaining parameters are known). For example, the resonance values of the wave number k and the distance l between the barriers were shown to satisfy Eq. (4) in [2] and [3], respectively.

3. THE BEHAVIOR OF THE TRANSMISSION COEFFICIENT NEAR RESONANCE

The analysis of the energy dependence of the transmission coefficient $P(k) = |A_T(k)|^2$ near resonance can be simplified considerably by introducing the functions

$$u = \cosh^2(qa) - \frac{1}{4}\delta^2\sinh^2(qa), \tag{5}$$

$$v = \delta\cosh(qa)\sinh(qa), \quad w = \frac{1}{4}\sigma^2\sinh^2(qa)$$

that are related by

$$u^2 + v^2 = (1 + w)^2, \quad uu' + vv' = (1 + w)w', \tag{6}$$

$$u'^2 + v'^2 - w'^2 = (u'v - uv')^2,$$

where the prime denotes differentiation with respect to one of the parameters, a, k, l, m, or U_0. Using these functions, the denominator $D(k)$ in Eq. (1) can be represented as

$$D = u + w\cos(2kl) + i[v + w\sin(2kl)]. \tag{7}$$

*e-mail: olkhovsk@kinr.kiev.ua

Retaining the first two terms in the expansion of $D(k)$ in a power series of the deviation of particle energy E from the resonance value E_r, we obtain near resonance

$$D(k) = D_r + C_r(E - E_r) \quad (8)$$
$$= C_r(E - E_r + D_r C_r^*/|C_r|^2),$$

where $D_r = D(k_r)$, $k_r = (2mE_r)^{1/2}/\hbar$, $C_r = mD_r'/(\hbar^2 k_r)$, and the prime denotes differentiation with respect to k. It follows from Eq. (4) that, at the resonance, we have

$$\cos(2k_r l) = -u_r/(1 + w_r), \quad (9)$$
$$\sin(2k_r l) = -v_r/(1 + w_r),$$

where u_r, v_r, and w_r are the values of the functions u, v, and w at $k = k_r$. Using formulas (5)–(7) and (9), we can easily verify that

$$D_r C_r^* = i/\beta, \quad |C_r|^2 = \beta^{-2}, \quad (10)$$

where

$$\beta = \frac{\hbar^2 k_r}{m}\left[\frac{u_r' v_r - u_r v_r'}{1 + w_r} + 2l w_r\right]^{-1}. \quad (11)$$

Differentiating functions (5) with respect to k and substituting the derivatives obtained into (11) yields

$$\beta = (\hbar^2 k_r q_r/m)[\delta_r k_r a + \sigma_r^2 \cosh(q_r a)\sinh(q_r a)]^{-1}, \quad (12)$$

where δ_r, σ_r, and q_r are the values of δ, σ, and q at $k = k_r$.

It follows from formulas (8) and (10) that

$$D(k) = C_r(E - E_r + i\beta). \quad (13)$$

Substituting (13) into (1) and taking into account (10), we find that the energy dependence of the transmission coefficient near resonance is described by the Breit–Wigner formula

$$P(k) = \frac{\beta^2}{(E - E_r)^2 + \beta^2} \quad (14)$$

with the half-width (12). The same formula for $P(k)$ is also obtained in the quasi-classical approximation [7].

4. THE ENERGY DEPENDENCE OF THE PHASE TUNNELING TIME NEAR RESONANCE

According to the general definition, the particle phase tunneling time through two barriers is given by the expression [8]

$$\tau = \hbar\partial \arg\{A_T \exp[ik(2a + l)]\}/\partial E. \quad (15)$$

It follows from (1) and (15) that

$$\tau = \hbar\partial \arg[\exp(ikl)/D]/\partial E. \quad (16)$$

Substituting (13) into (16), we obtain the expression for the energy dependence of the phase tunneling time near resonance

$$\tau = \frac{m}{\hbar k} l + \frac{\hbar\beta}{(E - E_r)^2 + \beta^2}. \quad (17)$$

The first term in this expression is the time it takes for the particles to freely traverse the distance between the barriers, and the second term is the time delay attributable to the localization of particles in the quasi-bound state in the space between the barriers.

5. COMPARISON WITH EXPERIMENTAL DATA

A neutron beam with a wavelength of $\lambda = 20.1$ Å at the half-width of the spectrum $\Delta\lambda/\lambda \cong 4.8\%$ was used in [1]. The calculated width of the angular distribution was 3.2 mrad. The measurements were carried out in a grazing-angle geometry.

During the experiment, neutrons tunneled through two identical rectangular barriers of width $a = 300$ Å and height $U_0 \simeq 230$ neV separated by a potential well of width $l = 195$ Å with a nearly zero potential. There was only one resonance level with an energy of $E_r = 127$ neV and a half-width of 4 neV in this potential structure. The neutron delay time in resonance was $(2.17 \pm 0.2) \times 10^{-7}$ s; the delay time far from resonance (1.9×10^{-8} s) was determined by the neutrons that were not involved in the tunneling.

The phase tunneling time in resonance calculated in [1] was 4.26×10^{-7} s.

At the experimental values of the parameters a and l, the resonance energy $E_r = 127$ neV is obtained from Eq. (4) at $U_0 = 243$ neV. At such a barrier height, the half-width of the resonance level β calculated using formula (12) is 1.6 neV, while the tunneling time in resonance calculated using formula (17) is 0.42 μs for this value of β.

As in [1], the calculated tunneling time in resonance is almost twice its experimental value. This discrepancy is most likely attributable both to the experimental factors (the neutron nonmonochromaticity, the angular divergence of the neutron beam, and the finite energy resolution of the detectors) and to the approximate nature of the phase tunneling time. The experimental factors result in an averaging of the resonance value of the tunneling time over a wide energy range; therefore, the value averaged over the entire transmission line is given in [1] along with the phase tunneling time at the resonance peak. It is the averaged phase tunneling time (2.27×10^{-7} s) that proved to be close to the experimental value. In our case, averaging the calculated tunneling time in resonance over the range $[E_r - 4$ neV, $E_r + 4$ neV$]$

also yields a value ($\bar{\tau} = 0.2$ μs) close to the experimental one. Wave packets [3, 9, 10] must be used to determine the tunneling time more accurately.

REFERENCES

1. A. I. Frank, I. V. Bondarenko, V. V. Vasil'ev, *et al.*, Pis'ma Zh. Éksp. Teor. Fiz. **75**, 729 (2002) [JETP Lett. **75**, 605 (2002)].
2. A. S. Davydov and V. N. Ermakov, Preprint ITP-86-90E (Kiev, 1986).
3. E. H. Hauge, J. P. Falck, and T. A. Fjeldly, Phys. Rev. B **36**, 4203 (1987).
4. A. Ya. Dzyublik and V. N. Rud'ko, Ukr. Fiz. Zh. **30**, 173 (1985).
5. B. N. Zakhar'ev and V. M. Chabanov, Fiz. Élem. Chastits At. Yadra **33**, 348 (2002) [Phys. Part. Nucl. **33**, 175 (2002)].
6. L. L. Chang, L. Esaki, and R. Tsu, Appl. Phys. Lett. **24**, 593 (1974).
7. A. A. Seregin, Zh. Éksp. Teor. Fiz. **73**, 1634 (1977) [Sov. Phys. JETP **46**, 859 (1977)].
8. V. S. Olkhovsky, E. Recami, and G. Salesi, Europhys. Lett. **57**, 879 (2002).
9. V. S. Olkhovsky and E. Recami, Phys. Rep. **214**, 339 (1992).
10. J. G. Muga, S. Brouard, and R. Sala, Phys. Lett. A **167**, 24 (1992).

Translated by E. Kozlovsky

Physics of Atomic Nuclei, Vol. 68, No. 7, 2005, pp. 1104–1119. Translated from Yadernaya Fizika, Vol. 68, No. 7, 2005, pp. 1149–1164.

NUCLEI
Experiment

Dynamic Reflection and Refraction of Neutrons at the Boundaries of Matter Characterized by a Variable Magnetic Induction

A. V. Kozlov[1)] and A. I. Frank*

Joint Institute for Nuclear Research, Dubna, Moscow oblast, 141980 Russia

Received June 21, 2004; in final form, September 22, 2004

Abstract—Optical phenomena that arise in the interaction of a neutron wave with matter characterized by a variable interaction potential are considered. The time dependence of the potential is assumed to be due to a change in the magnetization vector in matter with time. Since the interaction in question is time-dependent, the neutron energy is not conserved. If a neutron interacts with a sample that has a plane boundary, only the neutron-velocity component orthogonal to the matter boundary changes. Thus, reflected waves are characterized by a reflection angle that is different from the angle of incidence. Waves transmitted through a plane sample can also change direction. The changes in the neutron energy and in the neutron-velocity direction are closely related to the reversal of the neutron-spin projection. The question of whether a slab featuring a rotating magnetization vector can be used as a spin flipper or as a coherent wave splitter is considered. © *2005 Pleiades Publishing, Inc.*

1. INTRODUCTION

Time-dependent quantum phenomena have attracted an ever greater attention of physicists involved in neutron-optics studies. At the present time, we can say that there has appeared time-dependent neutron optics employing concepts such as diffraction in time, time focusing, and time interferometry. A time-dependent effect on a neutron wave makes it possible to change substantially all of its basic parameters—namely, polarization, intensity, wavelength, and the direction of propagation. One can hope that not only is this dynamical approach to neutron optics of purely theoretical interest, but it will also be of use in developing new experimental methods and quantum devices.

It seems that a radio-frequency spin flipper based on a concerted effect of a constant magnetic field and an alternating magnetic field crossed with it was the first nonstationary device used in neutron optics. The theory of this phenomenon was formulated by Rabi [1], who also proposed employing this device for resonance neutron-spin flip with the aim of measuring the neutron-magnetic moment. The viability of the method was demonstrated in experiments with molecular beams [2]. Before long, Alvarez and Bloch measured the neutron magnetic moment by this method [3]. Over many decades, Rabi's flipper, as well as Ramsey's resonance method [4], which was proposed on its basis, has been employed in neutron experiments.

A resonance spin flip in a magnetic field is accompanied by a change in the total neutron energy. Drabkin and Zhitnikov [5] proposed employing this circumstance to slow down neutrons by applying a combination of a resonance flipper and a flipper based on the use of static fields. Twenty years later, a similar idea was discussed by Kruger [6]. Before long, this was followed by the observation of a change in the neutron energy upon a resonance spin flip in the experiments reported in [7, 8] and a direct detection of a change in the frequency ω of the neutron wave function in experiments with neutron interferometers [9, 10]. Obviously, a change in the neutron energy can be interpreted as the result of photon exchange with an electromagnetic field. Multiphoton exchange in the interaction of a neutron with a variable field was studied theoretically and experimentally in [11–13].

An observation of a change in the energy of neutrons interacting with a crystal where ultrasonic vibrations were excited was reported in [14] and in some of the earlier studies. A nonstationary neutron-wave diffraction at surface acoustic waves was experimentally observed in [15]. This possibility was previously indicated in [16]. In such cases, one can speculate about the exchange of energy between a neutron and phonons.

The presence of a variable field is not a necessary condition for the emergence of a nonstationary state. It is sufficient that any parameters of the quantum

[1)]The address at the present time is Weizmann Institute of Science, Rehovot, 76100 Israel.

*e-mail: frank@nf.jinr.ru

problem at hand be time-dependent. A vivid illustration of this circumstance is provided by the classic study of Moshinsky [17], who considered the problem of neutron-wave evolution after the instantaneous removal of an ideal absorber positioned at the coordinate origin, $x = 0$, from a beam of monochromatic neutrons. The solution $\psi(x, t)$ has the form of a Fresnel integral and describes both the propagation of the wave front along the x axis and its gradual smearing, which has the same character as the spreading of a wave packet. The situation here is similar to the wave pattern in the case of spatial wave diffraction at the sharp boundary of a screen. Taking advantage of the symmetry in the Schrödinger equation between the variables x and k, on one hand, and the variables ω and t, on the other hand, Moshinsky called this phenomenon diffraction in time. Interest in Moshinsky's study was revived in connection with the articles written by Golub and Gäler together their coathors, who discussed the possibility of experimentally observing short time cold-neutron bunches prepared with the aid of a fast quantum chopper from a beam that was originally monochromatic [18–20]. This experiment was implemented later [21].

In the Moshinsky problem, a beam is subjected to a single aperiodic action. A generalization to the case of a periodic action of an absorber (chopper) was given in [22]. In accordance with the idea of quasienergy [23], the spectrum of states appears to be discrete in that case, the transmitted beam having a complicated structure characterized by beats. A similar situation must arise in the case of a periodic modulation of the transmitted-wave phase. In that case, one deals with a phase modulator of a wave rather than with a chopper. It was found that, under certain conditions, the original monochromatic wave can be restored upon transmitting the resulting multiwave state through a second modulator. The effect of two modulators can be interpreted as diffraction in time at two diffraction gratings. In this way, there arose the idea of a time interferometer [24, 25]. The problems of time interferometry were also considered in [26].

In order to prepare a state that has a discrete energy spectrum, it is not necessary to interrupt or modulate a neutron beam over its entire cross section simultaneously. It is quite sufficient that such a periodic modulation occur at each point of the beam, with the modulation phase changing from one point to another. Thus, there arose the problem of the motion of a periodic structure across the beam. Nonstationary phenomena in neutron diffraction at a moving grating were analyzed in [27] and were experimentally demonstrated in [28]. The idea of a spacetime interferometer involving two moving gratings was discussed in [26].

In the articles quoted above, the authors considered, as a rule, motion along one coordinate axis, in which case a change in the neutron velocity appeared to be the result of a time-dependent action. The possibility of applying a time-dependent action to a neutron in order to implement the time focusing of neutrons was discussed in [29]. That a quantum time lens for neutrons can be realized was recently demonstrated in the experiment reported in [30]. A similar idea was put forth and implemented for the time focusing of cold atoms [31]. A discrete spectrum arising upon wave modulation was observed in experiments with slow atoms as well [32].

Time-dependent action on a wave can also change the transverse component of the wave vector, this leading to a change in the direction of wave propagation. A dynamic nonspecular reflection of neutrons from a vibrating surface was observed in [33]. Obviously, only the wave-number component orthogonal to the matter surface changes in that case. If the amplitude of such vibrations is commensurate with $(k_\perp)^{-1}$, where $k_\perp$ is the wave-vector component orthogonal to the surface, this phenomenon can be interpreted as the result of reflected-wave modulation.

The dynamic reflection of neutrons is also possible in the case of an immobile surface of matter if an effective potential that is responsible for particle interaction with matter oscillates. This idea dates back to the study of Gerasimov and Kazarnovsky [34], who considered a number nonstationary quantum phenomena that can in principle be observed in experiments with ultracold neutrons, including the problem of neutron reflection from an oscillating potential. The last problem was solved in terms of perturbation theory—that is, for a relatively small amplitude of oscillations. An exact mathematical formulation of this problem reduces to an infinite number of equations [35]. The study reported in [34] is noteworthy in a different respect. In that study, the authors considered for the first time the interaction of neutrons with a variable field in the presence of matter. The interaction with matter was described by a constant effective potential, the variable part of the total potential being generated by the time-dependent magnetization. The conceptual framework of the present study is intimately related to this idea. Below, we consider a number of nonstationary neutron-optics phenomena arising in coherent neutron interaction with matter that is characterized by a variable magnetization vector.

This article is organized as follows. In Section 2, we describe an approximate method that can be used to solve the problem of reflection from an oscillating potential at not overly high frequencies of oscillations. Obviously, this problem is of quite general importance, but, within neutron optics, the situation corresponding to it is realized most easily via a quick

reversal of the magnetization of a magnet. The content of this section was previously exposed in [36]. We deemed it reasonable to reproduce it here because it is intimately related to the issues considered in the subsequent parts of our article. In Section 3, we present an exact solution to the problem of neutron reflection and refraction at the boundaries of matter whose magnetic-induction vector rotates. In Subsections 3.1 and 3.2, we consider in detail the problems of, respectively, dynamic reflection from a semi-infinite medium and neutron transmission through a thin film of magnetic substance.[2)] In Subsection 3.3, it is shown that, by slightly modifying the formulas presented in Subsection 3.2, one can arrive at the solution to the problem of Rabi's flipper in the presence of matter. In that case, the magnetic field in matter is described by the sum of two vectors: a constant vector and a rotating vector orthogonal to it.[3)] Section 4 is devoted to the possibility of an experimental observation and applications of dynamic effects considered above.

2. REFLECTION OF A WAVE FROM AN OSCILLATING POTENTIAL BARRIER: QUASISTATIONARY APPROACH

Let us consider reflection of the plane wave

$$\psi(x,t) = \exp[i(kx - \omega t)] \tag{2.1}$$

from the boundary of matter that occupies the half-space $x > 0$ and which is characterized by an effective potential

$$V(t) = U + u(t) \tag{2.2}$$

that changes periodically with time, the period being T. By virtue of the invariance of the problem with respect to translations along the boundary of matter, the longitudinal component of the wave number undergoes no change upon reflection, so that the problem is effectively one-dimensional. We will show that an approximate solution can be found in the general form, provided that the frequency $\Omega = 2\pi/T$ is not overly high ($\Omega \ll \omega$).

The time variation of the effective potential leads to a synchronous variation of the complex-valued amplitudes $r(t)$ and $\theta(t)$ of the reflected and transmitted waves. At small distances from the surface, the resulting state can be represented in the form

$$\psi(x,t) \tag{2.3}$$
$$= \begin{cases} \exp[i(kx - \omega t)] + r(t)\exp[-i(kx + \omega t)], & x < 0, \\ \theta(t)\exp[i(kx - \omega t)], & x > 0, \end{cases}$$
$$|x| \ll 1/k\gamma_1, 1/k\gamma_2,$$

where

$$\gamma_1 = \frac{\hbar\Omega}{E}, \quad \gamma_2 = \frac{\hbar\Omega}{|E-U|}, \tag{2.4}$$
$$\gamma_{1,2} \ll 1, \quad \Omega = \frac{2\pi}{T}.$$

The state of reflected waves,

$$\psi_r(x,t) = r(t)\exp[-i(kx - \omega t)], \tag{2.5}$$

can easily be found by applying the procedure used in [24, 25] for the case of a quantum modulator. We represent the amplitude $r(t)$ in the form of a Fourier expansion in the frequencies $n\Omega$ and substitute this expansion into (2.5). In the vicinity of the boundary, the wave function of the reflected wave then takes the form

$$\psi_r(x,t) \cong \sum_n a_n \exp[-i(kx + \omega_n t)], \tag{2.6}$$
$$\omega_n = \omega + n\Omega, \quad x < 0, \quad |x| \ll 1/k\gamma_1,$$

where a_n are the Fourier coefficients for the function $r(t)$.

Since the reflected waves propagate in free space, the usual dispersion relation holds for them. At arbitrary distances from the boundary, we therefore have

$$\psi_r(x,t) = \sum_n a_n \exp[-i(k_n x + \omega_n t)], \tag{2.7}$$
$$k_n = k(1 + n\gamma_1)^{1/2}, \quad x < 0.$$

Thus, the state in the left half-space is a nonstationary superposition of waves characterized by different frequencies and wave numbers. From Eq. (2.7), one can see that, at small distances from the boundary, $|x| \ll 1/k\gamma_1$, the phases of all waves are virtually coincident ($k_n x \cong kx$), this proving the validity of the approximation specified by Eqs. (2.3) and (2.6).

In order to solve the problem at hand, it only remains to find the modulation function for the reflected wave, $r(t)$. We know the wave functions at the boundary, and the continuity condition for these functions and their derivatives leads to the usual Fresnel formulas. For the quasistationary amplitude of the reflected wave, we find in this way that

$$r(t) = \frac{\sqrt{E} - \sqrt{E - V(t)}}{\sqrt{E} + \sqrt{E - V(t)}}. \tag{2.8}$$

[2)] A brief exposition of these results was given in [37].

[3)] The recent article of V. Ignatovich and F. Ignatovich [38] was devoted to the same problem. Referring to [37], those authors erroneously stated that only the case of a semi-infinite medium was considered there.

We note that the form of the wave function in the interior of matter remains unknown. The partial-wave amplitudes a_n, which are the Fourier coefficients in the expansion of $r(t)$, are therefore determined by the form of the time dependence of the potential and can be found for any periodic function $V(t)$.

In the case of grazing incidence to the boundary, the above formulas remain valid if one employs, instead of the wave vector k, its component $k_\perp$ orthogonal to the surface and by energy means the quantity $E_\perp = (\hbar^2/2m)k_\perp^2$. In accordance with Eqs. (2.7) and (2.8), reflection gives rise to a set of waves characterized by different normal wave-number components,

$$k_{\perp n} = k_\perp \left[1 + n\left(\frac{2m\Omega}{\hbar k_\perp^2}\right)\right]^{1/2}. \qquad (2.9)$$

Since the longitudinal component of the wave vector undergoes no change upon reflection, reflected waves corresponding to different satellites labeled with the index n differ in energy and have different reflection angles. The emerging pattern is qualitatively illustrated in Fig. 1.

The situation here resembles that in the case of diffraction at a plane grating; however, this similarity is purely apparent. Ordinary diffraction is described by the Fourier transform of coordinates and wave vectors, the difference of the wave vectors characterizing diffracted waves being determined by the reciprocal-lattice vector. In the case being considered, time and frequency (and, accordingly, energy) are conjugate variables of the Fourier transformation. All components of the pattern that arises upon reflection are associated with one quasienergy of the particle involved [23]. The energies of neighboring satellites differ by $\hbar\Omega$, the difference of their wave numbers being dependent on the satellite number n in a more a complicated way. Following the terminology proposed in [35], we will refer to this phenomenon as dynamic reflection.

Specifying the problem in order to adapt it to the potential of neutron optics and following [34], we assume that matter is a ferromagnet characterized by a time-dependent magnetic induction. The constant part of the potential V is then the effective rescattering potential

$$U = \frac{2\pi\hbar^2}{m}\rho b, \qquad (2.10)$$

which determines the neutron-optic properties of matter. Here, m is the neutron mass, ρ in the number of nuclei of matter per unit volume, and b is the coherent-scattering length. The time-dependent part of the potential is due to magnetic interaction and is given by

$$u(t) = -(\boldsymbol{\mu}\cdot\mathbf{B})(t), \qquad (2.11)$$

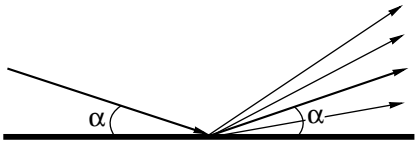

Fig. 1. Dynamic multiray reflection.

where $\boldsymbol{\mu}$ is the neutron-magnetic-moment operator and $\mathbf{B}$ is the magnetic-induction vector in matter. We assume that the incident neutron beam is polarized. In order to eliminate the spin-flip effect, we consider the situation where the magnetic-induction vector is aligned with the neutron spin.

By way of example, we consider a simple case where the intrinsic induction $\mathbf{B}$ changes sign instantaneously at regular time intervals of $T/2$. We then have

$$r_\pm(t) = \frac{\sqrt{E_p} - \sqrt{E_p - U_{\rm opt} \pm \mu B}}{\sqrt{E_p} + \sqrt{E_p - U_{\rm opt} \pm \mu B}}. \qquad (2.12)$$

The partial-wave amplitudes have the form

$$a_0 = \frac{r_+ + r_-}{2}, \quad a_n = \frac{r_+ - r_-}{\pi(2n-1)}, \qquad (2.13)$$

where n is an integer.

To conclude this section, we note that a nonstationary character of dynamic reflection considered above distinguishes it from the phenomenon that consists in nonspecular neutron reflection from magnets in the case of noncollinear orientation of the neutron spin and the magnetization vector and which was discovered a few years ago [39, 40]. In the latter case, the spin is flipped without any change in the total energy because the problem is stationary. In the presence of an external magnetic field B_0, the change in the potential energy by $2\mu B_0$ is accompanied by a change in the wave number and, hence, in the direction of wave propagation. There is no such effect in the absence of an external field.

3. NEUTRON REFLECTION AND REFRACTION AT THE BOUNDARIES OF MATTER FEATURING A ROTATING MAGNETIC-INDUCTION VECTOR

3.1. Reflection from a Semi-infinite Medium

In the preceding section, we excluded the problem of reflected-wave polarization from our consideration, assuming that the magnetic-induction vector is aligned with the neutron spin. We now consider the case where the magnetic induction in matter rotates at a constant frequency Ω. In contrast to the problem considered above, this problem can be solved exactly. Spin effects now become significant, and it is convenient to orient the initial spin along the z axis. We

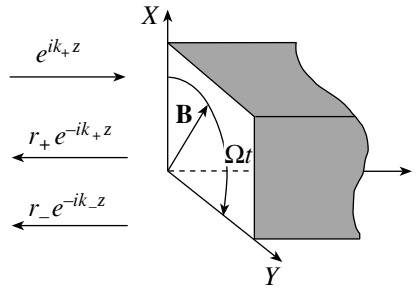

Fig. 2. Reflection of neutrons from a mirror featuring a rotating magnetization vector.

assume that, in a magnet, there is a magnetic field **B** that rotates in the xy plane and that the angular-velocity vector is aligned with the positive direction of the z axis. The orientation of the matter surface is arbitrary in a sense. The case where the induction-rotation plane is parallel to the matter boundary $z = 0$ seems realistic. The formulation of the problem is illustrated in Fig. 2.

Assuming an idealized picture, we set the magnetic field beyond matter to zero. As before, we solve the problem for the case of normal neutron incidence to the interface. Formulas (2.2), (2.10) and (2.11) for the interaction potential remain valid for this case as well.

For the region occupied by matter, the Schrödinger equation has the form

$$i\hbar\frac{\partial\Psi_\pm(z,t)}{\partial t} = -\frac{\hbar^2}{2m}\frac{\partial^2\Psi_\pm(z,t)}{\partial z^2} + [U - \hat{\boldsymbol{\mu}}\cdot\hat{\mathbf{B}}]\Psi_\pm(z,t), \quad z > 0. \tag{3.1}$$

Considering that

$$B_x = B\cos(\Omega t), \quad B_y = B\sin(\Omega t), \tag{3.2}$$

$$\hat{\boldsymbol{\mu}}\cdot\hat{\mathbf{B}}\Psi_\pm(z,t) = \mu(\sigma_x B_x + \sigma_y B_y)\Psi_\pm(z,t) = \mu B\exp(\mp i\Omega t)\Psi_\mp(z,t), \tag{3.3}$$

where σ_i are the Pauli matrices, we recast Eq. (3.1) into the form

$$i\hbar\frac{\partial\Psi_\pm(z,t)}{\partial t} = -\frac{\hbar^2}{2m}\frac{\partial^2\Psi_\pm(z,t)}{\partial z^2} + U\Psi_\pm(z,t) - \mu B\exp(\mp i\Omega t)\Psi_\mp(z,t), \tag{3.4}$$

where $\Psi_\pm$ are the wave functions corresponding to two spin projections onto the z axis. For the sake of definiteness, we assume that a plane wave incident to the mirror from the left is polarized along the positive direction of the z axis. From Eq. (3.4), it immediately follows that, in the solution, the time dependence factorizes explicitly in the form

$$\Psi_+(z,t) = \exp\left(-\frac{iEt}{\hbar}\right)\psi_+(z), \tag{3.5}$$

$$\Psi_-(z,t) = \exp\left(-\frac{i}{\hbar}(E-\hbar\Omega)t\right)\psi_-(z), \quad E \geq \hbar\Omega. \tag{3.6}$$

Since the wave functions $\psi_\pm(z)$ depend only on the coordinate, we will omit in the following the argument z for the sake of brevity. In the left half-space, where the motion being considered is free, the Schrödinger equation has the standard form

$$i\hbar\frac{\partial\Psi_\pm(z,t)}{\partial t} = -\frac{\hbar^2}{2m}\frac{\partial^2\Psi_\pm(z,t)}{\partial z^2}, \quad z < 0. \tag{3.7}$$

Substituting into it the wave functions (3.5) and (3.6) and following the conventional procedure, we obtain

$$\frac{\partial^2\psi_\pm}{\partial z^2} + k_\pm^2\psi_\pm = 0, \tag{3.8}$$

$$k_+ = \sqrt{\frac{2m}{\hbar^2}E}, \quad k_- = \sqrt{\frac{2m}{\hbar^2}(E-\hbar\Omega)}, \quad z < 0.$$

From (3.8), it immediately follows that spin-flip reflection is accompanied by changes in the energy and in the wave number. In the left half-space $z < 0$, the wave function has a conventional plane-wave form,

$$\psi_+ = \exp(ik_+z) + r_+\exp(-ik_+z), \qquad \psi_- = r_-\exp(-ik_-z), \tag{3.9}$$

where $r_\pm$ are the spin-flip and non-spin-flip amplitudes of reflected waves.

In the right half-space, which is occupied by matter, we have

$$\frac{\hbar^2}{2m}\frac{\partial^2\psi_+}{\partial z^2} + \varepsilon_\pm\psi_+ + \mu B\psi_\mp = 0, \tag{3.10}$$

$$\varepsilon_+ = E - U, \quad \varepsilon_- = E - U - \hbar\Omega, \quad z > 0.$$

The solution within matter will also be sought in the form of plane waves,

$$\psi_\pm = \tau_\pm\exp(i\eta z), \quad z > 0. \tag{3.11}$$

We must rely on the assumption—and our subsequent calculation confirms this assumption—that several waves having different wave numbers η correspond to the solution within matter. In order to find them, we substitute (3.11) into (3.10). We have

$$\left(\varepsilon_\pm - \frac{\hbar^2}{2m}\eta^2\right)\tau_\pm + \mu B\tau_\mp = 0. \tag{3.12}$$

For nonzero values of the amplitudes $\tau_\pm$, we find an expression for the square of the wave number of a neutron wave in matter. The result is

$$(\eta_{1,2})^2 = \frac{2m}{\hbar^2}\left(\frac{\varepsilon_+ + \varepsilon_-}{2} \pm \sqrt{\frac{(\varepsilon_+ - \varepsilon_-)^2}{4} + (\mu B)^2}\right). \tag{3.13}$$

Since, in taking yet another square root, one must use both signs, four solutions are possible in general for the wave number in matter; that is,

$$\psi_\pm = A_\pm \exp(i\eta_1 z) + B_\pm \exp(-i\eta_1 z) + C_\pm \exp(i\eta_2 z) + D_\pm \exp(-i\eta_2 z), \tag{3.14}$$

where

$$\eta_{1,2} = +\sqrt{\frac{2m}{\hbar^2}\left(\left(\varepsilon_+ - \frac{\hbar\Omega}{2}\right) \pm \sqrt{\left(\frac{\hbar\Omega}{2}\right)^2 + (\mu B)^2}\right)}; \tag{3.15}$$

here, only a positive sign is now taken in front of the outer radical. The indices 1 and 2 correspond to the plus and minus signs in front of the inner radical.

By assumption, the medium is not absorptive; therefore, $\eta_{1,2}$ can take only real or pure imaginary values. Since, in the region $z > 0$, there are no neutrons moving to the left and since the amplitude of a wave cannot grow, only the terms in (3.14) that feature the exponent $+i\eta_{1,2}z$ can have a physical meaning, irrespective of whether the wave number η has a real or a pure imaginary value. Therefore, the solution within the medium is sought in the form

$$\psi_\pm = A_\pm \exp(i\eta_1 z) + C_\pm \exp(i\eta_2 z), \quad z > 0. \tag{3.16}$$

The relation between the amplitudes of the waves corresponding to two spin projections can easily be found from the set of Eqs. (3.12):

$$A_- = \xi_1 A_+, \quad C_- = \xi_2 C_+, \tag{3.17}$$
$$\xi_{1,2} = \frac{1}{\mu B}\left(\frac{\hbar^2}{2m}\eta_{1,2}^2 - \varepsilon_+\right).$$

Matching the wave functions and their derivatives at the boundary of the medium in a conventional way, we find for the amplitudes of reflected waves that

$$r_+ = \frac{2(1-\nu)}{(1+\Lambda_1) - \nu(1+\Lambda_2)} - 1, \tag{3.18}$$
$$r_- = \frac{2(\xi_1 - \nu\xi_2)}{(1+\Lambda_1) - \nu(1+\Lambda_2)},$$

where

$$\Lambda_1 = \frac{\eta_1}{k_+}, \quad \Lambda_2 = \frac{\eta_2}{k_+}, \quad \nu = \frac{\xi_1}{\xi_2}\frac{k_- + \eta_1}{k_- + \eta_2}. \tag{3.19}$$

As to the reflection coefficients, their determination in the present case of waves featuring different wave numbers is somewhat different from the traditional one. Assuming, as usual, that the reflection coefficient specifies the reflected flux, we obtain

$$R_+ = |r_+|^2, \quad R_- = \frac{k_-}{k_+}|r_-|^2 \tag{3.20}$$

if the incident flux is normalized to unity.

For the normal-incidence case, which was considered above, the reflected waves corresponding to two spin projections are superposed in space. They differ in frequency and wave vector. In this case, the state of the reflected waves can be represented in a spinor form,

$$\Psi(z,t) = \begin{pmatrix} r_+ e^{-i(k_+ z + \omega_+ t)} \\ r_- e^{-i(k_- z + \omega_- t)} \end{pmatrix} \tag{3.21}$$
$$= \begin{pmatrix} r_+ e^{-ik_+ z} \\ r_- e^{i[-k_+(1-\gamma)^{1/2} z + \Omega t]} \end{pmatrix} e^{-i\omega t},$$

where $\gamma = \hbar\Omega/E$. A wave function of this form corresponds to a state that features a precessing spin. The precession angle is determined by the phase difference between the two spin components:

$$\varphi(z,t) = (k_- - k_+)z + \Omega t, \quad k_- = k_+(1-\gamma)^{1/2}, \tag{3.22}$$
$$k_+^2 - k_-^2 = \frac{2m}{\hbar}\Omega.$$

Taking this into account and introducing the average velocity $\tilde{v}$ for the two components in question [41], we arrive at an expression for the azimuthal angle of the spin vector. We have

$$\varphi(z,t) = \Omega\left(t - \frac{z}{\tilde{v}}\right), \quad \tilde{v} = \frac{\hbar}{m}\frac{k_+ + k_-}{2}. \tag{3.23}$$

In the approximation of low frequencies, $\gamma \ll 1$, the effective velocity $\tilde{v}$ coincides with the classical velocity. From (3.23), it follows that the direction of neutron spin is conserved in the rest fame moving at the neutron velocity $\tilde{v}$. However, it depends periodically on time, with the frequency Ω, at a fixed observation point z.

We will now analyze our results from the point of view of the energy dependence of the reflection coefficient. On the basis of formula (3.15), which determines the wave vectors $\eta_{1,2}$ in the medium, we can draw some conclusions on the character of reflection. For the sake of convenience, we introduce

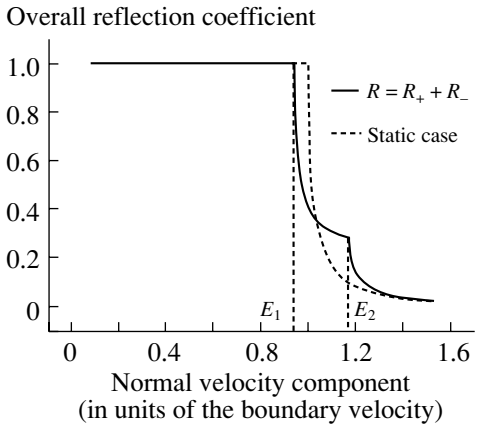

Fig. 3. Total reflection coefficient as a function of velocity. The calculation was performed at $U = 150$ neV, $B = 0.5$ T, and $f = 10$ MHz.

the following notation for two characteristic values of energy:

$$E_1 = U + \frac{\hbar\Omega}{2} - \sqrt{\left(\frac{\hbar\Omega}{2}\right)^2 + (\mu B)^2}, \qquad (3.24)$$

$$E_2 = U + \frac{\hbar\Omega}{2} + \sqrt{\left(\frac{\hbar\Omega}{2}\right)^2 + (\mu B)^2}. \qquad (3.25)$$

In the limit of low frequencies, this reduces to the trivial relation $E_{1,2} \cong U \mp \mu B$.

The range of incident-neutron energies can be partitioned into four regions. At extremely low energies, $E < \hbar\Omega$, the incident wave is completely reflected without changes in the spin projection or the frequency. In the subbarrier region $\hbar\Omega \le E < E_1$, there are two reflected waves differing in spin projection and frequency. Since the wave numbers $\eta_{1,2}$ are pure imaginary in this case, reflection is complete, so that the total flux in the reflected waves is equal to the incident flux. In the transition region near the barrier, $E_1 < E < E_2$, the wave vector η_1 is still imaginary, while η_2 is real-valued. The total reflection coefficient is less than unity. Finally, η_1 and η_2 are both real-valued in the above-barrier region $E > E_2$. In this case, both waves propagate freely in the medium, the reflection coefficient decreasing fast with increasing energy.

Figure 3 shows the calculated dependence of the total reflection factor $R = R_+ + R_-$ on the velocity. The ratio of the neutron velocity to the boundary velocity $v_0 = \sqrt{2U/m}$ is plotted along the abscissa. For the sake of comparison, we also present the curve representing the reflection coefficient for the usual static case, where matter is characterized exclusively by the effective potential. It can clearly be seen that the curve is characterized by two threshold velocities, which correspond to the energies $E_{1,2}$.

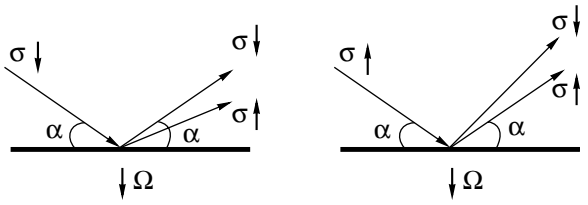

Fig. 4. Pattern of dynamic reflection from matter with a rotating induction vector for two orientations of the incident-wave spin.

In the case of grazing incidence, all of the calculations remain valid if, by k_+ and k_-, one means the wave-number components orthogonal to the surface of matter. In this case, we have two reflected waves that possess different normal and identical tangential components of the wave vector. As to the wave of initial polarization, it can be called a "usual" wave. For this wave, the reflection angle is equal to the incidence angle. A wave of inverse polarization is "unusual" in a sense. For it, reflection is not specular—that is, the reflection angle is not equal to the incidence angle. This distinction is determined by the frequency Ω exclusively. Both waves are coherent; therefore, the state of reflected waves can be described by a unified wave function

$$\Psi(z,t) = \begin{pmatrix} r_+ e^{i(k_x x + k_y y + k_+ z)} \\ r_- e^{i[k_x x + k_y y + k_+(1-\gamma)^{1/2} z - \Omega t]} \end{pmatrix} e^{-i\omega t}, \qquad (3.26)$$

which is similar to that in (3.21).

It is obvious that, if the incident wave is polarized in the negative direction of the z axis—that is, against the direction of the vector of the angular velocity of the magnetic induction—then the wave whose spin projection has changed has the frequency $E/\hbar + \Omega$, its wave number being greater than that of the incident wave. Both cases are illustrated in Fig. 4. In the case of an arbitrary spin orientation, there arise three reflected waves whose wave numbers have normal components equal to k, $k(1+\gamma)^{1/2}$, and $k(1-\gamma)^{1/2}$.

3.2. Transmission of Neutrons through a Thin Film Featuring a Rotating Magnetization Vector

The intensity of the unusual wave is sizable if the energy of incident neutrons does not differ significantly from the boundary energy (see Fig. 7 below). Above the barrier, the total reflection coefficient decreases fast. For neutrons of higher energy, it is

therefore of interest to consider the problem of neutron transmission through a slab of matter featuring a rotating magnetization vector.

Suppose that matter occupies the region $-L < z < L$. The problem at hand differs from that considered above by the presence of transmitted waves, their amplitudes being denoted by $\theta_\pm$. As before, a plus sign corresponds to the wave whose spin projection remains unchanged. In addition, there are now four waves propagating in the region $|z| < L$, which is occupied by matter, and having the wave numbers $\eta_{1,2}$ determined, as above, by Eq. (3.15). The corresponding wave function is still given by (3.14), while the relation between the amplitudes of the waves differing only by the spin projection is specified by formulas that are similar to (3.17).

In the region $z < -L$, the solution has the form (3.9), as before; for $z > L$, we obtain

$$\psi_+ = \theta_+ \exp(ik_+ z), \quad \psi_- = \theta_- \exp(ik_- z). \quad (3.27)$$

The calculations are simplified considerably if use is made of a well-known trick that consists in breaking down the wave function $\psi_\pm$ into the odd and the even component [42]. After that, the problems characterized by opposite parities are separated. For $|z| > L$, one can write

$$\psi_\pm(z) = \Phi_\pm + \varphi_\pm, \quad \psi_\pm(-z) = \Phi_\pm - \varphi_\pm, \quad |z| > L, \quad (3.28)$$

where $\Phi_\pm$ and $\varphi_\pm$ are, respectively, the even and the odd component of the wave function.

From (3.28), we obtain

$$\Phi_\pm = \frac{\psi_\pm(z) + \psi_\pm(-z)}{2}, \qquad \varphi_\pm = \frac{\psi_\pm(z) - \psi_\pm(-z)}{2}. \quad (3.29)$$

Substituting into (3.29) the solutions given by (3.9) and (3.27), we obtain

$$\Phi_+ = \frac{1}{2}[\exp(-ik_+ z) + \alpha_+ \exp(ik_+ z)], \qquad \Phi_- = \frac{1}{2}\alpha_- \exp(ik_- z), \quad (3.30)$$

where

$$\alpha_+ = r_+ + \theta_+, \quad \alpha_- = r_- + \theta_-. \quad (3.31)$$

Within matter, the even component of the wave function can be represented in the form

$$\psi_+ = A\cos(\eta_1 z) + B\cos(\eta_2 z), \qquad \psi_- = \xi_1 A\cos(\eta_1 z) + \xi_2 B\cos(\eta_2 z). \quad (3.32)$$

Matching the wave functions $\Phi_\pm$ with $\psi_\pm$ at the point $z = L$ in a conventional way, we obtain expressions for α_+ and α_- in the form

$$\alpha_+ = \exp(-2ik_+ L)\frac{\xi(\Theta + \Lambda_1\Lambda_2 g_1 g_2) + i[\Lambda_2 g_2(\xi_2 + \xi_1\Theta) - \Lambda_1 g_1(\xi_1 + \xi_2\Theta)]}{\xi(\Theta - \Lambda_1\Lambda_2 g_1 g_2) + i[\Lambda_2 g_2(\xi_2 - \xi_1\Theta) - \Lambda_1 g_1(\xi_1 - \xi_2\Theta)]}, \quad (3.33)$$

$$\alpha_- = \exp[-i(k_+ + k_-)L]\frac{2i\xi_1\xi_2(\Lambda_2 g_2 - \Lambda_1 g_1)}{\xi(\Theta - \Lambda_1\Lambda_2 g_1 g_2) + i[\Lambda_2 g_2(\xi_2 - \xi_1\Theta) - \Lambda_1 g_1(\xi_1 - \xi_2\Theta)]}, \quad (3.34)$$

where we have introduced the notation

$$g_{1,2} = \tan\eta_{1,2}L, \quad (3.35)$$

$$\Theta = \frac{k_-}{k_+} = \sqrt{\frac{E - \hbar\Omega}{E}}, \quad (3.36)$$

$$\Lambda_{1,2} = \eta_{1,2}/k_+, \quad \xi = \xi_1 - \xi_2. \quad (3.37)$$

For the odd solution in the region $|z| > L$, we have

$$\varphi_+ = \frac{1}{2}[\beta_+ \exp(ik_+ z) - \exp(-ik_+ z)], \qquad \varphi_- = \frac{1}{2}\beta_- \exp(ik_- z), \quad (3.38)$$

where

$$\theta_+ - r_+ = \beta_+, \quad \theta_- - r_- = \beta_-. \quad (3.39)$$

The odd component of the wave function in matter is

$$\varphi_+ = B\sin(\eta_1 z) + D\sin(\eta_2 z), \qquad \varphi_- = \xi_1 B\sin(\eta_1 z) + \xi_2 D\sin(\eta_2 z), \quad |z| < L. \quad (3.40)$$

From the continuity equations, we find for $\beta_\pm$ that

$$\beta_+ = \exp(-2ik_+L)\frac{\xi(\Theta g_1 g_2 + \Lambda_1\Lambda_2) + i[\Lambda_1 g_2(\xi_1 + \xi_2\Theta) - \Lambda_2 g_1(\xi_2 + \xi_1\Theta)]}{\xi(\Lambda_1\Lambda_2 - \Theta g_1 g_2) + i[\Lambda_2 g_1(\xi_2 - \xi_1\Theta) - \Lambda_1 g_2(\xi_1 - \xi_2\Theta)]}, \tag{3.41}$$

$$\beta_- = \exp[-i(k_+ + k_-)L]\frac{2i\xi_1\xi_2(\Lambda_1 g_2 - \Lambda_2 g_1)}{\xi(\Lambda_1\Lambda_2 - \Theta g_1 g_2) + i[\Lambda_2 g_1(\xi_2 - \xi_1\Theta) - \Lambda_1 g_2(\xi_1 - \xi_2\Theta)]}. \tag{3.42}$$

We can now readily find the amplitudes of the reflected and transmitted waves by using relations (3.31) and (3.39). We have

$$r_+ = \frac{\alpha_+ - \beta_+}{2}, \quad \theta_+ = \frac{\alpha_+ + \beta_+}{2}, \tag{3.43}$$
$$r_- = \frac{\alpha_- - \beta_-}{2}, \quad \theta_- = \frac{\alpha_- + \beta_-}{2}.$$

Defining, as before, the reflection and transmission coefficients as the densities of, respectively, the reflected- and the transmitted-wave flux under the assumption that the incident flux is equal to unity, we obtain

$$R_+ = |r_+|^2, \quad R_- = \frac{k_-}{k_+}|r_-|^2, \tag{3.44}$$
$$T_+ = |\theta_+|^2, \quad T_- = \frac{k_-}{k_+}|\theta_-|^2.$$

It is obvious that, in the case of normal incidence, the reflected and transmitted waves are superposed in space and are described by spinors that are similar to (3.21). For transmitted waves, we have

$$\Psi(z,t) = \begin{pmatrix} \theta_+ e^{ik_+ z} \\ \theta_- e^{i[k_+(1-\gamma)^{1/2}z + \Omega t]} \end{pmatrix} e^{-i\omega t}, \quad z > L. \tag{3.45}$$

Since transmitted waves corresponding to different spin projections differ in frequency and in the wave number, we deal, in the case of oblique incidence, with spatially separated waves, as before, the unusual wave, whose spin projection has changed, propagating in a direction that is different from the direction of incident-wave propagation. This difference is determined exclusively by the frequency Ω of rotation of the magnetic-induction vector. The emerging pattern is illustrated in Fig. 5.

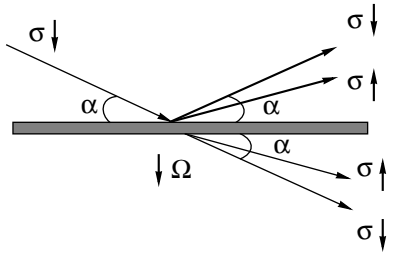

Fig. 5. Dynamic neutron reflection and refraction at the boundaries of a slab featuring a rotating magnetization vector.

3.3. Crossed Fields: Rabi's Flipper in the Presence of Matter

Having considered the case of neutron transmission through a slab featuring a single rotating field, we now address, for the sake of completeness, the case where there are in matter a constant magnetic field and a rotating magnetic field orthogonal to it [38]. Obviously, this is the problem of Rabi's resonance flipper in the presence of matter. As a matter of fact, a solution to this problem can be obtained from the above formulas. Suppose that we have a magnetic field of thickness $2L$, as before, and that, within it, there is a variable magnetic induction B whose components are

$$B_z = B_0, \quad B_x = B_1\cos(\Omega t), \quad B_y = B_1\sin(\Omega t). \tag{3.46}$$

As before, the spin of a neutron incident to this film is aligned with the z axis. The neutron now moves along the x axis (see Fig. 6).

For the region occupied by matter, the Schrödinger equation has the same form as that in (3.1). Substituting (3.46) into it, we obtain

$$i\hbar\frac{\partial\Psi_\pm(x,t)}{\partial t} = -\frac{\hbar^2}{2m}\frac{\partial^2\Psi_\pm(x,t)}{\partial z^2} \tag{3.47}$$

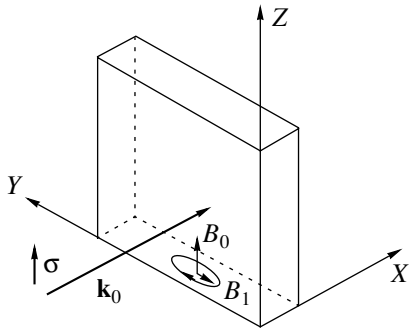

Fig. 6. Rabi's flipper in the presence of matter.

$$+ (U \mp \mu B_0)\Psi_\pm(x,t) - \mu B_1 \exp(\mp i\Omega t)\Psi_\mp(x,t).$$

The Schrödinger equation for the coordinate part of the wave function differs from (3.10) in the form of the magnetic field and in the definition of the quantities $\varepsilon_\pm$. We now have

$$\frac{\hbar^2}{2m}\frac{\partial^2\psi_+}{\partial x^2} + \varepsilon_\pm\psi_\pm + \mu B_1\psi_\mp = 0, \qquad (3.48)$$

$$\varepsilon_+ = E - U + \mu B_0,$$

$$\varepsilon_- = E - U - \mu B_0 - \hbar\Omega.$$

With allowance for (3.48), all formulas of the preceding section remain valid upon the substitution of B_1 for B. Further, we have

$$\eta_{1,2} \qquad (3.49)$$

$$= +\sqrt{\frac{2m}{\hbar^2}\left(\left(\varepsilon_+ - \frac{\hbar\Omega}{2}\right) \pm \sqrt{\left(\frac{\hbar\Omega}{2}\right)^2 + (\mu B_1)^2}\right)},$$

$$\xi_{1,2} = \frac{1}{\mu B_1}\left(\frac{\hbar^2}{2m}\eta_{1,2}^2 - \varepsilon_+\right). \qquad (3.50)$$

The solution to the problem at hand is given by (3.33)–(3.37) and (3.41)–(3.43) with allowance for the definitions in (3.48)–(3.50).

4. POSSIBILITY OF OBSERVATION AND APPLICATION

We have considered above a number of optical phenomena that arise in neutron-wave interaction with matter characterized by a variable potential. As far as we know, none of this has been observed experimentally so far. We will now briefly discuss the possibilities for an experimental observation of these phenomena and, in some cases, for their applications.

4.1. Dynamic Reflection and Refraction and Possibility for Controlling the Direction of Wave Propagation

In Subsection 3.1, we have obtained the reflection coefficients for the usual and unusual waves in the case of neutron reflection from a magnet featuring a time-dependent magnetization. Their behavior and specific values depend on several parameters, including the optical potential U, the magnetic induction B in matter, and the frequency Ω of rotation of the magnetic-induction vector. (In the quasistationary case, there is of course no dependence on the frequency.)

For the two waves, the reflection coefficients R_+ and R_- versus the velocity are shown in Fig. 7 according to the calculations based on Eqs. (3.17)–(3.20). We recall that the subscript "–" labels the wave undergoing spin-flip reflection and a change in the frequency. For the potential U, the magnetic induction in matter, and the frequency $f = \Omega/2\pi$ of rotation of the magnetic-induction vector, we used the values in this calculation that are identical to those in the calculation for Fig. 3. All of these seem quite realistic. As before, the ratio of the neutron-velocity component to the boundary velocity $v_0 = \sqrt{2U/m}$ is plotted along the abscissa.

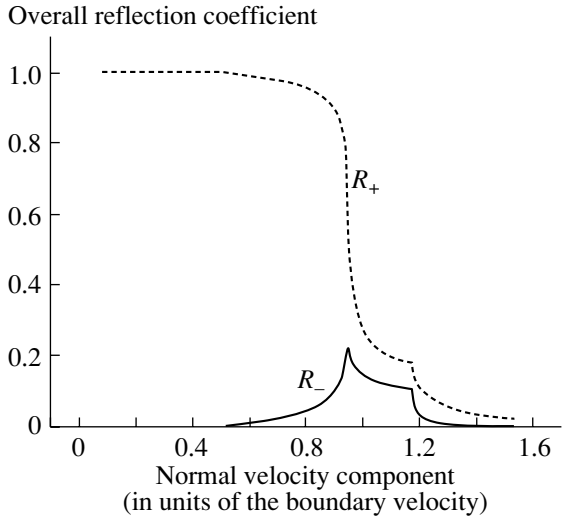

Fig. 7. Reflection coefficients for two waves. The potential U, the magnetic induction in matter, and the frequency of rotation of the magnetic-induction vector are identical to their counterparts in Fig. 3.

The reflection coefficient R_- for the unusual wave as a function of the velocity is displayed in Fig. 8 for various values of the frequency of rotation of the magnetization vector. Also shown there for the sake of comparison is the analogous curve calculated in the quasistationary approximation by formulas (2.12) and (2.13). The intensities of $n > 0$ waves are summed in order to obtain a more instructive picture. One can see that the reflection coefficient for the nonspecular wave depends rather weakly on the frequency and that its magnitude may be quite sizable. At low frequencies, the quasistationary calculation yields results that are rather close to precise ones. The effect is maximal at the incident-neutron energy close the threshold energy, $E \approx U$, and decreases fast with increasing energy.

In order to observe nonspecular dynamic reflection, it is necessary to ensure a sufficient angular separation of waves. From (3.8), it follows that the ratio of the normal components of two waves is

$$\frac{k_{-\perp}}{k_{+\perp}} = (1-\gamma)^{1/2}, \quad \gamma = \frac{\hbar\Omega}{E_\perp}, \quad E_\perp = \frac{\hbar^2}{2m}k_\perp^2, \qquad (4.1)$$

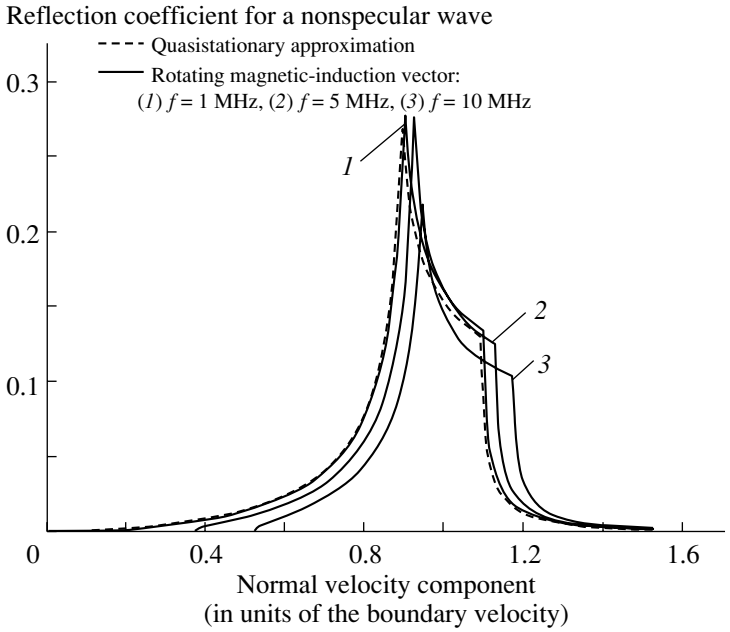

Fig. 8. Reflection coefficient R_- calculated in the quasistationary approximation and in the case of a rotating magnetic-induction vector. The potential U and the magnetic induction B in matter are identical to their counterparts in Figs. 3 and 7.

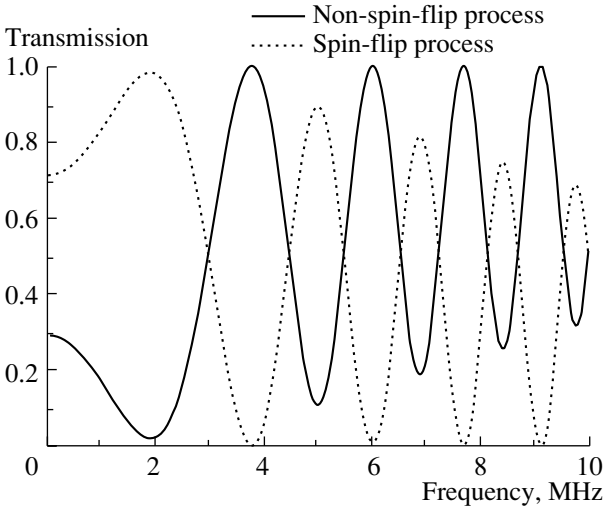

Fig. 9. Transmitted-wave intensity as a function of the frequency of rotation of the magnetic-induction vector. The calculation was performed at $B = 0.5$ T, $2L = 0.28$ mm, and $\lambda = 20$ Å.

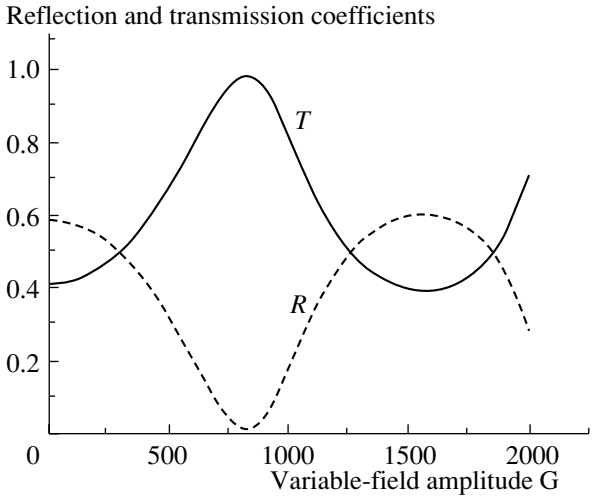

Fig. 10. Dynamic enhancement of the magnetic-field transparency featuring a variable field versus the amplitude of the radio-frequency field at $U = 150$ neV, $B_0 = -0.7$ T, $2L = 0.44$ μm, and $v = 6.4$ m/s.

where, in the last formula, it is assumed that $k_\perp \approx k_{\pm\perp}$. Since reflection is the strongest near the barrier and since the effective potential is about 10^{-7} eV for the majority of substances, we set $E_\perp \approx U \approx 150$ neV for estimates. Considering that a magnetization-reversal frequency of about 5 to 10 MHz is quite accessible in good magnetic materials, we set the cyclic frequency to $\Omega \approx 5 \times 10^7$ s^{-1}. The resulting estimate is $\gamma \approx 0.2$. Thus, the normal components of the two reflected waves differ quite sizably. Therefore, the effect of nonspecular reflection from matter featuring a rotating polarization vector can be detected with the aid of neutron reflectometers (see, for example, [43]). We note that the effect of nonspecular reflection from a vibrating surface was reliably measured in [33] at substantially lower frequencies of $f \approx 0.6-2.2$ MHz.

Let us now address the case of neutron transmission through a finite-thickness slab featuring a

rotating polarization vector. In this case, which we have already considered in Subsection 3.2, the energy of the motion in the direction orthogonal to the matter boundary, $E_\perp$, obviously must not fall below the potential U. If the excess of this energy above the barrier is not overly small, the total transmission factor tends to unity with increasing energy. (We disregard neutron absorption in the sample material.) In general, the amplitudes of transmitted waves depend on the same parameters as the amplitudes of reflected waves. In the case being considered, the slab thickness $2L$ is also an important parameter of the problem. For the case of a normal incidence of neutrons at a velocity of 200 m/s to a thin slab of matter, the transmitted-wave intensity calculated by formulas (3.33)–(3.37) and (3.41)–(3.43) is shown in Fig. 9 versus the frequency Ω of rotation of the magnetic-induction vector. The sample thickness and the magnetic-induction value used in the corresponding calculation are indicated in the caption under Fig. 9.

From this figure, it can be seen that one of the waves can be efficiently suppressed by varying the frequency of rotation, whereby a polarized wave that is characterized by the required direction of polarization is obtained at the output. Also, the intensities of the two waves can be equalized, in which case a state of transverse polarization is formed. Thus, we see that, in the geometry of transmission, the amplitude of the unusual wave can be commensurate with unity at rather large values of the normal neutron velocity as well.

In the geometry of grazing incidence, the waves are spatially separated, as is shown in Fig. 5. At small incidence angles α, the angle δ between the directions of propagation of the two waves is given by $\delta \approx \alpha\gamma/2$. We note that, since $k_\perp \approx \alpha k$ (where k is the total wave number), it follows from the definition in (4.1) that $\gamma \propto \alpha^{-2}$ and $\delta \propto \alpha^{-1}$. Estimates show that the spatial separation of the waves can easily be observed experimentally in this case inclusive.

We emphasize once again that the angle δ is proportional to the frequency Ω. Thus, there arises the unusual possibility of controlling the direction of the reflected or the transmitted wave by merely varying the frequency of rotation of the magnetization vector.

4.2. Dynamic Enhancement of Thin-Film Transparency

Let us briefly dwell upon yet another intriguing circumstance. The presence of many parameters in the problem of neutron transmission through matter in the presence of a variable magnetic field makes it possible to vary the optical properties of the system within a wide range. By way of example, we consider

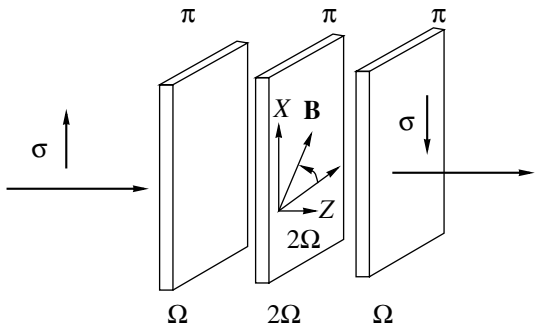

Fig. 11. Nonstationary spin interferometer employing nonseparated beams.

ultracold-neutron transmission through a resonance flipper in the presence of matter (see Subsection 3.3). In this case, the parameters of the device can be chosen in such a way that the total transmission of the system proves to be strongly dependent on the amplitude of the variable field. This situation is illustrated in Fig. 10. The values of the optical potential and of the constant magnetic field, as well as the film thickness, are indicated in the caption under the figure. The frequency corresponds to the resonance value $\Omega = 2\mu B_0/\hbar$.

Since the effect of the dynamic suppression of reflection (dynamic enhancement of film transmission) exists only in a very narrow range of the above parameters, it is difficult to state whether this effect may be of any practical importance.

4.3. Spin Flipper on the Basis of a Magnet Featuring a Variable Induction, Resonance Spin Echo, and Time Interferometer

Leaving aside, for the time being, the problem of the direction of unusual-wave propagation, we now focus on the polarization state of waves that traversed the slab of matter characterized by a variable magnetic induction. As can be seen from Fig. 9, a sample featuring a rotating magnetization vector is an efficient spin flipper. At specific values of the optical potential, magnetic induction, and sample thickness, one can always choose the frequency of rotation of the magnetic-induction vector in such a way as to obtain the preset relation between the intensities of waves that have opposite spin projections.

Herein lies the distinction between this device and the flipper featuring crossed fields, which was considered in Subsection 3.3. In the latter case, it is necessary to ensure fulfillment of two conditions simultaneously. First, the frequency of the variable field B_1 must be close to the resonance frequency $\Omega = 2\mu B_0/\hbar$; second, the amplitude of the field B_1 must be unambiguously related to the time of flight through matter.

By way of example, we indicate that, for the sign of polarization to be reversed (spin rotation through an angle π), the time of flight through the slab must satisfy the condition

$$t = \frac{2L}{v} = \frac{\pi\hbar}{2\mu B_1},$$

where v is the neutron velocity in matter.

The main advantage of a flipper featuring a magnet over a conventional resonance flipper is likely to be associated with its well-defined dimensions. This is of paramount importance, for example, in devices that employ the method of a resonance spin echo in zero field [44–47]. Below, we illustrate this circumstance for a specific example.

In this connection, we will consider one of the possibilities of the application of a flipper featuring a rotating magnetic induction. We mean a device that, on an equal footing, can be referred to as a spin [48] or a time [24–26] neutron interferometer. It is shown schematically in Fig. 11. Suppose that a neutron traverses successively three slabs featuring a rotating magnetization vector, the parameters of the devices being such that each of them reverses the spin direction—that is, each is a π flipper. In addition, the frequency of rotation of the magnetic-induction vector in the second slab is twice as high as that in the first and third slabs. (At a preset neutron energy, this imposes constraints on the relations between the slab thicknesses.) We also assume that the initial spin direction is parallel to the slab plane and, hence, to the plane of rotation of the magnetic-induction vector and that the slabs are equally spaced, the distance between them being denoted by D.

Choosing the z axis for a quantization axis, we represent the input neutron wave function in the form

$$\psi(z,t) = \frac{1}{\sqrt{2}}\begin{pmatrix}1\\1\end{pmatrix}\exp[i(kz-\omega t)]. \qquad (4.2)$$

Without considering here reflected waves, we assume, for the sake of simplicity, that the flipper under study is perfect, so that $|\theta_+| = 0$ and $|\theta_-| = 1$. In accordance with (3.45), the wave function immediately after the first flipper has the form

$$\psi(z,t) = \frac{1}{\sqrt{2}}\begin{pmatrix}e^{i[k(1+\gamma)^{1/2}z - \Omega t]}\\ e^{i[k(1-\gamma)^{1/2}z + \Omega t]}\end{pmatrix}e^{-i\omega t}. \qquad (4.3)$$

We recall that, for states in which the spin has opposite orientations with respect to the angular-velocity vector, the change in the energy, $\Delta E = \hbar\Omega$, has opposite signs. From (4.3), it follows that, at the point of fixed coordinates, the spin precesses about the z axis at the frequency 2Ω. When the neutron wave being considered reaches the second flipper, the corresponding phases are

$$\varphi_\pm^{(2)} \cong k(1\pm\gamma/2)D \mp \Omega t_1, \quad t_1 = \frac{D}{\tilde{v}}, \qquad (4.4)$$
$$\tilde{v} = \frac{\hbar}{m}\frac{k_+ + k_-}{2} \cong v \ (\gamma \ll 1),$$

the precession angle being equal to the difference of these phases. The second π flipper interchanges the spinor components and changes the frequency of each wave-function component by 2Ω. Immediately downstream of this flipper, we have

$$\psi(z,t) \qquad (4.5)$$
$$= \frac{1}{\sqrt{2}}\begin{pmatrix}e^{i[\varphi_-^{(2)} + k(1+\gamma/2)(z-D) - \Omega(t-t_1)]}\\ e^{i[\varphi_+^{(2)} + k(1-\gamma/2)(z-D) + \Omega(t-t_1)]}\end{pmatrix}e^{-i\omega t}.$$

From (4.4) and (4.5), one can see that, immediately upstream of the third flipper, the phase difference between two wave-function components is zero since the distance between the second and the third flipper is also equal to D. Thus, the third flipper will restore the original neutron energy by changing once again the frequencies of both wave-function components by Ω. As to the polarization of the final state, it will be opposite to the initial polarization.

We will show that this device is indeed analogous to an interferometer. Suppose that a matter slab of thickness d that is characterized by the refraction factor n and which is transparent to neutrons is inserted into the gap between one of the flipper pairs. On the basis of classical concepts, we find that the time of neutron propagation between the flippers will increase by

$$\Delta t = \frac{1-n}{n}\frac{d}{v} \approx (1-n)\frac{d}{v}, \qquad (4.6)$$

this being due to the difference of the neutron velocity in matter, nv, from the vacuum value v. Accordingly, the phase difference between the wave-function components—it can be associated with the angle of precession about the z axis—will increase by $\Delta\phi = 2\Delta t\Omega$. Thus, the direction of polarization upon the traversal of the system will change by $\Delta\phi$, and this is measurable experimentally. The same result can be obtained on the basis of wave concepts by calculating, for each wave-function component individually, the phase shift associated with refraction in matter [48]. The effect of time delay due to refraction in the sample [see Eq. (4.6)] was reliably measured in experiments with neutrons whose spin precessed in a constant magnetic field [49, 50]. We note that the time delay (4.6) is proportional to the cube of the wavelength, so that the effect is especially pronounced for ultracold neutrons. In view of this, the possibility of creating

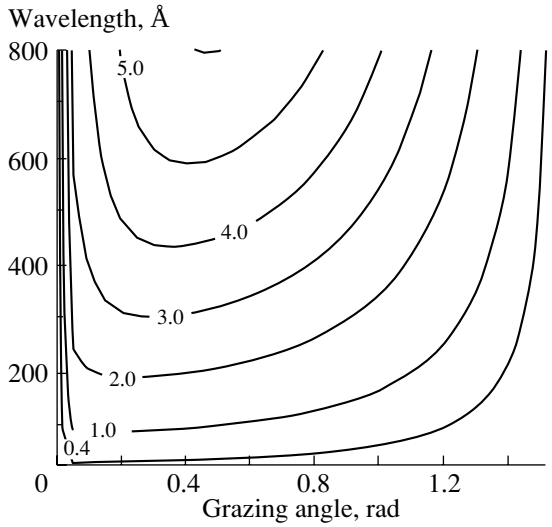

Fig. 12. Ratio of the splitting powers of a nonstationary wave splitter at frequency $\Omega = 7$ MHz and of a diffraction grating of spatial period 1 μm.

an interferometer of this type for ultracold neutrons seems appealing [51].

In this connection, we will now estimate the required accuracy in positioning flippers in such an interferometer. Obviously, fulfillment of the criterion

$$\Delta D \ll (k\gamma)^{-1} \tag{4.7}$$

is a necessary condition.

On the basis of the neutron-velocity and frequency values of $v = 8$ m/s and $\Omega = 2\pi f \approx 2.5 \times 10^6$ s^{-1}, respectively, which seem realistic, we obtain the estimate $(k\gamma)^{-1} \approx 2 \times 10^{-4}$ cm. Thus, the positions of the flippers must be fixed to a submicron precision. In the case of flippers based on thin magnetic films, which is considered here, this nontrivial problem can be solved, in all probability, but the application of conventional resonance flippers is absolutely impossible. We also note that, at a fixed flipper frequency, the factor $(k\gamma)^{-1}$ is proportional to neutron velocity.

4.4. Wave-Front Splitting and Spacetime Interferometer

The spin interferometer considered above is one of the interferometers that involve spatially superposed waves and which have been proposed in recent years. In this section, we consider the question of whether a slab featuring a rotating induction vector can be applied as a coherent wave splitter, which, as is well known, is the main element of an interferometer involving a spatial separation of waves. It is reasonable to compare this device with a conventional diffraction grating since not only do neutron interferometers employing diffraction gratings exist, but they also were

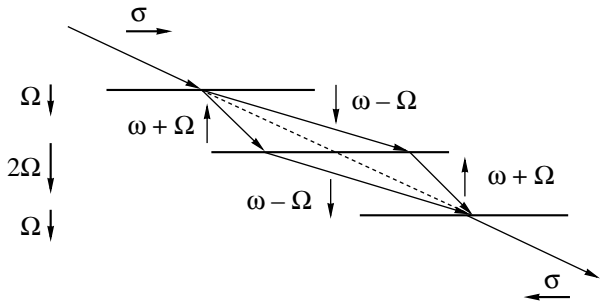

Fig. 13. Interferometer involving a spatial separation of waves on the basis of nonstationary spin flippers.

successfully applied in a number of fundamental experiments [52–56]. In the case of a normal incidence of a wave to a grating of period a, the angular separation of waves is obviously $\delta = 2\lambda/a$. In the case of a normal incidence of a wave to a nonstationary device, there is no angular separation. However, the situation changes in the case of grazing incidence. At small grazing angles, the effective grating period is αa, so that $\delta \propto \lambda/\alpha$. For a nonstationary wave splitter, we have

$$\delta \approx \alpha\frac{\gamma}{2} = \alpha\frac{\hbar\Omega}{2E} \propto \alpha\frac{\Omega}{k_\perp^2}.$$

Since $k_\perp = \alpha k$, we have $\delta \propto \lambda^2/\alpha$ in this case. Therefore, it turns out that, over a rather wide region of wavelengths and grazing angles, a nonstationary wave splitter possesses better splitting properties than a diffraction grating [37]. This circumstance is illustrated in Fig. 12. We also note that, in a resonance splitter, the entire wave intensity is partitioned between two waves, but, in the case of a grating, there is always a set of waves differing in the diffraction order; of these, only two take part in the formation of the interference pattern.

To be more specific, we also present a scheme of a possible interferometer that involves a spatial separation of waves and which employs nonstationary spin flippers (see Fig. 13). Shown on the left of the figure are the vector of the magnetization angular velocity and the frequencies for three flippers. The frequency of the wave function and the spin direction are indicated near the corresponding waves.

5. CONCLUSION

We have considered some optical phenomena that arise in the interaction of a neutron wave with matter characterized by a variable potential. The time dependence of the interaction potential is due to a time variation of the magnetization vector in matter. A nonstationary character of the interaction implies a change in the neutron energy. Since it has been

assumed in all cases that the incident wave interacts with a sample that has a plane surface, a change in the neutron energy leads to a change only in the neutron-velocity component orthogonal to the matter boundary. Thus, reflected waves are characterized by a reflection angle differing from the incidence angle. Waves transmitted through a plane sample may also change the direction of their propagation. A change in the energy of a neutron and in the direction of its velocity is closely related to the reversal of the neutron-spin projection. This relation is unambiguous in the case of a rotating magnetization vector. The wave that retains the initial polarization upon the interaction with a sample is referred to as a usual wave, the direction of its propagation is identical to that in the static case.

Thin samples of a magnetic substance featuring a rotating magnetization vector can serve as efficient spin flippers and coherent wave splitters. In some cases, such coherent splitters may be more efficient than modern diffraction gratings.

ACKNOWLEDGMENTS

We are grateful to A.A. Skoblin for significant assistance at the initial stage of this research. We are also indebted to V.G. Nosov and E.I. Kats for stimulating discussions.

This work was supported by INTAS (grant no. 00-00043).

REFERENCES

1. I. I. Rabi, Phys. Rev. **51**, 652 (1937).
2. I. I. Rabi, J. R. Zacharias, S. Milman, and R. Kush, Phys. Rev. **53**, 318 (1938).
3. L. W. Alvarez and F. Bloch, Phys. Rev. **57**, 111 (1940).
4. N. F. Ramsey, Phys. Rev. **76**, 996 (1949).
5. G. M. Drabkin and R. A. Zhitnikov, Zh. Éksp. Teor. Fiz. **38**, 1013 (1960) [Sov. Phys. JETP **11**, 729 (1960)].
6. E. Kruger, Nucleonics **25**, 889 (1980).
7. B. Alefeld, G. Badurek, and H. Rauch, Z. Phys. B **41**, 231 (1981).
8. H. Wenfurter, G. Badurek, H. Rauch, and D. Schwahn, Z. Phys. B **72**, 195 (1988).
9. G. Badurek, H. Rauch, and J. Summhammer, Phys. Rev. Lett. **51**, 1015 (1983).
10. G. Badurek , H. Rauch, and D. Tuppinger, Phys. Rev. A **34**, 2600 (1986).
11. J. Summhammer, Phys. Rev. A **47**, 556 (1993).
12. J. Summhammer, K. A. Hamacher, H. Kaiser, *et al.*, Phys. Rev. Lett. **75**, 3206 (1995).
13. J. Summhammer, Phys. Rev. A **54**, 3155 (1996).
14. E. Iolin, B. Farago, F. Mezei, *et al.*, Physica B (Amsterdam) **241–243**, 1213 (1998).
15. W. A. Hamilton, A. G. Klein, G. I. Opat, and P. A. Timmins, Phys. Rev. Lett. **58**, 2770 (1987).
16. I. M. Frank, Report No. R4-8851, OIYaI (Joint Inst. Nucl. Res., Dubna, 1975).
17. M. Moshinsky, Phys. Rev. **88**, 625 (1952).
18. R. Gähler and R. Golub, Z. Phys. B **56**, 5 (1984).
19. J. Felber, R. Gähler, and R. Golub, Physica B (Amsterdam) **151,** 135 (1988).
20. J. Felber, G. Muller, R. Gähler, and R. Golub, Physica B (Amsterdam) **162**, 191 (1990).
21. Th. Hils, J. Felber, R. Gähler, *et al.*, Phys. Rev. A **58**, 4784 (1998).
22. V. G. Nosov and A. I. Frank, J. Mosc. Phys. Soc. **1**, 1 (1991).
23. Ya. B. Zel'dovich, Zh. Éksp. Teor. Fiz. **51**, 1492 (1966) [Sov. Phys. **24**, 1006 (1966)].
24. A. I. Frank and V. G. Nosov, Yad. Fiz. **57**, 1029 (1994) [Phys. At. Nucl. **57**, 968 (1994)].
25. A. I. Frank and V. G. Nosov, Ann. N.Y. Acad. Sci. **755**, 293 (1995).
26. J. Felber, R. Gähler, R. Golub, *et al.*, Found. Phys. **29**, 381 (1999).
27. V. G. Nosov and A. I. Frank, Phys. Lett. A. **188**, 120 (1994).
28. A. I. Frank, S. N. Balashov, I. V. Bondarenko, *et al.*, Phys. Lett. A **311**, 6 (2003).
29. A. I. Frank and R. Gähler, Yad. Fiz. **63**, 605 (2000) [Phys. At. Nucl. **63**, 545 (2000)].
30. A. I. Frank, R. Geltenbort, G. V. Kukulin, and A. N. Strepetov, Pis'ma Zh. Éksp. Teor. Fiz. **78**, 224 (2003) [JETP Lett. **78**, 188 (2003)].
31. A. Stean, P. Szriftgiser, P. Desbiolles, and J. Dalibard, Phys. Rev. Lett. **74**, 4972 (1995).
32. M. Arndt, P. Szriftgiser, J. Dalibard, and A. M. Steane, Phys. Rev. A **53**, 3369 (1996).
33. J. Felber, R. Gähler, C. Rausch, and R. Golub, Phys. Rev. A **53**, 319 (1996).
34. A. S. Gerasimov and M. V. Kazarnovskiĭ, Zh. Éksp. Teor. Fiz. **71**, 1700 (1976) [Sov. Phys. JETP **44**, 892 (1976)]
35. D. L. Haaving and R. Reifenberge, Phys. Rev. B **26**, 6408 (1982).
36. A. I. Frank and D. B. Amandzholova, Ann. N.Y. Acad. Sci. **755**, 858 (1995); A. B. Amandzholova, V. G. Nosov, and A. I. Frank, Poverkhnost': Rentgenovskie, sinkhrotronnye i neĭtronnye issledovaniya **9**, 78 (1996).
37. A. I. Frank and A. V. Kozlov, in *Proceedings of the V International Seminar on Interaction of Neutrons with Nuclei (ISINN-5), Dubna, Russia, 1997*, E3-97-213 (Dubna, 1997), p. 411.
38. V. Ignatovich and F. Ignatovich, Am. J. Phys. **71**, 1013 (2003).
39. G. P. Felcher, S. Adenwalla, V. O. de Haan, and A. A. van Well, Nature **377**, 409 (1995).
40. D. A. Korneev, V. I. Bodnarchuk, and V. K. Ignatovich, J. Phys. Soc. Jpn., Suppl. A **65**, 7 (1996).
41. A. M. Kamchatnov, V. G. Nosov, and A. I. Frank, in *Proceedings of the 1st International Conference on Neutron Physics, Kiev, 1987* (TsNIIatominform, Moscow, 1988), Vol. 1, p. 241.

42. S. Flugge, *Practical Quantum Mechanics* (Springer-Verlag, Berlin, 1971; Mir, Moscow, 1974).
43. *Neutron Optical Devices and Applications*, Ed. by C. Majkrzak and J. Wood, SPIE Proc., Vol. 1738 (1992).
44. R. Golub and R. Gähler, Phys. Lett. A **123**, 43 (1987).
45. R. Gähler and R. Golub, J. Phys. (France) **49**, 1195 (1988).
46. T. Keller, P. Zimmermann, R. Golub, and R. Gahler, Physica B **162**, 327 (1990).
47. T. Keller, B. Keimer, K. Habicht, *et al.*, in *Neutron Spin Echo Spectroscopy: Basics, Trends and Applications* (Lecture Notes in Physics, Vol. 601), Ed. by F. Mezei, C. Pappas, and T. Gutbertlet (Springer, 2002), p. 74.
48. V. G. Baryshevskii, S. V. Cherepitsa, and A. I. Frank, Phys. Lett. A **153**, 299 (1991).
49. A. I. Frank, I. V. Bondarenko, A. V. Kozlov, *et al.*, Physica B **297**, 307 (2001).
50. A. I. Frank, I. Anderson, I. V. Bondarenko, *et al.*, Yad. Fiz. **65**, 2066 (2002) [Phys. At. Nucl. **65**, 2009 (2002)].
51. A. I. Frank, I. V. Bondarenko, A. V. Kozlov, *et al.*, in *Neutron Spin Echo Spectroscopy: Basics, Trends and Applications* (Lecture Notes in Physics, Vol. 601), Ed. by F. Mezei, C. Pappas, and T. Gutbertlet (Springer, 2002), p. 165.
52. A. I. Ioffe, Nucl. Instrum. Methods Phys. Res. **204**, 565 (1983).
53. A. I. Ioffe, Nucl. Instrum. Methods Phys. Res. A **268**, 169 (1988).
54. A. Ioffe, V. Zabiyakin, and G. Drabkin, Phys. Lett. A **111**, 373 (1985).
55. M. Gruber, K. Eder, A. Zeilinger, *et al.*, Phys. Lett . A **140**, 363 (1989).
56. G. van der Zouw, M. Weber, J. Felber, *et al.*, Nucl. Instrum. Methods Phys. Res. A **440**, 568 (2000).

Translated by A. Isaakyan

Physics of Atomic Nuclei, Vol. 68, No. 7, 2005, pp. 1120–1132. Translated from Yadernaya Fizika, Vol. 68, No. 7, 2005, pp. 1165–1178.

NUCLEI
Theory

Puzzle of the ^{6}Li Quadrupole Moment: Steps toward Solving It

L. D. Blokhintsev, V. I. Kukulin, and V. N. Pomerantsev

Institute of Nuclear Physics, Moscow State University, Vorob'evy gory, Moscow, 119899 Russia

Received June 10, 2004; in final form, December 10, 2004

Abstract—The problem of the origin of the quadrupole deformation in the ^{6}Li ground state is investigated with allowance for the three-deuteron component of the ^{6}Li wave function. Two long-standing puzzles related to the tensor interaction in the ^{6}Li nucleus are known: that of an anomalous smallness of the ^{6}Li quadrupole moment (being negative, it is smaller in magnitude than the ^{7}Li quadrupole moment by a factor of 5) and that of an anomalous behavior of the tensor analyzing power T_{2q} in the scattering of polarized ^{6}Li nuclei on various targets. It is shown that a large (in magnitude) negative exchange contribution to the ^{6}Li quadrupole moment from the three-deuteron configuration cancels almost completely the "direct" positive contribution due to the αd folding potential. As a result, the total quadrupole moment proves to be close to zero and highly sensitive to fine details of the tensor nucleon–nucleon interaction in the ^{4}He nucleus and of its wave function. © *2005 Pleiades Publishing, Inc.*

1. INTRODUCTION AND FORMULATION OF THE PROBLEM

At the present time, it seems that $A = 6$ nuclei have been quite thoroughly studied on the basis of various nuclear models, including fully microscopic [1–3], few-particle [4–10], and macroscopic ones. Almost all of the observables of their ground and low-lying excited states were explained in this way. In particular, the multicluster $(\alpha + 2N)$ model without antisymmetrization (MDMP) or with a subsequent antisymmetrization of variational wave functions (AMDMP) [4–8], where the symmetric S-wave alpha-particle component $|s^4[4]L = S = T = 0\rangle$ was taken for a nonexcited core, proved to be quite successful. Similar fully symmetric S-wave components of alpha-cluster wave functions are postulated in almost all of the alpha-cluster nuclear models (for example, in the Brink alpha-cluster model), as well as in numerous calculations of the structure of light nuclei and of the interaction of clusters by the resonating-group method [11, 12]. In the AMDMP approach, it was tacitly assumed that the D-wave component in the ^{4}He wave function—this component corresponds to an admixture of highly excited shell-model configurations of the $|s^2p^2[22]L = S = 2, T = 0\rangle$ type—does not play any significant role in the structure of light nuclei that include alpha-particle clusters, so that it can be disregarded without spoiling the quality of respective predictions [4–12]. It seemed that this assumption is well confirmed by the success of multicluster models in predicting the properties of $A = 6$, 7, and 9 nuclei [4–10, 13, 14]. Here, there is one important exception, however—the ^{6}Li quadrupole moment ($Q^{\text{expt}}(^6\text{Li}) = -0.083$ fm^2) was not reproduced, either in magnitude or in sign, by dynamical calculations based on the $(\alpha + 2N)$ model with a subsequent antisymmetrization or without it [4–9].

In simple αd-cluster models of the ^{6}Li nucleus, a negative value can be readily obtained for the quadrupole moment in question by assuming that the tensor αd potential has the form of a short-range purely attractive well [15–17], since, for the small D-wave component of the αd-cluster wave function, this leads to a sign that is opposite to the sign of the S-wave component, which is dominant. However, this character of the tensor αd potential is unsatisfactory in two respects. First, the tensor analyzing powers in polarized-deuteron scattering on ^{4}He nuclei [18–20] cannot be reproduced with such a potential. Second, potentials of this form are in a glaring contradiction with the tensor αd potential obtained from the folding model. It should be emphasized that, in all other cases of polarized-deuteron scattering on medium-mass nuclei, experimental data on tensor analyzing powers are rather well described with the tensor interaction obtained on the basis of the folding model [18–20]. Moreover, a series of recent studies reported in [21–23] showed that the tensor αd potential has a strong even–odd splitting (that is, it depends strongly on the parity of the angular momentum), the tensor αd potential being highly dissimilar to the folding-model potential in even waves and rather close to it in odd waves [23]. Moreover, those studies revealed a strong and nonmonotonic energy dependence of both the tensor and

the spin–orbit component of the αd potential, and this also calls for an explanation.

At the same time, fully microscopic six-nucleon calculations performed within the multiconfiguration shell model (so-called no-core shell model [3]) with realistic two- and three-nucleon forces lead to rather accurate predictions for the ^{6}Li quadrupole moment and for other properties of $A = 6$ nuclei. Moreover, microscopic six-nucleon calculations by the Monte Carlo method [1, 2] also yield a negative value of the ^{6}Li quadrupole moment, but it is overestimated in magnitude by a factor of 5. In those calculations, tensor mixing was fully taken into account in ^{4}He (that is, the D-wave component of the ^{4}He wave function was incorporated in the calculations). In view of this, it would be tempting to assume that the disregard of this component in traditional alpha-cluster models and in the AMDMP is precisely the factor that is responsible for the discrepancies in the results for the ^{6}Li quadrupole moment. However, the actual situation is more intricate. The point is that, in the case of the ^{6}Li nucleus, the aforementioned fully microscopic models lead to large errors in the binding energy of this nucleus in the αd cluster channel. In this channel, either the ^{6}Li nucleus proves to be unbound [1–3], or its binding energy appears to be strongly underrated in relation to its experimental counterpart. As was indicated in [14], so strong a change in the binding energy in the αd cluster channel is expected to change the quadrupole moment significantly (as occurs, for example, in the deuteron or in the ^{7}Li nucleus). In view of this, the authors of [14] assume that the agreement attained for the ^{6}Li quadrupole moment within the microscopic models in [1, 2] is accidental to a considerable extent and cannot underlie a reliable explanation of the nature of the quadrupole deformation in the ^{6}Li nucleus.

There are two more paradoxes closely related to the puzzle of the quadrupole deformation and the origin of the tensor interaction in the ^{6}Li nucleus. The first problem concerns the tensor analyzing power for the scattering of polarized $^6\overrightarrow{\text{Li}}$ and $^7\overrightarrow{\text{Li}}$ nuclei on medium-mass target nuclei (for example, Ni or Zr). Although the quadrupole moments of ^{6}Li and ^{7}Li are negative (that is, the charge distributions in these nuclei are oblate in the spin direction), the quantities T_{2q} have opposite signs for the scattering of $^6\overrightarrow{\text{Li}}$ and $^7\overrightarrow{\text{Li}}$ on Ni or Zr nuclei. Although the relationship between the quadrupole deformation of the projectile nucleus and the sign of T_{2q} was successfully explained in [17] for the case of ^{7}Li, the analogous explanation is inapplicable to the case of ^{6}Li.

Thus, there is quite a wide range of as-yet-unresolved problems that are associated with the origin of the quadrupole deformation and tensor interaction in the ^{6}Li nucleus. Our present study is devoted to clarifying these problems on the basis of available information about the structure of the D-wave component in ^{4}He and about the properties of the central ^{4}Hed potential. We formulate here a model of the tensor ^{4}Hed interaction, relying on the exchange mechanism where there occurs the interchange of a projectile ("external") deuteron and one of the deuterons entering into the composition of the ^{4}He core. The tensor potential generated by this mechanism is entirely due to the contribution of the D-wave state of the core, the corresponding shell-model configuration being $|s^2p^2[22]L = 2, S = 2, J = 0\rangle$. The main result of the present study can be formulated as follows: the above exchange mechanism makes a negative contribution of large magnitude to the ^{6}Li quadrupole moment, and this contribution cancels almost completely the positive contribution from the direct mechanism that is caused by the D-wave component of the wave function describing the motion of the external deuteron with respect to the ^{4}He core. To put it otherwise, we show that the puzzle of the quadrupole deformation of the ^{6}Li nucleus can be solved by employing the special tensor properties of the three-deuteron component in the wave function for this nucleus.

2. ORIGIN OF TENSOR MIXING IN THE ^{4}He AND ^{6}Li NUCLEI

2.1. Tensor Mixing and Internal Quadrupole Deformation in ^{4}He

Let us first discuss some special features of the tensor mixing in ^{4}He, which were partly missed in previous studies (see [24] and references therein to the studies of other authors). It is well known that the D-wave component in the alpha particle, the weight of this component varying between 10 and 16% in various models [25], includes, in addition to other configurations, that whose structure is $|s^2p^2[22]L = 2, S = 2, T = 0\rangle$. This is precisely the configuration that is directly related to the cluster dd configuration in ^{4}He, although the weight of the latter is about 2.2% [26], constituting only a small fraction of the total weight of the D wave in ^{4}He. Within the oscillator shell model, the wave function for the ^{4}He ground state is represented as the superposition

$$\begin{aligned}|^4\text{He}\rangle &= a_1|(0s)^4[4]L = 0, ST = 00\rangle \\ &+ a_2|(0s)^2(1p)^2[4]L = 0, ST = 00\rangle \\ &+ a_3|(0s)^2(1p)^2[22]L = 2, ST = 20\rangle \\ &+ b_1|(0s)^3(2s)[4]L = 0, ST = 00\rangle + \ldots,\end{aligned} \quad (1)$$

where the second, the third, and the fourth component are two-quantum configurations of total angular momentum $J = 0$, while the ellipsis stands for excited components involving a greater number of quanta. In the cluster dd representation, the second and the fourth component (more precisely, their superposition) can be represented in the form $\Psi_1 = \mathcal{A}\{\varphi_d(\mathbf{r}_{12}) \otimes \varphi_d(\mathbf{r}_{34}) \otimes \chi^S_{dd}(\mathbf{r}_{dd})\}$, where $\mathcal{A}$ is the operator of antisymmetrization with respect to permutations of nucleons between two deuterons, φ_d is the internal deuteron wave function, and $\chi^S_{dd}(\mathbf{r}_{dd})$ is the wave function describing the relative motion in the dd channel having the $2S$ structure and involving two oscillator excitation quanta in relative dd motion. The third component in Eq. (1) can be recast into the form $\Psi_2 = \mathcal{A}\{\varphi_d(\mathbf{r}_{12}) \otimes \varphi_d(\mathbf{r}_{34}) \otimes \chi^D_{dd}(\mathbf{r}_{dd})\}$, where $\chi^D_{dd}(\mathbf{r}_{dd})$ has the character of a D wave in the dd channel. The first component is dominant in the wave function for the ^{4}He ground state. Obviously, the first and the second, as well as the first and the fourth component, can be mixed with central nucleon–nucleon forces, while the third component ($L = 2$ for it) is admixed to other ones only by tensor nucleon–nucleon interactions. It is highly probable that the third component (that is, the D wave) is admixed to the ^{4}He ground state only through tensor mixing with the second and (or) the fourth component, which involve two excitation quanta, but not with the first component, which is the main one. The reason is that, from the point of view of the oscillator shell model, all three components (second, third, and fourth ones) belong to the same $2\hbar\omega$ shell—that is, they have a relatively small energy splitting—whereas the main configuration $|(0s)^4\rangle$ corresponds to the nonexcited (ground-state) shell shifted below by the large energy value $2\hbar\omega$. From this point of view, the weight of the D-wave cluster dd configuration is therefore of the second order of smallness (since it is mixed by tensor forces not with the main component but with the second or the fourth component, which in turn can only be considered as admixtures to the main configuration). Recent realistic calculations of four-nucleon systems seem to support this conclusion [25], since they yield only a rather small contribution of the D-wave dd component to the ^{4}He wave function.

The above specific tensor mixing in ^{4}He (within the excited $2\hbar\omega$ shell) leads to a very interesting consequence [27]: the S- and D-wave projections $\Phi^S(r_{dd})$ and $\Phi^D(r_{dd})$ of the total four-nucleon ^{4}He wave function onto the dd channel,

$$\Phi^S(r_{dd}) = \langle\varphi_{d_1}(\boldsymbol{\xi}_1)\varphi_{d_2}(\boldsymbol{\xi}_2)Y_{00}(\hat{\mathbf{r}}_{dd})|\Phi_\alpha(\boldsymbol{\xi}_1, \boldsymbol{\xi}_2, \mathbf{r}_{dd})\rangle,$$
$$\Phi^D(r_{dd}) = \langle\varphi_{d_1}(\boldsymbol{\xi}_1)\varphi_{d_2}(\boldsymbol{\xi}_2)Y_{2m}(\hat{\mathbf{r}}_{dd})|\Phi_\alpha(\boldsymbol{\xi}_1, \boldsymbol{\xi}_2, \mathbf{r}_{dd})\rangle,$$

have opposite signs. This in turn leads to a highly nontrivial conclusion: the spheroidal shape of the alpha particle is oblate.

Indeed, the presence of the D-wave component in the total alpha-particle wave function in the form described above implies that the matter (and charge) distribution features an internal deformation that does not manifest itself experimentally (that is, in the laboratory frame) because the total spin of the alpha particle is zero.[1)] Since the signs of the S- and D-wave projections onto the dd channel are opposite, this internal quadrupole moment of the alpha particle—it is determined by the off-diagonal matrix element $Q \sim \langle\varphi_{d_1}\varphi_{d_2}\Phi^S|\hat{Q}|\varphi_{d_1}\varphi_{d_2}\Phi^D\rangle$ between the S- and the D-wave component—must be negative! (Strictly speaking, one should take additionally into account other components of the alpha-particle D-wave function having the $3 + 1$ structure.)

Thus, we see that, if this D-wave dd component makes a dominant contribution to the internal quadrupole deformation of ^{4}He, then the alpha particle must have an oblate spheroidal shape in the body-frame axes, the respective quadrupole moment being negative. In [29], the degree of the internal deformation of the alpha particle was estimated at about 20%.

2.2. Origin of Quadrupole Deformation in ^{6}Li

In a free ^{4}He nucleus, a negative internal quadrupole deformation is unobservable because of zero total spin of this nucleus, while, in the ^{6}Li ground state, whose spin is equal to unity, this deformation can in principle be observed in the ^{4}He subsystem if the distortion of the ^{4}He cluster in the ^{6}Li nucleus is not overly strong. In a series of studies of our group [4–8], as well as in some studies of other authors [10–12], it was clearly demonstrated that, on the basis of the $(\alpha + 2N)$ three-cluster model (involving a subsequent antisymmetrization), one can explain quantitatively, without resort to any free parameters, all of the properties of the ground and low-lying excited states of the $A = 6$ nuclei (^{6}He, ^{6}Li, ^{6}Be), with the exception of the quadrupole moment.

In the aforementioned studies of our group, the total wave function for the $A = 6$ nuclei was represented in the form

$$\Psi^{(A=6)}_{\alpha np}(x_1, \ldots, x_6) \qquad (2)$$
$$= \mathcal{A}\{\Phi_\alpha(\boldsymbol{\xi}_1, \boldsymbol{\xi}_2, \mathbf{r}_{dd})\chi_{\alpha np}(\mathbf{r}, \mathbf{R})\},$$

[1)] The situation here resembles that of the internal quadrupole deformation of the nucleon, in which case it disappears upon averaging in the laboratory frame since the nucleon spin is 1/2 [28].

where $\Phi_\alpha(\boldsymbol{\xi}_1, \boldsymbol{\xi}_2, \mathbf{r}_{dd})$ is the wave function for the ^{4}He core, $\chi_{\alpha np}$ is the wave function describing the relative motion of the clusters in the $\alpha + 2N$ system, and $\mathcal{A}$ is the operator of antisymmetrization with respect to permutations between core nucleons and two external nucleons [5, 8]. In the calculations reported in [4–8], the internal wave function for the alpha-particle cluster was represented by the S-wave component, which is dominant; that is, the D-wave component, whose weight in Φ_α is small, was not expected to change the results significantly. However, this is illegitimate for operators that are rank-2 tensors—in particular, for the operator representing the quadrupole moment of a nucleus and having the form

$$Q_{ij} = \sum_{k=1}^{A} \hat{e}_k (3x_i^{(k)} x_j^{(k)} - r_{(k)}^2 \delta_{ij}),$$

where $\hat{e}_k = \dfrac{1+\tau_k}{2} e$ is the charge of the kth nucleon and $\mathbf{x}^{(k)}$ is its single-particle radius vector.

Because of the structure of the quadrupole-moment operator, the main contribution to the corresponding observable comes from the region of large distances near the boundary or beyond the range of nuclear forces [30]. In calculating the quadrupole deformation, the (αd) two-cluster wave functions $\chi^S_{\alpha d}(\mathbf{R})\varphi_d(\mathbf{r})$ and $\chi^D_{\alpha d}(\mathbf{R})\varphi_d(\mathbf{r})$, which correspond to the S and the D wave of the relative motion in the αd system, are therefore a good approximation for the wave function describing the relative motion in the $(\alpha + 2N)$ system. Concurrently, the deuteron wave function $\varphi_d(\mathbf{r})$, which includes both the S- and the D-wave component, is factored out from the total three-particle wave function $\chi_{\alpha np}(\mathbf{R}, \mathbf{r})$. Further, the antisymmetrization operator $\mathcal{A}$ includes both one- and two-nucleon permutations; of these, the former do not play any significant role in estimating the ^{6}Li quadrupole moment [5], while the latter are of crucial importance for this. Therefore, the antisymmetrization operator in (2) can be replaced by the sum of the identity operator and two deutron-permutation operators P_{dd}; since the deuteron spin is integral, the permutation operator P_{dd} must be taken with a plus sign. In this approximation, the total wave function for the ^{6}Li nucleus can be represented in the form

$$\Psi(^6\mathrm{Li}) = \mathcal{N}^{-1/2}\{1 + P_{dd}(13) + P_{dd}(23)\} \times \{\Phi_\alpha(12)\varphi_d(3)\chi_{\alpha d}\}, \quad (3)$$

where $\mathcal{N}$ is a normalization factor and the figures 1, 2, and 3 stand for the three deuterons in the ^{6}Li nucleus (see Fig. 1). The matrix element for the ^{6}Li quadrupole moment can be written in the form

$$Q = \langle \Psi(^6\mathrm{Li}) | \hat{Q} | \Psi(^6\mathrm{Li}) \rangle \equiv Q_{\mathrm{dir}} + Q_{\mathrm{exch}}, \quad (4)$$

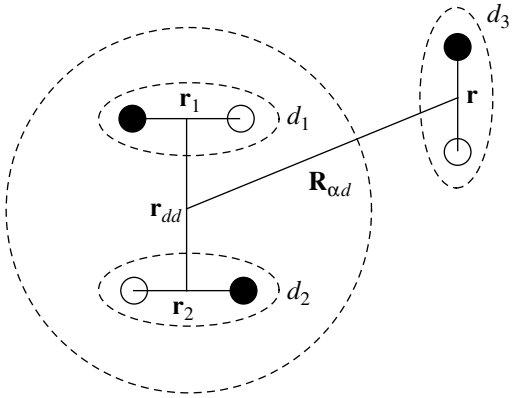

Fig. 1.

the direct (Q_{dir}) and the exchange (Q_{exch}) contribution to the total quadrupole moment having opposite signs, with the result that they can compensate each other to a considerable extent.[2)]

It should also be borne in mind that the weight of the D-wave component Φ^D_α does not exceed a few percent; therefore, its contribution is of importance only for some special observables (of the quadrupole-moment type) where other contributions are small or vanish completely. Moreover, the weight of the D-wave component in the wave function describing the relative motion in the αnp (or αd) system is also quite small (about 1%) in relation to the weight of the S-wave component, which is dominant. Therefore, the main contribution to the ^{6}Li quadrupole moment will come from two "mixed" configurations: $\Phi^S_\alpha \chi^D_{\alpha d}$ and $\Phi^D_\alpha \chi^S_{\alpha d}$.[3)]

In the present study, we show explicitly that, if use is made of the most precise alpha-particle wave functions adopted currently, which were obtained with realistic two- and three-nucleon interactions, and if αd-interaction dynamics describing empirical S- and D-wave phase shifts for d^4He scattering is accurately taken into account, the cancellation of the contributions Q_{dir} and Q_{exch} from relative motion in the αd system is indeed almost complete, so that the resulting ^{6}Li quadrupole moment is determined by the free-deuteron quadrupole moment exclusively.

[2)] The idea that such a compensation of the direct and exchange contributions to the ^{6}Li quadrupole moment is possible was first put forth in [5, 6] (see also [24]), but it has not been verified so far.

[3)] Obviously, the pure S-wave component $\Phi^S_\alpha \chi^S_{\alpha d}$ does not make any contribution to the quadrupole moment, while the component $\Phi^D_\alpha \chi^D_{\alpha d}$ involves a second-order smallness.

2.3. Admixture of a D Wave as a Small Parameter in the Expansion of a Nuclear Wave Function

Let us consider a three-deuteron structure in ^{6}Li (see Fig. 1).

It can easily be seen that, upon taking into account tensor nucleon–nucleon forces, there arise admixtures of D-wave components in each of the five Jacobi coordinates: $\mathbf{r}_1$, $\mathbf{r}_2$, $\mathbf{r}_{dd}$, $\mathbf{r}$, and $\mathbf{R}_{\alpha d}$. As a result, the tensor structure of the total wave function for the ^{6}Li nucleus proves to be extremely intricate. In particular, it can be shown that, even upon factoring out all three deuteron wave functions in the total wave function, the total number of possible configurations of S and D waves (in any of the Jacobi coordinates) is as large as $2^5 = 32$.

However, the problem of tensor mixing can be radically simplified by considering that the amplitude of the D wave is proportional to the small parameter β (for realistic nucleon–nucleon interactions, $\beta^2 \sim 0.03-0.05$). Therefore, the amplitude of the total-wave-function component involving two D waves (in two of the five Jacobi coordinates) is of order β^2, while the component involving D waves in all five Jacobi coordinates has the β^5 order of smallness. To a precision of 1%, one can therefore retain, in the total wave function for the ^{6}Li nucleus, only those components that involve not more than one D wave in any of the five Jacobi coordinates. By way of example, we indicate that, in considering, in this approximation, a D wave of relative motion in the αd system (that is, a D wave in the coordinate $\mathbf{R}_{\alpha d}$), only S waves in all coordinates must be retained in the ^{4}He wave function. If, on the contrary, a D wave in the $\mathbf{r}_{dd}$ coordinate in ^{4}He is included, only the S wave components must be taken into account in the relative motion in the αd system, as well as in the internal deuteron wave functions. In the ensuing analysis, we will follow this rule, which simplifies the problem considerably.

3. DIRECT AND EXCHANGE POTENTIAL OF αd INTERACTION

The problem of finding correct αd interaction—that is, an interaction that is matched not only with d^4He phase shifts but also with the ground state and low-lying excited states of the ^{6}Li nucleus—has been considered in a great number of studies (see the review article of Kukulin and Mackintosh [31], which contains an exhaustive list of references to earlier studies, and a more recent article of Cooper and Mackintosh [23]). There are many reasons behind increased interest in this problem [31], and one of the main of these is that, here, one can study, in the purest form, general features of the interaction of deuterons (spin-1 particles in general) with typical nuclear targets [18–20]. In contrast to heavier and more loosely bound targets, the ^{4}He nucleus is a pure scalar both in spin and isospin spaces and undergoes virtually no transitions to excited states up to projectile-deuteron energies of about 30 MeV. Therefore, this problem provides an almost ideal testing ground for three-particle models of deuteron–nucleus interaction.

No wonder that, since the mid-1950s, many groups have performed calculations of elastic d^4He scattering on the basis of the resonating-group method [32], as well as on the basis of Faddeev equations and other three-particle approaches. Although basic features of the observed cross sections for elastic scattering and breakup were successfully reproduced in those calculations, many subtler special features of αd interaction have remained unexplained so far. The main "white spots" in this pattern are associated with two problems: that of describing odd partial waves, which is intimately related with the origin of the Majorana forces between nuclei [23], and that of establishing the origin of tensor αd interaction in even and odd states [21, 23, 31]. Both the direct and the exchange αd potential include spin-dependent terms (spin–orbit and tensor ones), as well as the imaginary parts of these components, which are inadequately known at the present time [30, 31]. Thus, we will distinguish between a direct and an exchange term in each component of the αd interaction.

In the present study, we consider only one of the aforementioned problems, that of the origin of tensor αd interaction in even partial waves—more specifically, in the ground state of the ^{6}Li nucleus. Obviously, the structure and the magnitude of this tensor potential is closely related to the ^{6}Li quadrupole moment, since the degree of clustering in ^{6}Li is very high owing to an anomalous smallness of the binding energy in the αd channel, so that this nucleus can be considered as a two-cluster αd system to a good approximation.[4)]

According to the meaning of the components of the direct potential, it is natural to determine them by relying on the double folding of the effective nucleon–nucleon potential with the projectile (deuteron) and target (^{4}He) wave functions or on the single folding of the $N\alpha$ potential with the deuteron wave functions. In the present study, we adopt the latter procedure.

[4)] One reservation must be made here: this cluster configuration in ^{6}Li should not be taken too literally since the deuteron in it is strongly polarized in the field of the alpha particle and since the antisymmetrization of the αd cluster wave function must be performed in order to understand many aspects of the structure of ^{6}Li. However, these effects are negligible in the peripheral region of the nucleus, and this is precisely the region considered here.

While the central components of the direct and exchange d^4He potentials were thoroughly investigated in previous years [31, 33, 34] and while some information is available for direct tensor interaction, exchange tensor interaction has received virtually no study. The main objective of our present analysis is to reveal the origin and basic features of this force, which, as we show here, is precisely that which determines the ^{6}Li quadrupole moment.

Thus, we consider the tensor αd interaction in ^{6}Li on the basis of the two-component αd model, taking into account the interchange of the internal and external deuterons. We assume that the even partial waves (S and D) of elastic d^4He scattering and the ground state of the ^{6}Li nucleus can be described on the basis of the two-channel Schrödinger equation involving the matrix of potentials

$$\hat{V} = \begin{pmatrix} V_{00} & V_{02} \\ V_{20} & V_{22} \end{pmatrix}, \qquad (5)$$

where each element $V_{LL'}$ is in turn the sum of the direct and the exchange contribution. The direct contribution is determined by the folding procedure outlined above. As a matter of fact, the effective central αd potential V^{centr} found by solving the inverse scattering problem [35] was used for the diagonal interaction terms V_{00} and V_{22}. This phenomenological potential, which assumes that $V_{00} = V_{22}$, describes well $d\alpha$ phase shifts with allowance for Coulomb interaction and, hence, effectively includes both the direct and the exchange contribution to the diagonal part of the potential $\hat{V}$. In principle, the exchange terms in the potential can be either calculated within some approach like the resonating-group method or extracted from a fit to experimental data as the difference of the empirically reconstructed potential and the direct interaction.

In order to determine the total off-diagonal (tensor) potentials V_{02} and V_{20} (that is, the sum of the direct and exchange terms), it is necessary to know the mixing parameter ε_1 as a function of energy, but this parameter is poorly known at the present time [23, 34]. We will calculate these off-diagonal potentials as the sum of direct and exchange contributions. We will determine the direct tensor potentials by means of the single-folding procedure [36] and find the exchange potentials on the basis of the deuteron-exchange model developed in the present study.

3.1. Direct αd Potential

As was indicated above, the direct αd interaction is determined by folding the $N\alpha$ interaction with the known nucleon-distribution density in the deuteron. In the coordinate representation, its central (V_C^{fold}) and tensor (V_T^{fold}) components are given by [36]

$$V_C^{\text{fold}}(\mathbf{R}) = \frac{2}{4\pi}\int d^3r V_{N\alpha}(|\mathbf{R}+\mathbf{r}/2|)(\varphi_0^d(r))^2, \quad (6)$$

$$V_T^{\text{fold}}(\mathbf{R}) = V_T^{\text{fold}}(R)[(\mathbf{S}\cdot\mathbf{R})^2 - 2/3], \qquad (7)$$

$$V_T^{\text{fold}}(R) = \frac{6\sqrt{2}}{4\pi} \times \int d^3r V_{N\alpha}(|\mathbf{R}+\mathbf{r}/2|)\varphi_0^d(r)\varphi_2^d(r)P_2(\cos\theta),$$

where $\hat{S}_T = (\mathbf{S}\cdot\mathbf{R})^2 - 2/3$ is one of the possible forms of the operator of tensor interaction between a spin-1 particle and a spinless target; $\mathbf{R}$ is the point-to-point vector between the deuteron and alpha-particle centers of mass; $\mathbf{S}$ is the deuteron-spin operator; $V_{N\alpha}$ is the nuclear potential of the $N\alpha$ interaction; P_2 is a Legendre polynomial; $\cos\theta = \mathbf{R}\cdot\mathbf{r}/(Rr)$; and $\varphi_0^d(r)$ and $\varphi_2^d(r)$ are the radial functions for, respectively, the S- and the D-wave state in the deuteron, these functions being normalized according to the standard condition $\int_0^\infty [|\varphi_0^d(r)|^2 + |\varphi_2^d(r)|^2]r^2dr = 1$. The tensor component (7) is due exclusively to the D-wave component of the deuteron wave function; along with the tensor component of the exchange interaction, it must be taken into account in considering effects associated with the D-wave admixture in the total wave function for the ^{6}Li nucleus.

For $V_{N\alpha}$, we took the single-term Gaussian potential from [6], $V_{N\alpha} = V_0^{N\alpha}e^{-\gamma r^2}$, while, for $\varphi_0^d(r)$ and $\varphi_2^d(r)$, we employed the deuteron wave functions calculated with the Moscow nucleon–nucleon potential [37] and parametrized as the sum of Gaussian terms,

$$\varphi_l^d(r) = r^l\sum_{i=1}^{40} D_i^l \exp(-\alpha_i^{(l)}r^2). \qquad (8)$$

For this choice of $V_{N\alpha}$ and φ_l^d, fully analytic expressions can readily be obtained for the tensor folded potential V_T^{fold} both in the coordinate and in the momentum representation (see Appendix).

Figure 2 shows the radial dependences of the central [$V_C^{\text{fold}}(R)$] and tensor [$V_T^{\text{fold}}(R)$] folded potentials, along with the radial dependence of the phenomenological central potential $V^{\text{centr}}(R)$ used in our calculations. It is the difference of $V^{\text{centr}}(R)$ and $V_C^{\text{fold}}(R)$ that is a local representation of the exchange central potential.

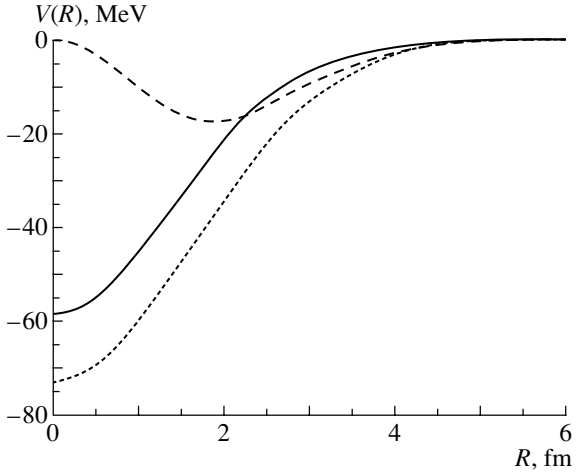

Fig. 2. Graphs of the (solid curve) direct central and (dashed curve) tensor αd potentials (the latter being multiplied by ten), along with the graph of the (dotted curve) phenomenological local central potential [6], which makes it possible to reproduce empirical d^4He phase shifts.

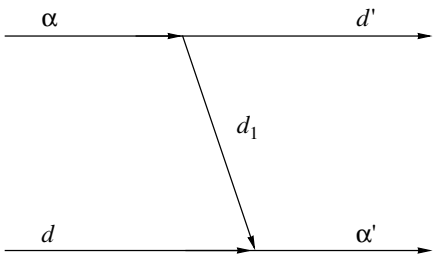

Fig. 3. Diagram corresponding to deuteron exchange in αd interaction.

3.2. Exchange αd Potential

Let us further consider deuteron exchange in the d^4He system (diagram in Fig. 3, where primes label final-state particles, while d_1 stands for the transferred deuteron). This exchange mechanism was disregarded in $(\alpha + 2N)$ three-particle models widely used to calculate states of the discrete and continuous spectra of the $d\alpha$ system [35, 38]. As to calculations of d^4He scattering by the resonating-group method [32], exchange contributions were considered there only for zero orbital angular momentum in the initial and final states—that is, also without taking into account tensor interaction.

The amplitude $V^{\rm exch}$ corresponding to the diagram in Fig. 3 can be treated as an exchange potential of αd interaction. Solving the Schrödinger (or Lippmann–Schwinger) equation with this potential is then equivalent to summing all ladder diagrams generated by deuteron exchange. It is obvious that, upon taking into account the D-wave component in the wave function describing the relative motion of two deuteron clusters in ^{4}He, this potential will develop a tensor component in addition to the central one. It should be emphasized that this exchange potential is nonlocal.

According to general rules of constructing amplitudes for nonrelativistic Feynman diagrams (see, for example, [39]), the deuteron-exchange amplitude is given by (spin variables are suppressed for the sake of brevity)

$$V^{\rm exch} = G_{\alpha\to d'd_1}(\mathbf{q}_{d'd_1})G_{dd_1\to\alpha'}(\mathbf{q}_{dd_1}) \times (E_{d_1} - \mathbf{k}^2_{d_1}/(2m_d) + i0)^{-1}, \quad (9)$$

where $G_{i\leftrightarrow jk}(\mathbf{q}_{jk})$ is the vertex function for the respective breakup (or fusion) reaction, $i \leftrightarrow jk$; $\mathbf{q}_{jk}$ is the momentum of the relative motion of particles j and k; m_i is the mass of particle i; and E_{d_1} and $\mathbf{k}_{d_1}$ are, respectively, the kinetic energy and the momentum of the virtual deuteron d_1, which are expressed, with the aid of the energy–momentum conservation laws, in terms of the energies and momenta of the external particles. We note that, in considering the problem of d^4He scattering or the problem of bound states in ^{6}Li, one has to deal with iterations of the diagram in Fig. 3 where a four dimensional integration corresponds to each intermediate state. However, integration with respect to the energy variable can be performed trivially by taking the residue at the pole corresponding to the intermediate deuteron, which appears to be on the mass shell upon doing this, the alpha particle formed from two deuterons remaining off the mass shell. In the following, we will consider bound states of the $d\alpha$ system, in which case the quantity $E_{d_1} - \mathbf{k}^2_{d_1}/(2m_d)$ is always negative, so that an infinitesimal imaginary term $i0$ can be discarded.

The vertex functions $G_{\alpha\to d'd_1}$ and $G_{dd_1\to\alpha'}$ can be represented in the form of the sum of S- and D-wave components [40]:

$$G_{\alpha\to d'd_1} = \sqrt{4\pi} \times \sum_{l=0,2;m} (1\mu'1\mu_1|lm)(lmlm|00)G_l(q_{d'd_1})Y_{lm}(\hat{q}_{d'd_1}). \quad (10)$$

Here, $(a\alpha b\beta|c\gamma)$ are Clebsch–Gordan coefficients; μ' and μ_1 are deuteron-spin projections; Y_{lm} are spherical harmonics; and $G_l(q)$ is the vertex form factor, which is expressed in terms of the Fourier component of the radial overlap integral $I_l(r)$ of the wave functions for the alpha particle and two deuterons as

$$G_l(q) = -(4\pi N)^{1/2} \times \left(\frac{q^2}{2\mu_{dd}} + \varepsilon_\alpha\right) \int_0^\infty I_l(r) j_l(qr) r^2 dr, \quad (11)$$

where μ_{ij} is the reduced mass of particles i and j, $\varepsilon_\alpha = 2m_d - m_\alpha$ is the binding energy of the alpha

particle with respect to breakup into two deuterons, $j_l(z)$ is a spherical Bessel function, $N = 6$ is a factor that takes into account the identity of nucleons, and $I_l(r)$ is determined from the expansion of the total overlap integral $I(\mathbf{r})$. We have

$$I(\mathbf{r}) = \int \varphi_d^+(\mathbf{r}_1)\varphi_d^+(\mathbf{r}_2)\Phi_\alpha(\mathbf{r}_1,\mathbf{r}_2;\mathbf{r})d^3r_1 d^3r_2 \quad (12)$$
$$= \sum_{l=0,2;m} i^l(1\mu'1\mu_1|lm)(lmlm|00)I_l(r)Y_{lm}(\hat{r}),$$

where φ_i is the total wave function describing the internal state of particle i with allowance for spin–isospin variables. The expression for $G_{dd_1\to\alpha'}$ is obtained from Eq. (10) upon the substitutions $\mathbf{q}_{d'd_1} \to \mathbf{q}_{dd_1}$, $Y_{lm}(\hat{q}) \to Y^*_{lm}(\hat{q})$, and $\mu' \to \mu$.

In order to determine the total exchange-scattering amplitude, the amplitude $V^{\rm exch}$ given by (9) must be iterated until reaching convergence of the relevant rescattering series. However, it is more straightforward to follow the way outlined above—namely, one identifies the Born amplitude $V^{\rm exch}$ with the exchange potential and substitutes this nonlocal exchange potential into the two-channel Lippmann–Schwinger equation, and it is the solution of this equation that yields the sum of the entire infinite rescattering series. In the present study, we relied on precisely this procedure. Moreover, the potential $V^{\rm exch}$ can be included, upon supplementing it with the corresponding operator of projection onto the deuteron state, in full three-particle calculations of the properties of the ^{6}Li nucleus. However, it can be used more straightforwardly within the two-channel αd cluster model of the ^{6}Li nucleus. In this model, the total wave function for the ^{6}Li nucleus includes the sum of the S- and D-wave components (respectively, χ_S and χ_D[5]); that is,

$$\Psi(^6\mathrm{Li}) = \psi_M(\mathbf{k})\Phi_\alpha; \quad (13)$$
$$\psi_M(\mathbf{k}) = \chi_0(k)\frac{1}{\sqrt{4\pi}}\varphi_M^d + \chi_2(k)$$
$$\times \sum_{m\mu}(2m1\mu|1M)Y_{2m}(\hat{\mathbf{k}})\varphi_\mu^d,$$

where $\mathbf{k}$ is the momentum of the relative motion of the d and α clusters in ^{6}Li, M is the projection of the ^{6}Li spin, and φ_μ^d is the deuteron wave function for the spin projection μ. The functions χ_L are assumed to be normalized as follows:

$$\int_0^\infty [\chi_0^2(k) + \chi_2^2(k)]\frac{k^2dk}{(2\pi)^3} = 1. \quad (14)$$

The potential $V^{\rm exch}$ acts as an integral operator.[6]

In order to obtain one-dimensional integral equations of the Lippmann–Schwinger type for the partial-wave components χ_0 and χ_2, it is necessary to construct a partial-wave expansion of the exchange potential $V^{\rm exch}$. After that, the result of applying the potential $V^{\rm exch}$ to the two-component wave function χ can be represented in the matrix form

$$\hat{V}^{\rm exch}\hat{\chi} = \begin{pmatrix} V_{00}^{\rm exch} & V_{02}^{\rm exch} \\ V_{20}^{\rm exch} & V_{22}^{\rm exch} \end{pmatrix}\begin{pmatrix} \chi_0 \\ \chi_2 \end{pmatrix}. \quad (15)$$

In order to obtain explicit expressions for the partial-wave potentials $V_{LL'}^{\rm exch}$, it is necessary to represent expression (9) as a function of the variables $\mathbf{k}$ and $\mathbf{k}'$. This problem can be simplified by approximating the vertex form factors appearing in (9) by a linear combination of Gaussian functions as

$$G_l(q) = q^l\sum_{i=1}^{N_l} a_{li}\exp(-\beta_{li}^2q^2), \quad (16)$$
$$l = 0, 2.$$

After straightforward but rather cumbersome calculations with the aid of the expansions in (16) for the potentials $V_{LL'}^{\rm exch}(k,k')$, one can obtain analytic expressions presented in the Appendix. We recall that, in the present study, we calculate only the off-diagonal ($L \neq L'$) elements of the exchange potential.

4. CHOOSING ^{4}He WAVE FUNCTION AND SOLVING COUPLED EQUATIONS

4.1. Solving Coupled Lippmann–Schwinger Equations

The wave function describing the relative motion of the d and α clusters in the ^{6}Li nucleus was found by solving the homogeneous two-channel Lippmann–Schwinger equation for the S- and D-wave components. We have

$$\chi_l(k) = \sum_{L'=0,2}\int_0^\infty \frac{V_{LL'}(k,k')}{E - k'^2/2\mu_{d\alpha}}\chi_{L'}(k')\frac{k'^2\mathrm{d}k'}{2\pi^2}, \quad (17)$$
$$L = 0, 2.$$

[5] The weight of the αd projection of the wave function for the ^{6}Li ground state is about 50% if use is made of the free-deuteron wave function. However, this weight increases to 90% or even to a higher value upon taking into account a complete antisymmetrization and the deformation of the deuteron cluster [41].

[6] We note that $V^{\rm exch}$ is a nonlocal operator both in the momentum and in the coordinate representation. Moreover, the operator $V^{\rm exch}$ depends on the energy of the system.

Table 1. Parameters of ^{4}He wave functions used in calculating the exchange potential

Version	ε_B, MeV	$\lvert F_0\rvert^2$	$\lvert F_2\rvert^2$	$S = \lvert F_0\rvert\lvert F_2\rvert$
$M1$	21.9	0.50073	0.02226	0.10558
$M2$		0.46725	0.00432	0.04492
$C1$(AV14)	27.8	0.4477	0.01132	0.07119
$C2$(UV14)	28.2	0.4201	0.01889	0.08907

For the potential $\hat{V}$ in (17), we took the sum of the phenomenological central potential V^{centr} [35], the off-diagonal (tensor) components of the folded potential V_T^{fold}, and the exchange potential V^{exch}, the Coulomb αd potential V^{Coul} being also included; that is,

$$V_{LL} = V_l^{\text{centr}} + V_l^{\text{Coul}}, \qquad (18)$$
$$V_{LL'} = (V_T^{\text{fold}})_{LL'} + V_{LL'}^{\text{exch}}, \quad L \neq L'.$$

According to formulas (9)–(12), the exchange potential V^{exch} is completely determined by the overlap integrals of the alpha-particle wave function and the wave functions for two deuterons.

4.2. Parametrization of the ^{4}He Wave Functions

For the alpha-particle wave functions, we employed, in our calculations, four versions associated with four versions of the potential V^{exch}, which are denoted by $M1$, $M2$, $C1$, and $C2$. Versions $M1$ and $M2$ correspond to a parametrization of the radial overlap integrals $I_0(r)$ and $I_2(r)$ found on the basis of ^{4}He wave functions obtained by Morita *et al.* [27] ($M1$) and, more recently, by Buchmann and Henley [42] ($M2$) from a variational solution to the four-nucleon problem with the realistic nucleon–nucleon potential proposed by Reid.

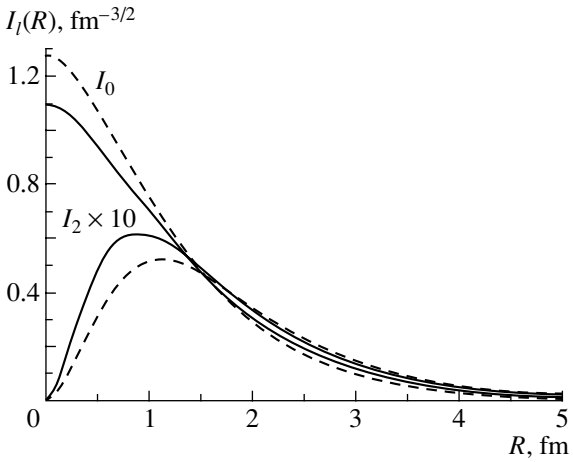

Fig. 4. Overlap integrals $I_0(R)$ and $I_2(R) \times 10$ of the ^{4}He wave functions and the deuteron wave functions: (solid curves) $C1$ version and (dashed curves) $C2$ version.

Table 2. ^{6}Li quadrupole moment found within the two-channel αd model with various tensor potentials

Tensor potential	ε_B, MeV	P_D, %	$\langle R^2\rangle$, fm^2	$\tilde{Q}$, fm^2
V_T^{exch} ($M1$)	1.495	0.30	19.3	−0.3525
V_T^{exch} ($M2$)	1.480	0.185	19.5	−0.2606
V_T^{exch} ($C1$, AV14)	1.501	0.63	19.4	−0.5372
V_T^{exch} ($C2$, UV14)	1.5088	1.00	19.3	−0.6092
V_T^{fold}	1.529	1.25	19.0	+0.5725
$V_T^{\text{exch}}(C2) + V_T^{\text{fold}}$	1.483	0.14	19.4	−0.009

Versions $C1$ and $C2$ correspond to choosing the four-nucleon ^{4}He wave functions found by using the Argonne nucleon–nucleon potential AV14 ($C1$) and the Urbana nucleon–nucleon potential UV14 ($C2$) with allowance for three-particle forces (UVII model) [43]. In the present study, we employed the analytic approximations of the overlap integrals I_0 and I_2 for these functions from [44]. Table 1 gives the alpha-particle binding energies ε_B, the norms of the overlap integrals $|F_l|^2 = \int |I_l(r)|^2 r^2 \mathrm{d}r$ for all four versions used here for the ^{4}He wave functions, and the parameter $S = |F_0||F_2|$ determining the strength of the exchange tensor potential and, through it, the exchange contribution to the ^{6}Li quadrupole moment.

Figure 4 shows the behavior of the overlap integrals $I_l(R)$ ($l = 0, 2$) for two versions of the ^{4}He wave functions ($C1$ and $C2$).

For the Coulomb αd interaction, we took the Coulomb potential acting between the alpha-particle and deuteron centers of mass. We note that the inclusion of the Coulomb interaction has virtually no effect on the quadrupole moment Q.

4.3. ^{6}Li Quadrupole Moment

By definition (see, for example, [30]), the quadrupole moment Q of the ^{6}Li nucleus is given by

$$Q = \left\langle \Psi_1 \left| 2\sqrt{4\pi/5} \sum_{i=1}^{3} r_i^2 Y_{20}(\hat{r}_i) \right| \Psi_1 \right\rangle, \qquad (19)$$

where Ψ_1 is the total wave function in the coordinate representation for ^{6}Li having the spin projection of unity and $\mathbf{r}_i$ is the coordinate of the ith proton in the ^{6}Li nucleus with respect to its center of mass. Using

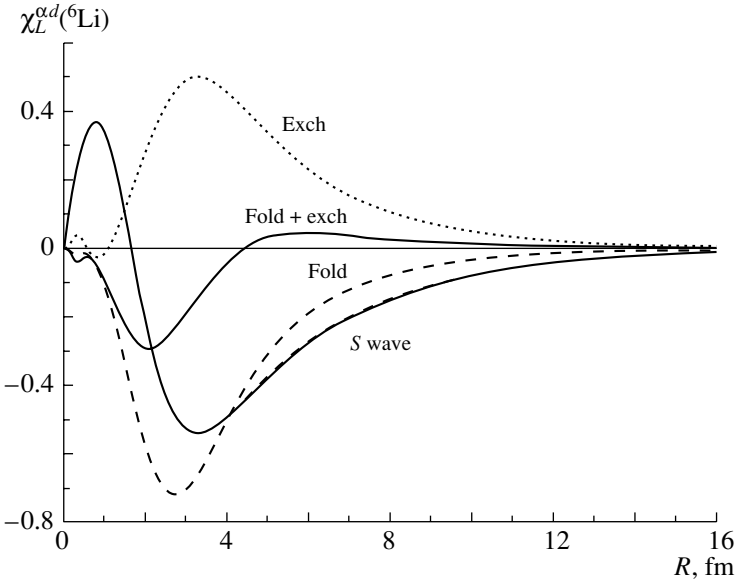

Fig. 5. D-wave component of the αd wave function describing relative motion in the ^{6}Li ground state according to calculations with various tensor αd potentials: (exch) exchange potential (version $C2$), (fold) direct potential, and (fold + exch) their sum. Also shown is (S wave) the S-wave component of this wave function (three versions of the S-wave component are virtually indistinguishable in the figure).

for Ψ_1 an expression that is similar to (13), we find, after some simple algebra, that

$$Q = (P_0 + P_2/10)Q_d + (4\sqrt{2}/15) \qquad (20)$$
$$\times \int_0^\infty \left[\chi_0(R)\chi_2(R) - \frac{1}{2\sqrt{2}}\chi_2^2(R)\right] R^4 dR,$$

where $\chi_0(R)$ and $\chi_2(R)$ are the radial wave functions describing the relative motion of the d and α clusters in the S- and D-wave states, respectively; $P_L = \int_0^\infty \chi_l^2(R)R^2dR\,(L = 0, 2)$ is the weight of the cluster αd state of relative orbital angular momentum L; and $Q_d = 0.2860 \pm 0.0015$ fm^2 is the deuteron quadrupole moment [45].

5. NUMERICAL RESULTS AND DISCUSSION OF THE RESULTS

The set of homogeneous integral Lippmann–Schwinger equations (17) was solved numerically by means of Gauss' quadrature with 48 and 96 mesh points of integration. The numerical accuracy of the solution was tested by the convergence of the results with increasing number of mesh points. In order to calculate the quadrupole moment by formula (20), we approximated the resulting numerical solutions by the sums of Gaussian functions and transformed therm analytically to the coordinate representation. The radial wave functions found in this way for relative motion in the αd system are displayed in Fig. 5. One can clearly see their peripheral character—the far tails of these functions extend to large distances of $R_{\alpha d} \simeq 8$–10 fm. This is associated with an anomalously low binding energy of ^{6}Li in the αd channel ($\varepsilon_B \simeq 1.47$ MeV).

The resulting values of the quadrupole moment $\tilde{Q}$ corresponding to relative motion in the αd system in the ^{6}Li nucleus [second term on the right-hand side of Eq. (20)] are given in Table 2. All of the results displayed in this table and in Fig. 5 were obtained by employing, for the diagonal elements V_{LL} ($L = 0, 2$) of the potential in (18), the local Gaussian potential $V_0 e^{-r^2/a^2}$ with the parameter values of $V_0 = -72.133$ MeV and $a = 2.305$ fm; the latter yields the value of $\varepsilon_B = 1.4754$ MeV for the binding energy of the ^{6}Li ground state (second state in this deep potential), the tensor mixing being omitted in the diagonal term.

In addition to the quadrupole moment, Table 2 also gives the binding energies, the weights P_D of the D wave, and the mean-square radius $\langle R^2\rangle$ for the relative motion in the αd system in ^{6}Li according to our two-channel calculations with the various tensor αd potentials.

From the data in Table 2, it can clearly be seen that the four-nucleon ^{4}He wave functions calculated in [27, 42] yield a strongly underestimated asymptotic behavior of the αd-channel wave function, this leading to underestimated contributions to the ^{6}Li

quadrupole moment. In contrast to those wave functions, more precise four-nucleon ^{4}He wave functions found in [43] have a more correct asymptotic behavior in the αd channel both in the S and in the D wave, version C2 leading to the largest (in magnitude) negative value of the ^{6}Li quadrupole moment due to the exchange tensor αd potential.

The result given in the last row of Table 2 shows that the contributions to the quadrupole moment from the direct and exchange tensor interactions nearly compensate each other.[7)] This comes as no surprise if one considers that, as follows from the data in Fig. 5, the D-wave functions in the αd channel, χ_2, in the external region $r \geq 4$ fm, which makes a dominant contribution to the quadrupole moment, are nearly equal in magnitude and opposite in sign for the versions of the calculation with the direct and exchange tensor potentials. Thus, the resulting D-wave function in the αd channel almost dies out at distances of $r \sim 4$ fm, so that the ^{6}Li quadrupole moment calculated with this function appears to be anomalously small.

6. CONCLUSION

We have found the exchange tensor d^4He potential on the basis of an admixture of the three-deuteron component in the ^{6}Li wave function. Within this model of tensor αd interaction, we have studied the ^{6}Li quadrupole moment and have compared the exchange potential in question with the direct tensor potential obtained by folding the $N\alpha$ potential with the two-component deuteron wave function. Our calculations have revealed for the first time that an anomalously small quadrupole deformation in the ^{6}Li ground state is due to an almost complete cancellation of the direct and exchange contributions, which are both large in magnitude, the latter being caused by deuteron exchange between the two clusters in the ^{6}Li nucleus. A negative sign of the exchange contribution is in turn a direct corollary of the fact that the S- and D-wave components of the wave functions describing relative motion in the dd system in ^{4}He have opposite signs. In all probability, this result follows from a specific character of the tensor interaction in ^{4}He (where the D wave in the dd channel is mixed by tensor nucleon–nucleon interaction with the $2\hbar\omega$-excited admixture of ^{4}He rather than with its main component). Thus, we have shown that the quadrupole deformation in the ^{6}Li nucleus is not related directly (as might have been thought) to the three-particle dynamics of the $\alpha + 2N$ system, but that it is caused to a considerable extent by the tensor polarization of the alpha-particle core by the external deuteron. It is interesting that this tensor polarization of the alpha-particle core does not manifest itself in any other observables (that is, those that are not of a tensor character), which are faithfully reproduced on the basis of the $(\alpha + 2N)$ three-particle model [4–9].

The result obtained here may have a number of important corollaries for nuclear physics. First, it demonstrates that, in ^{6}Li, the $3d$ component manifests itself in addition to cluster configurations (αd or $\alpha + 2N$ and $t\tau$), despite the smallness of its weight. It is precisely this component that determines, to a considerable extent, the asymptotic behavior of the D wave in the bound αd state. There is every reason to believe that this component also controls the energy dependence of the parameter ε_1 of the tensor mixing of the S and D waves in low-energy d^4He scattering.

Second, our result makes it possible to understand the distinction between the magnitudes and signs of the tensor analyzing powers T_{2q} for the scattering of polarized ^{6}Li and ^{7}Li projectiles on medium-mass nuclei. In light of the results obtained here, it is indeed obvious that, while the ^{7}Li quadrupole moment is due to direct ^{4}Het interaction, so that the main contribution to $Q(^7\mathrm{Li})$ comes from the asymptotic part of the wave function for relative motion in the αt system (as a result, this leads to a large negative value for it), the very small ^{6}Li quadrupole moment stems from an almost complete cancellation of the two D wave components (a direct and an exchange one) in the wave function for relative motion in the αd system. In other words, the ^{6}Li quadrupole deformation (in contrast to the ^{7}Li quadrupole deformation) is almost completely due to the exchange process, which will also radically change the dynamics of the spin-dependent interaction of ^{6}Li with nuclei. In particular, the same problems arise in studying the tensor analyzing powers for $^6\vec{\mathrm{Li}} + {}^4$He scattering and for scattering in other similar systems.

Finally, one can invert the formulation of the problem, assigning the ^{6}Li quadrupole moment a preset value and treating the D-wave component of the wave function for relative motion in the αd system as a sought quantity. This formulation makes it possible to deduce information about the values of the asymptotic normalization constant and the weight (spectroscopic factor) of the D wave in the wave function for relative dd motion in the ^{4}He system. We remind the reader that it is the exact value of this asymptotic constant for the virtual decay $^4\mathrm{He} \to d + d$ that controls the matrix element for the radiative-capture reaction $d + d \to {}^4\mathrm{He} + \gamma$, which plays an important role in Big Bang theory. We also note that a correct value of

[7)] Here, we mean the quadrupole moment $\tilde{Q}$ associated with the relative motion in the αd system. The free-deuteron quadrupole moment remains noncompensated in our case.

the matrix element for the radiative-capture reaction $d + {}^4\mathrm{He} \to {}^6\mathrm{Li} + \gamma$ [46, 47] at low deuteron energies is of paramount importance for understanding the origin of ^{6}Li in the Universe.

Thus, the puzzle of the ^{6}Li quadrupole deformation is of importance not only in itself; it is related to many fundamental problems in nuclear physics and astrophysics.

ACKNOWLEDGMENTS

We are grateful to H. Morita for placing at our disposal the spectroscopic *dd* amplitudes obtained for ^{4}He in the $4N$ calculations reported in [27, 42].

This work was supported in part by the Russian Foundation for Basic Research (project no. 04-02-16602).

APPENDIX

Here, we present explicit expressions for the potentials V_T^{fold} and V^{exch} appearing in the total nondiagonal potential $V_{LL'}(k,k')$.

By using expressions (7) and (8) and a Gaussian form for the potential $V_{N\alpha}$ ($V_{N\alpha} = V_0^{N\alpha} e^{-\gamma\rho^2}$), we can easily find in the coordinate representation that

$$V_T^{\mathrm{fold}}(R) = 6\sqrt{2} V_0^{N\alpha} R^2 \sum_{ij} A_{ij}^{(02)} e^{-\alpha_{ij}^{02} R^2}, \quad \text{(A.1)}$$

where

$$A_{ij}^{(02)} = \frac{\sqrt{\pi}}{16}\gamma^2 D_i^0 D_j^2 \left(\alpha_i^{(0)} + \alpha_j^{(2)} + \frac{\gamma}{4}\right)^{-7/2}, \quad \text{(A.2)}$$

$$\alpha_{ij}^{02} = \gamma \frac{\alpha_i^{(0)} + \alpha_j^{(2)}}{\alpha_i^{(0)} + \alpha_j^{(2)} + \gamma/4}.$$

In order to go over to the momentum representation, we will use the relation

$$V_{T,LL'}^{\mathrm{fold}}(k,k') = \frac{1}{\sqrt{kk'}} \quad \text{(A.3)}$$
$$\times \int_0^\infty J_{L+1/2}(kR) J_{L'+1/2}(k'R) V_T^{\mathrm{fold}}(R) R dR,$$

where $J_\lambda(x)$ is a Bessel function. Upon the substitution of (A.1) into expression (A.3), the resulting integral can be evaluated analytically. The result is

$$V_{T,02}^{\mathrm{fold}}(k,k') = 6\sqrt{2} V_0^{N\alpha} \quad \text{(A.4)}$$
$$\times \sum_{ij} A_{ij}^{02} \frac{1}{\sqrt{kk'}} J_{1/2,5/2}(k,k';\alpha_{ij}^{02}),$$

where

$$J_{1/2,5/2}(k,k';\alpha) \quad \text{(A.5)}$$
$$\equiv \int_0^\infty J_{1/2}(kR) J_{5/2}(k'R) e^{-\alpha R^2} R^3 dR$$
$$= \frac{\exp(-(k^2+k'^2)/4\alpha)}{8a^3}$$
$$\times \left\{k^2 I_{5/2}(x) - 2kk' I_{3/2}(x) + k'^2 I_{1/2}(x)\right\}.$$

Here, $x = kk'/(2\alpha)$ and $I_\lambda(x)$ is a modified Bessel function.

The exchange potential $V_{LL'}^{\mathrm{exch}}(k,k')$ has the form

$$V_{02}^{\mathrm{exch}}(k,k') \quad \text{(A.6)}$$
$$= \sum_{i,i'}\sum_{n=0}^\infty a_{0i} a_{2i'} \frac{I_{n+1/2}[(\beta_{0i}^2 + \beta_{2i'}^2)kk']}{\sqrt{\beta_{0i}^2 + \beta_{2i'}^2}}$$
$$\times (\exp\{-[\beta_{0i}^2(k^2 + k'^2/4)$$
$$+ \beta_{2i'}^2(k^2/4 + k'^2)]\} B_n^{02}(k,k')$$
$$+ \exp\{-[\beta_{2i'}^2(k^2 + k'^2/4)$$
$$+ \beta_{0i}^2(k^2/4 + k'^2)]\} B_n^{20}(k,k')).$$

Here, a_{li} and β_{li} are the parameters appearing in expansion (16) and the functions $B_n^{LL'}(k,k')$ are given by

$$B_n^{02}(k,k') = -\frac{2\sqrt{\pi} m_d}{\sqrt{3}(kk')^{3/2}} \quad \text{(A.7)}$$
$$\times \sum_{l_1+l_2=2} \sum_{l=0}^\infty \sum_{l'=0}^\infty (-1)^l 2^{-l_1} \frac{(2l+1)(2l'+1)}{\sqrt{(2l_1)!(2l_2)!}}$$
$$\times (l_1 0 l 0 | n 0)(l_2 0 l' 0 | n 0)(l 0 l' 0 | 2 0)$$
$$\times W(l_1 l_2 l l'; 2n) k^{l_1} (k')^{l_2} Q_l[\zeta(k,k')],$$

where $(a\alpha b\beta|c\gamma)$ are Clebsch–Gordan coefficients, $W(abcd;ef)$ is a Racah coefficient, $Q_l(x)$ is a Legendre function of the second kind, and

$$\zeta(k,k') = \frac{k^2 + k'^2 + m_d(\varepsilon_{\alpha dd} - E)}{kk'}. \quad \text{(A.8)}$$

Here, m_d is the deuteron mass, $\varepsilon_{\alpha dd} = 2m_d - m_\alpha$ is the α-particle binding energy in the dd channel, and E is the energy of the relative motion of α and d in the system of six nucleons; in our case, $E = -\varepsilon_{\alpha d}^{{}^6\mathrm{Li}} = m_{{}^6\mathrm{Li}} - m_\alpha - m_d < 0$. The expression for $B_n^{20}(k,k')$ can be obtained from (A.7) by means of the substitution $2^{-l_1} \to 2^{-l_2}$. The expression for $V_{20}^{\mathrm{exch}}(k,k')$ follows from expressions (A.6)–(A.8) upon the substitution $(-1)^l Q_l(\zeta) \to (-1)^{l'} Q_{l'}(\zeta)$.

REFERENCES

1. R. B. Wiringa, S. C. Pieper, J. Carlson, and V. R. Pandharipande, Phys. Rev. C **62**, 014001 (2000).
2. R. B. Wiringa and R. Schiavilla, Phys. Rev. Lett. **81**, 4317 (1998); Phys. Rev. C **56**, 1720 (1997); R. B. Wiringa *et al.*, Annu. Rev. Nucl. Part. Sci. **51**, 53 (2001).
3. D. C. Zheng *et al.*, Phys. Rev. C **52**, 2488 (1995).
4. V. I. Kukulin, V. M. Krasnopolsky, V. T. Voronchev, and P. B. Sazonov, Nucl. Phys. A **417**, 128 (1984); **453**, 365 (1986).
5. G. G. Ryzhikh, R. A. Eramzhyan, V. I. Kukulin, and Yu. M. Tchuvilsky, Nucl. Phys. A **563**, 247 (1993).
6. V. I. Kukulin, V. N. Pomerantsev, Kh. D. Razikov, *et al.*, Nucl. Phys. A **586**, 151 (1995).
7. P. B. Sazonov, V. I. Kukulin, V. M. Krasnopol'skiĭ, and V. T. Voronchev, Yad. Fiz. **43**, 1149 (1986) [Sov. J. Nucl. Phys. **43**, 735 (1986)].
8. V. I. Kukulin and G. G. Ryzhikh, Prog. Part. Nucl. Phys. **34**, 397 (1995).
9. I. J. Thomson *et al.*, Phys. Rev. C **61**, 024318 (2000).
10. M. V. Zhukov *et al.*, Phys. Rep. **231**, 151 (1993).
11. K. Arai, Y. Suzuki, and R. G. Lovas, Phys. Rev. C **59**, 1432 (1999).
12. R. Beck, F. Dickmann, and R. G. Lovas, Ann. Phys. (N.Y.) **173**, 1 (1987).
13. V. T. Voronchev, V. I. Kukulin, V. N. Pomerantsev, and G. G. Ryzhikh, Few-Body Syst. **18**, 191 (1995).
14. A. Csótó and R. G. Lovas, Phys. Rev. C **53**, 1444 (1996).
15. B. Buck and A. C. Merchant, J. Phys. G **14**, 211 (1988).
16. S. B. Dubovichenko and A. V. Dzhazairov-Kakhramanov, Yad. Fiz. **58**, 635 (1995) [Phys. At. Nucl. **58**, 579 (1995)].
17. H. M. Nishioka, R. C. Johnson, J. A. Tostevin, and K.-I. Kubo, Nucl. Phys. A **440**, 557 (1985); H. M. Nishioka, J. A. Tostevin, and R. C. Johnson, Phys. Lett. B **124**, 17 (1983); A. C. Merchant and N. Rowley, Phys. Lett. B **150**, 35 (1985).
18. R. Frick *et al.*, Phys. Rev. Lett. **44**, 14 (1980).
19. L. D. Knutson and W. Haeberli, Phys. Rev. C **12**, 1469 (1975).
20. R. Frick *et al.*, Z. Phys. A **319**, 133 (1984); **314**, 49 (1983).
21. S. G. Cooper, V. I. Kukulin, R. S. Mackintosh, and V. N. Pomerantsev, Phys. Rev. C **59**, 2361 (1999); V. I. Kukulin, V. N. Pomerantsev, S. G. Cooper, and S. B. Dubovichenko, Phys. Rev. C **57**, 2462 (1998).
22. S. B. Dubovichenko, Yad. Fiz. **61**, 210 (1998) [Phys. At. Nucl. **61**, 162 (1998)].
23. S. G. Cooper and R. S. Mackintosh, Nucl. Phys. A **723**, 45 (2003).
24. V. I. Kukulin, V. N. Pomerantsev, S. G. Cooper, and R. S. Mackintosh, Few-Body Syst., Suppl. **10**, 439 (1999); Yad. Fiz. **62**, 1187 (1999) [Phys. At. Nucl. **62**, 1114 (1999)].
25. A. Nogga, H. Kamada, W. Glöckle, and B. R. Barrett, Phys. Rev. C **65**, 054003 (2002).
26. D. Wachter *et al.*, Phys. Lett. B **200**, 246 (1988).
27. H. Morita, Y. Akaishi, O. Endo, and H. Tanaka, Prog. Theor. Phys. **78**, 1117 (1987).
28. A. J. Buchmann and E. M. Henley, Phys. Rev. C **63**, 015202 (2001).
29. B. C. Carp, Nucl. Phys. A **457**, 15 (1986); F. Mertz *et al.*, Nucl. Phys. A **489**, 399 (1988).
30. A. G. Sitenko and V. K. Tartakovskiĭ, *Lectures on the Theory of the Nucleus* (Atomizdat, Moscow, 1972; Pergamon, Oxford, 1975).
31. V. I. Kukulin and R. S. Mackintosh, J. Phys. G **30**, R1 (2004).
32. H. Kanada *et al.*, Nucl. Phys. A **457**, 93 (1986); H. Kanada, T. Kaneko, and Y. C. Tang, in *Book of Contributed Papers, V International Conference on Clustering Aspects in Nuclear and Subnuclear Systems, Kyoto, 1988*, p. 322.
33. S. G. Cooper, V. I. Kukulin, R. S. Mackintosh, and V. N. Pomerantsev, Nucl. Phys. A **677**, 187 (2000); R. S. Mackintosh, Preprint, MGOU (Moscow State Open University, Moscow, 2002).
34. S. G. Cooper, V. I. Kukulin, R. S. Mackintosh, and E. V. Kuznetsova, Phys. Rev. C **58**, R31 (1998); H. R. Bürgl *et al.*, Nucl. Phys. A **334**, 413 (1980); **321**, 445 (1979); **307**, 91 (1978).
35. V. I. Kukulin and V. N. Pomerantsev, Yad. Fiz. **51**, 376 (1990) [Sov. J. Nucl. Phys. **51**, 240 (1990)]; V. I. Kukulin, V. N. Pomerantsev, and S. B. Zuev, Yad. Fiz. **59**, 428 (1996) [Phys. At. Nucl. **59**, 403 (1996)].
36. P. W. Keaton, Jr., and D. D. Armstrong, Phys. Rev. C **8**, 1692 (1973).
37. V. I. Kukulin, V. M. Krasnopolsky, V. N. Pomerantsev, and P. B. Sazonov, Phys. Lett. B **165**, 7 (1985).
38. K. Hahn, E. W. Schmid, and P. Doleschall, Phys. Rev. C **31**, 325 (1985).
39. L. D. Blokhintsev and É. Truglik, Izv. Akad. Nauk SSSR, Ser. Fiz. **33**, 88 (1969).
40. L. D. Blokhintsev, I. Borbely, and E. I. Dolinsky, Fiz. Élem. Chastits At. Yadra **8**, 1189 (1977) [Sov. J. Part. Nucl. **8**, 485 (1977)].
41. Yu. M. Chuvil'skiĭ and G. G. Ryzhikh, Izv. Akad. Nauk SSSR, Ser. Fiz. **54**, 2276 (1990).
42. H. Morita, private communication.
43. R. Schiavilla, V. R. Pandharipande, and R. B. Wiringa, Nucl. Phys. A **449**, 219 (1986).
44. E. R. Crosson *et al.*, Phys. Rev. C **47**, 2690 (1993).
45. D. M. Bishop and L. M. Chenug, Phys. Rev. A **20**, 381 (1979).
46. K. M. Nollett, R. B. Wiringa, and R. Schiavilla, Phys. Rev. C **63**, 024003 (2001).
47. A. M. Mukhamedzhanov, R. P. Schmitt, R. E. Tribble, and A. Sattarov, Phys. Rev. C **52**, 3483 (1995).

Translated by A. Isaakyan

Physics of Atomic Nuclei, Vol. 68, No. 7, 2005, pp. 1133–1137. Translated from Yadernaya Fizika, Vol. 68, No. 7, 2005, pp. 1179–1184.

NUCLEI
Theory

Magic Numbers of Ultraheavy Nuclei

V. Yu. Denisov

Institute for Nuclear Research, National Academy of Sciences of Ukraine, pr. Nauki 47, Kiev, 03028 Ukraine

Received March 30, 2004; in final form, May 12, 2004

Abstract—For nuclei where the number of protons lies in the range $76 \leq Z \leq 400$, proton and neutron shell corrections are calculated along the beta-stability line described by Green's formula. The magic numbers of protons and neutrons are determined for ultraheavy nuclei. Alpha-decay half-lives and fission barriers are estimated for ultraheavy doubly magic nuclei. © *2005 Pleiades Publishing, Inc.*

INTRODUCTION

Magic numbers corresponding to the filling of nuclear shells of single-particle levels have been known since the middle of the past century, and the role that they play in nuclear physics is of crucial importance [1–4]. Nuclei where the numbers of nucleons are magic are more stable and have a higher binding energy than their neighbors and are more abundant in nature than them [1–4]. Many quantities, such as the energies required for the separation of one and two nucleons, the energies of alpha and beta transitions, pairing energies, and the excitation energies of low-lying vibrational states, undergo discontinuities upon passing a magic number [1–4].

The magic numbers $Z = 82$ and $N = 126$ are the greatest magic numbers that have been empirically confirmed to date for protons and neutrons, respectively. It should be noted, however, that, at matter densities close to nuclear-matter densities, there occurs a transition in neutron stars from nuclei, neutron drops, neutrons, and protons to fusing and decaying heavy nuclei [5, 6], which transform, as the density increases further, into a more complicated state of nuclear matter [5–7]. Therefore, very heavy nuclei can be formed in neutron stars. The existence of neutron-rich nuclei where the number of neutrons is about 10^3–10^5 and of supercharged nuclei where the number of protons is about 1600 is discussed in [6]. It would be interesting to find magic numbers in ultraheavy nuclei where the number of nucleons falls within the range $300 \leq A \leq 1200$. In neutron stars, the relative production rate for ultraheavy nuclei involving a magic number of nucleons would be enhanced because of their higher stability. The results presented in [8] also provoke interest in studying magic numbers in the region of superheavy nuclei.

It is well known that magic numbers correspond to the filling of nucleon shells in spherical beta-stable nuclei [1–4, 9–12]. The shell correction has a deep local minimum in the vicinity of a magic number [4, 9–14]. Calculating shell corrections for spherical nuclei involving various numbers of protons and neutrons, one can therefore determine magic numbers from the positions of deep local minima in the proton and neutron shell corrections. It should be noted that nuclei lying along the beta-stability line and having empirically known magic numbers of nucleons ($Z =$ 8, 20, 28, 50, 82, $N = 8$, 20, 28, 50, 82, 126) are spherical [4, 11]. In the following, we will therefore also explore shell corrections in spherical nuclei.

CALCULATION OF SHELL CORRECTIONS

Figure 1 shows the proton (δ_P), neutron (δ_N), and total ($\delta_P + \delta_N$) shell corrections calculated for $76 \leq Z \leq 400$ even–even spherical nuclei lying along the beta-stability line approximated by Green's formula [15], from which it follows that a nucleus involving Z protons and $N_{\text{Green}}(Z) = (2/3)Z + (5/3) \times (10\,000 + 40Z + Z^2)^2 - 500/3$ neutrons corresponds to the beta-stability valley [15]. Green's formula describes well the beta-stability line, which is associated with a specific relation between the numbers of protons and neutrons for nuclei known to date. Let us assume that that the relation between the numbers of protons and neutrons in beta-stable nuclei that is described by Green's formula is valid for heavier nuclei inclusive. Figure 1 shows the shell corrections calculated for nuclei involving an even number Z of protons in the range from 76 to 400 and an even number N of neutrons in the range $N_{\text{Green}} - 10 \leq N \leq N_{\text{Green}} + 10$, where N_{Green} is the even number closest to $N_{\text{Green}}(Z)$. The numbers of neutrons and nucleons in nuclei were varied in the range $102 \leq N \leq 820$ and in the range $178 \leq A \leq$ 1218, respectively.

The energies of single-particle levels of nucleons were calculated for the nucleon mean field in the form of the Woods–Saxon potential with allowance

1063-7788/05/6807-1133$26.00

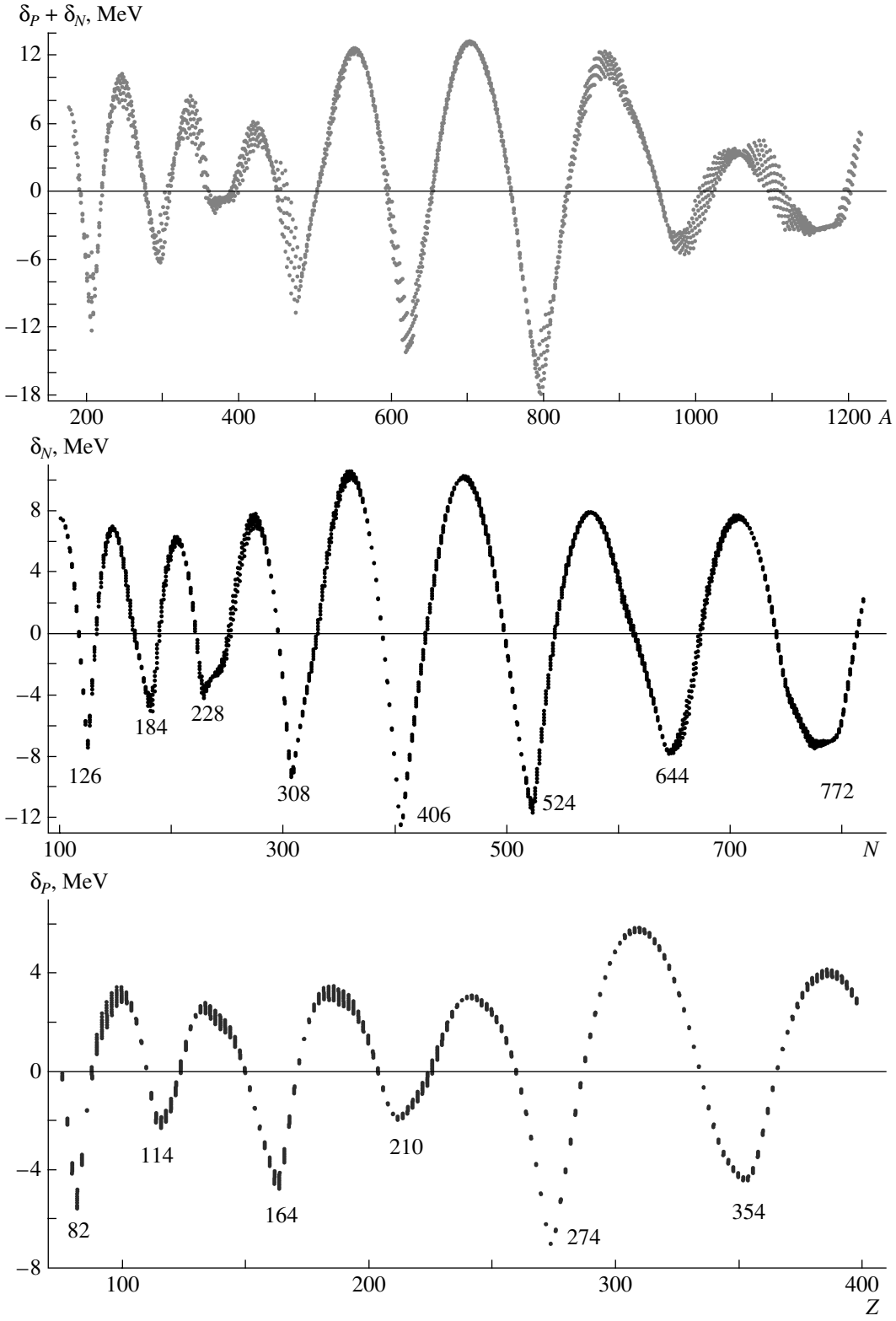

Fig. 1. Proton (δ_P), neutron (δ_N) and total ($\delta_P + \delta_N$) shell corrections for even–even spherical nuclei.

for spin–orbit and Coulomb interactions [2–4, 11, 16]. We employed a "universal" set of parameters of the Woods–Saxon potential [16]. This set makes it possible to describe well the spectra of single-particle levels in light, medium-mass, heavy, and superheavy spherical and deformed nuclei. Also, it was successfully used to calculate various properties of nuclei [14, 16, 17]. The residual pairing interaction of nucleons

was taken into account in the Lipkin–Nogami approximation [13, 18] , the coupling constant being set to $r_{\rm mic} = 3.30$ fm [13]. In order to calculate shell corrections, we employed a basis formed by oscillator wave functions for the lowest 35 shells of an axially deformed harmonic oscillator and took into account the lowest 2330 single-particle levels. The degree of the correcting polynomial was chosen to be six. This choice is conventional in calculating shell corrections for medium-mass, heavy, and superheavy nuclei [11]. The energies of single-particle levels of nucleons were calculated with the aid of the WSBETA code [16], which was refined in order to take into account greater numbers of shells and levels.

From the data in Fig. 1, it follows that the proton shell corrections have deep local minima at $Z =$ 82, 114, and 164 and that the neutron shell corrections have deep local minima at $N = 126$, 184, and 228. It should be noted that $Z = 82$, 114, and 164 and $N = 126$, 184, and 228 are or are assumed to be magic numbers [4]. For example, the empirically known magic numbers $Z = 82$ and $N = 126$ correspond to the doubly magic spherical nucleus $^{208}\mathrm{Pb}_{126}$. The values that we found for the shell corrections in the doubly magic nuclei $^{208}\mathrm{Pb}_{126}$ and $^{298}114_{184}$ are in good agreement with their counterparts calculated in [13, 14]. Thus, our calculations reproduce known results and make it possible to perform an extrapolation to the region of heavier nuclei.

The proton shell corrections have three deep local minima in the region $164 < Z \leq 400$ (Fig. 1). Therefore, $Z = 210$, 274, and 354 are the magic numbers of protons in this region. Analyzing deep local minima in the dependence of the neutron shell corrections on the number of neutrons in Fig. 1 in the range $228 < N \leq 820$, we can conclude that $N = 308$, 406, 524, 644, and 772 are the magic numbers of neutrons in this region.

ALPHA-DECAY HALF-LIVES

Among nuclei for which we have calculated shell corrections and which are close to the beta-stability line described by Green's formula, the $^{208}\mathrm{Pb}_{126}$, $^{298}114_{184}$, $^{472}164_{308}$, $^{616}210_{406}$, and $^{798}274_{524}$ nuclei are doubly magic. In Fig. 1, the total shell correction $\delta_P + \delta_N$ has deep local minima in the vicinities of these doubly magic nuclei. However, the heavier doubly magic nuclei $^{998}354_{644}$ and $^{1126}354_{772}$ are quite far off the beta-stability line described by Green's formula. For example, the $^{998}354_{644}$ nucleus is neutron-deficient, while the $^{1126}354_{772}$ nucleus is neutron-rich.

Alpha decay and fission are the main modes of decay of doubly magic beta-stable heavy nuclei. Let us estimate the alpha-decay half-lives and fission barriers for the super- and ultraheavy nuclei $^{298}114_{184}$, $^{472}164_{308}$, $^{616}210_{406}$, and $^{798}274_{524}$.

The alpha-decay half-lives for these nuclei will be found with the aid of the phenomenological Viola–Seaborg formula [19], which relates the alpha-decay half-life to the energy of alpha particles and the charge of the primary nucleus. For the constants of the phenomenological Viola–Seaborg formula, the authors of [20] found values that made it possible to reproduce faithfully the experimental half-lives of 58 nuclei heavier than $^{208}\mathrm{Pb}_{126}$. Knowing the total shell corrections calculated here and the macroscopic binding energies of nuclei as calculated by means of the mass formula from [13], we determine the energies of alpha particles (in MeV) emitted by the aforementioned super- and ultraheavy nuclei. We have

$$Q(^{298}114_{184}) \approx 9.4, \quad Q(^{472}164_{308}) \approx 13.1,$$
$$Q(^{616}210_{406}) \approx 20.9, \quad Q(^{798}274_{524}) \approx 35.0.$$

After that, we determine the half-lives with respect to the alpha decay of these nuclei with the aid of the modified Viola–Seaborg formula [20]. The results are (in s)

$$T_{1/2}(^{298}114_{184}) \approx 1.1 \times 10^{2},$$
$$T_{1/2}(^{472}164_{308}) \approx 2.3 \times 10^{4},$$
$$T_{1/2}(^{616}210_{406}) \approx 4.2 \times 10^{-6},$$
$$T_{1/2}(^{798}274_{524}) \approx 3 \times 10^{-21}.$$

The half-lives of the first three doubly magic nuclei with respect to alpha decay are quite long and can readily be measured. The results that we obtained for the energy of alpha particles from the $^{298}114_{184}$ nucleus and for its alpha-decay half-life are in good agreement with the results reported in [14].

Let us estimate fission barriers in doubly magic ultraheavy nuclei. In order to do this, we calculate the deformation energy of nuclei that is associated with the change in their shape. For very heavy nuclei, the fission barrier can be roughly estimated by taking into account only variations in the quadrupole deformation β_2 of the nuclear surface, since the quantity β_2 is small at the barrier, with the result that deformations of higher multipole orders have a weaker effect on the barrier shape. Figure 2 shows the deformation energy as a function of β_2 for the super- and ultraheavy doubly magic nuclei $^{298}114_{184}$, $^{472}164_{308}$, $^{616}210_{406}$, and $^{798}274_{524}$. In calculating nuclear deformation energies, we took into account variations in the liquid-drop and shell energies. The liquid-drop energy was found in the approximation where nuclear interaction is represented as the sum of the Yukawa and exponential terms [21].

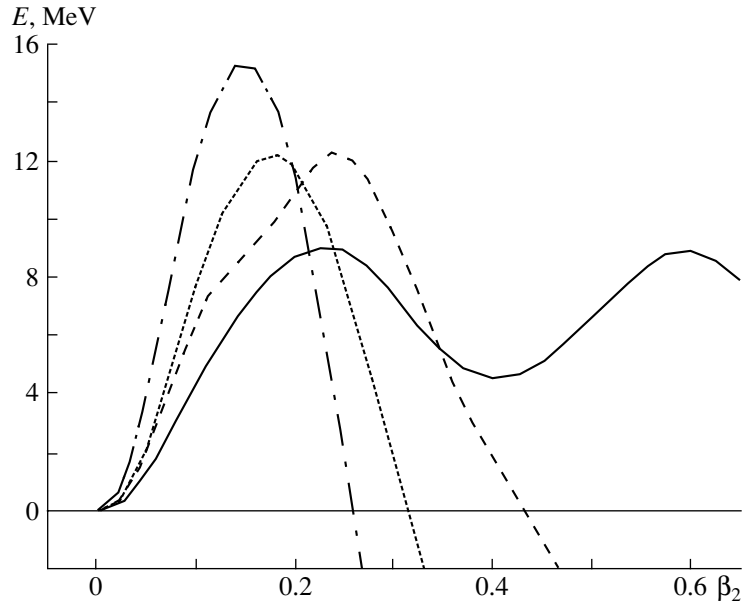

Fig. 2. Deformation energy for the super- and ultraheavy doubly magic nuclei (solid curve) $^{298}114_{184}$, (dashed curve) $^{472}164_{308}$, (dotted curve) $^{616}210_{406}$, and (dash-dotted curve) $^{798}274_{524}$.

From the data in Fig. 2, it follows that the fission barrier in the $^{298}114_{184}$ nucleus has a two-humped shape. The identical fission-barrier shape was obtained in [14] for the $^{298}114_{184}$ nucleus. The inner- and outer-barrier heights determined from the data in Fig. 2 are larger than their counterparts calculated in [14], this being due to the fact that the multipole surface deformations β_2, β_3, β_4, …, β_8 were taken into account in [14]. However, the inner-fission-barrier heights determined from Fig. 2 and in [14] are rather close, because, at small values of β_2, the effect of deformations of higher multipole orders on the barrier height is weak. This makes it possible to estimate the shape and the height of fission barriers in ultraheavy doubly magic nuclei.

From Fig. 2, one can see that the ultraheavy doubly magic nuclei $^{472}164_{308}$, $^{616}210_{406}$, and $^{798}274_{524}$ have rather high but narrow one-humped fission barriers. With increasing nuclear charge, the fission barrier becomes narrower and occurs at smaller values of β_2. An increase in the barrier height with increasing mass number in these doubly magic nuclei is due to an increase in the amplitude of the shell correction (see Fig. 1).

The fission half-life of the $^{298}114_{184}$ nucleus is about 10^{10} times longer than its alpha-decay half-life [14]. The lifetimes of the $114 \leq Z \leq 120$ neighboring nuclei are also determined by their alpha-decay periods [14, 17]. Similarly, the lifetimes of the $^{472}164_{308}$, $^{616}210_{406}$, and $^{798}274_{524}$ nuclei are related to their alpha-decay half-lives, since the fission barriers in these nuclei are rather high. As was indicated above, the half-lives of the doubly magic nuclei $^{472}164_{308}$ and $^{616}210_{406}$ could therefore readily be measured if they were formed.

The nucleus involving the magic number $Z = 164$ of protons can be formed, for example, in the fusion of two lead nuclei, whereas the nucleus involving the magic number $N = 308$ of neutrons can be generated in the fusion of two $^{252}Cf_{154}$ nuclei. However, nuclei arising in these reactions are rather far off the beta-stability line. Ultraheavy doubly magic nuclei can be produced in a collision of two heavy neutron-rich nuclei that is accompanied by the absorption of many neutrons.

DISCUSSION OF THE RESULTS AND CONCLUSION

Recently, there appeared the article of Zhang *et al.* [22], who studied magic numbers for $100 \leq Z \leq 140$ nuclei within the relativistic continuum Hartree–Bogolyubov approximation, employing various versions of microscopic forces. Various nuclear shapes were also taken into account in that article. It is well known that the inclusion of nuclear deformations leads to the emergence of additional local minima in the dependence of shell corrections on the number of nucleons [9–11, 14]. These minima, which are associated with the filling of shells in deformed nuclei, correspond to "quasimagic" numbers. It should be noted that deformed nuclei having filled shells—that is, quasimagic numbers of nucleons—also possess enhanced stability and other properties inherent in spherical beta-stable nuclei involving magic numbers of nucleons. However, the amplitude of magicity

effects in deformed nuclei is less than that in spherical nuclei. In the region $100 \le Z \le 140$, Zhang *et al.* [22] found a greater number of magic numbers than the present author and the authors of [4, 12]. Some of the magic numbers found in [22] are quasimagic. However, the magic numbers $Z = 114$, $N = 184$, and $N = 228$ for $100 \le Z \le 140$ nuclei were found here and in [4, 22] as well.

The shell corrections for $40 \le Z \le 200$, $40 \le N \le 420$ nuclei were calculated in [12] in the Hartree–Fock approximation with various versions of Skyrme forces and on the basis of the relativistic mean-field model. Within various versions of the calculations, magic numbers in the interval $Z \approx 114$–126, an interval around $Z \approx 164$, the interval $N \approx 172$–184, and an interval around $N \approx 308$ were found in that study. It is worth noting that, in the figures presented in [12], deep minima in the shell corrections are seen in the regions close to $N \approx 228$ and $N \approx 406$; unfortunately these minima are not discussed there.

Because of the Coulomb repulsion of protons, a region depleted in nucleons can arise at the center of super- and ultraheavy nuclei [12, 23]. This effect was taken into account in [12]. However, the doubly magic nucleus $^{472}164_{308}$ found here also proved to be doubly magic in the calculations performed in [12] by using some parametrizations of Skyrme forces. The Coulomb repulsion of protons at the center of a nucleus could affect the values of the magic numbers for heavier nuclei, but a detailed investigation of this effect would require substantially changing the parametrization of the nucleon-mean-field potential. It should be noted that a parametrization that would take into account a decrease in the density at the center of a nucleus has not yet been investigated. Therefore, the effect of the Coulomb repulsion of protons at the center of super- and ultraheavy nuclei was not considered in the present study.

In [12, 22], it was indicated that the values of magic numbers in super- and ultraheavy nuclear regions depend both on the choice of model and on the choice of parameters of forces in microscopic calculations. Therefore, it would be of interest to perform investigations similar to those in [12, 22] for heavier nuclei and to compare the results of such investigation with the results obtained here.

By studying shell corrections, we have determined the proton magic numbers $Z = 114$, 164, 210, 274, and 354 and the neutron magic numbers $N = 184$, 228, 308, 406, 524, 644, and 772 in super- and ultraheavy nuclear regions. Ultraheavy nuclei involving magic numbers of protons and neutrons are expected to be more stable and to possess higher binding energies than neighboring nuclei. The alpha-decay periods of some doubly magic ultraheavy nuclei and fission barriers in them are rather large; therefore, searches for such nuclei are of great interest.

REFERENCES

1. M. Goeppert-Mayer and J. Jensen, *Elementary Theory of Nuclear Shell Structure* (Wiley, New York, 1955; Inostrannaya Literatura, Moscow, 1958).
2. V. G. Solov'ev, *Theory of Atomic Nuclei* (Energoizdat, Moscow, 1981; Institute of Physics, Bristol, England, 1992).
3. P. Ring and P. Schuck, *The Nuclear Many-Body Problem* (Springer-Verlag, New York, 1980).
4. S. G. Nilsson and I. Ragnarsson, *Shapes and Shells in Nuclear Structure* (Cambridge Univ. Press, Cambridge, 1995).
5. S. L. Shapiro and S. A. Teukolsky, *Black Holes, White Dwarfs, and Neutron Stars: the Physics of Compact Objects* (Wiley, New York, 1983; Mir, Moscow, 1985).
6. A. B. Migdal, *Fermions and Bosons in Strong Fields* (Nauka, Moscow, 1978) [in Russian]; Rev. Mod. Phys. **50**, 107 (1978).
7. A. B. Migdal, E. E. Saperstein, M. A. Troitsky, and D. N. Voskresensky, Phys. Rep. **192**, 179 (1990).
8. S. V. Adamenko and A. S. Adamenko, nucl-ex/0307011.
9. V. M. Strutinsky, Nucl. Phys A **95**, 420 (1967).
10. V. M. Strutinsky, Nucl. Phys. A **122**, 1 (1968).
11. V. Brack, J. Damgaard, A. S. Jensen, *et al.*, Rev. Mod. Phys. **44**, 320 (1972).
12. M. Bender, M. Nazarewicz, and P.-G. Reinhard, Phys. Lett. B **515**, 42 (2001).
13. P. Moller, J. R. Nix, W. D. Myers, and W. J. Swiatecki, At. Data Nucl. Data Tables **59**, 185 (1995).
14. R. Smolanczuk, Phys. Rev. C **56**, 812 (1997).
15. A. E. S. Green, *Nuclear Physics* (McGraw-Hill, New York, 1955).
16. S. Cwiok, H. Dudek, W. Nazarewicz, and J.Skalsi, Comput. Phys. Commun. **46**, 379 (1987).
17. I. Muntian, Z. Patyk, and A. S. Sobczewski, Acta Phys. Pol. B **32**, 691 (2001); **34**, 2141 (2003).
18. H. C. Pradhan, Y. Nogami, and J. Law, Nucl. Phys. A **201**, 357 (1973).
19. V. E. Viola and G. T. Seaborg, J. Inorg. Nucl. Chem. **28**, 741 (1966).
20. R. Smolanczuk, J. Skalski, and A. Sobiczewski, in *Proceedigns of the International Workshop 24 on Gross Properties of Nuclei and Nuclear Excitations*, Ed. By H. Feldmeier *et al.* (GSI, Darmstadt, 1996), p. 35.
21. O. Moller and J. R. Nix, At. Data Nucl. Data Tables **26**, 165 (1981).
22. W. Zhang, J. Meng, S. Q. Zhang, *et al.*, nucl-ex/0403021.
23. O. Dechargé, J.-F. Berger, M. Girod, and Dietrich, Nucl. Phys. A **716**, 55 (2003).

Translated by A. Isaakyan

Physics of Atomic Nuclei, Vol. 68, No. 7, 2005, pp. 1138–1146. Translated from Yadernaya Fizika, Vol. 68, No. 7, 2005, pp. 1185–1194.

NUCLEI
Theory

Effect of Synchrotron Radiation on Nuclear Beta Decay

I. V. Kopytin and K. N. Karelin*

Voronezh State University, Universitetskaya pl. 1, Voronezh, 394893 Russia

Received May 13, 2004

Abstract—The stimulation of the endothermic beta decay of stable nuclei by the field of synchrotron radiation has been analyzed theoretically in the framework of the photobeta decay mechanism. In contrast to works devoted to the effect of laser fields on beta decay, the action of the field directly on a nucleus rather than on a beta electron is considered (a sufficiently intense flux of hard photons whose energies exceed 60 keV allows this action). The rates of such a beta decay are calculated for a number of "parent nucleus–daughter nucleus" pairs for the relativistic case including Coulomb effects. For the most intense available sources of synchrotron radiation, the rate of stimulated beta decay for most nuclei under investigation appears to be characteristic of third-forbidden β^- transitions. The effect of synchrotron radiation on highly forbidden natural nuclear β^- decays is also analyzed. In particular, irradiation increases the rate of the β^- decay of the $^{87}_{37}$Rb and $^{115}_{49}$In nuclei by 2% and by almost two orders of magnitude, respectively.

INTRODUCTION

Changes in the beta-decay characteristics of nuclei under external actions have been analyzed by many researchers for the last two decades. There are two directions of these investigations: first, analysis of the effect of a strong electromagnetic field (static or laser) on natural nuclear beta decay and, second, the stimulation of the beta decay of stable and naturally beta-active nuclei by collision and other processes.

The works of the first direction were reviewed in [1]. In these works, the natural beta decay of either the neutron or the triton was studied. The effect of the electromagnetic field only on the beta electron was analyzed, because energy transferred directly to a nucleus is much less than nuclear energies. The general conclusion was drawn that the differential probability of the above-indicated beta decay in this scheme depends generally on the wave intensity, but the experimental verification of the predictions is not yet possible. At the same time, variation in the energy flux density of the intense electromagnetic wave over a quite wide range scarcely affects the total probability of beta decay. In this approach, exceptions would be likely presented by beta processes that substantially involve the atomic electron shell such as electron capture or beta decay after which an electron appears in an atomic bound state [2, 3]. In this case, the strong external field can rearrange the atomic shell and thereby affect the rate of the beta process. However, the observation of the effects predicted for these processes also requires quite specific experimental conditions.

Among the works of the second direction, we point to [4–7] (where references to previous works of this cycle can be found) and to [8–11]. In [4–6], so-called collisional beta decay (CBD) was studied. In this case, the decay of a beta-stable nucleus (or a proton) is stimulated by its collisions with other nuclei or elementary particles. In these processes, energy that is transferred by a collisional partner to the target (parent) nucleus may be comparable with nuclear energies. This circumstance enables one to consider those beta transitions to the states of the daughter nucleus that were previously forbidden only by the energy conservation law; i.e., the external action directly on the parent nucleus rather than on the beta electron can be analyzed. In [6], this mechanism of CBD was also used to evaluate the possibility of highly forbidden natural beta transitions. Since cross sections for weak processes are small, the required intensities of incident particle fluxes are evidently too high for real realization of CBD. The investigations provided a conclusion that the observation of the CBD process is impossible, because the intensities of nucleon or ion beams are still insufficient. However, the occurrence of this process is not excluded in massive stars at high temperatures (about $(2–3) \times 10^9$ K), in particular, in the synthesis of "bypassed" (or p) nuclei [7].

Endothermic nuclear beta decay induced by electromagnetic radiation with the Planck frequency

*e-mail: dayna@mail.ru

spectrum (so-called photobeta decay) was analyzed in [8–11]. In contrast to works devoted to the effect of laser fields, temperatures comparable with nuclear energies were considered in [8–11]. As in the case of the CBD process, this circumstance opens the possibility of transferring the photon energy directly to the parent nucleus and realizing beta transitions that were previously forbidden by energy conditions. The first theoretical estimates of the cross section for photobeta decay were performed in [8] in application to the nuclear astrophysical problem and, more recently, in [9] for the problem of the synthesis of p nuclei in massive stars. However, the results that were obtained in [8, 9] are doubtful, because they were obtained in the plane wave approximation. Indeed, as was shown in [10, 11], where the photobeta decay of a stable nucleus in the field of thermal radiation was studied for the relativistic case with the exact inclusion of the effect of the Coulomb nuclear field on leptons, this process, as well as CBD, could contribute appreciably to the synthesis of p nuclei at certain stages of the evolution of a massive star for environmental temperatures $(1–5) \times 10^9$ K, when the energy of a photon absorbed by the parent nucleus at the maximum of the Planck spectrum is equal to 0.3–1.5 MeV. Such temperatures are evidently inaccessible on the Earth, and nuclear photobeta decay is hypothetical for accessible temperatures.

New sources of intense electromagnetic radiation, synchrotron radiation (SR), recently appear in a number of research centers. This radiation has unique characteristics [12] such as a wide spectral range up to the x-ray region with the possibility of obtaining hard photons with energies of several MeV, high power, sharp collimation that ensures high brightness of a source, and spontaneous polarization. All these properties of SR, together with a good theoretical description of its properties, open the way for a wide use of this radiation in physical experiments in atomic, molecular, and condensed matter physics (works in this area were reviewed in [13]; see also [14]). Since SR includes photons with energies above 50 keV and its power is high, the problem of the effect of electromagnetic radiation on nuclear beta decay again becomes urgent now for SR. Since energies transferred to the parent nucleus are sufficiently high and comparable with nuclear energies, for an appropriately chosen "parent nucleus–daughter nucleus" pair, it is possible to directly stimulate nuclear beta transitions that are forbidden under natural conditions only by the energy conservation law. Moreover, a similar mechanism can be used to analyze the possibility of accelerating highly forbidden natural beta decay. In this case, the absorption of a high-energy photon can induce the beta decay of the parent nucleus with those transitions to daughter nuclear states that are energetically forbidden under natural conditions but have quantum characteristics corresponding to allowed beta decay. Owing to a high power of real SR, one can hope, in contrast to CBD and beta decay stimulated by thermal radiation, to obtain rates such that the corresponding beta processes will be observable or, at least, to formulate necessary requirements for realizing this possibility.

The aim of this work is to study the effect of SR on nuclear beta decay. Analysis is based on the formalism developed in [10, 11]. In this formalism as in [8], nuclear beta decay is simulated by the electromagnetic field through the production of a virtual electron–positron pair with the subsequent absorption of a positron by a nucleus and the emission of an antineutrino. In this formalism in contrast to [8], the nuclear Coulomb field and relativism of leptons are exactly included. The characteristics of this endothermic beta decay are analyzed as functions of the parameters of SR, the threshold energy, and the charge number of the parent nucleus. Two situations are considered. In the first case, SR initiates the decays of nuclei that are beta stable under natural conditions and have a relatively low energy threshold. In the second case, SR acts on nuclei whose natural beta decay is possible but is highly forbidden, and the radiation-induced acceleration of their natural beta decay can be expected.

SYNCHROTRON RADIATION SPECTRUM

To date, a number of third-generation SR sources have been commissioned or will be commissioned in the near future. The most intense sources are SPring-8 (Japan), ESRF (France), and APS (USA) (operating at present) and the source PETRA-3 (Germany) under construction. They are characterized by a high energy of electrons in the orbit (6–8 GeV), considerable spectral brightness (the number of photons emitted from a unit area of a source per unit time into unit solid angle in the spectral range $\Delta\omega/\omega$), and a large number of output channels. As a rule, SR is emitted either in a rotating magnet or in special devices that consist of a number of magnets of different polarities and are mounted on the rectilinear section of the orbit of electrons. Depending on the magnetic field magnitude, these devices are classified as undulators (weak field) or wigglers (strong field). Synchrotron radiation that arises in each type of the above devices has the following features. Electrons in the rotating magnet move along a circular orbit and emit SR with a continuous spectrum. At the same time, an electron beam in an undulator deviates at a small angle and very bright and quasi-monochromatic light is formed due to interference effects. Electrons in a wiggler are subjected to a

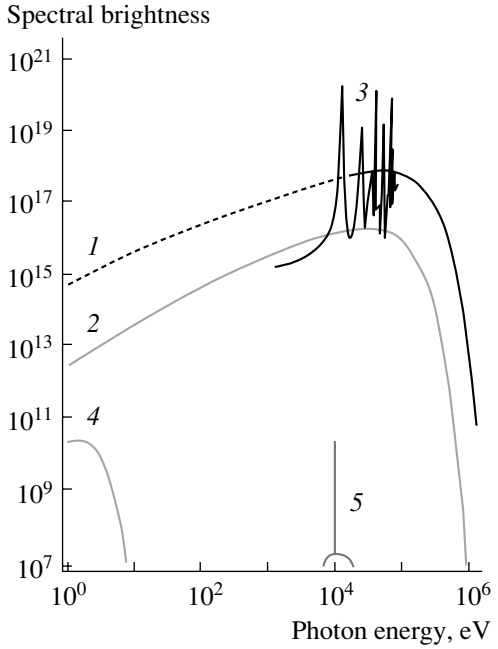

Fig. 1. Spectral brightness of SR sources (photon s^{-1} mm^{-2} $mrad^{-2}$ per 0.1% spectral range) vs. the photon energy for (*1*) wiggler, (*2*) rotating magnet, (*3*) undulator, (*4*) Sun, and (*5*) x-ray tube.

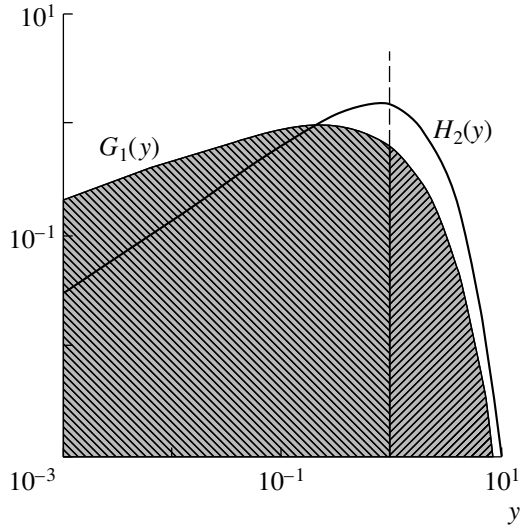

Fig. 2. Functions $G_1(y)$ and $H_2(y)$. Areas corresponding to 50% of the power of emitted SR are shaded.

strong deviating magnetic field and emit SR with high brightness and a continuous spectrum whose maximum is shifted towards higher energies. The SPring-8 setup is the brightest available source of SR of high photon energies ($\gtrsim$60 keV). Figure 1 shows the spectral brightness of this source as a function of the photon energy for various output channels (rotating magnet, wiggler, and undulators) in comparison with the brightnesses of the Sun and an x-ray tube [15].

Let us consider the theory of the above spectral properties. Synchrotron radiation that is formed in the rotating magnet is concentrated in a narrow cone with an angle of about $1/\gamma$, where $\gamma = E_e/m_e c^2$, E_e is the energy of electrons in the synchrotron, m_e is the electron mass, and c is the speed of light. Within this cone, the spectral–angular distribution of the flux of photons with frequency ω in relative frequency interval $d\omega/\omega$ is given by the expression [12]

$$\frac{d^3F(\omega,\theta,\psi)}{d\theta d\psi(d\omega/\omega)} = \frac{3\alpha_e}{4\pi^2}\gamma^2\frac{I}{e}y^2(1+X^2)^2 \times \left[K^2_{2/3}(\xi) + \frac{X^2}{1+X^2}K^2_{1/3}(\xi)\right]. \quad (1)$$

Here, θ and ψ are the observation angles in the horizontal and vertical planes, respectively (the horizontal plane coincides with the electron orbit plane); α_e is the fine structure constant; I is the current in the accelerator; e is the elementary charge; $y = \omega/\omega_c = E_\gamma/E_c$, where $E_\gamma = \hbar\omega$ is the photon energy, $E_c = \hbar\omega_c$, $\omega_c = 3\gamma^3 c/2\rho$ is the critical frequency (it divides the power spectrum into two equal parts), and ρ is the instantaneous radius of the electron trajectory; $X = \gamma\psi$, $\xi = y(1+X^2)^{3/2}/2$; and $K_n(x)$ is the modified Bessel function of the second kind. In terms of the commonly used units, $\rho(\text{in m}) = 3.3E_e/B$ and $E_c(\text{in keV}) = 0.665E_e^2 B$ (where E_e is given in GeV and the magnetic field B is given in tesla). In the horizontal direction ($\psi = 0$), distribution (1) has the form

$$\left.\frac{d^3F(\omega,\theta,\psi)}{d\theta d\psi(d\omega/\omega)}\right|_{\psi=0} = \frac{3\alpha_e}{4\pi^2}\gamma^2\frac{I}{e}H_2(y), \quad (2)$$

where

$$H_2(y) = y^2K^2_{2/3}(y/2),$$

or in the practical units (photon s^{-1} $mrad^{-2}$ into 0.1% of the spectral range)

$$\left.\frac{d^3F(\omega,\theta,\psi)}{d\theta d\psi(d\omega/\omega)}\right|_{\psi=0} = 1.33\times10^{13}E_e^2(\text{in GeV})I(\text{in A})H_2(y). \quad (3)$$

The integration of distribution (1) with respect to ψ yields

$$\frac{d^2F(\omega,\theta)}{d\theta(d\omega/\omega)} = \frac{\sqrt{3}}{2\pi}\alpha_e\gamma\frac{I}{e}G_1(y), \quad (4)$$

where

$$G_1(y) = y\int_y^\infty K_{5/3}(y')dy',$$

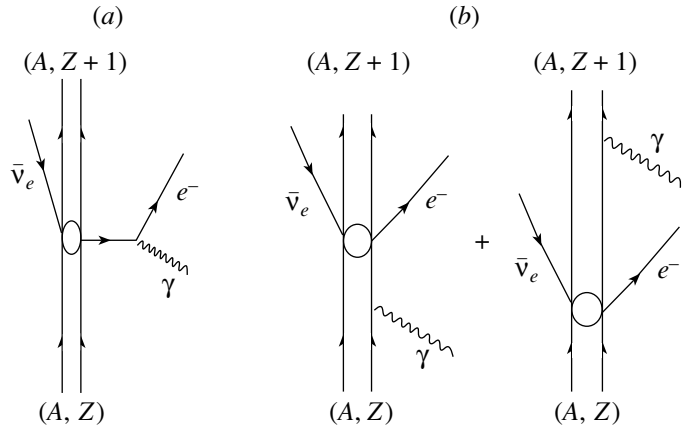

Fig. 3. Diagrams of endothermic β decay induced by electromagnetic radiation.

or in the practical units (photon s^{-1} $mrad^{-1}$ into 0.1% of the spectral range)

$$\frac{d^2F(\omega,\theta)}{d\theta(d\omega/\omega)} = 2.46\times10^{13}E_e(\text{in GeV})I(\text{in A})G_1(y). \tag{5}$$

The frequency dependence of distributions (2) and (4) is determined by the functions $H_2(y)$ and $G_1(y)$. Their plots are shown in Fig. 2. We note that, according to the definition of ω_c,

$$\int_0^1 G_1(y)dy = \int_1^\infty G_1(y)dy.$$

The wiggler radiation spectrum is identical in shape to the rotating-magnet spectrum, but it differs from the latter in a higher critical energy of emitted photons $E_c = \hbar\omega_c = 3e\hbar B\gamma^2/2m_e$ (because electrons move in a stronger magnetic field) and a larger number of these photons. Formulas (3) and (5) for the wiggler have the form

$$\left.\frac{d^3F(\omega,\theta,\psi)}{d\theta d\psi(d\omega/\omega)}\right|_{\psi=0} = 2.65\times10^{13}NE_e^2(\text{in GeV})I(\text{in A})H_2(y) \tag{6}$$

and

$$\frac{d^2F(\omega,\theta)}{d\theta\,(d\omega/\omega)} = 4.92\times10^{13}NE_e(\text{in GeV})I(\text{in A})G_1(y), \tag{7}$$

respectively, where N is the number of periodic elements in the wiggler.

RATE OF PHOTOBETA DECAY STIMULATED BY SYNCHROTRON RADIATION

Following [10, 11], we calculate the rate of the endothermic reaction

$$\gamma + (A,Z) \to (A,Z+1) + e^- + \overline{\nu}_e, \tag{8}$$

which has the energy threshold

$$\Delta \equiv [M(A,Z+1) - M(A,Z) + m_e]\,c^2 > 0. \tag{9}$$

Here, γ is the photon; A and Z are the mass and charge number of the $(A,\ Z)$ nucleus, respectively; e^- is the electron; $\overline{\nu}_e$ is the antineutrino; and $M(A,\ Z)$ is the mass of the nucleus $(A,\ Z)$. Owing to the energy threshold Δ, the natural β^- decay $(A,Z) \to (A,Z+1)$ is impossible and photons with energies $E_\gamma > \Delta$ are necessary in order to open this channel. Feynman diagrams corresponding to this process are shown in Fig. 3. Diagram 3*a* describes photobeta decay through the production of a virtual electron–positron pair in the Coulomb field of the nucleus (A,Z), and diagrams 3*b*, through the virtual excitation of nuclear states (so-called indirect nuclear transitions). For allowed β decays, the probability of an indirect transition obviously has smallness $(Zm_e/m_p)^2$ compared to the process described by diagram 3*a* (m_p is the proton mass), and contributions from bypass transitions will be disregarded below. According to general quantum mechanical rules, the probability of the photobeta transition from the $|\beta_i\rangle$ state of the parent nucleus (A,Z) to the $|\beta_f\rangle$ state of the daughter nucleus $(A,Z+1)$ (β_i, β_f are the sets of the quantum numbers of these states) that is initiated by a photon of energy E_γ is given by the expression

$$P^{(\gamma)}_{\beta,\omega}(\beta_i \to \beta_f) = 2\pi\int\frac{d^3p}{(2\pi)^3}\frac{d^3q}{(2\pi)^3}|M_{fi}|^2 \times \delta(M(A,Z) + \omega - M(A,Z+1) - \epsilon - q_0), \tag{10}$$

where M_{fi} is the amplitude of the $|\beta_i\rangle \to |\beta_f\rangle$ transition, and $\mathbf{p}$ and ϵ ($\mathbf{q}$ and q_0) are the momentum and energy of the electron (antineutrino) (we use the system of units where $\hbar = c = m_e = 1$). In [11], for $P^{(\gamma)}_{\beta,\omega}(\beta_i \to \beta_f)$ we obtained a general expression that can be represented for a particular case of allowed β^- transitions $|\beta_i\rangle \to |\beta_f\rangle$ (only these transitions will be discussed as most intense transitions) in the form

$$P^{(\gamma)}_{\beta,\omega}(\beta_i \to \beta_f) = 24\pi^2 \frac{\alpha_e \ln 2}{\Pi^2_{J_i} f_0 t} \times \sum_{j_\gamma l_\gamma j_e l_e L} \left(\Pi_{l_\gamma} \Pi_{j_e} C^{j_\gamma 1}_{11 l_\gamma 0}\right)^2 \times \int_1^{\omega-\Delta+1} |N^2||L_e|^2 \frac{(1+\omega-\Delta-\epsilon)^2}{\omega} \epsilon\sqrt{\epsilon^2-1}\, d\epsilon. \tag{11}$$

Here, J_i is the spin of the nucleus (A, Z); $f_0 t$ is the reduced lifetime of the β transition; $j_\gamma, l_\gamma (j_e, l_e)$ are the total and orbital angular momenta of the photon (electron), respectively; L is the orbital angular momentum transferred to the nucleus; $\Pi_l = \sqrt{2l+1}$; $C^{jm}_{j_1 m_1 j_2 m_2}$ is the Clebsch–Gordan coefficient; and the nuclear N and leptonic L_e components of the process amplitude are given by the respective expressions

$$N = \left(\frac{2\alpha_e R_{\text{nucl}}}{\nu_g}\right)^{\lambda_g - 1} \sqrt{\frac{\nu_g}{\alpha_e}} \times \left[\delta_{L0}(1+i)(\lambda_g - \eta_g - Z\nu_g - 1)\sqrt{1+E} - \delta_{L'0}(1-i)(\lambda_g - \eta_g + Z\nu_g + 1)\sqrt{1-E}\right], \tag{12}$$

$$L_e = i\frac{\Gamma(\lambda_g - \eta_g)}{\Gamma(2\lambda_g + 1)} \times \left(-(-1)^{l_e} \Pi_{l_e L'} C^{l_\gamma 0}_{l_e 0 L' 0} \begin{Bmatrix} l_e & j_e & 1/2 \\ L' & 1/2 & 1/2 \\ l_\gamma & j_\gamma & 1 \end{Bmatrix} I_1 + (-1)^{j_e} \Pi_{l'_e L} C^{l_\gamma 0}_{l'_e 0 L 0} \begin{Bmatrix} l'_e & j_e & 1/2 \\ L & 1/2 & 1/2 \\ l_\gamma & j_\gamma & 1 \end{Bmatrix} I_2 \right). \tag{13}$$

Here, R_{nucl} is the nuclear radius, $E = \omega - \epsilon$,

$$\nu_g = \frac{\alpha_e}{(1-E^2)^{1/2}}, \tag{14}$$

$$\lambda_g = (1 - (\alpha_e Z)^2)^{1/2}, \quad \eta_g = -EZ\nu_g,$$

$\Gamma(z)$ is the gamma function, $l'_e = 2j_e - l_e$, $L' = 1 - L$,

$$I_1 \equiv \int_0^\infty dr \sqrt{r} f_{l_e}(r) f_-(x) j_{l_\gamma}(\omega r), \tag{15}$$

$$I_2 \equiv \int_0^\infty dr \sqrt{r} g_{l_e}(r) f_+(x) j_{l_\gamma}(\omega r).$$

Here, $x = 2r\alpha_e/\nu_g$ and the large $f_{l_e}(r)$ and small $g_{l_e}(r)$ components of the radial function of the electron in the nuclear Coulomb field [16] are given by the expression

$$\begin{Bmatrix} f_{l_e}(r) \\ g_{l_e}(r) \end{Bmatrix} = 2^{3/2} \exp\left(\frac{\pi\xi_e}{2}\right) \frac{|\Gamma(\gamma_e + 1 + i\xi_e)|}{\Gamma(2\gamma_e + 1)} \frac{(2pr)^{\gamma_e}}{r} \begin{Bmatrix} \sqrt{\epsilon+1}/\epsilon \cdot \text{Im} \\ \sqrt{\epsilon-1}/\epsilon \cdot \text{Re} \end{Bmatrix} \times [e^{i(pr+\zeta_e)} {}_1\text{F}_1(\gamma_e - i\xi_e, 2\gamma_e + 1, -2ipr)], \tag{16}$$

where ${}_1\text{F}_1(a, c, z)$ is the confluent hypergeometric function, $\xi_e = \alpha_e Z\epsilon/p$, $p = (\epsilon^2 - 1)^{1/2}$, $\gamma_e = (\kappa_e^2 - (\alpha_e Z)^2)^{1/2}$, $\kappa_e = \mp(j_e + 1/2)$ for $j_e = l_e \pm 1/2$, $e^{2i\zeta_e} = (\kappa_e - i\xi_e/\epsilon)\,/\,(\gamma_e - i\xi_e)$; $j_{l_\gamma}(\omega r)$ is the spherical Bessel function;

$$f_\pm(x) = \sqrt{1+E} \times \left[(-Z\nu_g + 1) W_{\eta_g - \frac{1}{2}, \lambda_g}(x) \pm W_{\eta_g + \frac{1}{2}, \lambda_g}(x)\right], \tag{17}$$

where $W_{\kappa,\mu}(x)$ is the Whittaker function.

The cross section for photobeta decay induced by the photon of energy E_γ is expressed as [16]

$$\sigma(\omega) = \frac{P^{(\gamma)}_{\beta,\omega}(\beta_i \to \beta_f)}{j}, \tag{18}$$

where j is the photon flux density.

When a target [nucleus (A, Z)] is irradiated by a photon flux with a given frequency spectrum (such as SR that we discuss), the rate λ of the $(A, Z) \xrightarrow{\beta^-, \gamma} (A, Z+1)$ reaction and the yield $n(A, Z+1)$ of nuclei

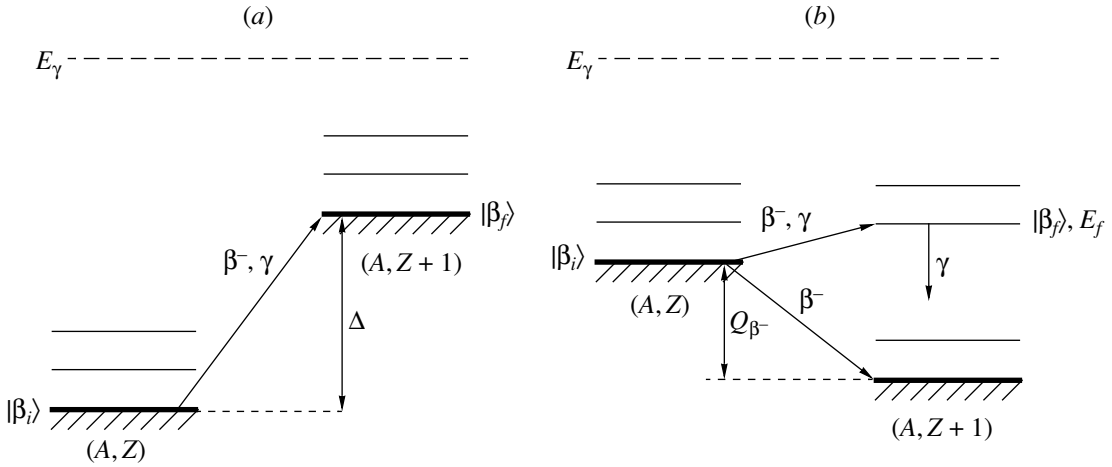

Fig. 4. Schemes of nuclear β^- decay (β^-, γ) stimulated by electromagnetic radiation for (a) a β^- stable nucleus and (b) a nucleus with natural β^- activity; the excited-state energy E_f is measured from the ground-state energy.

$(A, Z\ +\ 1)$ are given by the respective expressions

$$\lambda = V^{-1} \int\limits_{\Delta}^{\infty} d\omega \int d\theta d\psi\, F(\omega, \theta, \psi)\sigma(\omega), \qquad (19)$$

$$n(A, Z+1) = \frac{\rho(A, Z)d}{V} \qquad (20)$$

$$\times \int\limits_{\Delta}^{\infty} d\omega \int d\theta d\psi F(\omega, \theta, \psi)\sigma(\omega).$$

Here, $\rho(A, Z)$ is the density of parent nuclei in the target, d is the target thickness (determined by the penetration depth of photons into the substance, V is the target volume, and $F(\omega, \theta, \psi)$ is defined by Eq. (1). In the general case, $d = d(Z, \omega)$, but photon-energy dependence is disregarded in Eq. (20) (d can be taken at the critical frequency $\omega = \omega_c$, because the SR spectrum is sufficiently narrow). In what follows, the dependence of the photon flux F on the angle ψ will be disregarded. In this case, Eqs. (19) and (20) have the form

$$\lambda = V^{-1} \int\limits_{\Delta}^{\infty} d\omega \int\limits_{-1/2\gamma}^{1/2\gamma} d\theta\, F(\omega, \theta)\sigma(\omega), \qquad (21)$$

$$n(A, Z+1) = \frac{\rho(A, Z)d}{V} \qquad (22)$$

$$\times \int\limits_{\Delta}^{\infty} d\omega \int\limits_{-1/2\gamma}^{1/2\gamma} d\theta F(\omega, \theta)\sigma(\omega),$$

where $F(\omega, \theta)$ is defined by Eqs. (5) and (7) when SR is emitted in the rotating magnet and wiggler, respectively.

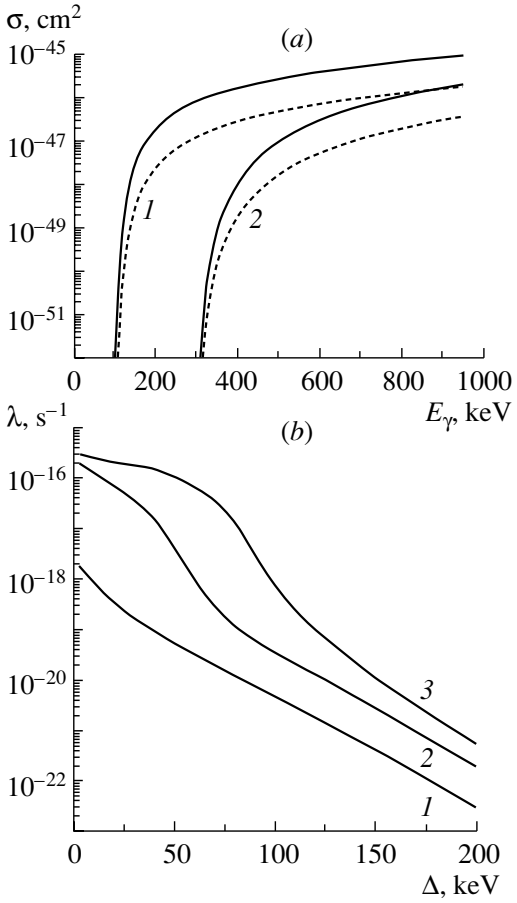

Fig. 5. (a) Cross section σ vs. the incident photon energy for threshold energy $\Delta = (1)$ 100 and (2) 300 keV and for $Z =$ (dashed curves) 40 and (solid curves) 73 and (b) the rate λ of stimulated β^- decay vs. threshold energy for $Z = (1)$ 30, (2) 66, and (3) 82.

STIMULATION OF THE DECAY OF β^- STABLE NUCLEI BY SYNCHROTRON RADIATION: CALCULATIONS

We consider the case where the β^- decay of the parent nucleus (A, Z) is impossible under natural conditions (see Fig. 4*a*). The channel of endothermic $|\beta_i\rangle \xrightarrow{\beta^-,\gamma} |\beta_f\rangle$ transition is open if $E_\gamma > \Delta$. The photon energy dependence of the process cross section [Eq. (18)] was analyzed for various values of the threshold energy Δ and charge number Z. In this analysis, a value of 10^5 s, which is characteristic of suppressed allowed β^- transitions, was used for the reduced lifetime $f_0 t$ of β decay. The calculation results are shown in Fig. 5*a*.

According to Fig. 5*a*, the cross section magnitude is characteristic of weak processes and is equal to $\sim 10^{-46}$–10^{-49} cm^2 in the E_γ energy range of interest. The process cross section decreases as Δ increases at a given Z value and increases appreciably with Z at a given Δ value. A similar Z dependence is observed for the rate of natural β^- decay if the nuclear Coulomb field is taken into account by introducing the universal Fermi function $F(Z, E)$ immediately into the integrand determining the function f_0.

Figure 5*b* shows the rate λ of stimulated β^- decay calculated as a function of Δ for various Z values [Eq. (21)]. The SR photon flux density was calculated with the data for the SPring-8 wiggler, which is the most intense source with a sufficiently wide hard part of the spectrum. Its parameters are as follows: the energy of electrons on the orbit $E_e = 8$ GeV, current $I = 0.1$ A, the critical energy $E_c = 43$ keV, and the periodic-element number $N = 37$ [12].

As is seen in Fig. 5*b*, the process rate depends strongly on the threshold energy. It decreases rapidly from values characteristic of the second-forbidden β transitions (for $\Delta < 40$ keV) to values corresponding to the third- or fourth-forbidden transitions (for $\Delta > 100$ keV). The Z dependence of λ is not as strong as the dependence on Δ.

In order to estimate the practical feasibility of the SR-stimulated nuclear photobeta decay of stable (against β^- decay) (A, Z) nuclei, we selected "parent nucleus (A, Z)–daughter nucleus $(A, Z+1)$" pairs that satisfy the following criteria: (i) the threshold energy Δ must be lower than 200 keV; (ii) the β^- transition between the ground states of these nuclei is allowed; and (iii) the daughter nucleus must be sufficiently long-lived with respect to the inverse $|\beta_f\rangle \to |\beta_i\rangle$ transition (β^+ decay and/or electron capture). The decay rate λ and the yield of daughter $n(A, Z+1)$ nuclei were calculated by Eqs. (21) and (22), respectively. The results obtained with the above parameters of SR are given in Table 1. It is seen that the highest rate of stimulated β^- decay of the $^{163}_{66}$Dy nucleus has an order of magnitude corresponding to the second-forbidden natural β decay (in this case, the threshold energy is anomalously low). In all other cases, λ is much lower and corresponds to third-forbidden transitions (for comparison, $\lambda = 4.7 \times 10^{-19}$ s^{-1} for the well-studied third-forbidden β^- decay of the $^{87}_{37}$Rb nucleus). Such rates are evidently too low for experimental verification of the above results. However, if the intensity of SR increases significantly or the peak of its spectrum is shifted towards higher energies, the rate of the stimulated β^- decay can increase to values corresponding to allowed or first-forbidden β transitions, which would make such an experiment more realizable. Obviously, when selecting candidate nuclei, it is necessary to take into account that the rate of endothermic decay depends strongly on the threshold energy Δ, as is shown in Fig. 5*b*.

ACCELERATION OF NATURAL β^- TRANSITIONS BY SYNCHROTRON RADIATION: RESULTS OF THE CALCULATIONS

We now consider the effect of the SR field on a naturally β^--active parent nucleus (A, Z). Let us describe a possible scheme of accelerating natural β^- decay. We do not discuss the effect of the electromagnetic field on the β electron. As was mentioned above, this effect has been well studied and the corresponding results were discussed in the Introduction. We only emphasize that the integral probability of β decay hardly changes when the field effect is taken into account in such a scheme. As in the case of the stimulation of the decay of β-stable nuclei, which was discussed in the preceding section, we are interested in the possibility of realizing β transitions that are forbidden in the absence of an electromagnetic field by the energy conservation law (see Fig. 4*b*). Owing to the presence of γ rays with energies above 50 keV in the SR spectrum, this β decay channel is not excluded. We now discuss this case in more detail. Let the parent nucleus (A, Z) be β^--unstable, but its natural decay be strongly suppressed. This condition is necessary in order to possibly enhance the effect. In addition, let quantum selection rules allow β transitions from the ground state of the parent nucleus to some of the excited states of the daughter nucleus $(A, Z+1)$ with excitation energies $E_f > Q_{\beta^-}$ (where Q_{β^-} is the energy release for the natural β^- decay). In this case, in order to increase the decay rate, E_f should be as low as possible ($E_f - Q_{\beta^-}$ serves as the energy threshold for photobeta decay, and, as was shown above, the decay probability depends strongly on this threshold). Under these conditions,

Table 1. Rate λ and yield $n(A, Z+1)$ for β^--stable nuclei (hereinafter, experimental data are taken from [17])

Nucleus (A, Z)	$J_i^{\pi_i} \to J_f^{\pi_f}$ transition	Δ, keV	$T_{1/2}$ of the nucleus (A, Z)	$T_{1/2}$ of the nucleus $(A, Z+1)$	λ, s^{-1}	$n(A, Z+1)$, s^{-1} cm^{-3}
$^{68}_{31}$Ga	$1^+ \to 0^+$	106	67.6 min	270 day	9.1×10^{-21}	3.0×10^{-10}
$^{163}_{66}$Dy	$5/2^- \to 7/2^-$	2.6	Stab.	4570 yr	2.0×10^{-16}	6.6×10^{-6}
$^{178}_{73}$Ta	$1^+ \to 0^+$	91	9.3 min	21.6 day	2.3×10^{-19}	7.5×10^{-9}
$^{179}_{72}$Hf	$9/2^+ \to 7/2^+$	110	Stab.	1.82 yr	2.3×10^{-20}	7.8×10^{-10}
$^{181}_{73}$Ta	$7/2^+ \to 9/2^+$	188	Stab.	121.2 day	1.3×10^{-21}	4.3×10^{-11}

Table 2. Decay rate λ for β^--active nuclei

Nucleus (A, Z)	Natural $J_i^{\pi_i} \to J_f^{\pi_f}$ transition	Q_{β^-}, keV	Stimulated $J_i^{\pi_i} \to J_f^{\pi_f *}$ transition	E_f, keV	$\lambda^{(\mathrm{spont})}$, s^{-1}	λ, s^{-1}
$^{79}_{34}$Se	$7/2^+ \to 3/2^-$	151	$7/2^+ \to 9/2^+$	207	$>3.4 \times 10^{-13}$	3.63×10^{-20}
$^{87}_{37}$Rb	$3/2^- \to 9/2^+$	283	$3/2^- \to 1/2^-$	388	$(4.63 \pm 0.04) \times 10^{-19}$	9.61×10^{-21}
$^{107}_{46}$Pd	$5/2^+ \to 1/2^-$	33	$5/2^+ \to 7/2^+$	93	$(3.4 \pm 0.3) \times 10^{-15}$	7.55×10^{-20}
$^{115}_{49}$In	$9/2^+ \to 1/2^+$	495	$9/2^+ \to 7/2^+$	612	$(4.98 \pm 0.25) \times 10^{-23}$	3.28×10^{-21}
$^{129}_{53}$I	$7/2^+ \to 1/2^+$	194	$7/2^+ \to 5/2^+$	321	$(1.40 \pm 0.04) \times 10^{-15}$	4.34×10^{-21}
$^{135}_{55}$Cs	$7/2^+ \to 3/2^+$	269	$7/2^+ \to 5/2^+$	480	$(9.6 \pm 0.3) \times 10^{-15}$	1.99×10^{-22}

SR makes the endothermic β^- transition possible from the ground state $|\beta_i\rangle$ of the nucleus (A, Z) to the excited state $|\beta_f\rangle$ of the daughter nucleus $(A, Z+1)$ with energy E_f through the above mechanism of stimulated β^- decay. It is assumed that the daughter nucleus $(A, Z+1)$ will be subsequently deexcited due to electromagnetic relaxation. In this case under certain conditions (a low rate of natural β decay and a relatively low energy threshold $E_f - Q_{\beta^-}$), a certain increase in the yield of the daughter nucleus $(A, Z+1)$ can be expected compared to their yield in the natural β process.

Taking into account the above requirements, we analyzed the schemes of the decay of β^--active nuclei with large lifetimes and listed candidates appropriate for investigations in Table 2. Some nuclei whose β^- decays are classified among second-forbidden transitions are not presented in Table 2, because the spins and parities of the appropriate excited states of these nuclei are uncertain.

The rate λ of the $(A, Z) \xrightarrow{\beta^-, \gamma} (A, Z+1)^*$ transition into the excited state $|\beta_f\rangle$ is calculated as previously by Eq. (21) for SR from the wiggler with the same parameters. The calculation results are also given in Table 2. For comparison, this table also presents the rate of the natural β^- decay of the nucleus (A, Z), which was calculated by the formula $\lambda^{(\mathrm{nat})} = \ln 2 / T_{1/2}$, where $T_{1/2}$ is the known half-life.

As is seen in Table 2, as in the case of the photobeta decays of stable nuclei, the rates λ correspond to the third-forbidden β transitions. These results are primarily attributed to the relatively high energy thresholds of endothermic reactions (60 keV or above). Therefore, for most suppressed β transitions presented in Table 2, radiation-induced change in the natural-decay rate is insignificant (no more than $2 \times 10^{-3}\%$). As was mentioned above, an increase in the SR flux density or a shift of the peak in its spectrum towards higher energies can significantly affect the rate of stimulated β decay. The third- and fourth-forbidden β decays of the $^{87}_{37}$Rb and $^{115}_{49}$In nuclei, respectively, are the only exceptions. In the former case, the rate of β^- decay increases by more than 2%, which is beyond the λ-measurement accuracy ($\lesssim 1\%$). In the latter case, the rate of β^- decay increases by a factor of almost 100, which is evidently due to a very strong suppression of the natural β^- transition.

CONCLUSIONS

The above study of endothermic β^- decays stimulated by synchrotron radiation provides the following conclusions.

(i) The rate of endothermic decay depends strongly on the energy threshold and, more slightly, on the charge number Z of the parent nucleus.

(ii) For all above cases of stimulated β decays of stable and naturally β^--active parent nuclei irradiated with synchrotron radiation from available intense sources, the order of magnitude of the decay rate is typical for third-forbidden β transitions. The endothermic β^- decay of the $^{163}_{66}$Dy nucleus with an anomalously low threshold energy is the only exception. The rate of this β^- decay corresponds to second-forbidden natural transitions. For this reason, the rate of the second-forbidden natural and first-forbidden β^- decays changes only slightly ($\lesssim 10^{-3}\%$). However, this change is already equal to 2% for the third-forbidden β^- transition of the $^{87}_{37}$Rb nucleus, and the rate of the strongly suppressed β decay of the $^{115}_{49}$In nucleus increases by almost two orders of magnitude.

(iii) Owing to relatively low rates of endothermic decays stimulated by the available synchrotron radiation sources, the effect can hardly be observed experimentally. However, real situations, where the stimulation of natural β^- decay is considered, are better, because stimulated β^- decay occurs to an excited state of the daughter nucleus. This circumstance allows the identification of decay by methods using γ rays, i.e., by detecting nuclear γ rays arising as a result of the deexcitation of the excited state. In this case, both the energy of the emitted photon and the lifetime of the excited state are important. In principle, "parent nucleus–daughter nucleus" pairs appropriate for experiment can be chosen. Rapid advance in the creation of intense sources of SR provides the hope that the corresponding experimental problem will be solved. A solution to this problem will give an answer to the fundamental question of whether external effects can stimulate nuclear decays—in particular, those that are forbidden by the energy-conservation law. Moreover, a positive answer to this question will possibly promote a solution to the problem of utilization of nuclear waste.

ACKNOWLEDGMENTS

We are grateful to A.N. Almaliev for stimulating discussions and valuable remarks. This work was supported by the Ministry of Education of the Russian Federation, project no. A03-2.9-450.

REFERENCES

1. I. M. Ternov, V. N. Rodionov, and O. F. Dorofeev, Fiz. Élem. Chastits At. Yadra **20**, 51 (1989) [Sov. J. Part. Nucl. **20**, 22 (1989)].
2. I. S. Batkin and I. V. Kopytin, Yad. Fiz. **53**, 930 (1991) [Sov. J. Nucl. Phys. **53**, 574 (1991)].
3. M. Jung, F. Bosch, K. Beckert, *et al.*, Phys. Rev. Lett. **69**, 2164 (1992).
4. I. S. Batkin, I. V. Kopytin, and O. V. Tyutina, Yad. Fiz. **53**, 1576 (1991) [Sov. J. Nucl. Phys. **53**, 968 (1991)].
5. I. V. Kopytin, M. A. Dolgopolov, É. G. Karpov, and T. A. Churakova, Yad. Fiz. **60**, 592 (1997) [Phys. At. Nucl. **60**, 513 (1997)].
6. I. V. Kopytin, É. G. Karpov, and T. A. Churakova, Izv. Ross. Akad. Nauk, Ser. Fiz. **61**, 49 (1997).
7. I. V. Kopytin and T. A. Krylovetskaya, Yad. Fiz. **61**, 1589 (1998) [Phys. At. Nucl. **61**, 1479 (1998)].
8. P. B. Shaw, D. D. Clayton, and F. C. Michel, Phys. Rev. **140**, 1433 (1965).
9. I. V. Kopytin and T. A. Krylovetskaya, Izv. Ross. Akad. Nauk, Ser. Fiz. **64**, 935 (2000).
10. I. V. Kopytin, K. N. Karelin, and A. A. Nekipelov, Izv. Ross. Akad. Nauk, Ser. Fiz. **67**, 670 (2003).
11. I. V. Kopytin, K. N. Karelin, and A. A. Nekipelov, Yad. Fiz. **67**, 1455 (2004) [Phys. At. Nucl. **67**, 1429 (2004)].
12. D. Attwood, *Soft X rays and Extreme Ultraviolet Radiation: Principles and Applications* (Cambridge Univ. Press, Cambridge, 1999).
13. I. M. Ternov, Usp. Fiz. Nauk **165**, 429 (1995) [Phys. Usp. **38**, 409 (1995)].
14. I. M. Ternov and V. V. Mikhaĭlin, *Synchrotron Radiation. Theory and Experiment* (Énergoatomizdat, Moscow, 1986) [in Russian].
15. http://www.spring8.or.jp/e/general_info/overview
16. V. B. Berestetskii, E. M. Lifshitz, and L. P. Pitaevskii, *Quantum Electrodynamics* (Nauka, Moscow, 1989; Pergamon, Oxford, 1982).
17. R. B. Firestone and V. S. Shirley, *Table of Isotopes*, 8th ed. (Wiley, New York, 1996).

Translated by R. Tyapaev

Physics of Atomic Nuclei, Vol. 68, No. 7, 2005, pp. 1147–1152. Translated from Yadernaya Fizika, Vol. 68, No. 7, 2005, pp. 1195–1200.

NUCLEI
Theory

Nature of Coulomb Shifts of Nuclear Scattering Resonances

N. Zh. Takibayev

Kazakh National Pedagogical University, Almaty, Kazakhstan

Received June 8, 2004; in final form, December 17, 2004

Abstract—Relations determining the shift of energies and widths of scattering resonances are obtained within the method of evolution in the coupling constant. These relations generalize the well-known relations for the shift of levels in a discrete spectrum. The problem of determining the Coulomb shifts of low-energy resonances manifesting themselves in the cross section for the scattering of some light nuclei is solved. Examples that are of importance for nuclear astrophysics and examples of problems that are associated with the production of chemical elements are considered. The character of Coulomb shifts is studied within simple nuclear models. Respective numerical estimates are given, which agree satisfactorily with experimental data. © *2005 Pleiades Publishing, Inc.*

1. INTRODUCTION

Low-energy resonances that manifest themselves in scattering processes involving light nuclei are likely to play an important role in the dynamics of nucleosynthesis occurring within stars and in the active region of galaxies [1–3]. In order to assess the role of such processes, it is of importance to determine reliably the parameters of some resonances whose energy is close to or less than the Coulomb barrier between interacting nuclei. The blocking effect of Coulomb forces hinders an experimental determination of nuclear cross sections in the region of astrophysical energies (from a few tens of electronvolts to a few kiloelectronvolts). Usually, nuclear data at such energies are deduced by means of extrapolation from the region of higher energies under the assumption that there are no resonances at such low energies, so that the cross sections in question change monotonically [1, 4].

At the same time, results obtained for few-body systems suggest that, in this energy region, narrow resonances can exist in some nuclear systems [5]. If so, advances in solving problems of nuclear synthesis and nucleogenesis (that is, the formation of chemical elements) will depend on the development of resonance physics and on the dynamics of complicated quantum systems [6].

Coulomb repulsion is of particular importance for low-energy nuclear resonances, since it reduces the probability for particles to approach each other closely and, hence, the probability of their nuclear interactions. Moreover, Coulomb repulsion can deform a resonance substantially—for example, push it to the region of higher energies.

As is well known, problems of scattering governed by both Coulomb and nuclear forces have special features inherent in them that are due to the "bad" behavior of Coulomb forces in the asymptotic region. This leads to the interplay of the nuclear and Coulomb transition operators, with the result that, even upon the separation of the purely Coulomb component from the total two-particle amplitude, the remainder involves irregular factors [7–9]. The situation becomes even more complicated in the problems where the scattering process involves three or more particles [10–12].

The aforesaid concerns the general problem of scattering in complicated systems governed by Coulomb and nuclear forces. However, the problem of describing the properties of resonance scattering becomes more tractable in the energy region around a narrow resonance. First of all, this applies to a determination of the Coulomb shift of resonance levels [13, 14].

In this connection, it is of importance to analyze the effect of Coulomb forces on the character of changes in the resonance position and width. Such estimates can be of use for many problems of nuclear astrophysics, as well as for problems of atomic and molecular physics and other branches of physics, where one often has to deal with interactions of different character and with resonance states of systems [15].

In the present study, we explore the character of the Coulomb shift of resonance nuclear states. Relations determining this shift—that is, the energy shift of such states and the change in their width—are obtained by the method of evolution in the coupling constant [13].

The ensuing exposition is organized as follows. Section 2 contains a brief account of the method of evolution in the coupling constant with special

emphasis on the details that are necessary for the ensuing calculations. Also, a generalization of the respective relations to the case of resonance scattering is given there. In Section 3, we consider examples involving simple model nuclear forces and admitting analytic solutions and generalizations of these examples to the cases incorporating Coulomb repulsion forces.

2. RELATIONS OF THE METHOD OF EVOLUTION IN THE COUPLING CONSTANT FOR THE SHIFT OF RESONANCE STATES

Let us briefly describe the method of evolution in the coupling constant [16, 17]. In doing this, we will give special attention to the points that are of importance for the ensuing exposition. We represent the total Hamiltonian of a quantum system in the form

$$H = H_0 + \lambda V + \alpha U, \tag{1}$$

where H_0 is a free Hamiltonian; λV is the potential of nuclear forces; λ is the respective coupling constant, which is factored out in this term; αU is the Coulomb potential; and $\alpha = e^2$ is the Coulomb coupling constant.

The method of evolution in the coupling constant describes the evolution of a quantum system in response to a variation in the coupling constant. The evolution of our system can be considered with respect to variations in the nuclear coupling constant λ, the Coulomb coupling constant α, or both coupling constants simultaneously. The final result must not depend on the method of analysis. In applying the method, it is assumed that the initial conditions of the problem (for example, solutions at $\lambda = 0$ or $\alpha = 0$) are known or preset.

We first consider the evolution of the system in the coupling constant λ, assuming that Coulomb forces are switched off. Differentiating the Schrödinger equation

$$(E_\nu - H)|\Psi_\nu\rangle = 0 \tag{2}$$

with respect to the parameter λ, we obtain the evolution equations for the wave function in the form

$$\frac{d}{d\lambda}|\Psi_\nu\rangle = G_+(E_\nu)V|\Psi_\nu\rangle \tag{3}$$

where $G_+(E) = (E - H + i\gamma)^{-1}$ and $\gamma \to 0_+$.

For levels of the discrete spectrum, there is the well-known relation [18]

$$\frac{d}{d\lambda}E_\nu = \langle\Psi_\nu|V|\Psi_\nu\rangle, \tag{4}$$

which is widely used.

In the scattering region, the method of evolution in the coupling constant leads to the equations

$$\frac{d}{d\lambda}S_{\mu\nu} = -2\pi i\delta(E_\mu - E_\nu)\sum_\sigma S_{\mu\sigma}V_{\sigma\nu} \tag{5}$$

for the scattering matrix $S_{\mu\nu} = \langle\Psi_\mu^-|\Psi_\nu^+\rangle$ and to the equations

$$\frac{d}{d\lambda}V_{\mu\nu} = \sum_\sigma V_{\mu\sigma}V_{\sigma\nu} \times \left(\frac{1}{E_\mu - E_\sigma - i\gamma} + \frac{1}{E_\nu - E_\sigma + i\gamma}\right) \tag{6}$$

for the matrix elements $V_{\mu\nu} = \langle\Psi_\mu|V|\Psi_\nu\rangle$, the initial conditions being $S_{\mu\nu}(\lambda = 0) = \delta_{\mu\nu}$ and $V^0_{\mu\nu} = V_{\mu\nu}(\lambda = 0)$.

It should be noted that Eqs. (5) reduce to the evolution equations for the phase shifts, which are defined by the relations $S_L(E) = \exp(2i\delta_L(E))$. We have

$$\frac{d}{d\lambda}\delta_L = -\pi i\rho(E_\nu)V_L(E_\nu, E_\nu), \tag{7}$$

where $\rho(E)$ is the density of states in the continuum region, the initial condition for the phase shift being $\delta^0 = \delta(\lambda = 0) = 0$. For the total S matrix to be unitary, it is necessary that the phase shift be real-valued (or the phase-shift matrix be Hermitian in the multichannel case). Therefore, the method of evolution is frequently referred to as a unitary approach in scattering theory [19].

The aforesaid also applies to the evolution equations with respect to the Coulomb coupling constant α—only the initial conditions will be different.

Let us now consider a simple isolated resonance, in which case the physical scattering amplitude exhibits a characteristic Breit–Wigner behavior,

$$f(E) \approx -\frac{1}{\pi\rho(E)}\frac{\Gamma/2}{E - E_R + i\Gamma/2}.$$

It is assumed that the off-shell amplitude $f(\mathbf{p}, \mathbf{p}'; Z)$, where $\mathbf{p}$ and $\mathbf{p}'$ are, respectively, the initial and the final momentum and the complex energy is $Z = k^2/(2\mu)$, has poles in the second sheet of energies at $Z = E_{\text{res}} = k^2_{\text{res}}/(2\mu)$ or in the complex plane of wave number at the points $k = k_{\text{res}}$, where $k_{\text{res}} = \pm k_R + ik_I$, $E_R = (k_R^2 - k_I^2)/(2\mu)$, and $\Gamma = -4k_Ik_R/(2\mu)$ with $k_I \le 0$. It is well known that, for $Z \to E = p_0^2/(2\mu)$ and $|\mathbf{p}| = |\mathbf{p}'| \to p_0$, the amplitude behaves as $f(p, p'; Z) \to f(E)$.

Let us represent $f(p, p'; Z)$ in the vicinity of the pole in the well-known form

$$f_{\text{res}}(p, p'; Z) = \langle p|\xi\rangle\frac{1}{Z - E_{\text{res}}}\langle\bar{\xi}|p'\rangle. \tag{8}$$

Using the Lippmann–Schwinger equation and equating the pole terms on its left and right-hand sides, we then obtain

$$\langle\bar{\xi}|p\rangle = (Z - E_{\rm res})\frac{[-\langle\Psi^0|\lambda V|\Psi^0\rangle + \ldots]}{\left[\langle\Psi^0|\xi\rangle - \sum\limits_{\sigma}\langle\Psi^0|\lambda V G_0(Z)|\xi\rangle\right]}, \tag{9}$$

where $G_0(Z) = (Z - H_0)^{-1}$. We note that, in a complicated multichannel problem, the form-factor representation will differ from (9) only by the bracketed expression in the numerator on the right-hand side of this relation.

The expression in the denominator on the right-hand side of (9) is of prime importance for the approximation used. From this expression, which vanishes at $Z = E_{\rm res}$, we can derive the following equation upon discarding wave vectors orthogonal to $\langle\Psi^0|$ and setting $|\xi\rangle = \lambda V|\varphi_{\rm res}\rangle$:

$$(E_{\rm res} - H_0 - \lambda V)|\varphi_{\rm res}\rangle = 0. \tag{10}$$

A similar result can be obtained for the vector $\bar{\varphi}_{\rm res}$ as well.

On the basis of equations belonging to the type in (10), we now derive, by means of the same procedure as that applied to Eq. (4), the evolution equation for the resonance energy [15]. The result is

$$\frac{dE_{\rm res}}{d\lambda} = \langle\bar{\varphi}_{\rm res}|V|\varphi_{\rm res}\rangle/\langle\bar{\varphi}_{\rm res}|\varphi_{\rm res}\rangle. \tag{11}$$

It is important to note that the $\varphi_{\rm res}$ and $\bar{\varphi}_{\rm res}$ (in contrast to the vectors Ψ_ν) are meaningful in a bounded region of energies—they are not eigenfunctions for the system in question and are not orthonormalized, the quantity $\langle\bar{\varphi}_{\rm res}|\varphi_{\rm res}\rangle$ not being real-valued. Moreover, $E_{\rm res}$ is complex-valued and has nothing to do with the eigenvalues of the Hamiltonian.

Relation (11) has a form that is close to the canonical form of Eq. (4) and is, in this sense, a generalization of (4), relating the features of the resonance $E_{\rm res}$ to the parameters of the interaction forces.

We will now extend the above procedure to resonance states where Coulomb forces are operative along with nuclear forces. We will consider the evolution of the system in response to variations in the Coulomb coupling constant α, assuming that nuclear forces are fixed, but that they are responsible for the existence of the scattering resonances being considered. Restricting, as before, the region under consideration to that around $Z \approx E_{\rm res}$, we obtain the relation

$$\frac{dE_{\rm res}}{d\alpha} = \langle\bar{\varphi}^{\rm C}_{\rm res}|U|\varphi^{\rm C}_{\rm res}\rangle/\langle\bar{\varphi}^{\rm C}_{\rm res}|\varphi^{\rm C}_{\rm res}\rangle, \tag{12}$$

which is of the same type as relation (11), but which involves modifications induced by Coulomb forces. With allowance for the initial conditions, the solution can be represented in the form

$$E_{\rm res}(\alpha) = E_{\rm res}(\alpha = 0) + \int\limits_0^\alpha d\alpha\langle\bar{\varphi}^{\rm C}_{\rm res}|U|\varphi^{\rm C}_{\rm res}\rangle/\langle\bar{\varphi}^{\rm C}_{\rm res}|\varphi^{\rm C}_{\rm res}\rangle. \tag{13}$$

In the following, we consider some simple example, employing relations (12) and (13).

3. MODEL PROBLEMS INVOLVING SEPARABLE NUCLEAR INTERACTION

By way of illustration, we consider a simple model problem that admits an exact analytic solution. The model in question employs a separable potential of the Yamaguchi type,

$$\{\lambda V\}^J_{L,S} = |\nu^J_{L,S}\rangle\lambda^J_{L,S}\langle\nu^J_{L,S}|. \tag{14}$$

Here, the coupling constant $\lambda^J_{L,S}$ is taken to be real-valued for the total Hamiltonian to be Hermitian.

Separable potentials are advantageous in that they make it possible to find a final solution. The amplitude can be represented in the analytic form

$$f = -|\nu\rangle\eta(Z)\langle\nu|, \tag{15}$$

where

$$\eta = \{1/\lambda - A(Z)\}^{-1}, \quad A(Z) = \langle\nu|G_0(Z)|\nu\rangle. \tag{16}$$

Here, the indices labeling states are suppressed for the sake of simplicity. If the sum of a few separable potentials appears in (14), then the expressions in (15) and (16) must treated as matrix-valued quantities in this new index as well.

Upon the inclusion of Coulomb forces, the distinction will consist in the modification of transition operators [7–10]. The Coulomb–nuclear amplitude $f_{\rm C}$ preserves the form (15), but the modified quantities then appear to be

$$\eta^{\rm C} = \{1/\lambda - A^{\rm C}(Z)\}^{-1}, \tag{17}$$

$$A^{\rm C}(Z) = \langle\nu^{\rm C}|G_0(Z)|\nu^{\rm C}\rangle = \langle\nu|G_{\rm C}(Z)|\nu\rangle, \tag{18}$$

where $G_{\rm C} = (Z - H_0 - \alpha U)^{-1}$ is the Coulomb Green's function.

It is important to note that the purely nuclear coupling constant appears in the expression on the right-hand side of (17) and that the following equality holds at the pole point:

$$1/\lambda = A^{\rm C}(E_{\rm res}). \tag{19}$$

By definition, its left-hand side is independent of the coupling constant α. Obviously, its right-hand side

will not change with α either, whence we readily obtain the condition $dA^{\mathrm{C}}(E_{\mathrm{res}})/d\alpha = 0$, which entails the relation

$$\frac{dE_{\mathrm{res}}}{d\alpha} = \frac{\langle\nu|G_{\mathrm{C}}(E_{\mathrm{res}})UG_{\mathrm{C}}(E_{\mathrm{res}})|\nu\rangle}{\langle\nu|G_{\mathrm{C}}(E_{\mathrm{res}})G_{\mathrm{C}}(E_{\mathrm{res}})|\nu\rangle} = \frac{\langle\bar{\xi}^{\mathrm{C}}|U|\xi^{\mathrm{C}}\rangle}{\langle\bar{\xi}^{\mathrm{C}}|\xi^{\mathrm{C}}\rangle}, \tag{20}$$

where we have used the notation

$$|\xi^{\mathrm{C}}\rangle = G_{\mathrm{C}}(E_{\mathrm{res}})|\nu\rangle, \quad \langle\bar{\xi}^{\mathrm{C}}| = \langle\nu|G_{\mathrm{C}}(E_{\mathrm{res}}). \tag{21}$$

In the model being considered, relation (20) is exact and determines the Coulomb shift of the pole point.

Within this simple model, we will further consider a few nuclear systems that are of importance for applications.

The first example is that of resonance nucleon scattering on alpha particles at low energies. The respective amplitudes have distinct resonances in the P-wave components $P^J_{L;S}$, where $J = 3/2$, $L = 1$, and $S = 1/2$. These resonances can be described satisfactorily by the simple separable potential (14) involving the form factor

$$\langle\nu^{3/2}_{1;1/2}|p\rangle = \nu_{3/2}(x) = \mathrm{const}\cdot x/(1+x^2), \tag{22}$$

where $\mathrm{const} = \sqrt{8\pi/(2\mu\beta)}$ and β is the inverse range of nuclear forces. Here, the dimensionless variable $x = p/\beta$ was introduced for the sake of convenience. We will employ it in the following as well, introducing the notation $x_Z = k/\beta$, $x_R = k_R/\beta$, and $x_I = -k_I/\beta$.

The amplitudes has a pole at the point $Z = E_{\mathrm{res}}$, where $A(E_{\mathrm{res}}) = 1/\lambda$. For the potential involving the form factor (22), it follows that $A(Z) = -(1 - 2ix_Z)/(1 - ix_Z)^2$.

For the $n\alpha$ system, experimental data yield $E_R = 0.9$ MeV and $\Gamma = 0.6$ MeV [4], whence it follows that the resonance parameters have the values of $x_R = 0.158$ and $x_I = -0.0256$, from which we can determine the features of the nuclear potential: $\lambda = -(1 + x_I)$ and $\beta = 1.175$ fm^{-1}.

Let us now estimate the Coulomb shifts in the mirror system—that is, find the features of the $p\alpha$ resonance. By numerically estimating the expression

$$\Delta E^{\mathrm{C}} = \alpha\frac{1}{t}\int\limits_0^t dy\frac{\langle\bar{\xi}^{\mathrm{C}}|U|\xi^{\mathrm{C}}\rangle}{\langle\bar{\xi}^{\mathrm{C}}|\xi^{\mathrm{C}}\rangle}, \tag{23}$$

we find that $\Delta E^{\mathrm{C}}/E_R \approx 1.056 - i0.73$ or $E^{\mathrm{C}}_R \approx 1.83$ MeV and that $\Gamma^{\mathrm{C}} \approx 1.54$ MeV, these values being in satisfactory agreement with their experimentally determined counterparts $E^{\mathrm{C}}_{R,\mathrm{exp}} = 1.9$ MeV and $\Gamma^{\mathrm{C}}_{\mathrm{exp}} = 1.5$ MeV [4].

Here, it should be noted that the resonance-position shift, which is determined by the real part of (23), is satisfactorily described by simple perturbation theory. At the same time, the shift of the resonance width depends on α and on the parameters of nuclear forces in an intricate way, so that it can be determined only numerically [13].

Indeed, the nuclear form factors of the potential that are modified by Coulomb forces acquire the characteristic factor

$$C^2_{L=1} = \frac{2\pi/(\zeta x)}{[\exp(2\pi/(\zeta x)) - 1]}\left(1 + \frac{1}{\zeta^2x^2}\right), \tag{24}$$

where $\zeta = \beta a_0$ and a_0 is the Bohr radius of the system, special features of the large-distance asymptotic behavior, which are insignificant for (23), being disregarded here.

For the system being considered, we have $\zeta \approx 19.35$, while the quantity $\Delta_R = \mathrm{Re}\{\langle\bar{\xi}^{\mathrm{C}}|\xi^{\mathrm{C}}\rangle/\langle\bar{\xi}^{\mathrm{C}}|\xi\rangle\}$ is close to unity for small x_{res}:

$$\Delta_R = \left(1 + \frac{1}{\zeta}(4 - 2\ln\zeta) - \frac{3}{\zeta^3} + \ldots\right). \tag{25}$$

We note that $1/\zeta \sim \alpha$. As to the quantity $\Delta_I = \mathrm{Im}\{\langle\bar{\xi}^{\mathrm{C}}|\xi^{\mathrm{C}}\rangle/\langle\bar{\xi}^{\mathrm{C}}|\xi\rangle\}$, it is a more complicated function of ζ and x_{res} [13].

An estimation of the quantity $\langle\bar{\xi}^{\mathrm{C}}|r^{-1}|\xi^{\mathrm{C}}\rangle$ yields nearly the same result. With increasing α, its real part undergoes virtually no change, while the imaginary part, albeit being dependent on ζ in a complicated way, makes a very small contribution. Thus, the resonance-energy shift is nearly linear in the constant α at small x_{res}.

Let us consider yet another example, that of resonance nucleon scattering on the nucleus of a ^{6}Li atom at very low energies. In the channel characterized by the quantum numbers $J^\pi = 5/2^-$, $L = 1$, $S = 3/2$, and $T = 1/2$, there are a resonance of width $\Gamma \approx 0.154$ MeV at $E_R \approx 0.225$ MeV for the $n\,^6$Li system and a resonance of width $\Gamma^{\mathrm{C}} \approx 0.836$ MeV at $E^{\mathrm{C}}_R \approx 1.6$ MeV for the $p\,^6$Li system [4].

Following the same line of reasoning as in the preceding case, we choose the potential in the form (14) with the form factor (22) and first determine the parameters for the $n\,^6$Li system. The results are $x_R = 0.149$, $x_I = -0.0229$, and $\beta = 0.683$ fm^{-1}. By using relation (23), we then estimate the Coulomb shift of the energy and the width of the resonance in the $p\,^6$Li system. We obtain the values of $E^{\mathrm{C}}_R \approx 1.72$ MeV and $\Gamma^{\mathrm{C}} \approx 0.78$ MeV, which are close to their experimental counterparts from [4].

In the calculations,we took into account the pronounced cluster structure of the lithium nucleus.

In evaluating the integrals in (23)—in particular, the quantity $\langle\bar{\xi}^{\mathrm{C}}|r^{-1}|\xi^{\mathrm{C}}\rangle$—we imposed a constraint on the minimum distance between charged clusters. Specifically, we set it to the alpha-particle size.

Finally, we consider low-energy resonance scattering in the system of two alpha particles. For the resonance energy and width, experimental data yield the values of, respectively, $E_R^{\mathrm{C}} \approx 92$ keV and $\Gamma^{\mathrm{C}} \approx 6.8$ eV [4]. The existence of such a narrow resonance is of paramount importance for the problem of the synthesis of light nuclei—for example, carbon nuclei [20, 21].

We will perform our analysis within the theory of scattering on two potentials, a Coulomb and a nuclear one, treating alpha particles in the region of very low energies as structureless elementary particles. The nuclear interaction of two alpha particles will be described by a simple separable S-wave potential—for example, that which involves the form factor $\langle\nu_{\alpha\alpha}|p\rangle = \mathrm{const}/(1+x^2)$.

In this case, the sign of the coupling constant specifies the character of the singularities of the amplitude. If $\lambda \le 0$, the pole of the amplitude corresponds to a bound (or a virtual) state in the system of two particles, the parameters of this state being $x_R = 0$ and $x_I = 1 - \sqrt{\lambda}$. If $\lambda > 0$, then the amplitude has poles at the points $x_{\mathrm{res}} = \pm x_R + x_I$, where $\lambda = x_R^2$ and $x_I = 1$. Thus, the inverse range β of forces and the coupling constant λ determine unambiguously resonances and the properties of the nuclear amplitude.

However, additional forces of Coulomb repulsion act between the particles, and this repulsion can change, as is well known, the resonance parameters substantially. In actual practice, we know the parameters of a shifted resonance rather than the parameters of the bare resonance. In this case, it is therefore necessary to invoke an inverse procedure—knowing the energy and the width of the observed resonance, one determines the position of the pole singularity of the amplitude in the absence of Coulomb forces and, accordingly, the parameters of the underlying nuclear potential. Within the potential model being considered, this can readily be done, for example, on the basis of the condition in (19) and expression (18).

With the aid of (18), we obtain

$$A^{\mathrm{C}}(Z) = \frac{4}{\pi}\int\limits_0^\infty \frac{x^2 dx}{(1+x^2)^2}\frac{F^{\mathrm{C}}(x)}{x_Z^2 - x^2 + i\gamma}, \qquad (26)$$

where $x_Z^2 = m_\alpha Z/\beta^2$ and the function $F^{\mathrm{C}}(x)$ reflects the modification of nuclear form factors that is induced by Coulomb forces ($y = 2\pi/\zeta x$),

$$F^{\mathrm{C}} = \frac{y}{1-\exp(-y)}\exp\left\{-y\left(1 - \frac{2}{\pi}\arctan(x)\right)\right\}. \qquad (27)$$

By using the small parameter $x_I/x_R \sim -0.185 \times 10^{-4}$ of the problem, we will determine the roots of Eq. (18) numerically. Here, an analytic continuation to the lower half-plane of the complex plane of k does not involve any difficulties, so that relevant estimations are straightforward by virtue of a pole dominance. For the potential of purely nuclear forces, one readily obtains the values of $\beta \sim 0.2784$ fm^{-1} and $\lambda \sim -5.38$. It is noteworthy that, although the coupling constant corresponds to attractive rather than repulsive forces, these values are close to typical nuclear-parameter values.

It is well known that there are no bound states in the system of two alpha particles. Therefore, it is possible that a potential involving a state forbidden by the Pauli exclusion principle is realized here. This nuclear potential, supplemented with Coulomb repulsion forces, generates a very narrow quasistationary state.

4. CONCLUSION

It is important to note that, even in the case of resonances close to the physical region, the character of the Coulomb shifts of scattering resonances is determined by the dimensionless parameters x_{res} and ζ characteristic of the system, which are related both to Coulomb quantities and to basic nuclear quantities.

The examples considered above have revealed that relations (12) and (13) and their model form (19) can be used in practical calculations. First of all, this concerns the description of pronounced pole singularities. This is exemplified by the resonances in the (n, α) and (p, α) systems.

It is clear that the n ^{6}Li and p ^{6}Li systems are more complicated than the model used here to simulate them—they feature a greater number of reaction channels and a greater number of singularities in the scattering amplitudes. However, the ^{6}Li nucleus has a pronounced cluster structure; owing to this, the respective estimates of the Coulomb shift of a single isolated low-energy resonance proved to be quite satisfactory.

In more complicated cases, it seems necessary to take into account a few close singularities (poles)—that is, to introduce higher rank potentials in the respective analysis.

In the model problem of two alpha particles, the Coulomb shift of the resonance width revealed a nontrivial behavior, this probably reflecting the intricate character of the interaction in this system at ultralow energies. At the same time, the nuclear forces themselves preserved conventional nuclear scales. This fact is of importance in the problems of the stellar synthesis of light nuclei.

The main objective of the present study was to derive simple relations for estimating resonance shifts and to demonstrate the viability of these relations by considering simple examples.

These relations are also of use in determining the properties of resonances in more complicated nuclear systems. At the first step, one can determine the positions of resonances and their width from calculations allowing for only nuclear forces, whereupon one can employ the relations in question to estimate the resonance-level shifts induced by Coulomb forces.

REFERENCES

1. U. A. Fowler, Usp. Fiz. Nauk **145**, 441 (1985) [Sov. Phys. Usp. **28**, (1985)].
2. S. Burles and D. Tytler, Astrophys. J. **499**, 699 (1998).
3. V. A. Bednyakov, Fiz. Élem. Chastits At. Yadra **33**, 915 (2002) [Phys. Part. Nucl. **33**, 583 (2002)].
4. F. Ajzenberg-Selove, Nucl. Phys. A **490**, 1 (1988).
5. N. Zh. Takibaev and F. M. Pen'kov, in *Proceedings of the Conference "Nuclear and Radiation Physics", Almaty, Kazakhstan, 1999*, Vol. 1, p. 25.
6. S. P. Merkur'ev and L. D. Faddeev, *Quantum Mechanics for Few-Particle Systems* (Nauka, Moscow, 1985) [in Russian].
7. V. S. Popov *et al.*, Zh. Éksp. Teor. Fiz. **80**, 1271 (1981) [Sov. Phys. JETP **53**, 650 (1981)].
8. N. Zh. Takibaev and B. A. Uruspaeva, Preprint No. 18, IFVÉ (Institute of High Energy Physics, Almaty, 1988).
9. E. O. Alt, Preprint MZ-TH/86-15 (Germany, 1986).
10. A. A. Kvittsinsky *et al.*, Fiz. Élem. Chastits At. Yadra **17**, 267 (1986) [Sov. J. Part. Nucl. **17**, 113 (1986)].
11. V. B. Belyaev *et al.*, Nucleonika **40**, 85 (1995).
12. V. B. Belyaev *et al.*, Preprint No. T-4-86-66, OIYaI, (Joint Inst. Nucl. Res., Dubna, 1986).
13. N. Zh. Takibaev, in *Selected Problems in Theoretical Physics and Astrophysics. To the 70th Anniversary of V. B. Belyaev* (OIYaI, Dubna, 2003), p. 66.
14. N. Zh. Takibaev, Vestn. Kaz. Nats. Pedagog. Univ. **2**, 14, (2004).
15. T. Dauxois *et al., Dynamics and Thermodynamics of Systems with Long-Range Interactions* (*Lecture Notes in Physics*) (Springer-Verlag, Berlin; Heidelberg, 2002).
16. D. A. Kirzhnits, G. Yu. Kryuchkov, and N. Zh. Takibaev, Fiz. Élem. Chastits At. Yadra, **10**, 741 (1979) [Sov. J. Part. Nucl. **10**, 289 (1979)].
17. D. A. Kirzhnits, *Works in Theoretical Physics and Memoirs* (Fizmatlitgiz, Moscow, 2001), Vol. 1 [in Russian].
18. H. Hellmann, *Einführung in die quanten chemie* (Leipzig, 1937).
19. D. A. Kirzhnits, F. M. Pen'kov, and N. Zh. Takibaev, Yad. Fiz. **38**, 1145, (1983) [Sov. J. Nucl. Phys. **38**, 689, (1983)].
20. F. Hoyle, Rev. Mod. Phys. **29**, 547 (1957).
21. R. Wagoner, W. Fowler, and F. Hoyle, Astrophys. J. **148**, 3 (1967).

Translated by A. Isaakyan

Physics of Atomic Nuclei, Vol. 68, No. 7, 2005, pp. 1153–1159. From Yadernaya Fizika, Vol. 68, No. 7, 2005, pp. 1201–1208.

NUCLEI
Theory

The Examination of the $^{12}C + ^{24}Mg$ Elastic Scattering around the Coulomb Barrier*

I. Boztosun, Y. Dagdemir, and O. Bayrak

Department of Physics, Erciyes University, Kayseri, Turkey

Received January 13, 2004; in final form, May 5, 2004

Abstract—The investigation of nuclear reactions near the Coulomb barrier poses a number of problematic issues which have remained unsolved for a long time: The out-of-phase problem between theoretical predictions and experimental data, the reproduction of the oscillatory structure near the Coulomb barrier, and the consistent description of angular distributions together with the excitation functions data are just some of these issues. To address and overcome them, we examine the elastic scattering of the $^{12}C + ^{24}Mg$ system within the framework of the optical model with two small potentials in addition to the nuclear potential. The experimental data have been analyzed in the laboratory system from 16.0 to 24.0 MeV and excellent agreement between theoretical results and the measured experimental data has been obtained by using this modified optical potential. We show that the presence of the two small additional potentials creates a deepening in the surface region of the nuclear potential, which is very effective for the interference of the internal and barrier waves. This work is important in showing the sensitivity of the cross section to the fine details of the optical potential. It is also argued that the two small additional potentials take into account the coupling effect like that of the coupled channels and as a result reduce the strength of the imaginary potential. In this context, the results of the optical model are compared with that of the coupled channels. © *2005 Pleiades Publishing, Inc.*

1. INTRODUCTION

The elastic and inelastic scattering of $n\alpha$-type nuclei which present a strongly oscillating backward rise in angular distributions and very structured excitation functions at both forward and backward angles have been studied extensively and research on these topics is still being conducted. A large body of experimental data has been accumulated from the systematic studies of such reactions and a number of problems have continued to plague the study of these systems. The explanation of anomalous large-angle-scattering data, the reproduction of the oscillatory structure near the Coulomb barrier, and the out-of-phase problem between theoretical predictions and experimental data are just some of them.

In this context, the $^{12}C + ^{24}Mg$ reaction [1–5] has been extensively investigated both experimentally and theoretically. Conventional optical-model analyses with shallow or deep potentials, either folding or phenomenological, have difficulty in explaining all or some of the experimental data [1, 2, 5]. The experimental data show striking oscillatory features at forward, intermediate, and backward angles. A similar oscillatory structure is also observed in the $^{16}O + ^{28}Si$ system, and the standard method has also failed to describe certain features of the experimental data.

A variety of theoretical approaches, based on dynamical models or purely phenomenological assumptions, have been proposed to explain or merely reproduce the experimental data [6]. However, although most of those descriptions give reasonably good fits to the angular distributions, and a few fit the elastic excitation functions, there is as yet no satisfactory physical explanation of all the observed phenomena. Theoretical frameworks proposed so far range from the occurrence of possibly overlapping shape resonances [7] and the scattering from surface-transparent optical potentials [8] to more exotic effects like explicit parity dependence of the ion–ion potential [9, 10].

The failure of these theoretical models might be due to the way the problem is modeled. That is to say, in the elastic and inelastic scattering of two nuclei, the projectile (A_p) or the target (A_t) nuclei may exist in any one particular excited state from among an infinite number of excited states, as well as in their ground state. In order to describe the scattering process fully and accurately, one would have to model all the different couplings to all the different excited states of A_p and A_t and, furthermore, to all the different mass partitions. This is an insurmountable task and therefore an approximation has to be made in practice. In modeling such as the optical

*The text was submitted by the authors in English.

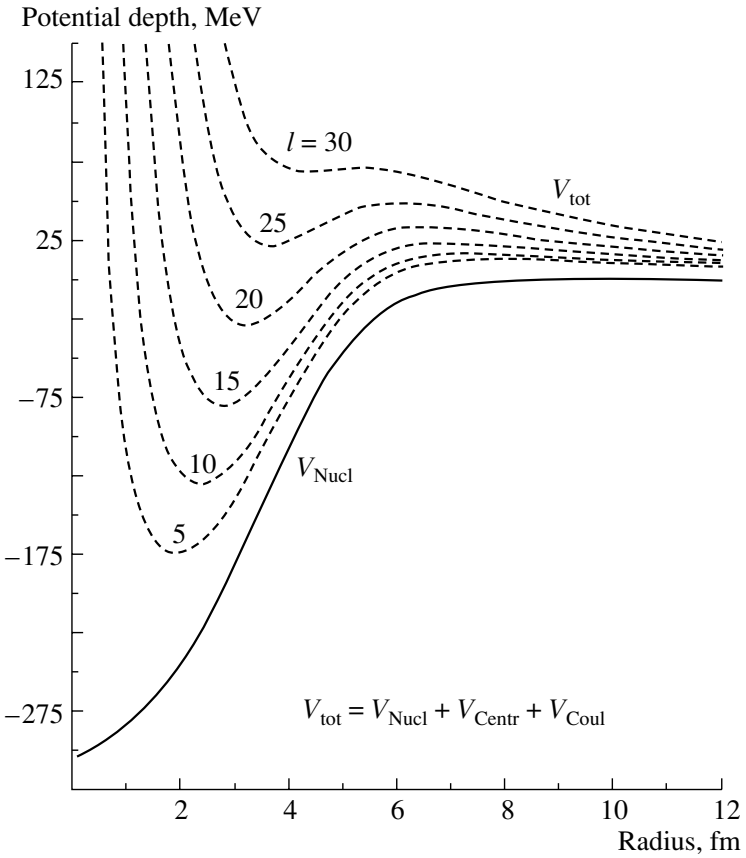

Fig. 1. Interaction potential between ^{12}C and ^{24}Mg vs. the separation R for various values of the orbital angular-momentum quantum number l.

model, the distorted-wave Born approximation, or the coupled-channel one, the infinite sets of equations are in fact truncated to a relatively few channels, which are theoretically expected or known by experiment to be strongly coupled to the entrance channel. The effect of other channels is taken into account using a complex optical potential (optical model) or a few excited states included in the coupled-channel calculations in addition to the complex potential. Furthermore, although the qualitative features of the optical potential are well determined, there is still ambiguity in determining its fine details.

Therefore, in this study, we have carried out notch tests for the different regions of the optical potential to determine the sensitivity of the calculations to the optical potential. We have noticed that the light–heavy ion reactions are extremely sensitive to the shape of the nuclear potential in the surface region. By noticing this sensitivity, we have introduced two small potentials which modify the shape of the nuclear potential in the optical-model calculations. We have then explained the modification of the optical potential by adding the two small additional potentials in the surface region and have introduced our optical model as well as potential parameters. In the paper, we show the results of the analyses in Section 3 from $E_{\rm lab} =$ 16.0 to 24.0 MeV and compare our results with the coupled-channel calculations. The effect of the two small potentials and the dispersion relation between real and imaginary potentials are also discussed in this section. Finally, our conclusion is given in Section 4.

Table 1. The parameters of the two small additional potentials

U_1, MeV	R_1, fm	a_1, fm	U_2, MeV	R_2, fm	a_2, fm
10.14	5.84	0.187	3.8	7.19	0.31

2. THE MODEL

With two small additional potentials $[U(r) = U_1 + U_2]$, the total real potential is given as

$$V_{\rm tot}(r) = \underbrace{V_{\rm Nucl}(r) + U(r)}_{\text{Real potential}} + V_{\rm Coul}(r) + V_{\rm Centr}(r). \quad (1)$$

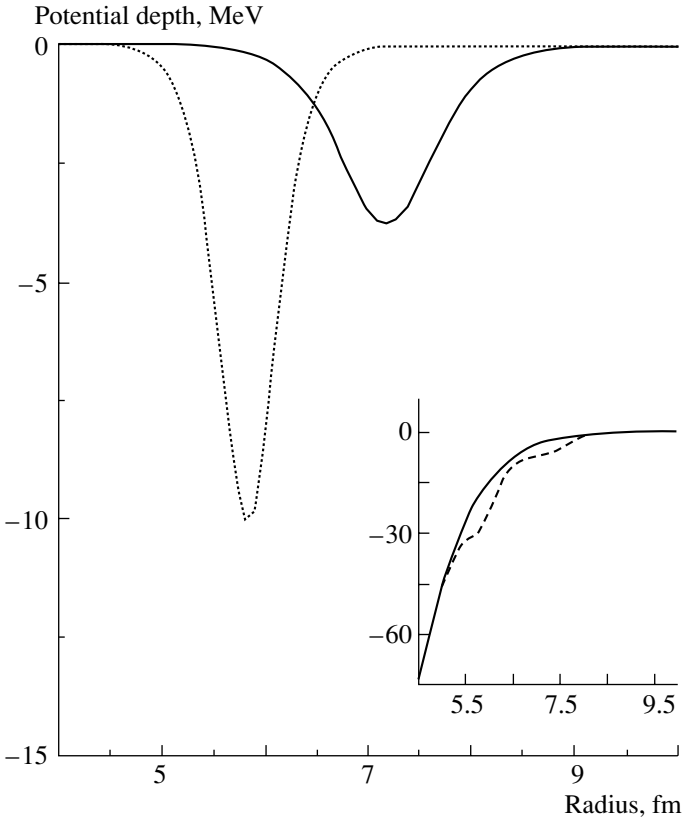

Fig. 2. The shapes of two small additional potentials U_1 (dotted curve) and U_2 (solid curve). The inset shows their effects on the nuclear potential with a dashed curve.

The nuclear potential is assumed to have the square of a Woods–Saxon shape taken as

$$V_{\rm Nucl}(r) = \frac{-V_0}{(1+\exp(r-R)/a)^2}, \qquad (2)$$

where $V_0 = 323.5$ MeV and $R = r_0(A_p^{1/3} + A_t^{1/3})$ with $r_0 = 0.848$ fm and $a = 1.3$ fm. The volume integral of the real potential is 289.28 MeV fm^3. The parameters of the nuclear potential are fixed as a function of energy and kept constant in the present calculations, although it has been observed that small changes could improve the quality of the fits.

The Coulomb potential [11] due to a charge $Z_p e$ interacting with a charge $Z_t e$, distributed uniformly over a sphere of radius $R_{\rm Coul}$, is also added:

$$V_{\rm Coul}(r)$$

$$= \begin{cases} \dfrac{1}{4\pi\epsilon_0}\dfrac{Z_p Z_t e^2}{r}, & r \geq R_{\rm Coul}, \qquad (3) \\ \dfrac{1}{4\pi\epsilon_0}\dfrac{Z_p Z_t e^2}{2R_{\rm Coul}}\left(3 - \dfrac{r^2}{R_{\rm Coul}^2}\right), & r < R_{\rm Coul}, \qquad (4) \end{cases}$$

where $R_{\rm Coul} = 6.2$ fm is the Coulomb radius, and Z_p and Z_t denote the charges of the projectile and the target nuclei, respectively.

The sum of the nuclear, Coulomb, and centrifugal potentials is shown in Fig. 1 for various values of the orbital angular momentum. The superposition of the attractive and repulsive potentials results in the for-

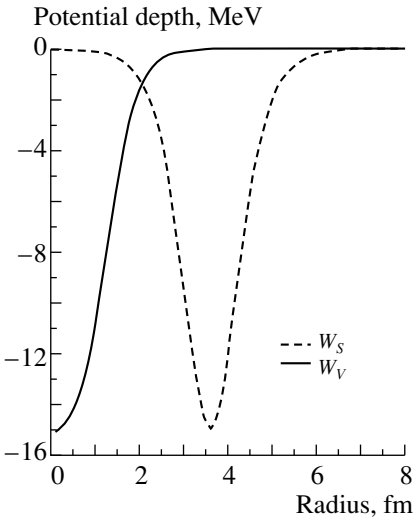

Fig. 3. The volume and surface components of the imaginary potential at $E_{\rm lab} = 21$ MeV.

Table 2. The parameters and volume integrals of the imaginary potentials and χ^2 values for some of the energies studied (note that 10% error has been assumed for the experimental data)

$E_{\rm lab}$, MeV	W_V, MeV	W_S, MeV	J_V, MeV fm^3	J_S, MeV fm^3	χ^2
16.0	1.0	1.0	0.051	1.004	1.43
17.0	3.0	1.0	0.153	1.004	3.06
18.5	5.0	5.0	0.256	5.020	1.37
19.0	7.0	7.0	0.358	7.028	4.23
19.5	9.50	9.0	0.486	9.037	2.92
20.0	17.50	15.0	0.596	15.061	2.03
20.5	14.50	13.0	0.741	13.053	1.26
21.0	15.50	15.0	0.793	15.061	1.30
21.5	18.50	17.0	0.946	17.069	2.58
22.0	19.50	18.0	0.997	18.073	0.78
22.5	20.50	19.0	1.049	19.077	3.62
23.0	22.00	20.0	1.125	20.081	3.73
23.5	23.50	23.0	1.202	23.093	1.74
24.0	25.50	25.0	1.304	25.102	3.74

mation of a potential pocket, which is very important for the interference of the barrier and internal waves, which creates the oscillatory structure observed in the cross section. The width and depth of the pocket depend on the orbital angular-momentum quantum number for a given nuclear potential.

Two small additional potentials are the derivatives of the Woods–Saxon shape

$$U(r) = 4U_1 a_1 df(r, R_1, a_1)/dr + 4U_2 a_2 df(r, R_2, a_2)/dr, \quad (5)$$

$$f(r, R_i, a_i) = \frac{1}{(1 + \exp((r - R_i)/a_i))}. \quad (6)$$

Their parameters are shown in Table 1. As shown in the inset of Fig. 2, they create two minima in the nuclear potential between ~5.8 and ~7.19 fm.

The imaginary part of the potential was taken as the sum of a Woods–Saxon volume and the surface potential [12]:

$$W(r) = -W_V f(r, R_V, a_V) + 4W_S a_S df(r, R_S, a_S)/dr, \quad (7)$$

$$f(r, R, a) = \frac{1}{(1 + \exp((r - R)/a))} \quad (8)$$

with $r_V = 0.25$ fm, $a_V = 0.326$ fm and $r_S = 0.70$ fm, $a_S = 0.42$ fm. The depths and volume integrals of the imaginary potentials are shown in Table 2, and for $E_{\rm lab} = 21$ MeV, they are displayed in Fig. 3.

3. THE RESULTS

Using this optical model with the above-described modifications in the nuclear potential, we have analyzed the experimental data from 16.0 to 24.0 MeV in the laboratory system for $^{12}C + ^{24}Mg$ elastic scattering. The comparison of the experimental data and the optical model fits are shown in Fig. 4. The results of the coupled-channels calculations are also shown in these figures for some of the energies studied for comparison purposes. The comparison of the optical-model calculations (solid curves) with the coupled-channel calculations (dashed curves) reveals that the optical-model results obtained by two small additional potentials are as good as or even better than the coupled-channel calculations.

However, it should be pointed out here that, with the standard optical-model calculations without two small additional potentials, we could not reproduce the oscillatory structure or obtain the correct phase for the experimental data. The oscillations in the theoretical results are completely out of phase with the measured ones even at intermediate angles. This is demonstrated in Fig. 5 at 21.0 MeV. Figure 5*d* presents the cross sections obtained when both potentials are omitted.

The effect of the two small potentials on the nuclear potential is shown in Fig. 2. As mentioned above, they create two minima in the nuclear potential between ~5.8 and ~7.19 fm, and as we argued in [13], one way to understand the effect of these potentials is in terms of the interference between the internal and barrier waves that correspond to a decomposition [14–16] of the scattering amplitude into two components, the inner and external waves. The inner wave comes from the reflection at the inner face of the total real potential pocket and the external wave comes from the reflection at the outer barrier (see Fig. 1 for the pocket in the total real potential). The presence of the two small potentials affects the phases and magnitudes of these internal and external components, and, as a result, we obtain excellent agreement with experimental data. We observe from the parameters in Table 1 that the two small additional potentials are not strong enough to produce pockets in the total real potential, although they have a very significant effect on the scattering.

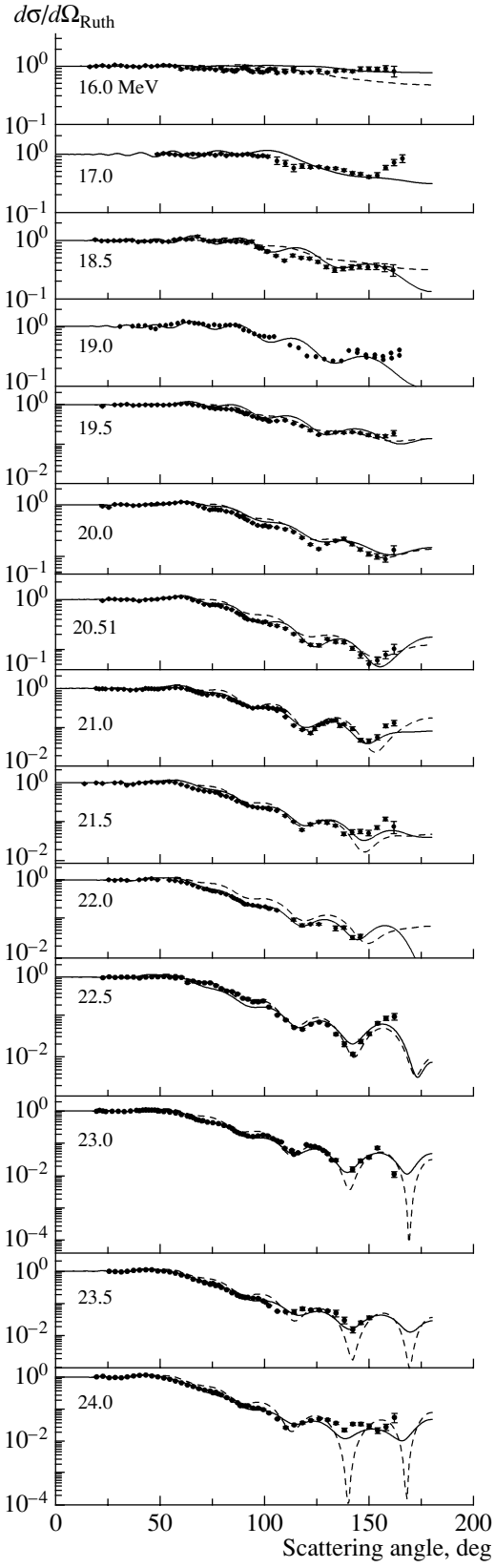

Fig. 4. The elastic scattering results obtained by using the optical-model calculations with two small additional potentials for the $^{12}C+^{24}Mg$ system (solid curves). The dashed curves show the results of the coupled-channel calculations.

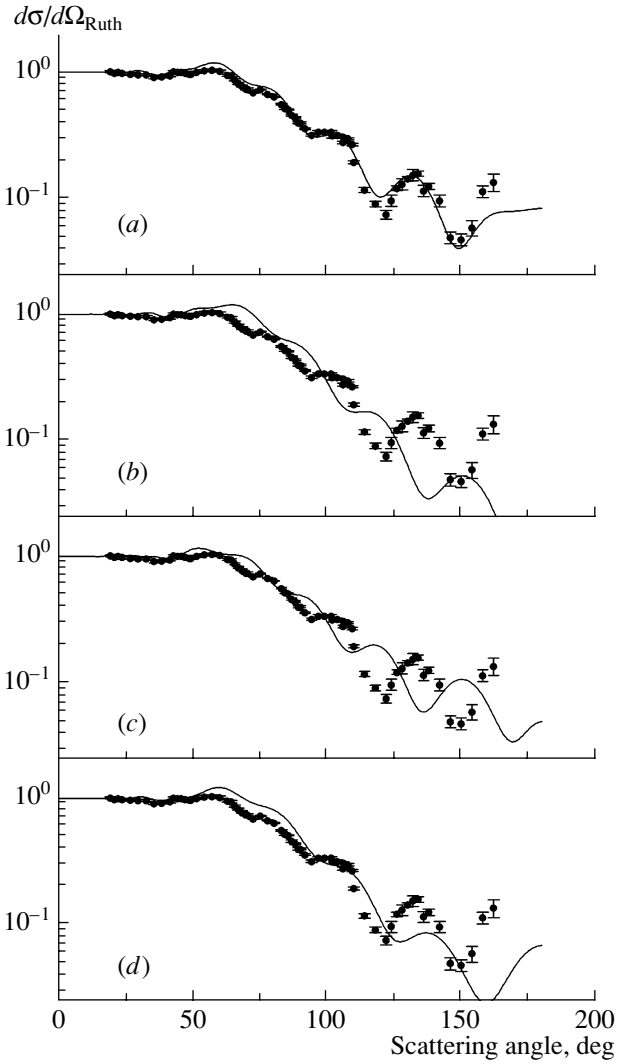

Fig. 5. Effect of the two small additional potentials for $E_{lab} = 21.0$ MeV: (a) the best fit obtained with the inclusion of both potentials, the fits obtained (b) without the inclusion of U_2, (c) without the inclusion of U_1, and (d) when both potentials are ignored [13].

Another way to look at the effect of the two small potentials is to plot the nuclear-plus-coupling potential (V_{CC}) in comparison with the nuclear potential and nuclear potential plus U_1 and U_2. V_{CC} consists of the nuclear potential plus the coupling potential, which is often treated to the first order and can be given as

$$V_{CC} = V_{Nucl}(r) + U(r) + \frac{1}{4\pi}\beta R\frac{dV_{Nucl}}{dr}, \quad (9)$$

where βR is the deformation length of the target nucleus. We see in Fig. 6 that V_{CC} departs from the nuclear potential in the surface region as a result of the effect of the coupling potential. We observe the similar effect for the two small additional potentials and both potentials generate similar results.

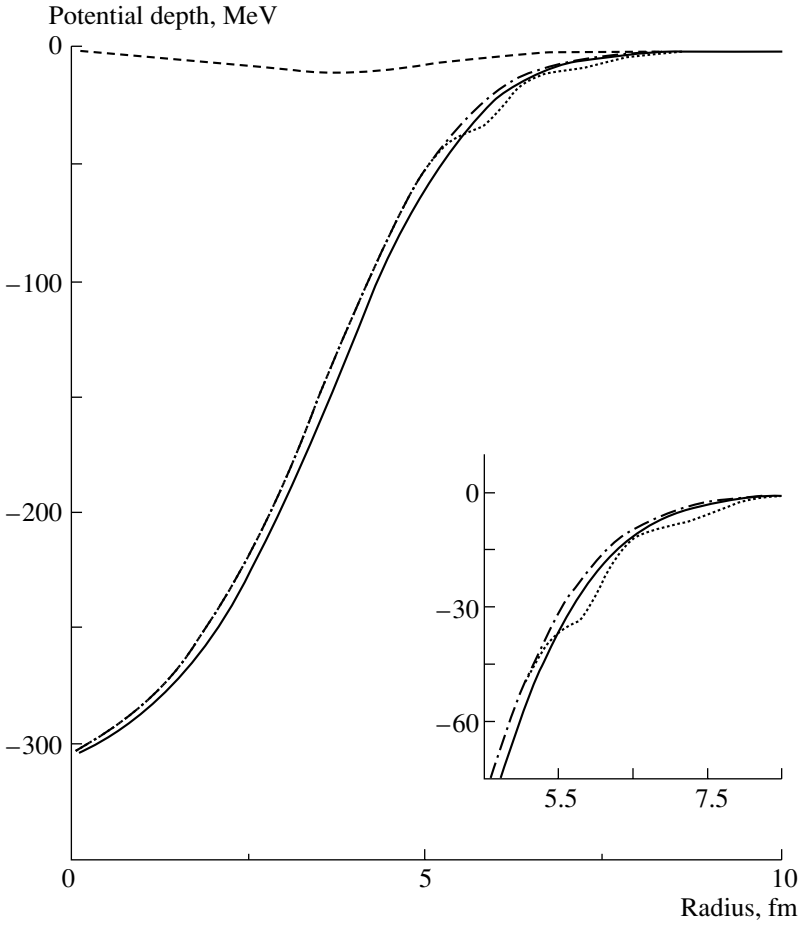

Fig. 6. The nuclear (V_{Nucl}) (dash-dotted curve), nuclear-plus-coupling (V_{CC}) (solid curve), and coupling potentials (dashed curve). The inset shows the comparison of V_{Nucl} (dash-dotted curve), V_{CC} (solid curve), and V_{Nucl} plus two small potentials ($U_1 + U_2$) (dotted curve).

The relative significance of the volume and surface components of the imaginary potential was evaluated for all the energies. For higher energies, omitting the volume term predominantly affected the amplitude of the cross section at large angles. However, this effect was small and negligible at lower energies. Omitting the surface term increased the cross sections at large angles, which were as much as two orders of magnitude. It was observed that this term had a significant effect at all the considered energies. This is clearly seen from the volume integrals of the imaginary potentials from Table 2.

We have also examined the dispersion relation between the real and imaginary potentials. The volume integrals of the real and imaginary potentials are calculated by using following formulas:

$$J_V(E) = \left[\frac{4\pi}{A_p A_t}\int_0^R V(r,E)r^2 dr\right], \qquad (10)$$

$$J_W(E) = \left[\frac{4\pi}{A_p A_t}\int_0^R W(r,E)r^2 dr\right].$$

From Table 2, it can be perceived that the strength of the depth of the imaginary potential increases rapidly at the top of the Coulomb barrier. However, we do not see a rapid change in the real potential parameters. It is expected that the real potential should accompany the rapid change in the parameters of the imaginary potential according to the dispersion relation. The reason why we do not observe this rapid variation might be due to the presence of the two small additional potentials. The two additional potentials take into account the coupling effect between different channels; therefore, both remove the rapid variation of the real potential parameters and reduce the strength of the imaginary potential. The code FRESCO [17] has been used for all the calculations.

4. SUMMARY

We have shown a consistent description of the elastic scattering of the $^{12}C + ^{24}Mg$ system from 16.0 to 24.0 MeV in the laboratory system by using the modified-optical-model calculations. The theoretical description of such systems has been very difficult due to the dominance of Coulomb interaction for bombarding energies close to or below the top of the Coulomb barrier as the elastic scattering cross sections approach the Rutherford values and tend to be featureless [11]. When the bombarding energy is over the Coulomb barrier, Coulomb excitation provides the major part of the reaction and absorption cross sections, and the effect of this absorption is represented by a long-range imaginary potential, which shadows the short-ranged nuclear terms. The absorption in higher partial waves beyond the grazing one causes the cross section to fall below the Rutherford value; Coulomb–nuclear interference occurs and, as a result, reduces the sensitivity of the scattering to the nuclear interaction.

Below and above the Coulomb barrier, the $^{12}C + ^{24}Mg$ system we examined in this paper shows all these features: The experimental data show very oscillatory features near the Coulomb barrier at very low energies and a striking backward rise and oscillatory features at forward, intermediate, and backward angles at high energies.

Similar to previous analyses performed so far, we failed to describe certain aspects of the data within the standard optical-model calculations. We then performed notch tests to see which part of the optical potential is more effective on the scattering of these two ions. We observed that the light–heavy ion reactions such as the one presented in this paper are very sensitive to the shape of the nuclear potential in the surface region. By taking this feature into account, we used two small additional potentials, which modify the shape of the nuclear potential in the surface region, and obtained excellent agreement with the experimental data over a wide energy range. The agreement between the optical-model and coupled-channel calculations in the results is very important in the sense that two additional potentials have effects very similar to that of the coupling of excited states to the ground state in the coupled-channel method.

It should be noted here that we have introduced two additional potentials in a phenomenological way by examining the sensitivity of the scattering to the optical potential. These two additional potentials are very small and do not create a pocket in the total nuclear potential, but they are very effective for the interference of the barrier and internal waves, which creates the oscillatory structure observed in the cross section. It could be very interesting to determine the potential by means of $S_l \rightarrow V$ inversion corresponding to the elastic scattering S matrix. This allows us to identify the dynamical polarization potential, and it is the properties of this which we can then relate to the characteristics of the coupling potential. Further work in order to obtain the inverted optical potential from the S matrix is still in progress.

ACKNOWLEDGMENTS

This paper is an output of the project supported by the Scientific and Technical Research Council of Turkey (TUBITAK), project no. TBAG-2398 and Erciyes University (FBA-03-27, FBT-04-15, FBT-04-16).

We wish to thank Professors G.R. Satchler, B. Buck, I.J. Thompson, R.S. Mackintosh, A. Lepine-Szily, and A.M. Merchant for useful comments and providing data and Mrs. N.A. Boztosun for proofreading.

REFERENCES

1. W. Sciani, A. Lepine-Szily, F. R. Lichtenthaeler, *et al.*, Nucl. Phys. A **620**, 91 (1997).
2. A. Lepine-Szily, W. Sciani, Y. K. Watari, *et al.*, Phys. Lett. B **304**, 45 (1993).
3. J. Carter, R. G. Clarkson, V. Hnizdo, *et al.*, Nucl. Phys. A **273**, 523 (1976).
4. J. Carter, J. P. F. Sellschop, R. G. Clarkson, and V. Hnizdo, Nucl. Phys. A **297**, 520 (1978).
5. R. L. Filho, A. Lépine-Szily, A. C. C. Villari, and O. P. Filho, Phys. Rev. C **39**, 884 (1989).
6. P. Braun-Munzinger and J. Barrette, Phys. Rep. **87**, 209 (1982).
7. J. Barrette, M. J. LeVine, P. Braun-Munzinger, *et al.*, Phys. Rev. Lett. **40**, 445 (1978).
8. S. Kahana, B. T. Kim, and M. Mermaz, Phys. Rev. C **20**, 2124 (1979).
9. D. Dehnhard, V. Shkolnik, and M. A. Franey, Phys. Rev. Lett. **40**, 1549 (1978).
10. S. Kubono, P. D. Bond, and C. E. Thorn, Phys. Lett. B **81**, 140 (1979).
11. G. R. Satchler, *Direct Nuclear Reactions* (Oxford Univ. Press, Oxford, 1983); *Introduction to Nuclear Reactions* (Macmillan, London, 1980).
12. A. M. Kobos and G. R. Satchler, Nucl. Phys. A **427**, 589 (1984).
13. I. Boztosun, Phys. Rev. C **66**, 024610 (2002); I. Boztosun *et al.*, Balkan Phys. Lett. **10**, 173 (2002).
14. S. Y. Lee, Nucl. Phys. A **311**, 518 (1978).
15. D. M. Brink and N. Takigawa, Nucl. Phys. A **279**, 159 (1977).
16. I. Boztosun and W. D. M. Rae, Phys. Rev. C **64**, 054607 (2001); Phys. Lett. B **518**, 229 (2001).
17. I. J. Thompson, FRESCO, A Coupled-Channels Code (unpublished).

Physics of Atomic Nuclei, Vol. 68, No. 7, 2005, pp. 1160–1170. From Yadernaya Fizika, Vol. 68, No. 7, 2005, pp. 1209–1219.

ELEMENTARY PARTICLES AND FIELDS
Experiment

A Study of the Nuclear-Medium Influence on Transverse Momentum of Hadrons Produced in Deep-Inelastic Neutrino Scattering*

N. M. Agababyan[1)], V. V. Ammosov, M. Atayan[2)], N. Grigoryan[2)], H. Gulkanyan[2)], A. A. Ivanilov[**], Zh. Karamyan[2)], and V. A. Korotkov

Institute for High Energy Physics, Protvino, Moscow oblast, 142284 Russia

Received September 21, 2004

Abstract—The influence of nuclear effects on the transverse momentum (p_T) of neutrino-produced hadrons is investigated using the data obtained with the SKAT propane–freon bubble chamber irradiated in the neutrino beam (with $E_\nu = 3$–30 GeV) at the Serpukhov accelerator. It has been observed that the nuclear effects cause an enhancement of $\langle p_T^2 \rangle$ of hadrons produced in the target fragmentation region at low invariant mass of the hadronic system ($2 < W < 4$ GeV) and at low energies transferred to the hadrons ($2 < \nu < 9$ GeV). At higher W and ν, no influence of nuclear effects on $\langle p_T^2 \rangle$ is observed. Measurement results are compared with predictions of a simple model, incorporating secondary intranuclear interactions of hadrons, which qualitatively reproduces the main features of the data. © *2005 Pleiades Publishing, Inc.*

1. INTRODUCTION

The experimental study of the hadron production in deep-inelastic scattering (DIS) of leptons on nuclei is an important source of information on the spacetime evolution of the leptoproduced quark strings. Depending on the features of the latter, the nuclear medium influences the inclusive spectra of final hadrons differently, in particular, affecting their yields and the mean transverse momentum in various domains of the phase space. Hitherto, no detailed data inferred in the same experiment are available for transverse momentum distributions in the lepton–nucleus DIS. This gap is partly filled by the present work, where the influence of the nuclear effects on the transverse momentum of neutrino-produced hadrons is explored using the data collected in the neutrino experiment with the bubble chamber SKAT.

In Section 2, the experimental procedure is briefly described. The experimental results are presented in Section 3, discussed in Section 4, and summarized in Section 5.

2. EXPERIMENTAL PROCEDURE

The experiment was performed with the SKAT bubble chamber [1], exposed to a wideband neutrino beam obtained with 70-GeV primary protons from the Serpukhov accelerator. The chamber was filled with a propane–freon mixture containing 87 vol % propane (C_3H_8) and 13 vol % freon (CF_3Br) with the percentage of nuclei H : C : F : Br = 67.9 : 26.8 : 4.0 : 1.3%. A 20-kG uniform magnetic field was provided within the operating chamber volume.

Charged-current interactions containing a negative muon with momentum $p_\mu > 0.5$ GeV are selected. Other negatively charged particles are considered to be π^- mesons. Protons with momentum below 0.6–0.65 GeV/c and a fraction of protons with momentum up to 0.85 GeV/c were identified by their stopping in the chamber. More details concerning the experimental procedure, in particular, the event-selection criteria and the reconstruction of the neutrino energy E_ν, can be found in our previous publications [2–5]. Each event is given a weight (depending on the charged particle multiplicity) which corrects for the fraction of events excluded due to improper reconstruction.

For further analysis, the events with $3 < E_\nu < 30$ GeV were accepted, provided that the invariant mass of the hadronic system $W > 2$ GeV and the transfer momentum squared $Q^2 > 1$ (GeV/c)^2. The full sample consists of 2222 events (3167 weighted events). The mean values of the kinematical variables are $\langle E_\nu \rangle = 10.8$ GeV, $\langle Q^2 \rangle = 3.6$ (GeV/c)^2, $\langle W \rangle = 3.0$ GeV, $\langle W^2 \rangle = 9.5$ GeV^2, and, for the energy ν transferred to the hadronic system, $\langle \nu \rangle = 6.5$ GeV.

The whole event sample is subdivided, using several topological and kinematical criteria [4, 5],

*The text was submitted by the authors in English.

[1)]Joint Institute for Nuclear Research, Dubna, Moscow oblast, 141980 Russia.

[2)]Yerevan Physics Institute, Armenia.

[**]e-mail: ivanilov@ihep.ru

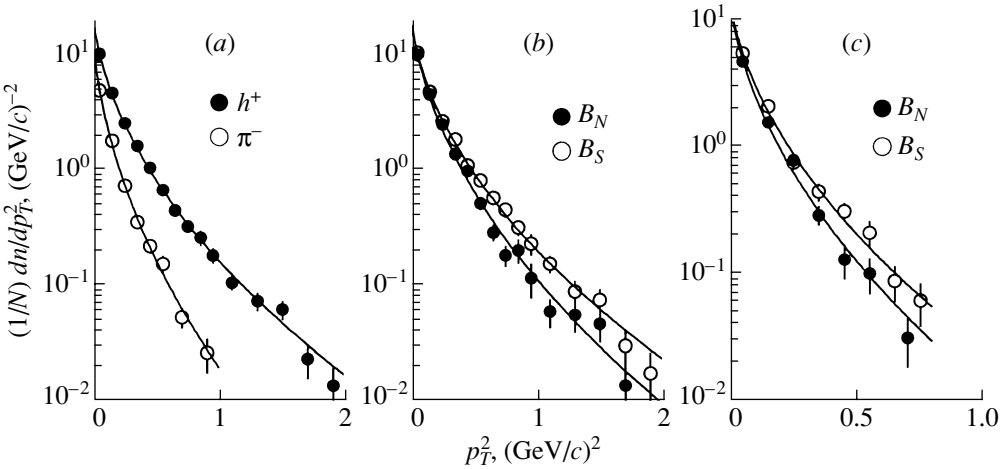

Fig. 1. The p_T^2 distributions (a) of h^+ and π^- for the whole event sample, (b) of h^+ for B_N and B_S subsamples, and (c) of π^- for B_N and B_S subsamples. The curves are results of the fit (see text).

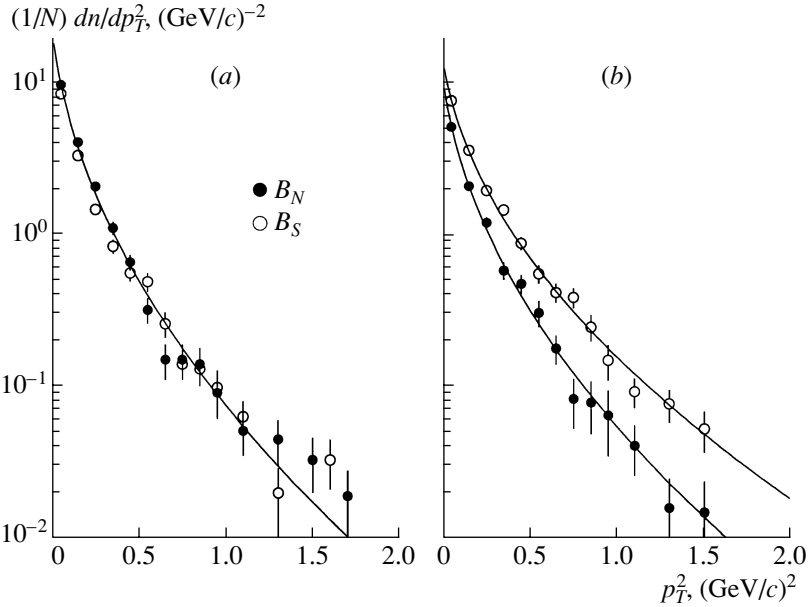

Fig. 2. The p_T^2 distributions of charged hadrons for B_N and B_S subsamples at (a) $x_F > 0$ and (b) $x_F < 0$. The curves are results of the fit (see text).

into three subsamples: the "cascade" subsample B_S with a sign of intranuclear secondary interactions and the "quasiproton" (B_p) and "quasineutron" (B_n) subsamples, the latter two composing the "quasinucleon" subsample ($B_N \equiv B_p + B_n$), for which no sign of secondary interactions is observed. The corresponding event numbers for the B_S, B_p, and B_n subsamples are 1190, 477, and 555 (weighted numbers $N_S = 1736$, $N_p = 680$, and $N_n = 751$), respectively.

About 40% of subsample B_p is contributed by interactions with free hydrogen. Weighting the "quasiproton" events with a factor of 0.6, one can compose a "pure" nuclear sample: $B_A = B_S + B_n + 0.6B_p$ (with an effective atomic weight $\bar{A} = 28$). It can also be shown [4, 5] that a subsample composed as $B_D = B_n + 0.6B_p$ approximately corresponds to the neutrino–deuterium interactions.

3. EXPERIMENTAL RESULTS

In the present analysis, the identified protons are not included. All the remaining positively (labeled as h^+) and negatively (labeled as π^-) charged hadrons

Table 1. The mean values of $\langle p_T^2 \rangle$ in $(\mathrm{GeV}/c)^2$ of h^+ and π^- for several subsamples and various regions of x_F and W^2

	$\langle p_T^2 \rangle_N$	$\langle p_T^2 \rangle_S$	$\langle p_T^2 \rangle_D$	$\langle p_T^2 \rangle_A$
	$4 < W^2 < 25\ \mathrm{GeV}^2$			
$h^+(x_\mathrm{F} > 0)$	0.180 ± 0.006	0.190 ± 0.007	0.182 ± 0.007	0.187 ± 0.005
$\pi^-(x_\mathrm{F} > 0)$	0.129 ± 0.009	0.128 ± 0.008	0.131 ± 0.009	0.129 ± 0.006
$h^+(x_\mathrm{F} < 0)$	0.207 ± 0.009	0.268 ± 0.009	0.205 ± 0.009	0.252 ± 0.007
$\pi^-(x_\mathrm{F} < 0)$	0.126 ± 0.009	0.141 ± 0.008	0.127 ± 0.009	0.137 ± 0.006
	$4 < W^2 < 9\ \mathrm{GeV}^2$			
$h^+(x_\mathrm{F} > 0)$	0.163 ± 0.007	0.170 ± 0.007	0.161 ± 0.007	0.166 ± 0.005
$\pi^-(x_\mathrm{F} > 0)$	0.101 ± 0.009	0.119 ± 0.010	0.104 ± 0.009	0.113 ± 0.007
$h^+(x_\mathrm{F} < 0)$	0.189 ± 0.011	0.266 ± 0.011	0.186 ± 0.011	0.245 ± 0.008
$\pi^-(x_\mathrm{F} < 0)$	0.106 ± 0.009	0.127 ± 0.009	0.108 ± 0.009	0.122 ± 0.007
	$9 < W^2 < 25\ \mathrm{GeV}^2$			
$h^+(x_\mathrm{F} > 0)$	0.205 ± 0.012	0.217 ± 0.013	0.214 ± 0.013	0.216 ± 0.009
$\pi^-(x_\mathrm{F} > 0)$	0.154 ± 0.015	0.134 ± 0.013	0.156 ± 0.016	0.144 ± 0.010
$h^+(x_\mathrm{F} < 0)$	0.228 ± 0.015	0.271 ± 0.014	0.229 ± 0.016	0.259 ± 0.011
$\pi^-(x_\mathrm{F} < 0)$	0.149 ± 0.018	0.157 ± 0.019	0.151 ± 0.018	0.155 ± 0.011

Table 2. The mean multiplicities of h^+ and π^- for several subsamples and various regions of x_F and W^2

	$\langle n \rangle_N$	$\langle n \rangle_S$	$\langle n \rangle_D$	$\langle n \rangle_A$
	$4 < W^2 < 25\ \mathrm{GeV}^2$			
$h^+(x_\mathrm{F} > 0)$	1.441 ± 0.023	1.198 ± 0.023	1.402 ± 0.023	1.279 ± 0.017
$\pi^-(x_\mathrm{F} > 0)$	0.449 ± 0.019	0.412 ± 0.017	0.474 ± 0.019	0.437 ± 0.013
$h^+(x_\mathrm{F} < 0)$	0.725 ± 0.023	1.303 ± 0.036	0.677 ± 0.023	1.052 ± 0.024
$\pi^-(x_\mathrm{F} < 0)$	0.325 ± 0.017	0.541 ± 0.022	0.339 ± 0.018	0.460 ± 0.015
	$4 < W^2 < 9\ \mathrm{GeV}^2$			
$h^+(x_\mathrm{F} > 0)$	1.349 ± 0.026	1.106 ± 0.027	1.319 ± 0.026	1.193 ± 0.019
$\pi^-(x_\mathrm{F} > 0)$	0.325 ± 0.019	0.309 ± 0.018	0.360 ± 0.021	0.329 ± 0.014
$h^+(x_\mathrm{F} < 0)$	0.632 ± 0.027	1.172 ± 0.040	0.589 ± 0.027	0.935 ± 0.027
$\pi^-(x_\mathrm{F} < 0)$	0.277 ± 0.019	0.480 ± 0.024	0.295 ± 0.020	0.405 ± 0.016
	$9 < W^2 < 25\ \mathrm{GeV}^2$			
$h^+(x_\mathrm{F} > 0)$	1.596 ± 0.042	1.349 ± 0.042	1.545 ± 0.042	1.425 ± 0.030
$\pi^-(x_\mathrm{F} > 0)$	0.660 ± 0.036	0.579 ± 0.032	0.671 ± 0.036	0.615 ± 0.024
$h^+(x_\mathrm{F} < 0)$	0.883 ± 0.043	1.516 ± 0.066	0.829 ± 0.043	1.248 ± 0.044
$\pi^-(x_\mathrm{F} < 0)$	0.408 ± 0.032	0.640 ± 0.041	0.417 ± 0.033	0.553 ± 0.028

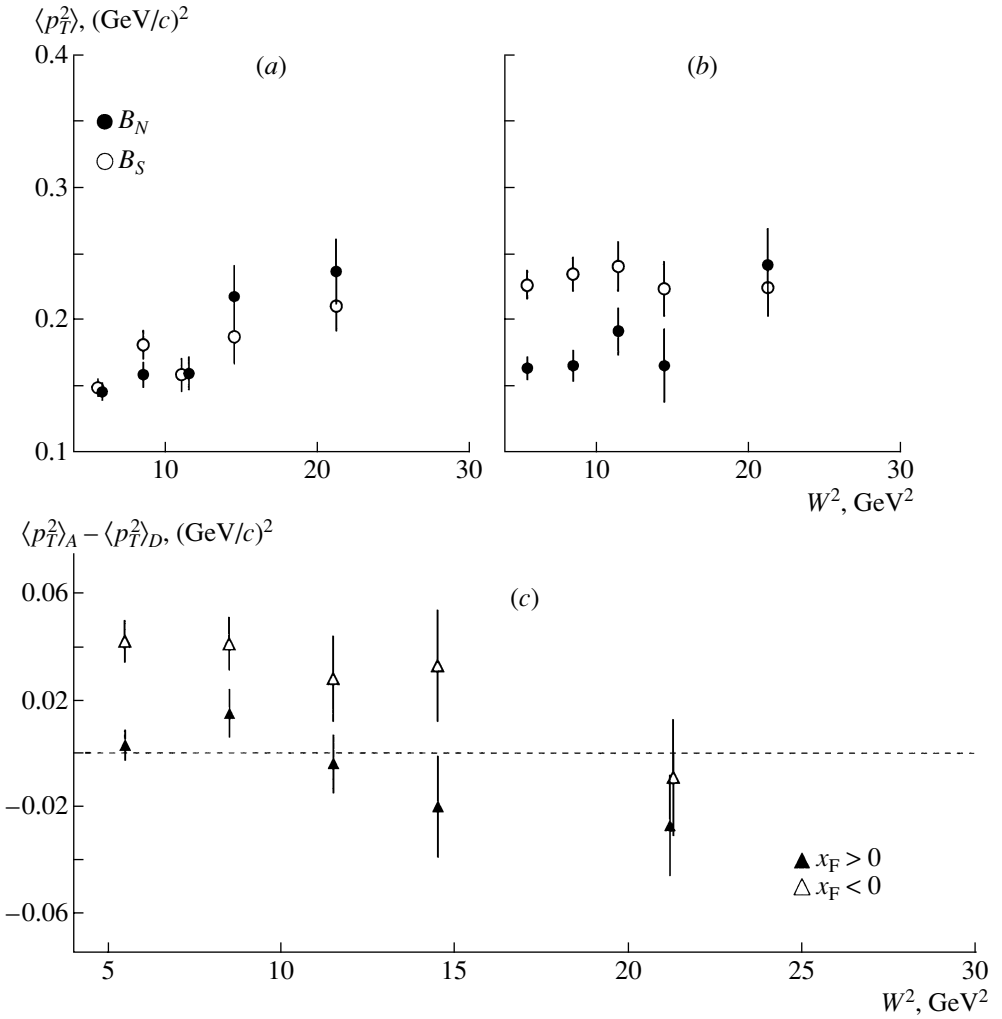

Fig. 3. The W^2 dependence of $\langle p_T^2 \rangle$ for B_N and B_S subsamples (a) at $x_F > 0$ and (b) at $x_F < 0$ and (c) of the difference $\langle p_T^2 \rangle_A - \langle p_T^2 \rangle_D$.

are given the pion mass m_π. The transverse momentum p_T of hadrons is defined with respect to the weak-current direction given by the vector difference of the neutrino and muon momenta. In Fig. 1a, the p_T^2 distributions for h^+ and π^- are plotted for the whole sample of events. Both distributions are fitted to the form $\exp[-b(p_T^2 + m_\pi^2)^{1/2}]$, with parameters $b(h^+) = 5.57 \pm 0.06$ GeV^{-1} and $b(\pi^-) = 7.48 \pm 0.15$ GeV^{-1}, respectively. The latter are close to those extracted from the neutrino interactions with a heavier composite target (CF_3Br) at the same incident energies [6]. The p_T^2 distributions for the B_S subsample are less steep than for the B_N subsample (both shown in Figs. 1b and 1c), owing to an additional transverse momentum acquired by final hadrons in the intranuclear scattering processes. These distributions can also be fitted to the same form, resulting in $b_S(h^+) = 5.30 \pm 0.08$ GeV^{-1} and $b_S(\pi^-) = 7.22 \pm 0.21$ GeV^{-1} for the "cascade" subsample, which are about 10–15% smaller than those in the "quasinucleon" subsample, $b_N(h^+) = 6.06 \pm 0.10$ GeV^{-1} and $b_N(\pi^-) = 7.99 \pm 0.25$ GeV^{-1}. Figure 2 shows the p_T^2 distributions for charged hadrons ($h^\pm$) produced in the current quark and target fragmentation regions (with Feynman variable $x_F > 0$ and $x_F < 0$, respectively). While at $x_F > 0$ the parameter b is almost the same for subsamples B_N and B_S, $b_N(x_F > 0) = 6.57 \pm 0.12$ (GeV/c)$^{-1}$ and $b_S(x_F > 0) = 6.43 \pm 0.13$ (GeV/c)$^{-1}$, at $x_F < 0$ $b_S(x_F < 0) = 5.29 \pm 0.10$ (GeV/c)$^{-1}$ is 16% smaller than $b_N(x_F < 0) = 6.13 \pm 0.15$ (GeV/c)$^{-1}$. The values of $b_N(x_F > 0)$ and $b_N(x_F < 0)$ for the "quasinucleon" subsample B_N are consistent with those measured in νp [7] and νD [8] interactions at somewhat higher $\langle W^2 \rangle$.

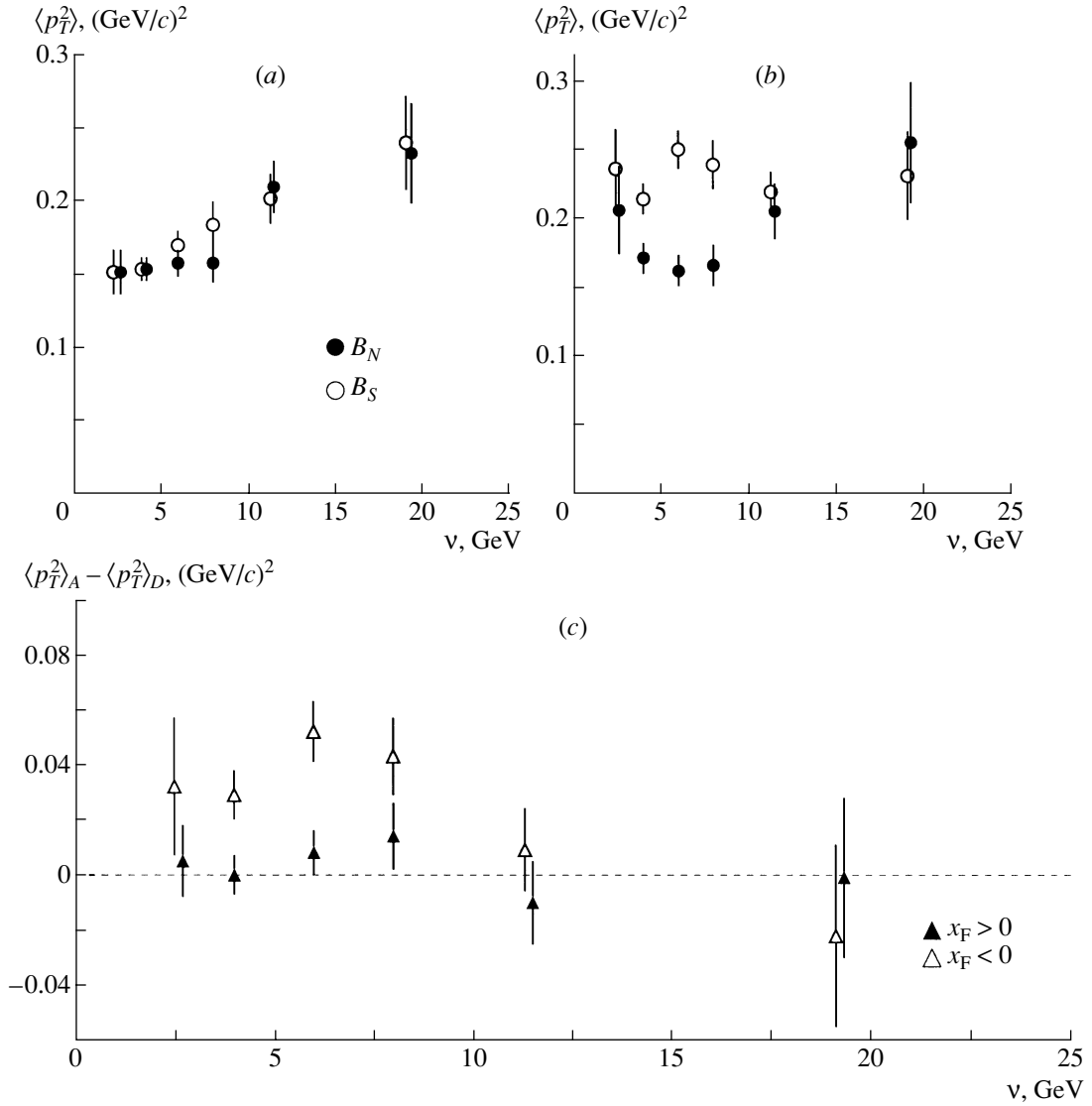

Fig. 4. The ν dependence of $\langle p_T^2 \rangle$ for B_N and B_S subsamples (a) at $x_F > 0$ and (b) at $x_F < 0$ and (c) of the difference $\langle p_T^2 \rangle_A - \langle p_T^2 \rangle_D$.

More informative (with respect to the nuclear effects) are the values of $\langle p_T^2 \rangle$ collected in Table 1 for several subsamples and various regions of x_F and W^2. As can be seen, the nuclear effects influence faintly the $\langle p_T^2 \rangle$ for π^- mesons, as well as for h^+ with $x_F > 0$, in both low ($4 < W^2 < 9$ GeV^2) and high ($9 < W^2 < 25$ GeV^2) regions of W^2. On the contrary, the $\langle p_T^2 \rangle$ for h^+ with $x_F < 0$ increases by $\Delta(p_T^2) = \langle p_T^2 \rangle_S - \langle p_T^2 \rangle_N = 0.061 \pm 0.013$ (GeV/c)^2 due to the secondary intranuclear interactions. One should emphasize that this rise is more prominent at $W^2 <$ 9 GeV^2, where $\Delta(p_T^2) = 0.077 \pm 0.016$ (GeV/c)^2, than at $W^2 > 9$ GeV^2, where $\Delta(p_T^2) = 0.043 \pm 0.021$ (GeV/c)^2. This is in accordance with the recent observations [4, 5, 9] that the effects of the secondary intranuclear interactions weaken with increasing W^2.

Another consequence of the intranuclear interactions is that the region of $x_F > 0$ turns out to be somewhat depleted, while the region of $x_F < 0$ is enriched for the subsample B_S relative to the subsample B_N. This can be clearly seen from the data on the mean multiplicities presented in Table 2. The depletion and enrichment effects can be characterized by the ratios $\rho(x_F > 0) = \langle n(x_F > 0) \rangle_S / \langle n(x_F > 0) \rangle_N$ and $\rho(x_F < 0) = \langle n(x_F < 0) \rangle_S / \langle n(x_F < 0) \rangle_N$, respectively. For π^- mesons, the depletion effect is rather weak, $\rho^-(x_F > 0) = 0.92 \pm 0.05$, while the multiplicity gain at $x_F < 0$ reaches $\rho^-(x_F < 0) = 1.66 \pm 0.11$. Slightly larger effects are observed for

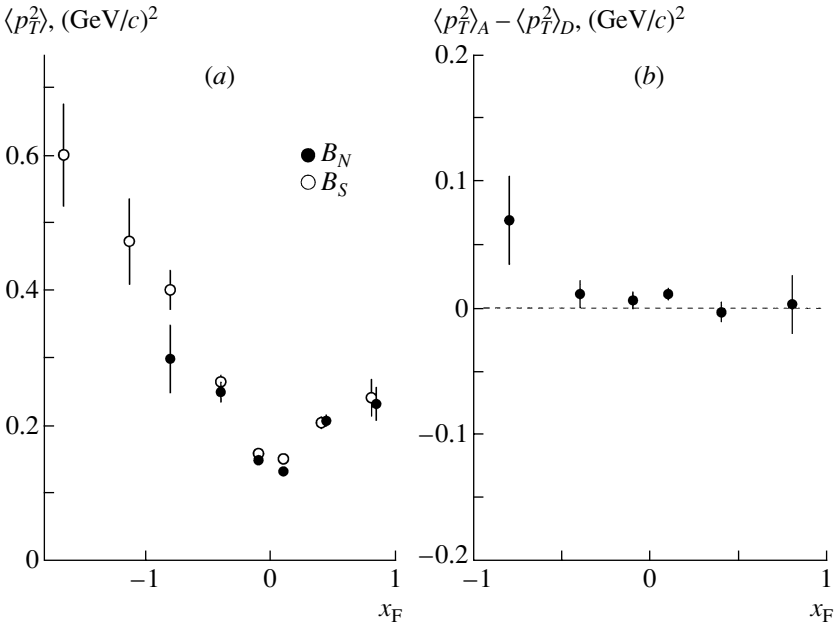

Fig. 5. The x_F dependence (a) of $\langle p_T^2\rangle$ for B_N and B_S subsamples and (b) of the difference $\langle p_T^2\rangle_A - \langle p_T^2\rangle_D$.

positively charged hadrons: $\rho^+(x_F > 0) = 0.83 \pm 0.02$ and $\rho^+(x_F < 0) = 1.80 \pm 0.08$. Note that the latter value can be somewhat influenced by the contamination from the nonidentified recoil protons emitted during the secondary interaction processes. The lower limit of the mean multiplicity of these protons, evaluated from the identification efficiency for protons with $0.6 < p_p < 0.85$ GeV/c (almost all having $x_F < 0$), turns out to be about 5% of $\langle n_{h^+}(x_F < 0)\rangle_S$. The data of Table 2 also indicate that the depletion and enrichment effects depend on W only slightly.

To compare our data with the results of other experiments, as well as to extract quantitative characteristics of the secondary intranuclear interactions, the data on $\langle p_T^2\rangle$, corresponding to νD and νA interactions, $\langle p_T^2\rangle_D$ and $\langle p_T^2\rangle_A$, respectively, are presented in Table 1. The values of $\langle p_T^2\rangle_D$ and $\langle p_T^2\rangle_A$ are defined as

$$\langle p_T^2\rangle_D = \frac{0.6N_p}{N_D}\langle p_T^2\rangle_p + \frac{N_n}{N_D}\langle p_T^2\rangle_n, \qquad (1)$$

$$\langle p_T^2\rangle_A = \frac{N_D}{N_A}\langle p_T^2\rangle_D + \frac{N_S}{N_A}\langle p_T^2\rangle_S. \qquad (2)$$

Here, $N_D = N_n + 0.6N_p$, $N_A = N_S + N_D$, and $\langle p_T^2\rangle_p$ and $\langle p_T^2\rangle_n$ are the values of $\langle p_T^2\rangle$ for subsamples B_p and B_n, respectively.

The average multiplicities $\langle n\rangle_A$ and $\langle n\rangle_D$ are defined similarly (see Table 2). The measured values of $\langle p_T^2\rangle_A - \langle p_T^2\rangle_D$ and $\langle n\rangle_A - \langle n\rangle_D$ will be compared with theoretical predictions in Section 4.

The dependence of the mean value of $\langle p_T^2\rangle$ of charged hadrons (combined h^+ and π^-) on the DIS kinematical variables W^2 and ν is presented in Figs. 3 and 4. It is seen from Fig. 3a that $\langle p_T^2\rangle$ for particles with $x_F > 0$ increases with W^2, as was observed in earlier investigations with neutrino and muon beams [8–14]. For the considered range of W^2, this rise is essentially caused by an increase in the available phase space. With increasing W^2, the QCD effects are predicted [15] to play a more and more significant role in the rise of $\langle p_T^2\rangle$. The data show (Figs. 3a, 3c) that the nuclear effects hardly affect $\langle p_T^2\rangle$ at $x_F > 0$. On the contrary, they cause a significant increase in $\langle p_T^2\rangle$ at $x_F < 0$ in the region of $W^2 < 15$ GeV^2, where the difference $\langle p_T^2\rangle_A - \langle p_T^2\rangle_D$ is about 0.04 (GeV/c)^2 and practically independent of W^2.

The dependence of $\langle p_T^2\rangle$ on ν (see Fig. 4) reveals analogous significant nuclear effects for particles with $x_F < 0$ in the region of $\nu < 9$ GeV, where the difference $\langle p_T^2\rangle_A - \langle p_T^2\rangle_D$ is around 0.03–0.05 (GeV/c)^2. At ν higher than 9 GeV, the nuclear effects on $\langle p_T^2\rangle$ are negligible. As for particles with $x_F > 0$, the effects of secondary intranuclear interactions hardly affect $\langle p_T^2\rangle$.

The dependence of $\langle p_T^2\rangle$ for charged hadrons on their kinematical variables is presented in Figs. 5 and 6. The dependence of $\langle p_T^2\rangle$ on x_F (Fig. 5a) has a typical "seagull" form (cf., for example, [6, 11]) for both B_N and B_S subsamples. For the latter, a small

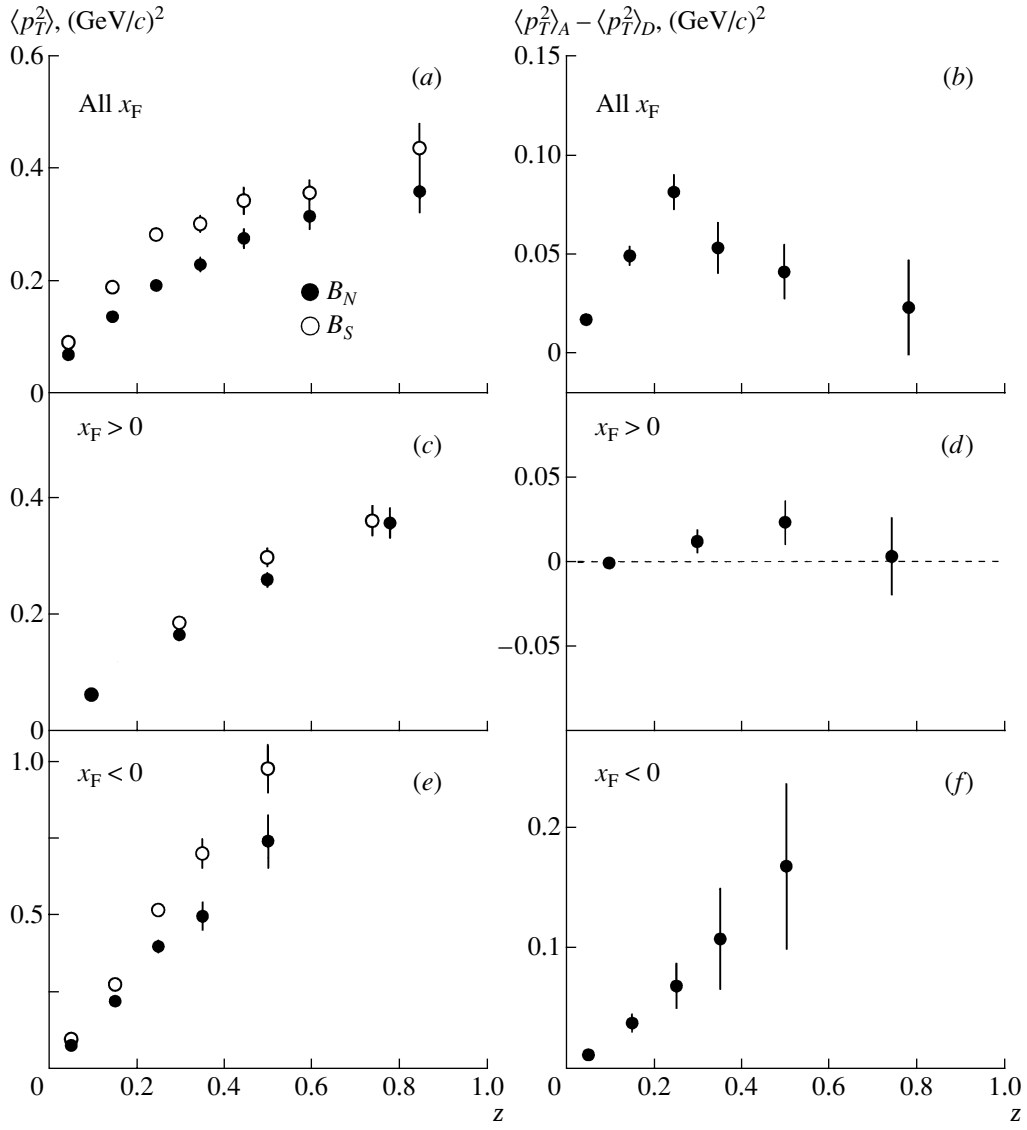

Fig. 6. The z dependence (a, c, e) of $\langle p_T^2\rangle$ for B_N and B_S subsamples and (b, d, f) of the difference $\langle p_T^2\rangle_A - \langle p_T^2\rangle_D$.

part (about 3%) of positively charged hadrons occupy the region of $x_F < -1$, kinematically forbidden for reactions on a free nucleon (the so-called "cumulative" region), where $\langle p_T^2\rangle_S$ reaches a rather high value of $\langle p_T^2\rangle_S \sim 0.6$ (GeV/c)^2. About one-third of these cumulative hadrons are estimated to be nonidentified protons with $0.6 < p_p < 0.85$ GeV/c and $\langle p_T^2\rangle = 0.51 \pm 0.06$ (GeV/c)^2. It is seen from Fig. 5b that the influence of nuclear effects is significant only at $x_F < -0.6$, where the difference $\langle p_T^2\rangle_A - \langle p_T^2\rangle_D$ is about 0.07 ± 0.03 (GeV/c)^2.

Figure 6 shows the dependences of $\langle p_T^2\rangle_N$, $\langle p_T^2\rangle_S$, and $\langle p_T^2\rangle_A - \langle p_T^2\rangle_D$ on the variable $z = E_h/\nu$, the fraction of the current quark energy carried by the hadron. The rise of $\langle p_T^2\rangle_N$ with z for forward hadrons (Fig. 6c), observed earlier in [10, 11, 13], is mainly caused by the intrinsic transverse momentum of the current quark inside the nucleon [16] (see Section 4 for details). It is seen from Fig. 6b that the secondary intranuclear interactions induce a significant difference of $\langle p_T^2\rangle_A - \langle p_T^2\rangle_D$ in almost the whole range of z. The rise of $\langle p_T^2\rangle_A - \langle p_T^2\rangle_D$ at $0 < z < 0.3$ is contributed by particles with $x_F < 0$ (cf. Fig. 6f), while its fall at $z > 0.3$ is caused by the increasing contribution of forward particles for which the difference $\langle p_T^2\rangle_A - \langle p_T^2\rangle_D$ is rather small (Fig. 6d), in accordance with recent observations in DIS of muons and positrons on light and intermediate mass nuclei [17, 18].

Table 3. The measured and predicted differences $\langle n\rangle_A - \langle n\rangle_D$ at $x_F > 0$ and $x_F < 0$

W^2, GeV^2	Particle type	$\langle n\rangle_A - \langle n\rangle_D$	
		measured	calculated
$4 < W^2 < 9$	$h^+(x_F > 0)$	-0.123 ± 0.019	-0.136 ± 0.045
	$\pi^-(x_F > 0)$	-0.037 ± 0.015	-0.008 ± 0.032
	$h^+(x_F < 0)$	0.375 ± 0.025	0.407 ± 0.084
	$\pi^-(x_F < 0)$	0.121 ± 0.017	0.241 ± 0.069
$9 < W^2 < 25$	$h^+(x_F > 0)$	-0.119 ± 0.036	-0.059 ± 0.041
	$\pi^-(x_F > 0)$	-0.056 ± 0.029	-0.006 ± 0.039
	$h^+(x_F < 0)$	0.418 ± 0.048	0.284 ± 0.051
	$\pi^-(x_F < 0)$	0.136 ± 0.032	0.186 ± 0.044

Table 4. The measured and predicted differences $\langle p_T^2\rangle_A - \langle p_T^2\rangle_D$ at $x_F > 0$ and $x_F < 0$

W^2, GeV^2	Particle type	$\langle p_T^2\rangle_A - \langle p_T^2\rangle_D$, $(\mathrm{GeV}/c)^2$	
		measured	calculated
$4 < W^2 < 9$	$h^+(x_F > 0)$	0.005 ± 0.006	0.003 ± 0.008
	$\pi^-(x_F > 0)$	0.009 ± 0.008	0.001 ± 0.011
	$h^+(x_F < 0)$	0.059 ± 0.009	0.032 ± 0.019
	$\pi^-(x_F < 0)$	0.014 ± 0.008	0.036 ± 0.024
$9 < W^2 < 25$	$h^+(x_F > 0)$	0.002 ± 0.011	0.000 ± 0.012
	$\pi^-(x_F > 0)$	-0.012 ± 0.013	-0.002 ± 0.015
	$h^+(x_F < 0)$	0.030 ± 0.013	0.010 ± 0.016
	$\pi^-(x_F < 0)$	0.004 ± 0.008	0.016 ± 0.019

4. MODEL CALCULATION AND DISCUSSION

The data on $\langle p_T^2\rangle_N$ of hadrons with $x_F > 0$ in the subsample B_N were checked for consistency with the conventional picture of the quark string fragmentation (see, e.g., [16] for a review). According to the latter, the z dependence of $\langle p_T^2\rangle_N$ for leading hadrons (containing the current quark) can be parametrized as [19]

$$\langle p_T^2\rangle_N = \langle p_T^2\rangle_{\mathrm{frag}} + z^2\langle k_T^2\rangle + \langle p_T^2\rangle_{\mathrm{QCD}}, \qquad (3)$$

where $\langle p_T^2\rangle_{\mathrm{frag}}$ is the contribution from the fragmentation process, k_T is the primordial transverse momentum of the current quark inside the nucleon, and $\langle p_T^2\rangle_{\mathrm{QCD}}$ is the contribution of QCD effects (involving hard gluon emission and $q\bar{q}$ production). At W^2 available in this experiment ($W^2 < 25$ GeV^2), the latter term can be approximately parametrized as [20]

$$\langle p_T^2\rangle_{\mathrm{QCD}} = a(W^2 - W_0^2), \qquad (4)$$

with $a = 3.5 \times 10^{-3}\,(\mathrm{GeV}/c)^2$ and $W_0^2 = 2$ GeV^2.

Figure 7 shows the z^2 dependence for $\langle p_T^2\rangle$ of positively charged hadrons in the current fragmentation region for two intervals of W^2, $W^2 < 9$ GeV^2 and $W^2 > 9$ GeV^2 (containing approximately equal statistics). The data for fast hadrons (with $z^2 > 0.16$), containing with a high probability the current quark, are fitted to dependence (3). The QCD term in (3) was fixed according to (4). At $z^2 > 0.16$, the mean value of $\langle W^2\rangle$ in the present experiment is practically independent of z^2: $\langle W^2\rangle \approx 6$ GeV^2, leading to $\langle p_T^2\rangle_{\mathrm{QCD}} = 0.014\ (\mathrm{GeV}/c)^2$ for the region $W^2 < 9$ GeV^2, and $\langle W^2\rangle \approx 14$ GeV^2, leading to $\langle p_T^2\rangle_{\mathrm{QCD}} = 0.042\,(\mathrm{GeV}/c)^2$ for the region $W^2 > 9$ GeV^2. The results of the fit are plotted in Fig. 7 (top). The fitted values of $\langle p_T^2\rangle_{\mathrm{frag}}$ and $\langle k_T^2\rangle$ turn out to be independent of W^2 within statistical uncertainties: $\langle p_T^2\rangle_{\mathrm{frag}} = 0.17 \pm 0.03\ (\mathrm{GeV}/c)^2$ and $\langle k_T^2\rangle = 0.23 \pm 0.10\ (\mathrm{GeV}/c)^2$ at

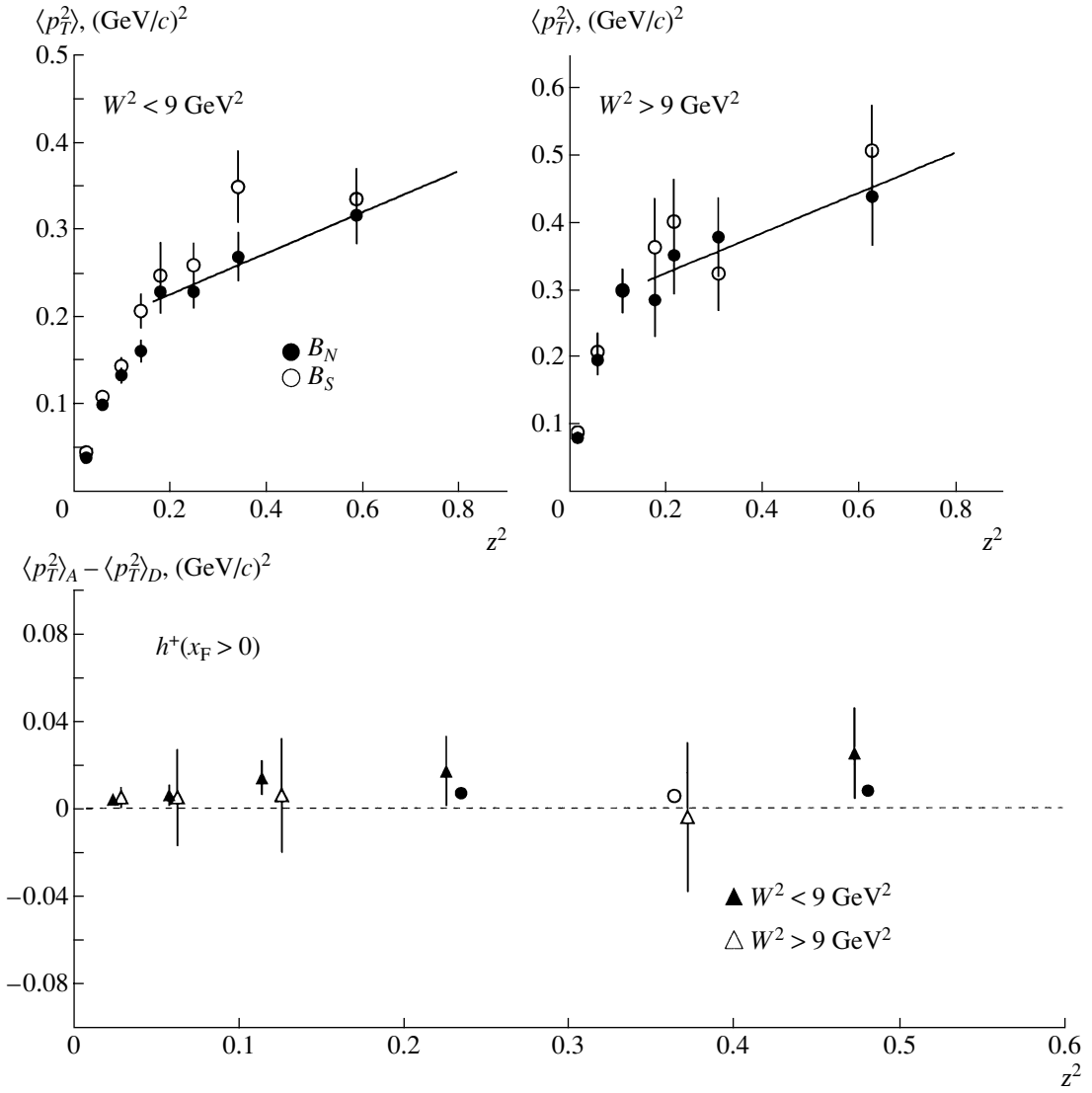

Fig. 7. The z^2 dependence of $\langle p_T^2\rangle$ and $\langle p_T^2\rangle_A - \langle p_T^2\rangle_D$ of positively charged hadrons with $x_F > 0$. The lines are the results of the fit (see text). The two closed circles in the bottom figure are predictions for leading particles with $0.16 < z^2 < 0.3$ and $z^2 > 0.3$ at $W^2 < 9$ GeV^2; the open circle is a prediction for particles with $z^2 > 0.2$ at $W^2 > 9$ GeV^2.

$W^2 < 9$ GeV^2, and $\langle p_T^2\rangle_{\text{frag}} = 0.22 \pm 0.07$ (GeV/c)^2 and $\langle k_T^2\rangle = 0.30 \pm 0.19$ (GeV/c)^2 at $W^2 > 9$ GeV^2. The quoted values of $\langle k_T^2\rangle$ are consistent with those extracted from the data on νp [21] and μp [22, 23] DIS at higher W^2 ($16 < W^2 < 400$ GeV^2). The values of $\langle p_T^2\rangle_{\text{frag}}$ are also consistent with that estimated in [21]; however, they somewhat underestimate the value of $\langle p_T^2\rangle_{\text{frag}} = 0.274 \pm 0.059$ extracted from e^+e^- annihilation at LEP energies [24].

In Fig. 7 (bottom), the difference $\langle p_T^2\rangle_A - \langle p_T^2\rangle_D$ versus z^2 is plotted. The data at low W^2, $W^2 <$ 9 GeV^2, indicate that the additional transverse momentum, acquired by forward hadrons (with $x_F > 0$) due to the intranuclear interactions, slightly increases with z, while at larger $W^2 > 9$ GeV^2 no significant nuclear effects are observed.

Below, an attempt is undertaken to describe the obtained experimental data on differences $\langle n\rangle_A - \langle n\rangle_D$ and $\langle p_T^2\rangle_A - \langle p_T^2\rangle_D$, which characterize the strength of nuclear effects, with the help of a simple model incorporating the secondary intranuclear interactions of produced pions [25]. We assume that the formation length l_π of pions is determined [26] in the framework of the Lund fragmentation model [27]:

$$l_\pi = \nu z \left[\frac{\ln(1/z^2) - 1 + z^2}{1 - z^2}\right] \Big/ k, \qquad (5)$$

where $k \approx 1$ GeV/fm is the quark string tension. Expression (5) has a maximum at $z \approx 0.3$ and be-

haves as $l_\pi \approx 2\nu z \ln(0.61/z)/k$ at $z < 0.2$ and approximately (with an accuracy better than 20%) as $l_\pi \approx \nu(1-z)/k$ at $z > 0.5$. The latter behavior (predicted also in [28]) was found to be consistent with recent experimental data [4, 5, 29]. We assume that a pion can interact in the nucleus, starting from the distance l_π from the νN-scattering point. The model considers both elastic and inelastic interactions of pions with $x_\mathrm{F} > 0$ produced in the νN scattering and having relatively large momenta, while only the elastic scattering of pions with $x_\mathrm{F} < 0$ (having small momenta) is considered. The contribution from nonidentified recoil protons (the overwhelming part of which occupy the region of $x_\mathrm{F} < 0$) is taken into account also.

A comparison with the experimental data is given in Tables 3 and 4. As can be seen from Table 3, a reasonable consistency with the data on $\langle n(x_\mathrm{F} > 0)\rangle_A - \langle n(x_\mathrm{F} > 0)\rangle_D$ is observed. Particularly, the model predicts a stronger depletion for the yield of h^+ than for π^- in the forward hemisphere in agreement with the data. The data description at $x_\mathrm{F} < 0$ is worse. The model overestimates the enhancement of the π^- yield at $W^2 < 9$ GeV^2 by a factor of 2, but is in agreement with the data at $W^2 > 9$ GeV^2 within experimental uncertainties. On the other hand, the predicted value of $\langle n_{h^+}(x_\mathrm{F} < 0)\rangle_A - \langle n_{h^+}(x_\mathrm{F} < 0)\rangle_D$ agrees with the measured one at $W^2 < 9$ GeV^2, but underestimates significantly that at $W^2 > 9$ GeV^2. Nevertheless, the model reproduces qualitatively the nuclear depletion and enhancement effects for the yield of h^+ and π^- and, in particular, predicts, in accordance with the experimental observation, these effects to be more significant for h^+ than for π^-. The model describes satisfactorily the data on the difference $\langle p_T^2\rangle_A - \langle p_T^2\rangle_D$ (Table 4). In particular, the model reproduces rather small values of this difference at $x_\mathrm{F} > 0$, as well as the data for π^- mesons with $x_\mathrm{F} < 0$.

The predicted values of $\langle p_T^2\rangle_A - \langle p_T^2\rangle_D$ for leading particles (with $z^2 > 0.16$) shown in Fig. 7 (bottom) are, in agreement with the data, rather small and do not contradict the trend of the latter with variation of z^2 and W^2.

Finally, one needs to note that, although the applied model reproduces the majority of the experimental data [presented in Tables 3 and 4 and Fig. 7 (bottom)], it is rather crude and uses several simplified assumptions which should be summarized: (i) the calculations concerning the secondary intranuclear interactions are performed for fixed average momenta of π^+ and π^- mesons, $\bar{p}_{\pi^\pm}(x_\mathrm{F} > 0)$ and $\bar{p}_{\pi^\pm}(x_\mathrm{F} < 0)$, instead of more extensive calculations averaged over the momentum spectra; (ii) the second-order effects of two or more intranuclear collisions of a pion are neglected; (iii) the model does not incorporate the production of hadronic resonances, in particular, ρ mesons (composing about 10% of charged pions [30, 31]), with a proper spacetime structure of their formation, intranuclear interactions, and decay.

5. SUMMARY

New experimental data concerning the influence of the nuclear medium on the transverse momentum of neutrino-produced hadrons are presented.

The p_T^2 distribution of hadrons (both positively and negatively charged) is less steep in "cascading" (and "nuclear") than in "quasinucleon" (and "quasideuteron") interactions, while in the quark fragmentation region ($x_\mathrm{F} > 0$) these subsamples have just the same p_T^2 distributions.

The influence of the nuclear medium on the dependence of $\langle p_T^2\rangle$ on kinematical variables of the DIS and of final hadrons is studied. The nuclear effects leading to an enhancement of $\langle p_T^2\rangle$ are more prominent for the following ranges of variables:

for $x_\mathrm{F} < 0$ at $W^2 < 15$ GeV^2 or $\nu < 9$ GeV, while no significant enhancement of $\langle p_T^2\rangle$ is observed at higher W^2 or ν;

for $x_\mathrm{F} < -0.6$, while at $x_\mathrm{F} > -0.6$ the manifestation of nuclear effects is faint;

for practically the whole range of z.

The observed z^2 dependence of $\langle p_T^2\rangle_N$ for fast hadrons in the "quasinucleon" subsample follows the conventional picture of the quark string fragmentation. The extracted parameters governing the transverse momentum of produced hadrons, $\langle p_T^2\rangle_\mathrm{frag} = 0.19 \pm 0.03$ (GeV/c)^2 and $\langle k_T^2\rangle = 0.24 \pm 0.09$ (GeV/c)^2 (estimated for the whole range of $4 < W^2 < 25$ GeV^2), are compatible with values obtained at higher energies.

The experimental data on nuclear effects are compared with predictions of a simple model incorporating the secondary intranuclear interactions of produced hadrons with the formation length taken into account. The model predicts a depletion of the particle yield at $x_\mathrm{F} > 0$ and an enhancement of that at $x_\mathrm{F} < 0$ (more pronounced for positively charged hadrons for both regions of $x_\mathrm{F} > 0$ and $x_\mathrm{F} < 0$) in agreement with the data. The model also describes satisfactorily the data on the difference $\langle p_T^2\rangle_A - \langle p_T^2\rangle_D$ for both h^+ and π^- with $x_\mathrm{F} > 0$ and $x_\mathrm{F} < 0$, as well as for the leading particles with $z > 0.4$.

ACKNOWLEDGMENTS

The YerPhI authors M.A., N.G., and H.G. acknowledge the supporting Grant of Calouste Gulbenkian Foundation and Swiss fund "Kidagan." The activity of one of the authors (Zh.K.) is supported by the Cooperation Agreement between DESY and YerPhI signed on December 6, 2002.

REFERENCES

1. V. V. Ammosov *et al.*, Fiz. Élem. Chastits At. Yadra **23**, 648 (1992) [Sov. J. Part. Nucl. **23**, 283 (1992)].
2. N. M. Agababyan *et al.*, Preprint No. 1535(9), YerFI (Yerevan Phys. Inst., Yerevan, 1999).
3. N. M. Agababyan *et al.*, Yad. Fiz. **65**, 1669 (2002) [Phys. At. Nucl. **65**, 1628 (2002)].
4. N. M. Agababyan *et al.*, Preprint No. 1578(3), YerFI (Yerevan Phys. Inst., Yerevan, 2002).
5. N. M. Agababyan *et al.*, Yad. Fiz. **66**, 1350 (2003) [Phys. At. Nucl. **66**, 1310 (2003)].
6. D. S. Baranov *et al.*, Z. Phys. C **21**, 197 (1984).
7. J. Bell *et al.*, Phys. Rev. D **19**, 1 (1979).
8. T. Kitagaki *et al.*, Phys. Lett. B **97**, 325 (1980).
9. E. S. Vataga *et al.*, Yad. Fiz. **63**, 1660 (2000) [Phys. At. Nucl. **63**, 1574 (2000)].
10. J. W. Chapman *et al.*, Phys. Rev. D **14**, 14 (1976).
11. M. Derrik *et al.*, Phys. Rev. D **17**, 1 (1978).
12. H. Deden *et al.*, Nucl. Phys. B **181**, 375 (1981).
13. J. J. Aubert *et al.*, Phys. Lett. B **95**, 306 (1980).
14. P. S. Bosetti *et al.*, Nucl. Phys. B **149**, 13 (1979).
15. G. Altarelli and G. Martinelli, Phys. Lett. B **76**, 89 (1978).
16. P. Renton and W. S. C. Williams, Annu. Rev. Nucl. Part. Sci. **31**, 193 (1981).
17. J. Ashman *et al.*, Z. Phys. C **52**, 1 (1991).
18. A. Airapetian *et al.*, Phys. Lett. B **577**, 37 (2003).
19. R. Odorico, Phys. Lett. B **89**, 89 (1979).
20. P. Mazzanti, R. Odorico, and V. Roberto, Phys. Lett. B **81**, 219 (1979).
21. P. Allen *et al.*, Nucl. Phys. B **188**, 1 (1981).
22. M. Arneodo *et al.* (EMC Collab.), Phys. Lett. B **149**, 415 (1984).
23. M. Arneodo *et al.* (EMC Collab.), Z. Phys. C **36**, 527 (1987).
24. M. Z. Akrawy *et al.* (OPAL Collab.), Z. Phys. C **47**, 505 (1990).
25. N. M. Agababyan *et al.*, Preprint No. 1582(3), YerFI (Yerevan Phys. Inst., Yerevan, 2003).
26. A. Bialas and M. Gyulassy, Nucl. Phys. B **291**, 793 (1987).
27. B. Andersson *et al.*, Phys. Rep. **97**, 31 (1983).
28. B. Z. Kopeliovich, Phys. Lett. B **243**, 141 (1990).
29. A. Airapetian *et al.* (HERMES Collab.), Eur. Phys. J. C **20**, 479 (2001).
30. D. Allasia *et al.*, Nucl. Phys. B **268**, 1 (1986).
31. V. V. Ammosov *et al.*, Yad. Fiz. **46**, 130 (1987) [Sov. J. Nucl. Phys. **46**, 80 (1987)].

Physics of Atomic Nuclei, Vol. 68, No. 7, 2005, pp. 1171–1175. Translated from Yadernaya Fizika, Vol. 68, No. 7, 2005, pp. 1220–1224.

ELEMENTARY PARTICLES AND FIELDS
Experiment

Backscattered Flux Generated by Protons with Energy above 1 TeV in a Lead Absorber

D. M. Podorozhnyi, I. D. Rapoport, and A. N. Turundaevsky*

Research Institute of Nuclear Physics, Moscow State University, Vorob'evy gory, Moscow, 119992 Russia

Received March 19, 2004; in final form, September 8, 2004

Abstract—Detailed simulations of cascade processes are used to analyze the properties of the backscattered particle flux from a lead absorber (in comparison with an iron absorber). The energy dependence of the albedo flux and the spatial and angular distributions of its various components are considered.

An ionization calorimeter is widely used for energy measurements to experimentally study high-energy particles [1]. In this case, certain difficulties in measuring the charge of the primary particle arise from the presence of a backscattered particle flux. The latter is formed by the secondary particles escaping from the absorbing material of the calorimeter in the direction opposite to the primary particle. The backscattered particle flux depends significantly on the absorber material for which high-density materials (iron, lead, and BGO) are used. The properties of the backscattered particle flux from an iron absorber were considered previously [2]. In this paper, our goal is to study the backscattered particle flux from a lead absorber in comparison with the data obtained previously for an iron absorber.

In this connection, we simulated the cascades triggered by 0.5-, 2-, 8-, and 32-TeV protons in a 90-cm-thick lead absorber. The primary particles were assumed to fall perpendicularly to the absorber surface. In this case, the secondary particles escaping through the surface are recorded (according to the conditions adopted previously for an iron absorber [2]). The simulations were performed using the GEANT 3.21 software package [3]; the high-energy and low-energy (below 50 GeV) hadron interactions in the cascade processes were described using the QGSJET [4, 5] and FLUKA [3] generators, respectively.

Below, we present the main properties of the backscattered particle flux obtained through simulations from a lead absorber in comparison with an iron absorber. Table 1 gives the mean numbers of backscattered particles for its various components as a function of the energy of the protons triggering a cascade in the absorber. As follows from these data, a stronger energy dependence of the number of backscattered particles is characteristic of the lead absorber. At all energies in the range under consideration, the neutron flux from the lead absorber is much higher than that from the iron absorber. At the same time, the spatial distribution of backscattered particles depends weakly on the absorber material. We can note only a narrower distribution of gamma-ray photons for the lead absorber (Table 2 and Fig. 1). The angular distributions of gamma-ray photons and neutrons of the backscattered flux change little when changing the absorber. The electron flux from lead is closer to the isotropic one than the backscattered particle flux from the iron absorber (Table 3 and Fig. 2).

An increase in the distance between the upper absorber boundary and the charge detector (i.e., in the gap between the charge detector and the absorber) causes the density of the backscattered particle flux near the primary particle track to decrease at a nearly isotropic angular distribution. Figure 3 shows the corresponding dependence for the various components. The decrease in the density is largest when the distance H increases from zero to about 5 cm. A further increase in the distance yields a relatively weak effect, because the value of H in this case becomes comparable to the emission depth of the backscattered particle flux.

The difference between the kinetic energies of the backscattered particle flux from different absorbing materials is largest for the electron component: the mean energy of the electrons escaping from lead is much lower (Table 4). This gives rise to two peaks in the energy distribution of backscattered charged particles, one of which arises from the electron component, while the other arises from the pion component (Fig. 4).

*e-mail: ant@eas.npi.msu.ru

1063-7788/05/6807-1171$26.00

Table 1. Mean numbers of backscattered particles produced by protons with energy E in the iron (pFe) and lead (pPb) absorbers

E, TeV	γ	e^+e^-	n	$\pi^+\pi^-$
		pFe		
0.5	43.8 ± 2.9	1.2 ± 0.1	178.9 ± 5.7	0.50 ± 0.05
2.0	76.0 ± 4.9	1.80 ± 0.16	411.8 ± 12.7	0.80 ± 0.07
8.0	174.0 ± 11.5	4.10 ± 0.29	1032.6 ± 32.7	1.60 ± 0.14
32.0	406.3 ± 30.2	10.5 ± 1.7	2597.3 ± 84.8	3.20 ± 0.21
		pPb		
0.5	35.7 ± 2.9	1.00 ± 0.09	482.5 ± 13.3	0.40 ± 0.05
2.0	86.2 ± 7.0	2.10 ± 0.16	1240.5 ± 34.0	1.00 ± 0.08
8.0	281.8 ± 28.3	7.70 ± 1.66	3401.0 ± 94.1	2.40 ± 0.17
32.0	673.5 ± 58.0	15.20 ± 1.48	8651.0 ± 234.7	4.70 ± 0.43

Table 2. Mean distances R (cm) of backscattered particles to the cascade axis at the upper boundaries of the iron (pFe) and lead (pPb) absorbers

E, TeV	γ	e^+e^-	n	$\pi^+\pi^-$
		pFe		
0.5	11.16 ± 0.07	10.38 ± 0.45	23.46 ± 0.05	6.27 ± 0.40
2.0	12.18 ± 0.06	10.99 ± 0.39	24.35 ± 0.03	8.16 ± 0.44
8.0	12.66 ± 0.04	11.55 ± 0.27	24.83 ± 0.02	7.77 ± 0.30
32.0	12.76 ± 0.03	10.33 ± 0.18	25.20 ± 0.01	8.46 ± 0.21
		pPb		
0.5	10.41 ± 0.09	11.74 ± 0.61	24.00 ± 0.03	7.52 ± 0.54
2.0	10.75 ± 0.06	13.53 ± 0.43	24.72 ± 0.02	7.18 ± 0.31
8.0	9.31 ± 0.03	10.83 ± 0.22	25.19 ± 0.01	7.48 ± 0.22
32.0	9.68 ± 0.02	13.19 ± 0.16	25.96 ± 0.01	7.60 ± 0.17

Table 3. Mean cosines of the exit angle of backscattered particles relative to the normal to the surfaces of the iron (pFe) and lead (pPb) absorbers

E, TeV	γ	e^+e^-	n	$\pi^+\pi^-$
		pFe		
0.5	0.7194 ± 0.0016	0.6786 ± 0.0109	0.7191 ± 0.0008	0.7433 ± 0.0151
2.0	0.7317 ± 0.0012	0.7104 ± 0.0086	0.7217 ± 0.0005	0.7768 ± 0.0112
8.0	0.7289 ± 0.0008	0.7061 ± 0.0059	0.7231 ± 0.0003	0.7910 ± 0.0078
32.0	0.7409 ± 0.0005	0.7406 ± 0.0036	0.7243 ± 0.0002	0.8010 ± 0.0051
		pPb		
0.5	0.7279 ± 0.0018	0.6614 ± 0.0127	0.7253 ± 0.0005	0.7607 ± 0.0148
2.0	0.7339 ± 0.0011	0.6502 ± 0.0087	0.7286 ± 0.0003	0.7630 ± 0.0099
8.0	0.7520 ± 0.0006	0.6798 ± 0.0045	0.7318 ± 0.0002	0.7707 ± 0.0064
32.0	0.7548 ± 0.0004	0.6540 ± 0.0032	0.7379 ± 0.0001	0.8046 ± 0.0042

Table 4. Mean kinetic energies (MeV) of the various components of the backscattered particle flux produced by protons with energy E in the iron (pFe) and lead (pPb) absorbers

E, TeV	γ	e^+e^-	n	$\pi^+\pi^-$
		pFe		
0.5	2.87 ± 0.08	14.04 ± 1.45	3.15 ± 0.04	193 ± 13
2.0	2.87 ± 0.07	14.42 ± 1.02	2.81 ± 0.03	312 ± 63
8.0	2.90 ± 0.07	15.73 ± 0.89	2.65 ± 0.02	620 ± 191
32.0	3.44 ± 0.08	26.41 ± 1.39	2.48 ± 0.01	513 ± 82
		pPb		
0.5	2.94 ± 0.06	7.98 ± 1.07	2.34 ± 0.02	1137 ± 774
2.0	2.79 ± 0.06	10.65 ± 3.35	2.20 ± 0.01	364 ± 193
8.0	3.23 ± 0.10	17.62 ± 2.42	2.07 ± 0.01	301 ± 38
32.0	2.83 ± 0.06	13.72 ± 2.14	1.89 ± 0.01	756 ± 103

Table 5. Best-fit parameters for the dependence of the number of backscattered particles on the depth of the first inelastic pFe interaction $N(X_{\text{int}}) = N_0 \exp(-X_{\text{int}}/L_{\text{abs}})$ (N_0 is the backscattered particle flux for the interaction at the upper absorber boundary, L_{abs} is the absorbing range, and χ^2/ν characterizes the quality of the fit)

E, TeV	N_0	L_{abs}, g cm^{-2}	χ^2/ν	N_0	L_{abs}, g cm^{-2}	χ^2/ν
	γ			e^+e^-		
0.5	118 ± 4	54 ± 3	1.8	4.1 ± 0.3	36 ± 4	1.2
2.0	223 ± 8	56 ± 2	2.2	5.7 ± 0.4	47 ± 4	1.2
8.0	384 ± 12	67 ± 3	3.6	11.0 ± 0.6	57 ± 4	0.7
32.0	839 ± 26	64 ± 3	2.3	18.8 ± 1.1	62 ± 5	0.9
	n			All charged particles		
0.5	303 ± 6	153 ± 8	0.8	5.6 ± 0.4	41 ± 5	0.8
2.0	727 ± 15	154 ± 7	2.5	8.7 ± 0.6	51 ± 4	0.6
8.0	1748 ± 35	162 ± 8	1.0	15.6 ± 0.8	59 ± 4	0.6
32.0	4397 ± 87	150 ± 7	1.0	34.3 ± 2.0	55 ± 4	0.5

Table 6. Same as Table 5 for pPb

E, TeV	N_0	L_{abs}, g cm^{-2}	χ^2/ν	N_0	L_{abs}, g cm^{-2}	χ^2/ν
	γ			e^+e^-		
0.5	65 ± 2	93 ± 7	8.5	3.9 ± 0.3	53 ± 7	1.8
2.0	133 ± 4	105 ± 6	10.6	6.0 ± 0.3	78 ± 9	2.6
8.0	262 ± 9	121 ± 9	12.6	15.1 ± 0.8	94 ± 10	3.8
32.0	860 ± 29	100 ± 6	9.6	30.3 ± 1.3	90 ± 12	4.7
	n			All charged particles		
0.5	784 ± 15	258 ± 14	1.3	4.9 ± 0.3	62 ± 9	2.4
2.0	2022 ± 35	269 ± 14	0.5	9.6 ± 0.5	73 ± 6	1.9
8.0	5512 ± 101	244 ± 12	0.4	22.8 ± 1.1	91 ± 7	2.5
32.0	$14\,622 \pm 246$	223 ± 10	1.4	42.0 ± 1.7	87 ± 10	4.3

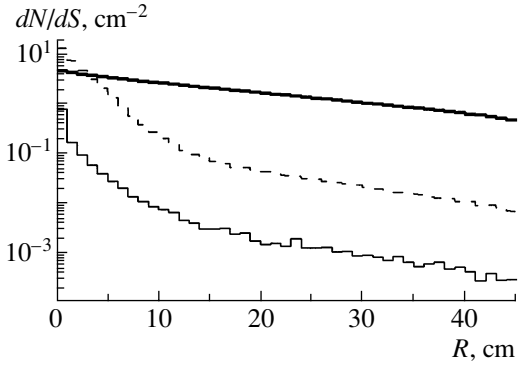

Fig. 1. Spatial distribution of backscattered particles for a 32-TeV primary proton. The dashed, thin solid, and heavy solid lines represent the gamma-ray photons, all charged particles, and the neutrons, respectively. dN/dS is the particle density per cm^2 as a function of the distance R to the cascade axis.

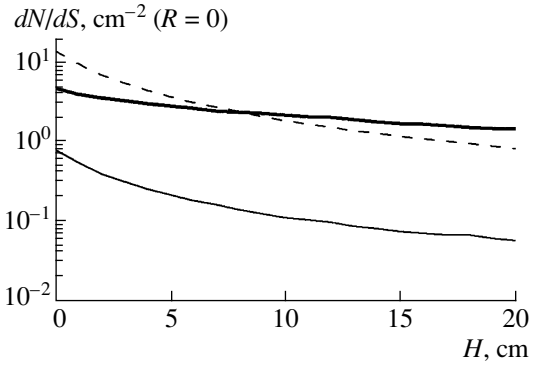

Fig. 3. Space density of the backscattered particle flux near the primary particle track versus distance H between the upper absorber boundary and the charge detector for a 32-TeV primary proton. The notation is the same as that in Fig. 1.

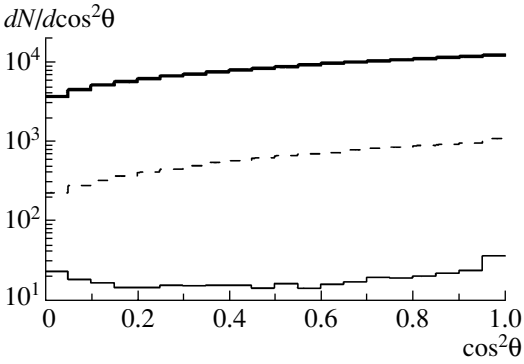

Fig. 2. Angular distribution of backscattered particles for a 32-TeV primary proton. The notation is the same as that in Fig. 1. θ is the exit angle of the backscattered particle relative to the normal to the absorber surface.

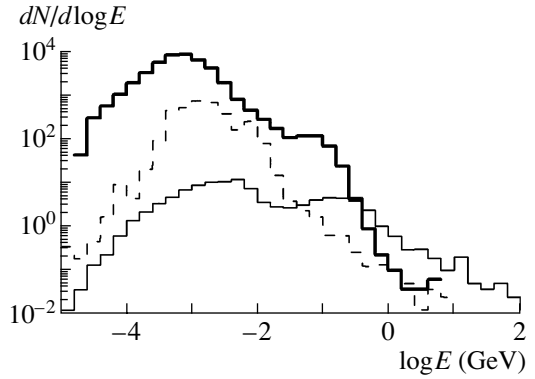

Fig. 4. Energy spectra of backscattered particles for a 32-TeV primary proton. The notation is the same as that in Fig. 1.

The number of backscattered particles fluctuates greatly for both the iron and lead absorbers. Events with a backscattered particle flux well above the mean values given in Table 1 are possible.

There is a correlation between the fluxes of various backscattered particle components. It should be noted that the neutron flux increases faster with primary energy than the fluxes of gamma-ray photons and electrons (see Table 1). This is attributable to a larger neutron range in the material; as result, a substantial part of the hadron cascade contributes to the backscattered particle flux, while the electromagnetic component is absorbed significantly.

Since the ratio of the cascade unit to the nuclear range in lead is smaller, the neutron flux depends weakly on the flux of the electromagnetic component at a large gamma-ray yield. The events with the highest flux of the electromagnetic component are distinguished by a small depth of the first inelastic interaction. The maximum of the hadron cascade gives a major contribution to the neutron component of the backscattered flux and a minor contribution to the electromagnetic component. The corresponding correlation for all charged particles differs only slightly from the curve for electrons, because the flux of charged pions is low.

The form of the dependence of the number of backscattered particles on the depth of the first inelastic interaction is also determined by the absorption range of the corresponding component. Figure 5 shows such dependences for gamma-ray photons, all charged particles, and neutrons. We see that this dependence is noticeably weaker for neutrons than for the electromagnetic component. For an exponential fit, $N(X_{\rm int}) = N_0 \exp(-X_{\rm int}/L_{\rm abs})$, the absorption range of the electromagnetic component is considerably lower than that for neutrons. For lead, this difference is larger than that for iron. The numerical

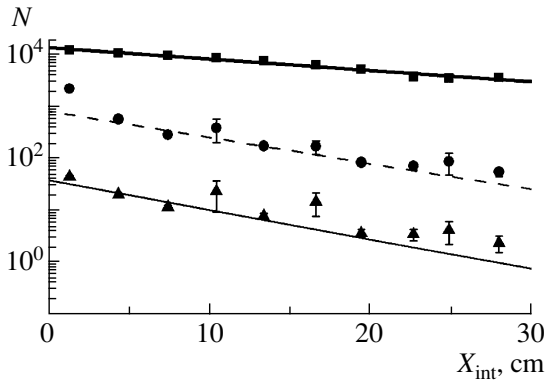

Fig. 5. Number of backscattered particles N versus depth X_{int} of the first inelastic interaction for a 32-TeV primary proton. The dots (●), triangles (▲), and squares (■) represent the gamma-ray photons, all charged particles, and the neutrons, respectively. The lines indicate the fits; the notation is the same as that in Fig. 1.

values of the best-fit parameters N_0 and L_{abs} for the various components with the corresponding values of χ^2/ν are given in Table 5 and Table 6 for the iron [2] and lead absorbers, respectively. The high values of χ^2/ν indicate that the absorption of the backscattered particle flux deviates from the strictly exponential law; this can be explained by the dependence of the absorption range on the energy of the backscattered particle. This is confirmed by the fact that the deviation from the exponential is more noticeable in the lead absorber, where the backscattered gamma-ray photons at low critical energy generate a well-defined electromagnetic cascade (Fig. 5).

Thus, a considerable fraction of the differences in the parameters of the backscattered particle flux from the lead (pPb) and iron (pFe) absorbers is attributable to the properties of the electromagnetic cascade. Since the critical energy in lead is significantly lower, the absorption range of the electromagnetic component increases, while the mean kinetic energy slightly decreases.

The neutron yield depends significantly on the nuclear mass of the absorber material. Heavy nuclei contain more neutrons; therefore, the fragmentation of these nuclei as they interact with hadrons from the cascade increases the flux of this component of the backscattered particle flux.

ACKNOWLEDGMENTS

This work was supported by the Russian Foundation for Basic Research (project no. 05-02-16783-a).

REFERENCES

1. N. L. Grigorov, V. S. Murzin, and I. D. Rapoport, Zh. Éksp. Teor. Fiz. **34**, 506 (1958) [Sov. Phys. JETP **7**, 348 (1958)].
2. D. M. Podorozhnyĭ, I. D. Rapoport, and A. N. Turundaevskiĭ, Yad. Fiz. **67**, 2200 (2004) [Phys. At. Nucl. **67**, 2176 (2004)].
3. GEANT User's Guide, CERN DD/EE/83/1 (Geneva, 1983).
4. N. N. Kalmykov and S. S. Ostapchenko, Preprint No. 98-36/537, NIIYaF MGU (Institute of Nuclear Physics, Moscow State University, Moscow, 1998).
5. N. N. Kalmykov, S. S. Ostapchenko, and A. I. Pavlov, Nucl. Phys. B (Proc. Suppl.) **52B**, 17 (1997).

Translated by E. Kozlovsky

Physics of Atomic Nuclei, Vol. 68, No. 7, 2005, pp. 1176–1182. Translated from Yadernaya Fizika, Vol. 68, No. 7, 2005, pp. 1225–1232.

ELEMENTARY PARTICLES AND FIELDS
Experiment

Albedo in the ATIC Experiment: Measurements and Simulations

N. V. Sokolskaya[1)*], J. H. Adams, Jr.[2)], H. S. Ahn[3)], K. E. Batkov[1)], G. L. Bashindzhagyan[1)], J. Z. Wang[3)], J. P. Wefel[4)], J. Wu[3)], O. Ganel[3)], T. G. Guzik[4)], R. M. Gunasingha[5)], V. I. Zatsepin[1)], J. Isbert[4)], K. C. Kim[3)], M. Christl[2)], E. N. Kouznetsov[1)], M. I. Panasyuk[1)], A. D. Panov[1)], E. S. Seo[3)], A. R. Fazely[5)], J. Chang[6),7)], and W. K. H. Schmidt[6)]

Received April 28, 2004; in final form, September 8, 2004

Abstract—We analyze the characteristics of the albedo, or the backscatter current, which constitutes a background for charge measurements in calorimetric experiments in high-energy cosmic rays. We compare the experimental data obtained in the flights of the ATIC spectrometer with the simulations performed using the GEANT 3.21 code. We discuss the influence of the backscatter on the charge resolution in the ATIC experiment. © *2005 Pleiades Publishing, Inc.*

1. INTRODUCTION

A number of experiments in which an ionization calorimeter was used to directly measure the spectra at high energies have been carried out to date. The experiments onboard the PROTON satellites [1] were performed in 1965–1968 first. However, the results obtained were inconclusive due to the possible signal distortion in the charge detector module by albedo particles from the calorimeter [2]. The albedo problem was completely solved in experiments with emulsion chambers owing to the high spatial resolution achieved in nuclear emulsion analysis. When applied to cosmic-ray studies, this technique has a number of shortcomings, namely, a high energy threshold and insufficient reliability of energy measurements. The technique is also very laborious. Therefore, the results obtained in three emulsion experiments differed significantly [3–5]. A successful method for solving the problem of the backscatter current was used in the SOKOL experiment [6], in which directional Cherenkov detectors were employed to determine the charges of light nuclei (protons and helium). Thin nondirectional Cherenkov counters were used to measure the charges of heavier nuclei. However, the charge resolution in this experiment was too low for nuclei heavier than helium to be resolved.

A different method for significantly reducing the albedo influence on charge measurements was used in the ATIC experiment. This experiment is aimed at performing new measurements of the energy spectrum for galactic cosmic rays with an individual charge resolution from protons to iron over a wide energy range, from 100 GeV to 100 TeV per particle. A matrix of silicon detectors has been used for the first time to measure the charge. The albedo problem is solved here through the fine segmentation of the charge detector. The matrix design of the charge detector offers a possibility for studying the pulse and lateral albedo signal distributions as a function of energy and type of primary particles. Comparison of experimental data with simulations verifies whether the simulations can be used in situations where no experimental data can be obtained.

2. THE ATIC SPECTROMETER

The layout of the spectrometer is shown in Fig. 1. A fully active calorimeter built from 320 bismuth-germanate (BGO) scintillator crystals, each $25 \times 2.5 \times 2.5$ cm in size, measures the energy of each cascade. The BGO crystals form eight layers, each 50×50 cm in area, with the crystal axes lying alternately along the X and Y axes. The calorimeter depth is 18 radiation units. The target module consists of three 10-cm-thick graphite layers (density $1.7\ \mathrm{g\,cm^{-3}}$) and lies above the calorimeter. The target thickness, including the constructional materials and scintillators, is 3/4 of the proton interaction length.

[1)]Skobeltsyn Institute of Nuclear Physics, Moscow State University, Vorob'evy gory, Moscow, 119992 Russia.
[2)]Marshall Space Flight Center, NASA, Huntsville, AL, USA.
[3)]University of Maryland, College Park, MD, USA.
[4)]Louisiana State University, Baton Rouge, LA, USA.
[5)]Southern University, Baton Rouge, LA, USA.
[6)]Max Planck Institut für Aeronomie, Lindau, Germany.
[7)]Purple Mountain Observatory, Chinese Academy of Sciences, China.
[*]e-mail: sok@dec1.sinp.msu.ru

The instrument has three hodoscopes built from 202 strips of plastic scintillators 1 cm thick and 2 cm wide. Each hodoscope consists of two mutually perpendicular strip layers. The hodoscopes are placed above, under, and inside the graphite target and form the first level trigger, which determines the aperture of the instrument, and provide additional measurements of the charge and trajectory of the primary particle reconstructed from the cascades in the calorimeter. The charge detector, a silicon matrix built from 4480 silicon pixels 1.5×2 cm in size, is the uppermost detector in the instrument. The silicon pixels are arranged in four planes with a small overlap along the X and Y axes to avoid the holes through which the primary particle could pass. Thus, each particle inside the aperture of the instrument passes at least through one silicon pixel, and about 15% of the particles pass through two pixels. The total matrix area is 99.2×111.2 cm. The ATIC silicon matrix and its properties are described in detail in [7, 8].

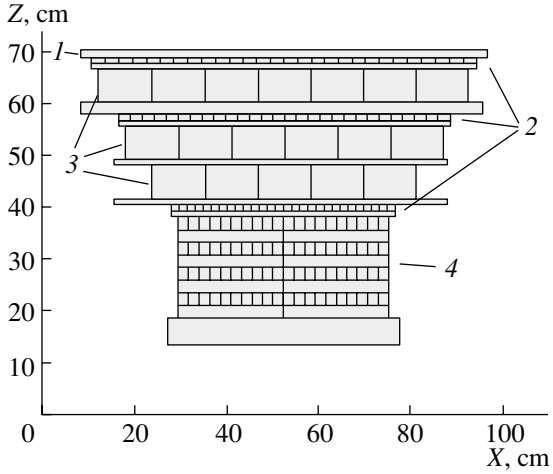

Fig. 1. Layout of the ATIC spectrometer: *1*—silicon matrix, *2*—scintillator hodoscopes, *3*—graphite target, *4*—BGO calorimeter.

3. FLIGHTS IN THE STRATOSPHERE

ATIC was launched for its first test flight on December 28, 2000, at McMurdo, Antarctica. Having made a complete turn around the South Pole, it landed on January 13, 2001. The altitude of the flight was 37 ± 1.5 km. Since ATIC landed successfully and was recovered in good condition, it could be flown again after refurbishment. The second, scientific, flight was also carried out in Antarctica from December 29, 2002, through January 18, 2003. A third flight is scheduled to increase the statistics, particularly at high energies. The goal of the ATIC-1 flight was to test the operation of all detectors and systems of the instrument. However, the first scientific data were obtained during this flight. We used ATIC-1 data to study the backscatter current and its influence on the charge resolution of the ATIC spectrometer.

4. RECONSTRUCTION OF EVENTS IN THE SPECTROMETER

Each high-energy event detected by the instrument is reconstructed from the signals in the detectors to determine the primary particle charge, energy, and trajectory in the instrument. The particle trajectory was reconstructed from the signals in the BGO calorimeter and was described by two projections in the XZ and YZ planes (see Fig. 2). Both projections are reconstructed independently using the Y- and X-oriented crystal layers, respectively. The crystal with the maximum energy deposition is determined in each layer. (If this crystal is found near the edge of the layer, then the event is considered to be a side event and is rejected.) Subsequently, the symmetrized weight center of the energy distribution in the layer is found by taking into account the crystals in both directions from the central crystal. The dispersions of the weight centers are determined from simulated cascades (see below): in each layer, the dispersion of the location of the weight center is determined as a function of the energy deposition in the layer. The parameters of the trajectory projections onto the XZ and YZ planes and their χ^2 values are calculated using these weight centers in the X- and Y-oriented layers of the

Table 1. Trajectory reconstruction accuracy and mean size of the search area for events of various energies

E_d, GeV	σ_X, cm	σ_Y, cm	Search area $\Delta X, \Delta Y$, cm
>10	10.3	9.6	±30
>100	4.6	4.6	±14
>1000	2.7	3.2	±9

Table 2. Probability of an albedo signal with $Q > 1.5$ (for protons) and $Q > 2.5$ (for helium nuclei) in various regions around the point of incidence of the primary particle (in %)

Search area	Protons			Helium		
	E_d, GeV			E_d, GeV		
$\Delta X, \Delta Y$, cm	>10	>100	>1000	>10	>100	>1000
±5	0.6	0.6	1.6	0.1	0.15	0.7
±10	1.7	2.2	6.3	0.1	1	2.2
±25	5.6	13.6	37.6	0.8	2.8	8.4

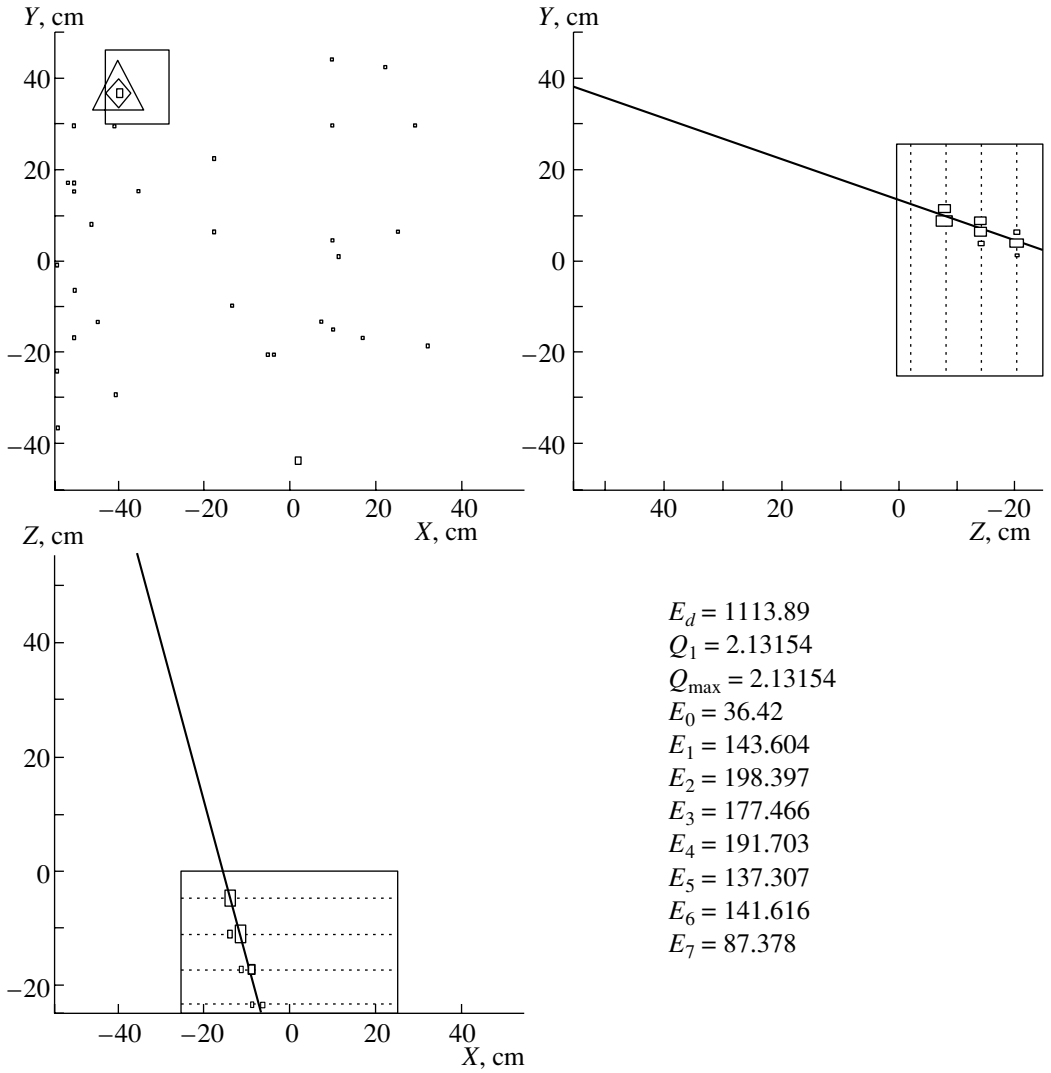

Fig. 2. Example of trajectory reconstruction and charge measurement for an event. The silicon matrix plane is shown in the upper left panel. The square delineates the search area; the triangle and the diamond indicate the locations of the detected charge and the maximum charge in the matrix, respectively. Q_1 is the maximum charge in the search area, $Q_{\max}$ is the maximum charge in the matrix, E_d is the energy deposition in the calorimeter, and E_0–E_7 are the energy depositions in the calorimeter layers (in GeV).

calorimeter. Subsequently, the trajectory projections are extended until they intersect the Si-matrix plane, and the rms errors in the coordinates of the points of intersection in the Si-matrix plane, σ_X and σ_Y, are determined. Then, the $\pm 3\sigma_X$, $\pm 3\sigma_Y$ area for primary particle search is delineated. The Si pixel with the maximum signal in the search area is selected, and the trajectory parameters are recalculated by taking into account the coordinates of the pixel center. The primary particle charge is determined from the formula $Z = \sqrt{A \cos\theta}$, where θ is the zenith angle of the trajectory, and A is the signal in the Si pixel in MIPs (MIP is the energy deposition of a vertical minimum ionizing particle in a silicon pixel). For each reconstructed event, the energy deposition in the calorimeter E_d is calculated by adding the energy depositions of all crystals in all layers of the calorimeter. The signals in the scintillator hodoscopes were not used at this stage of our analysis.

Figure 2 shows an example of event reconstruction. Figure 3 shows the experimental distributions of the distances along the x axis from the cascade axis to the center of the pixel with the maximum signal for three energy ranges. The width of these distributions is seen to decrease with increasing primary particle energy, since the nuclear dispersion decreases in importance and the Coulomb electron scattering begins to play a major role in the lateral distribution. The rms errors of these distributions in each coordinate, σ_X

and σ_Y, and the mean size of the $\pm 3\sigma$ search area as a function of the cascade energy are given in Table 1.

5. EXPERIMENTAL DATA

About 25 million events were detected in the ATIC-1 experiment. For our analysis of the backscatter current, we selected 7000 events with energy deposition $E_d > 10$ GeV and the same number of events with $E_d > 100$ GeV as well as all events (about 1600) with $E_d > 1$ TeV. When processing the raw data, in addition to information about the charge, energy deposition, and trajectory of the primary particle in these events, we recorded information about all signals in the silicon matrix. These signals, except the signal from the primary particle, were produced by the backscatter current or were noise signals. In Fig. 4, the number of albedo and noise signals in the entire matrix per event (n_a) is plotted against the equivalent charge $Q = \sqrt{A}$ for three ranges of energy deposition and three types of primary particles. The noise signals dominate at $Q < 1$, and their number does not depend on energy. On average, there were about 20 noise signals per event. The number of albedo signals decreases with increasing Q almost exponentially and increases with energy and charge of the primary particle. As the energy rises by an order of magnitude, the number of albedo particles increases by a factor of about 3.

6. SIMULATIONS

Initially, simulations were undertaken at the design stage of the instrument and were performed for the design with four 10-cm-thick graphite layers and for the silicon matrix with 3×3-cm pixels. For our simulations, we used the GEANT-3.21 software package, in which a hadron cascade was simulated using the FLUKA generator [9]. The primary particles were protons with energies of 10^2, 10^3, and 10^4 GeV. The results of these simulations were published in [7]. Electrons (bearing in mind both electrons and positrons), pions, photons, and protons were shown to give the main contribution to the albedo signal in the matrix. The relative contribution of pions and, especially, protons increases with the albedo signal. It was also shown that, for a pixel size of 3×3 cm, the frequency of events in which the albedo signal in the axis pixel exceeded 1 MIP is less than 1.5% even at an energy of 10 TeV; i.e., the albedo signals in the matrix are essentially separated from the primary particle signal.

We performed new simulations for the actual design of the instrument. An isotropic particle flux with a power-law energy distribution with index $\gamma = 1.6$ was incident on the silicon matrix plane over the aperture of the instrument. The simulations were carried out for three ranges of primary kinetic energies, $E > 10$, >100, and >1000 GeV, and cascades with energy deposition $E_d > 10$, >100, and >1000 GeV, respectively, were selected for the analysis. Protons and helium nuclei were taken as the primary particles. We used the QGSM generator [10] to simulate the interactions of helium nuclei. The statistics in our simulations were 10^4 cascades for protons and 10^3 cascades for helium in each energy range. To be

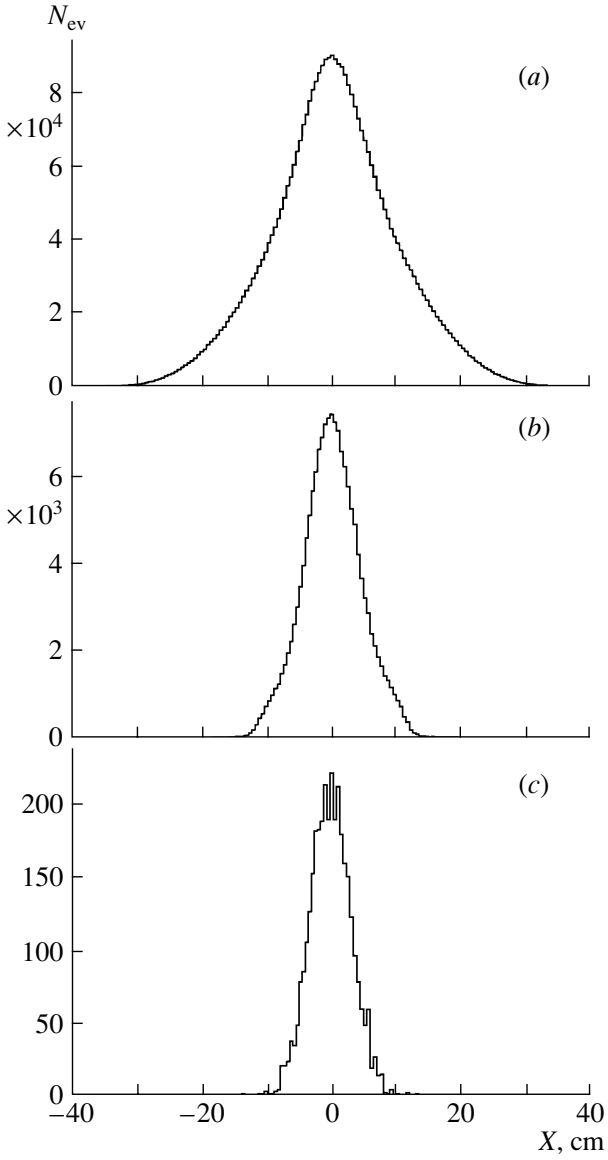

Fig. 3. Distribution of distances along the x axis from the primary particle location to the reconstructed trajectory: (a) $E_d > 10$, (b) $E_d > 100$, and (c) $E_d > 1000$ GeV. The number of events (N_{ev}) in the bin is along the vertical axis.

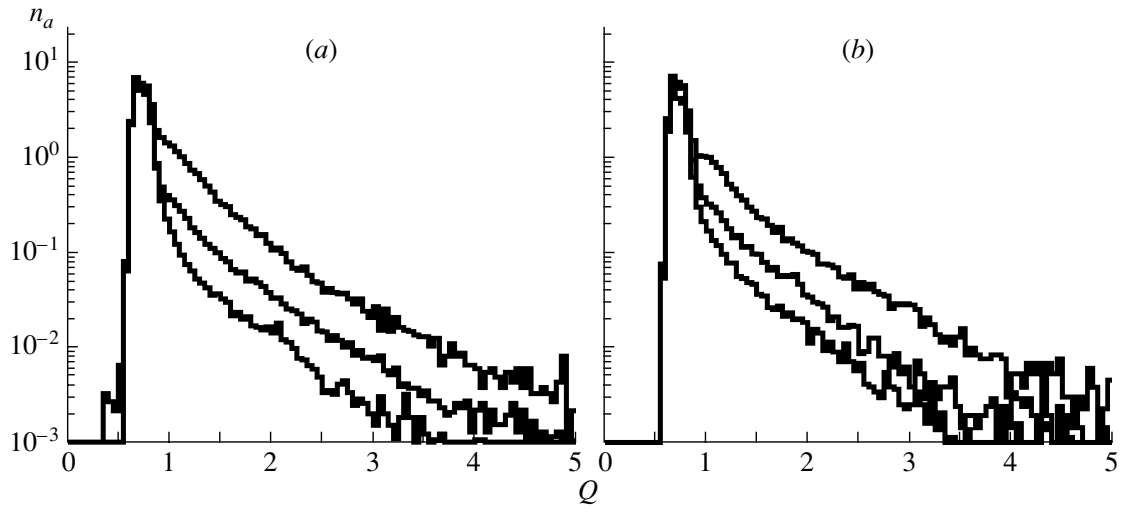

Fig. 4. Experimental albedo distribution in equivalent charge Q (n_a is the number of albedo signals per event in the entire matrix). (a) Three ranges of energy deposition: $E_d > 1000$ (upper histogram), $E_d > 100$ (middle histogram), and $E_d > 10$ GeV (lower histogram); (b) three types of primary particles for $E_d > 100$ GeV: nuclei with $Z > 3$ (upper histogram), helium nuclei (middle histogram), and protons (lower histogram).

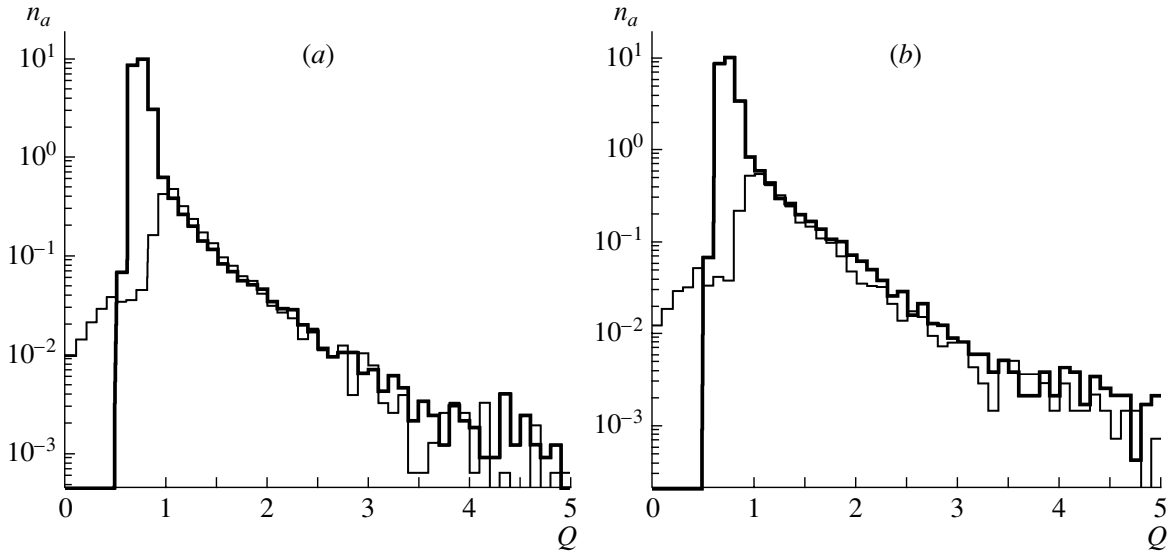

Fig. 5. Comparison of the experimental data with simulations (n_a is the number of albedo signals per event in the entire matrix for $E_d > 100$ GeV): (a) protons and (b) helium nuclei. The thin line represents our simulations.

sure that the simulation results are valid, they must be compared with experimental data.

Figure 5 compares the experimental and simulated distributions of albedo signals in Q for $E_d > 100$ GeV. We can see that the agreement is good at $Q > 1$, where the number of noise signals is negligible.

Figure 6 shows the simulated lateral distribution of albedo signals with $Q > 1$ in the silicon matrix for protons with $E_d > 100$ GeV. Also shown here is the experimental lateral distribution of albedo signals at $R > 20$ cm. The albedo particle density at $R < 20$ cm cannot be studied experimentally, since the maximum signal in this region (the search area) is considered as the signal from the primary particle. The region of $R > 80$ cm can be distorted in the experiment, because large distances are associated with particles near the edge of the matrix. In this case, there is a probability that the axis of the cascade produced by the nucleus that past by the matrix could be restored inside the matrix, and the signal from the backscat-

Table 3. Distortions of the proton and helium-nucleus fluxes due to the albedo δ_a, ionization loss fluctuations δ_i, and their sum δ (in %)

Row number	δ_a			δ_i			δ		
	E_d, GeV			E_d, GeV			E_d, GeV		
	>10	>100	>1000	>10	>100	>1000	>10	>100	>1000
1	−1.87	−2.29	−2.55	−3.68	−3.68	−3.68	−5.55	−5.97	−6.23
2	−0.47	−0.60	−0.90	−5.16	−5.16	−5.16	−5.63	−5.76	−6.06
3	+3.20	+2.39	+2.48	+7.80	+4.94	+4.19	+11.0	+7.33	+6.67
4	+2.73	+1.79	+1.58	+2.64	−0.22	−0.97	+5.37	+1.57	+0.61

Note: Row 1—decrease in proton flux, row 2—decrease in helium flux, row 3—increase in helium flux due to proton admixture, and row 4—sum of rows 2 and 3.

ter current of the nucleus could be mistaken for the proton signal. As we showed, the number of albedo signals from nuclei is larger than that from protons. Note that the values of albedo signal density D_a in the experiment and the simulations are not normalized to one another.

Thus, both the lateral distribution of albedo signals and their Q distribution are satisfactorily reproduced by the simulations. Therefore, we will use the results of our simulations for the subsequent analysis of the albedo influence when determining the charge from the maximum signal in the search area.

7. CHARGE RESOLUTION IN THE ATIC EXPERIMENT

To estimate the albedo influence, we must calculate the probability that the albedo signal rather than the signal from the primary particle will be the maximum signal in the search area, and, thus, the primary particle will be misidentified. Table 2 gives the calculated probabilities of detecting backscatter signals with $Q > 1.5$ for protons and $Q > 2.5$ for helium nuclei for three sizes of the search area and three ranges of energy deposition. Table 3 gives the distortions of the protons and helium fluxes due to the albedo δ_a when using the algorithm of primary particle search employed in the experiment for simulated events. For protons and helium, the flux is shown to decrease, because the measured charge Q exceeds 1.5 and 2.5, respectively (rows 1 and 2). The admixture to the helium flux from protons is given in row 3 (for this estimate, the relative number of cascades from protons and helium in the experiment was taken into account), and row 4 gives the total effect for helium in the range $1.5 < Q < 2.5$.

In addition to the albedo, the fluctuations of ionization losses in the silicon detector are another process that leads to misidentification of protons and helium nuclei. The fluctuations of ionization losses in the silicon detector of the ATIC instrument were analyzed in [8]. The distortions of the proton and helium fluxes due to this process δ_i and the total distortion $\delta = \delta_a + \delta_i$ are also given in Table 3. We see from this table (row 2) that the decrease in the helium flux is determined mainly by the ionization loss fluctuations, not by the albedo particles.

The experimental proton and helium charge res-

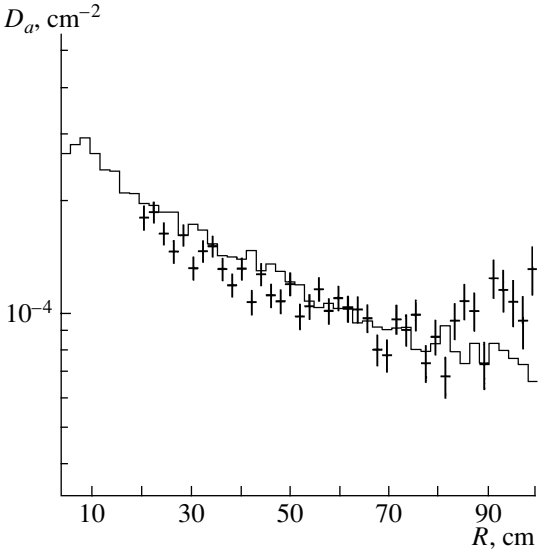

Fig. 6. Lateral distribution of the albedo signals from protons with $E_d > 100$ GeV in the silicon matrix. The points with error bars represent the experimental data, and the histogram represents the simulations.

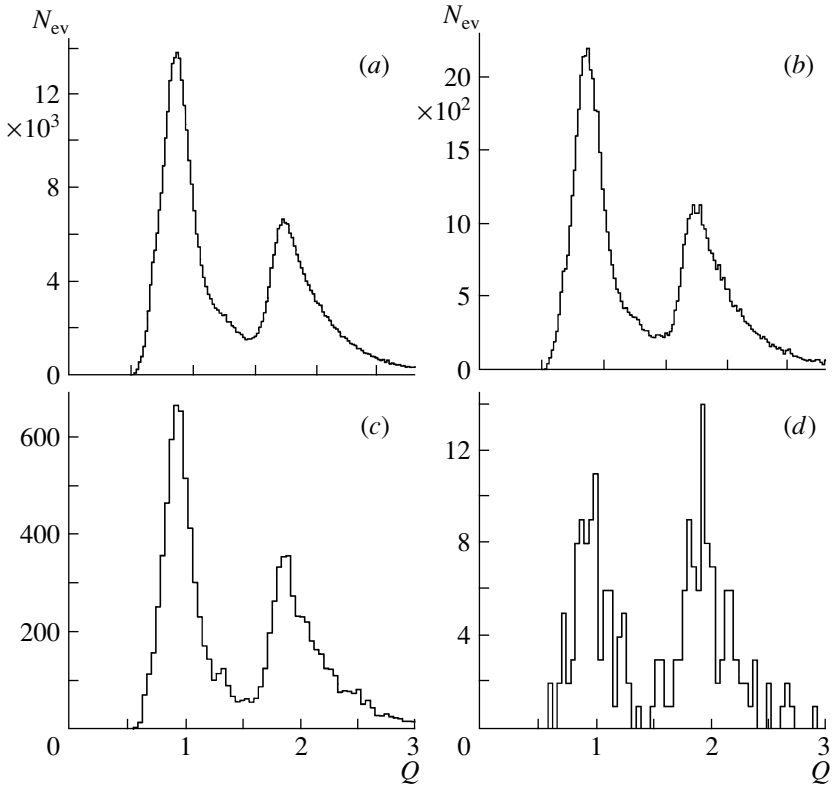

Fig. 7. Charge resolution for protons and helium nuclei in the experiment for four ranges of energy deposition: (*a*) $50 < E_d <$ 150 GeV, (*b*) $150 < E_d < 500$ GeV, (*c*) $500 < E_d < 5000$ GeV, and (*d*) $E_d > 5000$ GeV. The number of events (N_{ev}) in the bin is along the vertical axis.

olution is shown in Fig. 7 for four ranges of energy deposition.

8. CONCLUSIONS

The silicon matrix in the ATIC spectrometer has solved the problem of the backscatter current in this experiment and allowed a good charge resolution to be achieved for protons and helium and, consequently, the energy spectra of these particles to be measured. The required corrections to the measured proton and helium fluxes do not exceed 7%.

ACKNOWLEDGMENTS

This work was supported in Russia by the Russian Foundation for Basic Research (project nos. 02-98-16246 and 02-02-16545) and in the United States by NASA (grant nos. NAG5-5064, NAG5-5306, NAG5-5155, and NAG5-5308.

REFERENCES

1. N. L. Grigorov, G. P. Kakhidze, I. D. Rappoport, *et al.*, Kosm. Issled. **5**, 38 (1967).
2. R. W. Ellsworth *et al.*, Nucl. Instrum. Methods Phys. Res. **203**, 167 (1982).
3. V. I. Zatsepin, E. A. Zamchalova, A. Ya. Varkovitskaya, *et al.*, in *Proceedings of the 23rd ICRC, Calgary, 1993*, Vol. 2, p. 13; V. I. Zatsepin, T. V. Lazareva, G. P. Sazhina, and N. V. Sokol'skaya, Yad. Fiz. **57**, 684 (1994) [Phys. At. Nucl. **57**, 645 (1994)].
4. K. Asakimori *et al.* (JACEE Collab.), Astrophys. J. **502**, 278 (1998).
5. A. V. Apanasenko *et al.* (RUNJOB Collab.), Astropart. Phys. **16**, 13 (2001).
6. N. L. Grigorov, Yad. Fiz. **51**, 157 (1990) [Phys. At. Nucl. **51**, 99 (1990)].
7. J. H. Adams, Jr., G. L. Bashindzhagyan, V. I. Zatsepin, *et al.*, Prib. Tekh. Éksp. **44** (4), 38 (2001) [Instrum. Exp. Tech. **44** (4), 455 (2001)].
8. V. I. Zatsepin, J. H. Adams, Jr., *et al.*, Nucl. Instrum. Methods Phys. Res. A **524**, 195 (2004).
9. R. Brun, F. Brayant, M. Maire, GEANT Users Manual, CERN DD/EE/84-1 (Geneva, 1984); http://wwwasd.web.cern.ch/wwwasd/cernlib
10. I. D. Rappoport, A. N. Turundaevskiĭ, and V. Ya. Shestoperov, Yad. Fiz. **65**, 176 (2002) [Phys. At. Nucl. **65**, 170 (2002)]; N. S. Amelin, K. K. Gudima, and V. D. Toneev, Yad. Fiz. **51**, 512 (1990) [Sov. J. Nucl. Phys. **51**, 327 (1990)].

Translated by V. Astakhov

Physics of Atomic Nuclei, Vol. 68, No. 7, 2005, pp. 1183–1189. Translated from Yadernaya Fizika, Vol. 68, No. 7, 2005, pp. 1233–1239.

ELEMENTARY PARTICLES AND FIELDS
Theory

Some Features of the Production of Heavy-Quark-Containing Baryons in Electron–Positron Collisions

S. P. Baranov[1)] and V. L. Slad[*]

Institute of Nuclear Physics, Moscow State University, Vorob'evy gory, Moscow, 119899 Russia

Received July 6, 2004

Abstract—The production of various heavy-quark-containing baryons in electron–positron annihilation is considered. On the basis of exact formulas that we obtained previously within full perturbation theory, new numerical calculations of the respective cross sections are performed, and simple approximate expressions are then constructed for the results of these calculations. The dependence of the total cross sections on the masses of constituent quarks is discussed. The application of the Peterson fragmentation function and a Reggeon-type fragmentation function to describing differential cross sections is analyzed.
© *2005 Pleiades Publishing, Inc.*

1. INTRODUCTION

Investigation of the mechanisms responsible for the production of hadrons containing heavy quarks is of interest from the theoretical point of view since this provides the possibility for further testing QCD—more precisely, our understanding of it. In this way, one tests both its perturbative aspect used to describe the simultaneous production of several quark pairs and nonperturbative models constructed on the basis of QCD for bound states. We recall that, even in cases that are the simplest at first glance, the results of calculations appear to be in an unexpected contradiction with experimental data, as was, for example, in the hadronic production of J/ψ particles. At the same time, derivation of theoretical estimates for relevant cross sections is of importance for practical purposes, such as those associated with planning searches for such particles and investigations of their properties.

Available calculations of the cross sections for the production of baryons containing heavy c and b quarks rely, as a rule, on considering the production of respective diquarks, this corresponding to the fourth order of perturbation theory. A detailed review of the results obtained in this way and an exhaustive list of relevant references can be found in [1]. In the sixth order of perturbation theory [$\mathcal{O}(\alpha^2\alpha_s^4)$], the total and differential cross sections for the production of multiply heavy baryons Ω_{scb} and Ω_{ccc} at the Z pole in electron–positron collisions were calculated in our previous studies [2, 3]. For the squares of relevant matrix elements, we obtained exact analytic expressions, which, as might have been expected, are very cumbersome (they exist only in the form of computer codes). As a result, numerical calculations with these matrix elements would be extremely time-consuming.

By using these expressions and performing a series of new numerical calculations of various cross sections for the production of baryons containing three nonidentical quarks, we try here to impart, to the emerging results, a broader content, simplicity, and adaptability in the possible future application to constructing estimates for planning experiments. Specifically, we find, first of all, a simple approximate dependence of the total cross section for baryon production in electron–positron collisions on the mass of each constituent quark. On the basis of the concept of fragmentation, we then approximate the differential cross sections with the aid of the Peterson function for various sets of quark masses.

In this study, we also analyze some aspects of the description of the differential cross sections for the production of Ω_{scb} and Ω_{ccc} baryons in terms of a Reggeon-type fragmentation function.

2. DEPENDENCE OF THE TOTAL CROSS SECTIONS FOR BARYON PRODUCTION ON CONSTITUENT-QUARK MASSES

Let us consider some properties of the production of a $q_1q_2q_3$ baryon consisting of three nonidentical quarks q_1, q_2, and q_3 and having a mass M, a momentum $\mathbf{p}$, and an energy E at the Z pole in electron–positron collisions. We assume that the quark masses

[1)]Lebedev Institute of Physics, Russian Academy of Sciences, Leninskiĭ pr. 53, Moscow, 117924 Russia. e-mail: baranov@sci.lebedev.ru

[*]e-mail: vslad@sinp.msu.ru

m_1, m_2, and m_3 differ markedly from each other; that is,

$$m_1^2 \ll m_2^2 \ll m_3^2. \quad (1)$$

In QCD, the elementary process corresponding to the production of such a baryon is

$$e^+ + e^- \to q_1(p_1) + q_2(p_2) + q_3(p_3) + \bar{q}_1(p_4) + \bar{q}_2(p_5) + \bar{q}_3(p_6), \quad (2)$$

where the quark and antiquark 4-momenta are indicated in parentheses.

The formation of the baryon from three quarks is described in the well-known nonrelativistic approximation [4–6], whose details required for our purposes are as follows. First, the velocities of the quarks forming the baryon are assumed to be identical. Second, the differential cross section for baryon production is obtained from the standard differential cross section for the process in (2) by replacing the phase space of three quarks by an expression proportional to the baryon phase space; that is,

$$\frac{d^3p_1}{(2\pi)^3\cdot 2E_1}\frac{d^3p_2}{(2\pi)^3\cdot 2E_2}\frac{d^3p_3}{(2\pi)^3\cdot 2E_3} \to \frac{|\psi(0)|^2}{M^2}\frac{d^3p}{(2\pi)^3\cdot 2E}, \quad (3)$$

where $\psi(0)$ is the value of the wave function at the point where relative coordinates of all three quarks are zero.

In each of the Feynman diagrams corresponding to the process in (2), one can indicate a virtual gluon g such that it transforms into a quark–antiquark pair $q_i(p_i)\bar{q}_i(p_{i+3})$ without emitting a new gluon g'. The denominator of the propagator of the gluon g—it has the form $(p_i + p_{i+3})^2$—attains a minimum of $4m_i^2$ at $p_{i+3} = p_i$. But if a virtual gluon g transforms into two quark–antiquark pairs $q_i(p_i)q_j(p_j)\bar{q}_i(p_{i+3})\bar{q}_j(p_{j+3})$, the denominator of its propagator has a minimum of $4(m_i + m_j)^2$. Taking into account the inequalities in (1), we can deduce from the above that the leading contribution to the amplitude of the process in (2) comes from the diagrams where the production of quark–antiquark pairs proceeds hierarchically from the heaviest to the lightest. This sequence that ends up in the formation of a baryon from the quarks q_1, q_2, and q_3 is generally referred to as the fragmentation of the quark q_3 into a $q_1q_2q_3$ baryon. It is often described analytically in the form

$$d\sigma/dz = \sigma_{q_3\bar{q}_3}D(z), \quad (4)$$

where $\sigma_{q_3\bar{q}_3}$ is the total cross section for the process $e^+e^- \to q_3\bar{q}_3$ and $D(z)$ is the respective fragmentation function. For the variable z, one usually takes the quantity $x_p = p/p_{\max}$ or $x_E = E/E_{\max}$.

It is obvious that the amplitude of any process is a homogeneous function of the 4-momenta P_j, the masses M_j, and the widths Γ_j of real and virtual particles involved in the process. Therefore, the total cross section or one differential cross section or another can be represented in the form of the product of some power of the total energy $\sqrt{s}$ and a function of the reduced 4-momenta $P_j/\sqrt{s}$, the reduced masses $M_j/\sqrt{s}$, and the reduced widths $\Gamma_j/\sqrt{s}$. From here, it follows, among other things, that the fragmentation function $D(z)$ appearing in (4) depends parametrically on the reduced masses $m_i/\sqrt{s}$ of the product quarks. In the following, we will write the reduced masses explicitly only in the logarithmic factors on the right-hand side of formula (6) (see below).

In comparing experimental results obtained in electron–positron collisions with some fragmentation function, attention is given primarily to its form depending on one or two parameters but not to its normalization.

For want of experimentally observed events involving the production of $q_1q_2q_3$ baryons in electron–positron annihilation, it is reasonable to focus on the total cross section—namely, on the dependence of the total cross section on the masses of the quarks q_1, q_2, and q_3. The choice of a simple algebraic expression representing this dependence is based on the fact that the square of the matrix element of the process being considered is similar, in some respects, to a rational function of the momenta of product particles, its denominator at the minimum involving constituent quark masses and their sums as factors. It is well known that the integral of such a function can generally include logarithmic terms.

By using relation (3) and the results of numerical calculations of the total cross section for the production of $q_1q_2q_3$ baryons at the Z pole in electron–positron collisions for six sets of masses m_1, m_2, and m_3 for the same set of electroweak-interaction coupling constants (such as that for the production of *scb* baryons), we arrive at the formulas

$$\sigma_{\text{tot}} = \frac{|\psi(0)|^2}{(m_1+m_2+m_3)^2}G, \quad (5)$$

$$G \approx \frac{C}{m_1^2m_2^2}\ln\left(\frac{\sqrt{s}}{4m_1}\right)\ln\left(\frac{\sqrt{s}}{m_3}\right), \quad (6)$$

where $\sqrt{s} = 91.2$ GeV and $C = 0.0407 \pm 0.006$ pb.

In Table 1, we present the sets of masses m_1, m_2, and m_3; the values of G that are obtained from a Monte Carlo calculation of the integral of the square of the matrix element for the process in (2) over the phase space of four final particles (QCD column in the table); and the values of G that are obtained by formula (6).

Table 1

Quark mass, GeV			G, pb GeV^4		Parameter ε from (8)
m_1	m_2	m_3	QCD	Formula (6)	
0.5	1.5	4.8	$(7.85 \pm 0.16) \times 10^{-1}$	$(8.15 \pm 0.14) \times 10^{-1}$	0.124 ± 0.016
0.3	1.5	4.8	2.58 ± 0.07	2.57 ± 0.04	0.098 ± 0.012
0.075	1.5	4.8	$(5.59 \pm 0.20) \times 10^{1}$	$(5.42 \pm 0.09) \times 10^{1}$	0.066 ± 0.008
0.01	1.5	4.8	$(4.29 \pm 0.12) \times 10^{3}$	$(4.12 \pm 0.07) \times 10^{3}$	0.048 ± 0.006
0.01	0.5	4.8	$(3.90 \pm 0.28) \times 10^{4}$	$(3.71 \pm 0.06) \times 10^{4}$	0.016 ± 0.002
0.01	0.5	1.5	$(5.10 \pm 0.53) \times 10^{4}$	$(5.18 \pm 0.09) \times 10^{4}$	0.24 ± 0.08

We believe that the use of the factor $\ln(\sqrt{s}/(4m_1))$ in formula (6) is quite justified empirically. It seems plausible that the quantity G depends only slightly on the mass m_3 of the heaviest quark; relying on the results of our calculations exclusively, we cannot be confident, however, that the G depends on m_3 through the factor $\ln(\sqrt{s}/m_3)$, as follows from Eq. (6).

Strictly speaking, the dependence of the total cross section on the quark masses m_1, m_2, and m_3 is not exhausted by the explicit expressions in formulas (5) and (6), since the baryon-state wave function at the origin, $\psi(0)$, must change in response to a change in the masses. The dependence of $\psi(0)$ on the masses of constituent quarks is determined within potential quark models, which are not discussed in the present study. On the basis of the numerical values of $|\psi(0)|^2$ that are presented in [7] for six sets of quarks q_1, q_2, and q_3, we can nevertheless estimate cross sections by using the approximate expression

$$|\psi(0)|^2 \approx D m_2^{1.5} m_3, \quad \text{if} \quad m_1 \ll m_2 \leq m_3, \tag{7}$$

where $D = 0.065 \times 10^{-3}$ GeV$^{3.5}$.

Taken together, relations (5)–(7) indicate that the total cross section for the production of $q_1q_2q_3$ baryons in electron–positron annihilation is highly sensitive to the mass of the lightest of three quarks. This circumstance is especially important in the case where, for the quark q_1, one takes a u or a d quark, since, from the point of view of simple nonrelativistic concepts, their masses can be varied within rather wide intervals, from 50 MeV (in pions) to 300 MeV (in nucleons). In order to estimate cross sections for the production of baryons containing two heavy quarks and a u or a d quark, we set $m_u = m_d = 100$ MeV in Eqs. (5)–(7), bearing in mind that, according to the approximation specified by Eq. (6), these cross section are determined to within a factor of 10.

For want of something better and, to some extent, as a continuation of the strategies adopted in [7], we propose extending the procedure of the present study and of previous studies [2, 3] to the case of deriving estimates for the production of baryons containing one heavy quark c or b, a strange quark s, and a light quark u or d—namely, we propose supplementing the perturbative part of calculations (sixth order of perturbation theory) with the following nonrelativistic nonperturbative elements: the assumption of equal velocities of the quarks fusing into the baryon in question, relation (3), and the approximation specified by Eq. (7). What we inherit from nonrelativistic potential models reduces to the extrapolations in (3) and (7). It is reasonable to indicate here that, in contrast to u and d quarks, a strange quark of mass $m_s = 500$ MeV leads to an acceptable level of agreement with naive nonrelativistic expectations for the masses of the meson and baryon ground states [$s\bar{s}$ (ϕ) and sss (Ω), respectively].

All estimates that can be obtained on the basis of formulas (5)–(7) by setting $m_b = 4.8$ GeV, $m_s = 0.5$ GeV, and $m_u = m_d = 0.1$ GeV are given in Table 2 (the symbol q in the subscripts there stands for a u or a d quark). The factor C in (6) is set to 0.0407 pb in calculating cross sections for the production of Ω_{scb}, Ξ_{qcb}, and Ξ_{qsb} baryons and to $C = 0.0407\ \text{pb} \cdot ((g_V^c)^2 + g_A^c)^2/((g_V^b)^2 + g_A^b)^2 = 0.0317$ pb in dealing with Ξ_{qsc} baryons.

Table 2

Baryon	$\lvert\psi(0)\rvert^2 \times 10^3$, GeV^6	σ_{tot}, fb
Ω_{scb}	0.57	0.0097
Ξ_{qcb}	0.57	0.40
Ξ_{qsb}	0.11	0.98
Ξ_{qsc}	0.034	2.2

We would like to bring to the attention of the reader that, in [8], the quantity $|\psi(0)|^2$ was calculated at the following values of the constituent quark masses: $m_b = 5.29$ GeV, $m_c = 1.905$ GeV, $m_s = 0.6$ GeV, and $m_u = m_d = 0.3$ GeV. In our previous studies [2, 3], we employed the values of $|\psi(0)|^2$ from [8] without introducing any corrections. In the present study, all cross-section values, including those that are given in the figures, are calculated by using Eq. (7).

It should be emphasized that the approximate formula (6) was obtained for the constituent quark masses obeying the inequalities in (1). But if these inequalities are not satisfied and if, in addition, there are quarks identical in flavor among the quarks in question, formula (6) cannot be used even for a rough estimate of cross sections. Indeed, it can be seen that, for the production of an Ω_{ccc} baryon in electron–positron annihilation, a direct numerical calculation of the quantity G on the basis of formula (5) gives the value of 2.27 pb GeV^4, while expression (6) yields 0.090 pb GeV^4. The reasons for so significant a discrepancy between the values of G are rather obvious: if the inequalities in (1) hold, the main contribution to the cross section comes only from a few Feynman diagrams, but, if all three masses m_1, m_2, and m_3 are close to one another, all diagrams make approximately equal contributions (for the production of an Ω_{ccc} baryon, there are 504 such diagrams); additionally, interference effects arise if there are identical quarks.

3. DIFFERENTIAL CROSS SECTION AND PETERSON FRAGMENTATION FUNCTION

Let us now proceed to consider a simple algebraic description of the differential cross sections for the production of $q_1q_2q_3$ baryons in electron–positron collisions on the basis of the fragmentation approach. Experimental data on the production of heavy-quark hadrons in electron–positron annihilation are usually approximated in terms of the Peterson function [9]

$$D(z) \sim \frac{1}{z[1-(1/z)-\varepsilon/(1-z)]^2}, \qquad (8)$$

where ε is a phenomenological parameter. We used this function in [2] to describe approximately the production of Ω_{scb} baryons in electron–positron collisions.

We performed complete numerical calculations of the differential cross sections for the production of $q_1q_2q_3$ baryons for six sets of constituent quark masses (see Table 1) and then determined the values of the parameter ε of the Peterson function (8) that ensure the best agreement between the form of this fragmentation function and the form of the differential cross sections $d\sigma/dx_p$. The resulting values of the parameter ε are given in the last column of Table 1. The results of numerical calculations of $d\sigma/dx_p$ and their approximation in terms of the Peterson function are shown in Fig. 1.

The dependence of the parameter ε on the mass m_1 of the lightest quark can be approximated by a linear function,

$$\varepsilon \approx a + bm_1, \qquad (9)$$

where $a = 0.046$ and $b = 0.17$ GeV^{-1}. As the middle mass m_2 is decreased, the maximum of the distribution $d\sigma/dx_p$ is shifted toward the largest possible relative momentum value, $x_p = 1$, while the parameter ε becomes smaller. The shift of the maximum of the cross section $d\sigma/dx_p$ in response to the change in the mass m_3 of the heaviest quark is opposite to that in response to the analogous change in m_1 and m_2: with decreasing m_3, the extremal value of x_p decreases substantially, while the parameter ε in the function given by (8) grows.

The value that we found here for ε at the mass values of $m_1 = 0.01$ GeV, $m_2 = 0.5$ GeV, and $m_3 = 1.5$ GeV is very close to the values of ε that were obtained in experiments that studied the production of Λ_c, Σ_c, and Ξ_c baryons in electron–positron annihilation: $\varepsilon = 0.236^{+0.068}_{-0.048}$ for Λ_c [10], $\varepsilon = 0.29 \pm 0.06$ for Σ_c [11], and $\varepsilon = 0.24 \pm 0.08$ for Ξ_c [12].

For baryons containing quarks of identical flavor (for example, Ω_{ccc}), it is difficult to take into account effects of interference between identical particles; therefore, the fragmentation mechanism cannot be so well justified theoretically in this case as for $q_1q_2q_3$ baryons under the conditions in (1). At the same time, it remains quite useful in the phenomenological aspect. For example, it was found in [3] that the transverse-momentum distribution of Ω_{ccc} baryons that is obtained from direct numerical calculations cannot be adequately approximated with the aid of the Peterson function. However, the shape of this distribution can be faithfully reproduced by using the so-called Lund function [13]

$$D(z) \sim \frac{1}{z}(1-z)^a \exp(-c/z), \qquad (10)$$

where the parameters are set to $a = 2.4$ and $c = 0.70$.

4. DIFFERENTIAL CROSS SECTIONS AND REGGEON-TYPE FRAGMENTATION FUNCTION

Let us now consider the representation of numerical results for the production of heavy-quark-containing baryons in electron–positron collisions

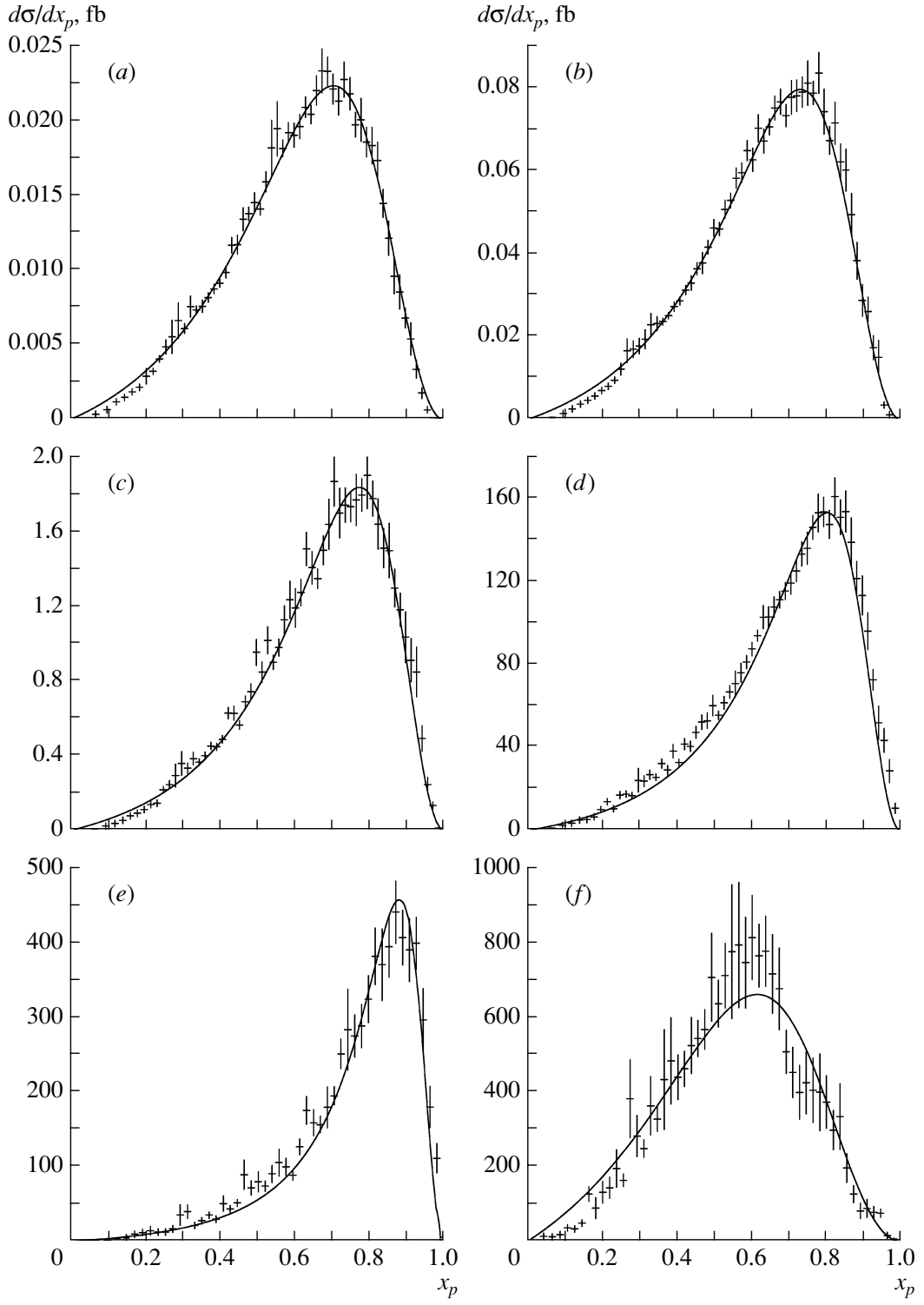

Fig. 1. Differential cross section $d\sigma/dx_p$ for the production of $q_1q_2q_3$ baryons in electron–positron collisions: (crosses) results of Monte Carlo calculations along with the errors in them and (solid curves) results of the calculation by formula (4) with the Peterson fragmentation function (8). The values of the masses of the quarks q_1, q_2, and q_3 (in GeV) and of the parameter ε in the Peterson function in Figs. 1*a*–1*f* are the following: (*a*) $m_1 = 0.5$, $m_2 = 1.5$, $m_3 = 4.8$, and $\varepsilon = 0.124$; (*b*) $m_1 = 0.3$, $m_2 = 1.5$, $m_3 = 4.8$, and $\varepsilon = 0.098$; (*c*) $m_1 = 0.075$, $m_2 = 1.5$, $m_3 = 4.8$, and $\varepsilon = 0.066$; (*d*) $m_1 = 0.01$, $m_2 = 1.5$, $m_3 = 4.8$, and $\varepsilon = 0.048$; (*e*) $m_1 = 0.01$, $m_2 = 0.5$, $m_3 = 4.8$, and $\varepsilon = 0.016$; and (*f*) $m_1 = 0.01$, $m_2 = 0.5$, $m_3 = 1.5$, and $\varepsilon = 0.24$.

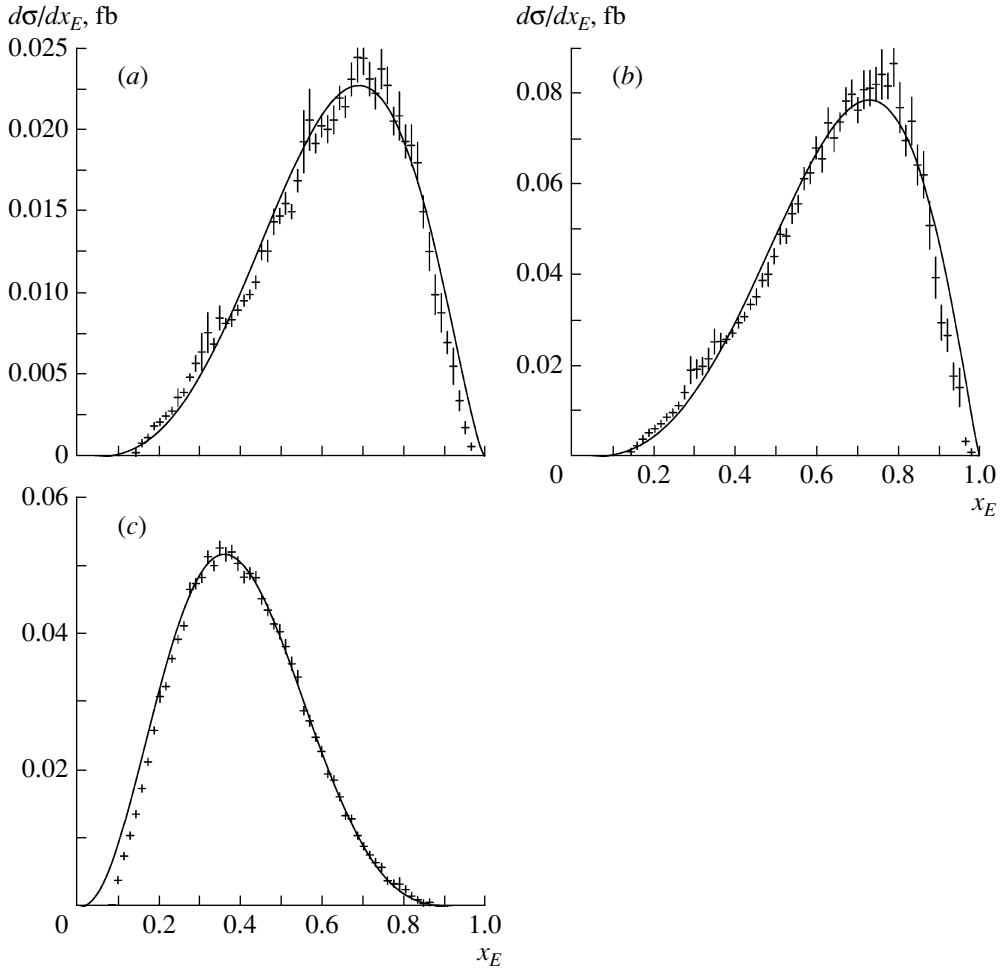

Fig. 2. Differential cross section $d\sigma/dx_E$ for the production of Ω_{scb} baryons [(a) $m_s = 0.5$ GeV and (b) $m_s = 0.3$ GeV] and Ω_{ccc} baryons (c) in electron–positron annihilation. The crosses show the results of Monte Carlo calculations and their errors. The solid curves correspond to the approximation of the cross sections with the aid of a Reggeon-type fragmentation function (11) with the parameters (a) $\beta = 3.3$ and $\gamma = 1.48$, (b) $\beta = 3.2$ and $\gamma = 1.18$, and (c) $\beta = 2.6$ and $\gamma = 4.6$.

in terms of the Reggeon-type fragmentation function [14]

$$D(z) \sim z^{\beta}(1-z)^{\gamma}. \qquad (11)$$

This function was employed in [15, 16] in discussing experimental data on the production of D and B mesons in electron–positron annihilation, the parameters β and γ not being related there to Regge trajectories.

An approximation of the numerical results obtained here for the production of Ω_{scb} and Ω_{ccc} baryons in electron–positron annihilation with the aid of the fragmentation function in (11) was performed for the differential cross sections $d\sigma/dx_E$ and is displayed in Fig. 2.

It is of interest to compare the values obtained for the parameters of the function in (11) by approximating the numerical results of our perturbative approach to determining cross sections and the values deduced from the expressions for these parameters in terms of the intercepts of the trajectories of appropriate hadrons. If the quark i fragments into a baryon consisting of the quarks i, j, and k, then [17]

$$\beta = 1 - \alpha_{i\bar{i}}, \quad \gamma = \alpha_{q\bar{q}} - 2\alpha_{jkq}, \qquad (12)$$

where the symbol q in the subscripts stands for a light quark u or d, while the quantities $\alpha_{l\bar{l}}$ and α_{jkq} are the intercepts of the meson (of $l\bar{l}$ quark content) and baryon (of jkq quark content) trajectories. An approximate linear relation between the intercepts of trajectories corresponding to different quark contents was obtained within the model of quark–gluon strings [18]:

$$2(\alpha_{ijk} - \alpha_{ijl}) = \alpha_{k\bar{k}} - \alpha_{l\bar{l}}. \qquad (13)$$

On the basis of relation (13) and the standard notation $\alpha_{u\bar{u}} = \alpha_{d\bar{d}} = \alpha_\rho$, $\alpha_{s\bar{s}} = \alpha_\phi$, $\alpha_{c\bar{c}} = \alpha_\psi$, $\alpha_{b\bar{b}} =$

α_Υ, and $\alpha_{uud} = \alpha_{udd} = \alpha_N$, the equalities in (12) can be recast into the form

$$\beta = 1 - \alpha_\Upsilon, \quad \gamma = 3\alpha_\rho - \alpha_\phi - \alpha_\psi - 2\alpha_N \qquad (14)$$

for Ω_{scb} baryons and into the form

$$\beta = 1 - \alpha_\psi, \quad \gamma = 3\alpha_\rho - 2\alpha_\psi - 2\alpha_N \qquad (15)$$

for Ω_{ccc} baryons.

For some intercepts, we will take the quite reliably established values of $\alpha_N = -0.4$, $\alpha_\rho = 0.5$, and $\alpha_\phi \approx 0$ [17], while, for the others, we will use the following estimates: $\alpha_\psi = -2.2$ [19] and $\alpha_\Upsilon = -8.0$ [20]. These estimates differ only slightly from those that were previously obtained in [7, 21].

Substituting the above values into relation (14) for Ω_{scb} baryons, we obtain $\beta = 9.0$ and $\gamma = 4.5$, but these results are in a glaring contradiction with the values of $\beta = 3.3$ and $\gamma = 1.48$ if $m_s = 500$ MeV and with the values of $\beta = 3.2$ and $\gamma = 1.18$ if $m_s = 300$ MeV, which we obtained from a comparison of the fragmentation function in (11) with the results of direct numerical calculations of the cross section $d\sigma/dx_E$. In turn, relation (15) for the production of Ω_{ccc} baryons yields $\beta = 3.2$ and $\gamma = 6.7$, which can be thought to be in very rough agreement with the values of $\beta = 2.6$ and $\gamma = 4.6$ resulting from the approximation of our numerical results for the cross section $d\sigma/dx_E$.

This suggests the simple conclusion that the perturbative and the nonperturbative (Reggeon) approach do not reduce to each other and, depending on the process being considered, they can lead either to close or to strongly different results.

REFERENCES

1. V. V. Kiselev and A. K. Likhoded, Usp. Fiz. Nauk **172**, 497 (2002) [Phys. Usp. **45**, 455 (2002)].
2. S. P. Baranov and V. L. Slad, Yad. Fiz. **66**, 1778 (2003) [Phys. At. Nucl. **66**, 1730 (2003)].
3. S. P. Baranov and V. L. Slad, Yad. Fiz. **67**, 829 (2004) [Phys. At. Nucl. **67**, 808 (2004)].
4. C.-H. Chang, Nucl. Phys. B **172**, 425 (1980).
5. R. Baier and R. Rückl, Phys. Lett. B **102**, 384 (1981).
6. D. Jones, Phys. Rev. D **23**, 1521 (1981).
7. V. G. Kartvelishvili and A. K. Likhoded, Yad. Fiz. **29**, 757 (1979) [Sov. J. Nucl. Phys. **29**, 390 (1979)].
8. E. Bagan, H. G. Dosch, P. Godzinsky, *et al.*, Z. Phys. C **64**, 57 (1994).
9. C. Peterson, D. Schlatter, J. Schmitt, and P. M. Zerwas, Phys. Rev. D **27**, 105 (1983).
10. ARGUS Collab. (H. Albrecht *et al.*), Phys. Lett. B **207**, 109 (1988).
11. ARGUS Collab. (H. Albrecht *et al.*), Phys. Lett. B **211**, 489 (1988).
12. ARGUS Collab. (H. Albrecht *et al.*), Phys. Lett. B **247**, 121 (1990).
13. B. Andersson, G. Gustafson, and B. Söderberg, Z. Phys. C **20**, 317 (1983).
14. V. G. Kartvelischvili, A. K. Likhoded, and V. A. Petrov, Phys. Lett. B **78**, 615 (1978).
15. G. Colangelo and P. Nason, Phys. Lett. B **285**, 167 (1992).
16. OPAL Collab. (G. Alexander *et al.*), Phys. Lett. B **364**, 93 (1995).
17. A. B. Kaĭdalov, Yad. Fiz. **45**, 1452 (1987) [Phys. At. Nucl. **45**, 902 (1987)].
18. A. B. Kaidalov, Z. Phys. C **12**, 63 (1982).
19. A. B. Kaĭdalov and O. I. Piskunova, Yad. Fiz. **43**, 1545 (1986) [Sov. J. Nucl. Phys. **43**, 994 (1986)].
20. O. I. Piskunova, Yad. Fiz. **57**, 538 (1994) [Phys. At. Nucl. **57**, 508 (1994)].
21. V. G. Kartvelischvili and A. K. Likhoded, Yad. Fiz. **42**, 1306 (1985) [Sov. J. Nucl. Phys. **42**, 823 (1985)].

Translated by A. Isaakyan

Physics of Atomic Nuclei, Vol. 68, No. 7, 2005, pp. 1190–1210. Translated from Yadernaya Fizika, Vol. 68, No. 7, 2005, pp. 1240–1259.

ELEMENTARY PARTICLES AND FIELDS
Theory

Is It Still Interesting to Search for Lepton-Flavor Violation in Rare Kaon Decays?[1)]

L. G. Landsberg*

Institute for High Energy Physics, Protvino, Moscow oblast, 142284 Russia

Received August 17, 2004; in final form, November 29, 2004

Abstract—Further possibilities of experiments aimed at searches for lepton-flavor violation in kaon decays at present and future intermediate-energy accelerators are considered. It is shown that such investigations are complementary to searches for muonic lepton-flavor-violating processes and can possess, in some models featuring approximately conserved generation quantum numbers of fundamental fermions, a very high and even record sensitivity. Searches for lepton-flavor-violating processes in kaon decays should be considered as a very important and independent part of the general program of searches for the violation of lepton flavors in processes involving charged leptons. © *2005 Pleiades Publishing, Inc.*

1. STANDARD MODEL AND LEPTON FLAVORS

Basic results in contemporary elementary-particle physics are in accord with the so-called Standard Model (SM) [1–5], which provides a good description of physical phenomena within the mass-scale region up to 100 GeV or even a few hundred gigaelectronvolts. The Standard Model involves three generations of fundamental fermions, quarks and leptons,

$$u, d, e, \nu_e (\text{ first generation}); \quad (1)$$

$$c, s, \mu, \nu_\mu (\text{ second generation}); \quad (2)$$

$$t, b, \tau, \nu_\tau (\text{ third generation}). \quad (3)$$

These fundamental families have the same structure, but they differ strongly in mass.

Strong interactions between quarks, which are characterized by special quantum numbers, quark flavors and quark colors, proceed via the exchange of eight types of massless color vector gluons. These interactions are described within the modern theory of strong-interaction processes, quantum chromodynamics (QCD). The QCD formalism enables one to realize quite well perturbative calculations in the leading logarithmic and the next-to-leading logarithmic approximation at rather short distances (<1–$2\ \text{GeV}^{-1}$). The fact that quarks and gluons carry color quantum numbers makes them unobservable as free particles (concept of confinement). Strong interactions conserve quark flavors: in such processes, quarks cannot transform into quarks of different flavor. They can only be rearranged into various combinations, be produced in pairs ($q\bar{q}$), or be annihilated in the form of such pairs.

Electroweak interactions involving both quarks and leptons are mediated by intermediate $W^\pm$ and Z bosons and by a photon γ. It is expected that scalar Higgs bosons must play an important role in weak interactions. These particles have yet to be discovered, but, the observed Higgs boson H^0 must exist in the Standard Model. As will be seen below, charged-current weak interactions mediated by $W^\pm$ bosons change quark flavors.

Let us now consider in detail the electroweak interactions of fundamental fermions. The interaction Lagrangian is based on the broken $SU(2)_L \times U(1)$ group involving left-handed quarks and leptons that form weak-isospin doublets,

$$\begin{pmatrix} \nu_e \\ e^- \end{pmatrix}_L, \quad \begin{pmatrix} \nu_\mu \\ \mu^- \end{pmatrix}_L, \quad \begin{pmatrix} \nu_\tau \\ \tau^- \end{pmatrix}_L, \quad (4)$$

$$\begin{pmatrix} u \\ d' \end{pmatrix}_L, \quad \begin{pmatrix} c \\ s' \end{pmatrix}_L, \quad \begin{pmatrix} t \\ b' \end{pmatrix}_L, \quad (5)$$

and right-handed quark and lepton singlets, q_R and l_R, respectively. The left- and right-handed fermions

*e-mail: lgl@mx.ihep.su

[1)] An extended version of the report presented at the Chicago Flavor Seminar, February 27, 2004 (Fermilab); hep-ph/0410261

1063-7788/05/6807-1190$26.00

can be represented in the form[2)]

$$\psi_L = \frac{1}{2}(1-\gamma_5)\psi \quad \text{and} \quad \psi_R = \frac{1}{2}(1+\gamma_5)\psi. \quad (6)$$

The electroweak interactions of quarks and leptons are realized via the exchange of intermediate heavy gauge $W^{\pm}$ and Z^0 bosons and massless photons. These interactions are described by the Lagrangian

$$L[SU(2)_L \times U(1)] = L_{\mathrm{CC}} + L_{\mathrm{NC}}. \quad (7)$$

The Lagrangian density L_{CC} is determined by the charged weak $(V-A)$ current; that is,

$$L_{\mathrm{CC}} = \frac{g}{2\sqrt{2}}(J_\mu^+ W^{+\mu} + J_\mu^- W^{-\mu}), \quad (8)$$

where

$$J_\mu^+ = (\bar{u}d')_{V-A} + (\bar{c}s')_{V-A} + (\bar{t}b')_{V-A} + (\bar{\nu}_e e)_{V-A} + (\bar{\nu_\mu}\mu)_{V-A} + (\bar{\nu_\tau}\tau)_{V-A}. \quad (9)$$

These interactions, induced by the exchange of intermediate $W^{\pm}$ bosons, are accompanied by a change in quark flavors.

The neutral-current Lagrangian density L_{NC} has the form

$$L_{\mathrm{NC}} = eJ_\mu^{\mathrm{em}} A^\mu + \frac{g}{2\cos\vartheta_{\mathrm{W}}} J_\mu^0 Z^\mu, \quad (10)$$

where J_μ^{em} is the vector electromagnetic current, while J_μ^0 is the weak neutral current featuring $(V-A)$ and $(V+A)$ components:

$$J_\mu^{\mathrm{em}} = \sum_f Q_f \bar{f}\gamma_\mu f, \quad J_\mu^0 = \sum_f \bar{f}\gamma_\mu(v_f - a_f\gamma_5)f.$$

Here, $v_f = T_3^f - 2Q_f \sin^2\vartheta_{\mathrm{W}}$ and $a_f = T_3^f$ are the coefficients of the vector and axial components of the neutral weak current; $\sin^2\vartheta_{\mathrm{W}} = 0.23147 \pm 0.00016$ is the square of the sine of the Weinberg angle; $g^2/8M_{\mathrm{W}}^2 = G_{\mathrm{F}}/\sqrt{2}$ is the Fermi constant for weak interaction; and Q_f and T_3^f are, respectively, the electric charge of the fermion f and the third component of its weak isospin.

The expressions for the charged weak quark currents involve the transformed components d', s', and b' of the down quarks. They are determined with the aid of the unitary Cabibbo–Kobayashi–Maskawa quark-mixing matrix V_{CKM} [6]:

$$\begin{pmatrix} d' \\ s' \\ b' \end{pmatrix} = V_{\mathrm{CKM}} \begin{pmatrix} d \\ s \\ b \end{pmatrix}. \quad (11)$$

The quark-mixing matrix has the form

$$V_{\mathrm{CKM}} = \begin{pmatrix} V_{ud} & V_{us} & V_{ub} \\ V_{cd} & V_{cs} & V_{cb} \\ V_{td} & V_{ts} & V_{tb} \end{pmatrix} = \begin{pmatrix} c_{12}c_{13} & s_{12}c_{13} & s_{13}e^{-i\delta} \\ -s_{12}c_{23} - c_{12}s_{23}s_{13}e^{i\delta} & c_{12}c_{23} - s_{12}s_{23}s_{13}e^{i\delta} & s_{23}c_{13} \\ s_{12}s_{23} - c_{12}c_{23}s_{13}e^{i\delta} & -s_{23}c_{12} - s_{12}c_{23}s_{13}e^{i\delta} & c_{23}c_{13} \end{pmatrix}. \quad (12)$$

This matrix depends on three quark-generation-mixing angles ϑ_{12}, ϑ_{13}, and ϑ_{23} ($s_{ij} = \sin\vartheta_{ij}$, $c_{ij} = \cos\vartheta_{ij}$) and on a nontrivial phase δ that determines CP violation in quark processes.

Thus, the processes occurring in the quark sector, quark mixing, and quark-flavor changes in weak decays are described in detail within the Standard Model.

At the same time, the situation in the lepton sector of the Standard Model had seemed different for a long time. The leptons of the different generations were characterized by the lepton flavors L_e, L_μ, and L_τ (see Table 1). The weak lepton interactions were described by the Standard Model Lagrangian where the neutrinos were taken to be massless particles and where lepton-flavor conservation was assumed.

It should be noted that lepton-flavor conservation is not caused by some new global gauge symmetries of the $U(1)$ type, as is the case, for example, for electric-charge conservation by virtue of the gauge symmetry of electromagnetic interactions. Therefore,

[2)] We recall the definition of the weak $(V-A)$ current in the Standard Model. The current J_μ^+ that corresponds to the $\Delta Q = +1$ weak $(i \to f)$ transition from the initial to the final fermion involves the differences of vector and axial terms of the type $\bar{f}\gamma_\mu(1-\gamma_5)i = 2\bar{f}_L\gamma_\mu i_L = \bar{f}\gamma_\mu i - \bar{f}\gamma_\mu\gamma_5 i = V_\mu - A_\mu = (\bar{f}i)_{V-A}$.

Table 1. Lepton flavors

Leptons belonging to different generations of fundamental Standard Model fermions		Lepton flavors		
		L_e	L_μ	L_τ
First-generation leptons	e^-, ν_e	1	0	0
Second-generation leptons	μ^-, ν_μ	0	1	0
Third-generation leptons	τ^-, ν_τ	0	0	1

Notes:
(1) For antileptons, lepton flavors change sign.
(2) The total lepton charge is $L = L_e + L_\mu + L_\tau$.

the question of whether lepton flavors are conserved or violated has always remained open. The question of whether the total lepton charge $L = L_e + L_\mu + L_\tau$ is conserved also aroused great interest. First of all, one bears in mind here the possibility of observing processes such as neutrinoless double-beta decay, $(Z, A) \to (Z + 2, A) + 2e^-$; the decays $K^+ \to \pi^- l^+ l^+$; and the neutrinoless conversion of muons to positrons, $\mu^- + (Z, A) \to e^+ + (Z - 2, A)$.

The discovery of neutrino oscillations in experiments with atmospheric and solar neutrinos [7, 8]; reactor neutrinos [9]; and, possibly, accelerator neutrinos [10] was one of the most important achievements in elementary-particle physics over the past years (see Table 2 and the review articles of Smirnov [11] and Alberico and Bilenky [12], who summarized the situation around neutrino oscillations). The hypothesis of neutrino oscillations was first put forth by Pontecorvo in 1957 [13] (see also [12], where the authors trace the evolution of the concept of neutrino oscillations). The observation of neutrino oscillations means that the neutrinos of the different fundamental generations have different masses and that lepton flavors are not strictly conserved quantum numbers. Therefore, neutrinos are mixed with one another and are able to transform into one another. The observation of neutrino oscillations [7–10] completed long-term searches for these effects and opened a new page in studying neutrino physics and the properties of lepton flavors [11, 12].

Although neutrino oscillations do not fit in the general pattern of the Standard Model, their discovery as it is did not generate the need for revising the fundamentals of this theory. It proved to be sufficient to modify somewhat the Standard Model by introducing in its Lagrangian terms that correspond to the neutrino masses and lepton-flavor violation. Concurrently, there arises the neutrino-mixing matrix, which is close in form to the Cabibbo–Kobayashi–Maskawa quark-mixing matrix. The neutrino-mixing

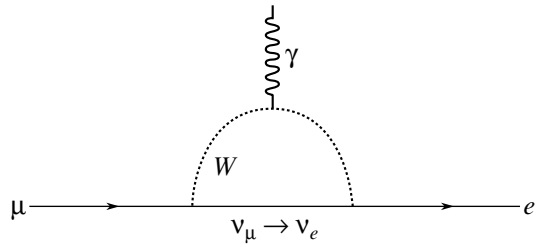

Fig. 1. Diagram for the decay $\mu \to e\gamma$ via the neutrino-mixing mechanism.

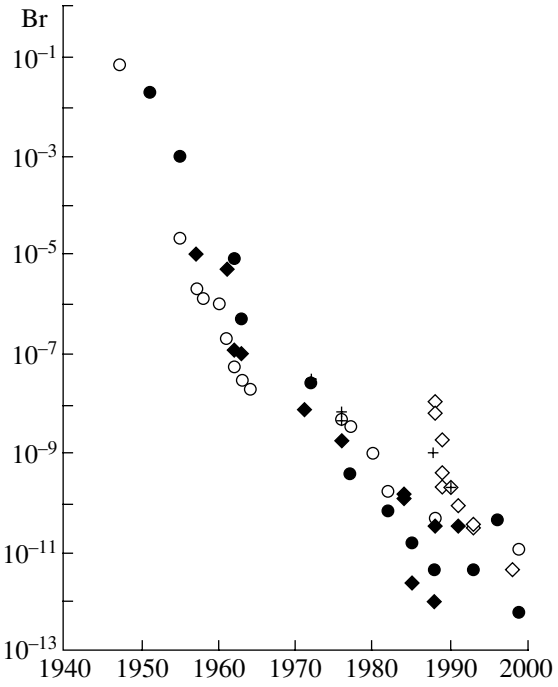

Fig. 2. Historic advances in experiments seeking the lepton-flavor violation in processes involving muons and kaons [28]: (○) $\mu \to e\gamma$, (◆) $\mu \to 3e$, and (●) $\mu^- + A \to e^- + A$ (muon processes) and (◇) $K_L^0 \to e\bar{\mu}$ and (+) $K^+ \to \pi^+ e\bar{\mu}$ (kaon processes). It can be seen from these data that the sensitivity of experiments seeking lepton-flavor-violating processes was constantly improved (on average, by two orders of magnitude per decade).

Table 2. Data on neutrino oscillations [11]

Best fit	Allowed values
$\Delta m^2_{12} = 7.1 \times 10^{-5}\ \mathrm{eV}^2$, $\tan^2\vartheta_{12} = 0.40$	$\Delta m^2_{12} < 10^{-4}\ \mathrm{eV}^2$, $\tan^2\vartheta_{12} < 0.64$
$\Delta m^2_{32} = 2.0 \times 10^{-3}\ \mathrm{eV}^2$, $\sin^2(2\vartheta_{23}) = 1$	$\Delta m^2_{32} \simeq (1.3\text{–}3.0) \times 10^{-3}\ \mathrm{eV}^2$, $\sin^2(2\vartheta_{23}) > 0.9$, $\sin^2\vartheta_{13} < 0.067$

matrix is referred to as the Pontecorvo–Maki–Nakagawa–Sakata matrix (see [12–15]). However, it should be emphasized that, while quark mixing leads to a great number of new effects in the quark sector of the Standard Model, the neutrino-mixing matrix may in general result only in quite limited phenomenology. It may even appear that neutrino oscillations will be unique experimental manifestations of lepton-flavor violation. If the neutrinos are Majorana particles, $|\Delta L| = 2$ neutrinoless double-beta decay can become another observable effect.

Indeed, let us consider other manifestations of lepton-flavor violation in processes involving charged leptons [below, they are referred to as lepton-flavor-violating (LFV) processes]. For example, the decay $\mu \to e\gamma$ is a lepton-flavor-violating process. At first glance, it seems that this decay may be due to neutrino mixing (see diagram in Fig. 1). However, the smallness of the neutrino masses results in that the probability of the decay $\mu \to e\gamma$ via the neutrino-mixing mechanism is very small—it is suppressed by the factors $(m_{\nu i}/M_W)^4$ [16, 17]. The branching ratio for the decay $\mu \to e\gamma$ is estimated as

$$\mathrm{Br}(\mu \to e\gamma) = \frac{\Gamma(\mu \to e\gamma)}{\Gamma(\mu \to e\bar{\nu}_e\nu_\mu)} \simeq \frac{3}{32}\frac{\alpha}{\pi}\left|\sum_i U^*_{\mu i}U_{ei}\left(\frac{m_{\nu i}}{M_W}\right)^2\right|^2. \quad (13)$$

Here,

$$\nu_\mu = \sum U_{\mu i}\nu_i, \quad \nu_e = \sum U_{ei}\nu_i, \quad (14)$$

where ν_i are the neutrino mass and lepton-flavor eigenstates and ν_μ and ν_e are the neutrino states produced in, respectively, muon and electron processes (they are neither mass eigenstates nor lepton-flavor eigenstates). In the case of $m_{\nu i} < 1$ eV, we then have $\mathrm{Br}(\mu \to e\gamma) \lesssim 10^{-48}$. Such an estimate is also valid for other lepton-flavor-violating processes involving charged leptons.

Searches for such forbidden lepton-flavor-violating decays ($\mu \to e\gamma$, $\mu \to 3e$, $K^0_L \to e\bar{\mu}$, $K^+ \to \pi^+\mu^+e^-$, and so on) are of great interest in the general context of searches for new physics beyond the Standard Model; over the past few decades, such searches have been performed in a number of experiments with an ever increasing accuracy. So far, none of these processes has been discovered. The upper limits established for them are presented in Table 3 [18–27] and in Fig. 2 [28] (where the history of these searches is demonstrated). Much attention has been given to lepton-flavor-violating processes involving charged leptons because their observation would obviously be beyond the Standard Model. The very fact that lepton-flavor violation was discovered in neutrino oscillations of course gave additional impetus to such searches. It will be seen below that, if lepton-flavor-violating decays occur, they generally manifest themselves at very short distances (for very high energy scales) that will remain inaccessible even to next-generation supercolliders. It seems that investigation of rare anomalous decays is the only way to probe this region of very high energies.

At the present time, a number of new projects have been proposed in which the sensitivity of searches

Table 3. Upper limits on the branching fractions of lepton-flavor-violating processes

Process	Upper limit on Br (90% C.L.)	References
$K^0_L \to e^\mp\mu^\pm$	4.7×10^{-12}	[18]
$K^0_L \to \pi^0 e^\mp\mu^\pm$	3.3×10^{-10}	[19]
$K^0_L \to e^\mp e^\mp\mu^\pm\mu^\pm$	4.12×10^{-11}	[19]
$K^+ \to \pi^+\mu^+e^-$	2.8×10^{-11}	[20]
$K^+ \to \pi^+\mu^-e^+$	5.2×10^{-10}	[21]
$K^+ \to \pi^-e^+e^+$	6.4×10^{-10}	[21]
$K^+ \to \pi^-e^+\mu^+$	5.0×10^{-10}	[21]
$K^+ \to \pi^-\mu^+\mu^+$	3.0×10^{-9}	[21]
$\mu \to e\gamma$	1.2×10^{-11}	[22]
$\mu \to 3e$	1.0×10^{-12}	[23]
$\Gamma(\mu^- + \mathrm{Ti} \to e^- + \mathrm{Ti})/\Gamma(\mu^- + \mathrm{Ti} \to \mathrm{capture})$	4.3×10^{-12}	[24]
$\tau \to e\gamma$	2.7×10^{-6}	[25]
$\tau \to \mu\gamma$	3.1×10^{-7}	[26]
$\tau \to l_1l_2l_3$	$(1.4\text{–}3.1) \times 10^{-7}$	[27]

for muon lepton-flavor-violating processes may be improved by a few orders of magnitude (up to $\mathrm{Br}(\mu \to e\gamma) \sim 10^{-14}$ and, in the future, to $\mathrm{Br}(\mu \to e\gamma)$ and $\mathrm{Br}(\mu \to 3e) \sim 10^{-15}$–$10^{-16}$ at neutrino factories). A new technique of superconducting magnetic traps was proposed for studying coherent μ–e conversion on nuclei to a precision of $\Gamma[\mu^- + (Z, A) \to e^- + (Z, A)]/\Gamma(\mu^- \to \text{capture}) \sim 10^{-17}$ (or even maybe up to 10^{-19}). The program of these new searches for muon lepton-flavor-violating processes and theoretical hypotheses associated with such processes are discussed in [28, 29] (see also references therein).

At the same time, there was some pessimism concerning the possibility of further improving accuracy in searches for lepton-flavor-violating processes in rare kaon decays. In this connection, two comments are in order:

First, lepton-flavor-violating processes in purely leptonic decays and in quark–lepton transitions can be caused by totally different mechanisms (for example, quark–lepton lepton-flavor-violating processes may be due to leptoquark exchange).

Second, a comparison of the quark–lepton processes $s \to d\mu\bar{e}$ and $d \to d\mu\bar{e}$ must be performed with allowance for their possible distinctions. In particular, it will be shown below that processes of the $s \to d\mu\bar{e}$ type, which manifest themselves in kaon decays, possess unique features that make respective experiments complementary to other searches for lepton-flavor-violating processes. Therefore, it is of paramount importance to consider possibilities of searches for lepton-flavor-violating kaon decays at the highest achievable sensitivity in new-generation experiments. This may become an important part of the general program of experiments aimed at searches for lepton-flavor violation in processes involving charged leptons.

The objective of the present article is to attract the attention of researchers to this problem and to emphasize the need for new investigations into lepton-flavor-violating kaon decays at the highest possible sensitivity.

2. PHENOMENOLOGY OF LEPTON-FLAVOR-VIOLATING KAON DECAYS

Let us consider the lepton-flavor-violating kaon decays

$$K_L^0 \to e^-\mu^+ \tag{15}$$

and

$$K \to \pi e^-\mu^+. \tag{16}$$

In this section, we present a phenomenological description of these processes [30–33]. Since kaons and pions are pseudoscalar particles, only axial and pseudoscalar currents can contribute to the decay process (15), where the $\langle 0|H_w|K_L^0\rangle$ transition occurs, while vector, scalar, and tensor hadron currents can contribute to the decay process (16) ($\langle \pi|H_w|K\rangle$ transition).

For the lepton-flavor-violating decay (15), the matrix element can be written in the form

$$M = \frac{G_\mathrm{F}}{\sqrt{2}}\big[J_A^\lambda(f'_A\bar{u}_e\gamma_\lambda v_\mu + f_A\bar{u}_e\gamma_5\gamma_\lambda v_\mu) + J_P(f'_P\bar{u}_e v_\mu + f_P\bar{u}_e\gamma_5 v_\mu)\big]. \tag{17}$$

The most general expression for the hadron currents appearing in the matrix element M was obtained by using the phenomenological decay parameters:

$$\left.\begin{aligned} &\text{axial vector} \quad J_A^\lambda = P^\lambda m_K a_A \varphi_K = P^\lambda m_K a_A \frac{1}{\sqrt{2m_K}} \\ &\text{pseudoscalar} \quad J_P = m_K^2 a_P \varphi_K = m_K^2 a_P \frac{1}{\sqrt{2m_K}} \end{aligned}\right\}. \tag{18}$$

Here, φ_K is the pseudoscalar kaon wave function normalized to $1/\sqrt{2m_K}$; P^λ is the kaon 4-momentum ($P^\lambda = P_\mu^\lambda + P_e^\lambda$); and a_A and a_P are the hadron parameters, which are defined below.

The constants $\frac{G_\mathrm{F}}{\sqrt{2}}f_A$, $\frac{G_\mathrm{F}}{\sqrt{2}}f'_A$, $\frac{G_\mathrm{F}}{\sqrt{2}}f_P$, and $\frac{G_\mathrm{F}}{\sqrt{2}}f'_P$ describe the new lepton-flavor-violating interactions of kaon hadron currents with lepton currents beyond the Standard Model. Because everything that is nec-

essary is taken into account in the definition of the new coupling constants f_A, f'_A, f_P, and f'_P, we do not include the Cabibbo mixing angle in the matrix element.

The relation between the axial currents J_A^λ for K_L^0 and K^+ decays is dictated by $SU(3)$ symmetry [30]

$$\langle 0|J_A^\lambda|K_L^0\rangle = \sqrt{2}\langle 0|J_A^\lambda|K^+\rangle = \sqrt{2}f_K\frac{P^\lambda}{\sqrt{2m_K}}. \quad (19)$$

Here, $f_K = 159.8 \pm 1.5$ MeV is the K^+-decay constant, which was determined from data on $K_{\mu 2}^+$ decays (see, for example, [1]). From here, the dimensionless constant $a_A = \sqrt{2}f_K/m_K$ is found to be 0.46. As was shown in [30], the relation between the constants a_A and a_P in (18) can be established on the basis of current algebra. We have

$$a_P = a_A\frac{m_K}{m_s + m_d} = 0.46 \times 4.6 = 2.1,$$

where $m_s \simeq 100$ MeV and $m_d \simeq 7.5$ MeV are the current quark masses.

Considering that the K_L^0-meson 4-momentum is $P^\lambda = P_\mu^\lambda + P_e^\lambda$ and using the Dirac equation for the lepton spinors μ and e, $(\hat{P}_\mu + m_\mu)v_\mu = (P_\mu^\lambda\gamma_\lambda + m_\mu)v_\mu = 0$ and $\bar{u}_e(\hat{P}_e - m_e) = 0$ (v_μ is the antispinor of μ^+, while u_e is the spinor of e^-), and the commutation properties of the Dirac matrices, one can represent the matrix element (17) in the form

$$\begin{aligned} M &= \frac{G_\mathrm{F}}{\sqrt{2}}\left\{\frac{m_K a_A}{\sqrt{2m_K}}\left[f'_A\bar{u}_e(\hat{P}_e + \hat{P}_\mu)v_\mu + f_A\bar{u}_e\gamma_5(\hat{P}_e + \hat{P}_\mu)v_\mu\right] + \frac{m_K^2 a_P}{\sqrt{2m_K}}\left[f'_P\bar{u}_e v_\mu + f_P\bar{u}_e\gamma_5 v_\mu\right]\right\} \\ &= \frac{G_\mathrm{F}}{\sqrt{2}}\left\{\frac{m_K a_A}{\sqrt{2m_K}}\left[f'_A(m_e\bar{u}_e v_\mu - m_\mu\bar{u}_e v_\mu) + f_A(-m_e\bar{u}_e\gamma_5 v_\mu - m_\mu\bar{u}_e\gamma_5 v_\mu)\right] + \frac{m_K^2 a_P}{\sqrt{2m_K}}\left[f'_P\bar{u}_e v_\mu + f_P\bar{u}_e\gamma_5 v_\mu\right]\right\} \\ &= \frac{1}{\sqrt{2m_K}}\left[A\bar{u}_e\gamma_5 v_\mu + B\bar{u}_e v_\mu\right]. \end{aligned} \quad (20)$$

Here, A and B are dimensionless amplitudes given by

$$\begin{aligned} A &= \frac{G_\mathrm{F}}{\sqrt{2}}m_K a_A \left[-f_A(m_\mu + m_e) + m_K\frac{a_P}{a_A}f_P\right] \\ &\simeq \frac{G_\mathrm{F}}{\sqrt{2}}m_K m_\mu a_A\left[-f_A + f_P\frac{m_K}{m_\mu}\frac{a_P}{a_A}\right] \\ &\simeq 2.00 \times 10^{-7}[-f_A + 9.9f_P], \end{aligned} \quad (21)$$

$$\begin{aligned} B &= \frac{G_\mathrm{F}}{\sqrt{2}}m_K a_A \left[-f'_A(m_\mu - m_e) + f'_P m_K\frac{a_P}{a_A}\right] \\ &\simeq \frac{G_\mathrm{F}}{\sqrt{2}}m_K a_A m_\mu[-f'_A + 9.9f'_P] \\ &\simeq 2.00 \times 10^{-7}[-f'_A + 9.9f'_P]. \end{aligned}$$

We can disregard the effect of the electron mass on the decay in (15) and find the width with respect to this decay in the form

$$\Gamma(K_L^0 \to e^-\mu^+) = \frac{1}{(2\pi)^2} \times \int\frac{d^3\mathbf{p}_\mu}{2E_\mu}\frac{d^3\mathbf{p}_e}{2E_e}|M|^2\delta^{(4)}(P_K + P_\mu + P_e), \quad (22)$$

where the square of the matrix element is

$$\begin{aligned} |M|^2 &= M^+M \\ &= \frac{1}{2m_K}\left[-A^*(\bar{v}_\mu\gamma_5 u_e) + B^*(\bar{v}_\mu u_e)\right]\left[A(\bar{u}_e\gamma_5 v_\mu) + B(\bar{u}_e v_\mu)\right] \\ &= \frac{1}{2m_K}\Big\{-A^*A(\bar{v}_\mu\gamma_5 u_e)(\bar{u}_e\gamma_5 v_\mu) + B^*B(\bar{v}_\mu u_e)(\bar{u}_e v_\mu) \\ &\quad - A^*B(\bar{v}_\mu\gamma_5 u_e)(\bar{u}_e v_\mu) + AB^*(\bar{v}_\mu u_e)(\bar{u}_e\gamma_5 v_\mu)\Big\} \\ &= \frac{1}{2m_K}\Big\{AA^*\mathrm{tr}\left[(\hat{P}_\mu - m_\mu)(\hat{P}_e - m_e)\right] + BB^*\mathrm{tr}\left[(\hat{P}_\mu - m_\mu)(\hat{P}_e + m_e)\right] \\ &\quad + A^*B\mathrm{tr}\left[(\hat{P}_\mu - m_\mu)(\hat{P}_e - m_e)\gamma_5\right] + B^*A\mathrm{tr}\left[(\hat{P}_e + m_e)(\hat{P}_\mu - m_\mu)\gamma_5\right]\Big\} \\ &= \frac{1}{2m_K}\Big\{|A|^2[P_\mu^\rho P_e^\sigma\cdot 4g_{\rho\sigma} + 4m_\mu m_e] + |B|^2[P_\mu^\rho P_e^\sigma\cdot 4g_{\rho\sigma} - 4m_\mu m_e]\Big\} \\ &= \frac{4}{2m_K}\left[|A|^2 + |B|^2\right](P_\mu P_e) + \frac{4}{2m_K}\left[|A|^2 - |B|^2\right](m_\mu m_e) \\ &\simeq \frac{4}{2m_K}\left[|A|^2 + |B|^2\right](P_\mu P_e). \end{aligned} \quad (23)$$

Here, terms of the A^*B type vanish upon evaluating the relevant trace because we have $\mathrm{tr}(\gamma_\rho\gamma_\sigma) = 4g_{\rho\sigma}$, $\mathrm{tr}I = 4$, $\mathrm{tr}(\gamma_\alpha\gamma_5\gamma_\beta) = 0$, $\mathrm{tr}(\gamma_\beta\gamma_5) = 0$, and $\mathrm{tr}\gamma_5 = 0$.

Further, we omit the terms proportional to the electron mass and introduce the 3-momentum $p = |\mathbf{p}_\mu|$ $[E_\mu = \sqrt{p^2 + m_\mu^2}$, $E_e = p$; $p = (m_K^2 - m_\mu^2)/(2m_K) = (m_K/2)(1 - m_\mu^2/m_K^2)]$. Upon integration, we then obtain

$$\Gamma(K_L^0 \to e^-\mu^+) = \frac{1}{4(2\pi)^2}\frac{1}{2m_K} \times 2[|A|^2 + |B|^2] \tag{24}$$

$$\times \int \frac{2(P_eP_\mu)}{E_\mu E_e} d^3\mathbf{p}_\mu \delta(m_K - E_\mu - E_e)$$

$$= \frac{1}{2(2\pi)^2}\frac{1}{2m_K} m_K^2 \left(1 - \frac{m_\mu^2}{m_K^2}\right)[|A|^2 + |B|^2]$$

$$\times \int \frac{4\pi p^2 dp}{E_\mu p}\delta\left(m_K - p - \sqrt{p^2 + m_\mu^2}\right)$$

$$= \frac{m_K}{8\pi}\left(1 - \frac{m_\mu^2}{m_K^2}\right)^2 [|A|^2 + |B|^2]$$

$$\simeq 18.1\ \mathrm{MeV} \times [|A|^2 + |B|^2].$$

Here, we have used the relation $m_K^2 = (P_e + P_\mu)^2 = 2(P_eP_\mu) + m_\mu^2 + m_e^2$, whence it follows that

$$2(P_eP_\mu) \simeq m_K^2\left(1 - \frac{m_\mu^2}{m_K^2}\right),$$

and the relations

$$\int \frac{pdp}{E_\mu}\delta\left(m_K - p - \sqrt{p^2 + m_\mu^2}\right)$$

$$= \frac{p}{E_\mu}\left(\frac{d}{dp}\left(p + \sqrt{p^2 + m_\mu^2}\right)\Big|_{p+E=m_K}\right)^{-1}$$

$$= \frac{E_\mu}{E_\mu + p}\frac{p}{E_\mu} = \frac{p}{E_\mu}\frac{E_\mu}{m_K} = \frac{p}{m_K} = \frac{1}{2}\left(1 - \frac{m_\mu^2}{m_K^2}\right),$$

$$\mathrm{Br}(K_L^0 \to e^-\mu^+) \tag{25}$$

$$= \frac{\Gamma(K_L^0 \to e^-\mu^+)}{\Gamma(K_L^0 \to \mathrm{tot})} = \frac{18.1\ \mathrm{MeV} \times [|A|^2 + |B|^2]}{1.273 \times 10^{-14}\ \mathrm{MeV}}$$

$$= 1.42 \times 10^{15}[|A|^2 + |B|^2].$$

Let us consider the model where $|f_A|^2 = |f_A'|^2$, $f_P = f_P' = 0$. We then have

$$\mathrm{Br}(K_L^0 \to e^\mp\mu^\pm) = 2\mathrm{Br}(K_L^0 \to e^-\mu^+)$$

$$= 2[1.42 \times 10^{15} \times 4.0 \times 10^{-14}|f_A|^2 \times 2]$$

$$= 2.27 \times 10^2|f_A|^2.$$

Taking into account the experimental limit $\mathrm{Br}(K_L^0 \to e^\mp\mu^\pm) < 4.7 \times 10^{-12}$ (see Table 3), we obtain the limitations

$$|f_A|^2 < 2.07 \times 10^{-14}, \quad f_A < 1.4 \times 10^{-7}. \tag{26}$$

In the model where $f_A = f_A' = 0$ and $|f_P| = |f_{P'}| \neq 0$, we have

$$\mathrm{Br}(K_L^0 \to e^\mp\mu^\pm) \tag{27}$$

$$= 2.27 \times 10^2 \times (9.9)^2|f_P|^2$$

$$= 2.22 \times 10^4|f_P|^2 < 4.7 \times 10^{-12}.$$

This leads to the limitations

$$|f_P|^2 \leq 2.1 \times 10^{-16}, \quad |f_P| < 1.5 \times 10^{-8}.$$

It is convenient to compare the decay $K_L^0 \to e^\mp\mu^\pm$ with the decay $K^+ \to \mu^+\nu_\mu$, which is kinematically close to the former. In the model where $|f_A| = |f_A'|$ and $f_P = f_P' = 0$, we have $[|A|^2 + |B|^2] = 2G_\mathrm{F}^2|f_A^2|f_K^2m_\mu^2$. From (24), we then have

$$\mathrm{Br}(K_L^0 \to e^-\mu^+)\tau^{-1}(K_L^0) \tag{28}$$

$$= \Gamma(K_L^0 \to e^-\mu^+)$$

$$= \frac{2G_\mathrm{F}^2|f_A|^2m_K}{8\pi}f_K^2m_\mu^2\left(1 - \frac{m_\mu^2}{m_K^2}\right)^2,$$

$$\mathrm{Br}(K_L^0 \to e^\mp\mu^\pm)\tau^{-1}(K_L^0)$$

$$= \Gamma(K_L^0 \to e^\mp\mu^\pm)$$

$$= \frac{4G_\mathrm{F}^2|f_A|^2m_K}{8\pi}f_K^2m_\mu^2\left(1 - \frac{m_\mu^2}{m_K^2}\right)^2.$$

For the decay $K^+ \to \mu^+\nu_\mu$, the results are [1]

$$\mathrm{Br}(K^+ \to \mu^+\nu_\mu)\tau^{-1}(K^+) \tag{29}$$

$$= \Gamma(K^+ \to \mu^+\nu_\mu)$$

$$= \frac{G_\mathrm{F}^2[\sin\vartheta_\mathrm{C}]^2m_K}{8\pi}f_K^2m_\mu^2\left(1 - \frac{m_\mu^2}{m_K^2}\right)^2;$$

$$B_1 = \left[\frac{\mathrm{Br}(K_L^0 \to e^\mp\mu^\pm)}{\mathrm{Br}(K^+ \to \mu^+\nu_\mu)}\frac{\tau(K^+)}{\tau(K_L^0)}\right] \tag{30}$$

$$= \frac{\Gamma(K_L^0 \to e^\mp\mu^\pm)}{\Gamma(K^+ \to \mu^+\nu_\mu)}$$

$$= \frac{4|f_A|^2(G_\mathrm{F}/\sqrt{2})^2}{\sin^2\vartheta_\mathrm{C}(G_\mathrm{F}/\sqrt{2})^2} \leq 1.75 \times 10^{-12}$$

{this follows from the data in Table 3 for the upper limit on the branching ratio for (15) and from [26]}.

For the lepton-flavor-violating decay $K_L^0 \to e^\mp\mu^\pm$, we will now consider the model in which this

process is induced by a horizontal boson X^0 changing lepton flavors (see Fig. 3). Within this model, the probability of the decay process (15) is proportional to

$$|f_A|^2\frac{G_F^2}{2}=\left(\frac{h'h''}{M_X^2}\right)^2. \quad (31)$$

From (30) and (31), we then obtain

$$B_1=\frac{4\left(\frac{h'h''}{M_X^2}\right)^2}{\sin^2\vartheta_C\left(\frac{g^2}{8M_W^2}\right)^2}=\frac{4}{\sin^2\vartheta_C}\frac{\left(\frac{h'h''}{M_X^2}\right)^2}{\left(\frac{g^2}{8M_W^2}\right)^2} \quad (32)$$

$$=4\left(\frac{M_W}{M_X}\right)^4\left[\left(\frac{h'h''}{g^2/8}\right)^2\frac{1}{\sin^2\vartheta_C}\right]$$

$$=\left(\frac{16}{\sin\vartheta_C\cdot g^2}\right)^2\left(\frac{h'}{h''}\right)^2\left[\frac{h''}{M_X}M_W\right]^4$$

$$=2.86\times10^4\left(\frac{h'}{h''}\right)^2\left[\frac{h''}{M_X}M_W\right]^4,$$

whence we find for M_X that

$$M_X^4=\frac{4M_W^4}{B_1}\left[\left(\frac{h'h''}{g^2/8}\right)^2\frac{1}{\sin^2\vartheta_C}\right].$$

Under the assumption that $\left(\frac{h'h''}{g^2/8}\right)^2\simeq1$, we have

$$M_X=3.0M_WB_1^{-1/4} \quad (33)$$

$$=2.6M_W\times10^3\ \text{GeV}\simeq210\ \text{TeV}.$$

It can be seen from here that the rare kaon decay (15) is sensitive to the region of very short distances (very large masses), which remains inaccessible even at next-generation supercolliders.

However, it should be noted that, in the model involving horizontal bosons, there exists yet another serious constraint on the parameters of the respective interaction. It can be seen from Fig. 4 that this interaction leads to $K^0\rightleftarrows X^0\rightleftarrows\bar{K}^0$ and will contribute to the mass difference Δm_K between the K_L^0 and K_S^0 mesons. It was shown in [30] that

$$\Delta m_K'\simeq\frac{8}{3}m_Kf_K^2\left(\frac{h''}{M_X}\right)^2. \quad (34)$$

If we make the extreme assumption that the kaon-mass splitting Δm_K is entirely due to this process (that is, $\Delta m_K'=\Delta m_K=3.49\times10^{-12}$ MeV) and represent $f_K=159.8$ MeV in the form $f_K=2.00\times10^{-3}M_W$, we can obtain

$$\left(\frac{h''}{M_X}M_W\right)^2=\frac{\Delta m_K}{m_K}\frac{3}{8}\frac{10^6}{4}=6.57\times10^{-10}. \quad (35)$$

Substituting (35) into (32), we then arrive at

$$B_1\le2.86\times10^4\left(\frac{h'}{h''}\right)^2\left[\frac{h''}{M_X}M_W\right]^4 \quad (36)$$

$$=1.23\times10^{-14}\left(\frac{h'}{h''}\right)^2.$$

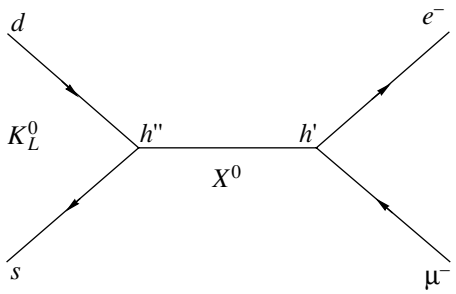

Fig. 3. Feynman diagram for the decay $K_L^0\to e^\mp\mu^\pm$ in the model involving horizontal bosons X^0 changing lepton flavors.

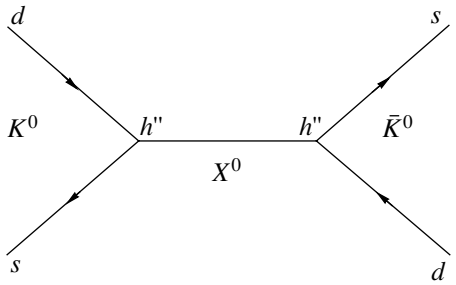

Fig. 4. Feynman diagram for the mixing processes $K^0\rightleftarrows X^0\rightleftarrows\bar{K}^0$ in the model involving horizontal bosons X^0.

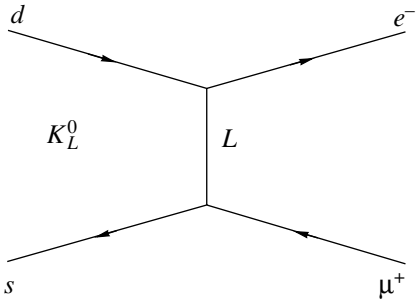

Fig. 5. Feynman diagram for the leptoquark-exchange-induced lepton-flavor-violating processes involving leptons and quarks.

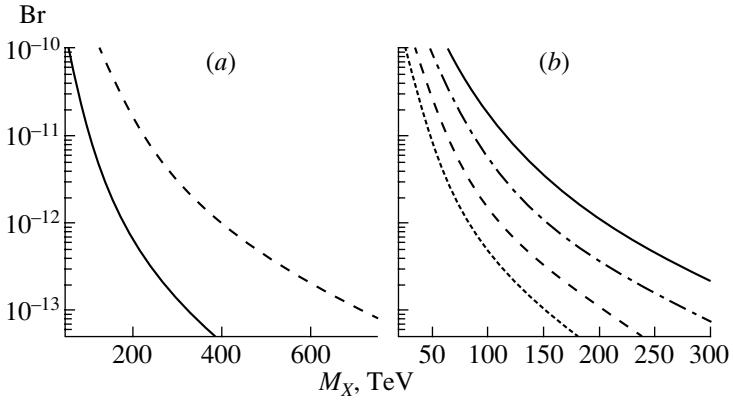

Fig. 6. Results of the calculation of the branching ratios (Br) for the decays (*a*) $K_L^0 \to e\bar{\mu}$ and (*b*) $K \to \pi e\bar{\mu}$ within the model proposed in [33] versus the mass of the horizontal boson X^0 [see (37)] under the assumption that $g_X = g$ is a weak coupling constant. In Fig. 6*a*, the solid and dashed curves correspond to the axial (A) and pseudoscalar (P) interactions violating lepton flavors in kaon decays. In Fig. 6*b*, the solid and dashed curves represent data on the decay $K_L^0 \to \pi^0 e\bar{\mu}$ for the scalar (S) and vector (V) interactions, respectively, while the dash-dotted and dotted curves show data on the decay $K^+ \to \pi^+ e\bar{\mu}$ for S and V interactions, respectively.

In fact, B_1 must be still smaller since $\Delta m'_K < \Delta m_K$—as is well known, a significant fraction of Δm_K can be explained by ordinary weak interactions within the Standard Model.

Thus, the only possible way to obtain a not overly small value of B_1 (close to the existing upper limit) is to introduce a large value of the ratio of the leptonic and hadronic coupling constants for the horizontal X^0 boson—$h'/h'' \gtrsim 10$. This condition does not seem absolutely unnatural. For example, one can see that, for weak interactions within the Standard Model, the ratio of the W-boson couplings to the leptons and strange quarks is $1/\sin\vartheta_C \simeq 5$ (for interactions with heavy quarks, this ratio is considerably higher). Nevertheless, it seems (in view of the possibility $\Delta m'_K < \Delta m_K$) that one can expect a relatively large branching ratio for the lepton-flavor-violating decay (15) only if there is a symmetry that suppresses the $K^0 \rightleftarrows X \rightleftarrows \bar{K}^0$ mixing processes or if an entirely different mechanism governs the decay process (15)—this may be, for example, leptoquark exchange (see Fig. 5). Such a mechanism must also contribute to other processes violating lepton flavor in lepton–hadron interactions—for example, the neutrinoless muon conversion $\mu^- + (Z, A) \to e^- + (Z, A)$. It is not peculiar to lepton-flavor-violating kaon decays.

The phenomenology of lepton-flavor-violating ($s \to d\mu e^-$) kaon decays was also investigated in [33] within the model involving the exchange of a horizontal boson X^0 and hadron interactions of the axial and pseudoscalar types (for the decays $K_L^0 \to e\bar{\mu}$) or of the vector and scalar types (in the decays $K \to \pi e\bar{\mu}$). The corresponding interactions are described by operators that have a rather general form; that is,

$$Q_{V,A} = \frac{g_X^2}{2M_X^2}\bar{d}\gamma_\alpha\left[C_{Lq}P_L + C_{Rq}P_R\right]s\bar{\mu}\gamma^\alpha \times \left[C_{Ll}P_L + C_{Rl}P_R\right]e + \text{h.c.}, \quad (37)$$

$$Q_{S,P} = \frac{g_X^2}{2M_X^2}\bar{d}\left[C'_{Lq}P_L + C'_{Rq}P_R\right]s\bar{\mu} \times \left[C'_{Ll}P_L + C'_{Rl}P_R\right]e + \text{h.c.},$$

where $P_L = (1-\gamma_5)/2$; $P_R = (1+\gamma_5)/2$; and g_X^2, C, and C' are coupling constants.

The branching ratios calculated with these operators for lepton-flavor-violating kaon decays are presented in Fig. 6 for $g_X^2 = g^2$ and $C = C' = 1$.

3. LEPTON-FLAVOR-VIOLATING KAON DECAYS AND CONCEPT OF FUNDAMENTAL FERMION GENERATIONS WITH CONSERVED QUANTUM NUMBERS

As was mentioned in Section 2, decays of the $s \to de\bar{\mu}$ type possess a unique special feature that distinguishes them from process of the $d \to de\bar{\mu}$ type (the neutrinoless conversion of muons into electrons) or from purely leptonic transitions accompanied by lepton-flavor violation ($\mu \to e\gamma$, $\mu \to 3e$, and so on).

Namely, quarks and leptons belonging to the different generations take part in lepton-flavor-violating

Table 4. Selection rule in the generation quantum number of fundamental fermions in the Standard Model

First-order processes	$\Delta G = 0$	$K^+ \to \pi^+\mu^+e^-, \quad K_L^0 \to e^\mp\mu^\pm, \quad K_L^0 \to \pi^0 e^\mp\mu^\pm$
Second-order processes	$\lvert\Delta G\rvert = 1$	$\mu \to 3e, \quad \mu \to e\gamma, \quad \mu^- + N \to e^- + N$
Third-order processes	$\lvert\Delta G\rvert = 2$	$K^0 \rightleftarrows \bar{K}^0\ (\Delta m(K_L^0 - K_S^0)), \quad \mu^-e^+ \to \mu^+e^-, \quad K^+ \to \pi^+\mu^-e^+$

Note: Some examples illustrating the effect of the ΔG selection rule:

a) $K^+ \to \pi^+\mu^+e^- : (\bar{s}u) \to (u\bar{d})\mu^+e^-$,

$$G_{\text{in}} = -1 + 2 = +1, \ \ G_{\text{fin}} = 0 + (-1) + 2 = +1, \ \ \Delta G = G_{\text{fin}} - G_{\text{in}} = 0;$$

b) $K^0 \to e^-\mu^+ : \ (\bar{s}d) \to e^-\mu^+$,

$$G_{\text{in}} = +1, G_{\text{fin}} = +1, \Delta G = 0;$$

$K^0 \to e^+\mu^- : \ G_{\text{in}} = +1, G_{\text{fin}} = -1, \Delta G = -2;$

$\bar{K}^0 \to e^-\mu^+ : \ \Delta G = +2;$

$\bar{K}^0 \to e^+\mu^- : \ \Delta G = 0;$

If dominant decays are characterized by $\Delta G = 0$, then one has

$$K_L^0 \simeq K_2^0 = \left| \frac{1}{\sqrt{2}}(K^0 \quad - \quad \bar{K}^0) \right\rangle \to e^\mp\mu^\pm,$$

$\hookrightarrow e^-\mu^+ \ \ \hookrightarrow \ e^+\mu^-$

but there is an additional factor of $1/2$ in the matrix elements for these decays;

c) $\mu^- + N \to e^- + N$: $G_{\text{in}} = +1 + G(N)$, $G_{\text{fin}} = +2 + G(N)$ $\Big\}\Delta G = +1;$

d) $K^0 \rightleftarrows \bar{K}^0$: $G_{\text{in}} = +1$, $G_{\text{fin}} = -1$ $\Big\}\Delta G = -2.$

kaon decays; therefore, it becomes possible to compensate for a change in the generation within the quark sector by the corresponding change in the generation within the lepton sector. This simple possibility was discussed many times, but it was most clearly formulated by Cahn and Harari [34], who introduced the quantum numbers G characterizing the fundamental fermion generations in the Standard Model and classified various processes in accordance with the possible change in this quantum number, $\Delta G = G_{\text{fin}} - G_{\text{in}}$.

If we consider only transitions between fermions of the first two generations, one can assign, in a purely phenomenological way, any differing quantum numbers to these generations—for example, $G_1 = 2$ for the first generation and $G_2 = 1$ for the second generation ($G_1 = -2$ and $G_2 = -1$ for antifermions). It can then be seen from Table 4 that we can partition all processes under consideration into classes in accordance with the change in G, ΔG, in the corresponding transitions.

In Fig. 7, the effect of the ΔG selection rule is shown for decays occurring via the exchange of horizontal boson X^0.

The physical meaning of the quantum number G is not quite clear. It is obvious that the special properties of lepton-flavor-violating kaon decays and their unique potential will manifest themselves only if the ΔG selection rule is rather stringent. Some lepton-flavor-violating decays corresponding to $\Delta G = 0$ may then have a markedly higher probability than other processes for which $|\Delta G| = 1$ at best. Moreover, horizontal interactions mediated by X^0-boson exchange, which were considered in the preceding section (see Figs. 3 and 4), are not sensitive in this case to constraints arising in $K^0 \rightleftarrows X^0 \rightleftarrows \bar{K}^0$ transitions since this mixing occurs in the third order ($|\Delta G| = 2$; see Table 4) and may be strongly suppressed. An unexpected distinction between the decay processes $K^+ \to \pi^+\mu^+e^-$ ($\Delta G = 0$) and $K^+ \to \pi^+\mu^-e^+$ ($|\Delta G| = 2$) is also worthy of note.

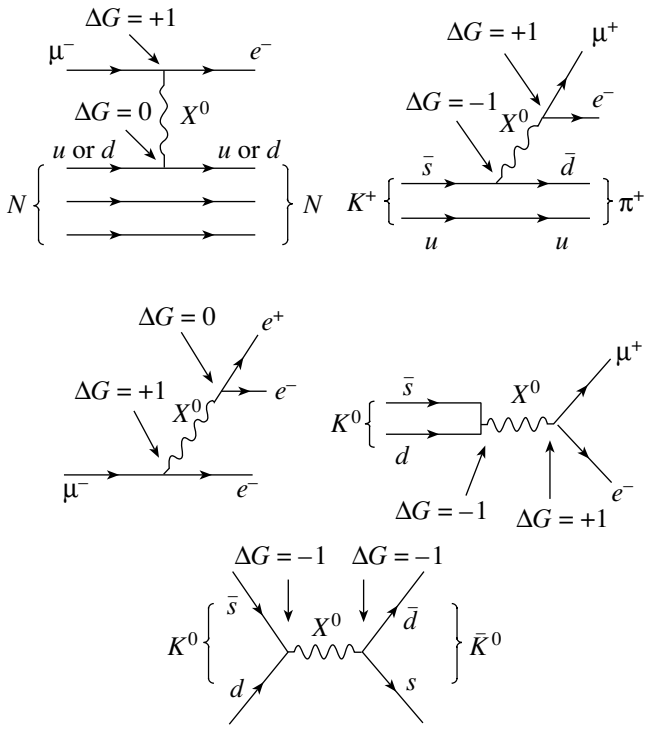

Fig. 7. Effect of the selection rule in the generation quantum numbers of fundamental fermions in the Standard Model within the mechanism involving the exchange of a horizontal boson X^0.

Thus, we see that, if the concept of fundamental generations that involves the quantum numbers G conserved in the first approximation is valid and if the $|\Delta G|$ selection rule imposes stringent constraints on the the branching ratios for the corresponding processes, further searches for lepton-flavor-violating kaon decays are of paramount importance.

Let us now illustrate the concept of the fundamental-fermion generations in the Standard Model that are characterized by the quantum numbers G conserved in the first approximation by considering the dynamical model involving extra spatial dimensions that was developed in [35] and especially in [36]. Below, we briefly formulate the main aspects of this model:

(A) A space that involves extra dimensions is characterized by an $M^4 \times S^2$ metric—that is, it corresponds to four-dimensional Minkowski spacetime and an additional two-dimensional manifold compactified within a sphere of radius R. In this six-dimensional spacetime, fundamental fermions form a single generation that further reduces to the three generations of fundamental fermions in the Standard Model [see (1)], these generations being localized in different regions of the multidimensional space and being characterized by the generation quantum numbers G_i that are conserved in the first approximation. These quantum numbers correspond to some angular momenta in the compactified S^2 space (sphere). Specifically, the first, second, and third generations of fundamental fermions are characterized, by the values of, respectively, $G_1 = 2$, $G_2 = 1$, and $G_3 = 0$ (for the corresponding antifermions, the signs of G are reversed).

(B) The existence of lepton-flavor-violating decays whose probability is determined by the structure of the extra space (that is, by the mass scale of the compactification of extra dimensions, $1/R$, and by the Kaluza–Klein structures for gauge bosons) is a distinctive feature of the model question.

(C) Because of a rather weak mixing of the fundamental generations in the Standard Model, $|\Delta G| \neq 0$ processes are strongly suppressed,

$$\mathrm{Br} \sim |\varepsilon^{|\Delta G|}|^2. \qquad (38)$$

Here, ε is the generation-mixing parameter, which plays a crucial role for the degree of suppression of processes accompanied by a change in the generation quantum number.

(D) The structure of the interactions of fermions, gauge bosons, and Higgs particles is tuned to reproduce the true hierarchy of masses and mixing angles in the quark sector for the matrix $V_{\rm CKM}$. Quark-mixing processes are determined by the mixing parameter $\varepsilon_q \simeq 10^{-2}$. For the lepton sector of the theory, it is presently impossible to determine the analogous mixing parameter ε_L in a model-independent way. Therefore, we are going to use two values of this parameter that are compatible with available experimental data: (i) $\varepsilon_L \simeq \varepsilon_q = 10^{-2}$ and (ii) $\varepsilon_L \ll \varepsilon_q$; we choose $\varepsilon_L \sim 10^{-3}$. It is obvious that, in the case of small lepton mixing, the ΔG selection rule becomes substantially more stringent.

Three types of processes characterized by different values of ΔG were considered. Since many model parameters were determined to a not very high precision, the branching ratios for lepton-flavor-violating decays were estimated quite roughly by comparing processes of similar kinematics that are allowed and forbidden in the Standard Model.

(1) Lepton-flavor-violating decays allowed by the selection rule $\Delta G = 0$ ($K_L^0 \to e^\mp\mu^\pm$, $K^+ \to \pi^+\mu^+e^-$). The branching ratio for the decay $K_L^0 \to e^\mp\mu^\pm$ is compared with the branching ratio for the allowed decay $K^+ \to \mu^+\nu_\mu$ (in just the same way as in Section 3). The quantity B_1 is then determined by the ratio of the squares of the corresponding matrix elements; that is,

$$B_1 = \left[\frac{\mathrm{Br}(K_L^0 \to e^\mp\mu^\pm)}{\mathrm{Br}(K^+ \to \mu^+\nu_\mu)}\frac{\tau(K^+)}{\tau(K_L^0)}\right] = \frac{\Gamma(K_L^0 \to e^\mp\mu^\pm)}{\Gamma(K^+ \to \mu^+\nu_\mu)} = \left|\frac{\langle \bar{e}\mu|\bar{s}d\rangle}{\langle \bar{\nu}\mu|\bar{s}u\rangle}\right|^2.$$

We recall that $B_1 \le 1.75 \times 10^{-12}$ [see (30)]. Within the model proposed in [36], one can obtain an equation that relates $\mathrm{Br}(K_L^0 \to e^\mp\mu^\pm)$ to the inverse compactification radius,

$$\frac{1}{R} > \frac{M_W}{\cos\vartheta_{\rm W}}\left[\frac{\mathrm{Br}(K^+ \to \mu^+\nu_\mu)}{\mathrm{Br}(K_L^0 \to e^\mp\mu^\pm)}\frac{\tau(K_L^0)}{\tau(K^+)}\right. \quad (39)$$
$$\left.\times\,(2\sin^4\vartheta_{\rm W} - \sin^2\vartheta_{\rm W} + 1/4)\right]^{1/4}\left(\frac{\zeta}{\sin\vartheta_{\rm C}}\right)^{1/2}$$
$$= \frac{M_W}{\cos\vartheta_{\rm W}}\left(\frac{\zeta}{\sin\vartheta_{\rm C}}\right)^{1/2}$$
$$\times\left[\mathrm{Br}(K_L^0 \to e^\mp\mu^\pm)^{-1} \times 0.64 \times 4.19\right]^{1/4} \times 0.595,$$

whence it follows that

$$1/R > 101\ \text{TeV} \times \sqrt{\zeta} \simeq 64\ \text{TeV}. \quad (40)$$

Here, $\zeta \simeq 0.4$ is a model parameter and $\mathrm{Br}(K_L^0 \to e^\mp\mu^\pm) = 4.7 \times 10^{-12}$.[3)]

For another $\Delta G = 0$ lepton-flavor-violating decay, $K^+ \to \pi^+\mu^+e^-$, it was found in [36] that

$$\frac{1}{R} > \frac{M_W}{\cos\vartheta_{\rm W}}\left(\frac{\zeta}{2\sin\vartheta_{\rm C}}\right)^{1/2} \quad (41)$$
$$\times\left[\frac{\xi\mathrm{Br}(K^+ \to \pi^0\mu^+\nu)}{\mathrm{Br}(K^+ \to \pi^+\mu^+e^-)}\right]^{1/4},$$

where

$$\xi = (4\sin^2\vartheta_{\rm W}/3 - 1)^2(1 + (4\sin^2\vartheta_{\rm W} - 1)^2) + \frac{\sin^4\vartheta_{\rm W}}{9}(16\cos^2\vartheta_{\rm W})^2 = 1.38.$$

From the constraint $\mathrm{Br}(K^+ \to \pi^+\mu^+e^-) < 2.8 \times 10^{-11}$, it follows for the compactification scale that

$$1/R > 18\ \text{TeV}. \quad (42)$$

(2) Lepton-flavor-violating decays corresponding to $|\Delta G| = 1$ suppressed transitions. Let us now consider the lepton-flavor-violating decay $\mu^+ \to e^+e^+e^-$, which proceeds in the next order in ΔG ($|\Delta G| = 1$; see Table 4). It can be compared with the main muon decay $\mu^+ \to e^+\nu_e\bar{\nu}_\mu$, which is kinematically close to it and which is allowed in the Standard Model [36]. We have

$$\frac{\mathrm{Br}(\mu^+ \to 3e)}{\mathrm{Br}(\mu^+ \to e^+\nu_e\bar{\nu}_\mu)} = (M_W R^4)(\varepsilon_L)^2\zeta^2\left[\frac{1 + 20\sin^4\vartheta_{\rm W}}{2\cos^4\vartheta_{\rm W}}\right] = (M_W R^4)(\varepsilon_L)^2\zeta^2 \times 1.90 < 1.0 \times 10^{-12}. \quad (43)$$

This yields

$$\frac{1}{R} > 60\ \text{TeV} \times \sqrt{\varepsilon_L} = \begin{cases} 6.0\ \text{TeV}\ \ (\varepsilon_L = 10^{-2}), \\ 1.9\ \text{TeV}\ \ (\varepsilon_L = 10^{-3}). \end{cases} \quad (44)$$

[3)] In estimating K_L^0-meson decays within the $\Delta G = 0$ model, we calculate $\mathrm{Br}(K_L^0 \to e^\mp\mu^\pm)$ with allowance for what was indicated in the note to Table 4: $K_L^0 \simeq K_2^0 = \left|\frac{1}{\sqrt{2}}(K^0 \underset{\hookrightarrow e^-\mu^+}{-} \bar{K}^0)\right\rangle \underset{\hookrightarrow e^+\mu^-}{\to} e^\mp\mu^\pm$. The amplitudes of the corresponding processes involve the factor of $1/2$.

In the model being considered, the decay $\mu \to e\gamma$ is additionally suppressed by a loop factor, so that its probability is small.

One of the most promising lepton-flavor-violating processes characterized by $|\Delta G| = 1$ is neutrinoless muon conversion to an electron in the field of a nucleus, $\mu^- + Z \to e^- + Z$. The best limit on the probability of this process is

$$F = \frac{\Gamma(\mu^- + \mathrm{Ti} \to e^- + \mathrm{Ti})}{\Gamma(\mu^- + \mathrm{Ti} \to \mathrm{capture})} \leq 4.3 \times 10^{-12}$$

(see Table 3).

Following [36], we find that the probability of this lepton-flavor-violating process and the compactification radius R are related by the equation

$$F = \frac{\Gamma(\mu^- + \mathrm{Ti} \to e^- + \mathrm{Ti})}{\Gamma(\mu^- + \mathrm{Ti} \to \mathrm{capture})} \tag{45}$$

$$= 2(\varepsilon_L)^2 \alpha_{\mathrm{QED}}^3 R^4 m_\mu^4 \left[\frac{\zeta F(q^2)}{\pi}\right]^2$$

$$\times Z_{\mathrm{eff}}^4 \left[\frac{\kappa m_\mu}{Z\Gamma(\mu^- \to \mathrm{capture})}\right] M_W^4 G_{\mathrm{F}}^2,$$

where $\Gamma(\mu^- \to \mathrm{capture}) = \Gamma(\mathrm{capture}) = 2.6 \times 10^6\ \mathrm{s}^{-1} = 1.71 \times 10^{-15}$ MeV for the Ti nucleus; $Z = 22$ and $N = 26$ are the numbers of, respectively, protons and neutrons in the nucleus; $Z_{\mathrm{eff}} = 17.6$ is the effective electric charge of the nucleus; $|F(q^2)| \simeq 0.54$ is the nuclear form factor; and $\kappa = 220$. From here, we obtain

$$\frac{1}{R} > m_\mu Z_{\mathrm{eff}} \left[\frac{2\alpha_{\mathrm{QED}}^2 m_\mu |F(q^2)|^2 \kappa}{\pi^2 \Gamma(\mathrm{capture}) ZF}\right]^{1/4} \tag{46}$$

$$\times M_W G_{\mathrm{F}}^{1/2} \zeta^{1/2} (\varepsilon_L)^{1/2}$$

or

$$\frac{1}{R} > 78\ \mathrm{TeV} \times \sqrt{\varepsilon}_L = \begin{cases} 7.8\ \mathrm{TeV}\ \ (\varepsilon_L = 0.01), \\ 2.5\ \mathrm{TeV}\ \ (\varepsilon_L = 0.001). \end{cases} \tag{47}$$

(3) Process $K^0 \to X \to \bar{K}^0$ characterized by $|\Delta G| = 2$. As was shown in [36], the hadronic transitions considered here, which proceed in the third order in ΔG, are strongly suppressed by the selection rule (38). The limitations for the compactification scale because of these processes appear to be very lenient:

$$\frac{1}{R} < 1.5\ \mathrm{TeV} \tag{48}$$

(from the mass difference, Δm_K),

$$\frac{1}{R} < 2.6\ \mathrm{TeV}\ \text{(from a possible effect} \tag{49}$$

on the CP-violation parameter, ε_K).

Therefore, the data on $K^0 \to X \to \bar{K}^0$ transitions, which proceed in the third order in $|\Delta G|$, impose no constraints on the branching ratio for the decay $K_L^0 \to e^\mp \mu^\pm$.

Thus, the possibility of considering various neutral lepton-flavor-violating processes from a unified point of view and with allowance for the selection in the generation quantum number of fundamental fermions, the ΔG selection rule, is an appealing feature of the studies reported in [35, 36]. Within this theory and with the aid of relations (39), (41), (43), and (46), we find that the branching ratios for lepton-flavor-violating processes admit the universal representation

$$\mathrm{Br}_i(\mathrm{LFV}) = a_i / R_{i\mathrm{eff}}^{-4}. \tag{50}$$

In accordance with the selection rule (38), we then have

$$R_{i\mathrm{eff}}^{-1} = [R^{-1}(\varepsilon^{|\Delta G|})^{1/2}]_i, \tag{51}$$

where R is the compactification radius expressed in TeV^{-1} units.

For the processes allowed by the selection rule in G (that is, if $\Delta G = 0$), we have $R_{\mathrm{eff}}^{-1} = R^{-1}$. For $|\Delta G| = 1$ lepton processes, we will use two assumptions on the lepton-mixing factors: (i) $\varepsilon_L \simeq \varepsilon_q \simeq 0.01$ and (ii) $\varepsilon_L = 10^{-3}$. Either assumption is compatible with available experimental data and is rather conservative. It is obvious that, with decreasing ε_L, the selection rule in the generation quantum number becomes more stringent.

Thus, we represent the branching ratios for lepton-flavor-violating decays in the form

$$\mathrm{Br}_i(\mathrm{LFV}) = a_i / [R^{-4}(\varepsilon^{|\Delta G|})^2]_i \tag{52}$$

or

$$a_i = \mathrm{Br}_i(\mathrm{LFV})[R^{-4}(\varepsilon^{|\Delta G|})^2]_i. \tag{53}$$

We conjecture that different lepton-flavor-violating processes corresponding to identical values of the effective inverse radius $R_{i\text{eff}}^{-1} = [R^{-1}(\varepsilon^{|\Delta G|})^{1/2}]_i$ (R is the compactification radius at which the lepton-flavor violation occurs for $\Delta G = 0$ allowed processes) are equally sensitive to possible lepton-flavor violation in processes involving charged leptons.

Relying on the currently available upper limit on the relevant branching ratios, $\text{Br}(K_L^0 \to e^\mp\mu^\pm) = 4.7 \times 10^{-12}$, and on the corresponding inverse compactification radius, $1/R = 64$ TeV (40), one can therefore estimate the branching ratios that must be achieved in searches for other lepton-flavor-violating processes in order to obtain commensurate sensitivities to lepton-flavor violation. The result is

$$\text{Br}_i(\text{LFV})|_{R_{\text{eff}}^{-1}=64\text{ TeV}} \tag{54}$$
$$= \left\{\text{Br}_i(\text{LFV})_{\text{exp}} = \frac{a_i}{[R^{-4}(\varepsilon^{|\Delta G|})^2]_i}\right\}$$
$$\times \frac{[R^{-4}(\varepsilon^{|\Delta G|})^2]_i}{(64\text{ TeV})^4} = a_i/(64\text{ TeV})^4.$$

If we assume that, in future kaon experiments, one can reach the sensitivity of $\text{Br}(K_L^0 \to e^\mp\mu^\pm) = 10^{-14}$ (this corresponds to $1/R = 298$ TeV), then the predicted branching ratios for other processes of the same sensitivity are

$$\text{Br}_i(\text{LFV})|_{R_{\text{eff}}^{-1}=298\text{ TeV}} = a_i/(298\text{ TeV})^4. \tag{55}$$

The corresponding numerical results are given in Table 5.

Thus, it was shown that the theory proposed in [35, 36], which involves a space featuring extra dimensions and an $M^4 \times S^2$ metric, the extra dimensions being compactified within a sphere of radius R, leads to the concept of approximately conserved generation quantum numbers of fundamental fermions in the Standard Model and to a significant suppression of $|\Delta G| \neq 0$ processes. In this theory, the sensitivity of lepton-flavor-violating kaon decays proceeding in the first order in G (that is, at $|\Delta G| = 0$), especially of the decays $K_L^0 \to e^\mp\mu^\pm$, is many orders of magnitude higher than muon lepton-flavor-violating processes, which proceed in the second order in G (that is, at $|\Delta G| = 1$) (see Table 5).

Of course, the model being considered is of an approximate character and calls for a further development and refinements. It is only one of the possible models involving lepton-flavor violation. In processes involving charged leptons, lepton-flavor violation may be of a very intricate character and may receive contributions from many other mechanisms, for which purely leptonic processes ($\mu \to e\gamma$, $\mu \to 3e$, $\tau \to 3\mu$, $\tau \to \mu + \gamma$, and so on) can be even more sensitive than kaon decays. For mixed quark–lepton processes, such as $s \to d\mu\bar{e}$ and $d \to d\bar{\mu}e$, it is of great interest to study in detail the relative potential of different mechanisms (involving the selection in the generation quantum number, leptoquark exchange, etc.). Finally, processes involving nonconservation of the total lepton charge L—such as neutrinoless double-beta decay [$(Z, A) \to (Z + 2, A) + 2e^-$] or exotic decays like $K^+ \to \pi^-\mu^+\mu^+$—may play an important role.

Problems associated with lepton-flavor violation attract much attention since lepton-flavor-violating processes can be sensitive to an energy scale that is far beyond the possibilities of next-generation supercolliders. These problems were considered in detail in a number of studies (see, for example, [28, 37–49] and references therein). At the present time, the main attention of researchers is given to an ambitious program of new searches for muon lepton-flavor-violating processes of the $\mu \to e + \gamma$ or $\mu^- + (Z, A) \to e + (Z, A)$ type. It is planned to improve the sensitivity of these searches by three to five orders of magnitude [28, 29]. Of course, this is a very important and promising line of future investigations.

However, it follows from the present analysis that searches for effects of lepton-flavor violation in rare kaon decays, where unique features of kaon processes may manifest themselves, are complementary to muon-decay experiments and also deserve an extensive development in future investigations. We will assess some possibilities of future kaon experiments in the next section.

4. PROSPECTS OF FUTURE SEARCHES FOR LEPTON-FLAVOR-VIOLATING KAON DECAYS

Future studies of rare lepton-flavor-violating kaon processes will be possible only upon realizing the following two main conditions:

Table 5. Sensitivities to various lepton-flavor-violating processes within the extradimensional model featuring approximately conserved generation quantum numbers of fundamental fermions [36]

Br(LFV) (90% C.L.) (experimental data on upper limits)	$\|\Delta G\|$	$[R^{-1}(\varepsilon^{\|\Delta G\|})^{1/2}]_i$, TeV	$[R^{-4}(\varepsilon^{\|\Delta G\|})^{2}]_i$, TeV^4	a_i(LFV), TeV^4	Branching ratios expected for lepton-flavor-violating processes and normalized to available data on the decays $K_L^0 \to e^{\mp}\mu^{\pm}$ and $R^{-1} = 64$ TeV [see (54)]	Branching ratios expected for lepton-flavor-violating processes and normalized to the sensitivity expected for the decays $K_L^0 \to e^{\mp}\mu^{\pm}$ in future kaon experiments [see (55)]	Expected precision in determining branching ratios for lepton-flavor-violating processes in the proposed experiments
$\mathrm{Br}(K_L^0 \to e^{\mp}\mu^{\pm}) < 4.7 \times 10^{-12}$	0	64	1.68×10^7	7.90×10^{-5}	Normalization: $\mathrm{Br}(K_L^0 \to e^{\mp}\mu^{\pm}) < 4.7 \times 10^{-12}$, $R^{-1} = 64$ TeV	Normalization: $\mathrm{Br}(K_L^0 \to e^{\mp}\mu^{\pm}) \sim 10^{-14}$, $R^{-1} = 298$ TeV	$\sim 10^{-13}$–10^{-14},
$\mathrm{Br}(K^+ \to \pi^+\mu^+e^-) < 2.8 \times 10^{-11}$	0	18	1.05×10^5	2.94×10^{-6}	1.75×10^{-13}	0.37×10^{-15}	10^{-12} (CKM) [51]
$\mathrm{Br}(\mu^- \to e^+e^-e^-) < 1.0 \times 10^{-12}$	1	6.07 ($\varepsilon_L = 10^{-2}$) 1.92 ($\varepsilon_L = 10^{-3}$)	1.36×10^3 1.36×10	1.36×10^{-9} 1.36×10^{-11}	0.81×10^{-16} 0.81×10^{-18}	0.17×10^{-18} 0.17×10^{-20}	10^{-14}–10^{-15} [29]
$F = \dfrac{\Gamma(\mu^- \to e^-)}{\Gamma(\mu \to \mathrm{capture})} < 4.3 \times 10^{-12}$	1	7.80 ($\varepsilon_L = 10^{-2}$) 2.47 ($\varepsilon_L = 10^{-3}$)	3.70×10^3 3.70×10	1.59×10^{-8} 1.59×10^{-10}	0.94×10^{-15} 0.94×10^{-17}	0.20×10^{-17} 0.20×10^{-19}	$\sim 10^{-17}$ (MECO) [29]

Note: For various processes, columns 6 and 7 give the expected branching ratios at which their sensitivity to lepton-flavor-violating processes will be commensurate with the existing data for the decays $K_L^0 \to e^{\mp}\mu^{\pm}$ and with data expected in the future for these decays.

(i) Intense kaon sources must be created in order to increase considerably statistics for enhancing the sensitivity to lepton-flavor-violating kaon decays.

(ii) Reliable methods must be developed for identifying rare lepton-flavor-violating kaon decays and for suppressing background processes that restrict the sensitivity of relevant experiments.

These conditions would require preparing a new generation of kaon experiments at the existing intermediate-energy (~25–120 GeV) accelerators, as well as at those that are currently under construction or are designed. Detectors for these investigations must be based on the latest achievements of experimental techniques in order to improve the efficiency of identification of decay products and the accuracy of spectrometric and time measurements, as well as to increase maximally the detector ability to operate at high rates.

Although there are presently no specific new proposals of searches for lepton-flavor-violating kaon decays, some investigations along these lines are under way [41, 50, 51]. In the project of the CKM experiment [50], in which it was planned to perform precision measurements of the rare decay $K^+ \to \pi^+\nu\bar{\nu}$, further searches for the lepton-flavor-violating decays $K^+ \to \pi^+\mu^+e^-$, $K^+ \to \pi^+\mu^-e^+$, and $K^+ \to \pi^-l^+l^+$ (first of all, $K^+ \to \pi^-\mu^+\mu^+$) were considered among accompanying measurements. It was shown that the high sensitivity of the CKM experiment and unique features of the CKM detector would make it possible to reach a statistical accuracy for their branching ratios at a level of $\mathrm{Br} \lesssim 10^{-12}$—that is, to improve the sensitivity of searches for lepton-flavor-violating kaon decays by more than one order of magnitude in relation to the results achieved in the E865 experiment (Table 3). Although a complete analysis of the background situation that would enable one to attain this improvement of the sensitivity was not performed in the SKM project, some studies were carried out, and their results proved to be very promising [51]. Note that the limit obtained in the E865 experiment for the decay $K^+ \to \pi^-\mu^+\mu^+$ ($\mathrm{Br} < 3 \times 10^{-9}$) was the least restrictive one. This limit was determined by the copious background from the decay $K^+ \to \pi^-\pi^+\pi^+$, in which two π^+ mesons decay in flight ($\pi^+ \to \mu^+\nu_\mu$) and are misidentified as muons. The results of the E865 experiment for this decay are presented in Fig. 8. For the CKM setup, it was shown via a CKM GEANT Monte Carlo simulation that, for standard processing methods (close to those used under conditions of the E865 experiment), the expected background for $\mathrm{Br}(K^+ \to \pi^-\mu^+\mu^+)$ proved to be at the same level ($\lesssim 2.5 \times 10^{-9}$, 90% C.L.). However, the set of equipment that must constitute the CKM detector made it possible to perform an optimized analysis on the basis of redundant momentum measurements for one of the muons with the aid of a magnetic spectrometer and a Cherenkov RICH spectrometer that was installed downstream of the magnetic spectrometer (and upstream of the muon detector) and which was intended for precisely measuring particle velocities. From an analysis of the data in Fig. 9, we see that this method would make it possible to reduce, at least by two orders of magnitude, the background of the decays $\pi \to \mu\nu$ in flight and to improve the expected sensitivity of searches to $\mathrm{Br}(K^+ \to \pi^-\mu^+\mu^+) \lesssim 10^{-11}$ [51]. Although the CKM experiment was initially approved at Fermilab, its future fate is unfortunately unclear because of the lack of funds. At the present time, the CKM Collaboration is preparing a revised plan for this experiment [52] with the aim of considerably reducing the cost of the project and, at the same time, achieving its main goals formulated in [50].

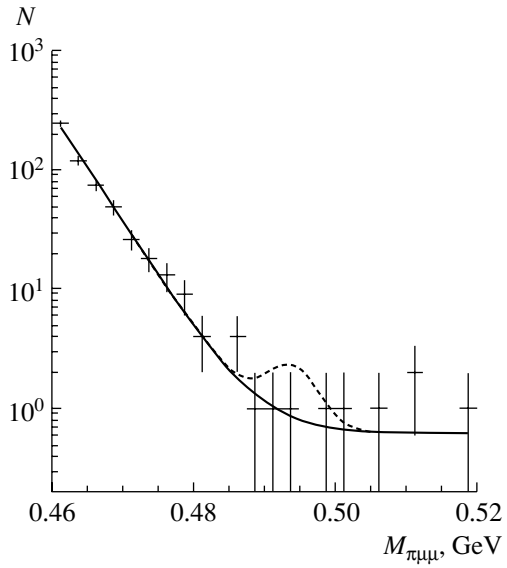

Fig. 8. Results of the E865 experiment for the decay $K^+ \to \pi^-\mu^+\mu^+$. The dashed curve corresponds to $\mathrm{Br}(K^+ \to \pi^-\mu^+\mu^+) \simeq 3 \times 10^{-9}$; N is the number of events.

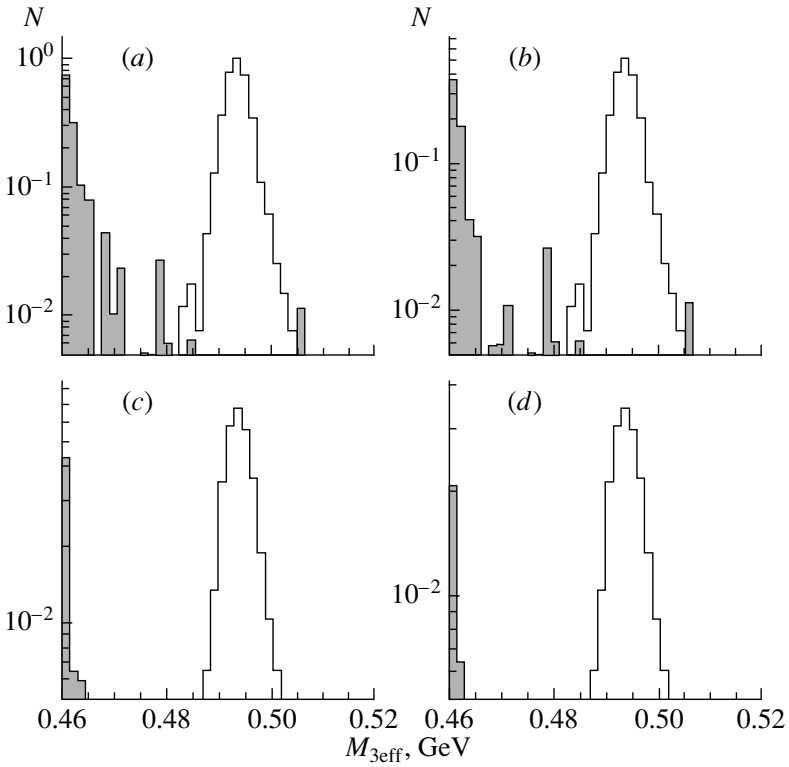

Fig. 9. Simulation of the background for the decay $K^+ \to \pi^-\mu^+\mu^+$ under the conditions of the CKM experiment [51]. The shaded histograms represent the background; N is the number of events in relative units; the unshaded peaks correspond to the decays $K^+ \to \pi^-\mu^+\mu^+$ (the vertical scale is changed). In Figs. 9*a* and 9*b*, the background is suppressed by standard kinematical methods for separating $K^+ \to \pi^-\mu^+\mu^+$ events with various cuts (which are close to the conditions in the E865 experiment); in Figs. 9*c* and 9*d*, the background is suppressed by using the procedure of a double identification of muons in the magnetic spectrometer and in the RICH spectrometer (see main body of the text). A comparison of the data in Figs. 9*d* and 8 shows that the background due to the decay $K^+ \to \pi^+\pi^-\pi^+$ (involving the decays $\pi^+ \to \mu^+\nu$ in flight) can be suppressed by more than two orders of magnitude under the conditions of a double muon constraint (CKM).

Although it is of importance to improve, to the maximum possible degree, the sensitivity of searches for various lepton-flavor-violating kaon decays, which may be induced by interactions of different types, searches for the decays $K_L^0 \to e^\mp\mu^\pm$ with the highest possible sensitivity seem to be the most promising. In this connection, we consider the estimates of the statistical potential of such searches at the present and future accelerators [41, 53, 54].

In order to illustrate the potential for obtaining intense K_L^0 beams at the Fermilab Main Injector, the estimates derived for one of the versions of the KAMI project (KAMI-NEAR [53]) are given in Table 6. As can be seen from this table, the sensitivity that can be achieved in such measurements is $\mathrm{Br}(K_L^0 \to e^\mp\mu^\pm) \lesssim 10^{-14}$.

At the 70-GeV IHEP accelerator, a statistical accuracy of $\mathrm{Br}(K_L^0 \to e^\mp\mu^\pm) \lesssim 10^{-13}$ can be achieved because of a lower intensity, a lower repetition frequency of the proton beam, and a shorter time of measurements. Nevertheless, prospects for increasing the solid angle and the intensity of the neutral beam should be explored by using a strongly asymmetric beam in order to reduce the losses of detection efficiency for the process under investigation. It should be recalled that, in the KOPIO experiment (BNL), the solid angle of a slow K_L^0 beam was increased up to about 500 μsr (the dimensions of the beam spot were about 120×10 cm^2—see Fig. 10) [55].

Information about the properties of future accelerators (the J-PARC project at KEK, accelerators for neutrino factories, and the proton driver at Fermilab [41, 56]) shows that, at the next-generation intermediate-energy hadron accelerators, the statistical sensitivity in searches for the decays $K_L^0 \to e^\mp\mu^\pm$ can be improved to a level of $<10^{-15}$ (or maybe higher). It seems that the sensitivity of these

Table 6. Evaluation of the potential of the K_L^0 beam at the Fermilab Main Injector in the KAMI-NEAR project [53]

Proton beam and properties of secondary neutral beam	Decay volume and data on K_L^0 decays	Results of an analysis of the decay $K_L^0 \to e^\mp\mu^\pm$
Proton beam: $E_p = 120$ GeV; $I_p = 3 \times 10^{13}$ protons per cycle $\to$ 3.6×10^{16} protons per hour; neutral-beam-production angle of $\vartheta \simeq 8$ mrad; beam acceptance of $d\Omega =$ (2.5 mrad) $\times$ (2.5 mrad) $= 6.3$ μsr; K_L^0-meson flux at the target of $1.5 \times 10^9 K_L^0$ per cycle; intensity ratio of $n/K_L^0 \simeq 20$	The distance from the primary target to the decay volume is 40 m; the decay length is 23 m; the decay probability in the decay volume is about 10%; the number of K_L^0 decays is 1.2×10^8/cycle $\to 1.4 \times 10^{11}$/hour; the mean momentum of decay kaons is 15 GeV	The total number of K_L^0 decays over two years of running (under the assumption of 50% losses because of dead time and inefficiency of accelerator system) is $N = 1.7 \times 10^{15} K_L^0$ decays; the detection efficiency for the decay $K_L^0 \to e^\mp\mu^\pm$ is $\sim$10%; the sensitivity is $\mathrm{Br}(K_L^0 \to e^\mp\mu^\pm) \lesssim 10^{-14}$. In the KAMI project characterized by a reduced intensity, the statistical sensitivity is $\mathrm{Br}(K_L^0 \to e^\mp\mu^\pm) \lesssim 10^{-13}$ [54]

experiments will be limited only by the background conditions of the experiments.

For experiments at the aforementioned level of sensitivity, the preparation of proposals will of course require a very careful elaboration of the experimental design and a detailed simulation of the background conditions of measurements. Only some of the possible recommendations for a further analysis are formulated here.

(i) A neutral beam must possess good properties and a minimum halo. In order to achieve this, the beam-formation scheme and the collimation system must be designed carefully. Figure 10 displays the results of a neutral-beam simulation for the KAMI project [54] that were obtained with allowance for data on neutral beams at the KTeV setup and for the beam in the KOPIO project [55]. The neutral beam must traverse the entire setup in a vacuum and not interact with the detector material.

(ii) The forward part of the setup contains the decay volume and two magnetic spectrometers upstream of it that are characterized by a very high resolution and which are located in the region of a high vacuum (about 10^{-6} Torr). The vacuum chamber must be within the yoke of the magnetic spectrometers. Thin-wall drift tubes of high resolution that were developed for the CKM setup and which operate in a high vacuum [50, 57] can be used as tracking detectors. Therefore, they can be located within the vacuum chamber of the magnetic spectrometer. The holes in the tubes make it possible to channel through them an intense neutral beam without interactions, so that the counting rate will be determined almost completely by the products of K_L^0-meson decay in the decay volume and in the spectrometers. The double measurement of the muon momentum reduces substantially the background from the decays $\pi \to \mu\nu_\mu$ in flight.

(iii) A muon- and electron-identification system must be located downstream of the magnetic spectrometers. In order to remove the neutral beam, it is channeled from the above system through a thin evacuated pipe. For a high-efficiency electron identification, one can employ a system formed by a shower spectrometer and a transition-radiation detector (as in the KTeV setup) or a gas Cherenkov detector. A conventional time-of-flight spectrometer can be used to identify muons and to perform additional independent measurements of their momenta (in the same way as was done in the E871 experiment [17]). However, it seems more efficient to employ in this region a high-precision RICH counter to identify simultaneously muons and electrons (as was proposed in the CKM project). This would also make it possible to perform a third measurement of the muon momentum and to suppress further the background from the decays $\pi \to \mu\nu_\mu$ in flight—this was discussed in [50, 51] by using the decay $K^+ \to \pi^-\mu^+\mu^+$ (see Fig. 9) as an example.

An analysis of possible background processes in separating the decays $K_L^0 \to e^\mp\mu^\pm$ was performed in [17, 32]. This resulted in indicating the following three main sources of the background:

The first source is the processes $K_L^0 \to \pi^\pm e^\mp\nu$ involving a very soft neutrino and the decays $\pi^+ \to \mu^\pm\nu$ in flight. Although the maximum mass of the

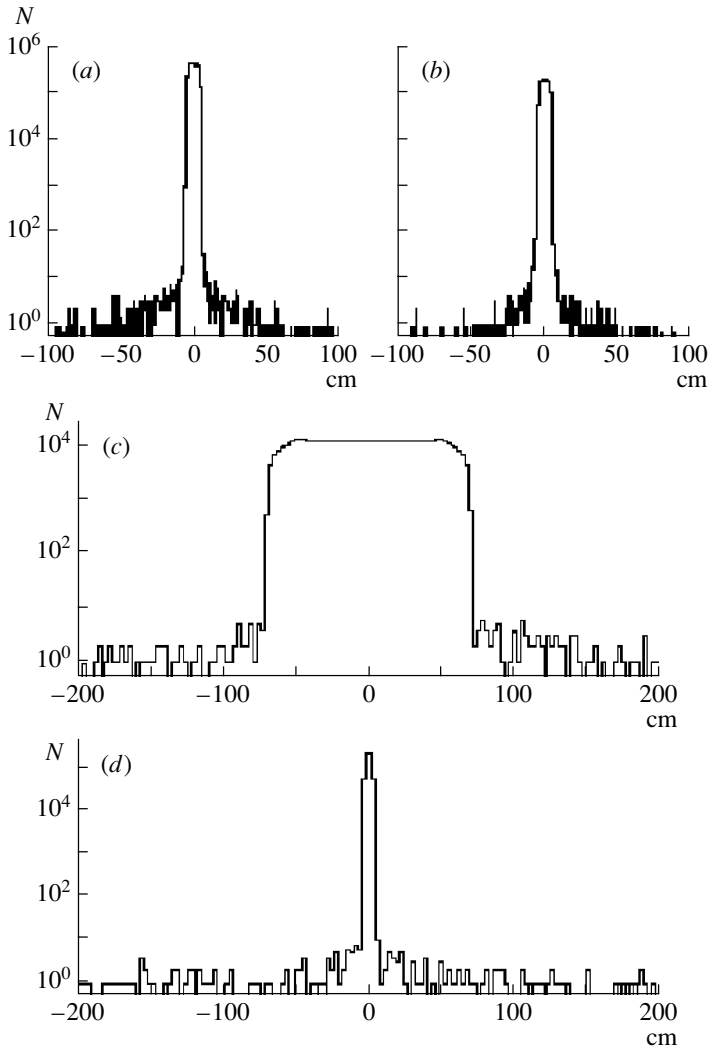

Fig. 10. Results of a simulation of the expected profiles for the low-halo neutral beams in the KAMI [54] and KOPIO [55] experiments: (*a*) the KAMI project, a K_L^0 beam; (*b*) the KAMI project, a neutron beam; (*c*) the KOPIO project, the horizontal profile of a neutral beam; and (*d*) the KOPIO project, the vertical profile of a neutral beam. In the KOPIO project, the neutral beam is characterized by a strong asymmetry in the vertical and horizontal coordinates and by a very large acceptance ($\sim$500 μsr).

detected system $e^{\mp}\mu^{\pm}$ is shifted, in this case, with respect to the K_L^0-meson mass ($(M_{e\mu})_{\max} = m_K -$ 8.43 MeV [32]), non-Gaussian errors in the momentum measurements can generate a hazardous background situation.

The second is a misidentification of secondary particles, which leads to errors in determining the effective mass of the system.

The third is random coincidences of secondary decay particles from two different K_L^0 mesons; such backgrounds become more dangerous under conditions of a high intensity that is necessary for achieving a high sensitivity of the experiment.

The possibility of independently suppressing these backgrounds should be studied carefully in designing the setup for searches for the decays $K_L^0 \to e\bar{\mu}$ (Monte Carlo simulation based on the GEANT package, dedicated calibration measurements). Particular attention should be given to non-Gaussian errors induced by the decays $\pi \to \mu\nu$ in flight and interactions of secondary particles in the tracking detectors of the magnetic spectrometers (the thickness of the detector material must be minimized). In order to reduce non-Gaussian effects to the maximum possible degree, tracks should be thoroughly fitted by using all available modern algorithms (see, for example, [58]).

In order to reduce the random background, it is necessary to chose carefully an optimum profile of the

neutral beam—for example, to use a sharply asymmetric profile (see Fig. 10 and [55]). It is also necessary to harness the latest achievements of electronics. It can be expected that considerable advances can be made by employing, in the beam-identification zone (that is, beyond the vacuum), new-generation tracking detectors that rely on the Micromega TPC technology (of the KABES type in the NA 48 experiment) and which enable one to operate under conditions of high counting rates [59].

For future experiments, it might be worth considering a system for focusing the products of the two-particle decay $K_L^0 \to e^-\mu^+$ with the aid of a superconducting solenoid whose magnetic field is directed along the neutral kaon beam (in a way analogous to that proposed in [60] for studying μ–e conversion). However, the proposed system may substantially complicate the design of the experimental setup.

5. CONCLUSION

In conclusion, it should be emphasized once again that, in view of unique features of lepton-flavor-violating kaon decays that are associated with the concept of approximately conserved generation quantum numbers G of fundamental fermions in the Standard Model and with the $\Delta G = 0$ selection rules, it is of paramount importance to perform a new generation of rare-kaon-decay experiments at the existing and future intermediate-energy (25–120 GeV) accelerators by using kaon beams of highest intensity. It is necessary to design new setups that would ensure the highest speed of operation and the most detailed reconstruction of event kinematics with the aim of suppressing the background and improving the sensitivity of experiments by two to four orders of magnitude in relation to the data in Table 3. These very complicated experiments should be considered as an independent and a complementary part of the general program of searches for lepton-flavor violation in processes involving charged leptons.

ACKNOWLEDGMENTS

I am grateful to M.V. Libanov, E.Yu. Nugaev, and S.V. Troitsky for numerous stimulating discussions, participants of the Chicago Flavor Seminar for enlightening comments, and A.V. Artamonov for his help in the preparation of the manuscript.

REFERENCES

1. L. B. Okun, *Leptons and Quarks* (Nauka, Moscow, 1990; North-Holland, Amsterdam, 1984).
2. L. B. Okun, *Particle Physics* (Nauka, Moscow, 1988; Harwood, Chur, 1985).
3. G. Kane, *Modern Elementary Particle Physics* (Addison-Wesley, New York, 1987; Mir, Moscow, 1990).
4. G. Buchalla *et al.*, Rev. Mod. Phys. **68**, 1125 (1996).
5. Fayyazuddin and Riazuddin, *A Modern Introduction to Particle Physics*, 2nd ed. (World Sci., Singapore, 1992).
6. N. Cabibbo, Phys. Rev. Lett. **10**, 531 (1963); M. Kobayashi and M. Maskawa, Prog. Theor. Phys. **49**, 652 (1973).
7. Super-Kamiokande Collab. (S. Fukuda *et al.*), Phys. Rev. Lett. **86**, 5651 (2001); SNO Collab. (Q. R. Ahmad *et al.*), Phys. Rev. Lett. **87**, 071301 (2001); **89**, 011302 (2002); Homestake Collab. (R. Davis), Rev. Mod. Phys. **75**, 985 (2003).
8. Super-Kamiokande Collab. (S. Fukuda *et al.*), Phys. Rev. Lett. **81**, 1562 (1998); **82**, 2644 (1999); **85**, 3999 (2000).
9. KamLAND Collab. (K. Eguchi *et al.*), Phys. Rev. Lett. **90**, 021802 (2003).
10. K2K Collab. (M. N. Ahn *et al.*), Phys. Rev. Lett. **90**, 041801 (2003) [hep-ex/0212007].
11. A. Yu. Smirnov, hep-ph/0311259.
12. W. A. Alberico and S. M. Bilenky, hep-ph/0311053.
13. B. M. Pontekorvo, Zh. Éksp. Teor. Phys. **33**, 549 (1957) [Sov. Phys. JETP **6**, 429 (1957)]; **34**, 247 (1958) [**7**, 172 (1958)].
14. B. M. Pontekorvo, Zh. Éksp. Teor. Phys. **46**, 984 (1964) [Sov. Phys. JETP **19**, 671 (1964)].
15. Z. Maki, M. Nakagawa, and S. Sakata, Prog. Theor. Phys. **28**, 870 (1962).
16. S. T. Petcov, Yad. Fiz. **25**, 641, 1336(E) (1977) [Sov. J. Nucl. Phys. **25**, 340, 698(E) (1977)].
17. S. M. Bilenky and B. M. Pontecorvo, Phys. Rep. **41**, 225 (1978).
18. D. Ambrose *et al.* (BNL E871 Collab.), Phys. Rev. Lett. **81**, 5734 (1998).
19. KTeV Collab. (M. Corcoran), in *Invited talk at the Workshop on e^+e^- Physics in the 1–2 GeV Range, Alghero, Italy, 2003*, hep-ex/0402033.
20. BNL E865 Collab. (R. Appel *et al.*), Phys. Rev. Lett. **85**, 2450 (2000).
21. BNL E865 Collab. (R. Appel *et al.*), Phys. Rev. Lett. **85**, 2877 (2000).
22. MEGA Collab. (M. L. Brooks *et al.*), Phys. Rev. Lett. **83**, 1521 (1999).
23. SINDRUM Collab. (U. Bellgardt *et al.*), Nucl. Phys. B **229**, 1 (1988).
24. SINDRUM II Collab. (C. Dohmen *et al.*), Phys. Lett. B **317**, 631 (1993).
25. BaBar Collab. (B. Auber *et al.*), hep-ex/0312027; Belle Collab. (K. Abe *et al.*), hep-ex/0310029.
26. K. Hagavara *et al.* (PDG), Phys. Rev. D **66**, 010001 (2002).

27. Y. Okada, hep-ph/0402027.
28. Y. Kuno and Y. Okada, Rev. Mod. Phys. **73**, 151 (2001) [hep-ph/9909265].
29. L. M. Barkov *et al.*, Research Proposal to PSI (1999), http://www.icepp.s.utokyo.ac.jpmeg; M. Bachman *et al.*, MECO Proposal to BNL (1997), http://meco.ps.uci.edu; S. Machida *et al.*, Letter of Intent to the J-PARK 50 GeV Proton Synchrotron Experiments. The PRIME Working Group (2003).
30. P. Herczeg, in *Proceedings of* "*Kaon Factory Workshop*," Ed. by M. K. Creddock, TRI-79-1 (TRIUMF, Vancouver, 1979), p. 20.
31. O. Shanker, Nucl. Phys. B **206**, 253 (1982).
32. J. L. Ritchie and S. Wojcicki, Rev. Mod. Phys. **65**, 1149 (1993).
33. T. G. Rizzo, hep-ph/9809526.
34. R. N. Cahn and H. Harari, Nucl. Phys. B **176**, 135 (1980).
35. M. V. Libanov and S. V. Troitsky, Nucl. Phys. B **599**, 319 (2001) [hep-ph/0011095]; J. M. Frere *et al.*, Phys. Lett. B **512**, 169 (2001) [hep-ph/0012306]; JHEP **0111**, 025 (2001) [hep-ph/0110045]; JHEP **0306**, 009 (2003) [hep-ph/0304117].
36. J. M. Frere *et al.*, hep-ph/0309014.
37. J. Bernabe *et al.*, Nucl. Phys. B **409**, 69 (1993).
38. J. D. Vergados, Phys. Rep. **133**, 1 (1986).
39. Z. Gagyi-Palffy *et al.*, Nucl. Phys. B **513**, 517 (1998).
40. A. Belyaev *et al.*, hep-ph/0008276.
41. A. Belyaev *et al.*, hep-ph/0107046.
42. L. S. Littenberg and R. Shrock, Phys. Lett. B **491**, 285 (2000).
43. K. Zuber, Phys. Lett. B **479**, 33 (2000).
44. S. Lavignac, hep-ph/0312304.
45. E. D. Iltan, hep-ph/0312311.
46. J. Ellis *et al.*, hep-ph/9911459.
47. K. Matsuda *et al.*, hep-ph/0003055.
48. J. L. Feng, hep-ph/0101122.
49. R. Shrock, presented at *Lepton Flavor Violation Theory, BNL Workshop on Future Kaon Experiments, 2004*.
50. CKM Collab. (J. Frank *et al.*), Fermilab Proposal for Precision Measurement of the Decay $K^+ \to \pi^+\nu\bar{\nu}$ and Other Rare K^+ Processes at Fermilab Using the Main Injector (Fermilab, 2001); http://www.fnal.gov/projects/ckm/welcome.html
51. L. G. Landsberg, Yad. Fiz. **65**, 1795 (2002) [Phys. At. Nucl. **65**, 1749 (2002)]; L. G. Landsberg and D. V. Vavilov, CKM Note 48 (2001).
52. E921 Collab., An Adaptation to Existing Facility of the E921 Precision Measurements in K^+ and π^+ Decays (Fermilab, 2004).
53. KAMI Collab. (E. Chen *et al.*), An Expression of Interest to Detect and Measure the Direct CP Violating Decay $K_L \to \pi^0\nu\bar{\nu}$ and Other Rare Decays at Fermilab Using the Main Injector (Fermilab 1997).
54. KAMI Collab. (T. Alexopoulos *et al.*), A Proposal for Precision Measurement of the Decay $K_L \to \pi^0\nu\bar{\nu}$ and Other Rare Processes at Fermilab Using the Main Injector—KAMI (Fermilab, 2001).
55. KOPIO Collab. (I.-H. Chiang *et al.*), KOPIO— a Search for $K^0 \to \pi^0\nu\bar{\nu}$, BNL Proposal (1999).
56. Letters of Intent for Nuclear and Particle Physics Experiments at the J-PARC, J-PARC 03–6, KEK (2003); W. Chou *et al.*, *The Proton Driver Design Study*, FERMILAB-TM-2; R. Raja, hep-ph/0402022.
57. C. Kendziora *et al.*, Fermilab Publ.-02-241E (2002).
58. R. M. Djilkibaev and R. V. Konoplich, hep-ex/0312022.
59. J. L. Collar and Y. Giomataris, hep-ex/0009063.
60. R. M. Dzhilkibaev and V. M. Lobashev, Yad. Fiz. **49**, 622 (1989) [Sov. J. Nucl. Phys. **49**, 384 (1989)].

Translated by A. Isaakyan

Physics of Atomic Nuclei, Vol. 68, No. 7, 2005, pp. 1211–1217. Translated from Yadernaya Fizika, Vol. 68, No. 7, 2005, pp. 1260–1267.

ELEMENTARY PARTICLES AND FIELDS
Theory

Pion Electromagnetic Form Factor in QCD Sum Rules

V. V. Braguta[1)] and A. I. Onishchenko[2)]

Received March 22, 2004; in final form, July 13, 2004

Abstract—The electromagnetic form factor of the π meson is calculated in terms of the QCD sum rules for a pion axial-vector current with allowance made for the radiative QCD corrections. The derived dependence of the pion form factor on the square of the transferred momentum Q^2 is in good agreement with the experimental data. The QCD corrections are shown to make a large contribution, and they should be taken into account in a rigorous theoretical analysis. © *2005 Pleiades Publishing, Inc.*

1. INTRODUCTION

The electromagnetic form factors of hadrons have been studied for a long time. The first calculations in this field appeared immediately after it had become clear that the perturbative approach in QCD could also be used to analyze the high-energy asymptotic behavior of exclusive processes [1–3]. However, a comparison of the experimental data with QCD predictions led to the conclusion that, at momentum transfers on the order of several GeV, the contribution of the power corrections to the asymptotic predictions is significant and should be taken into account in theoretical calculations (see, e.g., the discussion in [4]).

In this paper, we use the approach of QCD sum rules [5] to calculate the pion electromagnetic form factor with the goal of simultaneously allowing for the hard rescattering (hard contribution) and the overlap of the pion wave functions in the initial and final states (soft contribution). In this approach, the soft contribution is represented by the leading triangular diagram, while the hard contribution is represented by the single-gluon exchange diagrams, which have a higher order in the expansion in terms of the strong constant α_s, and, as a result, it is suppressed compared to the soft contribution by the factor $\alpha_s/\pi \sim 0.1$. The suppression of the hard contribution is in complete agreement with the high-energy asymptotics of the pion electromagnetic form factor calculated in terms of perturbative QCD [1–3]:

$$F_\pi^{\text{hard}}(Q^2) = \frac{8\pi\alpha_s(Q^2)}{9} \times \int_0^1 dx \int_0^1 dy \frac{\phi_\pi(x)\phi_\pi(y)}{xyQ^2} = \frac{8\pi\alpha_s f_\pi^2}{Q^2}, \quad (1)$$

where the asymptotic wave function of the pion is used in the last equality. At asymptotically large momentum transfers $\mathcal{O}(\alpha_s/\pi)$, the suppression of the hard contribution is compensated for with an excess by its slower decrease with increasing Q^2. However, in the range of low momentum transfers, the soft contribution, which behaves as $1/Q^4$, is significant and could become equal to the contribution of the hard rescattering.

The pion electromagnetic form factor has been studied in terms of various approaches, such as the QCD sum rules [6–9], the light-cone sum rules [10–12], and the perturbative approach with allowance made for the higher radiative corrections [13–17] and for the dependence of the pion wave function on the transverse momentum [18–20]. There are also estimates of this form factor that use pseudoscalar currents as the pion interpolation currents [21–23].

In this paper, we analyze the three-point QCD sum rules with allowance made for the radiative α_s corrections in order to determine the pion form factor in the low-energy range of small momentum transfers. We took an axial-vector current as the pion interpolation current. The main result of our work is an explicit analytic expression for the radiative QCD corrections to the double spectral density, which is one of the main components in the formulation of the QCD sum rules for the pion electromagnetic form factor. It should be noted that the radiative corrections only to the reduced spectral density are known to date [24, 25].

The results obtained are in good agreement with the available experimental data. Here, we would like to emphasize that allowing for the radiative corrections is very important for a systematic analysis, because only in this way can we simultaneously take into account the hard and soft contributions to the pion form factor. Moreover, the numerical value of the

[1)]Institute for High Energy Physics, Protvino, Russia.
[2)]Department of Physics and Astronomy, Wayne State University, Detroit, USA.

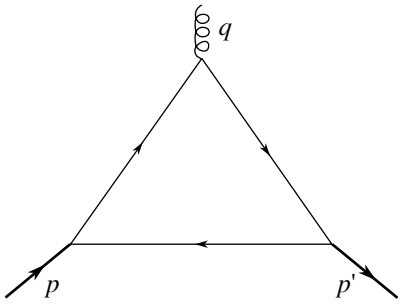

Fig. 1. Leading contribution.

corrections is fairly large, and they should be taken into account to make reliable theoretical predictions.

This paper is organized as follows. In Section 2, we describe the essence of the approach of QCD sum rules and give explicit expressions for the radiative corrections to the double spectral density. In Section 3, we perform a numerical analysis. Finally, in the last section, we discuss the results obtained.

2. DERIVATION OF THE QCD SUM RULES

We use the three-point QCD sum rules to determine the pion electromagnetic form factor. In this approach, the charged pion is described as the result of the action of an interpolation axial-vector current on the vacuum state. The matrix element of the axial-vector current in the vacuum–pion plates is defined as

$$\langle 0|\bar{u}\gamma_5\gamma_\mu d|\pi^-(p)\rangle = if_\pi p_\mu, \tag{2}$$

where $f_\pi = 131$ MeV. The pion electromagnetic form factor studied here is given by the hadron matrix element of the electromagnetic current:

$$\langle \pi(p')|j_\mu^{\rm el}|\pi(p)\rangle = F_\pi(Q^2)(p_\mu + p'_\mu), \tag{3}$$

where $j_\mu^{\rm el} = e_u\bar{u}\gamma_\mu u + e_d\bar{d}\gamma_\mu d$; p and p' are the pion momenta in the initial and final states, respectively; and $Q^2 = -q^2$ ($q = p - p'$) is the square of the transferred momentum.

In the QCD sum rules, the expression for the pion electromagnetic form factor is obtained from an analysis of the three-point correlation function

$$\Pi_{\mu\alpha\beta}(p,p',q) = i^2\int dxdye^{i(p'\cdot x - p\cdot y)} \tag{4}$$
$$\times\,\langle 0|T\{\bar{u}(x)\gamma_5\gamma_\alpha d(x), j_\mu^{\rm el}(0), (\bar{u}(y)\gamma_5\gamma_\beta d(y))^+\}|0\rangle.$$

This correlation function contains a large number of various tensor structures. The scalar functions at various Lorentz structures are functions of the kinematical invariants, i.e., $\Pi_i = \Pi_i(p^2, p'^2, q^2)$. In QCD, the expression for the three-point correlation function is calculated by using an operator-product expansion (OPE) for the time-ordered product of the currents in a deeply Euclidean region of momenta, $p^2, p'^2, q^2 < 0$. Apart from the leading perturbative contribution, OPE also yields the power-law corrections related to the vacuum condensates. Below, we will return to the discussion of the QCD expression for the three-point correlation function; now, we will discuss the relationship of our correlation function to the pion electromagnetic form factor. In the QCD sum rules, the relationship to the hadron characteristics is obtained by comparing the expression for the correlation function calculated in QCD with its spectral representation at $q^2 < 0$, where a model that describes the actual hadron spectrum most completely is taken as the spectral density. In our case, the following double spectral representation proves to be convenient:

$$\Pi_{\mu\alpha\beta}(p_1^2, p_2^2, q^2) = \frac{1}{(2\pi)^2} \tag{5}$$
$$\times\int\frac{\rho^{\rm phys}_{\mu\alpha\beta}(s_1,s_2,Q^2)}{(s_1-p_1^2)(s_2-p_2^2)}ds_1ds_2 + \text{subtractions}.$$

Under the assumption that the dispersion relation (5) converges rapidly, the physical spectral density is saturated by the low-lying hadron states plus the continuum that starts from certain threshold values of $s_1^{\rm th}$ and $s_2^{\rm th}$:

$$\rho^{\rm phys}_{\mu\alpha\beta}(s_1,s_2,Q^2) = \rho^{\rm res}_{\mu\alpha\beta}(s_1,s_2,Q^2) \tag{6}$$
$$+\,\theta(s_1-s_1^{\rm th})\theta(s_2-s_2^{\rm th})\rho^{\rm cont}_{\mu\alpha\beta}(s_1,s_2,Q^2),$$

where

$$\rho^{\rm res}_{\mu\alpha\beta}(s_1,s_2,Q^2) = \langle 0|\bar{u}\gamma_5\gamma_\alpha d|\pi^-(p')\rangle \tag{7}$$
$$\times\,\langle\pi^-(p')|j_\mu^{\rm el}|\pi^-(p)\rangle\langle\pi^-(p)|(\bar{u}\gamma_5\gamma_\beta d)^+|0\rangle$$
$$\times\,(2\pi)^2\delta(s_1)\delta(s_2) + \text{contribution from higher states}.$$

In the massless-quark approximation used in this paper, we set $m_\pi^2 = 0$. Thus, the pion contribution to the spectral density is given by $\rho^{\rm pion}_{\mu\alpha\beta} \sim f_\pi^2F_\pi(Q^2)p^\alpha p'^\beta(p^\mu + p'^\mu)$, and, as was pointed out in [6–9], the most convenient method of obtaining the sought form factor is to analyze the scalar amplitude Π at the most symmetric Lorentz structure $P_\mu P_\alpha P_\beta$ ($P = p_1 + p_2$).

Let us now return to the calculation of the QCD expression for the three-point correlation function. The contribution of the vacuum condensates has been well known for a long time [6–9] (its analytic expression can be found in Section 3). The perturbative contribution is convenient to calculate by using the double dispersion relation for the variables $s_1 = p^2$ and $s_2 = p'^2$ at $q^2 < 0$:

$$\Pi^{\rm pert}_{\mu\alpha\beta}(p^2,p'^2,q^2) = \frac{1}{(2\pi)^2} \tag{8}$$

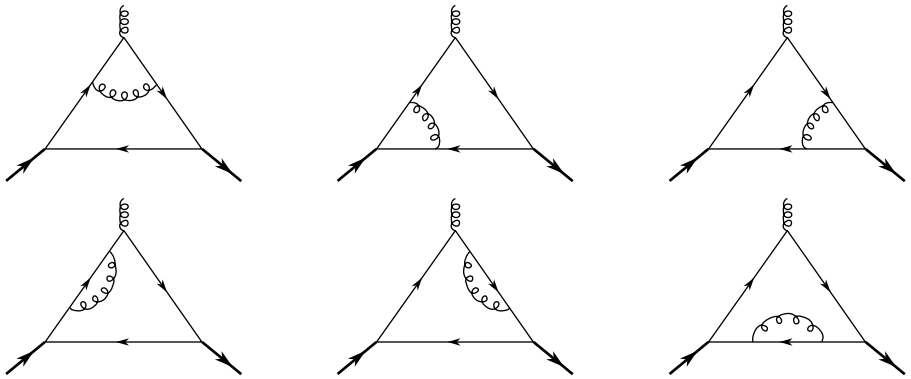

Fig. 2. Single-gluon radiative corrections.

$$\times \int \frac{\rho^{\text{pert}}_{\mu\alpha\beta}(s_1, s_2, Q^2)}{(s_1 - p^2)(s_2 - p'^2)} ds_1 ds_2 + \text{subtractions}.$$

The integration domain in (8) is defined by the inequality[3)]

$$-1 \le \frac{s_2 - s_1 - q^2}{\lambda^{1/2}(s_1, s_2, q^2)} \le 1, \tag{9}$$

where

$$\lambda(x_1, x_2, x_3) = (x_1 + x_2 - x_3)^2 - 4x_1x_2. \tag{10}$$

We will seek the double spectral density $\rho^{\text{pert}}_{\mu\alpha\beta}(s_1,s_2,Q^2)$ in the form of a series in the strong coupling constant:

$$\rho^{\text{pert}}_{\mu\alpha\beta}(s_1, s_2, Q^2) = \rho^{(0)}_{\mu\alpha\beta}(s_1, s_2, Q^2) + \frac{\alpha_s}{4\pi}\rho^{(1)}_{\mu\alpha\beta}(s_1, s_2, Q^2) + \dots. \tag{11}$$

Only the diagram shown in Fig. 1 contributes to the correlation function in the leading approximation in coupling constant. In the next order, we already have six diagrams shown in Fig. 2. We use the standard Cutkosky rules to calculate the double spectral density. Note also that the kinematical region $q^2 < 0$ is free from non-Landau singularities, and using the Cutkosky rules to determine the spectral density and the domain of integration over the variables s_1 and s_2 is completely justifiable. In the Born approximation, the expression for the scalar spectral density at the most symmetric Lorentz structure $P_\mu P_\alpha P_\beta$ can be easily derived and is given by

$$\rho^{(0)}_{\mu\alpha\beta}(s_1, s_2, Q^2) = \frac{3Q^4}{4}\frac{1}{k^{7/2}} \times \Big(3k(s_1 + s_2 + Q^2)(s_1 + s_2 + 2Q^2) - k^2 - 5Q^2(s_1 + s_2 + Q^2)^3\Big) P_\mu P_\alpha P_\beta + \dots, \tag{12}$$

[3)]In our case, this inequality holds for any $s_1, s_2 > 0$.

where $k = \lambda(s_1, s_2, -Q^2)$. The complete analytic expression for $\rho^{(0)}_{\mu\alpha\beta}$ can be found in [7]. The procedure for calculating the radiative corrections to the double spectral density is also quite clear. Here, it is necessary to consider all the possible sections of the diagrams in Fig. 2. However, the presence of collinear and soft infrared divergences calls for regularizing the emerging divergences at the intermediate stages, which makes the analytic calculation fairly complicated. The particular features of this calculation will be presented in the near future in a separate publication. Here, we only give the final result. The calculation can be simplified significantly by expanding the spectral density with respect to the various tensor structures under the conditions $\rho_{\mu\alpha\beta}q_\mu = \rho_{\mu\alpha\beta}p_\alpha = \rho_{\mu\alpha\beta}p'_\beta = 0$:

$$\begin{aligned}
\rho_{\mu\alpha\beta} &= A_1[(Q^2 + x)p_1^\alpha - (x + y)p_2^\alpha] \\
&\times [(y - x)p_1^\beta + (Q^2 + x)p_2^\beta] \\
&\times [(Q^2 + y)p_1^\mu + (Q^2 - y)p_2^\mu] \\
&- \frac{1}{2}A_2[(Q^2 + y)p_1^\mu + (Q^2 - y)p_2^\mu] \\
&\times [(Q^2 + x)g^{\alpha\beta} - 2p_1^\beta p_2^\alpha] \\
&- \frac{1}{2}A_3[(Q^2 + x)p_1^\alpha - (x + y)p_2^\alpha] \\
&\times [2(p_2^\beta - p_1^\beta)p_2^\mu + (Q^2 + y)g^{\mu\beta}] \\
&- \frac{1}{2}A_4[(x - y)p_1^\beta - (Q^2 + x)p_2^\beta] \\
&\times [2(p_2^\alpha - p_1^\alpha)p_1^\mu + (y - Q^2)g^{\mu\alpha}],
\end{aligned} \tag{13}$$

where $x = s_1 + s_2$ and $y = s_1 - s_2$. The four independent structures A_i (we omitted the dependence on the kinematical variables) can be determined by solving

the system of linear equations

$$I_1 = \rho_{\mu\alpha\beta} p_1^\mu p_2^\alpha p_1^\beta \tag{14}$$
$$= \frac{k^2}{8}\Big(kA_1 - A_2 - A_3 - A_4\Big),$$
$$I_2 = \rho_{\mu\alpha\beta} p_1^\mu g^{\alpha\beta} \tag{15}$$
$$= \frac{k}{4}(x+Q^2)\Big(kA_1 - 3A_2 - A_3 - A_4\Big),$$
$$I_3 = \rho_{\mu\alpha\beta} p_2^\alpha g^{\mu\beta} \tag{16}$$
$$= \frac{k}{4}(y+Q^2)\Big(kA_1 - A_2 - 3A_3 - A_4\Big),$$
$$I_4 = \rho_{\mu\alpha\beta} p_1^\beta g^{\mu\alpha} \tag{17}$$
$$= -\frac{k}{4}(y-Q^2)\Big(kA_1 - A_2 - A_3 - 3A_4\Big).$$

The analytic expressions for I_i (the functional dependence on the kinematical variables is implied) are derived when calculating the diagrams and are given by ($s_3 = Q^2$)

$$k^{1/2} I_1 = -s_1^3 + s_2 s_1^2 + s_2^2 s_1 - s_2^3 \tag{18}$$
$$+ (s_1+s_2)s_3^2 - s_1^2 s_3 - s_2^2 s_3 + s_1 s_2 s_3$$
$$\times \Big[-16\log^2(v_1) - 16\log(v_3)\log(v_1)$$
$$- 16\log(v_4)\log(v_1) + 2\log(v_1) - 4\log^2(v_3)$$
$$- 4\log^2(v_4) - 2\log(v_2) - 2\log(v_3)$$
$$- 8\log(v_3)\log(v_4) - 8\mathrm{Li}_2\left(\frac{x_2}{x_1}\right) - 8\mathrm{Li}_2\left(\frac{y_1}{y_2}\right)$$
$$- 8\mathrm{Li}_2\left(\frac{z_1}{s_1}\right) - 8\mathrm{Li}_2\left(\frac{z_1}{s_2}\right) + 8\mathrm{Li}_2\left(\frac{z_1}{z_2}\right)\Big],$$
$$k^{1/2} I_2 = -2s_1^2 - 2s_2^2 + 2s_3^2 - 8s_1 s_2 \tag{19}$$
$$+ s_1 s_2 \Big[-32\log^2(v_1) - 32\log(v_3)\log(v_1)$$
$$- 32\log(v_4)\log(v_1) + 4\log(v_1) - 8\log^2(v_3)$$
$$- 8\log^2(v_4) - 4\log(v_2) - 4\log(v_3)$$
$$- 16\log(v_3)\log(v_4) - 16\mathrm{Li}_2\left(\frac{x_2}{x_1}\right) - 16\mathrm{Li}_2\left(\frac{y_1}{y_2}\right)$$
$$- 16\mathrm{Li}_2\left(\frac{z_1}{s_1}\right) - 16\mathrm{Li}_2\left(\frac{z_1}{s_2}\right) + 16\mathrm{Li}_2\left(\frac{z_1}{z_2}\right)\Big],$$
$$k^{1/2} I_3 = -2s_1^2 + 2s_2^2 + 2s_3^2 - 8s_2 s_3 \tag{20}$$
$$+ s_2 s_3 \Big[-32\log^2(v_1) - 32\log(v_3)\log(v_1)$$
$$- 32\log(v_4)\log(v_1) + 4\log(v_1) - 8\log^2(v_3)$$
$$- 8\log^2(v_4) - 4\log(v_2) - 4\log(v_3)$$
$$- 16\log(v_3)\log(v_4) - 16\mathrm{Li}_2\left(\frac{x_2}{x_1}\right) - 16\mathrm{Li}_2\left(\frac{y_1}{y_2}\right)$$
$$- 16\mathrm{Li}_2\left(\frac{z_1}{s_1}\right) - 16\mathrm{Li}_2\left(\frac{z_1}{s_2}\right) + 16\mathrm{Li}_2\left(\frac{z_1}{z_2}\right)\Big],$$
$$k^{1/2} I_4 = 2s_1^2 - 2s_2^2 + 2s_3^2 - 8s_1 s_2 \tag{21}$$
$$+ s_1 s_3 \Big[-32\log^2(v_1) - 32\log(v_3)\log(v_1)$$
$$- 32\log(v_4)\log(v_1) + 4\log(v_1) - 8\log^2(v_3)$$
$$- 8\log^2(v_4) - 4\log(v_2) - 4\log(v_3)$$
$$- 16\log(v_3)\log(v_4) - 16\mathrm{Li}_2\left(\frac{x_2}{x_1}\right) - 16\mathrm{Li}_2\left(\frac{y_1}{y_2}\right)$$
$$- 16\mathrm{Li}_2\left(\frac{z_1}{s_1}\right) - 16\mathrm{Li}_2\left(\frac{z_1}{s_2}\right) + 16\mathrm{Li}_2\left(\frac{z_1}{z_2}\right)\Big],$$

where we used the following notation:

$$x_1 = \frac{1}{2}(s_1 - s_2 - Q^2) - \frac{1}{2}\sqrt{k}, \tag{22}$$
$$x_2 = \frac{1}{2}(s_1 - s_2 - Q^2) + \frac{1}{2}\sqrt{k}, \tag{23}$$
$$y_1 = \frac{1}{2}(s_1 + Q^2 - s_2) - \frac{1}{2}\sqrt{k}, \tag{24}$$
$$y_2 = \frac{1}{2}(s_1 + Q^2 - s_2) + \frac{1}{2}\sqrt{k}, \tag{25}$$
$$z_1 = \frac{1}{2}(s_1 + s_2 + Q^2) - \frac{1}{2}\sqrt{k}, \tag{26}$$
$$z_2 = \frac{1}{2}(s_1 + s_2 + Q^2) + \frac{1}{2}\sqrt{k}, \tag{27}$$
$$v_1 = \frac{1}{2s_1}(s_1 - s_2 - Q^2) + \frac{1}{2s_1}\sqrt{k}, \tag{28}$$
$$v_2 = \frac{1}{2s_2}(s_1 - s_2 + Q^2) + \frac{1}{2s_2}\sqrt{k}, \tag{29}$$
$$v_3 = \frac{1}{2s_1}(s_1 + s_2 + Q^2) + \frac{1}{2s_1}\sqrt{k}, \tag{30}$$
$$v_4 = \frac{s_1}{Q^2}, \tag{31}$$
$$v_5 = \frac{s_2}{Q^2}, \tag{32}$$
$$v_6 = 1 - \frac{z_1}{z_2}. \tag{33}$$

We checked that all infrared and ultraviolet divergences cancel out in the sum of the diagrams, as they must when use is made of axial-vector interpolation currents. The radiative corrections to the scalar density at the most symmetric Lorentz structure $P_\mu P_\alpha P_\beta$ are given by

$$\rho^{(1)}_{\mu\alpha\beta} = \frac{Q^2}{k^3}\Big\{\frac{1}{2}(x_1+x_2)kI_3 \tag{34}$$
$$+ (k - 5(x_1+x_2)(y_1+y_2))I_1$$

$$+\frac{1}{2}(y_1+y_2)kI_4+\frac{1}{2}\frac{k}{z_1+z_2}$$
$$\times((x_1+x_2)(y_1+y_2)-k)I_2\Big\}P_\mu P_\alpha P_\beta+\ldots.$$

The expression for the radiative corrections to the spectral density in the limit $Q^2\to\infty$ takes the form

$$\rho^{(1)}_{\mu\alpha\beta}=\left\{\frac{2}{Q^2}-10\frac{s_1+s_2}{Q^4}\right. \tag{35}$$
$$\left.-2\frac{s_1+s_2}{Q^4}\log\left(\frac{s_1s_2}{Q^4}\right)\right\}P_\mu P_\alpha P_\beta+\ldots.$$

Here, we wish to make several remarks. First, we see that there are no double logarithms in our result. In general, their presence might be expected, because the diagrams in Fig. 2 contain the Sudakov vertex, the corrections to the q vertex. In fact, the result for the gluon corrections to the electromagnetic vertex (with the addition of the self-energy insets divided by two to cancel the ultraviolet divergences) contains double logarithms and agrees with the result of [24, 25] in the limit $Q^2\to\infty$. However, our results for the corrections to the vertices p_1 and p_2 also contain double logarithms (an analog of the double logarithms that appear in the perturbative description of the pion electromagnetic form factor [18, 19]). The double logarithms cancel out in the sum of all diagrams. Second, using the expression for the spectral density at large Q^2 and the threshold values of $s_1^{\rm th}$ and $s_2^{\rm th}$ equal to $4\pi^2f_\pi^2$, we can easily show that, in the limit $Q^2\to\infty$, the QCD sum rules reproduce the leading high-energy asymptotics for the pion electromagnetic form factor (1) predicted by perturbative QCD using the asymptotic wave function of the pion ($\phi_\pi^{\rm as}(x)=6f_\pi x(1-x)$). Let us now consider a numerical analysis.

3. NUMERICAL RESULTS

We used the Borel scheme of the QCD sum rules to obtain the numerical results. In this scheme, the use of the Borel transformation in two variables, s_1 and s_2, also makes it possible to get rid of the unknown polynomial terms in p_1^2 and p_2^2 in the spectral representation for the correlation function. The Borel transformation of the three-point correlation function is defined as

$$\Phi(M_1^2,M_2^2,q^2)\equiv\hat{B}_{12}\Pi_i(s_1,s_2,q^2) \tag{36}$$
$$=\lim_{n,m\to\infty}\left\{\frac{s_2^{n+1}}{n!}\left(-\frac{d}{ds_2}\right)^n\frac{s_1^{m+1}}{m!}\left(-\frac{d}{ds_1}\right)\Big|_{s_1=mM_1^2,s_2=nM_2^2}\right\}\Pi_i(s_1,s_2,q^2).$$

The Borel transformations (36) of expressions (8) and (5) then yield

$$\Phi^{(\rm pert|phys)}(M_1^2,M_2^2,q^2)=\frac{1}{(2\pi)^2} \tag{37}$$
$$\times\int_0^\infty ds_1\int_0^\infty ds_2\exp\left[-\frac{s_1}{M_1^2}-\frac{s_2}{M_2^2}\right]$$
$$\times\rho^{(\rm pert|phys)}(s_1,s_2,q^2),$$

where $\rho^{(\rm pert|phys)}(s_1,s_2,q^2)$ is the scalar spectral density at the most symmetric Lorentz structure $P_\mu P_\alpha P_\beta$. Below, we assume that $M_1^2=M_2^2=M^2$. In the case where M^2 is chosen to be ~1 GeV^2, the right-hand side of (37) for the physical spectral density is saturated by the lightest hadron state, while the contribution of the higher states is suppressed.

Equating the Borel images of the theoretical and physical parts of the QCD sum rules yields

$$F_\pi(Q^2) \tag{38}$$
$$=\frac{4}{f_\pi^2}\left(\Phi(M^2,q^2)+\frac{\alpha_s}{48\pi M^2}\langle0|G^a_{\mu\nu}G^a_{\mu\nu}|0\rangle\right.$$
$$\left.+\frac{52\pi}{81M^4}\alpha_s\langle0|\bar\psi\psi|0\rangle^2\left(1+\frac{2Q^2}{13M^2}\right)\right),$$

where

$$\Phi(M^2,q^2)=\frac{1}{(2\pi)^2} \tag{39}$$
$$\times\int_0^{s_0}dx\exp\left[-\frac{x}{M^2}\right]\int_0^x dy\rho^{\rm pert}(s_1,s_2,q^2).$$

We subtracted the continuum contribution by using the so-called triangular model. To check the stability of our results to the choice of a model for the

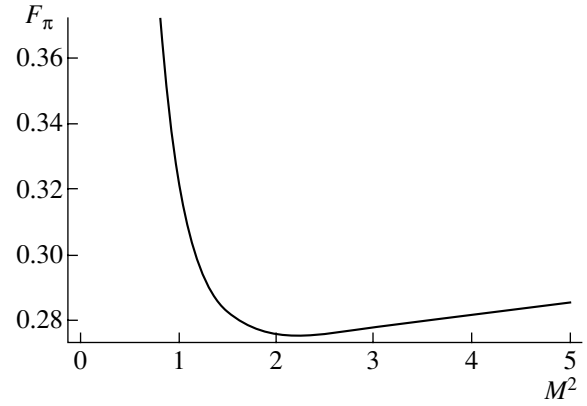

Fig. 3. M^2 dependence of the electromagnetic form factor F_π at $Q^2 = 1$ GeV^2.

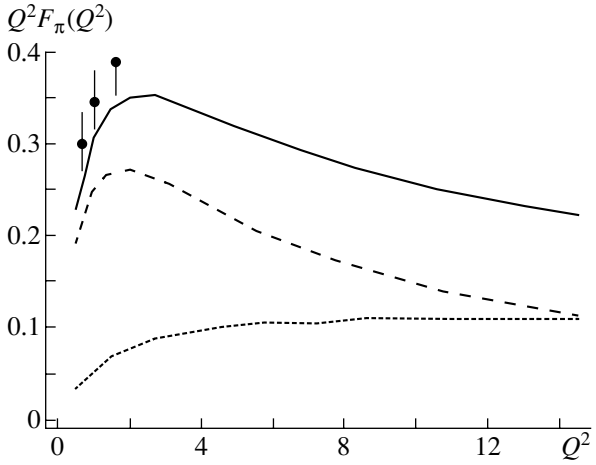

Fig. 4. Q^2 dependence of the pion electromagnetic form factor. The solid curve corresponds to the sum of the leading approximation (dashed curve) and the radiative corrections (dotted curve); the dots represent the experimental data [27].

continuum subtraction, we also performed calculations with the standard "square" model. Both models were found to yield similar results for the pion electromagnetic form factor, provided that the continuum thresholds were chosen so that $s_0 \sim 1.5 s_1^{\text{th}}$.[4)] In our calculations, we took $s_0 = 0.9$ GeV.[5)]

This value agrees with the continuum threshold of about 0.6 GeV^2 used in the two-point sum rules with axial-vector currents. In our numerical calculations, we used a two-loop running strong coupling constant with $\Lambda_{\text{QCD}} = 325$ MeV and fixed the scale μ of the coupling constant at 2 GeV. This choice agrees with the results of [25], where it is argued that the strong coupling constant should be "frozen" at $\alpha_s \sim 0.3$ when describing the pion electromagnetic form factor in the region $Q^2 < 10$ GeV^2. In Fig. 3, the pion electromagnetic form factor is plotted against the Borel parameter M^2 at $Q^2 = 1$ GeV^2. As we see from this figure, the "stability plateau" lies in the region $M^2 > 2$ GeV^2. Choosing the Borel parameter $M^2 = 2$ GeV^2, we can immediately construct the dependence of the form factor under study on the transferred momentum. However, having fixed the Borel parameter, we restrict the Q^2 region where our results may be considered reliable. This is easy to understand if we note that the perturbative contribution to the form factor decreases in proportion to Q^{-2} in the limit of high momentum transfers, while the power-law corrections increase in proportion to Q^2. It turns out that the sum rules are inapplicable even at $Q^2 > 4$. Therefore, we consider the limit of an infinite Borel parameter in order to obtain the dependence of the pion form factor in the entire Q^2 region accessible to experimental study. In other words, we employ an approach known as local duality; the continuum threshold [25, 26] is fixed by the relation $s_1^{\text{th}} = s_2^{\text{th}} = 4\pi^2 f_\pi^2/(1 + \alpha_s/\pi) = 0.6$ GeV^2 following from the requirement that the Ward identity for the pion electromagnetic form factor with the inclusion of the electromagnetic corrections be satisfied ($F_\pi(0) = 1$). Figure 4 presents our estimates for the dependence of the pion electromagnetic form factor on the momentum transfer as obtained in terms of local duality.

4. CONCLUSION

In this paper, we have calculated the pion electromagnetic form factor in terms of the QCD sum rules using axial-vector interpolation currents for pions in the initial and final states. In our calculations, we have taken into account the single-gluon QCD radiative corrections. The derived Q^2 dependence of the pion form factor is in agreement with the available experimental data. The radiative corrections to the double spectral density used to construct the sum rules with axial-vector interpolation currents have been calculated for the first time. Since the numerical value of these corrections is large, they should be taken into account in calculations.

ACKNOWLEDGMENTS

The work by V.V. Braguta was supported in part by the Russian Foundation for Basic Research (project no. 01-02-16585), the Ministry of Education of the Russian Federation (project no. E02-31-96), the

[4)] More detailed information about the various subtraction schemes can be found in [7].

[5)] In general, the continuum threshold can be determined from the ratio of the nonperturbative corrections to the leading perturbative contribution.

CRDF (grant no. MO-011-0), and the Dinastiya Foundation. The work by A.I. Onishchenko was supported in part by the NSF (grant no. PHY-0244853) and the US Department of Energy (grant no. DE-FG02-96ER41005).

REFERENCES

1. G. P. Lepage and S. J. Brodsky, Phys. Rev. D **22**, 2157 (1980).
2. A. V. Efremov and A. V. Radyushkin, Phys. Lett. B **94**, 245 (1980).
3. V. L. Chernyak, A. R. Zhitnitsky, and V. G. Serbo, Pis'ma Zh. Éksp. Teor. Fiz. **26**, 760 (1977) [JETP Lett. **26**, 594 (1977)].
4. A. V. Radyushkin, Few Body Syst., Suppl. **11**, 57 (1999); A. Szczepaniak, A. Radyushkin, and C. R. Ji, Phys. Rev. D **57**, 2813 (1998).
5. M. A. Shifman, A. I. Vainshtein, and V. I. Zakharov, Nucl. Phys. B **147**, 385, 448 (1979).
6. B. L. Ioffe and A. V. Smilga, Phys. Lett. B **114**, 353 (1982).
7. B. L. Ioffe and A. V. Smilga, Nucl. Phys. B **216**, 373 (1983).
8. V. A. Nesterenko and A. V. Radyushkin, Phys. Lett. B **115**, 410 (1982).
9. V. A. Nesterenko and A. V. Radyushkin, Pis'ma Zh. Éksp. Teor. Fiz. **39**, 576 (1984) [JETP Lett. **39**, 707 (1984)].
10. V. M. Braun and I. E. Halperin, Phys. Lett. B **328**, 457 (1994).
11. V. M. Braun, A. Khodjamirian, and M. Maul, Phys. Rev. D **61**, 073004 (2000).
12. J. Bijnens and A. Khodjamirian, Eur. Phys. J. C **26**, 67 (2002); hep-ph/0206252.
13. R. D. Field, R. Gupta, S. Otto, and L. Chang, Nucl. Phys. B **186**, 429 (1981).
14. F. M. Dittes and A. V. Radyushkin, Yad. Fiz. **34**, 529 (1981) [Sov. J. Nucl. Phys. **34**, 293 (1981)].
15. A. V. Radyushkin and R. S. Khalmuradov, Yad. Fiz. **42**, 458 (1985) [Sov. J. Nucl. Phys. **42**, 289 (1985)].
16. E. Braaten and S. M. Tse, Phys. Rev. D **35**, 2255 (1987).
17. B. Melic, B. Nizic, and K. Passek, Phys. Rev. D **60**, 074004 (1999); hep-ph/9802204.
18. J. Botts and G. Sterman, Nucl. Phys. B **325**, 62 (1989).
19. H. n. Li and G. Sterman, Nucl. Phys. B **381**, 129 (1992).
20. R. Jakob and P. Kroll, Phys. Lett. B **315**, 463 (1993); **319**, 545(E) (1993); hep-ph/9306259.
21. H. Forkel and M. Nielsen, Phys. Lett. B **345**, 55 (1995); hep-ph/9408396.
22. P. Faccioli, A. Schwenk, and E. V. Shuryak, Phys. Rev. D **67**, 113009 (2003); hep-ph/0202027.
23. V. V. Braguta and A. I. Onishchenko, hep-ph/0311146.
24. A. P. Bakulev, private communication.
25. A. P. Bakulev, A. V. Radyushkin, and N. G. Stefanis, Phys. Rev. D **62**, 113001 (2000); hep-ph/0005085.
26. A. P. Bakulev, K. Passek-Kumericki, W. Schroers, and N. G. Stefanis, hep-ph/0405062.
27. J. Volmer *et al.* (The Jefferson Lab F(pi) Collab.), Phys. Rev. Lett. **86**, 1713 (2001); nucl-ex/0010009.

Translated by M. Kobrinsky

Physics of Atomic Nuclei, Vol. 68, No. 7, 2005, pp. 1218–1226. Translated from Yadernaya Fizika, Vol. 68, No. 7, 2005, pp. 1268–1276.

ELEMENTARY PARTICLES AND FIELDS
Theory

On the Stability of a Self-Similar Spherical Bubble of a Scalar Higgs Field in de Sitter Space

N. A. Voronov*, A. L. Dyshko[1)], and N. B. Konyukhova[1)]**

Institute of Theoretical and Experimental Physics,
Bol'shaya Cheremushkinskaya ul. 25, Moscow, 117259 Russia

Received April 7, 2004; in final form, September 14, 2004

Abstract—An exact generalized discontinuous solution of the spherical-bubble type is obtained for a scalar Higgs field in de Sitter space. It is shown that the radius of such a generalized bubble evolves in accordance with one of the exact solutions to a dynamical problem considered previously for the bubble radius in the thin-wall approximation, where the bubble-wall thickness is negligible in relation to the bubble radius. Both the generalized solution and the self-similar bubble-type solution that was obtained earlier for the Higgs field in de Sitter space are studied for stability: it is shown that the former is stable, while the latter is unstable in this space. A physical interpretation of the reasons for the instability of the self-similar solution is given. © *2005 Pleiades Publishing, Inc.*

1. INTRODUCTION: ON SOLUTIONS TO THE NONLINEAR EQUATION FOR THE BUBBLE RADIUS IN THE THIN-WALL APPROXIMATION

In de Sitter space, the problem of the collapse of a spherical bubble formed by a scalar Higgs field described by the action functional

$$S_{\rm H} = \int \sqrt{-g}[g^{ik}\varphi_{,i}\varphi_{,k}/2 - U(\varphi)]d^4x, \qquad (1.1)$$

where the potential is

$$U(\varphi) = \lambda^2(\varphi^2 - \nu^2)^2, \qquad (1.2)$$

was considered in [1]. The above equations are written in the system of units where $c = \hbar = 1$. In terms of spherical coordinates (r, θ, ϕ), the metric of de Sitter space has the form [2, 3]

$$ds^2 = dt^2 - a^2(t)[dr^2 + r^2(d\theta^2 + \sin^2\theta d\phi^2)], \qquad (1.3)$$
$$a(t) = a_0\exp(Ht),$$

where H is the Hubble constant and $0 < a_0 = \text{const}$. By a bubble, we mean a spherically symmetric solution $\varphi(r,t)$ to the field equation such that it is defined and bounded over the whole space, tends to one of the vacua for $r \to \infty$ at any t, and differs from $\varphi_\pm \equiv \pm\nu$. A solution to the equation $\varphi(R(t),t) = 0$ is referred to as the radius $R(t)$ of a bubble (if this equation has more than one solution, we say that we are dealing here with embedded bubbles).

In [1], the problem of a bubble in de Sitter space was considered in the approximation of an infinitely thin wall, in which case the thickness of the bubble wall can be disregarded against the bubble radius, the intrinsic gravitational field of the bubble not being taken into account. In this approximation, the time evolution of the bubble radius is described by the equation

$$\ddot{R} + \{2/[a^2(t)R] + 3H\dot{R}\} \times [1 - a^2(t)\dot{R}^2] + H\dot{R} = 0, \quad t > 0, \qquad (1.4)$$

the initial conditions being taken in the form

$$R(0) = R_0 > 0, \quad \dot{R}(0) = 0. \qquad (1.5)$$

Equation (1.4) follows from the "folded action" [1]

$$S_w = -4\pi\mu\int a^2R^2\sqrt{1 - a^2\dot{R}^2}dt$$

($\mu = 4\sqrt{2}\lambda\nu^3/3$ is the surface energy density), which is obtained by integrating the total action functional $S_{\rm H}$ (1.1) with respect to the radius r with the field φ in the form of a wall. Equation (1.4) was also obtained in [1] from the exact equation for the Higgs field in de Sitter space in the spherically symmetric case, that is, from the equation

$$\varphi_{tt} + 3H\varphi_t - \varphi_{rr}/a^2 - 2\varphi_r/(a^2r) + 4\lambda^2\varphi(\varphi^2 - \nu^2) = 0, \qquad (1.6)$$

by constructing a solution in the form $\varphi_b(r,t) \approx \nu\tanh(\alpha(r,t)/l)$, where α is an unknown function,

[1)]Dorodnitsyn Computing Center, Russian Academy of Sciences, ul. Vavilova 40, Moscow, Russia.
*e-mail: voronov@heron.itep.ru
**e-mail: nadja@ccas.ru

$l = 1/(a_0\lambda\nu\sqrt{2})$ [$R(t)$ is a solution to the equation $\alpha(R(t), t) = 0,\ t \geq 0$], and by formally going over to the limit $l \to 0$ ($\lambda \to \infty$). We note that, for a flat spacetime, there exist a few different methods for deriving an equation that describes the evolution of the spherical-bubble radius (see, for example, [4] and references therein).

In order to analyze Eq. (1.4), it is convenient to go over to the conformal time τ,

$$\tau = -\exp(-Ht)/(a_0H), \qquad (1.7)$$
$$\tau(0) = \tau_0, \quad \tau(\infty) = 0,$$

where $\tau_0 = -(a_0H)^{-1}$, $(-\infty < t < \infty) \Leftrightarrow (-\infty < \tau \leq 0)$. As a result, the metric (1.3) of de Sitter space becomes conformally flat:

$$ds^2 = H^{-2}\tau^{-2}[d\tau^2 - dr^2 - r^2(d\theta^2 + \sin^2\theta d\phi^2)]. \qquad (1.8)$$

If, in expression (1.8), we extend the domain of the variable τ to the whole real axis, $-\infty < \tau < \infty$, then the coordinate system will cover the entire de Sitter space; that is, it will be geodesically complete [2].

The problem specified by Eqs. (1.4) and (1.5) reduces to the following form in terms of the conformal time τ (1.7) ($dR/d\tau \equiv R'$):

$$R'' = -(2/R - 3R'/\tau)(1 - R'^2), \qquad (1.9)$$
$$\tau_0 \leq \tau < 0,$$

$$R(\tau_0) = R_0, \quad R'(\tau_0) = 0. \qquad (1.10)$$

In [1], it was shown that Eq. (1.9), which describes the evolution of the bubble radius $R(\tau)$, possesses the following properties:

(i) For the problem specified by Eqs. (1.9) and (1.10), there exists a value of the initial radius R_0 (we denote it by R_c and refer to it as a critical radius) such that, for any $R_0 > R_c$, the bubble does not undergo a collapse in the course of its evolution, $R(0) = R_f \neq 0$ (or, in terms of the originally used time t, $R(\infty) = R_f \neq 0$), the following estimate being valid:

$$2/[\sqrt{3}(1+\sqrt{2})a_0H] < R_c < 6\sqrt{2/3}/(7a_0H). \qquad (1.11)$$

From numerical calculations, it was found that $R_c = D/(a_0H)$, where $D \approx 0.6204032$. We also present a rough estimate of the final radius R_f as a function of the initial radius $R_0 > R_c$ (for large R_0):

$$R_f \approx \left[R_0 + \sqrt{R_0^2 - (a_0H)^{-2}}\right]/2. \qquad (1.12)$$

(ii) Equation (1.9) possesses the family of particular solutions

$$R(\tau, d) = \pm\tau + d, \qquad (1.13)$$

where d is an arbitrary constant, and the solutions

$$R(\tau) = \pm\sqrt{2/3}\tau. \qquad (1.14)$$

Comment 1. Equation (1.9) is invariant under the transformation $R_{\text{new}} = NR$, $\tau_{\text{new}} = N\tau$, where N is a dimensional constant. We can then treat R and τ in Eq. (1.9) as dimensionless quantities and consider this equation on the interval $(-1, 0)$ under the conditions $R(-1) = \tilde{R}_0 > 0$ and $R'(-1) = 0$, whence, for the solution to the problem specified by Eqs. (1.9) and (1.10) for $R_0 = \tilde{R}_0/(a_0H)$, one obtains $R(\tau, \tau_0) = R(\tau, -1)/(a_0H)$. It follows, among other things, that, in the estimate for $R_c(\tau_0) = D/(a_0H)$, $D = R_c(-1)$; from Eqs. (1.11) and (1.12), it follows that $2/[\sqrt{3}(1+\sqrt{2})] < R_c(-1) < 6\sqrt{2/3}/7$, $R_f(-1) \approx [\tilde{R}_0 + \sqrt{\tilde{R}_0^2 - 1}]/2$.

2. SELF-SIMILAR BUBBLE-TYPE SOLUTIONS WITH A WALL OF FINITE WIDTH AND GENERALIZED DISCONTINUOUS SOLUTIONS

For a scalar field in de Sitter space, we write Eq. (1.6) in terms of the conformal time (1.7) as

$$\varphi_{\tau\tau} - 2\varphi_\tau/\tau - \varphi_{rr} - 2\varphi_r/r \qquad (2.1)$$
$$+ 4\lambda^2\varphi(\varphi^2 - \nu^2)/(H\tau)^2 = 0.$$

In this equation, it is convenient to go over to the dimensionless variables $\varphi_{\text{new}} = \varphi/\nu$, $\tau_{\text{new}} = (a_0H/\nu)\tau$, and $r_{\text{new}} = (a_0H/\nu)r$. Equation (2.1) then assumes the final form (we suppress the index "new" here)

$$\varphi_{\tau\tau} - 2\varphi_\tau/\tau - \varphi_{rr} - 2\varphi_r/r \qquad (2.2)$$
$$+ 4C^2\varphi(\varphi^2 - 1)/\tau^2 = 0,$$

where

$$C = \lambda\nu/H \qquad (2.3)$$

is a dimensionless constant. We now estimate C for a realistic physical situation, setting $H \approx 10^{-10}\ \text{yr}^{-1}$ [3] and $\lambda\nu \sim m_p$ [5] (where m_p is the proton mass). This yields $C \sim 10^{41}$.

We are interested in the solution $\varphi(r, \tau)$ to Eq. (2.2) such that it is defined and bounded over the entire space, satisfies the condition

$$\lim_{r\to\infty} \varphi^2(r, \tau) = 1 \qquad (2.4)$$

for any τ, and differs from $\varphi_\pm \equiv \pm 1$. As was indicated above, such a solution is referred to as a spherical bubble; if a given solution depends on C, it corresponds to a bubble whose wall has a finite width $l \sim 1/C$. Further, we define the bubble radius $R(\tau)$ as a solution to the equation $\varphi(R(\tau), \tau) = 0$.

Table

C	c_0	b_0	ξ_b
2	0.6774	−0.8500	−0.7950
4	0.9892	−0.9993	−0.8139
5	0.9980	−0.99994	−0.8150
10	$1-5\times10^{-7}$	$-1+2\times10^{-10}$	$-0.8161\approx-\sqrt{2/3}$

There arises the natural question of whether Eq. (2.2) has solutions belonging to the type of a bubble whose radius would possess, as the wall width tends to zero ($l\to 0$; that is, $C\to\infty$), the properties that were listed in Section 1 for solutions to Eq. (1.9).

First of all, it would be of interest to verify whether a bubble undergoes a collapse if its initial radius exceeds a critical value. However, we are unaware of relevant calculations [among the reasons behind the computational difficulties that arise in solving the problem specified by Eqs. (2.2) and (2.4), we can indicate the absence of a conserved energy integral, which would make it possible to test the correctness of the computations, and the emergence of large gradients in the solution].

The problem of bubbles collapsing at $\tau=0$ (that is, within an infinite time t) can be solved more successfully. In particular, the problem specified by Eqs. (2.2) and (2.4) has C-independent generalized discontinuous solutions of the shock-wave type; that is,

$$\tilde\varphi(r,\tau)=\theta(\tau\pm r), \tag{2.5}$$

where $\theta(x)$ is the signum function of x—specifically, $\theta(x)=x/|x|$ for $x\neq 0$, $\theta(0)=0$, and $\theta'(x)=2\delta(x)$. Indeed, we have

$$\tilde\varphi_{\tau\tau}=\tilde\varphi_{rr},\quad \tilde\varphi_r/r=\pm2\delta(\tau\pm r)/r=-\tilde\varphi_\tau/\tau,$$
$$\tilde\varphi(\tilde\varphi^2-1)\equiv 0.$$

The bubble radius for the function in (2.5) changes with the time τ according to the law

$$r=R(\tau)=\mp\tau.$$

Thus, the original problem specified by Eqs. (2.2) and (2.4) possesses solutions (2.5) to which particular solutions $R(\tau)=\mp\tau$ from the family (1.13) of solutions to Eq. (1.9) correspond, and this seems quite natural since the function in (2.5) is independent of C and originally describes a zero-width wall.

In order to find an analog of the solutions in (1.14) for a finite-width wall, we note first of all that a bubble whose radius also moves in time τ at a constant velocity corresponds to these solutions. We will seek a solution to the problem specified by Eqs. (2.2) and (2.4) in the form $\varphi=\varphi_b(r/\tau)$—that is, in the form of self-similar functions (see [6, 7]). A zero of the function φ_b will then automatically move at a constant velocity in time τ. As has already been mentioned, we concurrently assume that the radius at which the function φ_b vanishes coincides with the bubble radius R_b, this being natural since the bubble-energy density peaks at the zero of the function φ_b. In [6, 7], the velocity of motion of the zero of the function φ_b was found numerically versus the wall width l, and the limit of this velocity was determined there for $l\to 0$ ($C\to\infty$) in order to compare the velocity of the collapse of the self-similar function φ_b with the velocities in the solutions given by (1.13) and (1.14). We note from the outset that the collapse of a self-similar bubble in the limit of an infinitely thin wall proceeds according to the law specified by Eq. (1.14) (see in the table the C dependence of $\xi_b=R_b/\tau$, where $\xi_b(C)$: $\psi_b(\xi_b,C)=\varphi_b(R_b/\tau,C)=0$).

We will now proceed to consider briefly self-similar solutions, setting

$$\varphi=\psi(\xi),\quad \xi=r/\tau. \tag{2.6}$$

For $\psi(\xi)$ from Eqs. (2.2) and (2.4), we obtain the equation

$$[\xi^2(1-\xi^2)\psi']'=4C^2\xi^2\psi(\psi^2-1), \tag{2.7}$$

$$-\infty<\xi<-1,\quad -1<\xi<0,\quad 0<\xi<1,$$
$$1<\xi<\infty,$$

and the condition

$$\lim_{|\xi|\to\infty}\psi^2(\xi)=1, \tag{2.8}$$

where C is the same dimensionless constant (2.3) as in (2.2). Writing the expression for φ in Eq. (2.6) as a function of the original variables t and r, we obtain

$$\varphi(r,t)=\nu\psi(-a_0Hr\exp(Ht)).$$

Similar substitutions for a scalar field specified by the Higgs potential in de Sitter space were previously used by Basu and Vilenkin [8], but only for one-dimensional walls (as well as for string- and monopole-type solutions in the systems of two and three scalar Higgs fields). However, those authors did not notice the self-similar character of these variables (in conformal time).

The points $\xi=0$, $\xi=-1$, and $\xi=-\infty$ are regular singular points of Eq. (2.7) [9, 10], and it is necessary first of all to impose boundary conditions at finite singular points of this equation—namely, one formulates, in the interval $(-1,0)$, a singular boundary-value problem, imposing the conditions

$$\lim_{\xi\to-1+0}\psi(\xi)=c_0,\quad \lim_{\xi\to-1+0}[(1+\xi)\psi'(\xi)]=0, \tag{2.9}$$

$$\lim_{\xi\to-0}\psi(\xi)=b_0,\quad \lim_{\xi\to-0}[\xi\psi'(\xi)]=0, \tag{2.10}$$

where c_0 and b_0 are the parameters to be determined. By using theorem 5 from [10], it was shown in [6] that, at any fixed c_0 (fixed b_0), the singular Cauchy problem specified by Eqs. (2.7) and (2.9) [the Cauchy problem specified by Eqs. (2.7) and (2.10)] has only one solution; this solution is holomorphic at the point $\xi=-1$ (at the point $\xi=0$). Thus, the boundary-value problem specified by Eqs. (2.7), (2.9), and (2.10) has been formulated correctly in what is concerned with the number of indeterminate boundary parameters. It is shown that this problem is solvable if and only if $|c_0|\le 1$ and $|b_0|\le 1$; moreover, there are many solutions, and all of them satisfy the constraint

$$|\psi(\xi)|\le 1,\quad \forall\xi\in[-1,0]. \tag{2.11}$$

In particular, the constants $\psi_f\equiv 0$ and $\psi_\pm\equiv\pm1$ are solutions to the problem specified by Eqs. (2.7), (2.9), and (2.10). The number of solutions grows with increasing C, the first solution differing from the above constants appearing at $C\sim 1.581$. This solution is characterized by the presence of one zero in the interval $-1<\xi<0$. At any fixed $C\gtrsim 1.581$, such a solution to the problem specified by Eqs. (2.7), (2.9), and (2.10) is a solution of the bubble type (embedded-bubble type at a greater value of zeros in the interval $(-1,0)$), since it admits a continuation to the interval $(-\infty,-1)$ and, oscillating, tends to one of the vacuum solutions—that is, it satisfies the condition in (2.8) for $\xi\to-\infty$ [this condition is a natural condition for any nontrivial solution to the problem specified by Eqs. (2.7), (2.9), and (2.10)]. The solution in question admits an even continuation to the interval $(0,\infty)$.

The asymptotic behavior of the solution at large $|\xi|$ is [6, 7]

$$\psi^{\pm}(\xi)=\pm1\pm\frac{A}{|\xi|^{3/2}} \times\left[\cos\left(\frac{\sqrt{32C^2-9}}{2}\ln|\xi|+\eta\right)+o(1)\right],\quad |\xi|\to\infty, \tag{2.12}$$

where $C^2>9/32$ (for $C^2\le 9/32$, the asymptotic behavior of the solution is of no interest since, for such C, the boundary-value problem specified by Eqs. (2.7), (2.9), and (2.10) obviously does not have nontrivial solutions differing from $\psi_\pm=\pm1$), A and η being constants that are unambiguously determined from the Cauchy data at the singular points $\xi=\pm1$—that is, upon determining the value of c_0 for the solution to the boundary-value problem specified by Eqs. (2.7), (2.9), and (2.10).

Comment 2. As was indicated above, the number of solutions to the problem specified by Eqs. (2.7), (2.9), and (2.10) depends on C. From a qualitative analysis and from numerical experiments reported in [6, 7], it follows that the eigenvalues $C=C_n$ of the corresponding spectral problem for the linear equation

$$[\xi^2(1-\xi^2)\psi']'=-4C^2\xi^2\psi,\quad -1<\xi<0, \tag{2.13}$$

are global-bifurcation points.

This equation was obtained from (2.7) by means of a linearization around a trivial solution. Upon the substitution $\chi(\xi)=\xi\psi(\xi)$, Eq. (2.13) reduces to the Legendre equation

$$[(\xi^2-1)\chi']'-2(2C^2+1)\chi=0,\quad -1<\xi<0, \tag{2.14}$$

with the boundary conditions

$$|\lim_{\xi\to-1+0}\chi(\xi)|<\infty, \tag{2.15}$$

$$\lim_{\xi\to-1+0}[(1+\xi)\chi'(\xi)]=0,$$

$$\chi(0)=0. \tag{2.16}$$

For each $C=C_n$ such that $2(2C^2+1)=(2n+1)(2n+2)$, $n=0,1,\ldots$, which is equivalent to

$$C_n=\sqrt{[(2n+1)(n+1)-1]/2},\quad n=0,1,\ldots, \tag{2.17}$$

functions that are proportional to odd-order Legendre polynomials $P_{2n+1}(\xi)$, are then solutions to the problem specified by Eqs. (2.14), (2.15), and (2.16). It was natural to expect that, at $C\approx C_n$, the original nonlinear problem specified by Eqs. (2.7), (2.9), and (2.10) would possess small solutions (as perturbations of a trivial vacuum) that are nearly proportional to $P_{n+1}(\xi)/\xi$, and this was confirmed in the calculations reported in [6]. These solutions grow in amplitude with increasing C. It follows that, for each C such that $C_n<C<C_{n+1}$, $n=1,2,\ldots$, the boundary-value problem specified by Eqs. (2.7), (2.9), and (2.10) has precisely (apart from the sign) n solutions $\psi_1(\xi,C),\ldots,\psi_n(\xi,C)$ different from $\psi_\pm\equiv\pm1$, where $\psi_k(\xi,C)$ has precisely k zeros in the interval $(-1,0)$, $k=1,\ldots,n$. In particular, we find from (2.17) that $C_1=\sqrt{5/2}\approx 1.5811388$ (the value of C_1 for a flat wall was first obtained in [8] on the basis of a similar argument).

At large values of C^2 in Eq. (2.7), one can describe a wall-type solution qualitatively. In the region where ψ changes quite slowly, that term in Eq. (2.7) which involves a large numerical factor can be compensated only by a cofactor—that is, $\psi\approx\pm1$. But in the region

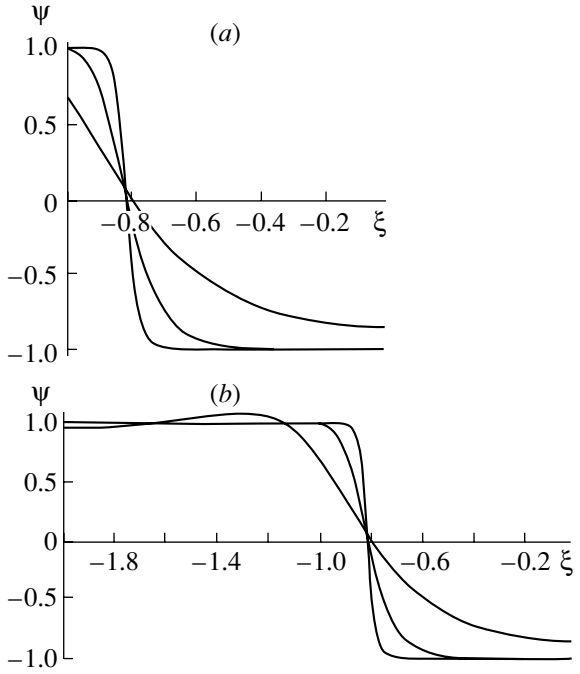

Fig. 1. (*a*) Graphs of basic bubble-type solutions to the boundary-value problem specified by Eqs. (2.7), (2.9), and (2.10) at $C = 2$, 4, and 10 (with increasing C, the wall becomes ever steeper); (*b*) graphs of the same solutions continued to the left of the point $\xi = -1$ [see the asymptotic expressions in (2.12)].

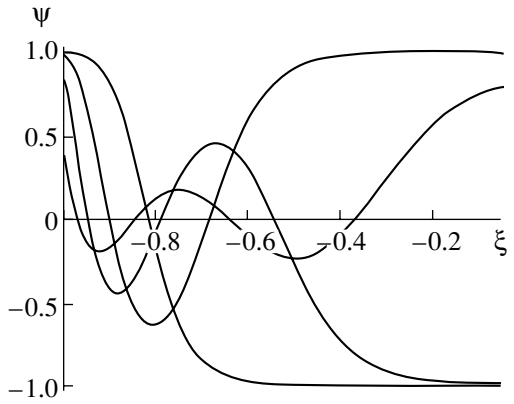

Fig. 2. Graphs of all (apart from those differing in sign) solutions (different from $\psi_\pm \equiv \pm 1$) to the boundary-value problem specified by Eqs. (2.7), (2.9), and (2.10) for $C = 5$.

where the function ψ changes sign, the coefficient of $4C^2$ is about unity in absolute value, and this term can be compensated only owing to derivatives. In this region, we have $\psi'' \approx \psi/l^2 \approx 4C^2\psi$, where l is a characteristic size of the region where the function ψ changes sign; that is, l is the wall thickness. From here, we obtain the estimate $l \approx 1/C$ (in dimensionless units). More precise information about the qualitative agreement between the results obtained in [6, 7] and the results of the theory of singular perturbations (including the results for multinode solutions) can be found in [6].

For various values of the constant C, Fig. 1*a* shows the graphs of solutions $\psi = \psi_b(\xi, C)$ to the problem specified by Eqs. (2.7), (2.9), and (2.10), while Fig. 1*b* displays the graphs of the same solutions continued to the left beyond the interval $(-1, 0)$. The table gives the values of C, c_0, b_0, and ξ_b for these solutions, where $\xi_b(C)$: $\psi_b(\xi_b(C), C) = 0$, $\xi_b \in (-1, 0)$. Apart from the change in sign, Fig. 2 presents the graphs of all solutions (different from $\psi_\pm \equiv \pm 1$) to the problem specified by Eqs. (2.7), (2.9), and (2.10) at $C = 5$.

Equation (2.7) also possesses the generalized solutions [6]

$$\tilde{\psi}(\xi) = \theta(1 \pm \xi). \tag{2.18}$$

Indeed, we have $\tilde{\psi}(1 - \tilde{\psi}^2) \equiv 0$, $\tilde{\psi}' = \pm 2\delta(1 \pm \xi)$, $\tilde{\psi}'' = -2\delta(1 \pm \xi)/(1 \pm \xi)$, whence it follows that $(1 - \xi^2)\tilde{\psi}'' - 2(2\xi - 1/\xi)\tilde{\psi}' = 0$. As can easily be verified, the solutions in (2.18) coincide with the generalized solutions (2.5). [For a geodesically complete space, there are, in addition to (2.18), generalized solutions of the form $\hat{\psi}(\xi) = \theta(1 \pm \xi)\theta(\pm\xi)$.]

Comment 3. For a solution to the boundary-value problem specified by Eqs. (2.7), (2.9), and (2.10) at fixed C, the following relation holds:

$$\int_{-1}^{0} \psi(\xi, C)[\psi^2(\xi, C) - 1]\xi^2 d\xi = 0.$$

For the main bubble, it follows from this relation that

$$\int_{-1}^{\xi_b(C)} \psi(\xi, C)[\psi^2(\xi, C) - 1]\xi^2 d\xi$$
$$= -\int_{\xi_b(C)}^{0} \psi(\xi, C)[\psi^2(\xi, C) - 1]\xi^2 d\xi,$$

which can serve as an additional test of the correctness of calculations.

3. ON THE STABILITY OF GENERALIZED AND SELF-SIMILAR SOLUTIONS

Let us now proceed to discuss the problem of stability of the solutions obtained in Section 2.

1. Stability of Generalized Discontinuous Solutions

We begin by considering the shock-wave-type solutions (2.5) [or (2.18)]. Substituting into Eq. (2.2) the expression

$$\varphi(r,\tau) = \theta(r \pm \tau) + u(r,\tau) \tag{3.1}$$

and assuming that $|u| \ll 1$, we find that, in the linear approximation, u satisfies the equation

$$u_{\tau\tau} - \frac{2}{\tau}u_\tau - u_{rr} - \frac{2}{r}u_r + \frac{8C^2}{\tau^2}u + \frac{12C^2}{\tau^2}[\theta^2(r \pm \tau) - 1]u = 0, \tag{3.2}$$

which differs from the equation describing an excitation above the vacua $\varphi_\pm = \pm 1$ [2, 3] by the term $(12C^2/\tau^2)(\theta^2 - 1)u$, which is responsible for the interaction of the field u with a well of finite depth and zero width, but this cannot radically change the character of the spectrum for perturbations above the vacua; that is, the solutions given by (2.5) are stable to small perturbations.

2. Instability of Self-Similar Solutions as Bubbles with Walls of Finite Width

Let us consider the stability of a self-similar solution, which we denote here by $\varphi(\xi)$. We are unaware of any attempts at addressing the problem of stability of a self-similar solution against small perturbations. Moreover, an analysis of solutions obtained numerically for stability is a cumbersome computational problem. Here, it becomes even more involved because of the need for studying the asymptotic behavior of perturbations at large C. Such difficulties do not arise if, in analyzing a self-similar bubble for stability, one employs a variational approach—for example, the Derrick–Hobart method [11]. Within this approach, one makes use of only those properties of a bubble-type self-similar solution that were studied in Section 2—in particular, the asymptotic behavior of the solution at large $|\xi|$ [see (2.12)]. Let us consider the functional

$$I(\varphi) = \int_{-\infty}^{\infty} \left[(1-\xi^2)(\varphi_\xi)^2/2 + C^2(1-\varphi^2)^2\right]\xi^2 d\xi \tag{3.3}$$

on the manifold specified by solutions to the problem formulated in terms of Eqs. (2.7) and (2.8). For this functional, Eq. (2.7) is the Euler–Lagrange equation; therefore, the substitution of solutions to the problem specified by Eqs. (2.7) and (2.8) must yield $\delta I(\varphi) = 0$.

We note that the integrand in the functional (3.3) coincides with the expression for the energy density of the field φ in de Sitter space in the so-called static coordinates, in which the metric has the form

$$ds^2 = (1-r^2H^2)dt^2 - (1-r^2H^2)^{-1}dr^2 - r^2(d\theta^2 + \sin^2\theta d\phi^2), \tag{3.4}$$

where the radial variable r is reduced to a dimensionless form with the aid of the Hubble constant H. One can show that this coincidence is not accidental and that the self-similar variable ξ is indeed equal to $-rH$, where r is the radial variable in the system of static coordinates. [Thus, self-similar solutions in the space specified by the metric in (1.8) coincide with stationary solutions in the space specified by the metric in (3.4).] Concurrently, the energy integral in the system of static coordinates (3.4) is the integral in (3.3) taken from $-\infty$ to 0.

2.1. First of all, we note that, for the C-independent discontinuous solution (2.18), which represents a bubble with a wall of zero width, the integral in (3.3) is equal to zero. Indeed, the integral $\int_{-\infty}^{\infty}(\varphi^2-1)\xi^2 d\xi$ vanishes since the integrand is different from zero only at one point. The second term involves the square of the derivative of the solution in (2.18). For the derivative of the function in (2.18), we obtain $\varphi_\xi = \pm 2\delta(1 \pm \xi)$. The square of a delta function is in general indeterminate, but, in the case being considered, it appears in the integral together with the factor $(1-\xi^2)$; since $(1-\xi^2)\delta(1\pm\xi) = 0$ [12], we have

$$\int_{-\infty}^{\infty}(1-\xi^2)\delta^2(1\pm\xi)\xi^2 d\xi = \int_{-\infty}^{\infty}\delta(1\pm\xi)[(1-\xi^2)\delta(1\pm\xi)]\xi^2 d\xi = 0 \times \left[2\int_{-\infty}^{\infty}\delta(1\pm\xi)d\xi\right] = 0.$$

We will now give a more rigorous proof of the last statement. We will calculate the kinetic part of the functional in (3.3) for the one-parameter family of functions $\varphi_\beta^\pm(\xi) = \tanh(\beta(1\pm\xi))$. For $\beta \to \infty$, the functions $\varphi_\beta^\pm(\xi)$ reduce to $\theta(1\pm\xi)$. For the sake of definiteness, we first consider the family of functions $\varphi_\beta^+(\xi)$. For these functions, the kinetic part of the functional in (3.3) is given by

$$I_k(\varphi_\beta^+, \beta) = \tilde{I}(\beta) = \beta^2 \int_{-\infty}^{\infty}[(1-\xi^2)/\cosh^4(\beta(1+\xi))]\xi^2 d\xi. \tag{3.5}$$

Let us make the change of variable $\beta(1+\xi)=y$. At large β, we then have

$$\tilde{I}(\beta)=2\int\limits_{-\infty}^{\infty}[y/\cosh^4(y)]dy+O(1/\beta)=O(1/\beta), \tag{3.6}$$

whence we obtain the result that is coincident with the above conclusion. The proof for the function $\theta(1-\xi)$ can be conducted in a similar way.

We will now prove that, upon the substitution of the functions in (2.18) into the functional in (3.3), the result will remain zero upon restricting the domain of integration to that from $-\infty$ to 0; that is, the energy of the solutions given by (2.18) in the system of static coordinates is zero. Since this result is obvious for the function $\theta(1-\xi)$, we will consider only the solution $\theta(1+\xi)$. In just the same way as in the above proof, we approximate this function by the expression $\tanh(\beta(1+\xi))$, but, instead of formula (3.5), we obtain the following result at large β:

$$\tilde{I}_0(\beta)=\beta^2\int\limits_{-\infty}^{0}[(1-\xi^2)/\cosh^4(\beta(1+\xi))]\xi^2d\xi \tag{3.7}$$

$$=2\int\limits_{-\infty}^{\beta}[y/\cosh^4(y)]dy+O(1/\beta).$$

For $\beta\to\infty$, the function $\tilde{I}_0(\beta)$ (3.7) tends to zero. Thus, the energy integral [the functional in (3.3)] retains a zero value upon this discontinuous continuation of the vacuum solutions to the interval $(-\infty,-1)$ [or to the interval $(-\infty,\infty)$].

2.2. Let us now proceed to study the stability of a C-dependent self-similar solution, which represents a bubble with a wall of finite width. In doing this, we assume that a solution is stable if it minimizes (this may be a local minimum) the functional in (3.3) and that it is otherwise unstable (see, for example, [11]). First of all, we show that the functional in (3.3) is finite for bubble-type solutions—that is, for functions whose asymptotic behavior is given by (2.12). Substituting formula (2.12) into expression (3.3), we find that, for $|\xi|\to\infty$, the integrand has the form

$$\frac{A^2}{8|\xi|}(32C^2-9)\cos(\sqrt{32C^2-9}\ln|\xi|+2\eta) \tag{3.8}$$

$$-\frac{3A^2}{8|\xi|}\sin(\sqrt{32C^2-9}\ln|\xi|+2\eta)+O(1/\xi^2).$$

The integrals of the terms proportional to $1/\xi^2$ in expression (3.8) converge at large $|\xi|$. In the first two terms, we introduce the variable $y=\ln|\xi|$, whereupon the integrand in the functional (3.3) for the functions $\varphi^{\pm}$, whose asymptotic behavior is given by (2.12), assumes the following form at large y:

$$[A^2(32C^2-9)/8]\cos\Big(\sqrt{32C^2-9}y+2\eta\Big)$$

$$-[3A^2\sqrt{32C^2-9}/8]\sin\Big(\sqrt{32C^2-9}y+2\eta\Big);$$

that is, the integral is bounded at large $|\xi|$. At the singular points $\xi=\pm1,0$, the solution to the problem specified by Eqs. (2.7), (2.9), and (2.10) is given by holomorphic functions [6, 7].

We will seek the minimum of the functional in (3.3) among functions that are bounded at finite ξ and whose asymptotic behavior at large $|\xi|$ is

$$\varphi^{\pm}\approx\pm1\pm(A/|\xi|^{3/2}) \tag{3.9}$$

$$\times\cos((\sqrt{32C^2-9}/2)\alpha\ln|\xi|+\eta),$$

where α is a parameter. For functions whose asymptotic behavior has the form (3.9), the integrand in the functional given by (3.3) then develops a term that involves a nonintegrated singularity at infinity,

$$A^2(32C^2-9)(1-\alpha^2)/(16|\xi|). \tag{3.10}$$

For trial functions of asymptotic behavior in the form (3.9), the functional in (3.3) is then $-\infty$ for $\alpha>1$ and $+\infty$ for $\alpha<1$. Thus, $\alpha=1$ is not a point of minimum for this functional (it is some kind of inflection point); that is, the self-similar solution whose asymptotic behavior is given by (2.12) is unstable in the class of functions whose asymptotic behavior has the form (3.9). [We note that the functional in (3.3) cannot be differentiated with respect to the parameter α since the respective integral diverges for $\alpha\neq1$.]

A similar conclusion can be drawn by studying the self-similar solution $\varphi(\xi)$ for stability by the Derrick–Hobart method [11]. Substituting into the functional in (3.3) the family of functions $\varphi_\gamma(\xi)=\varphi(\gamma\xi)$, where γ is a parameter, and making the change of variable $\xi_{\text{new}}=\gamma\xi$, we obtain

$$I(\varphi_\gamma)\equiv J(\gamma)=\frac{1}{\gamma^3}I(\varphi)+\frac{\gamma^2-1}{2\gamma^3}K(\varphi), \tag{3.11}$$

$$K=\int\limits_{-\infty}^{\infty}\left[\frac{\partial\varphi}{\partial\xi}(\xi)\right]^2\xi^2d\xi.$$

Since the quantities I and K in Eq. (3.11) are finite, we can differentiate $J(\gamma)$ with respect to γ. We have

$$\left.\frac{dJ(\gamma)}{d\gamma}\right|_{\gamma=1}=K-3I,$$

whence it follows that $I = K/3$, since $\varphi(\xi)$ is a solution to the Euler equation (2.7). For the second derivative, we obtain

$$\left.\frac{d^2J(\gamma)}{d\gamma^2}\right|_{\gamma=1} = -5K + 12I = -K < 0, \qquad (3.12)$$

since the functional K is positive definite. The inequality in (3.12) implies that a solution of the finite-width-wall type to Eq. (2.7) is unstable in the aforementioned class of functions. The above argument can be extended to the case where integration in the functional given by (3.3) is performed over the range between $-\infty$ and 0—that is, to the energy integral in the system of static coordinates (3.4). If, however, the interval of integration is finite in the functional given by (3.3), this argument becomes illegitimate, so that a dedicated consideration is required. We only note that, at large C, the Derrick relation $I = K/3$ is valid numerically to a high accuracy over the integration range $[-1, 0]$ (for $\xi < -1$, the solutions are very close to $\varphi_\pm \equiv \pm 1$); in particular, it was found for the main solution at $C = 6$ that $|I - K/3| \sim 10^{-5}$.

Comment 4. If one considers the singular boundary-value problem specified by Eqs. (2.7), (2.9), and (2.10) in the interval $(-1, 0)$, this problem is equivalent to the following problem: it is necessary to find solutions to Eq. (2.7) such that the integral

$$E(\varphi) = \int_{-1}^{0} [(1-\xi^2)(\varphi_\xi)^2/2 + C^2(1-\varphi^2)^2]\xi^2 d\xi \qquad (3.13)$$

is finite for them.

For this functional, Eq. (2.7) is the Euler–Lagrange equation, so that $\delta E(\varphi) = 0$ on the manifold spanned by the solutions to the problem specified by Eqs. (2.7), (2.9), and (2.10). The integral in (3.13) is a nonnegative definite, and the vacuum solutions $\varphi_\pm \equiv \pm 1$ minimize it absolutely, so that $E(\varphi_\pm) = 0$. For the spurious vacuum $\varphi_f \equiv 0$, which corresponds to an unstable field state, we obtain $E(\varphi_f) = C^2/3$, this being the maximum value of the integral in (3.13) for solutions to the problem specified by Eqs. (2.7), (2.9), and (2.10). For the remaining solutions to this problem, which admit an interpretation as perturbations of the trivial vacuum, we obtain intermediate values of E. Figure 3 shows the quantities given by (3.13): $E_n(C) = E(\varphi_n(\xi, C))$, where n is the number of nodes of the self-similar solution $\varphi_n(\xi, C)$ in the interval $(-1, 0)$.

In conclusion, we will discuss the possible reasons for the instability of self-similar solutions. To do this, we will return to de Sitter space in the variables (r, τ). The metric in (1.8) in terms of these variables

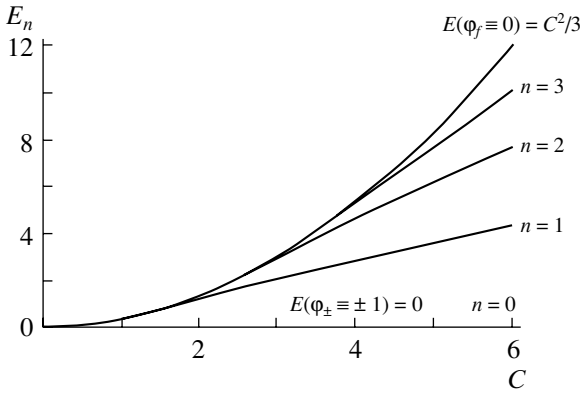

Fig. 3. Graphs of the quantities in (3.13): $E_n(C) = E(\varphi_n(\xi, C))$, where $\varphi_n(\xi, C)$ is the function that represents a solution to the boundary-value problem specified by Eqs. (2.7), (2.9), and (2.10) and which has n zeros in the interval $(-1, 0)$.

is conformally flat; therefore, a causal structure of a flat space survives in it. This means that the motion of test bodies $r = \kappa|\tau|$ for $\kappa > 1$ is impossible since $ds^2 \geq 0$ for real bodies. In a self-similar solution, the field φ is constant on the trajectories $r = \xi\tau$, so that a given value of the field φ moves at the velocity ξ, this not being a phase velocity since there is no periodic process. It is then natural to assume that the field φ resists motion off the light cone, but this means precisely an instability of a self-similar solution. The field will either discharge part of energy by radiation, going over to a stable state of the shock-wave type, or dissipate into the vacuum.

These arguments do not apply to the shock-wave-type solution (2.5), since the field is constant for $|\xi| > 1$, so that the concept of the velocity of motion of a given field value is meaningless. For the same reason, the stability of the self-similar solution is restored for $C \to \infty$, since, in this limit, it reduces to the corresponding θ function.

ACKNOWLEDGMENTS

We are grateful to A.E. Kudryavtsev and B.V. Pal'tsev for stimulating discussions.

This work was supported by the Russian Foundation for Basic Research (project no. 05-01-00257) and a grant no. (2328.2003.2) for support of leading scientific schools. The work of N.A. Voronov was supported and by the Ministry of Science of the Russian Federation (grant no. 40.052.1.1.1122). The work of A.L. Dyshko and N.B. Konyukhova was supported by the Russian Foundation for Basic Research (project no. 02-01-00050).

REFERENCES

1. T. I. Belova and N. A. Voronov, Pis'ma Zh. Éksp. Teor. Fiz. **61**, 337 (1995) [JETP Lett. **61**, 341 (1995)]; N. A. Voronov, A. L. Dyshko, I. Yu. Kobzarev, and N. B. Konyukhova, Yad. Fiz. **60**, 140 (1997) [Phys. At. Nucl. **60**, 130 (1997)]; N. A. Voronov, A. L. Dyshko, N. B. Konyukhova, and I. B. Staroverova, Zh. Vychisl. Mat. Mat. Fiz. **37**, 1506 (1997).
2. N. D. Birrell and P. C. W. Davies, *Quantum Fields in Curved Space* (Cambridge University Press, Cambridge, 1982; Mir, Moscow, 1984).
3. A. D. Linde, *Particle Physics and Inflationary Cosmology* (Nauka, Moscow, 1991; Harwood Academic Publishers, Chur, 1990).
4. H. Arodz and A. L. Larsen, Phys. Rev. D **49**, 4154 (1994).
5. L. B. Okun, *Leptons and Quarks* (Nauka, Moscow, 1981; North-Holland, Amsterdam, 1982).
6. A. L. Dyshko and N. B. Konyukhova, Zh. Vychisl. Mat. Mat. Fiz. **39**, 124 (1999); **41**, 467 (2001).
7. A. L. Dyshko, N. B. Konyukhova, and N. A. Voronov, Comput. Phys. Commun. **126**, 57 (2000).
8. R. Basu and A. Vilenkin, Phys. Rev. D **50**, 7150 (1994).
9. W. R. Wasow, *Asymptotic Expansions for Ordinary Differential Equations* (Wiley, New York, 1985; Mir, Moscow, 1968).
10. N. B. Konyukhova, Zh. Vychisl. Mat. Mat. Fiz. **23**, 629 (1983).
11. G. H. Derrick, J. Math. Phys. (N.Y.) **5**, 1252 (1964); R. H. Hobart, Proc. Phys. Soc. London **82**, 201 (1963).
12. I. M. Gel'fand and G. E. Shilov, *Generalized Functions* (Fizmatgiz, Moscow, 1959; Academic Press, New York, 1967).

Translated by A. Isaakyan

Physics of Atomic Nuclei, Vol. 68, No. 7, 2005, pp. 1227–1258. From Yadernaya Fizika, Vol. 68, No. 7, 2005, pp. 1277–1308.

ELEMENTARY PARTICLES AND FIELDS
Theory

Quasilinearization Method: Nonperturbative Approach to Physical Problems*

V. B. Mandelzweig[1)]

Racah Institute of Physics, Hebrew University, Jerusalem, Israel

Received May 13, 2004; in final form, September 3, 2004

Abstract—The general properties of the quasilinearization method (QLM), particularly its fast quadratic convergence, monotonicity, and numerical stability, are analyzed and illustrated on different physical problems. The method approaches the solution of a nonlinear differential equation by approximating the nonlinear terms by a sequence of linear ones and is not based on the existence of a small parameter. It is shown that QLM gives excellent results when applied to different nonlinear differential equations in physics, such as Blasius, Lane–Emden, and Thomas–Fermi equations, as well as in computation of ground and excited bound-state energies and wave functions in quantum mechanics (where it can be applied by casting the Schrödinger equation in the nonlinear Riccati form) for a variety of potentials most of which are not treatable with the help of perturbation theory. The convergence of the QLM expansion of both energies and wave functions for all states is very fast and the first few iterations already yield extremely precise results. The QLM approximations, unlike the asymptotic series in perturbation theory and $1/N$ expansions, are not divergent at higher orders. The method sums many orders of perturbation theory as well as of the WKB expansion. It provides final and accurate answers for large and infinite values of the coupling constants and is able to handle even supersingular potentials for which each term of the perturbation series is infinite and the perturbation expansion does not exist. © *2005 Pleiades Publishing, Inc.*

1. INTRODUCTION

I first came to the Institute of Theoretical and Experimental Physics (ITEP) sometime during 1960 as a student of the fourth year at the Moscow University to start my diploma work. I was twenty years old. The theoretical department then was still rather small, about 15 staff members and a similar number of diploma and PhD students. Soon I noticed a tall PhD student a few years older than myself who made lasting impression on me by being energetic and very ambitious. His name was Yuri Simonov. He was intensively working on analyticity and dispersion relations in field theory. A few years later, however, after losing in the Moscow subway a thick, ready for publication manuscript on analytic properties and connected with it numerous pages of complicated derivations, he decided overnight not to spend many months reconstructing it and instead switched to a different field: he turned to the few-body problem. It was then a virgin field—mathematical methods such as the Faddeev equations and the hyperspherical approach had just started to be developed and computer facilities and even computer languages (many programs at ITEP were at this time still written using machine addresses) were not at all adequate for intrinsically complicated calculations involving three or more particles. The series of his works in this new field [1], developing the hyperspherical harmonics method recently pioneered in physics, were elegantly and carefully written and heralded a new era in the treatment of several interacting particles. They made him well known among nuclear physicists and in the emerging few-body field. Twenty years later, this approach evolved into the correlation function hyperspherical harmonics method (CFHHM) combining the correlation function and hyperspherical harmonics methods, which enabled very accurate calculations of the few-body atomic and molecular bound states and resonances [2–5], of atomic cross sections [6], and of nuclear levels and reactions [7].

Another work which very much appealed to me at that time was the pioneering approach by Badalyan and Simonov to relating energy shifts in pionic atoms to low-energy πN-scattering data [8]. The extention of this work led a few years later to the general radius perturbation theory [9] for potentials consisting of two parts, an external potential and the internal "core." The small parameters in this theory are the ratios of the core radius to the characteristic length parameters of the outer potential, such as its radius, the

*The text was submitted by the authors in English.

[1)]This article is dedicated to the 70th birthday of Yu.A. Simonov [see Phys. At. Nucl. **68**, nos. 4, 5 (2005)].

1063-7788/05/6807-1227$26.00

size of the bound-state orbit, and so on. The simple formula for core corrections to scattering amplitudes, wave functions, and bound-state levels of the external potentials were obtained. The theory includes from the beginning the finite size of the core interaction and therefore gives much better results than the usual zero-range approximation to which it reduces in the limit of zero core size.

I am not qualified to review all the contributions of Prof. Simonov to nuclear and high-energy physics, but if I try to sum them up in one sentence, it will be developing nonperturbative methods, from the analyticity and unitarity approach in field theory, Regge theory, multiple dispersion relations, and hyperspherical analysis to the nonperturbative approach to QCD, which is his main interest now. As a homage to Yuri, I would like therefore to devote this article to reviewing an emerging additional nonperturbative approach to treatment of different physical problems called the quasilinearization method (QLM). The origin of this very powerful approximation technique lies in the theory of linear programming. The method, whose iterations are carefully constructed to yield rapid quadratic convergence and often monotonicity, was pioneered more than 30 years ago by Bellman and Kalaba [10, 11] to solve a wide variety of nonlinear ordinary and partial differential equations or their systems arising in different engineering and biology problems such as orbit determination, detection of periodicities, radiative transfer, and cardiology. The modern developments and applications of the method to different fields are given in the monograph [12]. QLM, however, was never systematically studied or extensively applied in quantum physics, though references to it can be found in well-known monographs [13, 14] dealing with the variable phase approach to potential scattering as well as in a few scattered research papers [15–18]. This could be explained by the fact that convergence of the method has been proved only under rather restrictive conditions [10, 11] which generally are not fulfilled in physical applications, such as, for example, for a rather small domain of variables or for forces which are finite everywhere in the domain. Recently, however, the convergence was proved [19, 20] for realistic physical conditions of infinite domains and forces which could be singular at certain points of the domains. It was shown also [21] how to deal with solutions which themselves could be infinite at certain values of parameters such as, for example, scattering amplitudes at bound-state energies.

The review is arranged as follows. In the second section, we start, for purposes of simplicity and transparency, with the first-order ordinary nonlinear differential equation and present the main features of the quasilinearization approach for this case. In the third section, we give the proof of the convergence of QLM for an nth-order ordinary nonlinear differential equation. The generalization to an nth-order partial nonlinear differential equation in N-dimensional space is straightforward. In order to highlight the power of the method, in the fourth section, we apply it to second- and third-order nonlinear differential equations well known in physics, namely, to the Lane–Emden, Thomas–Fermi, and Blasius equations. The comparison of QLM with quantum-mechanical perturbation theory is discussed in the fifth section, while the sixth, seventh, eighth, and ninth sections deal with comparison of the QLM and WKB. The results, convergence patterns, numerical stability, advantages of the method, and its possible future applications are summed in the final, tenth, section.

2. THE QUASILINEARIZATION METHOD FOR THE FIRST-ORDER ORDINARY NONLINEAR DIFFERENTIAL EQUATION

In order to introduce the method in the simplest possible way in this section, we limit ourselves to the case of the first-order ordinary nonlinear differential equation. Physically, this covers the quantum mechanics of one particle in a central field since in this case the Schrödinger equation for a wave function could be rewritten as the Ricatti equation for its logarithmic derivative. The presentation in this section closely follows the proofs and derivations of [19].

The aim of QLM is to obtain the solution $v(z)$ of a nonlinear first-order differential equation

$$\frac{dv(z)}{dz} = g(v(z), z) \tag{1}$$

with the boundary condition $v(a) = c$ as a limit of a sequence of linear differential equations. This goal is easily understandable in view of the fact that there is no useful technique of presenting the general solution to Eq. (1) in terms of a finite set of particular solutions as in the linear case, where, as a result of the superposition property, the equation could be solved analytically or numerically in a convenient fashion. In addition, the sequence should be constructed in such a way as to obtain quadratic convergence and, if possible, monotonicity.

The shift of the coordinate $z = x + a$ and of the solution itself $u(x) = v(x + a) - c$ reduces Eq. (1) to the canonical form [22]

$$\frac{du(x)}{dx} = f(u(x), x), \quad u(0) = 0, \tag{2}$$

where $f(u(x), x) \equiv g(u(x) + c, x + a)$.

The QLM prescription [10, 11] determines the $(n+1)$th iterative approximation $u_{n+1}(x)$ to the solution of Eq. (2) as a solution of the equation

$$u'_{n+1}(x) = f(u_n, x) + (u_{n+1}(x) - u_n(x)) f_u(u_n, x), \quad u_{n+1}(0) = 0, \tag{3}$$

where function $f_u(u,x) = \partial f(u,x)/\partial u$ is a functional derivative of a functional $f(u(x),x)$. If one defines m as an upper limit of a maximum of absolute values of the functional and its first and second functional derivatives

$$\max\left(|f(u(x),x)|, |f_u(u,x)|, \left|\frac{1}{2} f_{uu}(u,x)\right|\right) \leq m < \infty, \tag{4}$$

one can prove that the sequence of iterations $u_n(x)$, $n = 1, 2, \ldots$, converges uniformly and quadratically on the interval $[0,b]$ to solution $u(x)$ of Eq. (2) for bm sufficiently small. Indeed, introducing the norm $||g||$ of function $g(x)$ as a maximum of the function on the interval $[0,b]$,

$$||g|| = \max|g(x)|, \quad 0 \leq x \leq b, \tag{5}$$

and introducing the notation $\Delta u_{n+1}(x) = u(x) - u_n(x)$, $\delta u_{n+1}(x) = u_{n+1}(x) - u_n(x)$, one proves [10, 11] the following inequalities:

$$||\Delta u_{n+1}|| \leq k||\Delta u_n||^2, \tag{6}$$

$$||\delta u_{n+1}|| \leq k||\delta u_n||^2, \tag{7}$$

$$k = \frac{bm}{1-bm}, \tag{8}$$

which establish the uniform quadratic convergence of sequence $u_n(x)$ on $[0,b]$ for sufficiently small bm. A simple induction of Eq. (7) shows [11] that $\delta u_{n+1}(x)$ for an arbitrary $l < n$ satisfies the inequality

$$||\delta u_{n+1}|| \leq (k||\delta u_{l+1}||)^{2^{n-l}}/k, \tag{9}$$

or for $l = 0$

$$||\delta u_{n+1}|| \leq (k||\delta u_1||)^{2^n}/k. \tag{10}$$

The convergence therefore depends on the quantity $q_1 = k||u_1 - u_0||$, where zero iteration $u_0(x)$ satisfies condition $u_0(0) = 0$ and is chosen from physical and mathematical considerations. In view of Eq. (8), the convergence is reached if bm is sufficiently small. However, from Eq. (9), it follows that, for the convergence, it is sufficient that just one of the quantities $q_m = k||\delta u_{m+1}||$ be small enough. Consequently, one can always hope [11] that, even if first convergent coefficient q_1 is large, a well-chosen initial approximation u_0 results in a smallness of at least one of the convergence coefficients q_m, $m > 1$, which enables a rapid convergence of the iteration series for $n > m$.

One can prove in addition [10, 11] that the convergence is monotonic from below (above) if functional $f(u(x),x)$ is strictly convex (concave), that is, if the second functional derivative $f_{uu}(u,x)$ in interval $[0,b]$ exists and is strictly positive (negative).

The QLM approaches the solution of a nonlinear differential equation by approximating the nonlinear terms by a sequence of linear ones and is not based on existence of some kind of small parameter. In the proof of R.E. Bellman and R. Kalaba, a small parameter bm, however, does appear sort of through the back door. The requirement of small bm is unfortunately too restrictive in most physical problems, where m and b are often large or infinite, since x normally changes in an infinite region and many potentials are infinite at some points in the domain. For example, in the case of a variable phase equation [see Eq. (72) later on], since most of the realistic forces, like Yukawa, Coulomb, van der Waals, or hard core potentials, are infinite at the origin, a function

$$f(a(x),x) = -V(x)(x + a(x))^2 \tag{11}$$

or its first

$$f_a(a(x),x) = -2V(x)(x + a(x)) \tag{12}$$

or second

$$f_{aa}(a(x),x) = -2V(x) \tag{13}$$

functional derivatives are infinite at the origin. This means $m = \infty$, that is, a zero convergence interval. However, it has already been well known for a long time [13, 14, 23] that a first approximation of QLM gives finite and reasonable results even for super singular $1/r^n$, $n > 4$, potentials for which all the terms of the usual perturbation theory are strongly divergent. It indicates that the condition bm being small may be too restrictive and should be relaxed.

Our goal now is to modernize the proof of uniform quadratic convergence of QLM, so the requirement of smallness of an interval for large m, as well as the requirement of m being finite, is removed. Let us subtract from both sides of Eq. (2) a term $h(w(x),x)u(x)$, where $w(x)$ and $h(w(x),x)$ are some arbitrary function and functional, respectively, which we will choose later. We obtain

$$\frac{du(x)}{dx} - h(w(x),x)u(x) = f(u(x),x) - h(w(x),x)u(x), \quad u(0) = 0. \tag{14}$$

The integral form of this equation is

$$u(x) = \int_0^x ds(f(u(s),s) \tag{15}$$

$$- h(w(s),s)u(s))\exp\int_s^x dth(w(t),t)$$

or, in the case of nonzero boundary condition $u(0)=c$,

$$u(x)=c\exp\int_0^x dth(w(t),t) \tag{16}$$
$$+\int_0^x ds(f(u(s),s)-h(w(s),s)u(s))$$
$$\times\exp\int_s^x dth(w(t),t),$$

which can be checked easily by a simple differentiation.

We consider three different forms of function $w(x)$ and its functional $h(w(x),x)$:

$$h(w(x),x))\equiv 0, \tag{17}$$

$$h(w(x),x)=f_w(w(x),x),\quad w(x)\equiv 0, \tag{18}$$

$$h(w(x),x)=f_w(w(x),x),\quad w(x)\equiv u(x). \tag{19}$$

We can define now the iteration scheme by setting function $u(x)$ on the right equal to its nth approximation $u_n(x)$ and obtaining the $(n+1)$th approximation on the left. The zero approximation $u_0(x)$ is chosen from some mathematical or physical considerations and satisfies the boundary condition $u_0(0)=0$. We get three different iteration schemes, corresponding Eqs. (17)–(19), respectively:

$$u_{n+1}(x)=\int_0^x ds(f(u_n(s),s), \tag{20}$$

$$u_{n+1}(x)=\int_0^x ds(f(u_n(s),s) \tag{21}$$
$$- f_u(0,s)u_n(s))\exp\int_s^x dtf_u(0,t),$$

and

$$u_{n+1}(x)=\int_0^x ds(f(u_n(s),s) \tag{22}$$
$$- f_u(u_n(s),s)u_n(s))\exp\int_s^x dtf_u(u_n(t),t).$$

In the case of nonzero boundary condition $u(0)=c$, the iteration sequence should be slightly modified. For example, in this case, according to Eq. (16), Eq. (22) has a somewhat different form, namely,

$$u_{n+1}(x)=c\exp\int_0^x dtf_u(u_n(t),t) \tag{23}$$
$$+\int_0^x ds(f(u_n(s),s)-f_u(u_n(s),s)u_n(s))$$
$$\times\exp\int_s^x dtf_u(u_n(t),t).$$

Let us concentrate in the beginning to Eq. (22), which, being the solution to Eq. (3), displays the iteration sequence of the QLM. The subtraction of Eq. (3) for n and $n-1$ gives a similar differential equation for difference $\delta u_{n+1}(x)=u_{n+1}(x)-u_n(x)$:

$$\delta u'_{n+1}(x)=f(u_n(x),x)-f(u_{n-1}(x),x) \tag{24}$$
$$+\delta u_{n+1}(x)f_u(u_n(x),x)-\delta u_n(x)f_u(u_{n-1}(x),x),$$
$$\delta u_{n+1}(0)=0.$$

By use of the mean-value theorem [24], one can write

$$f(u_n(x),x)=f(u_{n-1}(x),x) \tag{25}$$
$$+\delta u_n(x)f_u(u_{n-1}(x),x)+\frac{1}{2}f_{uu}(\bar{u}_n(x),x)\delta u_n^2(x),$$

where $\bar{u}_n(x)$ lies between $u_n(x)$ and $u_{n-1}(x)$. As a result, Eq. (24) could be written as the following equation:

$$\delta u'_{n+1}(x)-\delta u_{n+1}(x)f_u(u_n(x),x) \tag{26}$$
$$=\frac{1}{2}f_{uu}(\bar{u}_n(x))\delta u_n^2(x),$$

whose solution has the form

$$\delta u_{n+1}(x)=\frac{1}{2}\int_0^x dsf_{uu}(\bar{u}_n(s),s)\delta u_n^2(s) \tag{27}$$
$$\times\exp\int_s^x dtf_u(u_n(t),t).$$

Obviously,

$$|\delta u_{n+1}(x)|\le\frac{1}{2}\int_0^x ds|f_{uu}(\bar{u}_n(s),s)| \tag{28}$$
$$\times|\delta u_n(s)|^2\exp\int_s^x dtf_u(u_n(t),t)$$

$$\leq k_n(x)|\delta u_n(\bar{x})|^2 \leq k_n(b)||\delta u_n||^2.$$

Here, $\bar{x}$ is the point on the interval $[0,x]$ where $|\delta u_n(x)|$ is maximal,

$$k_n(x) = \frac{1}{2}\int_0^x ds|f_{uu}(\bar{u}_n(s),s)|\exp\int_s^x dtf_u(u_n(t),t), \tag{29}$$

and positiveness of the integrand in Eq. (29) and definition (5) are used. Since Eq. (28) is correct for any x in the interval $[0,b]$, it is correct also for a value of $x \in [0,b]$ for which $|\delta u_{n+1}(x)|$ reaches its maximal value. This gives

$$||\delta u_{n+1}|| \leq k_n(b)||\delta u_n||^2. \tag{30}$$

Let us assume the boundness of the first two functional derivatives of $f(u(x),x))$, that is, existence of bounding functions $F(x)$ and $G(x)$ which for any u and x satisfy

$$f_u(u(x),x)) \leq F(x), \quad |f_{uu}(u(x),x)| \leq G(x). \tag{31}$$

In this case, $k_n(b) \leq k(b)$, where

$$k(b) = \frac{1}{2}\int_0^b dsG(s)\exp\int_s^b dtF(t), \tag{32}$$

and Eq. (30) could be written in the form

$$||\delta u_{n+1}|| \leq k(b)||\delta u_n||^2, \tag{33}$$

which is identical to Eq. (7) but with $k = k(b)$ instead of k given by Eq. (8). We can reproduce the results of Bellman and Kalaba [10, 11] by following their bounding restriction Eq. (4) and setting $F(x) = m$, $G(x) = 2m$. In this case, the integrals in Eq. (32) can be easily calculated and give $k(b) = (1-e^{-mb})/e^{-mb}$, which for small mb reduces to expression for k given by Eq. (8). However, as we will see in different examples in the next section, $k(b)$ given by Eq. (32), unlike k given by Eq. (8), can be sufficiently small also for an infinite interval length b and for singular functions $G(x)$ and $F(x)$. This means that the quantity $q_1(b)$,

$$q_1(b) = k(b)||u_1 - u_0||, \tag{34}$$

which is responsible for the convergence [see discussion after Eq. (10)], can be less than unity and thus assures the convergence even in this case. As was pointed out there, for the rapid convergence, it is actually enough that an initial guess for zero iteration be sufficiently good to ensure the smallness of just one of the convergence coefficients $q_m(b) = k(b)||u_{m+1} - u_m||$.

With the uniform quadratic convergence of the sequence $u_n(x)$ for the intervals $[0,b]$ in which at least one of the convergence coefficients $q_m(b) < 1$ is now proven, one can conclude from Eq. (27) that, in addition, for strictly convex (concave) functionals $f(u(x),x)$, the difference $u_{n+1}(x) - u_n(x)$ is strictly positive (negative), which establishes the monotonicity of the convergence from below (above), respectively, on this interval.

If $F(x)$ is a sign-definite function and $G(x) = |F(x)|$, the integral in Eq. (32) can be taken explicitly and produces a simple expression for $k(b)$,

$$k(b) = \frac{1}{2}\left|\exp\int_0^b dtF(t) - 1\right|. \tag{35}$$

The subtraction of Eq. (3) from Eq. (2) gives the equation

$$\Delta u'_{n+1}(x) = f(u,x) - f(u_n(x),x) \tag{36}$$
$$+ \Delta u_{n+1}(x)f_u(u_n(x),x) - \Delta u_n(x)f_u(u_n(x),x),$$
$$\Delta u_{n+1}(0) = 0,$$

which is similar to Eq. (24), which was a starting point for our derivation of Eq. (33). The derivation along the same lines, starting from Eq. (36), gives the analog of Eq. (6) with k changed to $k(b)$:

$$||\Delta u_{n+1}|| \leq k(b)||\Delta u_n||^2. \tag{37}$$

This equation again confirms the uniform quadratic convergence of sequence u_n to a solution $u(x)$ of Eq. (2). One can show in exactly the same fashion as before that, for strictly convex (concave) functionals $f(u(x),x)$, the difference Δu_{n+1} is strictly positive (negative), proving in this case the monotonic convergence to a limiting function u from below (above), respectively.

In the case where the solution $u(x)$ and, respectively, its iterations $u_n(x)$ go to infinity at some points on the interval $[0,b]$, Eq. (22) could become meaningless. To deal with it, it is necessary to regularize Eq. (2), that is, reformulate it in terms of a new function $v(x)$ which is finite, as, for example, to change to function $v(x) = 1/u(x)$ for $|u(x)| > 1$, the prescription which is used in the present work, or to set $u(x) = \tan v(x)$, as was suggested in [25, 26] and utilized in [21]. The corresponding nonlinear equations for $v(x)$ have the form

$$\frac{dv(x)}{dx} = -v(x)^2 f\left(\frac{1}{v(x)}, x\right), \tag{38}$$
$$v(0) = u(c), \quad |u(c)| = 1,$$

and

$$\frac{dv(x)}{dx} = \cos^2 v(x) f(\tan v(x), x), v(0) = 0, \tag{39}$$

respectively.

Let us now turn our attention to the iteration sequences given by Eqs. (20) and (21). These successive approximation schemes were considered by Picard [27] and Babikov, Calogero, and Fluegge (BCF) [14, 13, 23], respectively. The quadratic convergence reached in QLM is based on a specific choice of function $w(x)$ and its functional $h(w(x), x)$ given by Eq. (19), which, in view of the mean-value theorem of Eq. (25), assures cancellation of the first power of $\delta u_n(x)$ and $\Delta u_n(x)$ in recurrence relations of Eqs. (24) and (36), respectively. Such cancellation will not happen for the Picard and BCF choices of $w(x)$ and $h(w(x), x)$ given by Eqs. (17) and (18). One obtains, therefore, for these approximation schemes the usual inequality characteristic of first-order convergence

$$||\delta u_{n+1}|| < p||\delta u_n||, \tag{40}$$

p being a correspondent convergence coefficient. This leads, instead of very rapid 2^n-power type of convergence, displayed in Eqs. (33) and (37), to much slower geometric convergence

$$||\delta u_{n+1}|| < p^n||\delta u_1||. \tag{41}$$

3. THE QUASILINEARIZATION METHOD FOR THE nth-ORDER NONLINEAR DIFFERENTIAL EQUATION

For simplicity, we limit our discussion here to nonlinear ordinary differential equation on the interval $[0, b]$, which could be infinite:

$$L^{(n)}u(x) = f(u(x), u^{(1)}(x), \ldots, u^{(n-1)}(x), x), \tag{42}$$

with n boundary conditions

$$g_k(u(0), u^{(1)}(0), \ldots, u^{(n-1)}(0)) = 0, \quad k = 1, \ldots, l, \tag{43}$$

and

$$g_k(u(b), u^{(1)}(b), \ldots, u^{(n-1)}(b)) = 0, \quad k = l+1, \ldots, n. \tag{44}$$

Here, $L^{(n)}$ is a linear nth-order ordinary differential operator and f and $g_1, g_2, \ldots, g_n$ are nonlinear functions of $u(x)$ and its $n-1$ derivatives $u^{(s)}(x)$, $s = 1, \ldots, n-1$. The more general case of partial differential equations in N-dimensional space can be considered in exactly the same fashion by changing the definition of $L^{(n)}$ to be a linear nth-order differential operator in partial derivatives and x to be the N-dimensional coordinate array.

We will follow here the derivation outlined in [19, 20], which is not based, unlike the derivations in [10, 11], on a smallness of the interval and on the boundness of the nonlinear term and its functional derivatives, conditions which usually are not fillfilled in physical applications.

The QLM prescription [10, 11, 19, 20] determines the $r+1$ iterative approximation $u_{r+1}(x)$ to the solution of Eq. (42) as a solution of the linear differential equation

$$\begin{aligned} L^{(n)}u_{r+1}(x) &= f(u_r(x), u_r^{(1)}(x), \ldots, u_r^{(n-1)}(x), x) \\ &+ \sum_{s=0}^{n-1}\left(u_{r+1}^{(s)}(x) - u_r^{(s)}(x)\right) \\ &\times f_{u^{(s)}}(u_r(x), u_r^{(1)}(x), \ldots, u_r^{(n-1)}(x), x), \end{aligned} \tag{45}$$

where $u_r^{(0)}(x) = u_r(x)$, with linearized two-point boundary conditions

$$\begin{aligned} &\sum_{s=0}^{n-1}\left(u_{r+1}^{(s)}(0) - u_r^{(s)}(0)\right) \\ &\times g_{ku^{(s)}}(u_r(0), u_r^{(1)}(0), \ldots, u_r^{(n-1)}(0), 0) = 0, \\ &k = 1, \ldots, l, \end{aligned} \tag{46}$$

and

$$\begin{aligned} &\sum_{s=0}^{n-1}\left(u_{r+1}^{(s)}(b) - u_r^{(s)}(b)\right) \\ &\times g_{ku^{(s)}}(u_r(b), u_r^{(1)}(b), \ldots, u_r^{(n-1)}(b), b) = 0, \\ &k = l+1, \ldots, n. \end{aligned} \tag{47}$$

Here, the functions $f_{u^{(s)}} = \partial f/\partial u^{(s)}$ and $g_{ku^{(s)}} = \partial g_k/\partial u^{(s)}$, $s = 0, 1, \ldots, n-1$, are functional derivatives of the functionals $f(u(x), u^{(1)}(x), \ldots, u^{(n-1)}(x), x)$ and $g_k(u(x), u^{(1)}(x), \ldots, u^{(n-1)}(x), x)$, respectively. For example, in the case of a simple nonlinear boundary condition $u'(b)u(b) = c$, where c is a constant, one has $g(r) \equiv g(u(r), u'(r), r) = u'(r)u(r)$, so that $g_u = u'(r)$ and $g_{u'} = u(r)$. The linearized boundary condition (47) has the form $(u_{r+1}(b) - u_r(b))u_r'(b) + (u_{r+1}'(b) - u_r'(b))u(b) = 0$ or $(u_{r+1}(b)u_r(b))' = (u_r(b)u_r(b))'$, so the nonlinear boundary condition for the initial guess $u_0(b)u_0'(b) = c$ will be propagated to the linear boundary condition for the next iterations. The zeroth approximation $u_0(x)$ is chosen from mathematical or physical considerations.

To prove that the above procedure yields a quadratic and often monotonic convergence to the solution of Eq. (42) with boundary conditions (43) and (44), we follow the previous section and [19] and consider

a differential equation for the difference $\delta u_{r+1}(x) \equiv u_{r+1}(x) - u_r(x)$ between two subsequent iterations:

$$L^{(n)}\delta u_{r+1}(x) \tag{48}$$
$$= [f(u_r(x), u_r^{(1)}(x), \ldots, u_r^{(n-1)}(x), x)$$
$$- f(u_{r-1}(x), u_{r-1}^{(1)}(x), \ldots, u_{r-1}^{(n-1)}(x), x)]$$
$$+ \sum_{s=0}^{n-1}[\delta u_{r+1}^{(s)}(x)$$
$$\times f_{u^{(s)}}(u_r(x), u_r^{(1)}(x), \ldots, u_r^{(n-1)}(x), x) - \delta u_r^{(s)}(x)$$
$$\times f_{u^{(s)}}(u_{r-1}(x), u_{r-1}^{(1)}(x), \ldots, u_{r-1}^{(n-1)}(x), x)].$$

The boundary conditions are similarly given by the difference of Eqs. (46) and (47) for two subsequent iterations:

$$\sum_{s=0}^{n-1}[\delta u_{r+1}^{(s)}(0) \tag{49}$$
$$\times g_{ku^{(s)}}(u_r(0), u_r^{(1)}(0), \ldots, u_r^{(n-1)}(0), 0) - \delta u_r^{(s)}(0)$$
$$\times g_{ku^{(s)}}(u_{r-1}(0), u_{r-1}^{(1)}(0), \ldots, u_{r-1}^{(n-1)}(0), 0)] = 0,$$
$$k = 1, \ldots, l,$$

and

$$\sum_{s=0}^{n-1}[\delta u_{r+1}^{(s)}(b) \tag{50}$$
$$\times g_{ku^{(s)}}(u_r(b), u_r^{(1)}(b), \ldots, u_r^{(n-1)}(b), b) - \delta u_r^{(s)}(b)$$
$$\times g_{ku^{(s)}}(u_{r-1}(b), u_{r-1}^{(1)}(b), \ldots, u_{r-1}^{(n-1)}(b), b)] = 0,$$
$$k = l+1, \ldots, n.$$

In view of the mean-value theorem [24],

$$f(u_r(x), u_r^{(1)}(x), \ldots, u_r^{(n-1)}(x), x) \tag{51}$$
$$- f(u_{r-1}(x), u_{r-1}^{(1)}(x), \ldots, u_{r-1}^{(n-1)}(x), x)$$
$$= \sum_{s=0}^{n-1}\delta u_r^{(s)}(x)$$
$$\times f_{u^{(s)}}(u_{r-1}(x), u_{r-1}^{(1)}(x), \ldots, u_{r-1}^{(n-1)}(x), x)$$
$$+ \frac{1}{2}\sum_{s,t=0}^{n-1}\delta u_r^{(s)}(x)\delta u_r^{(t)}(x)$$
$$\times f_{u^{(s)}u^{(t)}}(\bar{u}_{r-1}(x), \bar{u}_{r-1}^{(1)}(x), \ldots, \bar{u}_{r-1}^{(n-1)}(x), x),$$

where $\bar{u}_{r-1}^{(s)}(x)$ lies between $u_r^{(s)}(x)$ and $u_{r-1}^{(s)}(x)$, Eq. (48) can be written as

$$L^{(n)}\delta u_{r+1}(x) - \sum_{s=0}^{n-1}\delta u_{r+1}^{(s)}(x) \tag{52}$$
$$\times f_{u^{(s)}}(u_r(x), u_r^{(1)}(x), \ldots, u_r^{(n-1)}(x), x)$$
$$= \frac{1}{2}\sum_{s,t=0}^{n-1}\delta u_r^{(s)}(x)\delta u_r^{(t)}(x)$$
$$\times f_{u^{(s)}u^{(t)}}(\bar{u}_{r-1}(x), \bar{u}_{r-1}^{(1)}(x), \ldots, \bar{u}_{r-1}^{(n-1)}(x), x).$$

Denoting $G_r^{(n)}(x,y)$ as the Green's function, which is the inverse of the following differential operator and incorporates linearized boundary conditions (46) and (47),

$$\tilde{L}^{(n)} = L^{(n)} \tag{53}$$
$$- \sum_{s=0}^{n-1} f_{u^{(s)}}(u_r(x), u_r^{(1)}(x), \ldots, u_r^{(n-1)}(x), x)\frac{d^s}{dx^s},$$

one can express the solution to the difference function δu_{r+1} as

$$\delta u_{r+1}(x) = \frac{1}{2}\int_0^b G_r^{(n)}(x,y) \tag{54}$$
$$\times \sum_{s,t=0}^{n-1}\delta u_r^{(s)}(y)\delta u_r^{(t)}(y)$$
$$\times f_{u^{(s)}u^{(t)}}(\bar{u}_{r-1}(y), \bar{u}_{r-1}^{(1)}(y), \ldots, \bar{u}_{r-1}^{(n-1)}(y), y)dy.$$

The functions $\delta u_r^{(s)}(y)\delta u_r^{(t)}(y)$ could be taken outside of the sign of the integral at some point $y = \bar{x}$ belonging to the interval, so one obtains

$$\delta u_{r+1}(x) = \frac{1}{2}\sum_{s,t=0}^{n-1}\delta u_r^{(s)}(\bar{x})\delta u_r^{(t)}(\bar{x})M_{\mathrm{st}}(x), \tag{55}$$

where $M_{\mathrm{st}}(x)$ equals

$$M_{\mathrm{st}}(x) = \int_0^b G_r^{(n)}(x,y) \tag{56}$$
$$\times f_{u^{(s)}u^{(t)}}(\bar{u}_{r-1}(y), \bar{u}_{r-1}^{(1)}(y), \ldots, \bar{u}_{r-1}^{(n-1)}(y), y)dy.$$

If $M_{\mathrm{st}}(x)$ is a strictly positive (negative) matrix for all x in the interval, then $\delta u_{r+1}(x)$ will be positive (negative), and the monotonic convergence from below (above) results.

Obviously, from Eq. (54) follows

$$|\delta u_{r+1}(x)| \le k_r(x)||\delta u_r||^2, \tag{57}$$

where k_r is given by

$$k_r(x) = \frac{1}{2}\int_0^b |G_r^{(n)}(x,y)| \sum_{s,t=0}^{n-1} dy \tag{58}$$
$$\times |f_{u^{(s)}u^{(t)}}(\bar{u}_{r-1}(y), \bar{u}_{r-1}^{(1)}(y), \ldots, \bar{u}_{r-1}^{(n-1)}(y), y)|$$

and $||\delta u_r||$ is a maximal value of any of $|\delta \bar{u}_r^{(s)}|$ on the interval $(0, b)$.

Since Eq. (57) is correct for any x on the interval $(0, b)$, it is correct also for some $x = \bar{x}$, where $|\delta u_{r+1}(x)|$ reaches its maximum value $||\delta u_{r+1}||$. One therefore has

$$||\delta u_{r+1}|| \leq k_r(\bar{x})||\delta u_r||^2. \tag{59}$$

Assuming the boundness of the integrand in expression (58), that is, the existence of the bounding function $F(x)$ such that integrand at $x = \bar{x}$ and at any y is less than or equal to $F(y)$, one finally has

$$||\delta u_{r+1}|| \leq k||\delta u_r||^2, \tag{60}$$

where

$$k = \int_0^b F(x)dx. \tag{61}$$

The linearized boundary conditions (46) and (47) are obtained from exact boundary conditions (43) and (44) by using the mean-value theorem (51) and neglecting the quadratic terms, so that the error in using linearized boundary conditions vis-à-vis the exact ones is quadratic in the difference between the exact and linearized solutions. The maximum difference between boundary conditions (46) and (47) corresponding to two subsequent quasilinear iterations is therefore quadratic in $||\delta u_r||$. In view of this result and of Eq. (60), the difference between the subsequent iterative solutions to Eq. (45) with boundary conditions (46) and (47) decreases quadratically with each iteration. In a similar way, one can show (see previous section and [19]) that the difference $\Delta u_{r+1}(x) = u(x) - u_r(x)$ between the exact solution and the rth iteration decreases quadratically as well:

$$||\Delta u_{r+1}|| \leq k||\Delta u_r||^2. \tag{62}$$

A simple induction of Eq. (60) shows [11] that $\delta u_{n+1}(x)$ for an arbitrary $l < r$ satisfies the inequality

$$||\delta u_{r+1}|| \leq (k||\delta u_{l+1}||)^{2^{r-l}}/k, \tag{63}$$

or, for $l = 0$, we can relate the $(n+1)$th-order result to the first iterate by

$$||\delta u_{n+1}|| \leq ((k||\delta u_1||)^{2^n}/k. \tag{64}$$

The convergence depends therefore on the quantity $q_1 = k||u_1 - u_0||$, where, as we have mentioned earlier, the zeroth iteration $u_0(x)$ is chosen from physical and mathematical considerations. Usually, it is advantageous (see discussion below) that $u_0(x)$ satisfy at least one of the boundary conditions. From Eq. (63), it follows, however, that, for convergence, it is sufficient that just one of the quantities $q_m = k||\delta u_m||$ be small enough. Consequently, one can always hope [11] that, even if the first convergent coefficient q_1 is large, a well-chosen initial approximation u_0 results in the smallness of at least one of the convergence coefficients q_m, $m > 1$, which then enables a rapid convergence of the iteration series for $r > m$. It is important to stress that, in view of the quadratic convergence of the QLM method, the difference $||\Delta u_{r+1}||$ between the exact solution and the QLM iteration always converges to zero if the difference $\delta u_{r+1}(x)$ between two subsequent QLM iterations becomes infinitesimally small.

Indeed, if $\delta u_r(x)$ is close to zero, it means, since $\delta u_{r+1}(x) = \Delta u_r(x) - \Delta u_{r+1}(x)$, that $\Delta u_r(x) = \Delta u_{r+1}(x)$ or $Q_r = Q_{r+1}$, where $Q_r = k||\Delta u_r||$. When one assumes the possibility that Q_r and Q_{r+1} could not be small, one could conclude that the iteration process "stagnates," which means convergence to the wrong answer or no convergence at all.

However, such a conclusion is wrong since Eq. (62), which can be written as $Q_{r+1} \leq Q_r^2$, for $Q_r \leq 1$ (this last inequality, starting from some r, is a necessary condition of convergence), cannot be satisfied unless both $||Q_{r+1}||$ and $||Q_r||$ equal zero. This proves that stagnation of the iteration process is impossible and convergence of $||\delta u_{r+1}||$ to zero automatically leads to convergence of the QLM iteration sequence to the exact solution. Hence, the QLM assures not only convergence but also convergence to the correct solution.

Another corollary of this iteration process is that, if the solution and its derivatives are continuous functions of x, the convergence of the QLM in the whole region will follow. Indeed, even if the zero iteration $u_0(x)$ is chosen not to satisfy the boundary conditions, the next iteration $u_1(x)$, being a solution to a linear equation with linearized boundary conditions (46) and (47), will automatically satisfy the exact boundary conditions (43) and (44), at least up to the second order in difference δu_1 at the boundaries. This means that the difference between the exact and first QLM iterations at some intervals near the boundaries will be small, so that the QLM iterations in this interval would converge. Because the subsequent values of $k\delta u_m(x)$, $m > 2$, become much smaller for this interval, in view of assumed continuity of the solution and its derivatives, these differences will also be small at the neighboring intervals. The subsequent iterations will extend the convergence to the next neighboring intervals and so on, until the convergence in the whole region is reached. The predicted trend is therefore that the QLM yields rapid convergence starting at the regions where the boundary conditions are imposed and then spreading from there to all other regions.

An additional important corollary is that, in view of Eq. (63), once the quasilinear iteration sequence starts to converge, it will continue to do so, unlike the perturbation expansion, which is often given by an asymptotic series and therefore converges only up to a certain order and diverges thereafter.

Based on this summary of the QLM, one can deduce the following important features of the quasilinearization method:

(i) The method approximates the solution of nonlinear differential equations by treating the nonlinear terms as a perturbation about the linear ones and is not based, unlike perturbation theories, on the existence of some kind of small parameter.

(ii) The iterations converge uniformly and quadratically to the exact solution. In the case of matrix $M_{\rm st}$ in Eq. (56) being strictly positive (negative) for all x in the interval, the convergence is also monotonic from below (above).

(iii) For rapid convergence, it suffices that an initial guess for the zeroth iteration be sufficiently good to ensure the smallness of just one of the quantities $q_r = k||u_{r+1} - u_r||$. If the solution and its derivatives are continuous, convergence follows from the fact that, starting from the first iteration, all QLM iterations automatically satisfy the quasilinearized boundary conditions (46) and (47). The convergence is extremely fast: if, for example, q_1 is of the order of $1/3$, only four iterations are necessary to reach the accuracy of eight digits, since $(1/3)^{2^n}$ is of the order of $(1/10)^{2^{n-1}}$.

(iv) Convergence of $||\delta u_{r+1}||$ to zero automatically leads to convergence of the QLM iteration sequence to the exact solution.

(v) Once the quasilinear iteration sequence at some interval starts to converge, it will always continue to do so. Unlike an asymptotic perturbation series, the QLM yields the required precision once a successful initial guess generates convergence after a few steps.

4. EXAMPLES: COMPARISON OF QUASILINEARIZATION RESULTS WITH EXACT SOLUTIONS

In order to investigate the applicability of the QLM and its convergence and numerical stability, we present in this review the results of computations [20] on different ordinary second- and third-order nonlinear differential equations applied in physics, namely, the Lane–Emden, Thomas–Fermi, and Blasius equations, and compare the results obtained by the QLM with the exact solutions. Although all our examples deal only with linear boundary conditions, the nonlinear boundary conditions can be handled readily after their quasilinearization as explained in the previous section.

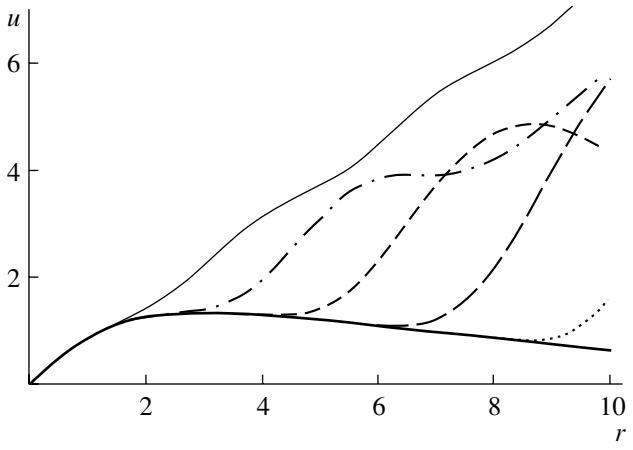

Fig. 1. Convergence of QLM iterations for the Lane–Emden equation and comparison with the numerically obtained exact solution. Thin solid, dash-dotted, short-dashed, long-dashed, and dotted curves correspond to the first, second, third, fourth, and fifth QLM iterations, respectively, while the thick solid curve displays the exact solution. The difference between the exact solution and the eighth QLM iteration for all r in the figure is less than 10^{-11}.

4.1. Lane–Emden Equation

The Lane–Emden equation

$$y''(r) + \frac{2}{r}y'(r) + y^n(r) = 0, \qquad (65)$$
$$y(0) = 1, \quad y'(0) = 0,$$

is a nonlinear second-order differential equation which arises in the study of stellar structure. It describes the equilibrium density distribution in a self-gravitating sphere of polytropic isothermal gas. The parameter n corresponds to a particular choice for an equation of state with its physically interesting range being $0 \le n \le 5$. The equation also appears in other contexts, e.g., in the case of radiatively cooling self-gravitating gas clouds, in the mean-field treatment of a phase transition in critical absorption, or in the modeling of clusters of galaxies. The equation can be solved analytically for the special cases $n = 0$, 1, and 5. For other values of n, power series approximations, as well as nonperturbative approaches, have been developed (see, for example, [28] and references therein). Setting $y = u/r$ transforms the equation to a more convenient form without a first derivative:

$$u''(r) + \frac{u^n(r)}{r^{n-1}} = 0, \quad u(0) = 0, \quad u'(0) = 1. \quad (66)$$

Let us consider this nonlinear equation for the physically interesting and analytically nonsolvable

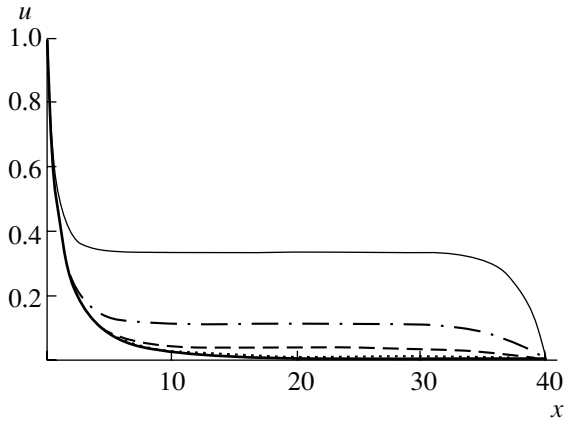

Fig. 2. Convergence of QLM iterations for the Thomas–Fermi equation and comparison with the numerically obtained exact solution. Thin solid, dash-dotted, short-dashed, and dotted curves correspond to the first, second, third, and fourth QLM iterations, respectively, while the thick solid curve displays the exact solution. The difference between the exact solution and the eighth QLM iteration for all x in the figure is less than 10^{-7}.

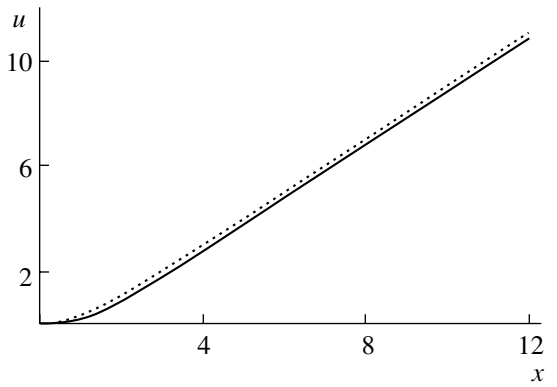

Fig. 3. Comparison of the first QLM iteration for the Blasius equation with the numerically obtained exact solution (dotted and solid curves, respectively). The difference between the exact solution and the fifth QLM iteration for all x in the figure is less than 10^{-10}.

case of $n = 4$. The quasilinearized form of Eq. (66) is

$$u''_{k+1}(r) + n\frac{u_k^{n-1}(r)}{r^{n-1}}u_{k+1}(r) = \frac{n-1}{r^{n-1}}u_k^n(r), \quad (67)$$
$$u_{k+1}(0) = 0, \quad u'_{k+1}(0) = 1.$$

The simplest initial guess satisfying the boundary conditions will be $u_0(r) = r$. A comparison of the quasilinear solutions corresponding to the first five iterations with the numerically computed exact solution is given in Fig. 1. The figure shows that the convergence to the exact solution is very fast. It starts at the left boundary and spreads with each iteration to larger values of r as expected from the discussion in Section 3. The difference between the exact solution and the eighth QLM iteration for all r in the range between 0 and 10, where our calculations were performed, is less than 10^{-11}.

4.2. Thomas–Fermi Equation

The Thomas–Fermi equation [29, 30]

$$\sqrt{x}u''(x) = u^{3/2}(x), \quad u(0) = 1, \quad u(\infty) = 0, \quad (68)$$

is an equation for the electron density around the nucleus of an atom. The left-hand side of the above equation equals zero for $u < 0$. The Thomas–Fermi equation is also very useful for calculating form factors and for obtaining effective potentials which can be used as initial trial potentials in self-consistent field calculations. It is also applicable to the study of nucleons in nuclei and electrons in metal. It has long been known (see [31] and references therein) that solution of this equation is very sensitive to a value of the first derivative at zero which ensures smooth and monotonic decay from $u(0) = 1$ to $u(\infty) = 0$ as demanded by the boundary conditions. Finding the value of $u'(0)$ accurately is a tedious procedure requiring considerable computer time. By contrast, the computation is much simpler for the quasilinearized version of this equation. The QLM procedure in this case reduces to setting $u''_{k+1}(r) = f(u_k) + (u_{k+1}(r) - u_k(r))f_u(u_k)$, where $f = u^{3/2}(r)/\sqrt{x}$ and the functional derivative is $f_u = (3/2)u^{1/2}/\sqrt{x}$, so that the QLM equation has the form

$$\sqrt{x}u''_{k+1}(x) - \frac{3}{2}u_k^{1/2}(x)u_{k+1}(x) = -\frac{1}{2}u_k^{3/2}(x), \quad (69)$$
$$u_{k+1}(0) = 1, \quad u_{k+1}(\infty) = 0,$$

which is easily solved by specifying directly the boundary condition at infinity without searching first for the proper value of the first derivative. The initial guess satisfying the boundary condition at zero was chosen to be $u_0(x) \equiv 1$. The results of QLM calculations with Eq. (69) are presented in Fig. 2, which displays the exact solution together with the first four QLM iterations.

The convergence starts at the boundaries, exactly as expected from the discussion in the previous section, and expands with each iteration to a wider range of values of the variable x. The difference between the exact solution and the eighth QLM iteration for all x in the range between 0 and 40, where our calculations were performed, is less than 10^{-7}.

4.3. Blasius Equation

The Blasius equation [32]

$$u'''(x) + u''(x)u(x) = 0, \quad (70)$$

$$u(0) = u'(0) = 0, \quad u'(\infty) = 1,$$

is a third-order nonlinear differential equation which describes the velocity profile of the fluid in the boundary layer which forms when fluid flows along a flat plate. The Blasius equation is similar to the Thomas–Fermi equation in that it has a two-point boundary condition. However, it differs from the Thomas–Fermi case in that it is of higher order and also contains a second-derivative term times $u(x)$. Therefore, Eq. (70) is even more difficult to solve. The QLM procedure in this case is given by $u'''_{k+1}(x) = f(u_k, u''_k) + (u_{k+1} - u_k) f_u(u_k, u''_k) + (u''_{k+1} - u''_k) f_{u''}(u_k, u''_k)$, where $f(u, u') = -u''u$, $f_u(u, u') = -u''$, and $f_{u''}(u, u') = -u$. The quasilinearized version of the Blasius equation thus has the form

$$u'''_{k+1}(x) + u_k(x)u''_{k+1}(x) + u_{k+1}(x)u''_k(x) - u_k(x)u''_k(x) = 0, \quad u_{k+1}(0) = u'_{k+1}(0) = 0, \quad u'_{k+1}(\infty) = 1. \tag{71}$$

The initial guess satisfying the boundary condition for the derivative at zero was chosen to be $u_0(x) \equiv 1$. The results of QLM calculations with Eq. (71) are presented in Fig. 3, which displays the exact solution together with the first QLM iteration.

The convergence starts at the left boundary, as follows from the discussion in Section 3, and expands with each iteration to larger values of the variable x. The difference between the exact solution and the fifth QLM iteration for all x in the range between 0 and 10, where our calculations were performed, is less than 10^{-10}.

We see in all our examples that QLM is able to handle large values of the coupling constant and any degree of the nonlinearity and provides extremely accurate and numerically stable answers for a wide range of nonlinear physics problems.

5. COMPARISON WITH PERTURBATION THEORY

In the previous sections, we have proved that the QLM successive approximations to exact solution converge quadratically and uniformly to an exact solution. In this section, we consider examples of different singular and nonsingular, attractive and repulsive potentials for which the nonlinear first-order ordinary differential equation for an S-wave scattering length,

$$\frac{da(r)}{dr} = -V(r)(r + a(r))^2, \quad a(0) = 0, \tag{72}$$

obtained in variable-phase approach [13, 14], could be solved exactly. We will compare the iterations obtained by QLM with perturbation theory and with exact solutions.

5.1. Square-Well Potential

1. Repulsive square well. Let us start from the repulsive square-well potential

$$V(r) = \frac{\lambda}{R^2}\Theta(R - r), \tag{73}$$

where $\Theta(R - r)$ is the Heaviside function and λ is a potential strength which for now is assumed to be positive. The change of variables to dimensionless variable $x = \sqrt{\lambda}r/R$ and dimensionless function $A(x) = \sqrt{\lambda}a(xR/\sqrt{\lambda})/R$ allows one to express Eq. (72) for $x \le x_0$, $x_0 = \sqrt{\lambda}$ in the form

$$\frac{dA(x)}{dx} = -(x + A(x))^2, \quad A(0) = 0. \tag{74}$$

For $x > x_0$, $A(x)$ is a constant equal dimensionless scattering length $A_0 = \sqrt{\lambda}a_0/R$, the scattering length itself being $a_0 \equiv a(R)$. A further change of the function to $u(x) = x + A(x)$ gives a familiar equation for the hyperbolic tangent

$$\frac{du(x)}{dx} = 1 - u^2(x), \quad u(0) = 0. \tag{75}$$

Exact variable scattering length $a(r)$ for the repulsive square-well potential is therefore

$$a(r) = \frac{R}{\sqrt{\lambda}} \tanh\left(\sqrt{\lambda}\frac{r}{R}\right) - r, \tag{76}$$

while the scattering length is given by

$$a_0 = R\left(\frac{\tanh\sqrt{\lambda}}{\sqrt{\lambda}} - 1\right) \equiv R\left(\frac{\tanh x_0}{x_0} - 1\right). \tag{77}$$

We use here the Calogero definition of the scattering length [13]

$$a_0 = \lim_{k\to 0} \frac{\tan\delta(k)}{k}, \tag{78}$$

δ being a scattering phase, which is different in sign from the definition used in most publications.

Before considering the QLM, let us turn to the usual perturbation theory. Displaying explicitly the dependence of the potential on the coupling constant $V(r) = \lambda v(r)$ and expanding $a(r)$ in powers of λ, one obtains from Eq. (72)

$$\sum_{k=1}^{\infty} \lambda^k a'_k(r) = -\lambda v(r)\left(r + \sum_{n=1}^{\infty} \lambda^n a_n(r)\right)^2. \tag{79}$$

Comparisons of coefficients before the powers of λ gives the recurrence relation

$$a'_k(r) = -v(r) \tag{80}$$

$$\times \left(r^2\delta_{k1} + 2ra_{k-1}(r) + \sum_{n=1}^{k-2} a_{k-n-1}(r)a_n(r) \right).$$

For the repulsive square-well potential, the successive integrations of these equations produce the expansion $a(r)$ in the powers of the coupling constant. The first three terms of the perturbation expansion of the variable scattering length, for example, are

$$a_1(r) = -\int_0^r ds s^2 v(s), \tag{81}$$

$$a_2(r) = -\int_0^r ds \cdot 2sv(s)a_1(s),$$

$$a_3(r) = -\int_0^r dsv(s)(2sa_2(s) + a_1^2(s)),$$

and so on. In terms of function $u(x)$, this expansion has the form

$$u(x) = x - \frac{1}{3}x^3 + \frac{2}{15}x^5 - \frac{17}{315}x^7 + \frac{62}{2835}x^9 - \frac{1382}{155925}x^{11} + \frac{21844}{6081075}x^{13} - \frac{929569}{638512875}x^{15} + \frac{6404582}{10854718875}x^{17} + O(x^{19}). \tag{82}$$

These series, of course, could also be obtained by using the power series expansion of $\tanh(x)$. The power expansion of scattering length is given by Eqs. (82) and (77); the latter can be written in the form $a_0 = R(u(x_0)/x_0 - 1)$.

Let us consider now the approximate QLM solutions to Eq. (75), choosing as a zeroth approximation a solution to this equation for a very small x: $u_0(x) = x$. Recurrence relation (22) now has the form

$$u_{n+1}(x) = \int_0^x ds(1 + u_n^2(s)) \exp\left(-2\int_s^x dt u_n(t) \right), \tag{83}$$

while the nth approximation to the scattering length is given by

$$a_{0,n} = R\left(\frac{u_n(x_0)}{x_0} - 1 \right). \tag{84}$$

The substitution of the zeroth iteration in Eq. (83) leads to a first-order approximation

$$u_1(x) = -i\frac{\sqrt{\pi}}{4}\mathrm{erf}(ix)e^{-x^2} + \frac{x}{2}, \tag{85}$$

where $\mathrm{erf}(x)$ is the error function [33]. Expansion of (85) in a power series enables a comparison with perturbation series (82),

$$u_1(x) = x - \frac{1}{3}x^3 + \frac{2}{15}x^5 - \frac{4}{105}x^7 + \frac{8}{945}x^9 + O(x^{11}), \tag{86}$$

which shows that the first approximation reproduces exactly three terms of the perturbation series, that is, two more terms than was given correctly by the zero QLM approximation $u_0(x) = x$. This improvement of the representation of the perturbation series not by one but by two powers of λ is, of course, precisely what one should expect from the quadratic convergence. In addition, the fourth term is also mostly correct, being $-12/315$ vis-à-vis exact $-17/315$. The second iteration $u_2(x)$ cannot be calculated analytically, but can be computed numerically or expressed by a power series expansion with the help of a symbolic computation program [34]. The latter gives

$$u_2(x) = x - \frac{1}{3}x^3 + \frac{2}{15}x^5 - \frac{17}{315}x^7 + \frac{62}{2835}x^9 - \frac{1382}{155925}x^{11} + \frac{21844}{6081075}x^{13} - \frac{918844}{638512875}x^{15} + \frac{39944}{70945875}x^{17} + O(x^{19}). \tag{87}$$

One can see that the second iteration of QLM reproduces correctly the first seven terms of the perturbation series, an improvement by four powers of λ compared with the previous QLM approximation $u_1(x)$. In addition, the eighth and ninth terms of the power-series expansion of $u_2(x)$ are very close to their precise values in perturbation theory, being $-\frac{918844}{638512875}$ and 5.63×10^{-4} vis-à-vis exact values $-\frac{929569}{638512875}$ and 5.90×10^{-4}, respectively.

Aside from the fact that first QLM approximations already sum many orders of the usual perturbation theory, the QLM iterations, unlike the perturbation series, have meaning also for a large or even infinite values of coupling constant. Indeed, for $\lambda \to \infty$, any term of the perturbation series is infinite. Even for a finite moderately large potential strength $\lambda \geq 2.5$, perturbation expansion (82) diverges since the power-series expansion of the hyperbolic tangent of x_0 converges [33] only for $x_0 < \pi/2$, that is, for $\lambda < \pi^2/4$. On the other hand, the QLM approximations to the scattering length are finite. The first QLM approximation to scattering length (85) in view of an asymptotic expression

$$\mathrm{erf}(z) \simeq \left(1 - \frac{e^{-z^2}}{\sqrt{\pi}z} \right) \tag{88}$$

for $|z| \to \infty$ [33] shows that the scattering length in this approximation equals $-R/2$, a reasonable approximation to exact value $a_0 = -R$. The computation of the scattering length in the second QLM approximation gives again a finite and improved result $a_0 = -3R/4$.

To tackle more rigorously the question of convergence of the iteration series for dimensionless scattering length $A_{0,n} = a_{0,n}/R$ given by Eqs. (83), (84) to the exact result $A_0 = a_0/R$, let us turn to the convergence condition demanding the smallness of convergence coefficient (34), which in this case is given by

$$q_1(b) = k(b)||a_{0,1} - a_{0,0}|| \tag{89}$$
$$= k(b)\left|\left|\frac{u_1(x) - u_0(x)}{x}\right|\right| = k(b)\max_{0\le x\le b}\left|\frac{u_1(x)}{x} - 1\right|.$$

To calculate $q_1(b)$, one first has to estimate $k(b)$ using, for example, Eq. (35). From Eq. (75) and the boundary condition, there follows $u(-x) = -u(x)$. We can consider therefore only the positive branch of the solution whose extremum is reached when $u'(x) = 1 - u^2(x) = 0$, that is, when $u(x) = 1$. This means that $0 \le u(x) \le 1$. Since the first and second functional derivatives of $f(u(x), x) = 1 - u^2(x)$ equal $-2u(x)$ and -2, respectively, one can set $F(x) = -2$ and $G(x) = |F(x)| = 2$, which gives

$$k(b) = \frac{1}{2}|e^{-2b} - 1| \le \frac{1}{2}. \tag{90}$$

In view of the fact that, due to the properties [33] of the error function, $|u_1(x)/x - 1| \le 1/2$ for all positive x, one obtains $q_1(b) \le 1/4$ for all values of b. Thus, the convergence of QLM approximations (84), (84) to the exact scattering length in the case of a repulsive square well is uniform and quadratic for all values of x_0, that is, for all values of coupling constant λ.

2. Attractive square well. The same conclusions are correct also for the attractive square-well potential the equations for which are obtained by changing λ to $-\lambda$. The equation for $u(x)$ now has the form

$$\frac{du(x)}{dx} = 1 + u^2(x), \quad u(0) = 0. \tag{91}$$

Its solution is

$$u(x) = \tan x, \tag{92}$$

and the scattering length is given by

$$a_0 = R\left(\frac{\tan\sqrt{\lambda}}{\sqrt{\lambda}} - 1\right) \equiv R\left(\frac{u(x_0)}{x_0} - 1\right). \tag{93}$$

The QLM subsequent approximations are obtained with the help of recursion equations

$$u_{n+1}(x) = \int_0^x ds(1 - u_n^2(s))\exp\left(2\int_s^x dt u_n(t)\right). \tag{94}$$

Choosing the zeroth QLM approximation as before in the form $u_0(x) = x$ leads to the first QLM approximation

$$u_1(x) = \frac{\sqrt{\pi}}{4}\mathrm{erf}(x)e^{x^2} + \frac{x}{2}. \tag{95}$$

Now there is, however, an additional difficulty, since scattering length $a_0(x_0)$ is a singular function of $x_0 = \sqrt{\lambda}$ and becomes infinite at values of the coupling constant corresponding to zero bound-state energies $\lambda = ((2n+1)\pi/2)^2$. This finds reflection in the fact that $u_1(x_0)$ increases very fast for x_0 around $\pi/2$. To deal with it, let us, in accordance with the discussion in the previous section, regularize Eq. (91), that is, reformulate it for $|u(x)| > 1$ in terms of a new function

$$v(x) = \frac{1}{u(x)}. \tag{96}$$

Defining c as a singular point, where $u(c) = \infty$, one obtains, according to Eq. (38), the following nonlinear equation for $v(x)$:

$$\frac{dv(x)}{dx} = -(1 + v(x)^2), \quad v(c) = \frac{1}{u(c)} = 0. \tag{97}$$

In view of Eq. (91), a solution to this equation is $v(x) = u(c - x)$. Equation (96) then gives

$$u(x) = \frac{1}{u(c - x)}. \tag{98}$$

Setting $x = c/2$ allows to write an equation

$$u^2\left(\frac{c}{2}\right) = 1 \tag{99}$$

for constant c. Since the solution to Eq. (91) should be an odd function of x,

$$u(-x) = -u(x), \tag{100}$$

it is enough to choose only a positive branch of Eq. (99), that is,

$$u\left(\frac{c}{2}\right) = 1. \tag{101}$$

From Eqs. (98) and (100) follows the $2c$ periodicity of solution $u(x)$: $u(x + 2c) = 1/[u(c - (x + 2c))] = -1/[u(x + c)] = -u(c - (c + x)) = u(x)$. Thus, it is enough to find a solution only on the interval $(0, 2c)$. We can now formulate the following result:

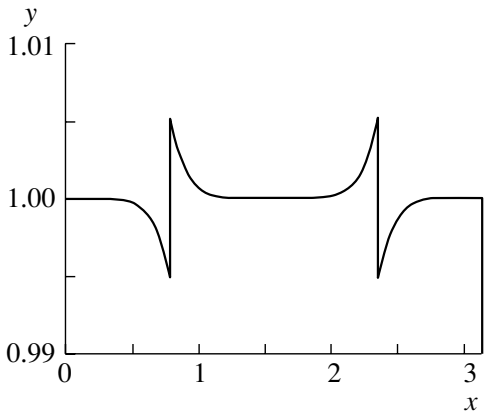

Fig. 4. The ratio of the first QLM iteration to the exact solution for the attractive square well as a function of the potential strength λ (axis x).

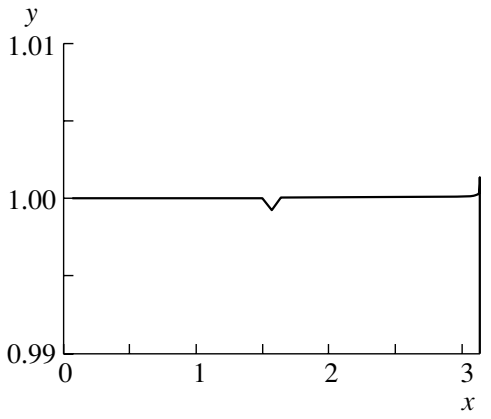

Fig. 5. The same as in Fig. 4, but for the second QLM approximation.

The nth QLM approximation $U_n(x)$ to the solution of Eq. (91) on the interval $[0, 2c_n]$, which is able to properly describe a singularity, is given by

$$U_n(x) = u_n(x)\Theta\left(\frac{c_n}{2} - x\right)\Theta(x) \qquad (102)$$
$$+ \frac{1}{u_n(c_n - x)}\Theta\left(x - \frac{c_n}{2}\right)\Theta\left(\frac{3c_n}{2} - x\right)$$
$$+ u_n(x - 2c_n)\Theta\left(x - \frac{3c_n}{2}\right)\Theta(2c_n - x),$$

where the nth QLM approximation $u_n(x)$ on the interval $(0, c_n/2)$ is found with the help of recurrence relations Eq. (94) and the nth approximate value c_n of c is given by

$$u_n\left(\frac{c_n}{2}\right) = 1. \qquad (103)$$

Computation of $c_n/2$ shows that the differences between exact value $c = \pi/2$ and approximate values c_n are very small even for the first and second QLM iterations, namely, $c_1 - \pi/2$ and $c_2 - \pi/2$ are 0.00529 and 0.00000132, the errors being 0.5 and $10^{-4}\%$, respectively. Since the nth QLM approximation, Eq. (102), has a pole at $x_0 = c_n$, $\lambda = c_n^2$ gives a value of potential strength corresponding to a zero-energy bound state. One sees that the QLM description of such a state is extremely accurate even in the first and especially in the second approximations.

To prove the uniform quadratic convergence of the QLM iterations, it is enough, in view of Eqs. (100) and (102), to consider $u_n(x)$ only on intervals $(0, c_n/2)$ which are very close to interval $(0, \pi/4)$. Since the first and second functional derivatives on the left-hand side of Eq. (91) are $2u(x)$ and 2, respectively, and $|u(x)| \le 1$, one can choose $F(x) = G(x) = 2$ and use Eq. (35), which produces a simple expression for $k(b)$,

$$k(b) = \frac{1}{2}(e^{2b} - 1). \qquad (104)$$

This leads to the following result for $q_1(b)$:

$$q_1(b) = \frac{1}{2}(e^{2b} - 1)\left(\frac{\sqrt{\pi}}{4}\mathrm{erf}(b)e^{b^2} - \frac{b}{2}\right). \qquad (105)$$

A simple computation shows that $0 < q_1(b) < 1$ for $0 < b < 0.92$, which proves the uniform quadratic convergence of the QLM iterations on an even larger interval $(0, 0.92)$ than the interval $(0, \pi/4)$ and thus the convergence of the sequence $U_n(x_0)$ to the exact solution $\tan x_0$ on the interval $(0, 2c_n) \approx (0, \pi)$. In view of its $2c_n \approx \pi$ periodicity, the nth QLM approximation $U_n(x_0)$ converges therefore to the exact solution for all x_0, that is, for all values of the coupling constant λ.

The extremely fast convergence of QLM approximations given by Eq. (102) is evident from the ratios of first [Eq. (95)] and second [Eq. (94)] QLM iterations to exact solution (92), which are shown in Figs. 4 and 5, respectively.

5.2. δ-Function Potential

In the case of the δ-function potential

$$V(r) = \frac{\lambda}{R}\delta(r - R), \qquad (106)$$

Eq. (72) for the scattering length has the form

$$A'(x) = \lambda(x - A(x))^2\delta(x - 1) \qquad (107)$$
$$\equiv \lambda(1 - A(x))^2\delta(x - 1), \quad A(0) = 0,$$

where $x = r/R$ and $A(x) = -a(r)/R$ are a dimensionless variable and variable scattering length, respectively; note that, in the last equation, $A(x)$ cannot be set equal to $A(1)$, since $A(x)$ is discontinuous at $x = 1$, its derivative being proportional to the δ function. Introduction of a new function $y(x) = \lambda\Theta(x - 1)$, $y(0) = 0$, $y(\infty) = \lambda$, with a derivative $dy(x) = \lambda\delta(x - 1)dx$ reduces Eq. (107) to the form

$$\frac{dA(y)}{dy} = (1 - A(y))^2, \quad A(y)|_{y=0} = 0. \tag{108}$$

A solution to this equation is

$$A(y) = \frac{y}{1 + y}. \tag{109}$$

An exact solution to Eq. (72) for the δ potential thus is given by $a(r) = -RA(y) \equiv -R\lambda\Theta(r - R)/[1 + \lambda\Theta(r - R)]$. The scattering length a_0 equals $a(r)|_{r=\infty} \equiv -R\lambda/(1 + \lambda)$. It is singular at $\lambda = -1$, reflecting the existence of the zero-energy bound state for the unit potential strength.

Let us now consider QLM approximations to exact solution (109) in the case of the repulsive δ-function potential, $\lambda > 0$. According to Eq. (22), they are given by the following iteration sequence,

$$A_{n+1}(y) = \int_0^y ds(1 - A_n^2(s)) \tag{110}$$
$$\times \exp\left[-2\int_s^y dt(1 - A_n(t))\right],$$

since the functional derivative of the right-hand part of Eq. (108) equals $-2(1 - A(y))$. The introduction of the nth approximation $u_n(y) = 1 - A_n(y)$ to a function $u(y) = 1 - A(y) = 1/(1 + y)$ helps to write recurrence relationship (110) in a simpler form

$$u_{n+1}(y) = \exp\left(-2\int_0^y dtu_n(t)\right) \tag{111}$$
$$+ \int_0^y dsu_n^2(s)\exp\left[-2\int_s^y dtu_n(t)\right],$$

which coincides with the QLM iteration scheme (23) for Eq. (108), rewritten with the help of function $u(x) = 1 - A(x)$ as

$$u'(x) = -u(x)^2, \quad u(0) = 1. \tag{112}$$

Since for $x = \infty$ $y = \lambda$, $u_n(\lambda)$ gives the nth approximation to $u(\lambda) = 1 - A_0(\lambda) = 1/(1 + \lambda)$, where $A_0(\lambda)$ is the exact dimensionless scattering length.

Let us choose as a zero approximation $u_0(y) \equiv u(0) = 1$. The substitution in Eq. (111) for $n = 0$ gives

$$u_1(y) = \frac{1}{2}(1 + e^{-2y}). \tag{113}$$

One can see that, already, the first approximation $u_1(\lambda)$ for $\lambda \to \infty$ is finite and equals $1/2$, which gives a value of $1/2$ for the approximate dimensionless scattering length vis-à-vis exact value $A_0 = 1$. Each term in the perturbation series for $u(\lambda)$,

$$u(\lambda) = \sum_{m=0}^{\infty}(-\lambda)^m, \tag{114}$$

in this case is infinite, while the perturbation expansion itself is divergent already for $|\lambda| \geq 1$. The comparison of perturbation expansion (114) with the perturbative expansion of first QLM approximation (113)

$$u_1(\lambda) = \frac{1}{2}(1 + e^{-2\lambda}) = 1 - \lambda + \lambda^2 \tag{115}$$
$$- \frac{2}{3}\lambda^3 + \frac{1}{3}\lambda^4 - \frac{2}{15}\lambda^5 + O\left(\lambda^6\right)$$

shows that, in this approximation, the perturbation series is correct up to the fourth term. The next, second, approximation also can be calculated analytically with the help of a symbolic computation program [34] and gives a rather cumbersome expression,

$$u_2(\lambda) = -\frac{1}{4}\frac{-2\sqrt{e^{e^{-2\lambda}}} - e^{1/2-\lambda} + \sqrt{2\pi}\,\mathrm{erf}(e^{-\lambda}/\sqrt{2})\sqrt{e^{e^{-2\lambda}}}e^{1/2} - e^{1/2+\lambda} - \sqrt{2\pi}\,\mathrm{erf}(1/\sqrt{2})e^{1/2}\sqrt{e^{e^{-2\lambda}}}}{\sqrt{e^{e^{-2\lambda}}}e^{1/2\left(-e^{-2\lambda}+2\lambda+1\right)}}. \tag{116}$$

For $\lambda \to \infty$, the largest term in both numerator and denominator is $e^{1/2+\lambda}$. Therefore, $u_2(\infty) = 1/4$, which corresponds to the second QLM approximation to A_0 being $3/4$, a significant improvement compared with the result obtained in this limit in the first QLM approximation (113). The computation of the power-series expansion yields

$$u_2(\lambda) = 1 - \lambda + \lambda^2 - \lambda^3 + \lambda^4 - \lambda^5 + \lambda^6 \tag{117}$$
$$- \frac{62}{63}\lambda^7 + \frac{79}{84}\lambda^8 - \frac{4931}{5670}\lambda^9 + O(\lambda^{10}).$$

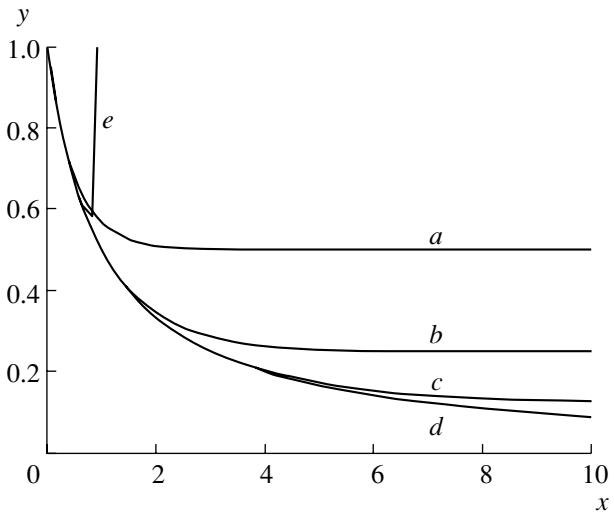

Fig. 6. Comparison of first three QLM approximations $u_n(\lambda), n = 1, 2, 3$ (curves a, b, c, respectively) with exact solution $u(\lambda) = 1/(1+\lambda)$ (curve d) and its perturbation expansion (114) (curve e) containing 15 terms (up to λ^{14}, inclusively) for the δ-function potential with the potential strength λ (axis x) changing in the interval $(0, 10)$.

The perturbation series in the second QLM approximation is given correctly up to the seventh term, while the coefficients of the eighth and ninth terms are different only by $1/63$ and $5/84$, that is, by 1.6 and 6%, respectively.

Analytic calculation of the third QLM approximation seems impossible, but the power series expansion can be evaluated with the help of the same program [34], which yields

$$u_3(\lambda) = 1 - \lambda + \lambda^2 - \lambda^3 + \lambda^4 - \lambda^5 + \lambda^6 \quad (118)$$
$$- \lambda^7 + \lambda^8 - \lambda^9 + \lambda^{10} - \lambda^{11} + \lambda^{12} - \lambda^{13} + \lambda^{14}$$
$$- \frac{59534}{59535}\lambda^{15} + \frac{1904891}{1905120}\lambda^{16} - \frac{12139457}{12145140}\lambda^{17}$$
$$+ \frac{161721779}{161935200}\lambda^{18} - \frac{113880892943}{114225041700}\lambda^{19} + O\left(\lambda^{20}\right).$$

In the third QLM approximation, the first 15 terms of the perturbation series are given exactly, while the next five terms have coefficients extremely close to being exact.

Summing up, the number of the terms given precisely in the zero, first, second, and third QLM approximations equals 1, 3, 7, and 15, increasing by 2, 2^2, and 2^3, respectively, that is, according to geometric progression with $q = 2$, exactly as one should expect from the quadratic law of convergence. The number N_n of perturbation series terms reproduced exactly in the nth QLM approximation is therefore

$$N_n = \sum_{k=0}^{n} q^k = \frac{q^{n+1} - 1}{q - 1} = 2^{n+1} - 1 \quad (119)$$

and for larger n approximately doubles with n increasing by each unit. For example, the 6th QLM approximation reproduces exactly $2^7 - 1 = 127$ terms of the perturbation expansion, while the 12th approximation reproduces $2^{13} - 1 = 8191$ terms, and so on.

The numerical computation of $u_3(\infty)$ gives 0.125, corresponding to $A_0 = 0.875$, a finite and gratifying result.

Comparison of the first three QLM approximations $u_n(\lambda)$, $n = 1, 2, 3$, with exact solution $u(\lambda) = 1/(1+\lambda)$ and its perturbation expansion (114) containing 15 terms (up to λ^{14}, inclusively) for the δ-function potential with the potential strength λ changing in the interval $(0, 10)$ is shown graphically in Fig. 6. One can see that each subsequent QLM approximation reproduces the exact solution better than the previous one up to infinite values of the coupling constant, while even 15th-order perturbation theory is not able to describe the exact solution adequately beyond $\lambda = 1$.

To prove the uniform quadratic convergence of QLM iterations, let us note that the first and second functional derivatives on the left-hand side of Eq. (112) are $-2u(x)$ and -2, respectively, exactly as in the case of the repulsive square well which was discussed earlier. The extremal value of $u(x)$, reached when $u'(x) = -u^2(x) = 0$, is obviously zero, which in view of boundary condition $u(0) = 1$ means $0 \le u(x) \le 1$. This allows one to choose the same functions $F(x) = -2$, $G(x) = 2$ as for the repulsive square well and, consequently, results in the same expression (90) for $k(b)$. Since from Fig. 6 it follows that the maximal difference between zero and first QLM approximations $||u_1(x) - u_1(x)||$ equals $1/2$, one obtains as before $q_1(b) \le 1/4$, which proves the uniform quadratic convergence of the QLM iterations for all values of b. This means that the convergence of subsequent QLM approximations to the exact scattering length for the repulsive δ-function potential is uniform and quadratic for all values of coupling constant λ, including very large and infinite ones.

5.3. Inverse Square Potential

Let us consider now the inverse square potential

$$V(r) = \frac{\lambda}{r^2}\Theta(R - r), \quad (120)$$

where λ is the dimensionless coupling constant. As is well known [35], this potential produces a fall to the

center in the case of $\lambda < -1/4$. For $r \le R$, Eq. (72) for the scattering length can be written in the form

$$A'(x) = -\lambda\left(1 + \frac{A(x)}{x}\right)^2, \quad A(0) = 0, \qquad (121)$$

where $x = r/R$ and $A(x) = a(r)/R$ are a dimensionless variable and variable scattering length, respectively; for $x > 1$, $A(x) \equiv A(1)$ is a constant and represents the dimensionless scattering length A_0. Looking for a solution in the form $A(x) = x\alpha(x)$, we obtain for $\alpha(x)$ the following equation:

$$\alpha'(x) = -\frac{1}{x}[\alpha(x) + \lambda(1 + \alpha(x))]^2. \qquad (122)$$

Note that, in this equation, boundary condition $\alpha(0) = 0$ is not necessary: $\alpha(x)$ could be any function regular at $x = 0$, so that condition $A(0) = 0$ is satisfied. Setting $\alpha(x) = \text{const} \equiv A_0$ gives an algebraic equation $A_0 = -\lambda(1 + A_0)^2$ whose solution is given by $A_0 = -1 - (1/2\lambda)(1 \pm \sqrt{1 + 4\lambda})$. Since for $\lambda \to 0$ there should be no scattering, only the solution with the minus sign before the square root should be chosen, since only for this solution $A_0 \to 0$ when $\lambda \to 0$. Setting for convenience $g = 4\lambda$, we finally obtain

$$A_0 = -1 - \frac{2}{g}(1 - \sqrt{1 + g}). \qquad (123)$$

The solution has a singularity, namely, a branch point, at $g = -1$, that is, at $\lambda = -1/4$. The singularity marks the beginning of interval $-\infty < \lambda < -1/4$, where a fall to the center takes place [35] and the expression for the scattering length becomes complex, its real and imaginary parts for $g < -1$ being given by

$$\mathrm{Re}A_0 = -1 - \frac{2}{g}, \quad \mathrm{Im}A_0 = \frac{2}{g}\sqrt{-1 - g}. \qquad (124)$$

Note that, in view of our definition (78) of the scattering length, one has to choose $\mathrm{Im}A_0 \ge 0$ [35]. The perturbation series for the scattering length can be obtained by expansion of the square root in Eq. (123) in a power series, which gives

$$\begin{aligned} A_0 = {} & -\frac{1}{4}g + \frac{1}{8}g^2 - \frac{5}{64}g^3 + \frac{7}{128}g^4 \qquad (125)\\ & - \frac{21}{512}g^5 + \frac{33}{1024}g^6 - \frac{429}{16384}g^7 + \frac{715}{32768}g^8\\ & - \frac{2431}{131072}g^9 + \frac{4199}{262144}g^{10} - \frac{29393}{2097152}g^{11}\\ & + \frac{52003}{4194304}g^{12} - \frac{185725}{16777216}g^{13} + \frac{334305}{33554432}g^{14}\\ & - \frac{9694845}{1073741824}g^{15} + \frac{17678835}{2147483648}g^{16}\\ & - \frac{64822395}{8589934592}g^{17} + \frac{119409675}{17179869184}g^{18}\\ & - \frac{883631595}{137438953472}g^{19} + \frac{1641030105}{274877906944}g^{20}\\ & - \frac{6116566755}{1099511627776}g^{21} + \frac{11435320455}{2199023255552}g^{22}\\ & - \frac{171529806825}{35184372088832}g^{23}\\ & + \frac{322476036831}{70368744177664}g^{24}\\ & - \frac{1215486600363}{281474976710656}g^{25}\\ & + \frac{2295919134019}{562949953421312}g^{26}\\ & - \frac{17383387729001}{4503599627370496}g^{27}\\ & + \frac{32968493968795}{9007199254740992}g^{28}\\ & - \frac{125280277081421}{36028797018963968}g^{29}\\ & + \frac{238436656380769}{72057594037927936}g^{30}\\ & - \frac{14544636039226909}{4611686018427387904}g^{31}\\ & + \frac{27767032438524099}{9223372036854775808}g^{32} + O(g^{33}). \end{aligned}$$

The expansion is convergent [33] for $|g| < 1$, that is, for $|\lambda| < 1/4$.

Let us now turn our attention to QLM approximations and their convergence. The QLM iterations sequences are easiest to find by considering differential form (3) of Eq. (22), which can be written as

$$\begin{aligned} \alpha'_{n+1}(x) = -\frac{1}{x}\Big[&\frac{g}{4}(1 - \alpha_n^2(x)) \qquad (126)\\ &+\alpha_{n+1}\left(1 + \frac{g}{2}(1 + \alpha_n(x))\right)\Big]. \end{aligned}$$

The assumption that $\alpha_n(x)$ are constant functions, $\alpha_n(x) \equiv c_n$, immediately establishes the QLM recurrence relationship

$$c_{n+1} = -g\frac{1 - c_n^2}{4 + 2g(1 + c_n)}. \qquad (127)$$

Note that, since $c_{n+1} \to 0$ when $g \to 0$, each approximation to the scattering amplitude vanishes for $g = 0$, as it should, since in absence of the potential there is no scattering. The convergence of the QLM iteration sequence to exact solution (123) is obvious. Indeed,

for $n \to \infty$, Eq. (127) is

$$c_\infty = -g\frac{1-c_\infty^2}{4+2g(1+c_\infty)}, \tag{128}$$

whose solution vanishing for $g \to 0$ is given by the expression for A_0 in Eq. (123). The QLM approximation c_n to the dimensionless scattering length for an infinite n therefore indeed is $c_\infty \equiv A_0$, as we wanted to show.

The explicit calculation of the first few QLM approximations, starting from the usual initial guess $c_0 = 0$, gives

$$c_1 = -\frac{g}{4+2g}, \tag{129}$$

$$c_2 = -\frac{1}{4}\frac{\left(16+16g+3g^2\right)g}{\left(8+8g+g^2\right)(2+g)}, \tag{130}$$

$$c_3 = -\frac{1}{8}\frac{\left(4096+12288g+14080g^2+7680g^3+2016g^4+224g^5+7g^6\right)g}{\left(128+256g+160g^2+32g^3+g^4\right)(2+g)\left(8+8g+g^2\right)}. \tag{131}$$

These expressions, unlike that of perturbation theory, give finite values also for $g > 1$ or even for $g = \infty$, where the first, second, and third QLM approximations give $-1/2$, $-3/4$, and $-7/8$ vis-à-vis exact value $A_0 = -1$; the fourth approximation, not given here because of its cumbrous form, results in $-15/16$, and so on. The convergence of these values is from above in agreement with the law of convergence for the concave functions proved in Section 2, since the second functional derivative $-\lambda/x^2$ on the right-hand side of Eq. (121) is negative for the repulsive potential.

The expansion of the QLM approximations in the power series in the coupling constant shows, as in previous examples, that each QLM iteration sums exactly many perturbation series terms, whose number is given by Eq. (119). One obtains

$$c_0 = 0, \tag{132}$$

$$c_1 = -\frac{1}{4}g+\frac{1}{8}g^2-\frac{1}{16}g^3+\frac{1}{32}g^4-\frac{1}{64}g^5+O\left(g^6\right), \tag{133}$$

$$\begin{aligned} c_2 = {} & -\frac{1}{4}g+\frac{1}{8}g^2-\frac{5}{64}g^3+\frac{7}{128}g^4 \\ & -\frac{21}{512}g^5+\frac{33}{1024}g^6-\frac{107}{4096}g^7+\frac{177}{8192}g^8 \\ & -\frac{593}{32768}g^9+O\left(g^{10}\right), \end{aligned} \tag{134}$$

$$\begin{aligned} c_3 = {} & -\frac{1}{4}g+\frac{1}{8}g^2-\frac{5}{64}g^3+\frac{7}{128}g^4 \\ & -\frac{21}{512}g^5+\frac{33}{1024}g^6-\frac{429}{16384}g^7+\frac{715}{32768}g^8 \\ & -\frac{2431}{131072}g^9+\frac{4199}{262144}g^{10}-\frac{29393}{2097152}g^{11} \\ & +\frac{52003}{4194304}g^{12}-\frac{185725}{16777216}g^{13}+\frac{334305}{33554432}g^{14} \\ & -\frac{2423711}{268435456}g^{15}+\frac{4419705}{536870912}g^{16} \\ & -\frac{16205537}{2147483648}g^{17}+\frac{29852049}{4294967296}g^{18} \\ & -\frac{220900693}{34359738368}g^{19}+O\left(g^{20}\right), \end{aligned} \tag{135}$$

$$\begin{aligned} c_4 = {} & -\frac{1}{4}g+\frac{1}{8}g^2-\frac{5}{64}g^3+\frac{7}{128}g^4 \\ & -\frac{21}{512}g^5+\frac{33}{1024}g^6-\frac{429}{16384}g^7+\frac{715}{32768}g^8 \\ & -\frac{2431}{131072}g^9+\frac{4199}{262144}g^{10}-\frac{29393}{2097152}g^{11} \\ & +\frac{52003}{4194304}g^{12}-\frac{185725}{16777216}g^{13}+\frac{334305}{33554432}g^{14} \\ & -\frac{9694845}{1073741824}g^{15}+\frac{17678835}{2147483648}g^{16} \\ & -\frac{64822395}{8589934592}g^{17}+\frac{119409675}{17179869184}g^{18} \\ & -\frac{883631595}{137438953472}g^{19}+\frac{1641030105}{274877906944}g^{20} \\ & -\frac{6116566755}{1099511627776}g^{21}+\frac{11435320455}{2199023255552}g^{22} \\ & -\frac{171529806825}{35184372088832}g^{23}+\frac{322476036831}{70368744177664}g^{24} \\ & -\frac{1215486600363}{281474976710656}g^{25}+\frac{2295919134019}{562949953421312}g^{26} \\ & -\frac{17383387729001}{4503599627370496}g^{27} \\ & +\frac{32968493968795}{9007199254740992}g^{28} \\ & -\frac{125280277081421}{36028797018963968}g^{29} \\ & +\frac{238436656380769}{72057594037927936}g^{30} \end{aligned} \tag{136}$$

$$-\frac{3636159009806727}{1152921504606846976}g^{31} + \frac{6941758109631017}{2305843009213693952}g^{32} + O\left(g^{33}\right).$$

A comparison of Eqs. (132)–(136) with Eq. (125) shows that the QLM iterations with $n = 0$, 1, 2, 3, 4 reproduce exactly 1, 3, 7, 15, 31 terms of the perturbation series, respectively, in exact agreement with Eq. (119), while the next few terms have coefficients extremely close to being exact. The number of terms given precisely by the zero, first, second, third, and fourth QLM approximations increases by 2, 2^2, 2^3, and 2^4, exactly as we saw earlier in the case of the δ-function potential and in precise agreement with the quadratic law of convergence. Due to the simplicity of the algebraic recurrence relations (127), Eq. (119) for number N_n of the perturbation series terms given precisely by the nth QLM approximation can be checked for higher QLM approximations. For example, earlier from the example of the repulsive δ potential, we concluded that $N_6 = 127$. The simple calculation using a symbolic manipulation program [34] shows immediately that it is precisely the same for the inverse square potential. Indeed, the first seven nonzero terms of the expansion in powers of g of difference $A_0 - c_6$ between exact scattering length (123) and its sixth QLM approximation are

$$-\frac{1}{2894802230932904885589274625217197696331749616641014100986439600197828240998 4}g^{127} + \frac{127}{57896044618658097711785492504343953926634992332820282019728792003956564819968}g^{128} - \frac{16319}{231584178474632390847141970017375815706539969331281128078915168015826259279872}g^{129} + \frac{707135}{463168356949264781694283940034751631413079938662562256157830336031652518559744}g^{130} - \frac{92988123}{37053468555941182535542715202780130513046395093004980492626426882532201484779 52}g^{131} + \frac{2473622041}{74106937111882365071085430405560261026092790186009960985252853765064402969559 04}g^{132} - \frac{110916205323}{29642774844752946028434172162224104410437116074403984394101141506025761187823616}g^{133}, \quad (137)$$

exactly as one expects from Eq. (119). In addition, one can see that the next terms of the perturbation series are also reproduced extremely well, their difference from the precise terms being infinitesimally small. Namely, the coefficient of 127th power of g is about 3.45×10^{-76}, the coefficient of 128th power is about 2.19×10^{-74}, and so on.

For the attractive potential, expressions (129)–(131) become singular, with the number of zeros of denominators increasing with each iteration. This, of course, is a reflection of the fact that the exact scattering length A_0 has a branch point at $g = -1$ and a cut line along the real axis between $g = -1$ and $g = -\infty$. When n increases, the poles get closer and closer to each other and fuse together at $n = \infty$, where, as we saw earlier, the exact amplitude and its singularity are reproduced.

To handle the singularities, one can try, as we have discussed earlier, to consider, instead of function $\alpha(x)$, a new function $\beta(x)$ such that $\alpha(x) = 1/\beta(x)$. Substitution of the last expression into Eq. (121) leads to the equation

$$\beta'(x) = \frac{1}{x}[\beta(x) + \lambda(1 + \beta(x))]^2, \quad (138)$$

which is different from Eq. (122) only by the sign of the right-hand side. The QLM iteration sequence is found as before by considering differential form (45) of Eq. (22),

$$\beta'_{n+1}(x) = \frac{1}{x}\left[\frac{g}{4}(1 - \beta_n^2(x)) + \beta_{n+1}\left(1 + \frac{g}{2}(1 + \beta_n(x))\right)\right], \quad (139)$$

which leads under a previous assumption of β_n being a constant function, $\beta_n \equiv c_n$, to exactly the same QLM recurrence relations (127). Again, the convergence of the QLM series follows from the fact that, at $n \to \infty$, we have the same equation (128), as before, with the only distinction that, since now the scattering amplitude in the limit $n = \infty$ is given by $1/\beta_\infty$,

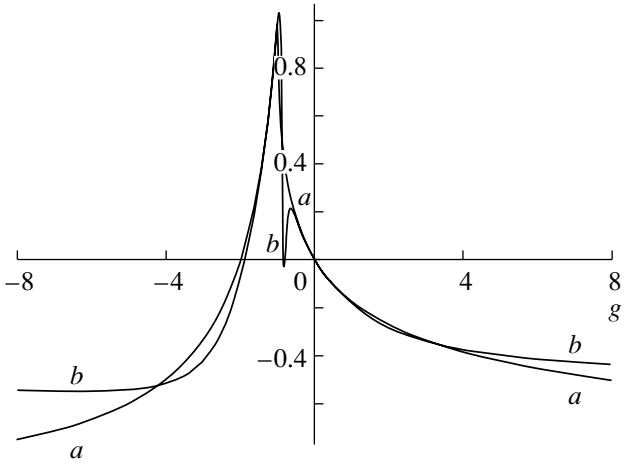

Fig. 7. Comparison of real parts of the exact scattering length (curve a) and of the second QLM approximation to it (curve b) for inverse square potential, $|g| \leq 8$.

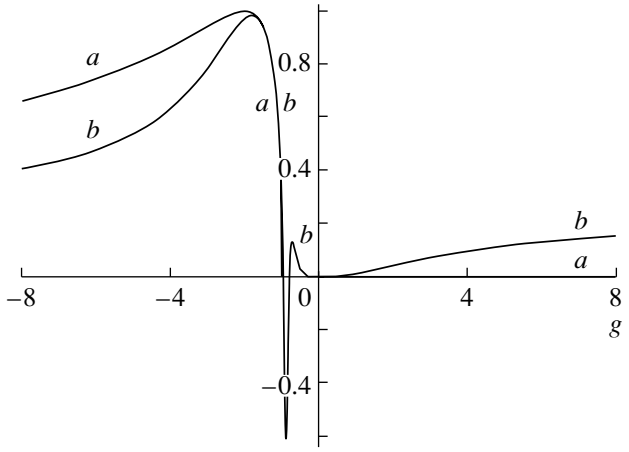

Fig. 8. Comparison of imaginary parts of the exact scattering length (curve a) and of the second QLM approximation to it (curve b) for inverse square potential, $|g| \leq 8$.

one should take a solution to this equation which goes to infinity at $g \to 0$ rather than to zero. Such a solution is given by

$$\beta_\infty = -1 - \frac{2}{g}(1 + \sqrt{1+g}). \qquad (140)$$

The $n = \infty$ QLM approximation to the scattering length A_0 thus equals

$$\frac{1}{\beta_\infty} = \frac{1}{-1 - (2/g)(1+\sqrt{1+g})} \qquad (141)$$
$$\equiv -1 - \frac{2}{g}(1 - \sqrt{1+g}),$$

which indeed coincides exactly with expression (123) for A_0.

Since the change to $\beta_n(x) = 1/\alpha_n(x)$ does not give anything new, the only way to avoid the singularities in the case of an attractive potential seems therefore to use the fact that the zero approximation could be an arbitrary, not necessarily real, number and to choose c_0 as a complex number with a positive imaginary part of the same order as the real part. The necessity of choosing c_0 complex in the case of the attractive potential follows also from the fact that, in this case, the fall to the center happens. The inelastic cross section for zero energies, determined by the imaginary part of the S-wave scattering length [35], cannot therefore be zero; however, from recurrence relations (127), it is obvious that, unless the initial guess c_0 is a complex number, all subsequent QLM approximations are real.

A comparison of real and imaginary parts of the scattering length with those calculated in the second and third QLM approximations for an arbitrary initial guess $\alpha_0 = 1 + i$ and for coupling constant values $|\lambda| \leq 2\ |g| \leq 8$ is shown in Figs. 7–10. One can see that, even for the second QLM iteration, the agreement between the exact scattering length and the QLM approximation to it is quite good. It improves visibly for the next QLM iteration. For the fourth and next iterations, the distinction between the exact and approximate scattering length is difficult to see and therefore the correspondent graphs are not shown.

5.4. Newton Supersingular Potential

Our next and last example [36] is the highly singular Newton potential [37]

$$V(r) = \frac{a^2}{(r/R)^4}(b^2 + c^2 e^{R/r}), \qquad (142)$$

which in canonical form, setting $(ab)^2 = g$, $(c/b)^2 = p$, and $R = 1$, can be written as

$$V(r) = \frac{g}{r^4}(1 + pe^{1/r}). \qquad (143)$$

This potential contains a fourth-order pole at the origin and for the nonzero p in addition an essential singularity there; g and p are inherently positive since the attractiveness of such a potential near the origin leads to the fall to the center [35, 37].

The scattering length is given by the analytical expression

$$a_0 = -\frac{z}{2}\frac{H_\nu^{(1)'}(z)}{H_\nu^{(1)}(z)}, \qquad (144)$$

where $\nu = 2\sqrt{g}$ and $z = 2i\sqrt{gp}$. In the limit of the inverse quartic potential, when $p = 0$, this equation, using the property of the Hankel function at zero argument, $H_\nu^{(1)'}(z)/H_\nu^{(1)}(z) = -2\nu/z$, reduces to $a_0 = -\sqrt{g}$, a well-known result [13, 23, 26]. Since for

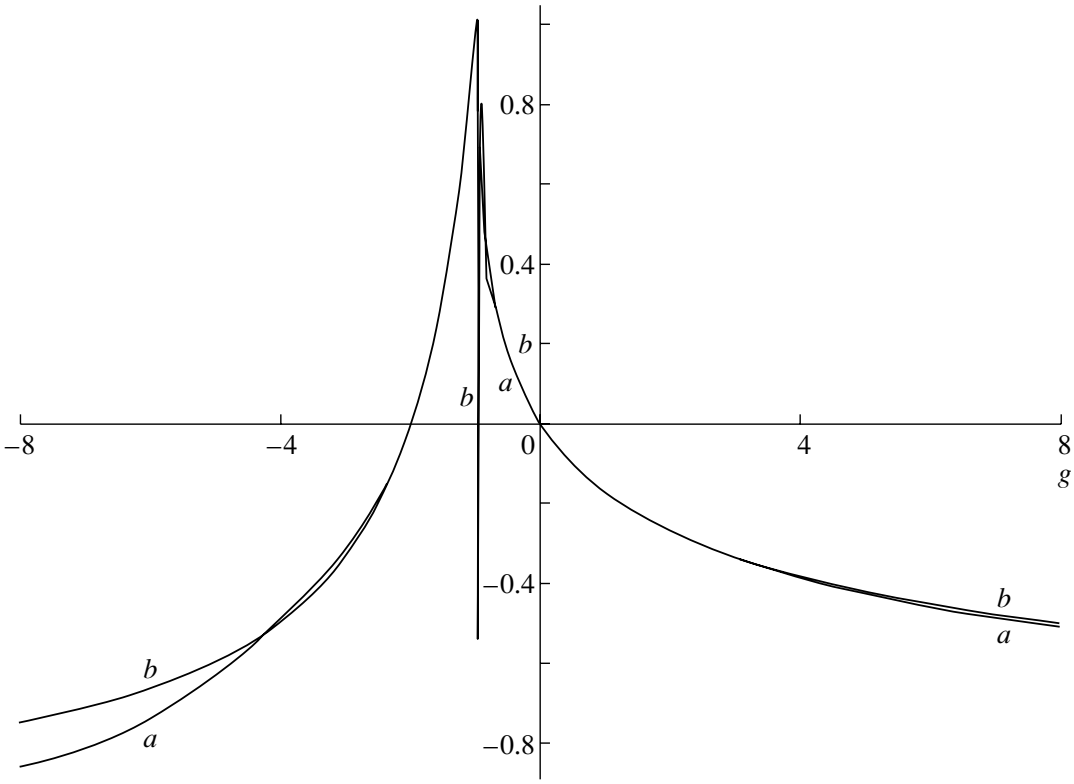

Fig. 9. The same as in Fig. 7, but in the third QLM approximation.

the repulsive potential no bound states are possible and the scattering length has no poles, we now use Eqs. (72) and (22) to obtain the scattering length in the QLM approximation. Tables 1–3 contain our results for potential strengths g between 1 and 10 and for different values of p: $p = 0$ corresponds to a pure inverse quartic potential, while $p = 1$ and $p = 10$ correspond to equal admixtures of the $1/r^4$ term and the term containing the essential singularity at the origin and to the dominant contribution of the latter term, respectively.

Since the patterns of convergence for different p are rather similar, we present the graphs only for one value of p. Namely, for $p = 1$, the first few iterations and the last iteration, as well as the exact solution, are displayed in Fig. 11, while Fig. 12 shows the dependence on the coupling strength of the number of iterations necessary to obtain five-digit accuracy of the scattering length. We see that, in this case, this number always equals 6 and, due to the extreme singularity of the Newton potential, does not depend on the strength of the potential.

One should stress that, unlike the QLM approach, which works perfectly well, giving an accuracy of five significant figures with just six iterations even for large values of coupling constants, the perturbation treatment in this case is not possible at all even for a very small coupling. Indeed, in view of the strong singularity of the potential at the origin, all the terms of the Born series for the scattering amplitude are divergent and no perturbation expansion exists for any coupling values, which is, of course, a direct consequence of the branch-point singularity of the exact scattering length (144) at $g = 0$. Since we now use Eq. (72), where the second functional derivative on the right-hand side,

$$-2V(r), \tag{145}$$

for the repulsive Newton potential is concave, the difference of subsequent QLM iterations should be strictly negative, ensuring the monotonic convergence to the exact solution from above. This, indeed, is what follows from Fig. 11, where the curve corresponding to the first iteration lies above the curve corresponding to the second iteration and both lie above the exact solution as expected.

6. QLM AND WKB

The derivation of the WKB solution starts by casting the radial Schrödinger equation into nonlinear Riccati form and solving that equation by expansion in powers of $\hbar$. It is interesting, instead,

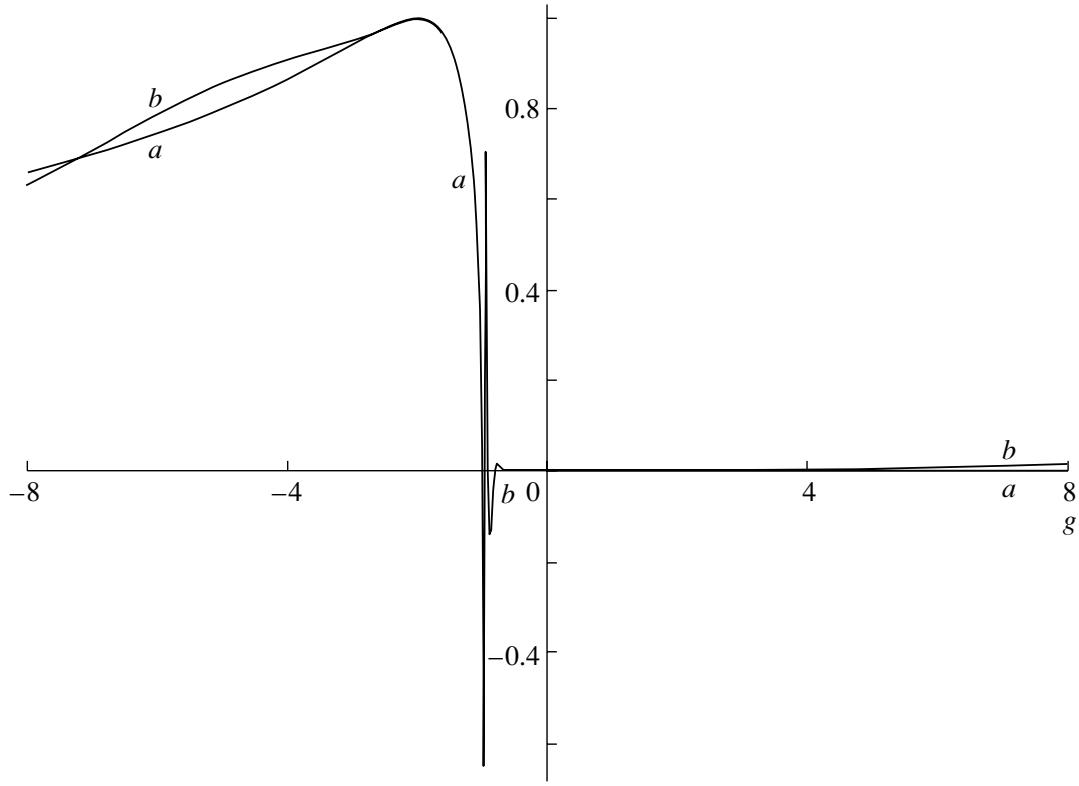

Fig. 10. The same as in Fig. 8, but in the third QLM approximation.

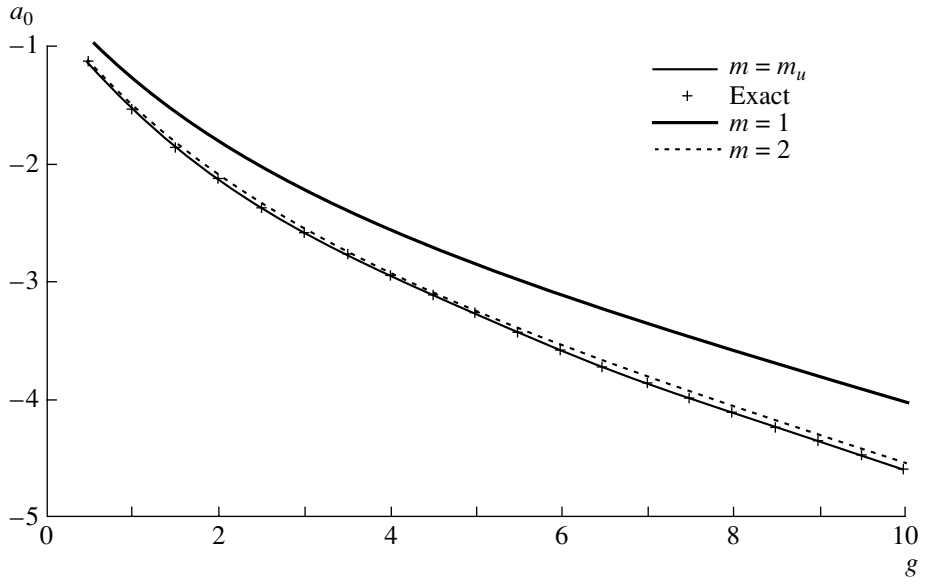

Fig. 11. Convergence of QLM iterations and comparison with the exact results for the scattering length a_0 for the Newton potential of Table 2 ($p = 1$).

to solve this nonlinear equation with the help of the QLM [19, 20] and compare the results with the WKB results. The QLM and its iterations were originally constructed [10, 11] as a generalization of the Newton–Raphson method [38, 39] to yield rapid quadratic and often monotonic convergence to the exact solution. The initial comparison of QLM and WKB was performed in [16, 17], where it was shown

that the first QLM iteration reproduces the structure of the WKB series, generating an infinite series of WKB terms, but with different coefficients. Besides being a better approximation than the usual WKB, the first QLM iteration is also expressible in a closed integral form.

The goal of this section is, following [40, 41], to point out that similar conclusions can be reached for higher QLM approximations as well. Namely, we show that the pth QLM iterate with $p > 1$ reproduces the WKB series exactly up to $\hbar^{2p}$: when expanded in powers of $\hbar$, it, besides providing the correct structure of the whole series, generates the coefficients of the first 2^n terms of the WKB series precisely and of a similar number of the next terms approximately. In addition, we prove that the exact quantization condition in any QLM iteration, including the first, leads to exact energies not only for the Coulomb and harmonic oscillator potentials, as was shown in [16, 17], but also for many other well-known physical potentials used in molecular and nuclear physics, such as the Pöschl–Teller, Hulthèn, Hyleraas, Morse, and Eckart.

The usual WKB substitution

$$\chi(r) = C \exp\left(\lambda \int^{r} y(r')dr'\right) \tag{146}$$

converts the radial Schrödinger equation

$$\frac{d^2\chi(r)}{dr^2} + \lambda^2 k^2 \chi(r) = 0 \tag{147}$$

to the nonlinear Riccati form

$$\frac{dy(z)}{dz} + (k^2(z) + y^2(z)) = 0. \tag{148}$$

Here, $k^2(z) = E - V - l(l+1)/z^2$, $\lambda^2 = 2m/\hbar^2$, and $z = \lambda r$.

The proper bound-state boundary condition for potentials falling off at $z \simeq z_0 \simeq \infty$ is $y(z) = \text{const}$ at $z \geq z_0$. This means that

$$y'(z_0) = 0, \tag{149}$$

so that Eq. (148) at $z \simeq z_0$ reduces to $k(z_0)^2 + y^2(z_0)) = 0$ or $y(z_0)) = \pm ik(z_0)$. We choose here to define the boundary condition with the plus sign, so that

$$y(z_0) = ik(z_0). \tag{150}$$

The quasilinearization [16, 19, 20] of this equation gives a set of recurrence differential equations

$$\frac{dy_p(z)}{dz} = y_{p-1}^2(z) - 2y_p(z)y_{p-1}(z) - k^2(z) \tag{151}$$

with the boundary condition deduced from Eq. (150):

$$y_p(z_0) = ik(z_0). \tag{152}$$

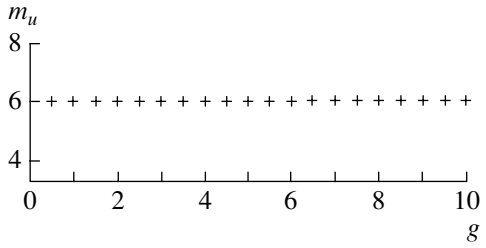

Fig. 12. Minimum QLM iteration number required in order that the absolute value of the difference between successive iterations be less than 10^{-5} for the potential of Fig. 11.

The analytic solution [16] of these equations expresses the pth iterate $y_p(z)$ in terms of the previous iterate:

$$y_p(z) = f_{p-1}(z) - \int_{z_0}^{z} ds \frac{df_{p-1}(s)}{ds} \times \exp\left[-2\int_{s}^{z} y_{p-1}(t)dt\right], \tag{153}$$

where

$$f_{p-1}(z) = \frac{y_{p-1}^2(z) - k^2(z)}{2y_{p-1}(z)}. \tag{154}$$

Indeed, differentiation of both parts of Eq. (154) leads immediately to Eq. (151), which proves that $y_p(z)$ is a solution to this equation. The boundary condition (150) is obviously satisfied automatically.

The second term in Eq. (153) could be written as

$$\int_{z_0}^{z} ds \left(-\frac{df_{p-1}(s)/ds}{2y_{p-1}(s)}\right) \times \left(2y_{p-1}(s)\exp\left[-2\int_{s}^{z} y_{p-1}(t)dt\right]\right). \tag{155}$$

The second expression in the parentheses in the integrand is the derivative of the exponential there. The integration by parts of this integral therefore gives

$$\left[\left(-\frac{1}{2y_{p-1}(s)}\frac{df_{p-1}(s)}{ds}\right) \times \exp\left[-2\int_{s}^{z} y_{p-1}(t)\right]\right]\Bigg|_{z_0}^{z} - \int_{z_0}^{z} ds \frac{d}{ds}\left(-\frac{df_{p-1}(s)/ds}{2y_{p-1}(s)}\right)\exp\left[-2\int_{s}^{z} y_{p-1}(t)dt\right]. \tag{156}$$

Table 1. Comparison of QLM and exact phases δ_0 (defined as $\delta_0 = \arctan a_0$, where a_0 is the scattering length) for the Newton potential $V(r) = (g/r^4)(1 + pe^{1/r})$, $p = 0$ [m_u is the minimum QLM iteration number required in order that the absolute value of the difference between successive iterations be less than 10^{-5}; the resulting absolute value of the difference $\Delta = \Delta u_{m_u+1}$ between the final QLM approximation and the exact solution is displayed in the last column, where square brackets denote the powers of 10 for the scattering length a_0 for the Newton potential $V(r) = g(1 + pe^{1/r})/r^4$ ($R = 1$); the choice $p = 0$ here reduces $V(r)$ to the special case $1/r^4$]

g	m_u	QLM	Exact	$\lvert\Delta\rvert$
1.0	5	−0.99999987	−1.00000000	1[−7]
2.0	6	−1.41421510	−1.41421356	2[−6]
3.0	6	−1.73205380	−1.73205081	3[−6]
4.0	6	−2.00000120	−2.00000000	1[−6]
5.0	6	−2.23606960	−2.23606798	2[−6]
6.0	6	−2.44949190	−2.44948974	2[−6]
7.0	6	−2.64575400	−2.64575131	3[−6]
8.0	6	−2.82843040	−2.82842712	3[−6]
9.0	6	−3.00000100	−3.00000000	1[−6]
10.0	6	−3.16227880	−3.16227766	1[−6]

Since the lower limit in the first term of this expression vanishes in view of Eq. (149), the integration of the second term of Eq. (153) by parts results in

$$y_p(z) = f_{p-1}(z) + \left(-\frac{1}{2y_{p-1}(z)}\frac{df_{p-1}(z)}{dz}\right) \quad (157)$$
$$-\int_{z_0}^{z} ds \frac{d}{ds}\left(-\frac{df_{p-1}(s)/ds}{2y_{p-1}(s)}\right)\exp\left[-2\int_{s}^{z} y_{p-1}(t)dt\right].$$

The successive integrations by parts of Eq. (157) lead [16] to the series

$$y_p(z) = \sum_{n=0}^{\infty} \mathcal{L}_n^{(p)}(z) \quad (158)$$

with $\mathcal{L}_n^{(p)}(z)$ given by recursive relation

$$\mathcal{L}_n^{(p)}(z) = \frac{1}{2y_{p-1}(z)}\frac{d}{dz}(-\mathcal{L}_{n-1}^{(p)}(z)) \quad (159)$$

and

$$\mathcal{L}_0^{(p)}(z) = f_{p-1}(z). \quad (160)$$

Since

$$\frac{d}{dz} = g\frac{d}{dr}, \quad g = \lambda^{-1} = \frac{\hbar}{\sqrt{2m}}, \quad (161)$$

Table 2. The same as in Table 1, but for $p = 1$

g	m_u	QLM	Exact	$\lvert\Delta\rvert$
1.0	6	−1.55117510	−1.55117440	7[−7]
2.0	6	−2.13431750	−2.13431460	3[−6]
3.0	6	−2.58243320	−2.58243170	2[−6]
4.0	6	−2.96048760	−2.96048510	2[−6]
5.0	6	−3.29370350	−3.29370260	9[−7]
6.0	6	−3.59504450	−3.59504330	1[−6]
7.0	6	−3.87221530	−3.87221380	2[−6]
8.0	6	−4.13024160	−4.13023970	2[−6]
9.0	6	−4.37261600	−4.37261370	2[−6]
10.0	6	−4.60188310	−4.60188040	3[−6]

Eq. (158) represents the expansion of the pth QLM iterate in powers of g, that is, in powers of $\hbar$, which one can compare with the WKB series, as will be done in the next section.

For the zeroth iterate $y_0(z)$, it seems natural to choose the zeroth WKB approximation, that is, to set

$$y_0(z) = ik(z), \quad (162)$$

which in addition satisfies boundary condition (150). However, one has to be aware that this choice has unphysical turning point singularities. According to the existence theorem for linear differential equations [42], if $y_{p-1}(z)$ in Eq. (151) is a discontinuous function of z in a certain interval, then $y_p(z)$ or its derivatives may also be discontinuous functions in this interval, so consequently the turning point singularities of $y_0(z)$ may propagate to the next iterates.

Substitution of the initial QLM approximation (162) into Eq. (153) gives an especially simple expression [16] for the first QLM iterate,

$$y_1(z) = ik(z) - i\int_{z_0}^{z} ds\, k'(s)\exp\left[-2i\int_{s}^{z} k(t)dt\right]. \quad (163)$$

The first QLM iteration is expressible in a closed integral form. However, it takes into account, though approximately, an infinite number of WKB terms corresponding to higher powers of $\hbar$, as will be shown in the next section. In view of this, it is a better approximation than the usual WKB.

7. COMPARISON OF EXPANSIONS OF QLM ITERATES AND WKB SERIES

To obtain the WKB series, one has to expand solution y of the Riccati equation (148) in powers of $\hbar$. This is easy to do by using Eq. (161) and looking for y in the form of series in g:

$$y = \sum_{m=0}^{\infty} g^m Y_m. \tag{164}$$

Substitution into (148) and equation of terms by the identical powers of g gives

$$\frac{dY_{m-1}}{dr} = -\sum_{k=0}^{m} Y_k Y_{m-k}. \tag{165}$$

This reduces to the recurrence relation

$$Y_m = -\frac{1}{2Y_0}\left(Y'_{m-1} + \sum_{k=1}^{m-1} Y_k Y_{m-k}\right). \tag{166}$$

The derivatives in this and subsequent expressions are in variable r. The zero WKB approximation Y_0 is given by $Y_0 = ik$. The subsequent terms Y_n of the expansion can be obtained from this recurrence relation by use of Mathematica [43].

We present here the WKB expansion (164) up to g^7 inclusively:

$$\begin{aligned} y = ik - \frac{gk'}{2k} + \frac{i}{8k^3}g^2(3k'^2 - 2kk'') \\ + \frac{g^3}{8k^5}(6k'^3 - 6kk'k'' + k^2k^{(3)}) + \frac{i}{128k^7} \\ \times g^4(-297k'^4 + 396kk'^2k'' - 52k^2k''^2 \\ - 80k^2k'k^{(3)} + 8k^3k^{(4)}) - \frac{g^5}{32k^9}(306k'^5 \\ - 510kk'^3k'' + 111k^2k'^2k^{(3)} - 3k^2k'(-48k''^2 \\ + 5kk^{(4)}) + k^3(-24k''k^{(3)} + kk^{(5)})) + \frac{i}{1024k^{11}} \\ \times g^6(50139k'^6 - 100278kk'^4k'' + 22704k^2k'^3k^{(3)} \\ + 12k^2k'^2(3679k''^2 - 290kk^{(4)}) + 16k^3k' \\ \times (-694k''k^{(3)} + 21kk^{(5)}) - 8k^3(301k''^3 \\ - 80kk''k^{(4)} + k(-49k^{(3)^2} + 2kk^{(6)}))) + \frac{g^7}{128k^{13}} \\ \times (38286k'^7 - 89334kk'^5k'' + 20721k^2k'^4k^{(3)} \\ + k'^3(53724k^2k''^2 - 3405k^3k^{(4)}) + 3k^3k'^2 \\ \times (-5426k''k^{(3)} + 129kk^{(5)}) + 2k^3k'(-3528k''^3 \\ + 735kk''k^{(4)} + 2k(225k^{(3)^2} - 7kk^{(6)})) \\ + k^4(1176k''^2k^{(3)} - 62kk''k^{(5)} \\ + k(-90k^{(3)}k^{(4)} + kk^{(7)}))). \end{aligned} \tag{167}$$

Table 3. The same as in Table 1, but for $p = 10$

g	m_u	QLM	Exact	$\lvert\Delta\rvert$
1.0	6	−3.53935640	−3.53935320	3[−6]
2.0	6	−4.91444300	−4.91444030	3[−6]
3.0	6	−5.96917320	−5.96917180	1[−6]
4.0	6	−6.85821230	−6.85821020	2[−6]
5.0	6	−7.64140310	−7.64140000	3[−6]
6.0	6	−8.34941940	−8.34941840	1[−6]
7.0	6	−9.00048470	−9.00048340	1[−6]
8.0	6	−9.60646440	−9.60646280	2[−6]
9.0	6	−10.17560100	−10.17559900	2[−6]
10.0	6	−10.71389400	−10.71389200	2[−6]

To compare expansion of the first QLM iterate y_1 in powers of $\hbar$ with the WKB expansion (167), we have to use, as we have already mentioned in the previous section, Eqs. (158) and (159) together with Eq. (162). The result up to power g^7 inclusively is again obtained with the help of Mathematica [43]:

$$\begin{aligned} y_1 = ik - \frac{k'g}{2k} + \frac{ig^2}{4k^3}(k'^2 - kk'') \\ + \frac{g^3}{8k^5}(3k'^3 - 4kk'k'' + k^2k^{(3)}) + \frac{ig^4}{16k^7} \\ \times (-15k'^4 + 25kk'^2k'' - 7k^2k'k^{(3)} \\ + k^2(-4k''^2 + kk^{(4)})) + \frac{g^5}{32k^9}(-105k'^5 \\ + 210kk'^3k'' - 60k^2k'^2k^{(3)} + k^2k'(-70k''^2 \\ + 11kk^{(4)}) + k^3(15k''k^{(3)} - kk^{(5)})) - \frac{ig^6}{64k^{11}} \\ \times (-945k'^6 + 2205kk'^4k'' - 630k^2k'^3k^{(3)} \\ + 14k^2k'^2(-80k''^2 + 9kk^{(4)}) + 2k^3k'(175k''k^{(3)} \\ - 8kk^{(5)}) + k^3(70k''^3 - 26kk''k^{(4)} + k(-15k^{(3)^2} \\ + kk^{(6)}))) + \frac{g^7}{128k^{13}}(10395k'^7 - 27720kk'^5k'' \\ + 7875k^2k'^4k^{(3)} - 126k^2k'^3(-150k''^2 + 13kk^{(4)}) \\ + 14k^3k'^2(-495k''k^{(3)} + 17kk^{(5)}) \\ + k^3k'(-2800k''^3 + 784kk''k^{(4)} + k(455k^{(3)^2} \\ - 22kk^{(6)})) + k^4(560k''^2k^{(3)} - 42kk''k^{(5)} \\ + k(-56k^{(3)}k^{(4)} + kk^{(7)}))). \end{aligned} \tag{168}$$

As we have already mentioned, the comparison of expansion of the first QLM iterate in powers of $\hbar$ and WKB series was originally performed in [16, 17]. There, it was shown that the expansion reproduces exactly the first two terms and also gives correctly the structure of the WKB series up to the power g^3 considered in these works, generating series with identical terms, but with different coefficients. Comparison of Eqs. (167) and (168) of the present work shows that this conclusion is also true if higher powers of g are taken into account.

The computation of the expansion of the second QLM iterate y_2 in powers of $\hbar$ is done by reexpanding the term $1/(2y_1)$ in Eq. (159) in the series in powers of g and keeping the powers up to g^7 inclusively in this expression as well as in the sum in Eq. (158). The result is given by

$$y_2 = ik - \frac{k'g}{2k} + \frac{ig^2}{8k^3}(3k'^2 - 2kk'') \tag{169}$$
$$+ \frac{g^3}{8k^5}(6k'^3 - 6kk'k'' + k^2k^{(3)}) + \frac{ig^4}{32k^7}(-74k'^4$$
$$+ 99kk'^2k'' - 20k^2k'k^{(3)} + k^2(-13k''^2$$
$$+ 2kk^{(4)})) + \frac{g^5}{64k^9}(-607k'^5 + 1017kk'^3k''$$
$$- 222k^2k'^2k^{(3)} + 6k^2k'(-48k''^2 + 5kk^{(4)})$$
$$- 2k^3(-24k''k^{(3)} + kk^{(5)})) - \frac{ig^6}{128k^{11}}(-6186k'^6$$
$$+ 12446kk'^4k'' - 2832k^2k'^3k^{(3)} + k^2k'^2$$
$$\times (-5503k''^2 + 435kk^{(4)}) + 2k^3k'(694k''k^{(3)}$$
$$- 21kk^{(5)}) + k^3(301k''^3 - 80kk''k^{(4)}$$
$$+ k(-49{k^{(3)}}^2 + 2kk^{(6)}))) + \frac{g^7}{256k^{13}}(75256k'^7$$
$$- 176659kk'^5k'' + 41224k^2k'^4k^{(3)} + 4k^2k'^3$$
$$\times (26687k''^2 - 1700kk^{(4)}) + 2k^3k'^2$$
$$\times (-16243k''k^{(3)} + 387kk^{(5)}) + k^3k'(-14071k''^3$$
$$+ 2940kk''k^{(4)} + 8k(225{k^{(3)}}^2 - 7kk^{(6)}))$$
$$+ 2k^4(1176k''^2k^{(3)} - 62kk''k^{(5)} + k(-90k^{(3)}k^{(4)}$$
$$+ kk^{(7)}))).$$

The expansion of y_2 reproduces exactly the first four terms of the WKB series. It also gives the proper structure of the other terms of the WKB series, generating series with identical terms which have approximately correct coefficients.

The expansion of y_3 is obtained in a similar fashion. It reproduces exactly the first eight terms of the WKB series, that is, all the terms up to the power g^7 inclusively listed in Eq. (167).

Summing up, we have proved that the expansion of the first, second, and third QLM iterates reproduces exactly two, four, and eight WKB terms, respectively. Since the zero QLM iterate y_0 was chosen to be equal to the zero WKB approximation ik, one can state that the pth QLM iterate contains 2^p exact terms. In addition, expansion of each QLM iterate has the correct structure whose terms are identical to the WKB series with approximate coefficients.

The 2^p law is, of course, not accidental. The QLM iterates are quadratically convergent [10, 11, 19, 20]; that is, the norm of the difference of the exact solution and the pth QLM iterate $||y - y_p||$ is proportional to the square of the norm of the differences of the exact solution and the $(p-1)$th QLM iterate:

$$||y - y_p|| \sim ||y - y_{p-1}||^2. \tag{170}$$

Since y_0 contains just one correct WKB term of power g^0 and thus $||y - y_0||$ is proportional to g, one has to expect that $||y - y_1|| \sim g^2$ and thus y_1 contains two correct WKB terms of powers g^0 and g^1. The difference $||y - y_2|| \sim ||y - y_1|| \sim g^4$, so that y_2 contains four correct WKB terms of powers g^0, g^1, g^2, and g^3. Finally, the difference $||y - y_3||$ should be proportional to g^8, and therefore y_3 has to contain eight correct terms with powers between g^0 and g^7 inclusively. This explains the 2^p law.

8. QLM AND WKB ENERGY CALCULATIONS

The exact quantum-mechanical quantization condition for the energy [44–46] has the form

$$J = \oint_C y(z)dz = 2\pi i n. \tag{171}$$

Here, $y(z)$ is the logarithmic derivative of the wave function, given by Eq. (148); $z = gr$; $n = 0, 1, 2, \ldots$ counts the number of poles of $y(z)$ and is the bound-state number; and the integration is along a path C in the complex plane encircling the segment of the Rez axis between the turning points.

The pth QLM iterate $y_p(z)$, as we have seen, contains in addition to 2^p exact WKB terms of powers $g^0, g^1, \ldots, g^{2^p-1}$ also an infinite number of structurally correct WKB terms of higher powers of g with approximate coefficients. One can expect therefore that the quantization condition (171) with $y(z)$ approximated by any QLM iterate $y_p(z)$, including the first,

$$J_p = \oint_C y_p(z)dz = 2\pi i n, \quad p = 1, 2, \ldots, \tag{172}$$

gives more accurate energy than the WKB quantization condition

$$\oint_C k(z)dz = 2\pi\left(n+\frac{1}{2}\right), \qquad (173)$$

which is obtained by substituting into exact quantization condition (171) the WKB expansion (167) up to the first power of $g \sim \hbar$, that is, $y(z) = ik(z) - \frac{dk(z)/dz}{2k(z)}$, and neglecting all higher powers of g in the expansion. Indeed, Eq. (172) leads to exact energies not only for the Coulomb and harmonic oscillator potentials, as was shown earlier in [16, 17], but also for many other well-known physical potentials [40, 41] used in molecular and nuclear physics, such as the cotangent, Pöschl–Teller, Hulthèn, Hyleraas, Morse, and Eckart.

The WKB quantization condition (173) yields the exact energy only for the first two potentials, but not for the rest of them.

Let us now consider some of the above-mentioned potentials:

1. Harmonic oscillator $V(x) = x^2/2$, $-\infty < x < \infty$. From now on, we will work in the units $\hbar = m = 1$ so that from $z = \lambda x$ follows $x = z/\sqrt{2}$ and $V(z) = z^2/4$.

In view of the boundary condition (152), $y_p(z)$ at infinity should behave like $i\sqrt{E - z^2/4} \simeq -z/2 + E/z$, where we omitted terms of order $1/z^2$ and higher. Here, we took into account that, for bound states, the logarithmic derivative at infinity should be negative. More accurately, the pole structure of $y_p(z)$ at $z \sim \infty$ can be found by looking for the solution there in the form $y_p(z) \simeq -z/2 + \alpha_p/z$. Substituting into the quasilinearized equation (151)

$$\frac{dy_p(z)}{dz} = y_{p-1}^2(z) - 2y_p(z)y_{p-1}(z) - \left(E - \frac{z^2}{4}\right) \qquad (174)$$

and again neglecting terms of order $1/z^2$ or higher, which do not contribute to the integral, yields $\alpha_p = E - 1/2$, so that the pole term in $y_p(z)$, $p = 1, 2, \ldots$, is given by $(E - 1/2)/z$.

The integration in Eq. (172) is counterclockwise along a path C in the complex plane encircling the segments of the Rez axis between the two turning points $-2\sqrt{E}$ and $2\sqrt{E}$. Since the only singularity outside contour C in the complex plane lies at infinity, the integral (172) can be done by distorting the contour to enclose the pole at $x = \infty$. The evaluation of the integral yields $2\pi i(E - 1/2) = 2\pi i n$ or $E = n + 1/2$, which is the exact equation for the energy levels.

2. Cotangent potential $V(x) = V_0\cot^2(\pi x/a)$, $V_0 > 0$, $0 < x < a$. Let us introduce a new variable

$$z = \sin^2\left(\frac{\pi x}{a}\right), \qquad (175)$$

so that

$$x = \frac{a}{\pi}\arcsin\sqrt{z}, \quad dx = \frac{a}{2\pi}\frac{1}{\sqrt{z(1-z)}}dz,$$
$$k(z) = \sqrt{2(E+V_0) - \frac{V_0}{z}}.$$

The QLM equation (151) will now have the form

$$\frac{2\pi}{a}\sqrt{(1-z)z}\frac{dy_p(z)}{dz} = y_{p-1}^2(z) - 2y_p(z)y_{p-1}(z) - k^2(z). \qquad (176)$$

One of the singularities of $k^2(z)$ is at $z = 0$. Near this point, the equation has the form

$$\frac{2\pi}{a}\sqrt{z}\frac{dy_p(z)}{dz} = y_{p-1}^2(z) - 2y_p(z)y_{p-1}(z) + \frac{2V_0}{z}. \qquad (177)$$

We look for a solution to this equation in the form $y_p(z) = a_p/\sqrt{z}$. Then we obtain for a_p the following recurrence relation:

$$a_p(2a_{p-1} - \pi/a) = a_{p-1}^2 + (\pi/a)^2\lambda(\lambda - 1). \qquad (178)$$

Here, we set $2V_0 = (\pi/a)^2\lambda(\lambda - 1)$, where $\lambda = 1/2 + \sqrt{1/4 + 2V_0a^2/\pi^2}$. The solution to this algebraic equation, which fullfils the demand that, at large p, $a_p = a_{p-1}$, is $a_p = \pi\lambda/a$. The $y_p(z)$ near zero thus has the form $y_p(z) = \pi\lambda/(a\sqrt{z})$. At $z \simeq \infty$, Eq. (176) reduces to

$$\frac{2\pi}{a}\sqrt{-z^2}\frac{dy_p(z)}{dz} = y_{p-1}^2(z) - 2y_p(z)y_{p-1}(z) - 2(E+V_0).$$

Looking for a solution in the form $y_p(z) = c_p$, where c_p is some constant, one obtains the recurrent relation for c_p, namely, $c_{p-1}^2 - 2c_pc_{p-1} - 2(E+V_0) = 0$. The solution to this algebraic equation, which fullfils the demand that, at large p, $c_p = c_{p-1}$, is $c_p = \sqrt{-2(E+V_0)}$.

The quantization condition (172) in variable z given by Eq. (175) has the form

$$J_p = \frac{a}{\pi}\oint_C \frac{y_p(z)}{\sqrt{z(1-z)}}dz = 2\pi i n, \qquad (179)$$
$$p = 1, 2, \ldots,$$

where integration is counterclockwise along a path C in the complex plane encircling the cut along the Rez axis between zero and $z = V_0/[2(E+V_0)]$. Since

$y_p(z)$ equals $\pi\lambda/(a\sqrt{z})$ and $\sqrt{-2(E+V_0)}$ at $z \simeq 0$ and $z \simeq \infty$, respectively, the integrand in Eq. (179) has poles with residues $\pi\lambda/a$ and $\sqrt{2(E+V_0)}$ there. The deformation of the contour to include these poles and computation of their contributions yields

$$J_p = 2\pi i\left(-\frac{a}{\pi}\lambda + \sqrt{2(E+V_0)}\right) = 2\pi i n, \quad (180)$$

or, upon substitution of the value of λ and inserting $\hbar$ and m from dimensional considerations,

$$E = -V_0 + \frac{\pi^2\hbar^2}{2ma^2}\left(n + \frac{1}{2} + \sqrt{\frac{2mV_0a^2}{\pi^2\hbar^2} + \frac{1}{4}}\right)^2.$$

This is the exact equation for the energy levels in the cotangent potential [47]. The correspondent WKB expression is different and is given by [47]

$$E = -V_0 + \frac{\pi^2\hbar^2}{2ma^2}\left(n + \frac{1}{2} + \sqrt{\frac{2mV_0a^2}{\pi^2\hbar^2}}\right)^2.$$

3. Modified Pöschl–Teller potential $V(x) = -V_0/\cosh^2(x/a)$, $V_0 > 0$, $-\infty < x < \infty$. Setting $z = \cosh^2(x/a)$ so that $dx = adz/[2z(z-1)]$, one finds that the QLM equation (151) now has the form

$$\frac{2}{a}\sqrt{(z-1)z}\frac{dy_p(z)}{dz} = y_{p-1}^2(z) \quad (181)$$
$$- 2y_p(z)y_{p-1}(z) - k^2(z),$$

where $k^2(z)$ is given by $2(-|E| + V_0/z)$. At $z \simeq 0$, this equation has the form

$$\frac{2\pi}{a}\sqrt{-z}\frac{dy_p(z)}{dz} = y_{p-1}^2(z) \quad (182)$$
$$- 2y_p(z)y_{p-1}(z) - \frac{\lambda(\lambda-1)}{z},$$

where we use the definition of $\lambda = 1/2 + \sqrt{1/4 + 2V_0a^2}$, so that $2V_0 = \lambda(\lambda-1)/a^2$. The solution near zero can be sought in analogy with previous cases in the form $y_p(z) = a_p/\sqrt{-z}$. Substitution into (182) gives $a_p = a_{p-1}^2 - 2a_pa_{p-1} + \lambda(\lambda-1)$, whose solution, satisfying the condition that, at large p, $a_p = a_{p-1}$, is $a_p = \lambda - 1$. Thus, near zero, $y_p(z) \simeq (\lambda-1)/\sqrt{-z}$. The solution at infinity $y_p(z) \simeq \sqrt{2|E|}$ is found in the same way as in the previous two sections. The integration in the quantization condition

$$J_p = a\oint_C \frac{y_p(z)}{\sqrt{z(z-1)}}dz = 2\pi i n, \quad (183)$$
$$p = 1, 2, \ldots,$$

is counterclockwise along a path C in the complex plane encircling the cut along the Rez axis between $z = \lambda(\lambda-1)/[2a^2|E|]$ and $z = \infty$. The deformation of the contour and computation of the integral upon substitution of values of λ and insertion of $\hbar$ and m from dimensional considerations yields

$$E = -\frac{\hbar^2}{2ma^2}\left[-\left(n + \frac{1}{2}\right) + \sqrt{\frac{2mV_0a^2}{\hbar^2} + \frac{1}{4}}\right]^2.$$

This is the exact equation for the energy levels in the Pöschl–Teller potential hole [23, 47]. The correspondent WKB expression is different [47] and is given by

$$E = -\frac{\hbar^2}{2ma^2}\left[-\left(n + \frac{1}{2}\right) + \sqrt{\frac{2mV_0a^2}{\hbar^2}}\right]^2.$$

Summing up, in this section, we have shown that the quantization condition in the first QLM iteration leads to exact energies for the harmonic oscillator, cotangent, and modified Pöschl–Teller potentials. In [41], it was shown that it is also true for many other potentials, such as the Coulomb, Hulthèn, Hylleraas, Morse, Eckart, and some other well-known potentials used in molecular and nuclear physics which have a simple analytic structure. By comparison, the WKB approximation reproduces exact energies only in the case of the oscillator and Coulomb potentials.

9. QLM AND WKB ENERGY AND WAVE FUNCTION CALCULATIONS

We will show now following our works [40, 48, 49] that, also in the general case of arbitrary potentials that do not have a simple analytic structure, both the wave functions and energies are very well reproduced by the first QLM iteration and demonstrate significant improvement over those obtained by the usual WKB approximation. In addition, we show that, if the initial QLM guess is properly choosen, the wave function in the first QLM iteration, unlike the WKB wave function, is free of unphysical turning point singularities. Since the first QLM iteration is given by an analytic expression [40, 41, 48, 49], it allows one to analytically estimate the role of different parameters and the influence of their variation on boundedness or unboundedness of, for example, critically stable quantum systems with much more precision than obtained by the WKB approximation, which often fails miserably, for systems on the border of stability. In addition, we show that five QLM iterations are usually enough to obtain both the wave function and energies with the extreme accuracy of ten significant figures.

In the previous section, the zero-order WKB approximation $ik(z)$ was chosen as the zeroth iterate $y_0(z)$. However, that choice has unphysical turning point singularities. Consequently, if $y_p(z)$ in Eq. (151)

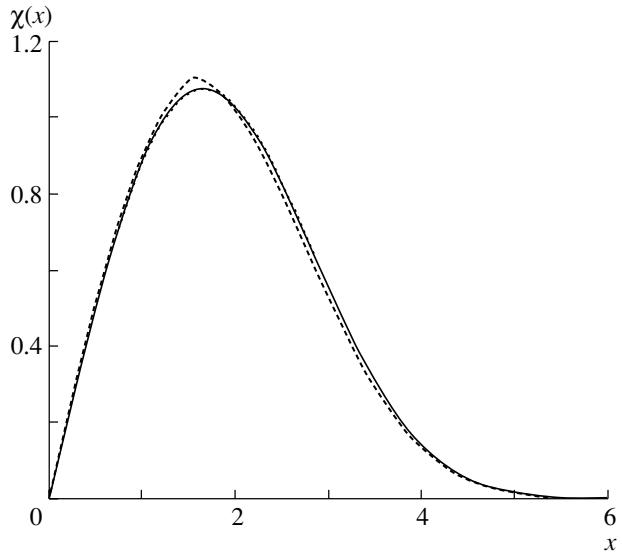

Fig. 13. Comparison of the Langer WKB solution (dashed curve), the exact solution (dotted curve), and the first QLM iteration (solid curve) for the ground state of the anharmonic oscillator. The last two are almost indistinguishable on the plot. Here, $x = \kappa r$, $\kappa^2 = 2mE/\hbar^2$.

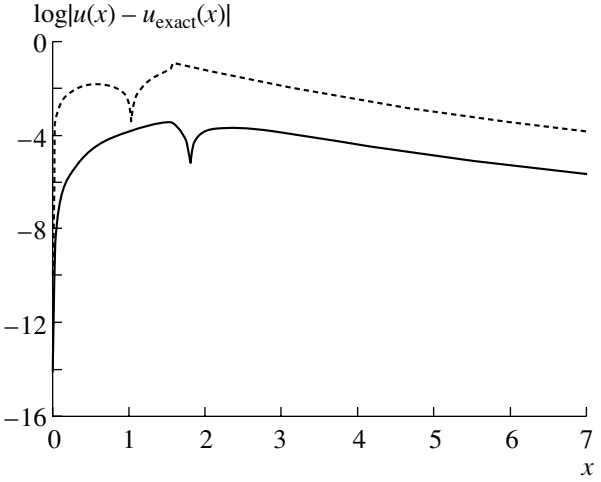

Fig. 14. Logarithm of the differences between exact u_{exact} and WKB solution (dashed curve) and between u_{exact} and the first QLM iteration u_1 (solid curve) for the ground state of the anharmonic oscillator; $u(x)$ is defined as $u(x) = -\arctan(\kappa\chi(r)/\chi'(r)) = -\arctan(E/y(\lambda r))$; QLM iteration here is performed on the monotonic function $u(x)$ and not on the singular function $y(\lambda r)$.

is a discontinuous function of z in a certain interval, then $y_{p+1}(z)$ or its derivatives could also be discontinuous functions in this interval [42], so the turning point singularities of $y_0(z)$ would unfortunately propagate to the next iterate, as we indeed saw in the QLM series containing powers of $k(z)$ in the denominators of different terms.

To avoid this, let us choose as the zero iteration the Langer [50] WKB wave function, which does not have the turning point singularities. This function near the turning points a and b is given by the simple analytic expression

$$\chi_i(r) = c_i\sqrt{\frac{S_i^{1/3}(r)}{|k(r)|}}\,\mathrm{Ai}\left[dS_i^{1/3}(r)\right], \qquad (184)$$

$$S_i(r) = \frac{3}{2}\lambda\left|\int_i^r |k(s)|\,ds\right|.$$

Here, Ai denotes the Airy function; $i = a, b$; $k(r) = (2m/\hbar^2)[(E - V(r)) - (l + 1/2)^2/(2mr^2)]$; d is -1 for $a < r < b$ and 1 for $r \le a, r \ge b$; and $c_a = 1$, $c_b = (-1)^n$, where $n = 0, 1, 2$ is the number of the bound state. It is easy to check that $\chi_a(r)$ and $\chi_b(r)$ coincide at some point in the interval (a, b) between the turning points, are continuous across them, and coincide with the usual WKB solutions far from them. Let us present a couple of examples considered originally in [48] (numerous other examples are considered in [49]):

1. Ground state of the anharmonic oscillator $V(r) = (r^2 + r^4)/2$. The exact energy of this state is 2.324406352 (in a.u.) with mass $m = 1$. The WKB energy is different by 2.14% and equals 2.27460 a.u., while the first-iteration QLM energy equals 2.32575 and differs from the exact energy only by 0.058%. The fifth-iteration QLM energy coincides with the exact energy in all ten digits.

The graphs corresponding to the Langer WKB solution, the exact solution, and the first QLM iteration are displayed in Fig. 13. One can see that, while the Langer solution is noticeably different from the exact solution, the curve of the first QLM iteration is almost indistinguishable from the exact curve.

This can be followed more precisely by looking at Fig. 14, where the logarithm of the difference between the exact and WKB solutions and the one between the exact solution and the first QLM iteration are shown. One can see that the difference between the exact solution and the first QLM iteration is two orders of magnitude smaller than the difference between the exact and the WKB solutions, that is, just one QLM iteration increases the accuracy of the result by a remarkable two orders of magnitude.

2. Second excited state of the linear potential $V(r) = 2^{7/2}r$. The exact energy in this case is 9.352429642 a.u. The WKB energy is different by 0.49% and equals 9.39863 a.u. The first-iteration QLM energy equals 9.3582123 and differs from the exact one only by 0.062%. The QLM energy, as in the

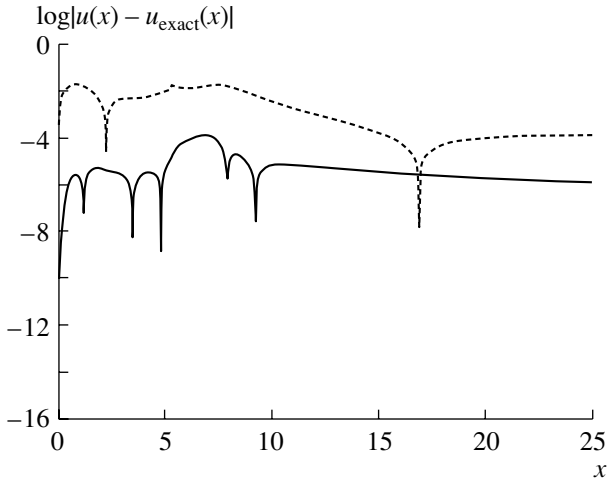

Fig. 15. The same as in Fig. 14, but for the second excited state of the linear potential.

case of the anharmonic potential, coincides with the exact one after the fifth iteration in all ten digits.

The accuracy of the WKB approximation increases for higher excitations. Therefore, in the case of the second excited state in the linear potential, both the Langer WKB and QLM curves are indistinguishable from the exact one. Figure 15 shows, however, that, also in this case, the difference between the exact solution and the first QLM iteration is two orders of magnitude smaller than the difference between the exact and WKB solutions.

10. CONCLUSIONS

Summing up, we have reviewed the basic properties of the quasilinearization method and its emerging applications in physics. The proof of the convergence of the method for nonlinear ordinary nth-order differential equations was reformulated [19, 20] by removing unnecessary restrictive conditions generally not fulfilled in physical applications and was adjusted for large or infinite domains of variables and for functionals which are singular at some points in the domain. The generalization of the proof to nonlinear partial nth-order differential equations in N-dimensional space is straightforward.

The results can be summed up as follows:

(i) The sequence $u_n(x), n = 1, 2, \ldots$, of QLM iterations converges uniformly and quadratically to the exact solution $u(x)$. For convergence, it is sufficient that an initial guess for the zeroth iteration be sufficiently good to ensure the smallness of just one of the convergence coefficients $q_m = k||u_{m+1} - u_m||$. For a first-order nonlinear ordinary equation, for example, k is given by Eqs. (32) or (35). [In addition, in this case, for strictly convex (concave) functionals $f(u(x), x)$, difference $u_{n+1}(x) - u_n(x)$ is strictly positive (negative), which establishes the monotonicity of the convergence from below (above), respectively.]

(ii) The method approaches the solution of a nonlinear differential equation by approximating the nonlinear terms by a sequence of linear ones and is not based on the existence of a smallness parameter. As a result, it is able to handle, unlike perturbation theory, large or even infinite values of the coupling constant.

(iii) Comparison of QLM with perturbation theory shows that each QLM iteration reproduces and sums many orders of perturbation theory exactly and, in addition, many more orders approximately. Namely, in agreement with the quadratic pattern of the convergence, the number N_n of terms of the perturbation series reproduced exactly in the nth QLM approximations equals $2^{n+1} - 1$, and approximately the same number of terms is reproduced approximately. The number of the exactly reproduced terms thus doubles with each subsequent QLM approximation and reaches, for example, 127 terms in the 6th QLM approximation 8191 terms in the 12th QLM approximation, and so on.

(iv) QLM handles without any problems not only singular potentials, like the inverse squared potential, for which perturbation theory is divergent outside a narrow interval of values of the coupling constant, but even supersingular potentials, like the Newton potential, for which perturbation series are not existent at all, since their calculation leads to infinities in each order of the perturbation expansion.

(v) The advantage of the quasilinear approach is that each pth QLM iteration is expressible in a closed integral form. We have proved that its expansion in powers of $\hbar$ reproduces the structure of the WKB series, generating an infinite number of WKB terms with 2^p terms of the expansion reproduced exactly and a similar number approximately. As a result, one expects that the exact quantization condition with the integrand replaced by any QLM iterate, including the first, gives more accurate energy than the WKB quantization condition which is obtained by substituting into the exact quantization condition the WKB expansion up to the first power of $\hbar$ and neglecting all higher powers of $\hbar$. Indeed, we have shown that the approximation by the first QLM iterate in Eq. (171) leads to exact energies for harmonic oscillator, cotangent, and modified Pöschl–Teller potentials. The same is true [41] for many other well-known physical potentials used in molecular and nuclear physics, such as the Coulomb, Hulthèn, Hyleraas, Morse, and Eckart.

(vi) For other potentials which have more complicated analytical structure, we have shown via examples of the anharmonic oscillator and linear po-

tentials that the use of the Langer WKB solution as an initial guess even in the first QLM approximation gives energies and wave functions at least two orders of magnitude more accurate than the WKB results; such a QLM solution, unlike the usual WKB solution, displays no unphysical turning point singularities. Since the first QLM iterate is given by an analytic expression, it allows one to estimate analytically the role of different parameters and their influence on properties of a quantum system with much higher precision than that provided by the WKB approximation. In addition, we have shown that five QLM iterations are usually enough to obtain both the wave function and the energy with accuracy of at least ten significant figures.

In view of all this, since most equations of physics, from classical mechanics to quantum field theory, are either nonlinear or can be transformed in a nonlinear form, the quasilinear method may turn out to be extremely useful and in many cases more advantageous than perturbation theory or its different modifications, like expansion in inverse powers of the coupling constant, $1/N$ expansion, etc.

ACKNOWLEDGMENTS

The numerous discussions with Dr. R. Krivec and Dr. F. Tabakin are gratefully acknowledged.

REFERENCES

1. Yu. A. Simonov, Yad. Fiz. **3**, 630 (1966) [Sov. J. Nucl. Phys. **3**, 461 (1966)]; Yu. A. Simonov and A. M. Badalyan, Yad. Fiz. **3**, 1032 (1966) [Sov. J. Nucl. Phys. **3**, 755 (1966)]; **5**, 88 (1967) [**5**, 60 (1967)]; V. V. Pustovalov and Yu. A. Simonov, Zh. Éksp. Teor. Fiz. **51**, 345 (1966) [Sov. Phys. JETP **24**, 230 (1967)]; F. Calogero and Yu. A. Simonov, Phys. Rev. **169**, 789 (1968), **183**, 869 (1969); Nuovo Cimento A **64**, 337 (1969).
2. V. B. Mandelzweig, Nucl. Phys. A **508**, 63c (1990); Few-Body Syst., Suppl. **7**, 371 (1994).
3. M. I. Haftel and V. B. Mandelzweig, Phys. Lett. A **120**, 232 (l987); Ann. Phys. (N.Y.) **189**, 29 (1989); Phys. Rev. A **38**, 5995 (l988); **39**, 2813 (l989); **41**, 2339 (1990); **46**, 142 (1992); **49**, 3338, 3344 (1994).
4. R. Krivec, M. I. Haftel, and V. B. Mandelzweig, Phys. Rev. A **46**, 6903 (1992); **47**, 911 (1993); **52**, 221 (1995); Few-Body Syst. **17**, 229 (1994); J. Comput. Phys. **123**, 149 (1996); S. Berkovic, R. Krivec, V. Mandelzweig, and L. Stotland, Phys. Rev. A **55**, 988 (1997).
5. R. Krivec and V. B. Mandelzweig, Phys. Rev. A **52**, 221 (1995); **56**, 3614 (1997); **57**, 4976 (1998); R. Krivec, V. Mandelzweig, and K. Varga, Phys. Rev. A **61**, 062503 (2000).
6. R. Krivec, M. Amusia, and V. Mandelzweig, Phys. Rev. A **62**, 064701 (2000); **63**, 052708 (2001); **64**, 012713 (2001); **67**, 062720 (2003); Surf. Rev. Lett. **9**, 1161 (2002); Few-Body Syst., Suppl. **14**, 147 (2003); M. Ya. Amusia, E. G. Drukarev, R. Krivec, and V. B. Mandelzweig, Phys. Rev. **66**, 052706 (2002); AIP Proc. **652**, 123 (2003).
7. A. Kievsky, S. Rosati, and M. Viviani, Nucl. Phys. A **551**, 241 (1993); **577**, 511 (1994); Few-Body Syst. **18**, 25 (1995); Phys. Rev. C **52**, R15 (1995); Phys. Rev. Lett. **81**, 1580 (1998); **82**, 3759 (1999).
8. A. M. Badalyan and Yu. A. Simonov, Yad. Fiz. **11**, 1112 (1970) [Sov. J. Nucl. Phys. **11**, 618 (1970)].
9. V. B. Mandelzweig, Nucl. Phys. A **292**, 333 (1977).
10. R. Kalaba, J. Math. Mech. **8**, 519 (1959).
11. R. E. Bellman and R. E. Kalaba, *Quasilinearization and Nonlinear Boundary-Value Problems* (Elsevier, New York, 1965; Mir, Moscow, 1968).
12. V. Lakshmikantham and A. S. Vatsala, *Generalized Quasilinearization for Nonlinear Problems*, in *Mathematics and its Applications* (Kluwer, Dordrecht, 1998), Vol. 440.
13. F. Calogero, *Variable Phase Approach to Potential Scattering* (Academic Press, New York, 1965; Mir, Moscow, 1972).
14. V. V. Babikov, *The Method of Phase Functions in Quantum Mechanics* (Nauka, Moscow, 1968) [in Russian].
15. A. A. Adrianov, M. I. Ioffe, and F. Cannata, Mod. Phys. Lett. A **11**, 1417 (1996).
16. K. Raghunathan and R. Vasudevan, J. Phys. **20**, 839 (1987).
17. M. Jameel, J. Phys. **21**, 1719 (1988).
18. M. A. Hooshyar and M. Razavy, Nuovo Cimento B **75**, 65 (1983).
19. V. B. Mandelzweig, J. Math. Phys. **40**, 6266 (1999).
20. V. B. Mandelzweig and F. Tabakin, Comput. Phys. Commun. **141**, 268 (2001).
21. R. Krivec and V. B. Mandelzweig, Comput. Phys. Commun. **152**, 165 (2003).
22. R. Courant and D. Hilbert, *Methoden der mathematischen physik* (Springer, Berlin, 1937; Gostekhizdat, Moscow, 1945), Vols. 1, 2.
23. S. Fluegge, *Practical Quantum Mechanics* (Springer, New York, 1974), Vols. 1, 2.
24. V. Volterra, *Theory of Functionals* (Blackie, London, 1931; Nauka, Moscow, 1983).
25. R. F. Dashen, Nuovo Cimento **28**, 229 (1963); J. Math. Phys. **4**, 388 (1963).
26. V. V. Babikov, Usp. Fiz. Nauk **92**, 3 (1967) [Sov. Phys. Usp. **10**, 271 (1967)].
27. E. Picard, J. Math. **6**, 145 (1990).
28. H. Goenner and P. Havas, J. Math. Phys **41**, 7029 (2000).
29. L. H. Thomas, Proc. Cambrige Phil. **23**, 542 (1927).
30. E. Fermi, Z. Phys. **48**, 73 (1928).
31. H. A. Bethe and R. W. Jackiw, *Intermediate Quantum Mechanics* (W. A. Benjamin Inc., New York, 1968; Mir, Moscow, 1965).
32. H. Schlichting, *Boundary Layer Theory* (McGrow-Hill, New York, 1978; Nauka, Moscow, 1974).

33. I. S. Gradshteyn and I. M. Ryzhik, *Table of Integrals, Series, and Products* (Nauka, Moscow, 1971; Academic Press, New York, 1994).
34. B. W. Char *et al.*, *Maple V Library Reference Manual and Computer Program* (Springer, New York, 1991).
35. L. D. Landau and E. M. Lifshitz, *Quantum Mechanics* (Nauka, Moscow, 1989; Pergamon Press, New York, 1977).
36. R. Krivec and V. B. Mandelzweig, Comput. Phys. Commun. **138**, 69 (2001).
37. R. G. Newton, *Scattering Theory of Waves and Particles* (Springer, New York, 1982; Mir, Moscow, 1969).
38. S. D. Conte and C. de Boor, *Elementary Numerical Analysis* (McGrow-Hill, New York, 1981).
39. A. Ralson and P. Rabinowitz, *A First Course in Numerical Analysis* (McGrow-Hill, New York, 1988).
40. R. Krivec and V. B. Mandelzweig, Phys. Lett. A **337**, 354 (2005).
41. V. B. Mandelzweig, *Comparison of Quasilinear and WKB Solutions in Quantum Mechanics* (submitted for publication).
42. E. L. Ince, *Ordinary Differential Equations* (Dover, New York, 1956; ONTI, Kharkov, 1939).
43. S. Wolfram, *The Mathematica Book,* 4th ed. (Wolfram Media/Cambrige Univ. Press, 1999).
44. J. L. Dunham, Phys. Rev. **41**, 713 (1932); C. M. Bender, K. Olaussen, and P. Wang, Phys. Rev. D **16**, 1740 (1977).
45. R. A. Leacock and M. J. Padgett, Phys. Rev. Lett. **50**, 3 (1983).
46. R. A. Leacock and M. J. Padgett, Phys. Rev. D **28**, 2491 (1983).
47. I. I. Goldman and V. D. Krivchenkov, *Problems in Quantum Mechanics* (Dover, New York, 1993).
48. R. Krivec, V. B. Mandelzweig, and F. Tabakin, Few-Body Syst. **34**, 57 (2004).
49. R. Krivec and V. B. Mandelzweig, *Quazilinearization Method and WKB*, Comput. Phys. Commun. (2005) (in press).
50. R. E. Langer, Phys. Rev. **51**, 669 (1937); C. M. Bender and S. A. Orszag, *Advanced Mathematical Methods for Scientists and Engineers I* (Springer, New York, 1999).

Physics of Atomic Nuclei, Vol. 68, No. 7, 2005, pp. 1259–1260. Translated from Yadernaya Fizika, Vol. 68, No. 7, 2005, pp. 1309–1310.

LETTERS TO THE EDITOR

Quadrupole Moments and Transition Probabilities $B(E2)$ for Light Nuclei in the Orthogonal-Scheme Basis with Symmetric Representations of the $O(A-1)$ Group

K. J. Yankauskas* **and A. K. Petrauskas**

Received June 7, 2004; in final form, November 4, 2004

The nuclear properties are studied in the $U(3(A-1))$ scheme using two bases (schemes): unitary and orthogonal [1]. In this work, we analyze some problems of spectroscopic calculations in the orthogonal scheme.

The basis wave function of the system of A nucleons in the orthogonal scheme (specified by the following chains of the subgroups of the $U(3(A-1))$ group [1]: $U(3(A-1)) \supset O(3(A-1)) \supset O(A-1) \times O^+(3)$, $O(A-1) \supset S(A)$, where U, O, and S are unitary, orthogonal, and symmetric groups, respectively) is denoted as

$$\psi(EK\beta\omega_{123}\alpha\lambda L\Gamma_0). \tag{1}$$

Here, E and K are the irreducible symmetric representations of the $U(3(A-1))$ and $O(3(A-1))$ groups, respectively; $\omega_{123} \equiv (\omega_1\omega_2\omega_3)$ is the irreducible representation of the $O(A-1)$ group; β and α are the repetition indices for the chains $O(3(A-1)) \supset O(A-1) \times O^+(3)$ and $O(A-1) \supset S(A)$, respectively; λ is the Young tableau of the $S(A)$ group; L is the orbital angular momentum; and Γ_0 are the remaining quantum numbers and spin–isospin characteristic. Functions (1) are the eigenfunctions of the $[3(A-1)]$-dimensional harmonic oscillator and E and K have the sense of the number of oscillatory quanta and multidimensional angular momentum, respectively. Functions with $E > K$ are multiquantum-excited $U(3(A-1))$ states (radial ρ excitations).

In this article, we propose simple expressions for calculating the quadrupole momenta Q and the transition probabilities $B(E2)$ in orthogonal-scheme bases. These bases involve the kinematically most important functions [2], i.e., functions that correspond to the most symmetric Young tableaus of the $S(A)$ group and symmetric representations of the $O(A-1)$ group of the form $\omega_{123} \equiv (K0\,0)$ and that are specified by the number of quanta $E = K + 2N$, where $N = 0, 1, 2, \ldots$.

The electric quadrupole moment of the nucleus is defined as the mean value of the $(16\pi/5)^{1/2}O_0^2$ operator in the state with $J = M$. The operator O_0^2 is given as

$$O_0^2 = \frac{e}{2}\sum_i^A (1 - 2t_0^1(i))Y_0^2(i)r^2(i). \tag{2}$$

Here, e is the elementary charge, $t_0^1(i)$ is the isospin projection, Y_0^2 is the spherical function, and $r(i)$ is the distance between the ith particle and the center of mass of the nucleus. Using the properties of the proton–neutron basis of the $U(3(A-1))$ scheme [3] and the relation between the functions of the unitary and orthogonal schemes [2], we represent the group quantities of the $SU(3)$ [4] and $O^+(3)$ groups for states with $E = K$ as

$$Q = -\left[\frac{(2J+1)(2J-1)J(2L+1)L(L+1)}{(2J+3)(J+1)(2L+3)(2L-1)}\right]^{1/2} \times \begin{Bmatrix} L & L & 2 \\ J & J & S \end{Bmatrix} \frac{(2l+3)\lambda_1}{K} er_\psi^2. \tag{3}$$

Here, λ_1 is determined from the $(\lambda_1 0)$ representation of the $SU(3)$ group for the proton subsystem of the proton–neutron basis [the representation of the $SU(3)$ group for the entire system has the form $(\lambda\mu) = (K0)$] and r_ψ is the parameter of the wave function. Then, using Eq. (3) and Eq. (16) from [5], we express the quadrupole moments in terms of the basis of functions (1) with $E = K + 2N$, $N = 0, 1, 2, \ldots$, where multiquantum ρ excitations are taken into account, as

$$Q = -\frac{3X(X+1) - 4J(J+1)L(L+1)}{2(J+1)(2J+3)(2L+3)(2L-1)} \times \frac{(2K+3)\lambda_1}{K}[D]er_\psi^2. \tag{4}$$

*e-mail: fizkat@jtf.ku.lt

1063-7788/05/6807-1259$26.00

Here, $X = S(S+1) - L(L+1) - J(J+1)$ and $[D]$ is the following sum of the coefficients C_N of the expansion of the wave function $\psi(J)$ in the above multiquantum basis:

$$[D] = \left[\sum_{N=0}^{N_{\max}} A(Nl_K, Nl_K)C_N^2 + 2\sum_{N=0}^{N_{\max}-1} A(Nl_K, N+1l_K)C_N C_{N+1}\right]. \quad (5)$$

Here, according to [5, Eq. (17)],

$$A(Nl_K, Nl_K) = \frac{l_K + 2N + 3/2}{l_K + 3/2}, \quad (6)$$

$$A(Nl_K, N+1\,l_K) = -\frac{\sqrt{(N+1)(l_K+N+3/2)}}{l_K+3/2},$$

where $l_K = K + 3(A-2)/2$ and $N = (E-K)/2$.

The probability of electric quadrupole transitions $B(E2)$ is expressed in terms of the matrix element of the O_0^2 operator [6], and it is similarly represented as

$$B(E2, J \to J-2) = \frac{15}{8\pi}\frac{\lambda_1^2}{K^2} \times \frac{(K-L+2)(K+L+1)L(L-1)}{(2L-1)}(2J-3) \times \begin{Bmatrix} S & L-2 & J-2 \\ 2 & J & L \end{Bmatrix}[D_1]^2 e^2 r_\psi^4. \quad (7)$$

Here,

$$[D_1] = \left[\sum_{N=0}^{N_{\max}} A(Nl_K, Nl_K)C_N C_N^1 + \sum_{N=0}^{N_{\max}-1} A(Nl_K, N+1\,l_K)(C_N C_{N+1}^1 + C_{N+1}C_N^1)\right], \quad (8)$$

where C and C^1 are the coefficients of the expansion of the functions $\psi(J)$ and $\psi(J-2)$, respectively, in basis (1) with $E = K + 2N$, where $N = 0, 1, 2, \ldots$. The expressions for the probabilities of other possible transitions are also easily obtained.

The above formulas are applicable for $U(3(A-1))$ states with symmetric $O(A-1)$ representations of the form $\omega_{123} = (K0\,0)$. Such states of the orthogonal scheme exist in nuclei with $A \le 16$ [1]. Formulas (4) and (7) take into account both isospin and spin dependences of Q and $B(E2)$ and generalize the known formulas of collective models [7].

REFERENCES

1. V. V. Vanagas, *Algebraic Methods in Nuclear Theory* (Mintis, Vilnius, 1971) [in Russian].
2. K. J. Yankauskas and A. K. Petrauskas, *Density Matrix of Excited U(3(A − 1)) States of Atomic Nuclei and Its Applications* (Klaipeda Univ., Klaipeda, 1997) [in Russian].
3. A. K. Petrauskas, L. Yu. Sabalyauskas, and V. M. Bondarenko, Lit. Fiz. Sb. **16**, 15 (1976).
4. J. D. Vergados, Nucl. Phys. A **111**, 681 (1968).
5. K. J. Yankauskas, Yad. Fiz. **65**, 984 (2002) [Phys. At. Nucl. **65**, 953 (2002)].
6. A. Bohr and B. R. Mottelson, *Nuclear Structure* (Benjamin, New York, 1969; Mir, Moscow, 1971), Vol. 1.
7. G. F. Filippov, V. I. Ovcharenko, and Yu. F. Smirnov, *Microscopic Theory of Collective Excitations of Atomic Nuclei* (Naukova Dumka, Kiev, 1981) [in Russian].

Translated by R. Tyapaev

Physics of Atomic Nuclei, Vol. 68, No. 7, 2005, pp. 1261–1262. Translated from Yadernaya Fizika, Vol. 68, No. 7, 2005, pp. 1311–1312.

FUTURE PUBLICATIONS

Special Features of the Boundary of Stability of Light Nuclei

K. A. Gridnev, D. K. Gridnev, V. G. Kartavenko, V. E. Mitroshin, V. N. Tarasov, D. V. Tarasov, and W. Greiner

The problem of stability of the $^{4-12}$He, $^{14-44}$O, and $^{38-80}$Ca isotopes with respect to the emission of one or two neutrons is studied in the Hartree–Fock approximation by using *Sly*4 and *Ska* effective Skyrme forces. A stability peninsula in the region of ^{40}O is discovered.

On Alignment in Jet Events

I. P. Lokhtin, A. K. Managadze, L. I. Sarycheva, and A. M. Snigirev

The hypothesis previously put forth in the literature that alignment of spots on films that is observed in emulsion experiments with cosmic rays is related to a predominant jet character of events at ultrahigh energies is verified. The Monte Carlo PYTHIA generator, which is known to have provided good results in describing jet events in hadron–hadron interactions, is used in the present analysis. Because of a strong correlation between the directions of the jet axes and particle momenta (collinearity) in them, the estimated degree of alignment is much higher than in a random sample of spots disposed chaotically on a film. For primary-interaction altitudes and collision energies satisfying some specific constraints, the degree of alignment appears to be strongly dependent on the hardness of the process and on the threshold for the total energy of selected clusters, increasing as they grow.

On the Possibility of Revealing Collective Pion Degrees of Freedom in a Nucleus by Means of Quasielastic Pion Knockout Induced by High-Energy Electrons

V. G. Neudatchin, L. L. Sviridova, N. P. Yudin, and S. N. Yudin

The kinematics of quasielastic knockout accompanying pion electroproduction and involving longitudinal virtual photons is considered, and a method for directly studying, in this way, the momentum distribution of pions in specific channels owing to the dominance of pole amplitudes is proposed. It is shown that, in view of the final-state interaction between the knock-on pion and the target nucleus, the existence of a pion condensate in nuclei can be efficiently revealed since the momentum distribution of collective pions is expected to have a pronounced maximum at a momentum of 0.3 GeV/c and since the excitation spectrum of the final recoil nucleus is concentrated in the low-energy region $E^* \approx K^2/(2AM_N) \leq 1$ MeV. The results for pion knockout from meson clouds of individual nucleons are of a totally different character. The analogous distributions are also given for rho mesons, this corresponding to the process $\rho^* + \gamma_T^* \to \pi$.

Searches for Light-Quark Exotic Baryons of Isotopic Spin 5/2

A. F. Nilov

The status of light-quark exotic baryons of isospin $I = 5/2$ is considered. A brief survey of theoretical studies devoted to this subject is given. Experimental searches for exotic baryons are traced from the first publication on the subject to the present day. Among possible candidates for an exotic baryon, the pentaquark baryon $E_{5/2\,5/2}$ of mass $M \approx 1.44$ GeV and width $\Gamma < 0.05$ GeV is the most probable. This state was recorded in six studies at five different facilities. Among these, there are two studies where the excess of the signal above the background is more than five standard deviations. Possibilities of further searches for exotic baryons in various reactions are discussed.

1063-7788/05/6807-1261$26.00

Electric Properties of Levels of ^{156}Dy Rotational Bands

A. A. Okhunov

A nonadiabatic character of $E0$ transitions from states of the 0_2^+ and 2_1^+ bands in ^{156}Dy is studied within a phenomenological model that takes into account the mixing of states of the $K^\pi = 0_1^+$, 0_2^+, 0_3^+, 2_1^+, and 1^+ bands. It is shown that a nonadiabatic character of these $E0$ transitions is due predominantly to the mixing of the 0_2^+ and 0_3^+ bands.

On Electrodisintegration of Nuclei

A. A. Pasichnyĭ and O. A. Prigodyuk

The kinematical dependences of cross sections for the electrodisintegration of nuclei that is induced by high-energy electrons is studied within the shell model of the nucleus. It is proposed to identify the quantum numbers of nuclear shells by a method that involves the subtraction of quasielastic peaks. The effect of Coulomb resonances and quasireal photons on the formation of angular and energy distributions of electrons and protons in $A(e, e'p)(A-1)$ reactions is explored. The phenomenon of quasielastic-peak shift and broadening is interpreted.

Charmed-Quark Component of the Photon Wave Function

V. V. Anisovich, L. G. Dakhno, V. N. Markov, V. A. Nikonov, and A. V. Sarantsev

We determine the $c\bar{c}$ component of the photon wave function on the basis of (i) data on the transitions $e^+e^- \to J/\psi(3096)$, $\psi(3686)$, $\psi(4040)$, $\psi(4415)$; (ii) the partial widths with respect to the two-photon decays $\eta_{c0}(2979)$, $\chi_{c0}(3415)$, $\chi_{c2}(3556) \to \gamma\gamma$; and (iii) the charmonium-states wave functions obtained by solving the Bethe–Salpeter equation for the $c\bar{c}$ system. Using the resulting $c\bar{c}$ component of the photon wave function, we calculate the $\gamma\gamma$-partial decay widths for a radial excitation of the $2S$ state, $\eta_{c0}(3594) \to \gamma\gamma$, and $2P$ states, $\chi_{c0}(3849)$, $\chi_{c2}(3950) \to \gamma\gamma$.

Random-Matrix Theory and Analysis of Nucleus–Nucleus Collisions at High Energies

E. I. Shahaliev, R. G. Nazmitdinov, A. A. Kuznetsov, M. K. Suleymanov, and O. V. Teryaev

We propose a novel method for analyzing experimental data obtained in relativistic nucleus–nucleus collisions. The method, based on the ideas of random-matrix theory, is applied to detecting systematic errors that occur in measuring momentum distributions of emitted particles. The unfolded momentum distribution is well described by a Gaussian orthogonal ensemble of random matrices if the uncertainty in the momentum distribution is maximal. The method is free from unwanted background contributions.